frontiers | Research Topics

Methods and applications in integrative physiology

Edited by
Ovidiu Constantin Baltatu, Chao Chen and Guido Caluori

Published in
Frontiers in Physiology

ISSN 1664-8714
ISBN 978-2-83251-049-0
DOI 10.3389/978-2-83251-049-0

About Frontiers

Frontiers is more than just an open access publisher of scholarly articles: it is a pioneering approach to the world of academia, radically improving the way scholarly research is managed. The grand vision of Frontiers is a world where all people have an equal opportunity to seek, share and generate knowledge. Frontiers provides immediate and permanent online open access to all its publications, but this alone is not enough to realize our grand goals.

Frontiers journal series

The Frontiers journal series is a multi-tier and interdisciplinary set of open-access, online journals, promising a paradigm shift from the current review, selection and dissemination processes in academic publishing. All Frontiers journals are driven by researchers for researchers; therefore, they constitute a service to the scholarly community. At the same time, the *Frontiers journal series* operates on a revolutionary invention, the tiered publishing system, initially addressing specific communities of scholars, and gradually climbing up to broader public understanding, thus serving the interests of the lay society, too.

Dedication to quality

Each Frontiers article is a landmark of the highest quality, thanks to genuinely collaborative interactions between authors and review editors, who include some of the world's best academicians. Research must be certified by peers before entering a stream of knowledge that may eventually reach the public - and shape society; therefore, Frontiers only applies the most rigorous and unbiased reviews. Frontiers revolutionizes research publishing by freely delivering the most outstanding research, evaluated with no bias from both the academic and social point of view. By applying the most advanced information technologies, Frontiers is catapulting scholarly publishing into a new generation.

What are Frontiers Research Topics?

Frontiers Research Topics are very popular trademarks of the *Frontiers journals series*: they are collections of at least ten articles, all centered on a particular subject. With their unique mix of varied contributions from Original Research to Review Articles, Frontiers Research Topics unify the most influential researchers, the latest key findings and historical advances in a hot research area.

Find out more on how to host your own Frontiers Research Topic or contribute to one as an author by contacting the Frontiers editorial office: frontiersin.org/about/contact

Methods and applications in integrative physiology

Topic editors

Ovidiu Constantin Baltatu — Anhembi Morumbi University, Brazil

Chao Chen — University of California, Davis, United States

Guido Caluori — INSERM Institut de Rythmologie et Modélisation Cardiaque (IHU-Liryc), France

Citation

Baltatu, O. C., Chen, C., Caluori, G., eds. (2022). *Methods and applications in integrative physiology*. Lausanne: Frontiers Media SA.

doi: 10.3389/978-2-83251-049-0

Table of contents

frontiers | Frontiers in Physiology

TYPE Editorial
PUBLISHED 30 November 2022
DOI 10.3389/fphys.2022.1096216

OPEN ACCESS

EDITED AND REVIEWED BY
Geoffrey A. Head,
Baker Heart and Diabetes Institute, Australia

*CORRESPONDENCE
Ovidiu Constantin Baltatu,
ocbaltatu@gmail.com,
ovidiu.baltatu@ulife.com.br
Chao-Yin Chen,
cych@ucdavis.edu
Guido Caluori,
guido.caluori@ihu-liryc.fr

SPECIALTY SECTION
This article was submitted to Integrative Physiology, a section of the journal Frontiers in Physiology

RECEIVED 11 November 2022
ACCEPTED 21 November 2022
PUBLISHED 30 November 2022

CITATION
Baltatu OC, Chen C-Y and Caluori G (2022), Editorial: Methods and applications in integrative physiology. *Front. Physiol.* 13:1096216. doi: 10.3389/fphys.2022.1096216

Editorial: Methods and applications in integrative physiology

Ovidiu Constantin Baltatu[1,2]*, Chao-Yin Chen[3]* and Guido Caluori[4,5]*

[1]Center of Innovation, Technology and Education (CITE) at Anhembi Morumbi University—Anima Institute, Sao Jose dos Campos, Brazil, [2]College of Medicine and Health Sciences, Khalifa University, Abu Dhabi, United Arab Emirates, [3]Department of Pharmacology, University of California, Davis, Davis, CA, United States, [4]IHU LIRYC, Electrophysiology and Heart Modeling Institute, Fondation Bordeaux Université, Pessac, France, [5]University of Bordeaux, INSERM U1045, Cardiothoracic Research Center of Bordeaux, Pessac, France

KEYWORDS

data collection, data analysis, technology, computational biology, computer simulation

Editorial on the Research Topic
Methods and applications in integrative physiology

Physiology is the science of function in living organisms that serves as the foundation of knowledge for clinical and experimental medicine. Physiology is an emerging property of tissues and organs. This definition gives us a direct feeling of its complexity and of the multifaceted approaches to investigating it.

Integrative physiology is concerned with the larger elements of physiology that entail the integration of processes and regulatory functions at all biological levels, from the molecular, cellular, tissue, and organ levels to clinical research. Integrative physiology utilizes knowledge from multidisciplinary research that blends life sciences and mathematical sciences. Therefore, its methodology—as in the procedures or strategies used to find, select, process, and evaluate evidence addressing a specific question—is often multi- and cross-disciplinary. Since knowledge in integrative physiology, clinical and experimental medicine is constantly expanding, so too are the methodologies and strategies to approach its questions. New or adapted technologies are the key to enable and expand these needed advancements.

This Research Topic is part of the Methods and Applications in Physiology series. This series showcases the recent advances in experimental techniques and methods used to understand the most fundamental questions in physiological research, ranging from molecular to organ function in living organisms. This Research Topic focuses on cutting-edge emerging technologies and techniques for new sensors, data gathering, processing, analysis, and modeling for various academic, clinical, and healthcare applications ranging from bench to bedside.

We, as Guest Editors, are pleased to present 13 papers and are grateful for the 74 contributions from 46 institutions in 11 countries. This Research Topic of articles includes the use of new methodologies for evaluating physiological (Hillman et al.; Liu

et al., 2022; Luck et al.; Švecová et al.) and pathological (Lu et al.; Odehnalová et al.) processes, how computational approaches can provide new insights into how molecular events leading to physiological behavior and guide the future wet bench research (Gerach et al.; Gionti et al.; Gurel et al.; Yoneda et al.), the benefits and disadvantages of methods in integrative physiological research (Horváth et al.; Stracina et al.) and the species difference in autonomic regulation (Bazmi and Escobar). We would like to introduce, for interested readers, the synopsis of each accepted contribution:

Cardiac imaging

Gross pathology examination is the gold standard for morphological evaluation of focal myocardial disease. The 9.4 T magnetic resonance imaging (MRI) is a new approach for visualizing myocardial pathology. Using an experimental radiofrequency (RF) ablation lesion in swine heart tissue, Odehnalová et al. demonstrated that lesions can be measured on high-resolution MRI images with the same accuracy as on pathological sections and compared these two methods for the evaluation of experimental radiofrequency (RF) ablation lesion in swine heart tissue.

Laser doppler flowmetry

Laser Doppler flowmetry (LDF) probes, which provide continuous, non-invasive assessment of skin blood flow, are routinely used to quantify cutaneous microcirculatory perfusion. When an LDF probe is removed and replaced, as is the case during pre- and post-intervention or between-day assessments, inhomogeneities in the skin's microvasculature density contribute to a deterioration in reproducibility. Luck et al. demonstrated that increasing the number of individual LDF probes in a custom-made holder improves LDF measurement reproducibility during test retests. These findings imply that cutaneous vascular conductance (CVC) measurements acquired with numerous laser Doppler probes (number ≥4) have a sufficiently high degree of repeatability after the probes are replaced within the same individual. As a result, we propose that the results from numerous laser Doppler probes in a holder be used in the intraindividual analysis for investigations in which the LDF probes must be removed and replaced in the same participants.

New method to estimate both the surface and t-tubular capacitance/area in cardiomyocytes

Švecová et al. have devised a new method for determining the fraction of t-tubular membrane by perfusing the tested cell with an isotonic solution with low conductivity. It can repeat measurements on the same cardiomyocyte, allowing for paired statistical testing, which is an advantage over previous approaches. The procedure is straightforward and noninvasive for the measured cell, and it can be applied to investigate short-term alterations in the t-tubular system.

A simulation model for investigating stretch activation in heart pumping

Yoneda et al. created a Monte Carlo (MC) cross-bridge model with a trapping mechanism to shed light on the role of stretch activation in heart pumping. In this Monte Carlo cross-bridge model, they included a mechanism for trapping the myosin molecule in its post-power stroke state. Yoneda et al. calculated the rate constants of transitions for trapping and escape in a thermodynamically consistent manner. They derive the following findings about the stretch activation process based on our numerical analysis: Because the population of trapped myosin molecules and their average force increase after stretching, the delayed force becomes larger than the original isometric force; ii) the delayed force has a duration of more than a few seconds due to a relatively small rate constant of escape from the trapped state.

Goldfish autonomic nervous system experimental model

Bazmi and Escobar examined ventricular action potentials, electrocardiograms, and Ca^{2+} transients from perfused Goldfish intact hearts with either a sympathetic or parasympathetic agonist to determine how stimulation of either autonomic nervous system branch impacted cardiac contractility and excitability. Their findings show that stimulating the Goldfish autonomic nervous system with these regularly used agonists resulted in a commensurate alteration in heart dromotropism, chronotropism, inotropism, and lusitropism, like what has been reported in humans. Although the Goldfish heart only has two chambers, the authors conclude that its similar electrical and autonomic features make it a valuable model for studying larger mammalian pathophysiology.

In-silico model for left ventricular dyssynchrony and impaired torsion

Gerach et al. investigated the specific hypothesis that dyssynchrony alone affects the kinetics of the left ventricle in patients with heart failure with reduced ejection fraction (HFrEF) and left bundle branch block (LBBB) in such a way that rotational behavior is qualitatively altered. If this was the case, they would

have been able to replicate the mechanical behavior found in the NOGA XP cardiac mapping system *in vivo*. The fact that this theory was falsified indicates that it is not the electromechanical activation sequence alone that controls rotational behavior, implying that other mechanisms are involved. The implications include that more research is needed to fully understand the drivers of rotating behavior and that these additional (and now unknown) mechanisms are likely equally crucial to address therapeutically.

Calcium transient high-throughput assay for the detection of acute cardiac hazard in early drug discovery

Lu et al. developed an acute cardiac hazard score system applied to the Ca^{2+} transient assay using different human-induced pluripotent stem cell-derived cardiomyocytes (hiPSC-CM) cell lines to easily identify the concentration-dependent level of cardiac risk by concentration for new chemical entities based on Ca^{2+} transient measurement in hiPSC-CMs using multiple functional parameters including beat rate, calcium transient duration at 90% of repolarization (CTD90), and amplitude. The human-induced pluripotent stem cell-derived cardiomyocytes assay system's calcium transient high-throughput assay is simple to use and inexpensive.

Using the action potential clamp technique to investigate cardiac ion channel coordination

Horváth et al. traced the evolution of the voltage clamp technique from its traditional application of the rectangular command to the onion-peeling method. These new methods expand the possibilities for investigating the function of individual ion channels as well as the coordination of membrane currents during AP. The onion-peeling technique is particularly well suited for studying the interaction of currents and thus has a distinct potential in integrative physiology. It was designed for cardiac myocytes but can be applied to skeletal and smooth muscle cells, neurons, and any excitable cell type where ionic currents and AP control cell function.

New parameters for stratifying arrhythmic risk

Gionti et al. used numerical simulations based on left ventricular models derived from post-myocardial infarction patients to identify some features of proarrhythmic geometric configurations of scars and border zones. A geometric pattern of scar and border zones, characterized by thin subendo- and subepicardial border zones and transmural border zone isthmuses, was identified at cardiac magnetic resonance as a major risk for sustained ventricular tachycardia inducibility at electrophysiology study. This data is simple to apply in daily life and could be combined with known non-invasive risk factors to identify patients with ischemic cardiomyopathy and moderate systolic dysfunction who should undergo an electrophysiology study.

A review and future outlook on ECG applications in clinical and experimental settings

Stracina et al. reviewed progress and presented perspectives on ECG recording and analysis. Through a multidisciplinary approach, the authors summarize the potential of advanced data analysis. Special emphasis is placed on innovative deep-learning techniques that have been intensively expanded in a wide range of clinical applications and offer promising prospects in experimental branches.

Cardiac neural network dynamics—opportunities and challenges

The fundamental investigations into the cardiac neural control hierarchy were reviewed by Gurel et al. They discuss the use of computational methods to investigate how information is processed while closed-loop control is in operation and to guide better experimental design. The large cardio-neural datasets produced by these experimental designs necessitate sophisticated signal processing and time series analysis techniques, as well as the usual large-scale computational challenges related to data sharing and reproducibility. These difficulties offer excellent chances for developing and approving cutting-edge methods to improve the understanding of the mechanisms underlying cardiac pathologies needed for clinical application.

An open-source hypoxia/hyperoxia exposure chamber

Hillman et al. created a simple hypoxia chamber using off-the-shelf components and controlled by open-source software to collect continuous data on oxygen levels and other environmental factors (temperature, humidity, pressure, light, sound, etc.). They created a low-cost and customizable system using FLOS (Free-Libre and Open-Source) software and hardware that can be used for a variety of experimental protocols. This hypoxia/hyperoxia exposure chamber enables

reproducible and transparent data acquisition as well as increased consistency with a high degree of customization for each experimenter's needs.

Human hypertension blood flow model

Bahloul et al. proposed a fractional model with high flexibility for characterizing the arterial complex tree network. Through a series of validations on human hypertensive patients, the results demonstrate the validity of the new model and the physiological interpretability of the fractional differentiation order. Furthermore, the findings show that the fractional-order modeling approach has a high potential for improving understanding of the structural and functional changes in the large and small arteries caused by hypertension disease.

We gratefully acknowledge the work of the 74 authors of the Frontiers Research Topic (RT) entitled *Methods and Applications in Integrative Physiology*, and eagerly anticipate future discoveries, research, and developments in integrative physiology.

Author contributions

OB, C-YC, and GC wrote this Editorial. All authors contributed to the article and approved the submitted version.

Conflict of interest

The authors declare that the research was conducted in the absence of any commercial or financial relationships that could be construed as a potential conflict of interest.

Publisher's note

Reference

Liu, Y., Zhu, Y., Zhang, Z., Bao, D., Deng, H., Liu, L., et al. (2022). N-Acetyl-L-Cysteine protects organ function after hemorrhagic shock combined with seawater immersion in rats by correcting coagulopathy and acidosis. *Front. Physiol.* 13, 831514. doi:10.3389/fphys.2022.831514

frontiers in Physiology

ORIGINAL RESEARCH
published: 09 February 2022
doi: 10.3389/fphys.2022.793305

Autonomic Regulation of the Goldfish Intact Heart

Maedeh Bazmi[1] *and Ariel L. Escobar*[2]*

[1]*Quantitative Systems Biology Program, School of Natural Sciences, University of California, Merced, Merced, CA, United States,*
[2]*Department of Bioengineering, School of Engineering, University of California, Merced, Merced, CA, United States*

Autonomic regulation plays a central role in cardiac contractility and excitability in numerous vertebrate species. However, the role of autonomic regulation is less understood in fish physiology. Here, we used Goldfish as a model to explore the role of autonomic regulation. A transmural electrocardiogram recording showed perfusion of the Goldfish heart with isoproterenol increased the spontaneous heart rate, while perfusion with carbamylcholine decreased the spontaneous heart rate. Cardiac action potentials obtained *via* sharp microelectrodes exhibited the same modifications of the spontaneous heart rate in response to isoproterenol and carbamylcholine. Interestingly, the duration of the cardiac action potentials lengthened in the presence of both isoproterenol and carbamylcholine. To evaluate cardiac contractility, the Goldfish heart was perfused with the Ca^{2+} indicator Rhod-2 and ventricular epicardial Ca^{2+} transients were measured using Pulsed Local Field Fluorescence Microscopy. Following isoproterenol perfusion, the amplitude of the Ca^{2+} transient significantly increased, the half duration of the Ca^{2+} transient shortened, and there was an observable increase in the velocity of the rise time and fall time of the Ca^{2+} transient, all of which are compatible with the shortening of the action potential induced by isoproterenol perfusion. On the other hand, carbamylcholine perfusion significantly reduced the amplitude of the Ca^{2+} transient and increased the half duration of the Ca^{2+} transient. These results are interesting because the effect of carbamylcholine is opposite to what happens in classically used models, such as mouse hearts, and the autonomic regulation of the Goldfish heart is strikingly similar to what has been observed in larger mammalian models resembling humans.

Keywords: electrocardiogram, local field fluorescence microscopy, intracellular microelectrodes, sympathetic regulation, parasympathetic regulation

OPEN ACCESS

Edited by:
Ovidiu Constantin Baltatu, Anhembi Morumbi University, Brazil

Reviewed by:
Kenneth Scott Campbell, University of Kentucky, United States
Norbert Szentandrássy, University of Debrecen, Hungary

***Correspondence:**
Ariel L. Escobar
aescobar4@ucmerced.edu

Specialty section:
This article was submitted to Integrative Physiology, a section of the journal Frontiers in Physiology

Received: *11 October 2021*
Accepted: *19 January 2022*
Published: *09 February 2022*

Citation:
Bazmi M and Escobar AL (2022) Autonomic Regulation of the Goldfish Intact Heart. Front. Physiol. 13:793305. doi: 10.3389/fphys.2022.793305

INTRODUCTION

In nearly all vertebrate species, direct input from the autonomic nervous system tightly controls cardiac contractility and excitability (Lee and Shideman, 1959; Katz, 1967; Lindemann and Watanabe, 1985; Cohn, 1989; Henning, 1992). Although there is an abundant amount of research on the autonomic control of cardiac contractility and excitability in numerous mammalian species, the characterization of pathophysiological mechanisms is still difficult to obtain for humans specifically. This is in part due to humans having strikingly dissimilar action potential (AP) characteristics and electrocardiographic morphology in comparison with commonly used animal

models such as mice, rats, and rabbits (Nakamura et al., 2002; Tsai et al., 2011; Bazmi and Escobar, 2020). Fish, on the other hand, are the largest and most diverse group of vertebrates, and as such, their autonomic nervous system regulation can often deviate from the classical vertebrate models used to study autonomic control of cardiac contractility and excitability. The most drastic difference in autonomic system regulation can be observed when comparing the hagfish, which have no known autonomic nervous system control, to the teleost, which exhibit fully functional autonomic regulation in cardiac function (Sandblom and Axelsson, 2011). Nevertheless, if a fish species does exhibit autonomic regulation, it is likely to be similar to what has been established for many mammalian species.

In vertebrate species exhibiting full autonomic control, the autonomic nervous system functions through two closely intertwined antagonistic branches: the sympathetic branch and the parasympathetic branch. The sympathetic branch of the nervous system, referred to as the sympathetic nervous system, modulates cardiac function through the release of transmitters referred to as catecholamines (Lee and Shideman, 1959; Evans, 1986; Marks, 2013). These catecholamines bind to and stimulate β-adrenergic receptors, which in turn, increase the speed of conduction through the atrioventricular node (positive dromotropic effect), increase heart rate (positive chronotropic effect), increase contractility (positive inotropic effect), and increase the velocity of myocardial relaxation during diastole (positive lusitropic effect). Locally released catecholamines, such as norepinephrine (NE), stimulate the β-adrenergic receptors by activating adenylyl cyclase (AC; Hildebrandt et al., 1983; Brum et al., 1984) and increasing cyclic adenosine monophosphate (cAMP) levels (Osterrieder et al., 1982). Increased cAMP levels activate protein kinase A (PKA; Krebs, 1972; Hayes and Mayer, 1981) and induce the dissociation of the catalytic subunit. Levels of cAMP and thus PKA are finely regulated by cyclic nucleotide phosphodiesterases (PDEs) which degrade cAMP into 5′-AMP. Nevertheless, the catalytic subunit of PKA phosphorylates several key Ca^{2+} handling proteins such as the L-type Ca^{2+} Channel (LTCC; Collins et al., 1981; Osterrieder et al., 1982), the ryanodine receptor 2 (Suko et al., 1993; Valdivia et al., 1995), and phospholamban (PLN; Weilenmann et al., 1987). These modifications not only alter the electrical activity of the myocardium, which have positive dromotropic and chronotropic effects, but also Ca^{2+} handling dynamics in the myocardium which lead to positive inotropic and lusitropic effects (Aguilar-Sanchez et al., 2019).

The sympathetic branch of the nervous system is highly antagonized by the parasympathetic branch. Referred to as the parasympathetic nervous system, this branch modulates cardiac contractility and excitability through the local release of the transmitter acetylcholine (ACh) from postganglionic cholinergic intracardiac neurons. The ACh subsequently binds to and stimulates muscarinic (M2) receptors. Activation of M2 receptors stimulates a G_i protein, which inhibits AC (Krebs, 1972). This inhibition leads to significantly lower levels of cAMP, a reduced fraction of activated PKA, and a decreased degree of phosphorylation in the key Ca^{2+} handling proteins. These modifications result in negative inotropic, chronotropic, dromotropic, and lusitropic effects, all of which are crucial in countering the sympathetic nervous system and maintaining homeostasis in the vertebrate central nervous system (Watanabe and Lindemann, 1984; Aguilar-Sanchez et al., 2019).

Although fish hearts contain a single atrium and ventricle and present a fundamentally different cardiovascular system when compared to other mammalian models, there are many developmental, structural, and functional commonalities between the two vertebrate species (Sandblom and Axelsson, 2011; Mersereau et al., 2015; Xing et al., 2017; Bazmi and Escobar, 2020). The Goldfish specifically, has remarkably similar electrical properties to humans. For example, the heart rate, AP morphology, and Ca^{2+} transient kinetics and dynamics of adult Goldfish closely parallel those of humans, even more so than mice and Zebrafish models (Bazmi and Escobar, 2020).

Previous literature suggests few fish models exhibit autonomic control in a similar manner to larger mammals; however, it is not clear how autonomically driven AP kinetics impact cardiac contractility in the fish intact heart specifically. To explore how stimulation of either autonomic nervous system branch would alter cardiac contractility and excitability, we performed experiments in which we perfused the Goldfish intact heart with either a sympathetic or parasympathetic agonist. Ventricular APs, electrocardiograms, and Ca^{2+} transients recorded from the Goldfish intact heart showed perfusion with either 100 nm isoproterenol (sympathetic agonist) or 5 µm carbamylcholine (parasympathetic agonist), was enough to stimulate the sympathetic branch or parasympathetic branch, respectively. Interestingly, our results indicate stimulation of the Goldfish autonomic nervous system by these commonly used agonists resulted in a corresponding change in cardiac dromotropism, chronotropism, inotropism, and lusitropism in a similar manner observed in humans.

MATERIALS AND METHODS

Ethical Approval

Our animal facilities are Association for Assessment and Accreditation of Laboratory Animal Care accredited and Office of Laboratory Animal Welfare certified and fully comply with all regulations, policies, and standards that protect animal welfare. Animal use in our studies were in accordance with the National Institutes of Health Guide for the Care and Use of Laboratory Animals (NIH Publication No. 85–23, Revised 1996) and the Institutional Animal Care and Use Committee guidelines of the University of California Merced (Protocol # 2008–201). The animals were bought from Toledo Goldfish, United States.

Adult Goldfish were anesthetized by immersion in ice-cold water containing 0.16 mg ml^{-1} tricaine methanesulfonate for 2–5 min. To assure the Goldfish were completely anesthetized prior to decapitation, the tail was held with a small, curved tweezer, and gently moved. Once the Goldfish were completely anesthetized, they were decapitated, and the intact heart was removed from the chest cavity.

Heart Cannulation and Perfusion

Goldfish hearts were dissected, and the bulbous arteriosus was cannulated onto a gauge 27 needle and perfused in a Langendorff system at a rate of 60 µl/min driven by gravity. Multiple solutions

were perfused through the bulbus arteriosus with the aid of a self-designed μ-manifold. Goldfish hearts were perfused with a fish ringer solution containing: NaCl 137 mm, KCl 5.4 mm, $CaCl_2$ 1.8 mm, $MgCl_2$ 0.5 mm, HEPES 10 mm, and glucose 5.5 mm. The Ca^{2+} dye Rhod-2 AM was perfused into the heart with a Harvard pump for 30–45 min. The temperature of the bath containing the heart was set to 28°C. The temperature was controlled with the aid of a Peltier unit positioned at the bottom of the recording chamber and measured with a linearized semiconductor temperature sensor.

Pharmacological Agents

The Goldfish heart was perfused with fish ringer solution containing 4 mm blebbistatin, prior to obtaining any electrophysiological recordings to suppress cardiac motion. In order to elicit a sympathetic response, the Goldfish heart was perfused with fish ringer solution containing 100 nm isoproterenol for 10 min before the start of any AP and Ca^{2+} transient recordings. To determine if the sympathetic response to isoproterenol could be reversed, the Goldfish heart was perfused with fish ringer solution for a prolonged amount of time. Indeed, the effects of isoproterenol could be completely reversed if the Goldfish heart were continuously perfused with fish ringer solution for 20 min. In contrast, to elicit a parasympathetic response the Goldfish heart was perfused with fish ringer solution containing 5 μm carbamylcholine for 10 min prior to the start of any AP and Ca^{2+} transient recording. The effects of carbamylcholine could be completely reversed after continuously perfusing the heart with fish ringer solution for 60 min. Recordings obtained prior to perfusion with isoproterenol or carbamylcholine were considered as control, and recordings obtained following isoproterenol or carbamylcholine perfusion were considered as experimental.

Experimental Setup

Optical Measurements

Ca^{2+} transients were recorded ($N = 8$ hearts) using Pulsed Local Field Fluorescence Microscopy (PLFFM; Mejía-Alvarez et al., 2003; Escobar et al., 2004, 2006; Valverde et al., 2006, 2010; Kornyeyev et al., 2010; Mattiazzi et al., 2015; Aguilar-Sanchez et al., 2017). The PLFFM technique assessed physiological parameters by exciting exogenous probes present in the tissue and detecting the light emitted by these fluorescent indicators. The excitation (532 nm Yag laser) and emitted light propagated through a multimode fiber optic (200 mm diameter, 0.67 NA) placed on the surface of the intact heart. The emitted light then traveled back through the multimode fiber, dichroic mirrors, and filters (610 nm) and was focused on an avalanche photodiode (Perkin Elmer, United States) with the aid of a microscope objective. The signal was digitized by an A/D converter (NI, United States) and acquired by a PC. The fluorescent indicator utilized to obtain Ca^{2+} transients in this study was Rhod-2 AM. Often referred to as a "Ca^{2+} indicator dye," Rhod-2 AM (50 μg) was prepared with 20 μl of 20% pluronic in 1 ml fish ringer solution.

Electrophysiological Measurements

Epicardial electrical recordings of the APs ($N = 4$ hearts) were obtained using sharp glass microelectrodes filled with 3 M KCl connected to a high input impedance differential amplifier (WPI, United States). Glass microelectrodes were fabricated with a micropipette puller (Sutter Instrument Co., United States) and had a resistance of 10–20 MΩ (Ferreiro et al., 2012; López Alarcón et al., 2019). Data were recorded with an acquisition system from National Instruments in conjunction with additional software built in our lab. All fluorescence and membrane potential recordings were obtained from the Goldfish ventricular epicardium. Goldfish hearts were continuously paced at 1 Hz with the aid of two acupuncture needles placed in the apex of the ventricle in the presence and absence of the pharmacological agents. However, the hearts were not paced in experiments assessing changes in the spontaneous heart rate.

Whole Heart Electrocardiographic Measurements

Transmural electrocardiographic recordings ($N = 6$ hearts) were performed by placing one Ag–AgCl micropellet inside the left ventricle and a second pellet outside the left ventricle (Kornyeyev et al., 2010; López Alarcón et al., 2019). Signals were amplified by a custom-made DC-coupled instrumentation amplifier and were digitally sampled identically to the AP recordings.

Statistical Analysis

In whole heart experiments, there are two main causes of variance. First, no two animals have entirely identical hearts, regardless of the species. Second, although we are measuring Ca^{2+} transients and APs in the same region (the mid-region of the left ventricle) of the heart, it is impossible to perform the recordings in the same precise location between different hearts. Thus, the data are presented as the measured times with their standard error (SEM). To assess electrical changes, AP traces were first normalized then evaluated at their respective repolarization times. Specifically, the time it takes for the AP to reach 30, 50%, or 90% repolarization, referred to here as APD30, APD50, or APD90, respectively.

Each wave of the electrocardiogram (QRS complex, T wave, and J wave) was measured using its corresponding half duration. The recorded Ca^{2+} transients were normalized between zero (minimum fluorescence) and one (maximum fluorescence) in order to evaluate the kinetics of the recorded Ca^{2+} transients. The kinetic parameters of the Ca^{2+} transients evaluated were the rise time (time for the Ca^{2+} transient to rise from, 10 to 90% of its maximum amplitude), half duration (duration of the Ca^{2+} transient at 50% of the maximum amplitude), and fall time (time for the Ca^{2+} transient to fall from 90 to 10% of the maximum amplitude). The AP parameters and Ca^{2+} transient kinetics obtained for the control and the experimental groups were evaluated and normalized to their respective control values for each heart used. After this normalization, data were compiled, and statistical analysis was performed.

The data are presented as multiple measurements (n; dot cloud) recorded for different measurements (n) on different hearts (N) with the mean ± SEM (solid lines). To determine

if the agonists produced a significant effect, the distribution of the data before and after administration was compared using a two-sample Kolmogorov–Smirnov test (OriginPro, 2019). The difference was significant if the value of $p < 0.01$.

RESULTS

Sympathetic Regulation of Action Potentials and Heart Rate

In order to elicit a sympathetic response and assess the β-adrenergic regulation of the Goldfish heart, we first perfused the heart with 100 nm isoproterenol. Goldfish ventricular chronotropic properties were examined *via* AP recordings and spontaneous heart rate recordings (**Figure 1**). Perfusion of the Goldfish intact heart with 100 nm isoproterenol altered the AP morphology (**Figure 1A**) and had a positive chronotropic effect, significantly increasing the heart rate by 46% (**Figures 1B,C**; from 0.87 ± 0.01 Hz to 1.27 ± 0.02 Hz). Interestingly, all kinetic parameters of the AP significantly changed following isoproterenol perfusion; APD30 increased from 228.10 ± 14.40 ms to 237.90 ± 11.80 ms (**Figure 2A**), APD50 decreased from 353.90 ± 30.40 ms to 300.30 ± 20.00 ms (**Figure 2B**), and APD90 increased from 455.40 ± 20.10 ms to 468.70 ± 27.00 ms (**Figure 2C**).

Sympathetic Prevalence in Electrocardiographic Signals

The effects of catecholamines on whole heart electrical activity were assessed through transmural electrocardiogram recordings (**Figure 3**). The 3 main components of the Goldfish electrocardiogram are presented in **Figure 3A** and consist of the QRS complex (ventricular depolarization), J wave (likely due to a voltage gradient due to the presence of a prominent AP notch in the epicardium but not the endocardium), ending with T wave (ventricular repolarization). Application of isoproterenol altered the morphology of the Goldfish electrocardiogram (**Figure 3A**) and increased the heart rate (**Figures 3B,C**; from 1.10 ± 0.40 Hz to 3.10 ± 0.70 Hz). Furthermore, application of isoproterenol also significantly altered the duration of the QRS wave, T wave, and J wave (**Figure 4**). The QRS complex significantly decreased from 22.70 ± 1.30 ms to 17.30 ± 2.80 ms (**Figure 4A**), the T wave significantly increased from 164.70 ± 53.20 ms to 292.10 ± 58.10 ms (**Figure 4B**), the J wave significantly increased from 126.10 ± 42.30 ms to 333.10 ± 105.30 ms (**Figure 4C**).

Sympathetic Regulation of Cardiac Contractility

In many vertebrate species, stimulation of either autonomic nervous system branch will not only alter cardiac excitability, but also cardiac contractility. In order to assess if eliciting a sympathetic response altered the inotropic and/or the lusitropic properties of the Goldfish ventricle, experiments were performed in which the amplitude and kinetics of the Ca^{2+} transient were examined in the presence and absence of 100 nm isoproterenol (**Figure 5**). Stimulation of β-adrenergic receptors altered the morphology of the Ca^{2+} transient (**Figure 5A**) and significantly increased the normalized amplitude of the Ca^{2+} transient (**Figure 5B**; from 1.00 ± 0.07 to 1.10 ± 0.04). To detect if isoproterenol significantly altered the kinetics of the Ca^{2+} transient, the three following parameters of the Ca^{2+} transient were assessed (**Figure 6**): rise time (RT), fall time (FT), and half duration (HD). A significant change in any aforementioned kinetical parameter is a reflection of a significant corresponding change in myocardial Ca^{2+} handling dynamics. Perfusion of isoproterenol significantly increased the velocity of every Ca^{2+} transient kinetic parameter in the Goldfish heart (**Figures 6A–C**; RT: from 27.98 ± 4.60 ms to 22.47 ± 3.50 ms, FT: from 150.08 ± 22.80 ms to 135.88 ± 20.30 ms, and HD: from 148.60 ± 8.10 ms to 134.87 ± 5.20 ms), implying

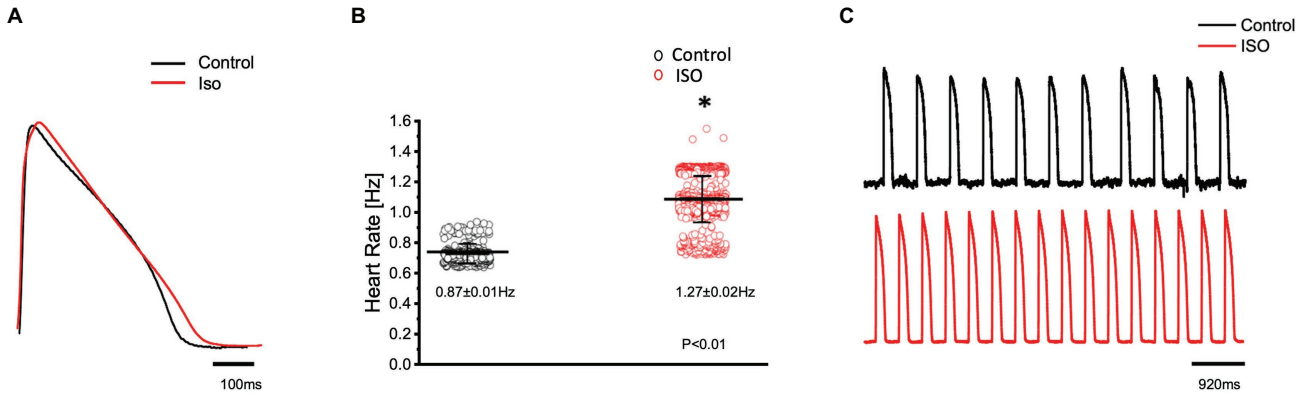

FIGURE 1 | Goldfish ventricular action potential and spontaneous heart rate recordings before (black) and after perfusion with 100 nm isoproterenol (red). Perfusion of the Goldfish intact heart with 100 nm isoproterenol altered the action potential morphology **(A)** and had a positive chronotropic effect, significantly increasing the heart rate (**B**; from 0.87 ± 0.01 Hz to 1.27 ± 0.02 Hz, $p < 0.01$, $n = 160$ for the control, $n = 263$ for ISO, $N = 4$). The positive chronotropic effect following isoproterenol perfusion is also reflected in spontaneous AP recordings from the left ventricle **(C)**. *Denotes a significant difference between the two distributions. The data are presented as multiple measurements (n; dot cloud) recorded for different measurements (*n*) on different hearts (*N*) with the mean ± SEM (solid lines).

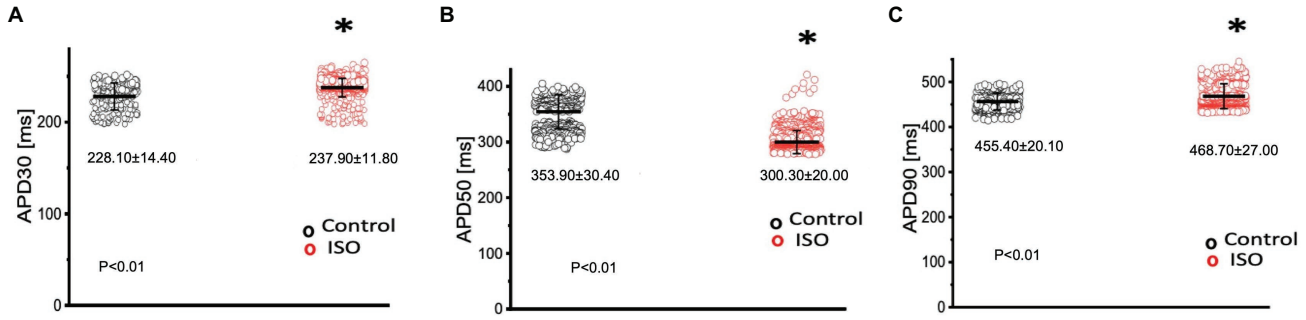

FIGURE 2 | Kinetic parameters of the Goldfish ventricular action potential before (black) and after (red) perfusion with 100 nm isoproterenol. Following isoproterenol perfusion, APD30s significantly increased from 228.10 ± 14.40 ms to 237.90 ± 11.80 ms ($p < 0.01$, $n = 113$ for the control, $n = 113$ for ISO, $N = 4$; **A**), APD50 decreased from 353.90 ± 30.40 ms to 300.30 ± 20.00 ms ($p < 0.01$, $n = 143$ for the control, $n = 316$ for ISO, $N = 4$; **B**), and APD90 significantly increased from 455.40 ± 20.10 ms to 468.70 ± 27.00 ms ($p < 0.01$, $n = 95$ for the control, $n = 256$ for ISO, $N = 4$; **C**). *Denotes a significant difference between the two distributions. The data are presented as multiple measurements (n; dot cloud) recorded for different measurements (*n*) on different hearts (*N*) with the mean ± SEM (solid lines).

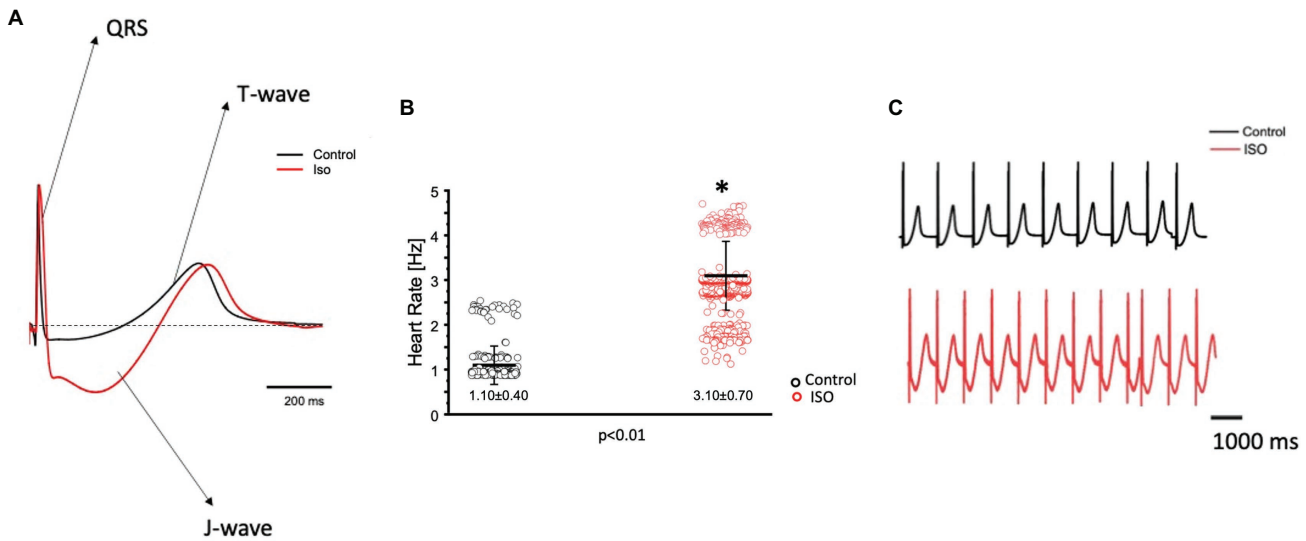

FIGURE 3 | Goldfish ventricular electrocardiogram recordings before (black) and after (red) perfusion with 100 nm isoproterenol. The three main components of the Goldfish electrocardiogram are presented: QRS complex, J wave, and T wave. Application of isoproterenol altered the morphology of the Goldfish electrocardiogram **(A)** and increased the spontaneous heart rate from 1.10 ± 0.40 Hz to 3.10 ± 0.70 Hz ($p < 0.01$, $n = 180$ for the control, $n = 412$ for ISO, $N = 6$; **B**). Electrocardiogram recordings before and after isoproterenol perfusion reflect an increased heart rate in response to isoproterenol **(C)**. *Denotes a significant difference between the two distributions. The data are presented as multiple measurements (n; dot cloud) recorded for different measurements (*n*) on different hearts (*N*) with the mean ± SEM (solid lines).

perfusion with isoproterenol increased the rate of relaxation of the Goldfish myocardium during diastole, resulting in a positive lusitropic effect (**Figure 6B**). The presence of a β-adrenergic drive suggests the presence of a parasympathetic one, as they are the two antagonistic branches of the autonomic nervous system.

Parasympathetic Regulation of Action Potentials and Heart Rate

The parasympathetic nervous system, on the other hand, is thought to be the dominant branch of the autonomic nervous system. To elicit a parasympathetic response and induce a cholinergic response, 5 µm carbamylcholine was administered to the Goldfish intact heart. As before, the chronotropic properties of the heart were assessed *via* AP and spontaneous heart rate recordings. Not surprisingly, the administration of carbamylcholine altered the AP morphology (**Figure 7A**) and had a negative chronotropic effect, reducing the heart rate by 92.2% (**Figures 7B,C**; from 0.98 ± 0.05 Hz to 0.13 ± 0.08 Hz). Not surprisingly, carbamylcholine administration significantly prolonged all three kinetic parameters of the AP (**Figures 8A–C**; APD30 increased from 235.90 ± 12.10 ms to 295.30 ± 11.50 ms, APD50 increased from 388.10 ± 23.90 ms to 651.40 ± 49.50 ms, and APD90 increased from 446.70 ± 14.60 ms to 833.60 ± 30.00 ms, respectively).

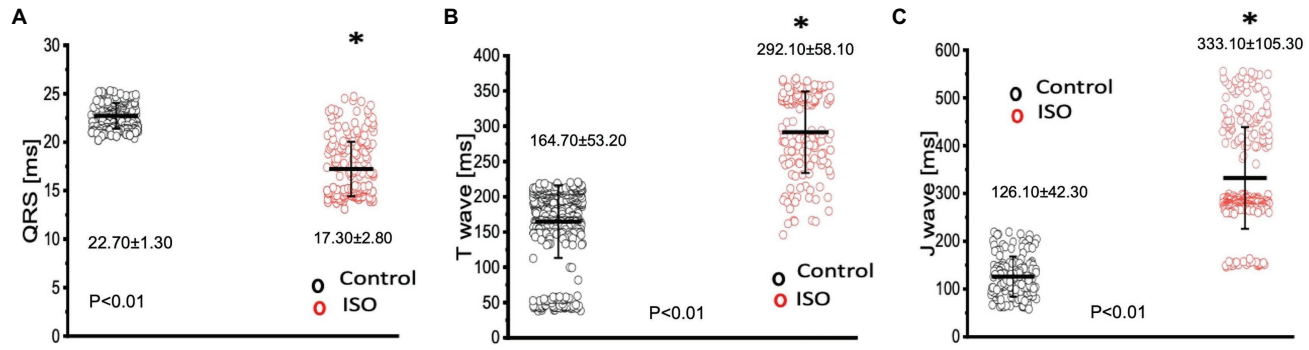

FIGURE 4 | Perfusion with 100 nm isoproterenol significantly altered the time course of all three components in the Goldfish electrocardiogram. The duration of the QRS complex significantly decreased from 22.70 ± 1.30 ms to 17.30 ± 2.80 ms ($p < 0.01$, $n = 80$ for the control, $n = 121$ for ISO, $N = 6$; **A**), T wave significantly increased from 164.70 ± 53.20 ms to 292.10 ± 58.10 ms ($p < 0.01$, $n = 110$ for the control, $n = 120$ for ISO, $N = 6$; **B**), and the J wave significantly increased from 126.10 ± 42.30 ms to 333.10 ± 105.30 ms ($p < 0.01$, $n = 74$ for the control, $n = 118$ for ISO, $N = 6$; **C**). *Denotes a significant difference between the two distributions. The data are presented as multiple measurements (n; dot cloud) recorded for different measurements (*n*) on different hearts (*N*) with the mean ± SEM (solid lines).

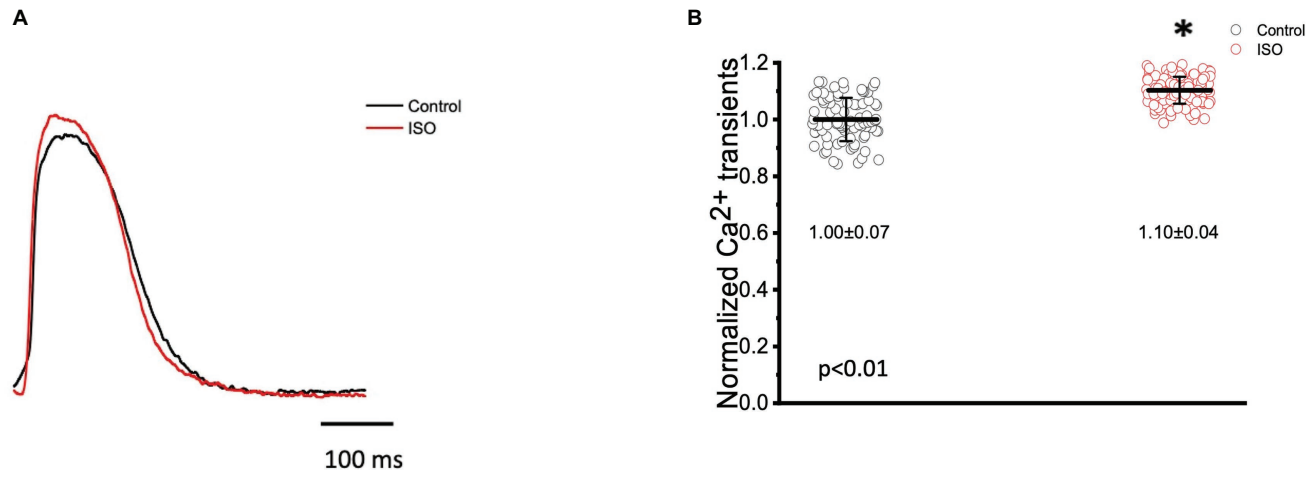

FIGURE 5 | Goldfish ventricular Ca^{2+} transient recording and normalized amplitude in the absence (black) and presence (red) of 100 nm isoproterenol. Stimulation of *β*-adrenergic receptors altered the morphology of the Ca^{2+} transient **(A)** and significantly increased the normalized amplitude of the Ca^{2+} transient from 1.00 ± 0.07 to 1.10 ± 0.04 ($p < 0.01$, $n = 65$ for the control, $n = 67$ for ISO, $N = 8$; **B**). *Denotes a significant difference between the two distributions. The data are presented as multiple measurements (n; dot cloud) recorded for different measurements (*n*) on different hearts (*N*) with the mean ± SEM (solid lines).

Parasympathetic Prevalence in Electrocardiographic Signals

To further assess how cholinergic stimulation altered whole heart electrical activity in the Goldfish model, transmural electrocardiograms were recorded in the presence and absence of 5 µm carbamylcholine (**Figure 9**). The morphology of the Goldfish electrocardiogram changed dramatically in response to cholinergic stimulation (**Figure 9A**) and significantly decreased the spontaneous heart rate (**Figures 9B,C**; from 1.00 ± 0.04 Hz to 0.15 ± 0.09 Hz).

Cholinergic stimulation significantly altered the duration of the QRS complex, the T wave, and the J wave (**Figure 10**). The QRS complex significantly decreased from: 33.20 ± 2.40 ms to 31.90 ± 1.80 ms (**Figure 10A**), the T wave significantly increased from 370.20 ± 3.70 ms to 379.70 ± 14.40 ms (**Figure 10B**), and the J wave significantly increased from 169.20 ± 30.20 ms to 326.60 ± 23.30 ms (**Figure 10C**). The increased J wave duration is likely reflective of the decreased heart rate observed in **Figures 7B**, **9C**.

Parasympathetic Regulation of Cardiac Contractility

In many vertebrate species, stimulation of either autonomic nervous system branch will not only alter cardiac excitability, but also cardiac contractility. To assess if stimulation of either autonomic nervous system branch altered the inotropic and/or the lusitropic properties of the Goldfish ventricle, experiments were performed in which the amplitude and kinetics of the Ca^{2+} transient were examined in the presence and absence of a cholinergic agonist.

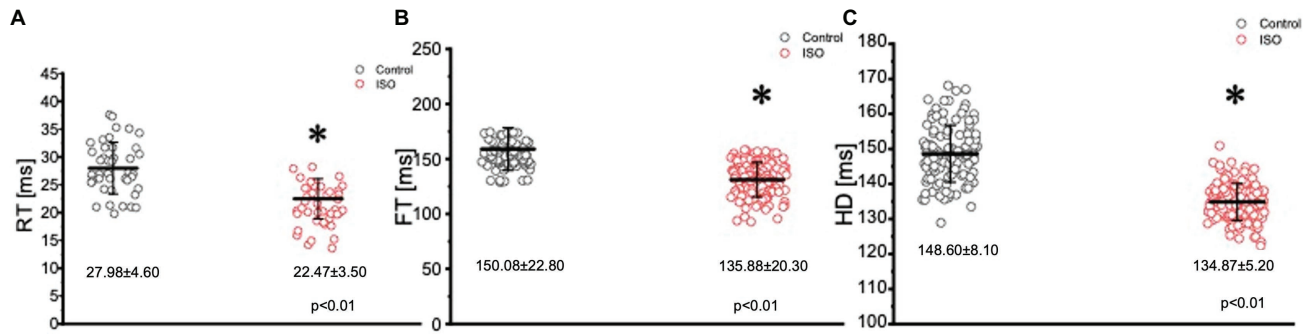

FIGURE 6 | Kinetic parameters of the Goldfish ventricular Ca^{2+} transients before (black) and after (red) perfusion with 100 nm isoproterenol. Perfusion of the Goldfish heart with 100 nM isoproterenol significantly decreased the rise time (RT) of the Ca^{2+} transient from 27.98 ± 4.60 ms to 22.47 ± 3.50 ms ($p < 0.01$, $n = 65$ for the control, $n = 96$ for ISO, $N = 8$; **A**), decreased the fall time (FT) of the Ca^{2+} transient from 150.08 ± 22.80 ms to 135.88 ± 20.30 ms ($p < 0.01$, $n = 76$ for the control, $n = 76$ for ISO, $N = 8$; **B**), and significantly decreased the half duration (HD) of the Ca^{2+} transient from 148.60 ± 8.10 ms to 134.87 ± 5.20 ms ($p < 0.01$, $n = 64$ for the control, $n = 72$ for ISO, $N = 8$; **C**). *Denotes a significant difference between the two distributions. The data are presented as multiple measurements (n; dot cloud) recorded for different measurements (*n*) on different hearts (*N*) with the mean ± SEM (solid lines).

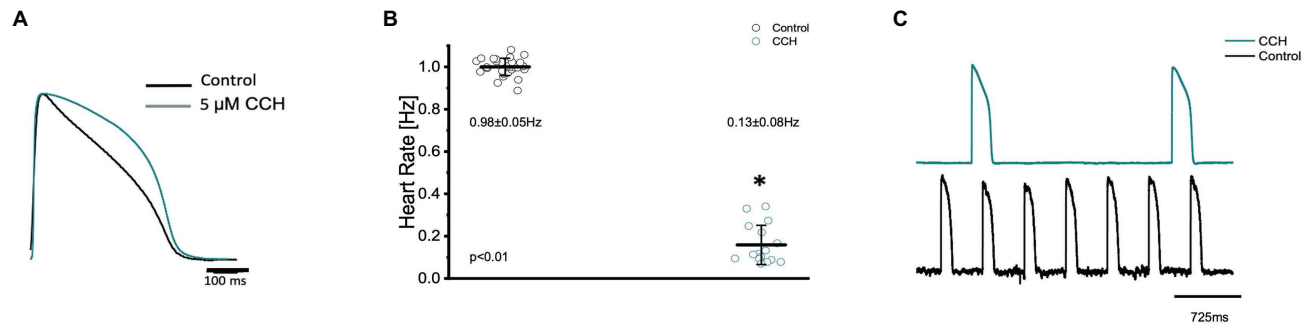

FIGURE 7 | Goldfish ventricular action potential and spontaneous heart rate recordings before (black) and after perfusion with 5 μm carbamylcholine (green). Administration of carbamylcholine altered the AP morphology **(A)** and had a negative chronotropic effect, reducing the heart rate from 0.98 ± 0.05 Hz to 0.13 ± 0.08 Hz ($p < 0.01$, $n = 29$ for the control, $n = 16$ for CCH, $N = 4$; **B**). The negative chronotropic effect following carbamylcholine perfusion is also reflected in spontaneous AP recordings from the left ventricle **(C)**. *Denotes a significant difference between the two distributions. The data are presented as multiple measurements (*n*; dot cloud) recorded for different measurements (*n*) on different hearts (*N*) with the mean ± SEM (solid lines).

To assess cholinergic regulation of contractility specifically, Ca^{2+} transients were recorded from the epicardial wall of the Goldfish ventricle in the presence and absence of 5 μm carbamylcholine (**Figure 11**). Administration of carbamylcholine had a negative inotropic effect, as the amplitude of the Ca^{2+} transient (**Figure 11A**) decreased in the presence of carbamylcholine. This negative inotropic effect is also presented in **Figure 11B**, where the normalized amplitude of the Ca^{2+} transient significantly decreased from 1.00 ± 0.10 to 0.49 ± 0.03 following cholinergic stimulation.

The three kinetical properties of the Ca^{2+} transient, including the rise time (RT), fall time (FT), and half duration (HD) were also evaluated to better understand how stimulation of the cholinergic pathway affected Ca^{2+} handling kinetics in the Goldfish myocardium (**Figure 12**). Although administration of 5 μm carbamylcholine did not significantly increase the rise time of the Ca^{2+} transient (**Figure 12A**; 30.20 ± 5.40 ms to 31.20 ± 3.20 ms), it did significantly increase the half duration of the Ca^{2+} transient (**Figure 12C**; from 151.80 ± 2.30 ms to 160.30 ± 4.00 ms). This effect can be due to the longer APs induced *via* cholinergic stimulation. Interestingly we were unable to observe a significant difference in the relaxation time (**Figure 12B**; from 161.50 ± 15.10 ms to 150.70 ± 12.10 ms) of the Ca^{2+} transient. This suggests carbamylcholine application did not significantly modify the lusitropic property of the Goldfish myocardium in these experiments; however, a significant change in the half duration of the Ca^{2+} transient does indicate the presence of an intrinsic parasympathetic tone in the Goldfish isolated heart, capable of modifying Ca^{2+} transient kinetics.

DISCUSSION

In most vertebrate hearts, both excitability and contractility are tightly regulated by the autonomic nervous system. Though there is a significant amount of research regarding the sympathetic and parasympathetic regulation of many vertebrate species, there is little known about how autonomic regulation impacts the electrical

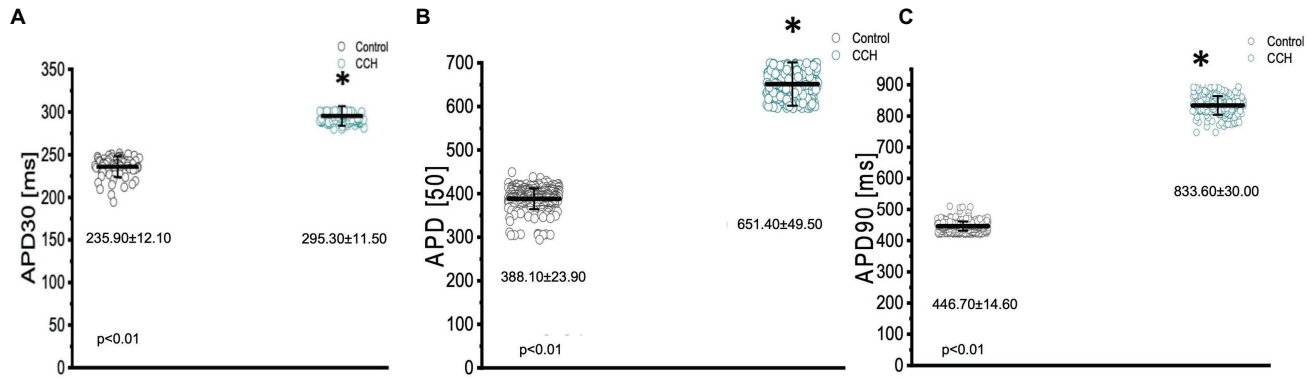

FIGURE 8 | Kinetic parameters of the Goldfish ventricular action potential before (black) and after (green) perfusion with 5 μm carbamylcholine. APD30 significantly increased from 235.90 ± 12.10 ms to 295.30 ± 11.50 ms ($p < 0.01$, $n = 80$ for the control, $n = 49$ for CCH, $N = 4$; **A**), APD50 significantly increased from 388.10 ± 23.90 ms to 651.40 ± 49.50 ms ($p < 0.01$, $n = 379$ for the control, $n = 308$ for CCH. $N = 4$; **B**), and APD90 significantly increased from 446.70 ± 14.60 ms to 833.60 ± 30.00 ms ($p < 0.01$, $n = 455$ for the control, $n = 201$ for CCH, $N = 4$; **C**). *Denotes a significant difference between the two distributions. The data are presented as multiple measurements (n; dot cloud) recorded for different measurements (n) on different hearts (N) with the mean ± SEM (solid lines).

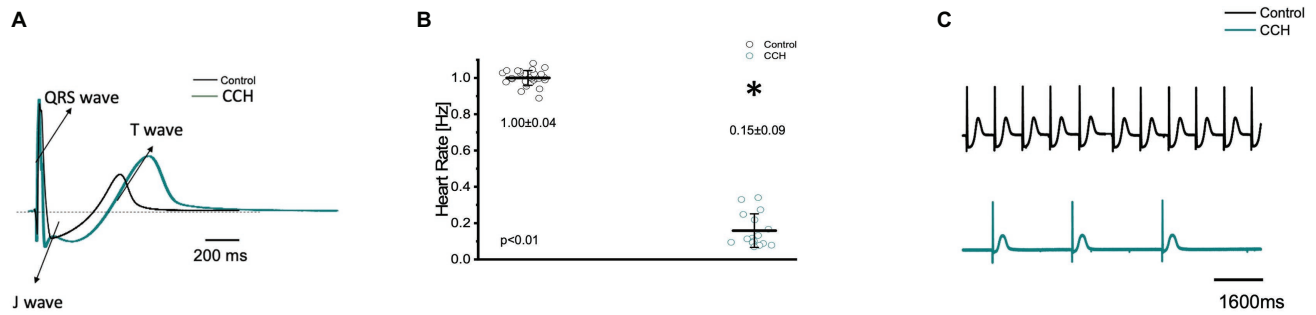

FIGURE 9 | Transmural ventricular electrocardiogram recordings in the absence (black) and presence (green) of 5 μm carbamylcholine. The three main components of the Goldfish electrocardiogram are presented: QRS complex, J wave, and T wave **(A)**. Carbamylcholine administration significantly altered the kinetic parameters of all the electrocardiographic signals. Administration of carbamylcholine significantly decreased heart rate from 1.00 ± 0.04 Hz to 0.15 ± 0.09 Hz ($p < 0.01$, $n = 29$ for the control, $n = 16$ for CCH, $N = 6$; **B**). Electrocardiogram recordings before and after carbamylcholine perfusion reflect a decreased heart rate in response to carbamylcholine **(C)**. *Denotes a significant difference between the two distributions. The data are presented as multiple measurements (n; dot cloud) recorded for different measurements (n) on different hearts (N) with the mean ± SEM (solid lines).

and mechanical function of fish hearts specifically. To our knowledge, it is not clear how autonomically driven AP kinetics impact contractility in the intact fish heart, which has become an increasingly popular model used to understand human cardiac physiology and pathophysiology. In this study, we investigated how stimulation of either autonomic branch regulated the time course of APs and electrocardiograms, and how these electrical changes correlated with changes in left ventricular Ca^{2+} transient measurements at the whole heart level. Our results indicate the presence of a fully developed dual control from both the adrenergic and cholinergic nerves in the Goldfish heart, highly resembling the pattern found in other vertebrate models.

β-Adrenergic Stimulation Increased Cardiac Excitability and Contractility

It is well-established stimulation of β-adrenergic receptors will have a positive chronotropic, dromotropic, inotropic, and lusitropic effect in any vertebrate species exhibiting full autonomic regulation. In the fish model, the autonomous rhythm of the heart is determined by the pacemaker region located near the atrial chamber, identified over 100 years ago (Keith and Mackenzie, 1910). Pacemaker APs are categorized by a gradual and slow diastolic depolarization (Phase 4), toward the threshold voltage of the AP upstroke (Phase 0; Saito, 1973; Harper et al., 1995; Haverinen and Vornanen, 2007; Tessadori et al., 2012). There are three main mechanisms by which an organism can modulate its heart rate, all of which end with an altered slope of the diastolic depolarization during diastole. This slope, set by the sinoatrial node, can be modified positively (by the sympathetic nervous system) or negatively (by the parasympathetic nervous system) by shifting the maximum diastolic potential, or decreasing the rate of depolarization, or (positively or negatively) shifting the membrane potential threshold; all of which could either increase or decrease

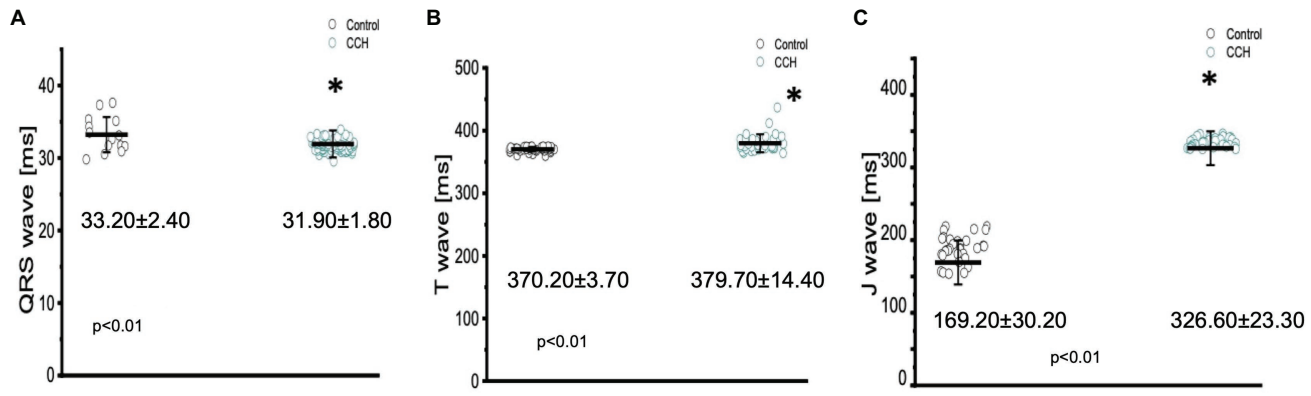

FIGURE 10 | Perfusion with 5 μm carbamylcholine significantly altered the time course of all three components in the Goldfish electrocardiogram. The duration of the QRS significantly decreased from 33.20 ± 2.40 ms to 31.90 ± 1.80 ms ($p < 0.01$, $n = 15$ for the control, $n = 59$ for CCH, $N = 6$; **A**), the T wave increased from 370.20 ± 3.70 ms to 379.70 ± 14.40 ms ($p < 0.01$, $n = 31$ for the control, $n = 36$ for CCH. $N = 6$; **B**), and the J wave show a significant increase from 169.20 ± 30.20 ms to 326.60 ± 23.30 ms ($p < 0.01$, $n = 32$ for the control, $n = 31$ for CCH. $N = 6$; **C**). *Denotes a significant difference between the two distributions. The data are presented as multiple measurements (n; dot cloud) recorded for different measurements (n) on different hearts (N) with the mean ± SEM (solid lines).

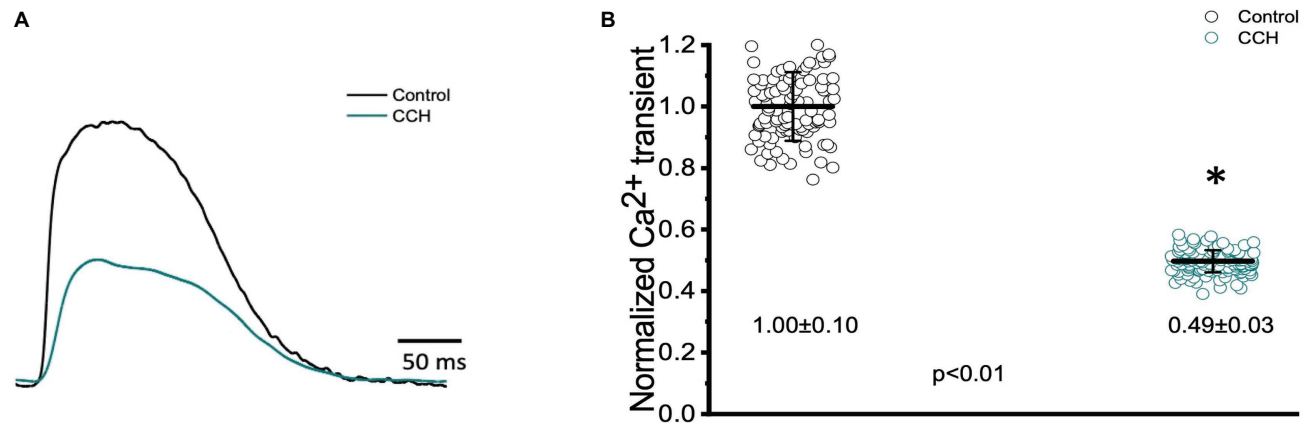

FIGURE 11 | Goldfish ventricular Ca^{2+} transient recording and normalized amplitude in the absence (black) and presence (green) of 5 μm carbamylcholine. Perfusion with carbamylcholine altered the morphology of the Ca^{2+} transient **(A)** and significantly decreased the normalized amplitude of the Ca^{2+} from 1.00 ± 0.10 to 0.49 ± 0.03 ($p < 0.01$, $n = 108$ for the control, $n = 143$ for CCH, $N = 8$; **B**). *Denotes a significant difference between the two distributions. The data are presented as multiple measurements (n; dot cloud) recorded for different measurements (n) on different hearts (N) with the mean ± SEM (solid lines).

the time required for the membrane potential to reach the threshold and fire an AP. In the Goldfish model, administration of isoproterenol altered ventricular AP morphology and had a positive chronotropic effect (**Figures 1A–C**). Remarkably, previous studies have observed isoproterenol to induce strikingly similar AP morphological changes in canine endocardial myocytes and guinea pig cardiomyocytes (O'Hara and Rudy, 2012; Szentandrássy et al., 2012; Sala et al., 2018).

The changes in the AP morphology can be better observed in **Figure 2**, where the kinetics of the ventricular AP are presented following adrenergic stimulation with isoproterenol. Perfusion with isoproterenol lead to a significant increase in APD30 and APD90 (**Figures 2A,C**, respectively) and a significant decrease in APD50 (**Figure 2B**). Interestingly, canine endocardial myocytes treated with isoproterenol exhibit lengthening of APD90 (Szentandrássy et al., 2012; Sala et al., 2018), similar to what we observed for the Goldfish. Unlike mammals, many fish species lack the slow component of the delay rectifier current (IKs), the main current system mediating repolarization effects of adrenergic stimulation on cardiac AP duration (Vornanen, 2017). The absence of this repolarizing current could explain the counterintuitive prolongation of APD30 and APD90 in the presence of an adrenergic stimulus. However, the role of I_{Ks} in response to adrenergic stimulation is not yet elucidated in the Goldfish heart, and further studies are necessary to corroborate this hypothesis.

Transmural electrocardiograms were recorded in the presence and absence of isoproterenol (**Figure 3**) to examine its effect on whole heart electrical activity. Indeed, isoproterenol perfusion not only altered the morphology of the electrocardiogram (**Figure 3A**) but also reaffirmed the positive chronotropic effect

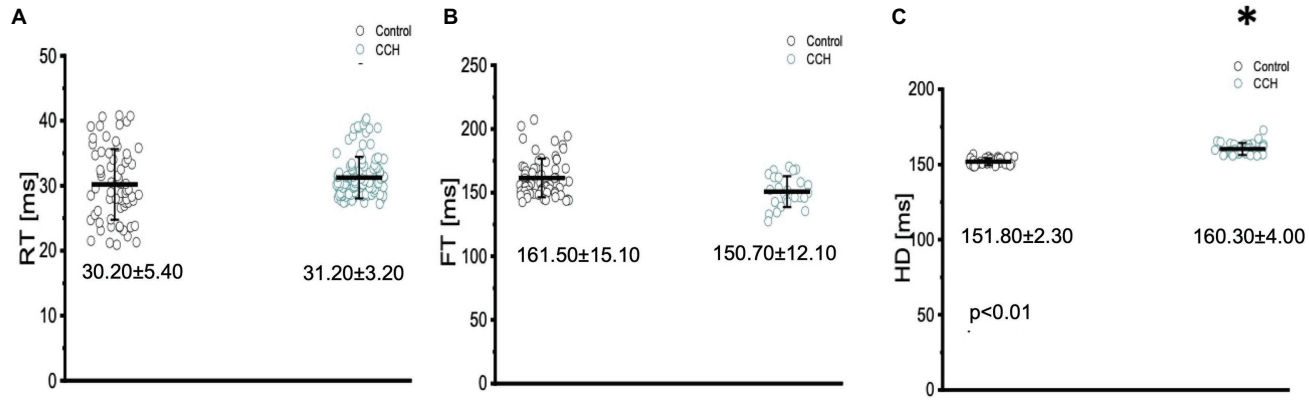

FIGURE 12 | The three kinetical properties of the Ca^{2+} transient, including the rise time (RT), fall time (FT), and half duration (HD) before (black) and after (green) perfusion with 5 μm carbamylcholine. Administration of 5 μm carbamylcholine did not significantly increase the rise time of the Ca^{2+} transient from 30.20 ± 5.40 ms to 31.20 ± 3.20 ms ($p > 0.01$, $n = 69$ for the control, $n = 85$ for CCH, $N = 8$; **A**) or decrease the fall time (FT) from 161.50 ± 15.10 ms to 150.70 ± 12.10 ms ($p > 0.01$, $n = 59$ for the control, $n = 27$ for CCH, $N = 8$; **B**). However, the half duration of the Ca^{2+} transient significantly increased from 151.80 ± 2.30 ms to 160.30 ± 4.00 ms ($p < 0.01$, $n = 29$ for the control, $n = 31$ for CCH, $N = 8$; **C**). *Denotes a significant difference between the two distributions. The data are presented as multiple measurements (n; dot cloud) recorded for different measurements (n) on different hearts (N) with the mean ± SEM (solid lines).

(**Figures 3B,C**) of isoproterenol presented in **Figure 1**. The positive chronotropic effect could be due to an increased slope of diastolic depolarization, as many other mammals exhibit the same pattern in response to adrenergic stimulation (Randall et al., 2020).

Isoproterenol's significant effect on whole heart excitability (**Figure 4**) not only reaffirms the presence of a positive chronotropic effect, but also suggests the instigation of a positive dromotropic effect. Because the QRS complex represents ventricular depolarization, its duration indirectly measures intraventricular impulse conduction. Thus, the positive dromotropic effect induced by isoproterenol can best be observed in **Figure 4A**, where administration of the catecholamine significantly reduced the duration of the QRS complex and increased the rate of intraventricular impulse conduction. Furthermore, isoproterenol significantly increased the duration of the T wave, and significantly prolonged the duration of the J wave (**Figures 4B,C**). An increased J wave duration is consistent with the prolongation of the APD30 in the presence of 100 nm of isoproterenol (**Figure 2A**). These modifications observed in the electrocardiogram further solidify the hypothesis that Goldfish exhibit sympathetic regulation, as perfusion with a catecholamine significantly modified cardiac excitability. The cardiac AP alters the mechanical function of vertebrate hearts by increasing intracellular free Ca^{2+} concentration, ultimately inducing cardiac contractions (Coraboeuf, 1978; Randall et al., 2020). In the Goldfish heart, Ca^{2+} influx through the LTCCs is the most likely trigger of Ca^{2+} release from the sarcoplasmic reticulum (Bazmi and Escobar, 2020), which ultimately augments cardiac contractile properties. Therefore, modifications in Ca^{2+} handling dynamics are essential for understanding how cardiac excitability alters cardiac contractility.

Epicardial Ca^{2+}transient recordings from the Goldfish ventricle show administration of isoproterenol altered the morphology of the Ca^{2+} transient and significantly increased the normalized amplitude of the Ca^{2+} transient (**Figures 5A,B**), a trend also observed in guinea pigs (Katra et al., 2004). The positive chronotropic effect (**Figures 1C**, **3C**) in response to adrenergic stimulation could be explained by the alterations present in the Ca^{2+} transient dynamics followed by isoproterenol perfusion. A significant increase in the Ca^{2+} transient amplitude following adrenergic stimulation (**Figure 5B**) suggests isoproterenol increased the Ca^{2+} current, likely through the LTCC (Bazmi and Escobar, 2020). As previously discussed, adrenergic stimulation activates a cascade of events that phosphorylate numerous Ca^{2+} handling proteins, including PLN on serine 16 and threonine 17. Phosphorylation of PLN removes its inhibitory effect on the cardiac sarcoplasmic endoplasmic reticulum ATPase, thus increasing Ca^{2+} load into the sarcoplasmic reticulum. An increased Ca^{2+} transient amplitude increases the influx of positive charges into the myocardium and reduces the AP threshold; both of which increase the conduction velocity of the AP, resulting in a positive dromotropic effect. Furthermore, an increased Ca^{2+} current will increase the amount of Ca^{2+} in the sarcoplasmic reticulum and ultimately increase Ca^{2+} induced Ca^{2+} release. This would then increase the strength of contraction, resulting in the positive inotropic effect observed in **Figure 5**. To our knowledge, a positive inotropic effect in response to adrenergic stimulation has yet to be observed in the ventricle of any other fish species (Vornanen and Tuomennoro, 1999; Molina et al., 2007; Vornanen et al., 2010; Abramochkin and Vornanen, 2017). However, it is likely previous studies did not observe positive dromotropic effects considering many of them performed similar experiments on isolated cardiomyocytes and not at the intact heart level. Looking at changes in the kinetic properties of the Goldfish heart, it is likely isoproterenol also had a positive lusitropic effect. Although all three kinetical parameters of the Goldfish Ca^{2+} transient decreased

following isoproterenol perfusion (**Figures 6A–C**), the lusitropic effect can be best observed in **Figure 6B**, as the fall time of the Ca^{2+} transient significantly decreased, suggesting isoproterenol increased the rate of myocardial relaxation during diastole.

Muscarinic Stimulation Decreased Cardiac Excitability and Contractility

As previously mentioned, an organism with an adrenergic drive could potentially also have a cholinergic drive, as they are the two antagonistic branches of the autonomic nervous system. Cholinergic control, however, is stronger than adrenergic control and has a negative chronotropic, dromotropic, inotropic, and lusitropic effect (Randall et al., 1968; Urbá-Holmgren et al., 1977; Laurent et al., 1983; Farrell, 1984; Axelsson et al., 1987). In the Goldfish model, perfusing the heart with 5 µm carbamylcholine prolonged the AP (**Figure 7A**) and had a negative chronotropic effect (**Figures 7B,C**). The strong negative chronotropic effect induced by cholinergic stimulation could be mediated by an ACh activated potassium current (IK_{Ach}); a major current found in fish atrial myocytes responsible for the repolarization of the membrane potential (Molina et al., 2007; Vornanen et al., 2010; Abramochkin and Vornanen, 2017). Furthermore, the activation of a muscarinic receptor will produce inhibition of the adenylyl cyclase reducing the levels of cAMP, preventing PKA-mediated phosphorylation. It is important to note, however, the levels of cAMP are finely regulated by PDEs, which contribute to the lowered cAMP concentrations. Nevertheless, lowered PKA levels result in a reduction in key phosphorylation sites, which ultimately decrease the slope of the diastolic depolarization and decrease heart rate. Furthermore, administration of carbamylcholine significantly prolonged all three kinetical parameters of the AP duration (**Figures 8A–C**). Considering previous research has shown the presence of Ca^{2+} dependent inactivation of the LTCC in Goldfish ventricular myocytes (Bazmi and Escobar, 2020), it is likely a decreased sarcolemmal Ca^{2+} influx mediated by carbamylcholine (**Figure 11B**) decelerated inactivation and prolonged the duration of the action potential.

In order to determine how the stimulation of cholinergic response modulated whole heart electrical activity, electrocardiograms were recorded in the presence and absence of carbamylcholine (**Figure 9**). Perfusion with carbamylcholine altered electrocardiogram morphology (**Figure 9A**) and reaffirmed the negative chronotropic effect (**Figures 9B,C**) presented in **Figure 7B**. Modification of whole heart excitability in response to muscarinic stimulation is presented in **Figure 10**. Interestingly, the duration of the QRS complex decreased in response to carbamylcholine administration, suggesting a slight positive dromotropic response, something typically observed in tachycardia. Currently, little is known about the depolarizing ventricular currents in the Goldfish which could provide further insight as to why cholinergic stimulation would reduce the duration of the QRS complex. Carbamylcholine perfusion also significantly increased the T and J wave durations (**Figures 10A–C**); however, the increased J wave was expected as there was a corresponding increase in APD30 (**Figure 8A**).

The negative chronotropic effect induced by stimulation of the muscarinic receptors could also be explained by modifications of the Ca^{2+} transient. Administration of 5 µM carbamylcholine modified Ca^{2+} transient morphology and significantly decreased the amplitude of the Ca^{2+} transient, suggesting stimulation of muscarinic receptors may have had a negative inotropic effect (**Figures 11A,B**). This is particularly interesting because previous studies conducted in isolated cardiac myocytes suggest muscarinic stimulation produced minor changes in cardiac chronotropic and inotropic properties in the fish heart (Laurent et al., 1983; Fritsche and Nilsson, 1990; Steele et al., 2009). This discrepancy, however, could be explained by the fact that other experiments were conducted in isolated myocytes, while our experiments were performed in the intact heart. As the heart is an electrically coupled organ, isolation of cardiac myocytes disrupts this electrical coupling, which may alter cardiac contractile properties.

A reduction in the Ca^{2+} current amplitude (**Figure 11B**) is likely to have reduced the slope of the diastolic depolarization and, as such, induced a negative chronotropic effect. As mentioned before, there are numerous mechanisms by which this slope may change. During cholinergic stimulation, PDEs and inhibition of adenylyl cyclase reduce cAMP levels which not only lower the activation of PKA, but also reduce stimulation of HCN channels. The current produced by these channels, I_f, typically increases the slope of the diastolic depolarization. However, in the presence of a cholinergic agonist, stimulation of If decreases, thus reducing the slope of the diastolic depolarization and ultimately reducing heart rate. Interestingly, HCN4 pacemaker channels have only been identified in the pacemaker region of the Goldfish and Zebrafish (Tessadori et al., 2012; Newton et al., 2014). Another possible mechanism by which muscarinic receptor stimulation induced a negative chronotropic response could be activation (IK_{Ach}), although the contribution of this current is still poorly elucidated in fish ventricular myocytes (Molina et al., 2007; Vornanen et al., 2010; Abramochkin and Vornanen, 2017). Activation of IK_{ACh} would induce hyperpolarization of the maximum diastolic potential, decreasing the heart rate. A decreased Ca^{2+} current and activation of IK_{ACh} also lead to a negative dromotropic effect as a decreased Ca^{2+} current will decrease the influx of positive charges, increase the threshold of the AP, and decrease the mean diastolic potential; all of which reduce AP conduction velocity and induce a negative dromotropic effect.

Modifications presented in the kinetic properties of the Goldfish heart following carbamylcholine perfusion (**Figure 12**) suggest stimulation of the muscarinic receptor induced a minor negative lusitropic effect. While the half duration of the Ca^{2+} transient significantly increased in response to carbamylcholine perfusion (**Figure 12C**), the rise time and fall time were not significantly altered (**Figures 12A,B**). These results are interesting because the effect of carbamylcholine is in the opposite direction

of what happens in mouse hearts and is very similar to larger mammals (Aguilar-Sanchez et al., 2019).

CONCLUSION

We conclude that the Goldfish heart is a very interesting model to study autonomic regulation due to its similarities with larger mammals. Although the Goldfish heart only has two chambers, its strikingly similar electrophysiological and autonomic characteristics make it a suitable model to study larger mammalian pathophysiology.

DATA AVAILABILITY STATEMENT

The raw data supporting the conclusions of this article will be made available by the authors, without undue reservation.

ETHICS STATEMENT

The animal study was reviewed and approved by Association for Assessment and Accreditation of Laboratory Animal Care (2008–201).

AUTHOR CONTRIBUTIONS

MB and AE designed and performed the research, analyzed data, and wrote the paper. All authors contributed to the article and approved the submitted version.

FUNDING

The study was supported by NIH (R01 HL-084487 to AE) and NIH (1R01HL152296 to AE).

REFERENCES

Abramochkin, D. V., and Vornanen, M. (2017). Seasonal changes of cholinergic response in the atrium of Arctic navaga cod (Eleginus navaga). *J. Comp. Physiol. B.* 187, 329–338. doi: 10.1007/s00360-016-1032-y

Aguilar-Sanchez, Y., Fainstein, D., Mejia-Alvarez, R., and Escobar, A. L. (2017). Local field fluorescence microscopy: imaging cellular signals in intact hearts. *J. Vis. Exp.* 121:55202. doi: 10.3791/55202

Aguilar-Sanchez, Y., Rodriguez de Yurre, A., Argenziano, M., Escobar, A. L., and Ramos-Franco, J. (2019). Transmural autonomic regulation of cardiac contractility at the intact heart level. *Front. Physiol.* 10:773. doi: 10.3389/fphys.2019.00773

Axelsson, M., Ehrenström, F., and Nilsson, S. (1987). Cholinergic and adrenergic influence on the teleost heart *in vivo*. *Exp. Biol.* 46, 179–186.

Bazmi, M., and Escobar, A. L. (2020). Excitation–contraction coupling in the goldfish (Carassius auratus) intact heart. *Front. Physiol.* 11:1103. doi: 10.3389/fphys.2020.01103

Brum, G., Osterrieder, W., and Trautwein, W. (1984). Beta-adrenergic increase in the calcium conductance of cardiac myocytes studied with the patch clamp. *Eur. J. Phys.* 401, 111–118. doi: 10.1007/BF00583870

Cohn, J. N. (1989). Sympathetic nervous system activity and the heart. *Am. J. Hypertens.* 2, 353S–356S.

Collins, J. H., Kranias, E. G., Reeves, A. S., Bilezikjian, L. M., and Schwartz, A. (1981). Isolation of phospholamban and a second proteolipid component from canine cardiac sarcoplasmic reticulum. *Biochem. Biophys. Res. Commun.* 99, 796–803. doi: 10.1016/0006-291X(81)91235-3

Coraboeuf, E. (1978). Ionic basis of electrical activity in cardiac tissues. *Am. J. Phys. Heart Circ. Phys.* 234, H101–H116. doi: 10.1152/ajpheart.1978.234.2.H101

Escobar, A. L., Fernández-Gómez, R., Peter, J.-C., Mobini, R., Hoebeke, J., and Mijares, A. (2006). IgGs and Mabs against the β2-adrenoreceptor block A-V conduction in mouse hearts: a possible role in the pathogenesis of ventricular arrhythmias. *J. Mol. Cell. Cardiol.* 40, 829–837. doi: 10.1016/j.yjmcc.2006.03.430

Escobar, A. L., Ribeiro-Costa, R., Villalba-Galea, C., Zoghbi, M. E., Pérez, C. G., and Mejía-Alvarez, R. (2004). Developmental changes of intracellular Ca^{2+} transients in beating rat hearts. *Am. J. Phys. Heart Circ. Phys.* 286, H971–H978. doi: 10.1152/ajpheart.00308.2003

Evans, D. B. (1986). Modulation of cAMP: mechanism for positive inotropic action. *J. Cardiovasc. Pharmacol.* 8(Suppl. 9), S22–S29. doi: 10.1097/00005344-198611001-00003

Farrell, A. P. (1984). A review of cardiac performance in the teleost heart: intrinsic and humoral regulation. *Can. J. Zool.* 62, 523–536. doi: 10.1139/z84-079

Ferreiro, M., Petrosky, A. D., and Escobar, A. L. (2012). Intracellular Ca^{2+} release underlies the development of phase 2 in mouse ventricular action potentials. *Am. J. Phys. Heart Circ. Phys.* 302, H1160–H1172. doi: 10.1152/ajpheart.00524.2011

Fritsche, R., and Nilsson, S. (1990). Autonomic nervous control of blood pressure and heart rate during hypoxia in the cod, Gadus morhua. *J. Comp. Physiol. B.* 160, 287–292. doi: 10.1007/BF00302594

Harper, A. A., Newton, I. P., and Watt, P. W. (1995). The effect of temperature on spontaneous action potential discharge of the isolated sinus venosus from winter and summer plaice (Pleuronectes platessa). *J. Exp. Biol.* 198, 137–140. doi: 10.1242/jeb.198.1.137

Haverinen, J., and Vornanen, M. (2007). Temperature acclimation modifies sinoatrial pacemaker mechanism of the rainbow trout heart. *Am. J. Phys. Regul. Integr. Comp. Phys.* 292, R1023–R1032. doi: 10.1152/ajpregu.00432.2006

Hayes, J. S., and Mayer, S. E. (1981). Regulation of Guinea pig heart phosphorylase kinase by cAMP, protein kinase, and calcium. *Am. J. Physiol. Endocrinol. Metab.* 240, E340–E349. doi: 10.1152/ajpendo.1981.240.3.E340

Henning, R. J. (1992). Vagal stimulation during muscarinic and β-adrenergic blockade increases atrial contractility and heart rate. *J. Auton. Nerv. Syst.* 40, 121–129. doi: 10.1016/0165-1838(92)90023-A

Hildebrandt, J. D., Sekura, R. D., Codina, J., Iyengar, R., Manclark, C. R., and Birnbaumer, L. (1983). Stimulation and inhibition of adenylyl cyclases mediated by distinct regulatory proteins. *Nature* 302, 706–709. doi: 10.1038/302706a0

Katra, R. P., Pruvot, E., and Laurita, K. R. (2004). Intracellular calcium handling heterogeneities in intact Guinea pig hearts. *Am. J. Phys. Heart Circ. Phys.* 286, H648–H656. doi: 10.1152/ajpheart.00374.2003

Katz, A. M. (1967). Regulation of cardiac muscle contractility. *J. Gen. Physiol.* 50, 185–196. doi: 10.1085/jgp.50.6.185

Keith, A., and Mackenzie, I. (1910). Recent researches on the anatomy of the heart. *Lancet* 175, 101–103. doi: 10.1016/S0140-6736(01)74711-3

Kornyeyev, D., Reyes, M., and Escobar, A. L. (2010). Luminal Ca^{2+} content regulates intracellular Ca^{2+} release in subepicardial myocytes of intact beating mouse hearts: effect of exogenous buffers. *Am. J. Phys. Heart Circ. Phys.* 298, H2138–H2153. doi: 10.1152/ajpheart.00885.2009

Krebs, E. G. (1972). Protein kinases. *Curr. Top. Cell. Regul.* 5, 99–133. doi: 10.1016/B978-0-12-152805-8.50010-1

Laurent, P., Holmgren, S., and Nilsson, S. (1983). Nervous and humoral control of the fish heart: structure and function. *Comp. Biochem. Physiol. A Physiol.* 76, 525–542. doi: 10.1016/0300-9629(83)90455-3

Lee, W. C., and Shideman, F. E. (1959). Role of myocardial Catecholamines in cardiac contractility. *Science* 129, 967–968. doi: 10.1126/science.129.3354.967

Lindemann, J. P., and Watanabe, A. M. (1985). Muscarinic cholinergic inhibition of beta-adrenergic stimulation of phospholamban phosphorylation and Ca^{2+} transport in Guinea pig ventricles. *J. Biol. Chem.* 260, 13122–13129. doi: 10.1016/S0021-9258(17)38847-6

López Alarcón, M. M., Rodríguez de Yurre, A., Felice, J. I., Medei, E., and Escobar, A. L. (2019). Phase 1 repolarization rate defines Ca^{2+} dynamics and contractility on intact mouse hearts. *J. Gen. Physiol.* 151, 771–785. doi: 10.1085/jgp.201812269

Marks, A. R. (2013). Calcium cycling proteins and heart failure: mechanisms and therapeutics. *J. Clin. Investig.* 123, 46–52. doi: 10.1172/JCI62834

Mattiazzi, A., Argenziano, M., Aguilar-Sanchez, Y., Mazzocchi, G., and Escobar, A. L. (2015). Ca2+ Sparks and Ca2+ waves are the subcellular events underlying Ca2+ overload during ischemia and reperfusion in perfused intact hearts. *J. Mol. Cell. Cardiol.* 79, 69–78. doi: 10.1016/j.yjmcc.2014.10.011

Mejía-Alvarez, R., Manno, C., Villalba-Galea, C. A., del Valle Fernández, L., Costa, R., Fill, M., et al. (2003). Pulsed local-field fluorescence microscopy: A new approach for measuring cellular signals in the beating heart. *Pflugers Arch.* 445, 747–758. doi: 10.1007/s00424-002-0963-1

Mersereau, E. J., Poitra, S. L., Espinoza, A., Crossley, D. A., and Darland, T. (2015). The effects of cocaine on heart rate and electrocardiogram in zebrafish (Danio rerio). *Comp. Bioche. Physiol. C Toxicol. Pharmacol.* 172-173, 1–6. doi: 10.1016/j.cbpc.2015.03.007

Molina, C. E., Gesser, H., Llach, A., Tort, L., and Hove-Madsen, L. (2007). Modulation of membrane potential by an acetylcholine-activated potassium current in trout atrial myocytes. *Am. J. Phys. Regul. Integr. Comp. Phys.* 292, R388–R395. doi: 10.1152/ajpregu.00499.2005

Nakamura, T., Lozano, P. R., Ikeda, Y., Iwanaga, Y., Hinek, A., Minamisawa, S., et al. (2002). Fibulin-5/DANCE is essential for elastogenesis *in vivo*. *Nature* 415, 171–175. doi: 10.1038/415171a

Newton, C. M., Stoyek, M. R., Croll, R. P., and Smith, F. M. (2014). Regional innervation of the heart in the goldfish, Carassius auratus: a confocal microscopy study: innervation of the goldfish heart. *J. Comp. Neurol.* 522, 456–478. doi: 10.1002/cne.23421

O'Hara, T., and Rudy, Y. (2012). Quantitative comparison of cardiac ventricular myocyte electrophysiology and response to drugs in human and nonhuman species. *Am. J. Phys. Heart Circ. Phys.* 302, H1023–H1030. doi: 10.1152/ajpheart.00785.2011

Osterrieder, W., Brum, G., Hescheler, J., Trautwein, W., Flockerzi, V., and Hofmann, F. (1982). Injection of subunits of cyclic AMP-dependent protein kinase into cardiac myocytes modulates Ca2+ current. *Nature* 298, 576–578. doi: 10.1038/298576a0

Randall, W. C., Randall, D. C., and Ardell, J. L. (2020). "Autonomic regulation of myocardial contractility," in *Reflex Control of the Circulation. 1st Edn*. eds. I. H. Zucker and J. P. Gilmore (United Kingdom: Taylor and Francis), 67–103.

Randall, W., Wechsler, J., Pace, J., and Szentivanyi, M. (1968). Alterations in myocardial contractility during stimulation of the cardiac nerves. *Am. J. Physiol.* 214, 1205–1212. doi: 10.1152/ajplegacy.1968.214.5.1205

Saito, T. (1973). Effects of vagal stimulation on the pacemaker action potentials of carp heart. *Comp. Biochem. Physiol. A Physiol.* 44, 191–199. doi: 10.1016/0300-9629(73)90381-2

Sala, L., Hegyi, B., Bartolucci, C., Altomare, C., Rocchetti, M., Váczi, K., et al. (2018). Action potential contour contributes to species differences in repolarization response to β-adrenergic stimulation. *Europace* 20, 1543–1552. doi: 10.1093/europace/eux236

Sandblom, E., and Axelsson, M. (2011). Autonomic control of circulation in fish: A comparative view. *Auton. Neurosci.* 165, 127–139. doi: 10.1016/j.autneu.2011.08.006

Steele, S. L., Lo, K. H. A., Li, V. W. T., Cheng, S. H., Ekker, M., and Perry, S. F. (2009). Loss of M_2 muscarinic receptor function inhibits development of hypoxic bradycardia and alters cardiac β-adrenergic sensitivity in larval zebrafish (*Danio rerio*). *Am. J. Phys. Regul. Integr. Comp. Phys.* 297, R412–R420. doi: 10.1152/ajpregu.00036.2009

Suko, J., Maurer-Fogy, I., Plank, B., Bertel, O., Wyskovsky, W., Hohenegger, M., et al. (1993). Phosphorylation of serine 2843 in ryanodine receptor-calcium release channel of skeletal muscle by cAMP-, cGMP- and CaM-dependent protein kinase. *Biochim. Biophys. Acta* 1175, 193–206. doi: 10.1016/0167-4889(93)90023-I

Szentandrássy, N., Farkas, V., Bárándi, L., Hegyi, B., Ruzsnavszky, F., Horváth, B., et al. (2012). Role of action potential configuration and the contribution of Ca^{2+} and K^+ currents to isoprenaline-induced changes in canine ventricular cells: isoprenaline in canine heart. *Br. J. Pharmacol.* 167, 599–611. doi: 10.1111/j.1476-5381.2012.02015.x

Tessadori, F., van Weerd, J. H., Burkhard, S. B., Verkerk, A. O., de Pater, E., Boukens, B. J., et al. (2012). Identification and functional characterization of cardiac pacemaker cells in Zebrafish. *PLoS One* 7:e47644. doi: 10.1371/journal.pone.0047644

Tsai, C.-T., Wu, C.-K., Chiang, F.-T., Tseng, C.-D., Lee, J.-K., Yu, C.-C., et al. (2011). *In-vitro* recording of adult zebrafish heart electrocardiogram—A platform for pharmacological testing. *Clin. Chim. Acta* 412, 1963–1967. doi: 10.1016/j.cca.2011.07.002

Urbá-Holmgren, R., González, R. M., and Holmgren, B. (1977). Is yawning a cholinergic response? *Nature* 267, 261–262. doi: 10.1038/267261a0

Valdivia, H. H., Kaplan, J. H., Ellis-Davies, G. C., and Lederer, W. J. (1995). Rapid adaptation of cardiac ryanodine receptors: modulation by Mg^{2+} and phosphorylation. *Science* 267, 1997–2000. doi: 10.1126/science.7701323

Valverde, C. A., Kornyeyev, D., Ferreiro, M., Petrosky, A. D., Mattiazzi, A., and Escobar, A. L. (2010). Transient Ca2+ depletion of the sarcoplasmic reticulum at the onset of reperfusion. *Cardiovasc. Res.* 85, 671–680. doi: 10.1093/cvr/cvp371

Valverde, C. A., Mundiña-Weilenmann, C., Reyes, M., Kranias, E. G., Escobar, A. L., and Mattiazzi, A. (2006). Phospholamban phosphorylation sites enhance the recovery of intracellular Ca^{2+} after perfusion arrest in isolated, perfused mouse heart. *Cardiovasc. Res.* 70, 335–345. doi: 10.1016/j.cardiores.2006.01.018

Vornanen, M. (2017). "Electrical excitability of the fish heart and its autonomic regulation," in *Fish Physiology. Vol. 36*. eds. A. K. Gamperl, T. E. Gillis, A. P. Farrell and C. J. Brauner (New York: Elsevier), 99–153.

Vornanen, M., Hälinen, M., and Haverinen, J. (2010). Sinoatrial tissue of crucian carp heart has only negative contractile responses to autonomic agonists. *BMC Physiol.* 10:10. doi: 10.1186/1472-6793-10-10

Vornanen, M., and Tuomennoro, J. (1999). Effects of acute anoxia on heart function in crucian carp: importance of cholinergic and purinergic control. *Am. J. Phys.* 277, R465–R475. doi: 10.1152/ajpregu.1999.277.2.R465

Watanabe, A. M., and Lindemann, J. P. (1984). "Mechanisms of adrenergic and cholinergic regulation of myocardial contractility," in *Physiology and Pathophysiology of the Heart. Vol. 34*. ed. N. Sperelakis (United States: Springer), 377–404.

Weilenmann, C. M., Vittone, L., Cingolani, G., and Mattiazzi, A. (1987). Dissociation between contraction and relaxation: the possible role of phospholamban phosphorylation. *Basic Res. Cardiol.* 82, 507–516. doi: 10.1007/BF01907220

Xing, N., Ji, L., Song, J., Ma, J., Li, S., Ren, Z., et al. (2017). Cadmium stress assessment based on the electrocardiogram characteristics of zebra fish (Danio rerio): QRS complex could play an important role. *Aquat. Toxicol.* 191, 236–244. doi: 10.1016/j.aquatox.2017.08.015

Conflict of Interest: The authors declare the research was conducted in the absence of any commercial or financial relationships that could be construed as a potential conflict of interest.

Publisher's Note: All claims expressed in this article are solely those of the authors and do not necessarily represent those of their affiliated organizations, or those of the publisher, the editors and the reviewers. Any product that may be evaluated in this article, or claim that may be made by its manufacturer, is not guaranteed or endorsed by the publisher.

frontiers in Physiology

REVIEW
published: 16 March 2022
doi: 10.3389/fphys.2022.864002

Exploring the Coordination of Cardiac Ion Channels With Action Potential Clamp Technique

*Balázs Horváth[1], Norbert Szentandrássy[1,2], Csaba Dienes[1], Zsigmond M. Kovács[1], Péter P. Nánási[1,2], Ye Chen-Izu[3], Leighton T. Izu[3] and Tamas Banyasz[1]**

[1] Department of Physiology, University of Debrecen, Debrecen, Hungary, [2] Department of Basic Medical Sciences, Faculty of Dentistry, University of Debrecen, Debrecen, Hungary, [3] Department of Pharmacology, University of California, Davis, Davis, CA, United States

The patch clamp technique underwent continual advancement and developed numerous variants in cardiac electrophysiology since its introduction in the late 1970s. In the beginning, the capability of the technique was limited to recording one single current from one cell stimulated with a rectangular command pulse. Since that time, the technique has been extended to record multiple currents under various command pulses including action potential. The current review summarizes the development of the patch clamp technique in cardiac electrophysiology with special focus on the potential applications in integrative physiology.

Keywords: cardiac electrophysiology, voltage clamp, action potential voltage clamp, ion current, pharmacology

OPEN ACCESS

Edited by:
Ovidiu Constantin Baltatu, Anhembi Morumbi University, Brazil

Reviewed by:
Timm Danker, University of Tübingen, Germany
Richard A. Gray, United States Food and Drug Administration, United States

****Correspondence:***
Tamas Banyasz
banyasz.tamas@med.unideb.hu

Specialty section:
This article was submitted to Integrative Physiology, a section of the journal Frontiers in Physiology

Received: *27 January 2022*
Accepted: *15 February 2022*
Published: *16 March 2022*

Citation:
Horváth B, Szentandrássy N, Dienes C, Kovács ZM, Nánási PP, Chen-Izu Y, Izu LT and Banyasz T (2022) Exploring the Coordination of Cardiac Ion Channels With Action Potential Clamp Technique. Front. Physiol. 13:864002. doi: 10.3389/fphys.2022.864002

INTRODUCTION

Cardiac action potential (AP) is shaped by numerous ionic currents flowing in and out of the cell through the sarcolemma. The ultimate goal in cellular cardiac electrophysiology is to characterize the dynamics of individual ionic currents and understand how the interplay of these currents will draw the profile of the AP in different experimental conditions. There are two conceptually different methods to determine the profile of a given ionic current during AP. To accomplish this goal in the traditional way, we have to determine the magnitude of each discrete current from moment to moment during the AP. This step is followed by the reconstruction of the AP from the interplay of the individual actors. The traditional way employs rectangular command pulses mapping the channel kinetic parameters and the voltage dependence of the parameters. Based on this information, the profile of the current can be reconstructed during the AP with the help of computer simulation. The other approach, termed the AP clamp method, uses prerecorded AP command and measures the current profile directly during the AP in question. Current experimental methods allow the researcher to record multiple currents under the same AP. The goal of this article is to review the evolution of the voltage clamp method in a classical way employing rectangular command pulse to the sequential the AP voltage clamp technique. We aimed to compare the benefits and disadvantages of the methodical variations of these techniques with special emphasis on the integrative approach.

Abbreviations: AP, action potential; $I_{Ca,L}$, L-type calcium current; I_{K1}, inward rectifying potassium current; I_{Kr}, rapid component of delayed rectifier potassium current; I_{Ks}, slow component of delayed rectifier potassium current; $I_{Na,L}$, late sodium current.

THE CONCEPTUAL DIFFERENCE BETWEEN TRADITIONAL VOLTAGE CLAMP AND ACTION POTENTIAL VOLTAGE CLAMP

The voltage clamp technique was developed by Kenneth Cole and George Marmont in 1947 to study giant axon electrophysiology (Verkhratsky and Parpura, 2014). Silvio Weidmann combined this method with the glass microelectrode and adapted it to the cardiac myocyte (Kléber et al., 2006). Regardless of the size, or the type of the cell being voltage-clamped, the concept of this technique is simple. The glass microelectrode, filled with an electrolyte, establishes an electric contact between the inner space of the cell and the amplifier. The other pole of the amplifier is connected to the extracellular reference electrode immersed into the perfusion fluid. In this simple circuit, all elements are connected in a chain (i.e., series circuit); hence, the current measured with the amplifier will represent the current flowing through a membrane (**Figure 1**). If the membrane contains multiple ion channel types (i.e., sodium, potassium, and chloride), the total membrane current is a composite current. During a voltage clamp experiment, the amplifier maintains the voltage pattern (e.g., rectangular, ramp, and sine) determined by the command voltage and measures the current in the circuit that is the membrane current.

TRADITIONAL VOLTAGE CLAMP TECHNIQUE USING RECTANGULAR COMMANDS

The primary research goal when using rectangular command voltage is to characterize the behavior of ion channels and understand how the changing membrane voltage modulates their function. The function of ion channels is determined by the conformation of the pore-forming protein. The transition between functional states (i.e., short states) is governed by membrane potential changes. Using a series of rectangular command voltages (i.e., rapid voltage step followed by sustained voltage levels) the kinetic properties (i.e., activation, inactivation, and recovery) of a given channel can be mapped. Hypothetically, having all the channel parameters determined, the magnitude of the current can be predicted during any voltage change with an appropriate mathematical model (Xu et al., 2002; Bondarenko et al., 2004; Shannon et al., 2004; Romero et al., 2011). There is only one serious technical difficulty to be handled in these studies: dissecting the individual current from the total membrane current. Since the cardiac cell membrane contains numerous channels, before we can start recording the one single current we are interested in, all other channels must be "silenced." Blocking all unwanted currents in cardiac cells is a difficult task. To achieve this goal, experimenters often use drugs or non-physiological conditions. The intracellular and extracellular ion species and concentrations are usually different from the physiological milieu during the traditional voltage clamp experiment. Then, the reconstruction of the current in the computer model is based on assumption that the channel behaves similarly in a physiological environment.

ACTION POTENTIAL VOLTAGE CLAMP—DIRECT MEASUREMENT OF ION CURRENT DURING ACTION POTENTIAL

The great quote "Measure what is measurable, and make measurable what is not so" attributed sometimes to Galileo Galilei, at other times to the French scholars Antoine-Augustin Cournot and Thomas-Henri Martin, could be a first-rate motto for this technique. This experimental method uses a "reverse approach" in order to determine the current profile directly during AP. To achieve this, a four-step protocol is employed. First, an AP is recorded from the cell in physiological ionic milieu under the current clamp mode. Second, the recorded AP is fed back to the amplifier as command voltage in the voltage clamp mode, and the compensation current is recorded. Under these circumstances, the compensation current will be a flat line with some minor artifacts before the upstroke caused by the exogenous stimuli in the previous step. In an ideal measurement, the compensation current will be zero because the cell membrane does not require any exogenous current from the amplifier to produce its own AP (**Figure 2**, green trace). This flat compensation current is saved and used later as reference current. In the third step, a selective ion channel blocker is applied to turn off the current to be recorded. If the compensation current is recorded following the full development of the inhibition, the mirror image of the blocked current will be seen. The current in interest is blocked, and the missing current is supplied by the amplifier (**Figure 2**, blue trace). In the fourth step, the second current trace is subtracted from the first. Since the first compensation current is practically a flat line in the optimal case, the subtraction results in flipping the second trace (**Figure 2**, red trace). Now, the produced trace reveals the current profile during the AP. Unlike in the first case, this trace is not a reconstruction but a direct record of the current studied in the physiological milieu.

THE TECHNICAL EVOLUTION OF THE CONCEPT

Action potential-shaped command voltages were already used for various purposes before the concept of the AP clamp was used for the current recording. Bastian and Nakajima employed prerecorded APs to study the T-tubule function in the skeletal muscle using the double sucrose gap method (Bastian and Nakajima, 1974; Nakajima and Bastian, 1974). Starzak et al. used the AP-shaped command pulse to test the effectiveness of the space clamp in the squid axon (Starzak and Starzak, 1978; Starzak and Needle, 1983). Although these authors made no attempt to record specific ion currents in these experiments, the essential elements of AP clamp technique can be identified. Remarkably, Starzak et al. consistently used the term "action potential clamp"

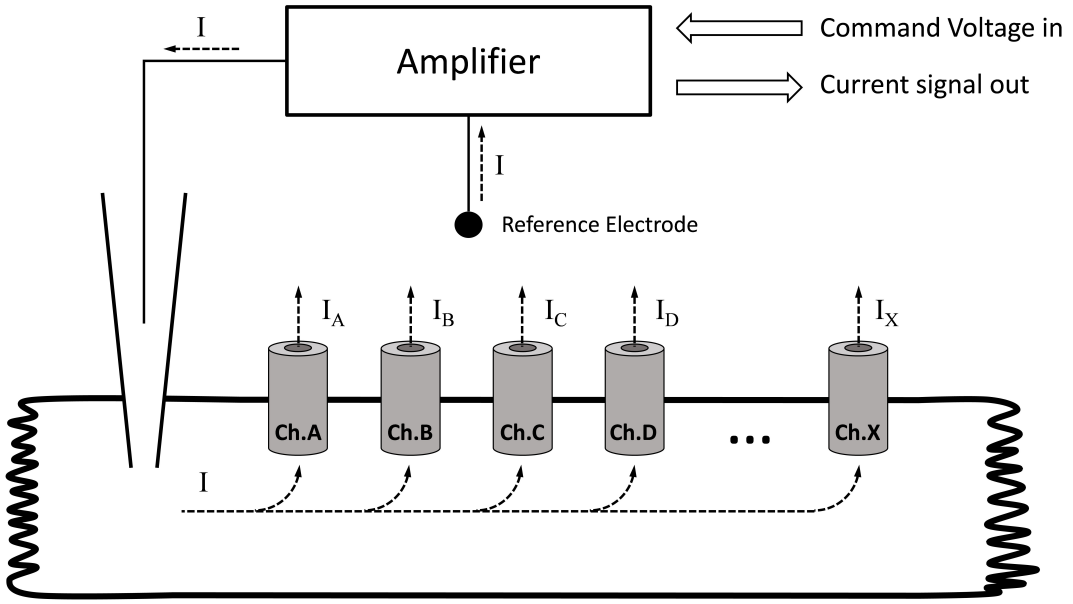

FIGURE 1 | Recording the membrane current with the single electrode (discontinuous) voltage clamp technique. Ch.A, Ch.B, . . . Ch.X indicate different channel types in the membrane. The amplifier measures the total current passing through the membrane. If the membrane contains different channels, the current measured by the amplifier will be the sum of the individual currents. If the goal is to determine the current generated by a single channel type, all other channels must be turned off.

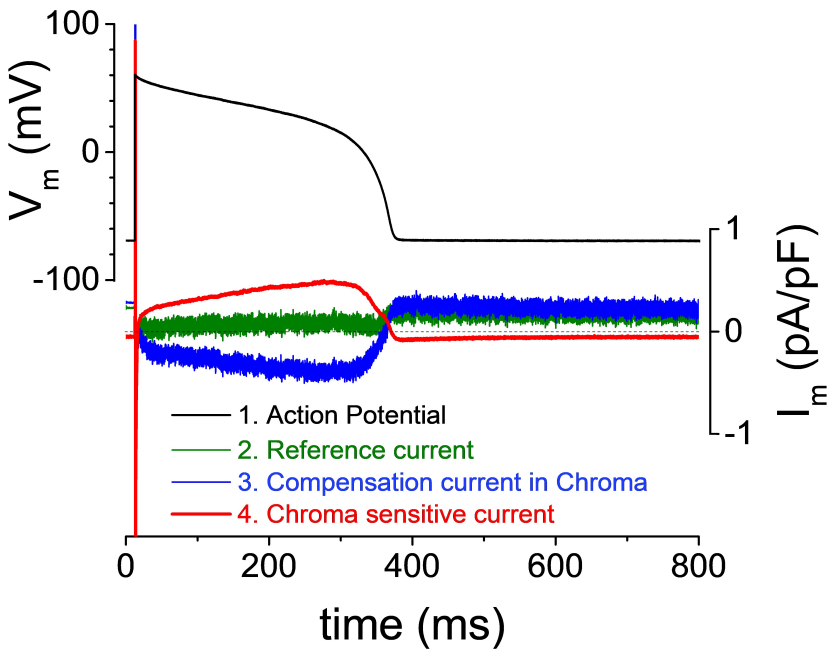

FIGURE 2 | Self-action potential clamp recording of an ion current. The cell's action potential (depicted in black) is used as command voltage. The reference current (depicted in green) is recorded immediately after steady state was achieved. After the application of Chroma (Chromanol-293B), I_{Ks} was blocked, and the compensation current (depicted in blue) was provided by the amplifier. The Chroma-sensitive current (depicted in red) was obtained by subtraction of the compensation current from the reference current.

in their publications and defined an essential criterion for the technique: "To produce the most accurate reproduction of this AP, the voltage clamp currents must include no contributions due to ineffective space clamp" (Starzak and Starzak, 1978).

Attempts to record ion currents directly during the AP can be traced back to the early 1970s. Bezanilla et al. (1970) published the first method in 1970 to record membrane conductance during AP in the squid axon. The cell was stimulated by a brief

current pulse, and then, the AP was allowed to develop in the current clamp mode. At the required point, the amplifier was switched to the voltage clamp mode in less than 10 μs and the current-voltage relationship of the membrane was determined. The instantaneous current-voltage relationship made it possible to obtain a good estimate of the sodium and potassium conductance at different points of the AP. The technique was adapted and improved by several followers, and at present, it is termed a discontinuous single-electrode voltage clamp (dSEVC) (Brennecke and Lindemann, 1971, 1974; Wilson and Goldner, 1975; Merickel, 1980).

Another approach employed two recording electrodes but not prerecorded AP (Jackson et al., 1982; Fischmeister et al., 1984; Mazzanti and DeFelice, 1987). The first electrode penetrated the membrane and accessed the interior of the cell; this electrode recorded the membrane potential in the current clamp mode. The other electrode was sealed to the membrane surface and recorded the current passing through the membrane patch under the tip in the voltage clamp mode. The high access resistance prevented clamping the whole cell. The cell can be stimulated *via* the voltage recording electrode, and the cell produces the AP in the "free running mode." The measured voltage served as the input voltage value for the second electrode. The method has two important limitations. First, the patch under the current recording electrode has usually a few ion channels. Second, the natural instability of the AP parameters increases the variability of the recorded current.

A big breakthrough came in 1989 with two pioneering publications from two independent teams. Doerr et al. used digitized AP in spontaneously beating rabbit sinoatrial node cells as command voltage and recorded the compensation current (Doerr et al., 1989). Similar experiments were conducted by de Haas and Vogel (1989) in single nerve fibers of *Xenopus laevis*. Specific channel blockers and current subtraction were used to dissect the current of interest during AP in both works. These publications reported the first current profiles obtained with direct recording during AP. The method gained popularity in a short time and grew into a valuable tool for mapping the ion currents that shape AP in various cells types including the cardiac myocytes (Doerr et al., 1990; Bouchard et al., 1995), neurons (Barra, 1996), and plant cells (Thiel, 2004). The subtraction method is used with various command pulses including rectangular steps or ramps especially to isolate small currents (Wagner et al., 2006; Maltsev and Kyle, 2009; Ton et al., 2021). Combined with fluorescent techniques, the AP clamp method became a powerful tool for studying the Ca^{2+} dynamics in cardiac myocytes (Arreola et al., 1991; Grantham and Cannell, 1996; Puglisi et al., 1999).

For a long time, the AP clamp was used to record only one single current from one cell. In this respect, it did not differ from the traditional voltage clamp method. Limitation resulted from the fact that in AP clamp experiments, the stability of the AP is judged by the flatness of the reference current after the seal is established. If the compensation current is not a flat, horizontal line, this is the indication that no steady state is reached, and the cell is not stable. Deviation of the current from the zero level to either positive or negative direction ("bumps" or "pits") results from changing the current magnitude during the AP. For a long time, nobody attempted to apply a second or third channel inhibitor upon the cell after the development of the effect of the first drug. The first report using multiple channel inhibitors in a sequential manner to record multiple currents in the same cell was published in 2011. The new method, named as "sequential dissection technique," added only one innovative idea to the regular AP clamp method: multiple channel inhibitors were applied cumulatively, and the compensation current, recorded after the development of the effect of a channel inhibitor, was used as a reference current for the next compensation current (Banyasz et al., 2011). Hypothetically, this new advancement allowed the experimenter to determine all current during the AP, assuming that each current has a specific inhibitor.

VARIANTS OF THE ACTION POTENTIAL CLAMP TECHNIQUE

Several variations of the AP clamp technique are used in various labs these days. These variants employ different modifications in order to circumvent technical limitations or extend certain capacities of the method. Discussing all possible modifications within one single article would be an overambitious aim leading to the loss of the focus of our article; therefore, we restricted ourselves to outline the main variants only.

USING SELF-ACTION POTENTIAL, CANONICAL ACTION POTENTIAL, OR MODIFIED ACTION POTENTIAL AS COMMAND

Individual cells display distinctive APs with some degree of cell-to-cell variations. The selection of the AP influences the current profiles obtained in the experiments. Using the cell's own AP is an obvious choice resulting in a decent, flat reference current in the first phase of experiments. This method is referred to as the self-AP clamp technique (^{Self}AP clamp) (Hegyi et al., 2020). The essence of this technique is to maintain the cell's own steady-state AP by satisfying the following requirements. First, the physiological ionic composition is used in both internal and external solutions containing no exogenous calcium buffer. Second, the cell is paced sufficiently long at a constant rate to stabilize AP prior to the current recording. These two conditions maintain the natural flow of ion currents and calcium cycling. Therefore, the recorded currents reflect the natural profile of the currents during the AP of the actual cell patched. The leading disadvantage of the self-AP clamp originates from the cell-to-cell variation. The AP parameters (e.g., length and plateau height) show considerable cell-to-cell variation that translates to increased variability of the currents due to the high-voltage sensitivity of the activation and inactivation of the ion channels. For instance, a few millivolt elevation of the plateau height was reported to increase potassium currents substantially in canine ventricular myocytes (Horvath et al., 2006). Another disadvantage results from using

pipette solution that mimics the physiological intracellular ionic milieu. Traditionally, ethylene glycol-*bis*(β-aminoethyl ether)-*N*,*N*,*N*',*N*'-tetraacetic acid (EGTA) is added to the internal solution to buffer calcium in voltage clamp experiments. Buffering cytosolic calcium eliminates the contraction of the cell, increasing the lifetime of the seal. Using "physiological" internal solutions without calcium buffer leave the cell's calcium cycling intact, and the cell will develop regular contractions during the experiment.

Using canonical (i.e., "typical," "average," and "standardized") AP can prevent the error introduced by the cell-to-cell fluctuation and offers reduced variability for the recorded current (Hezso et al., 2021; Horváth et al., 2021). An undesirable consequence of using canonical AP is that the reference current is not a flat line. Thus, it is challenging to judge the stability of the AP after the seal is established. Rundown of currents or other types of electric instabilities of the cell causes growing deflection or hump on the reference current. These changes are easier to recognize when the reference current is a straight line, like in the case of the self-AP clamp.

Modified APs can be used for various reasons in AP clamp experiments. One possible reason for using modified AP is to circumvent technical difficulties, like possible conflict between the resolution of the recording and voltage clamp fidelity. When small currents (<1 nA), like I_{Ks} or I_{Kr}, are recorded in the cardiac cells, it is practical to set the amplifier gain high in order to increase the resolution and record fine details of the current profile. Unfortunately, increasing the gain reduces the maximum output current of the amplifier. Therefore, high gain increases the chance to lose voltage control during the upstroke of the AP where sodium current may exceed 100 nA. The consequences are serious because the membrane voltage is uncertain until the control is not regained. There are two equally poor options here. If the amplifier gain is kept high, the resolution is maintained, but the clamp would be lost at the beginning of the AP. If the gain is set low, the voltage control is maintained, but the resolution of the recorded current is poor. The solution could make use of modified AP with a short, depolarizing voltage step (10 ms, −30 mV) prior to the upstroke. This depolarizing step can inactivate the voltage-activated sodium channels allowing the amplifier to maintain voltage control during the whole AP (Varro et al., 2000). Custom-tailored APs with modified length, plateau height, or diastolic interval can also be used to study the dynamics of ion currents that shape AP (Rocchetti et al., 2001).

DYNAMIC CLAMP

A unique variant of the AP clamp method is the dynamic clamp, where the AP command for the voltage-clamped cell (Cell 1) is obtained from a current clamped cell (Cell 2) or mathematical model (Berecki et al., 2005; Meijer van Putten et al., 2015). Then, the current recorded in Cell 1 is fed back to Cell 2 (or the mathematical model), so it can modify the morphology of the original AP. In this configuration, the two systems (cells) are in dynamic connection and real-time coupling. The dynamic clamp technique provides a powerful tool for studying the dynamic interaction between a current and the AP. For example, Mahajan et al. used the dynamic clamp method to investigate the Ca^{2+} modulation of ionic currents during AP in the cardiac myocyte (Mahajan et al., 2008). First, they eliminated Ca^{2+} cycling by depleting the sarcoplasmic reticulum, and the calcium transient was supplied by a mathematical model. The data were fed into the AP-clamped cell, and they recorded the L-type calcium current. Using this technique, they could explore the interaction between the calcium transient and L-type calcium current during AP. The greatest advantage of the dynamic clamp method is that the AP obtained from the current-clamped cell or mathematical model can be manipulated, and the interaction between the currents and the voltage profile can be studied. Furthermore, it can be determined how different ion currents communicate *via* the voltage during AP.

SEQUENTIAL DISSECTION ACTION POTENTIAL CLAMP OR "ONION-PEELING" TECHNIQUE

This further developed version of the self-AP technique allows the recording of multiple ion currents from the same cell (Banyasz et al., 2011, 2014; Horvath et al., 2013). Before the current recordings, the cell's AP is recorded under the current clamp condition. This AP is used during the whole experiment as the command voltage. Then, the reference current is recorded, and the first channel blocker is applied. Following the development of the drug effect, the compensation current is recorded. In a regular self-AP clamp measurement, the experiment is finished and the cell is discarded. Using the onion-peeling technique, the experiment is continued with the next channel blocker added upon the first blocker. After the development of the effect, the compensation current is recorded again. The cumulative application of the channel blockers can be continued *ad libitum*. During the data processing, any current can be determined by the subtraction of the compensation current recorded under the effect of its blocker from the previously recorded compensation current. Hypothetically (if the viability of the cell is appropriate), it is possible to record each current of the membrane during the AP. **Figure 3** shows four current traces recorded in a guinea pig cell during the AP with this method. Conventionally, these currents are referred to as drug-sensitive currents in the literature. Hence, the current dissected out with E4031 is termed "E4031-sensitive current" not I_{Kr}. The reason for this distinction is that the selectivity of pharmacological inhibitors is sometimes debated. **Table 1** lists channel inhibitors known to have sufficiently high selectivity.

The quality requirements are exceptionally high to successfully perform onion-peeling experiments. Robust cells with stable membrane potential and AP are vital. Cell isolation is basically the same as in other single cell methods, but the storage media should mimic the physiological milieu. If any media with non-physiological ionic composition are used during the cell isolation, the exposition time should be minimized. The pH and osmolarity of the solution must be tightly controlled, and using membrane-permeable buffers is known to increase

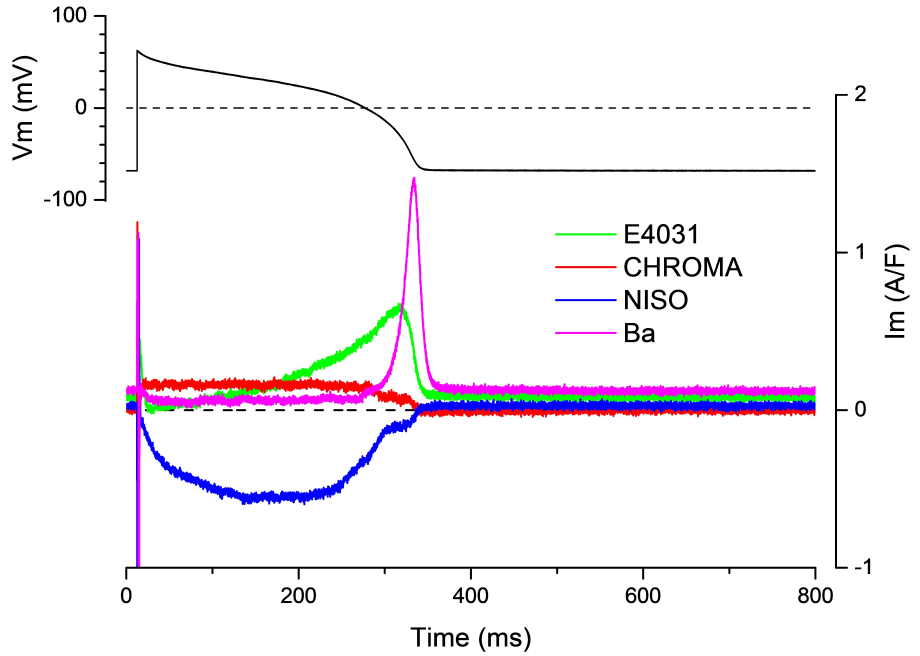

FIGURE 3 | Onion-peeling recording of multiple currents in the guinea pig ventricular myocyte. Representative current set.

the robustness of the cells. The pipette solution used in these experiments should mimic the intracellular ionic milieu of the cell. Pipette resistance and noise should be kept low. Since the pipette solution contains no exogenous calcium buffer, each AP evokes contraction of the cell; hence, the seal must be sufficiently stable to survive hundreds of contractions during the experiment. The instrumentation (i.e., A/D converter and stimulator) used in these experiments are basically the same as for any voltage clamp setup used for recording small (<1 nA) currents. A good external square wave/pulse generator is very useful in these experiments. Although most electrophysiology software offers the option of stimulating the cell with a rectangular pulse in current-clamp mode, adjustment of stimulation parameters is complicated. Old-fashioned external square pulse generators usually have control knobs that allow the experimenter to adjust any parameters without interrupting the actual experimental protocol.

THE POTENTIAL OF ACTION POTENTIAL CLAMP TECHNIQUE IN INTEGRATIVE PHYSIOLOGY

Cardiac arrhythmias are the primary cause of death in the developed world. Pathological conditions that serve as a substrate for arrhythmias are consequences of complex changes in ion channels/transporters and calcium handling molecule function. The dysfunction of these systems leads to alteration of one or more membrane currents causing abnormal AP generation with resultant arrhythmias. To understand how altered membrane currents with the deformed AP cause pathological rhythm generation, one needs to understand the interaction of the individual ion currents during the AP. The traditional approach to achieve this goal was combining voltage clamp experiments with mathematical modeling. Choosing this method inherently assumes that it is possible to determine the sufficient number of parameters with the required accuracy with rectangular command voltages for each ion current to successfully reconstruct the AP with computer model. Since the parameters of the individual currents are obtained in different experiments, *post hoc* adjustment/optimization is often needed during the model construction. The AP clamp technique determines the current profile directly during the AP without later adjustment of the obtained data.

PHARMACOLOGICAL APPLICATION: IDENTIFYING THE TARGET(S) OF UNKNOWN DRUGS

Each ionic current has a characteristic profile/trajectory during AP termed as fingerprint. The AP clamp technique is suitable for economic screening of new drugs with unknown target(s). After having all ion currents mapped, the suspected drug-sensitive current can be identified in a single AP clamp experiment (Szabo et al., 2008; Szentandrassy et al., 2011). Analyzing the profile of the drug-sensitive current recorded with the AP clamp can give a clue toward the identity of currents that might be affected by the drug. Prescreening a drug with an unknown effect prior to systematic pharmacological tests can save valuable time. Effects of receptor agonists/antagonist or hormones can also be readily screened with the AP clamp. Even in the case when an agonist/antagonist affects only one population of receptors,

TABLE 1 | Specific inhibitors for the major ionic currents in cardiac cells.

Ion Channel and transporter	Inhibitor	Effective concentration	References
I_{Na}	TTX	1–10 μM	Yuill et al., 2000; Chorvatova et al., 2004
$I_{Na-Late}$	Ranolazine	10 μM	Rajamani et al., 2009
$I_{Na-Late}$	Eleclazine (GS-6615)	10 μM	Rajamani et al., 2016
$I_{Na-Late}$	GS-967	1 μM	Potet et al., 2020
I_{Ca-L}	Nifedipine	1 μM	Horiba et al., 2008
I_{Ca-L}	Nisoldipine	0.1 μM	Banyasz et al., 2003
I_{Ca-T}	NNC 55-0396		Huang et al., 2004
I_{Ca-T}	R(-)efodipine		Tanaka et al., 2004
I_{NCX}	SEA0400	3 μM	Birinyi et al., 2005; Ozdemir et al., 2008
I_{to}	4-aminopyridine	1 mM	Patel and Campbell, 2005; Banyasz et al., 2007
I_{kr}	E4031	1 μM	Varro et al., 2000; Banyasz et al., 2007
I_{ks}	HMR-1556	30 nM	Gögelein et al., 2000; Thomas et al., 2003
I_{ks}	Chromanol-293B	1–10 μM	Yamada et al., 2008
I_{k1}	$BaCl_2$	50 μM	Banyasz et al., 2007; Banyasz et al., 2008
I_{K-Ca}	Apamin	100 pM, 1 nM	Xu et al., 2003; Ozgen et al., 2007
I_{Cl-Ca}	Niflumic acid	50 μM	Greenwood and Leblanc, 2007; Saleh et al., 2007
I_{Cl-Ca}	N-(p-amylcinnamoyl) anthranilic acid	5 μM	Gwanyanya et al., 2010
$I_{Cl-small}$	Chlorotoxin		Borg et al., 2007
I_{Cl-vol}	Tamoxifen		Borg et al., 2007
$I_{Cl,ligand}$	Picrotoxin		Etter et al., 1999

signal transduction pathways often couple to more than one ionic current; the AP clamp is uniquely suited for studying the drug concentration-dependent effects on multiple currents. As example, the frequency-dependent effects of isoproterenol on $I_{Ca,L}$, I_{Ks}, and I_{Cl} in guinea pig ventricular cells (Rocchetti et al., 2006) and the effects of acetylcholine and adenosine on I_{K1} in ferret cardiac myocytes (Dobrzynski et al., 2002) were clarified using the AP clamp technique.

REGIONAL DIFFERENCES WITHIN THE HEART/STUDY OF THE INDIVIDUAL CELL ELECTROPHYSIOLOGY

Action potential morphology has long been known to have characteristic regional differences within the heart. Apico-basal and transmural differences in AP morphology were demonstrated in several species (Banyasz et al., 2003; Szentadrassy et al., 2005). This inhomogeneity results from varying current densities in the different regions. When L-type calcium currents $I_{Ca,L}$ of epicardial and endocardial cells were compared with the traditional (i.e., rectangular pulse) voltage clamp technique, the voltage dependence, activation, and inactivation kinetics of the currents were found not statistically different. Interestingly, when the profile of $I_{Ca,L}$ was determined as nisoldipine-sensitive current with the AP clamp technique, marked differences were observed between epicardial and endocardial cells (Banyasz et al., 2003). $I_{Ca,L}$ exhibited a sharp spike followed by a rapid decay in both endocardial and epicardial canine ventricular cells following the upstroke of the AP. Following the spike, a hump developed on the $I_{Ca,L}$ was recorded in epicardial but not in endocardial cells. This hump, or second peak, arose following the deepest point of the incisura and reached its maximum during the crest of the dome. The amplitude of the first peak was greater in endocardial than in epicardial cells, and the amplitude of the second peak was smaller than the first one. No sustained current was recorded during the plateau in endocardial cells, in contrast to the slowly declining but non-zero current flowing during the dome of epicardial myocytes. There was a tight correlation between the parameters of AP and $I_{Ca,L}$, indicating that the development of the AP dome and the second $I_{Ca,L}$ peak are coupled tightly. This suggests that the second peak on $I_{Ca,L}$ may provide the depolarizing current responsible for the formation of the dome under physiological and development of EADs under pathological circumstances. The second activation of $I_{Ca,L}$ is also clearly demonstrated by the current-voltage relationship, obtained under AP clamp conditions. Essentially, similar results were obtained in ventricular myocytes dispersed from healthy human hearts (Fulop et al., 2004). This double-peaked performance of $I_{Ca,L}$ in epicardial canine and human ventricular cells and the relationship between the profile of AP and $I_{Ca,L}$ can be demonstrated exclusively under AP clamp conditions but not with the traditional voltage clamp method. Furthermore, these data established the first time direct connection between the trajectory of a membrane current and the AP.

Regional differences are not the only electrophysiological inhomogeneity within the myocardium. It has been widely known that cell-to-cell variations exist within small regions of the myocardium. Traditional voltage clamp studies investigate one current from any one cell and different current from different cell. Then, averaged data from multiple cells are used to construct canonical AP models. Nonetheless, the averaged canonical AP model may not reflect the behavior of all cells due to cell-to-cell variability (Marder and Taylor, 2011; Pathmanathan et al., 2019). It has been evident that discrepancies exist between model simulations, and the AP clamp measured current and model simulations still fail to reproduce some of the AP dynamics including EAD, adaptation, and restitution (Faber et al., 2007; Mahajan et al., 2008; Pasek et al., 2008; Decker et al., 2009; Banyasz et al., 2011). It is the unique potential of the onion-peeling technique that it can record the currents during individual AP providing input data accurate and realistic models allowing to study the interaction of currents in individual cells.

The onion-peeling technique allows to correlate AP parameters with membrane currents. In an earlier study, our team studied the membrane currents during the AP in guinea

pig ventricular myocytes (Banyasz et al., 2011). Four currents, namely, nisoldipine-sensitive current, Chromanol-293B-sensitive current, E4031-sensitive current, and Ba^{2+}-sensitive current, were recorded. Cardinal parameters of the current traces (i.e., peak amplitude, time to peak, and charge movement) were analyzed and compared. Analysis results showed that some cells had large current density for all four currents recorded, while others had small ones. The values span a wide range; for example, the ratio of the largest and smallest nisoldipine-sensitive current was higher than 10. The difference could not result from the cell size because all current magnitudes were normalized to cell capacitance. Data showed that cells exhibiting large inward currents also had large potassium currents. The statistical analysis revealed linear correlation between the inward going charge carried by Ca^{2+} and the outward moving charge carried by the sum of potassium currents during the AP. Interestingly, the AP parameters (i.e., length and plateau height) showed no correlation with the current magnitudes or the moving charge. These data provide the first observations to demonstrate that either large or small currents can generate similar APs as long as the inward going and outward going currents counterbalance each other in the cell. The possibility to measure multiple currents from the same cell has revealed hitherto unknown and unexpected characteristics of the ionic currents in myocardial cells. First, within a single cell, large outward current/charge movement is matched with large inward current/charge movement and vice versa; hence, the magnitudes of the depolarizing and repolarizing currents seem to be coordinated in such a way as to produce canonical AP, as seen in healthy guinea pig ventricular myocytes in this study. Second, there exists large variation in the current/charge movements between cells. These two findings suggest a more pluralistic view of cardiac cells. The magnitude of ionic currents can vary widely between cells, but the relative strength of the depolarizing and repolarizing currents is somehow constrained within a cell to produce similar APs. Variation and coordination of ionic currents in cardiac myocytes should have a significant impact on the AP and play important roles in arrhythmias.

COORDINATION OF MEMBRANE CURRENTS

Cardiac membrane currents are differentially modulated by various control mechanisms including sympathetic stimulation or humoral factors. Thus, the relative contribution of the individual currents to the AP may change during cardiac adaptation. The onion-peeling technique is a feasible method to study the changing balance among membrane currents in various conditions. For example, there is a consensus on that I_{Kr} and I_{K1} are the two chief repolarizing currents in the ventricular myocyte; the contribution of I_{Ks} to repolarization is minor. β-adrenergic stimulation is known to facilitate these currents in different extent. I_{Ks} is reported to be very sensitive to β-adrenergic stimulation; the sensitivity of the other two currents is less. In all previous studies, however, each potassium current was recorded from different cells and using different voltage clamp protocols. Thus, it remains unknown how β-adrenergic stimulation coordinately regulates these current in the same cell during AP. Previous experiments could not answer the question how β-stimulation changes the relative contribution of each potassium current to the repolarization reserve. Such knowledge is essential for designing antiarrhythmic strategies involving potassium channel blockers. Using the onion-peeling method, it became possible to measure and analyze the proportion of different potassium currents in the same cell during the AP in control condition and following β-stimulation (Banyasz et al., 2014). According to the data obtained, isoproterenol greatly increased I_{Ks}, making it to the most powerful repolarizing current in guinea pig cardiac myocytes. I_{Kr} was insensitive to isoproterenol, so its contribution to the repolarizing reserve was reduced. At high isoproterenol concentrations, the contribution of I_{Ks} surpassed the I_{Kr} contribution by 4- to 5-folds. The I_{K1} magnitude was marginally increased, but its relative contribution was unaltered. Previously, the contribution of different potassium current to the cell's repolarization power has been a subject of debate. The onion-peeling method can provide accurate measure to characterize the coordination of the three potassium current during the AP.

The onion-peeling technique was used to explore the coordination between inward and outward currents in a recently published work by Hegyi et al. (2020). Four inward currents and six outward currents were recorded and analyzed in rabbit and porcine ventricular cells. The authors demonstrated that the I_{Kr} and the late sodium current ($I_{Na,L}$) counterbalance each other during the ventricular AP. That is, robust linear correlation was found between the peak amplitude and the total moving charge of these two currents under various conditions. The correlation was present in young and old control animals and in a heart failure model as well. The correlation between these two currents was demonstrated after prolongation of the AP with anemone toxin II too. Additionally, the authors reported a strong correlation between the length of the AP and the current parameters (i.e., peak density and total charge movement). These correlations should be considered when building *in silico* AP models. Recently, Pathmanathan et al. (2019) demonstrated that correctly accounting for these types of correlations may be the key to successful uncertainty quantification when evaluating computational models.

CONCLUDING REMARKS

This review summarizes the development of the voltage clamp technique from the traditional version that applies rectangular command to the onion-peeling method. These new techniques widen the opportunities for exploring the function of individual ion channels as well as the coordination of membrane currents during AP. The onion-peeling technique is exceptionally suited for studying the interplay among the currents; thus, it has a unique potential in integrative physiology. It was developed for cardiac myocytes but can be adapted to the skeletal muscle or smooth muscle cells, neurons, and any excitable cell type where ionic currents and AP control cell function.

AUTHOR CONTRIBUTIONS

BH, NS, CD, ZK, PN, YC-I, and LI contributed to conception and design of the work, literature search, and review of the text. TB contributed to conception and design of the work, literature search, drafting, writing, and figure design and drawing. All authors contributed to the article and approved the submitted version.

FUNDING

This work was funded by the UD Faculty of Medicine Bridging Found to TB and the National Research Development and Innovation Office (NKFIH-K115397 to PN and NS; NKFIH-K138090 to CD, PN, and NS; and NKFIH-FK128116 to BH). Further support was provided by GINOP-2.3.2-15-2016-00040 and EFOP-3.6.2-16-2017-00006 (to PN), which are co-financed by the European Union and the European Regional Development Fund. Support was also obtained from the Thematic Excellence Program of the Ministry for Innovation and Technology in Hungary (TKP-2020-NKA-04) within the framework of the Space Sciences thematic program of the University of Debrecen. CD was supported by the EFOP-3.6.3-VEKOP-16-2017-00009 project co-financed by the EU and the European Social Fund and by the ÚNKP-21-3 New National Excellence Program of the Ministry for Innovation and Technology from the National Research Development and Innovation Fund. Funding sources had no involvement in the preparation of the article; in the study design; in the collection, analysis, and interpretation of data; in writing of the report; or in the decision to submit the article for publication.

REFERENCES

Arreola, J., Dirksen, R. T., Shieh, R. C., Williford, D. J., and Sheu, S. S. (1991). CA2+current and ca2 + transients under action-potential clamp in guinea-pig ventricular myocytes. *Am. J. Physiol. Cell Physiol.* 261, C393–C397. doi: 10.1152/ajpcell.1991.261.2.C393

Banyasz, T., Fulop, L., Magyar, J., Szentandrassy, N., Varro, A., and Nanasi, P. (2003). Endocardial versus epicardial differences in L-type calcium current in canine ventricular myocytes studied by action potential voltage clamp. *Cardiovasc. Res.* 58, 66–75. doi: 10.1016/s0008-6363(02)00853-2

Banyasz, T., Horvath, B., Jian, Z., Lzu, L. T., and Chen-Izu, Y. (2011). Sequential dissection of multiple ionic currents in single cardiac myocytes under action potential-clamp. *J. Mol. Cell. Cardiol.* 50, 578–581. doi: 10.1016/j.yjmcc.2010.12.020

Banyasz, T., Jian, Z., Horvath, B., Khabbaz, S., Izu, L. T., and Chen-Izu, Y. (2014). Beta-adrenergic stimulation reverses the I-Kr-I-Ks dominant pattern during cardiac action potential. *Pflug. Arch. Europ. J. Physiol.* 466, 2067–2076. doi: 10.1007/s00424-014-1465-7

Banyasz, T., Lozinskiy, I., Payne, C. E., Edelmann, S., Norton, B., Chen, B., et al. (2008). Transformation of adult rat cardiac myocytes in primary culture. *Exp. Physiol.* 93, 370–382. doi: 10.1113/expphysiol.2007.040659

Banyasz, T., Magyar, J., Szentandrassy, N., Horvath, B., Birinyi, P., Szentmiklosi, J., et al. (2007). Action potential clamp fingerprints of K + currents in canine cardiomyocytes: their role in ventricular repolarization. *Acta Physiol.* 190, 189–198. doi: 10.1111/j.1748-1716.2007.01674.x

Barra, P. F. A. (1996). Ionic Currents during the Action Potential in the Molluscan Neurone with the Self-Clamp Technique. *Comp. Biochem. Physiol.* 113, 185–194.

Bastian, J., and Nakajima, S. (1974). Action potential in the transverse tubules and its role in the activation of skeletal muscle. *J. General Physiol.* 63, 257–278. doi: 10.1085/jgp.63.2.257

Berecki, G., Zegers, J. G., Verkerk, A. O., Bhuiyan, Z. A., de Jonge, B., Veldkamp, M. W., et al. (2005). HERG channel (dys)function revealed by dynamic action potential clamp technique. *Biophys. J.* 88, 566–578. doi: 10.1529/biophysj.104.047290

Bezanilla, F., Rojas, E., and Taylor, R. E. (1970). Sodium and potassium conductance changes during a membrane action potential. *J. Physiol.* 211, 729–751. doi: 10.1113/jphysiol.1970.sp009301

Birinyi, P., Acsai, K., Banyasz, T., Toth, A., Horvath, B., Virag, L., et al. (2005). Effects of SEA0400 and KB-R7943 on Na + /Ca2 + exchange current and L-type Ca2 + current in canine ventricular cardiomyocytes. *Naunyn Schmiedeb. Archiv. Pharmacol.* 372, 63–70. doi: 10.1007/s00210-005-1079-x

Bondarenko, V. E., Szigeti, G. P., Bett, G. C. L., Kim, S. J., and Rasmusson, R. L. (2004). Computer model of action potential of mouse ventricular myocytes. *Am. J. Physiol. Heart Circulat. Physiol.* 287, H1378–H1403.

Borg, J. J., Hancox, J. C., Zhang, H., Spencer, C. I., Li, H., and Kozlowski, R. Z. (2007). Differential pharmacology of the cardiac anionic background current I(AB). *Europ. J. Pharmacol.* 569, 163–170. doi: 10.1016/j.ejphar.2007.05.012

Bouchard, R. A., Clark, R. B., and Giles, W. R. (1995). Effects of Action Potential Duration on Excitation-Contraction Coupling in Rat Ventricular Myocytes. *Circulat. Res.* 76, 790–801. doi: 10.1161/01.res.76.5.790

Brennecke, R., and Lindemann, B. (1971). A chopped-current clamp for current injection and recording of membrane polarization with single electrodes of changing resistance. *TITJ Life Sci.* 1, 53–58.

Brennecke, R., and Lindemann, B. (1974). Theory of a membrane-voltage clamp with discontinuous feedback through a pulsed current clamp. *Rev. Scient. Instrum.* 45, 184–188.

Chorvatova, A., Snowdon, R., Hart, G., and Hussain, M. (2004). Effects of pressure overload-induced hypertrophy on TTX-sensitive inward currents in guinea pig left ventricle. *Mol. Cell. Biochem.* 261, 217–226. doi: 10.1023/b:mcbi.0000028759.22274.cf

de Haas, V., and Vogel, W. (1989). Sodium and potassium currents recorded during an action potential. *EBJ* 17, 49–51. doi: 10.1007/BF00257145

Decker, K. F., Heijman, J., Silva, J. R., Hund, T. J., and Rudy, Y. (2009). Properties and ionic mechanisms of action potential adaptation, restitution, and accommodation in canine epicardium, American journal of physiology. *Heart Circulat. Physiol.* 296, H1017–H1026. doi: 10.1152/ajpheart.01216.2008

Dobrzynski, H., Janvier, N. C., Leach, R., Findlay, J. B., and Boyett, M. R. (2002). Effects of ACh and adenosine mediated by Kir3.1 and Kir3.4 on ferret ventricular cells, American journal of physiology. *Heart Circulat. Physiol.* 283, H615–H630. doi: 10.1152/ajpheart.00130.2002

Doerr, T., Denger, R., Doerr, A., and Trautwein, W. (1990). Ionic Currents Contributing To The Action-Potential In Single Ventricular Myocytes Of The Guinea-Pig Studied With Action-Potential Clamp. *Pflug. Arch. Europ. J. Physiol.* 416, 230–237. doi: 10.1007/BF00392058

Doerr, T., Denger, R., and Trautwein, W. (1989). Calcium Currents In Single Sa Nodal Cells Of The Rabbit Heart Studied With Action-Potential Clamp. *Pflug. Arch. Europ. J. Physiol.* 413, 599–603. doi: 10.1007/BF00581808

Etter, A. A., Cully, D. F., Liu, K. K. C., Reiss, B. T., Vassilatis, D. K., Schaeffer, J. M., et al. (1999). Picrotoxin blockade of invertebrate glutamate-gated chloride channels: subunit dependence and evidence for binding within the pore. *J. Neurochem.* 72, 318–26. doi: 10.1111/jnc.1999.72.1.318

Faber, G. M., Silva, J., Livshitz, L., and Rudy, Y. (2007). Kinetic properties of the cardiac L-type Ca2 + channel and its role in myocyte electrophysiology: a theoretical investigation. *Biophys. J.* 92, 1522–1543. doi: 10.1529/biophysj.106.088807

Fischmeister, R., Defelice, L. J., Ayer, R. K., Levi, R., and Dehaan, R. L. (1984). Channel Currents During Spontaneous Action-Potentials In Embryonic Chick Heart-Cells - The Action-Potential Patch Clamp. *Biophys. J.* 46, 267–272. doi: 10.1016/S0006-3495(84)84020-5

Fulop, L., Banyasz, T., Magyar, J., Szentandrassy, N., Varro, A., and Nanasi, P. P. (2004). Reopening of L-type calcium channels in human ventricular myocytes during applied epicardial action potentials. *Acta Physiol. Scand.* 180, 39–47. doi: 10.1046/j.0001-6772.2003.01223.x

Gögelein, H., Brüggemann, A., Gerlach, U., Brendel, J., and Busch, A. E. (2000). Inhibition of IKs channels by HMR 1556. *Naunyn Schmied. Archiv. Pharmacol.* 362, 480–488. doi: 10.1007/s002100000284

Grantham, C. J., and Cannell, M. B. (1996). Ca2 + influx during the cardiac action potential in guinea pig ventricular myocytes. *Circulat. Res.* 79, 194–200. doi: 10.1161/01.res.79.2.194

Greenwood, I. A., and Leblanc, N. (2007). Overlapping pharmacology of Ca2 + -activated Cl- and K + channels. *Trends Pharmacol. Sci.* 28, 1–5. doi: 10.1016/j.tips.2006.11.004

Gwanyanya, A., Macianskiene, R., Bito, V., Sipido, K. R., Vereecke, J., and Mubagwa, K. (2010). Inhibition of the calcium-activated chloride current in cardiac ventricular myocytes by N-(p-amylcinnamoyl)anthranilic acid (ACA). *Biochem. Biophys. Res. Commun.* 402, 531–536. doi: 10.1016/j.bbrc.2010.10.069

Hegyi, B., Chen-Izu, Y., Izu, L. T., Rajamani, S., Belardinelli, L., Bers, D. M., et al. (2020). Balance Between Rapid Delayed Rectifier K + Current and Late Na + Current on Ventricular Repolarization An Effective Antiarrhythmic Target? *Circulat. Arrhyth. Electrophysiol.* 4:13. doi: 10.1161/CIRCEP.119.008130

Hezso, T., Naveed, M., Dienes, C., Kiss, D., Prorok, J., Arpadffy-Lovas, T., et al. (2021). Mexiletine-like cellular electrophysiological effects of GS967 in canine ventricular myocardium. *Scient. Rep.* 11:9565. doi: 10.1038/s41598-021-88903-3

Horiba, M., Muto, T., Ueda, N., Opthof, T., Miwa, K., Hojo, M., et al. (2008). T-type Ca2 + channel blockers prevent cardiac cell hypertrophy through an inhibition of calcineurin-NFAT3 activation as well as L-type Ca2 + channel blockers. *Life Sci.* 82, 554–560. doi: 10.1016/j.lfs.2007.11.010

Horvath, B., Banyasz, T., Jian, Z., Hegyi, B., Kistamas, K., Nanasi, P. P., et al. (2013). Dynamics of the late Na + current during cardiac action potential and its contribution to afterdepolarizations. *J. Mol. Cell. Cardiol.* 64, 59–68. doi: 10.1016/j.yjmcc.2013.08.010

Horváth, B., Kiss, D., Dienes, C., Hézsõ, T., Kovács, Z., Szentandrássy, N., et al. (2021). Ion current profiles in canine ventricular myocytes obtained by the "onion peeling" technique. *J. Mol. Cell. Cardiol.* 158, 153–162. doi: 10.1016/j.yjmcc.2021.05.011

Horvath, B., Magyar, J., Szentandrassy, N., Birinyi, P., Nanasi, P. P., and Banyasz, T. (2006). Contribution of I-Ks to ventricular repolarization in canine myocytes. *Pflugers Arch. Europ. J. Physiol.* 452, 698–706. doi: 10.1007/s00424-006-0077-2

Huang, L., Keyser, B. M., Tagmose, T. M., Hansen, J. B., Taylor, J. T., Zhuang, H., et al. (2004). NNC 55-0396 [(1S,2S)-2-(2-(N-[(3-benzimidazol-2-yl)propyl]-N-methylamino)ethyl)-6-fluoro-1,2,3,4-tetrahydro-1-isopropyl-2-naphtyl cyclopropanecarboxylate dihydrochloride]: a new selective inhibitor of T-type calcium channels. *J. Pharmacol. Exp. Therap.* 309, 193–199.

Jackson, M. B., Lecar, H., Brenneman, D. E., Fitzgerald, S., and Nelson, P. G. (1982). Electrical development in spinal cord cell culture. *J. Neurosc.* 2, 1052–1061. doi: 10.1523/JNEUROSCI.02-08-01052.1982

Kléber, A. G., Niggli, E., McGuigan, J. A., and Weingart, R. (2006). The early years of cellular cardiac electrophysiology and Silvio Weidmann (1921-2005). *Heart Rhythm* 3, 353–359. doi: 10.1016/j.hrthm.2005.11.017

Mahajan, A., Shiferaw, Y., Sato, D., Baher, A., Olcese, R., Xie, L.-H., et al. (2008). A rabbit ventricular action potential model replicating cardiac dynamics at rapid heart rates. *Biophys. J.* 94, 392–410. doi: 10.1529/biophysj.106.98160

Maltsev, V. A., and Kyle, J. W. (2009). Undrovinas, Late Na(+) current produced by human cardiac Na(+) channel isoform Na(v)1.5 is modulated by its beta(1) subunit. *J. Physiol. Sci.* 59, 217–225. doi: 10.1007/s12576-009-0029-7

Marder, E., and Taylor, A. L. (2011). Multiple models to capture the variability in biological neurons and networks. *Nat. Neurosci.* 14, 133–138. doi: 10.1038/nn.2735

Mazzanti, M., and DeFelice, L. J. (1987). Na channel kinetics during the spontaneous heart beat in embryonic chick ventricle cells. *Biophys. J.* 52, 95–100. doi: 10.1016/S0006-3495(87)83192-2

Meijer van Putten, R. M. E., Mengarelli, I., Guan, K., Zegers, J. G., van Ginneken, A. C., Verkerk, A. O., et al. (2015). Ion channelopathies in human induced pluripotent stem cell derived cardiomyocytes: a dynamic clamp study with virtual IK1. *Front. Physiol.* 6:7. doi: 10.3389/fphys.2015.00007

Merickel, M. (1980). Design of a single electrode voltage clamp. *J. Neurosci. Methods* 2, 87–96. doi: 10.1016/0165-0270(80)90047-3

Nakajima, S., and Bastian, J. (1974). Double sucrose-gap method applied to single muscle fiber of Xenopus laevis. *J. Gen. Physiol.* 63, 235–256. doi: 10.1085/jgp.63.2.235

Ozdemir, S., Bito, V., Holemans, P., Vinet, L., Mercadier, J. J., Varro, A., et al. (2008). Pharmacological inhibition of na/ca exchange results in increased cellular Ca2 + load attributable to the predominance of forward mode block. *Circulat. Res.* 102, 1398–1405. doi: 10.1161/CIRCRESAHA.108.173922

Ozgen, N., Dun, W., Sosunov, E. A., Anyukhovsky, E. P., Hirose, M., Duffy, H. S., et al. (2007). Early electrical remodeling in rabbit pulmonary vein results from trafficking of intracellular SK2 channels to membrane sites. *Cardiovasc. Res.* 75, 758–769. doi: 10.1016/j.cardiores.2007.05.008

Pasek, M., Simurda, J., Christe, G., and Orchard, C. H. (2008). Modelling the cardiac transverse-axial tubular system. *Progr. Biophys. Mol. Biol.* 96, 226–243. doi: 10.1016/j.pbiomolbio.2007.07.021

Patel, S. P., and Campbell, D. L. (2005). Transient outward potassium current, 'Ito', phenotypes in the mammalian left ventricle: underlying molecular, cellular and biophysical mechanisms. *J. Physiol.* 569, 7–39. doi: 10.1113/jphysiol.2005.086223

Pathmanathan, P., Cordeiro, J. M., and Gray, R. A. (2019). Comprehensive Uncertainty Quantification and Sensitivity Analysis for Cardiac Action Potential Models. *Front. Physiol.* 10:721. doi: 10.3389/fphys.2019.00721

Potet, F., Egecioglu, D. E., Burridge, P. W., and George, A. L. (2020). GS-967 and Eleclazine Block Sodium Channels in Human Induced Pluripotent Stem Cell–Derived Cardiomyocytes. *Mol. Pharmacol.* 98, 540–547. doi: 10.1124/molpharm.120.000048

Puglisi, J. L., Yuan, W. L., Bassani, J. W. M., and Bers, D. M. (1999). Ca2 + influx through Ca2 + channels in rabbit ventricular myocytes during action potential clamp - Influence of temperature. *Circulat. Res.* 85, E7–E16. doi: 10.1161/01.res.85.6.e7

Rajamani, S., El-Bizri, N., Shryock, J. C., Makielski, J. C., and Belardinelli, L. (2009). Use-dependent block of cardiac late Na + current by ranolazine. *Heart Rhythm* 6, 1625–1631. doi: 10.1016/j.hrthm.2009.07.042

Rajamani, S., Liu, G., El-Bizri, N., Guo, D., Li, C., Chen, X. L., et al. (2016). The novel late Na(+) current inhibitor, GS-6615 (eleclazine) and its anti-arrhythmic effects in rabbit isolated heart preparations. *Br. J. Pharmacol.* 173, 3088–3098. doi: 10.1111/bph.13563

Rocchetti, M., Besana, A., Gurrola, G. B., Possani, L. D., and Zaza, A. (2001). Rate dependency of delayed rectifier currents during the guinea-pig ventricular action potential. *J. Physiol. London* 534, 721–732. doi: 10.1111/j.1469-7793.2001.00721.x

Rocchetti, M., Freli, V., Perego, V., Altomare, C., Mostacciuolo, G., and Zaza, A. (2006). Rate dependency of beta-adrenergic modulation of repolarizing currents in the guinea-pig ventricle. *J. Physiol. London* 574, 183–193. doi: 10.1113/jphysiol.2006.105015

Romero, L., Carbonell, B., Trenor, B., Rodriguez, B., Saiz, J., and Ferrero, J. M. (2011). Systematic characterization of the ionic basis of rabbit cellular electrophysiology using two ventricular models. *Progr. Biophys. Mol. Biol.* 107, 60–73. doi: 10.1016/j.pbiomolbio.2011.06.012

Saleh, S. N., Angermann, J., Sones, W. R., Leblanc, N. I, and Greenwood, A. (2007). Stimulation of Ca2 + -Gated Cl- Currents by the Calcium-Dependent K + Channel Modulators NS1619 [1,3-Dihydro-1-[2-hydroxy-5-(trifluoromethyl)phenyl]-5-(trifluoromethyl)-2H-benzimidazol-2-one] and Isopimaric Acid. *J. Pharmacol. Exp. Therap.* 321, 1075–1084. doi: 10.1124/jpet.106.118786

Shannon, T. R., Wang, F., Puglisi, J., Weber, C., and Bers, D. M. (2004). A mathematical treatment of integrated Ca dynamics within the ventricular myocyte. *Biophys. J.* 87, 3351–3371. doi: 10.1529/biophysj.104.047449

Starzak, M., and Needle, M. (1983). The Action Potential Clamp as a Test of Space-Clamp Effectiveness - The Lettvin Analog Axon. *IEEE Transact. Biomed. Engin.* 30, 139–140. doi: 10.1109/tbme.1983.325212

Starzak, M. E., and Starzak, R. J. (1978). An Action Potential Clamp to Probe the Effectiveness of Space Clamp in Axons. *IEEE Transact. Biomed. Engin.* 25, 201–204. doi: 10.1109/TBME.1978.326249

Szabo, A., Szentandrassy, N., Birinyi, P., Horvath, B., Szabo, G., Banyasz, T., et al. (2008). Effects of ropivacaine on action potential configuration and ton currents in isolated canine ventricular cardiomyocytes. *Anesthesiology* 108, 693–702. doi: 10.1097/ALN.0b013e3181684b91

Szentadrassy, N., Banyasz, T., Biro, T., Szabo, G., Toth, B. I., Magyar, J., et al. (2005). Apico-basal inhomogeneity in distribution of ion channels in canine and human ventricular myocardium. *Cardiovasc. Res.* 65, 851–860. doi: 10.1016/j.cardiores.2004.11.022

Szentandrassy, N., Nagy, D., Ruzsnavszky, F., Harmati, G., Banyasz, T., Magyar, J., et al. (2011). Powerful Technique to Test Selectivity of Agents Acting on Cardiac Ion Channels: the Action Potential Voltage-Clamp. *Curr. Med. Chem.* 18, 3737–3756. doi: 10.2174/092986711796642418

Tanaka, H., Komikado, C., Shimada, H., Takeda, K., Namekata, I., Kawanishi, T., et al. (2004). The R(-)-enantiomer of efonidipine blocks T-type but not L-type calcium current in guinea pig ventricular myocardium. *J. Pharmacol. Sci.* 96, 499–501. doi: 10.1254/jphs.rcj04001x

Thiel, G. (2004). Dynamics of chloride and potassium currents during the action potential in Chara studied with action potential clamp. *Europ. Biophys. J.* 24, 85–92.

Thomas, G. P., Gerlach, U., and Antzelevitch, C. (2003). HMR 1556, a potent and selective blocker of slowly activating delayed rectifier potassium current. *J. Cardiovasc. Pharmacol.* 41, 140–147. doi: 10.1097/00005344-200301000-00018

Ton, A. T., Nguyen, W., Sweat, K., Miron, Y., Hernandez, E., Wong, T., et al. (2021). Arrhythmogenic and antiarrhythmic actions of late sustained sodium current in the adult human heart. *Scient. Rep.* 11:12014. doi: 10.1038/s41598-021-91528-1

Varro, A., Balati, B., Iost, N., Takacs, J., Virag, L., Lathrop, D. A., et al. (2000). The role of the delayed rectifier component I-Ks in dog ventricular muscle and Purkinje fibre repolarization. *J. Physiol. London* 523, 67–81. doi: 10.1111/j.1469-7793.2000.00067.x

Verkhratsky, A., and Parpura, V. (2014). History of Electrophysiology and the Patch Clamp. *Methods Mole. Biol.* 1183, 1–19. doi: 10.1007/978-1-4939-1096-0_1

Wagner, S., Dybkova, N., Rasenack, E. C. L., Jacobshagen, C., Fabritz, L., Kirchhof, P., et al. (2006). Ca2 + /calmodulin-dependent protein kinase II regulates cardiac Na + channels. *J. Clin. Investig.* 116, 3127–3138. doi: 10.1172/JCI26620

Wilson, W. A., and Goldner, M. M. (1975). Voltage clamping with a single microelectrode. *J. Neurobiol.* 6, 411–422. doi: 10.1002/neu.480060406

Xu, X. P., Salata, J. J., Wang, J. X., Wu, Y., Yan, G. X., Liu, T. X., et al. (2002). Increasing I-Ks corrects abnormal repolarization in rabbit models of acquired LQT2 and ventricular hypertrophy. *Am. J. Physiol. Heart Circulat. Physiol.* 283, H664–H670. doi: 10.1152/ajpheart.00076.2002

Xu, Y. F., Tuteja, D., Zhang, Z., Xu, D. Y., Zhang, Y., Rodriguez, J., et al. (2003). Molecular identification and functional roles of a Ca2 + -activated K + channel in human and mouse hearts. *J. Biol. Chem.* 278, 49085–49094. doi: 10.1074/jbc.M307508200

Yamada, M., Ohta, K., Niwa, A., Tsujino, N., Nakada, T., and Hirose, M. (2008). Contribution of L-type Ca(2 +) channels to early afterdepolarizations induced by I(Kr) and I(Ks) channel suppression in guinea pig ventricular myocytes. *J. Membrane Biol.* 222, 151–166. doi: 10.1007/s00232-008-9113-9

Yuill, K. H., Convery, M. K., Dooley, P. C., Doggrell, S. A., and Hancox, J. C. (2000). Effects of BDF 9198 on action potentials and ionic currents from guinea-pig isolated ventricular myocytes. *Br. J. Pharmacol.* 130, 1753–1766. doi: 10.1038/sj.bjp.0703476

Conflict of Interest: The authors declare that the research was conducted in the absence of any commercial or financial relationships that could be construed as a potential conflict of interest.

frontiers in Physiology

ORIGINAL RESEARCH
published: 22 March 2022
doi: 10.3389/fphys.2022.838593

Human Hypertension Blood Flow Model Using Fractional Calculus

Mohamed A. Bahloul[1], *Yasser Aboelkassem*[2,3]* *and Taous-Meriem Laleg-Kirati*[1,4]

[1] Computer, Electrical, and Mathematical Sciences, and Engineering Division (CEMSE), King Abdullah University of Science and Technology (KAUST), Thuwal, Saudi Arabia, [2] College of Innovation and Technology, University of Michigan, Flint, MI, United States, [3] Michigan Institute for Data Science, University of Michigan, Ann Arbor, MI, United States, [4] National Institute for Research in Digital Science and Technology (INRIA), Paris, France

The blood flow dynamics in human arteries with hypertension disease is modeled using fractional calculus. The mathematical model is constructed using five-element lumped parameter arterial Windkessel representation. Fractional-order capacitors are used to represent the elastic properties of both proximal large arteries and distal small arteries measured from the heart aortic root. The proposed fractional model offers high flexibility in characterizing the arterial complex tree network. The results illustrate the validity of the new model and the physiological interpretability of the fractional differentiation order through a set of validation using human hypertensive patients. In addition, the results show that the fractional-order modeling approach yield a great potential to improve the understanding of the structural and functional changes in the large and small arteries due to hypertension disease.

Keywords: blood flow, hypertension, vascular compliance, fractional calculus, Windkessel model

OPEN ACCESS

Edited by:
Ovidiu Constantin Baltatu, Anhembi Morumbi University, Brazil

Reviewed by:
Jean-Claude Trigeassou, Université de Bordeaux, France
Soroush Safaei, The University of Auckland, New Zealand

***Correspondence:**
Yasser Aboelkassem
yassera@umich.edu

Specialty section:
This article was submitted to Original Research Article, a section of the journal Frontiers in Physiology

Received: *18 December 2021*
Accepted: *21 February 2022*
Published: *22 March 2022*

Citation:
Bahloul MA, Aboelkassem Y and Laleg-Kirati T-M (2022) Human Hypertension Blood Flow Model Using Fractional Calculus. Front. Physiol. 13:838593. doi: 10.3389/fphys.2022.838593

1. INTRODUCTION

Cardiovascular diseases (CVDs) are the leading cause of death worldwide, responsible for more than 17.9 million deaths in 2019 that representing 32% of global mortality. This number is expected to reach 23.6 million by 2030 (Mensah et al., 2019). A key risk factor for CVDs is high blood pressure, known as hypertension. Although the reduction in hypertension can restrain the onset of CVDs, current treatments techniques are only partially effective. In fact, hypertension is considered chronic pathology that can only be regulated with medication; however, it cannot be cured definitely. The primary pathological sign of high blood pressure is reduced vascular compliance due to structural remodeling and functional modifications in the arteries. In a normotensive state, any variation of the hemodynamic induces structural and functional adaptations within the different cell types and layers of the vascular wall. However, in hypertensive states, this adaptive response does not lead to normal hemodynamic control but instead inducts irregular vascular changes, defined as, vascular remodeling (Brown et al., 2018). Several clinical studies in-patient and experimental researches have revealed the marked correlation between vascular remodeling and the pathophysiology of hypertension. In particular, they observe that the vascular remodeling in resistive arteries is firmly associated with the progression and severity of hypertension's disease. Accordingly, deep understanding and analysis of the pathological mechanisms of hypertension vascular remodeling hold high significance for diagnosing CVDs and is crucial for the clinical treatment of hypertension (Li et al., 2017).

Over the last century, various physics-driven and data-driven modeling methods and diverse numerical computational approaches have been developed to characterize vascular biomechanics and arterial hemodynamics. Commonly, these approaches involve a compromise between precision and complexity. In the open literature, the arterial hemodynamics and mechanic modeling approaches are classified into two main classes: macro and micro modeling methods. The macro-scale class is considered a low dimensional strategy that usually implicates the well-known lumped parametric, the arterial Windkessel, (Frank, 1899). Typically this class used ordinary differential equations (ODEs) to describe the arterial hemodynamic as a function of time only. Accordingly, they are commonly explored to describe the global cardiovascular functions and biomechanical properties (Shi et al., 2011; Malatos et al., 2016). This class is considered computationally simple but less accurate than the microscale models. In addition, it is less insightful in terms of physiological interpretability, (Zhou et al., 2019). On the other hand, the microscale models are generally considered more insightful as they provide a precise estimate of cardiovascular function and accurately represent local as well as global arterial biomechanical properties. These modeling approaches are considered high-dimensional paradigms [one-dimensional (1D), two-dimensional (2D), and three-dimensional (3D)] as they involve more than one dimension along with the time scale to describe the complex geometries of the arterial network. Although micro-scale-based models provide detailed information about the arterial circulatory system, their complexity is not manageable in practical medical routines, (Zhou et al., 2019).

In recent decades, fractional-order models have surfaced as potential techniques that compromise between accuracy and computational cost for large-scale problems in different fields (Bahloul and Kirati, 2021). In particular fractional-order differential equations have been considerably explored in modeling complex biological systems (Magin, 2006). Basically, fractional-order approaches allow much modeling flexibility by extending the concepts of differentiability and integrating the non-local and memory properties through the fractional differentiation order. These features enable the characterization of complex phenomena over various time and space scales without splitting the problem into smaller sub-compartments.

The versatility and flexibility of fractional-order tools lead researchers to believe that the future of computational modeling in bio-engineering and bio-informatics (Magin, 2006). This paradigm shift extends from bio-engineering in general to cardiovascular system modeling and characterization specifically, as experimental studies find that fractional-order models are more suitable and interpretable in describing the arterial structure and biomechanical response of the heart and systemic circulation. *In-vivo* and *in-vitro* investigations have pointed that fractional-order calculus-based approaches are more convenient to precisely represent the viscoelasticity properties of soft collagenous tissues in the vascular bed. A fractional-order viscoelastic model in human arterial segments has been tested and validated in (Craiem et al., 2008). Results show that the extra fractional-differentiation order parameter (α) allowed predicting complex and frequency-dependent responses similar to reported complex elastic moduli in arteries. (Craiem and Armentano, 2007; Craiem et al., 2008; Zerpa et al., 2015) revealed that fractional models should be acknowledged adequate alternatives to model arterial viscoelasticity. In addition, the fractional differentiation order (α) plays a pivotal function, and it is considered the most valuable parameter to monitor and analyze, reflecting the structural and functional changes in the arteries. Most recently, we have used fractional-order derivative to model the apparent arterial compliance dynamics. The proposed model employs fractional-order capacitor (FOC) element that combine the complex and frequency dependence characteristics of arterial compliance. The FOC modeling approach accounted for both resistive and capacitive properties allowing a reduced-order representation of the vascular compliance and stiffness (Bahloul and Kirati, 2021).

This study presents a novel fractional-order modified Windkessel model to study the blood flow in the arterial system. Fractional-order tools have been adopted to represent the dynamic relationship between blood pressure and volume in the proximal and distal sites of the arterial network. Accordingly, the model includes two fractional-order capacitors to describe the apparent vascular compliance of large arteries close to the heart and one of the resistive arteries further away from the heart as illustrated in **Figure 1C**. The proposed model has been applied and validated using two hypertension datasets acquired from human subjects. The results show the accuracy and flexibility of the proposed method in modeling the aortic blood pressure measurements while maintaining a low model complexity. In addition, the proposed fractional-order representation draws a more appropriate framework to analyze and understand hypertension behavior and its pathophysiology connection with vascular remodeling.

2. MATERIALS AND METHODS

2.1. Fractional-Order Calculus

In the last decades, non-integer differentiation, the so-called fractional-order calculus, became a popular tool for characterizing real-world physical systems and complex behaviors from various fields such as biology, control, electronics, and economics (Gutiérrez et al., 2010; Magin, 2010). The long-memory and spatial dependence phenomena inherent to the fractional-order systems present unique and attractive peculiarities that raise exciting opportunities to represent complex phenomena subject to power-law behavior accurately. For instance, the power-law behavior has been demonstrated in describing human soft tissues visco-elasticity and characterizing the elastic vascular arteries. *In-vivo* and *in-vitro* experimental studies have pointed that fractional-order calculus-based approaches are more decent to precisely represent the hemodynamic; the viscoelasticity properties of soft collagenous tissues in the vascular bed; the aortic blood dynamics (Perdikaris and Karniadakis, 2014; Zerpa et al., 2015); red blood cell (RBC) membrane mechanical properties (Craiem and Magin, 2010); and the heart valve cusp (Doehring et al.,

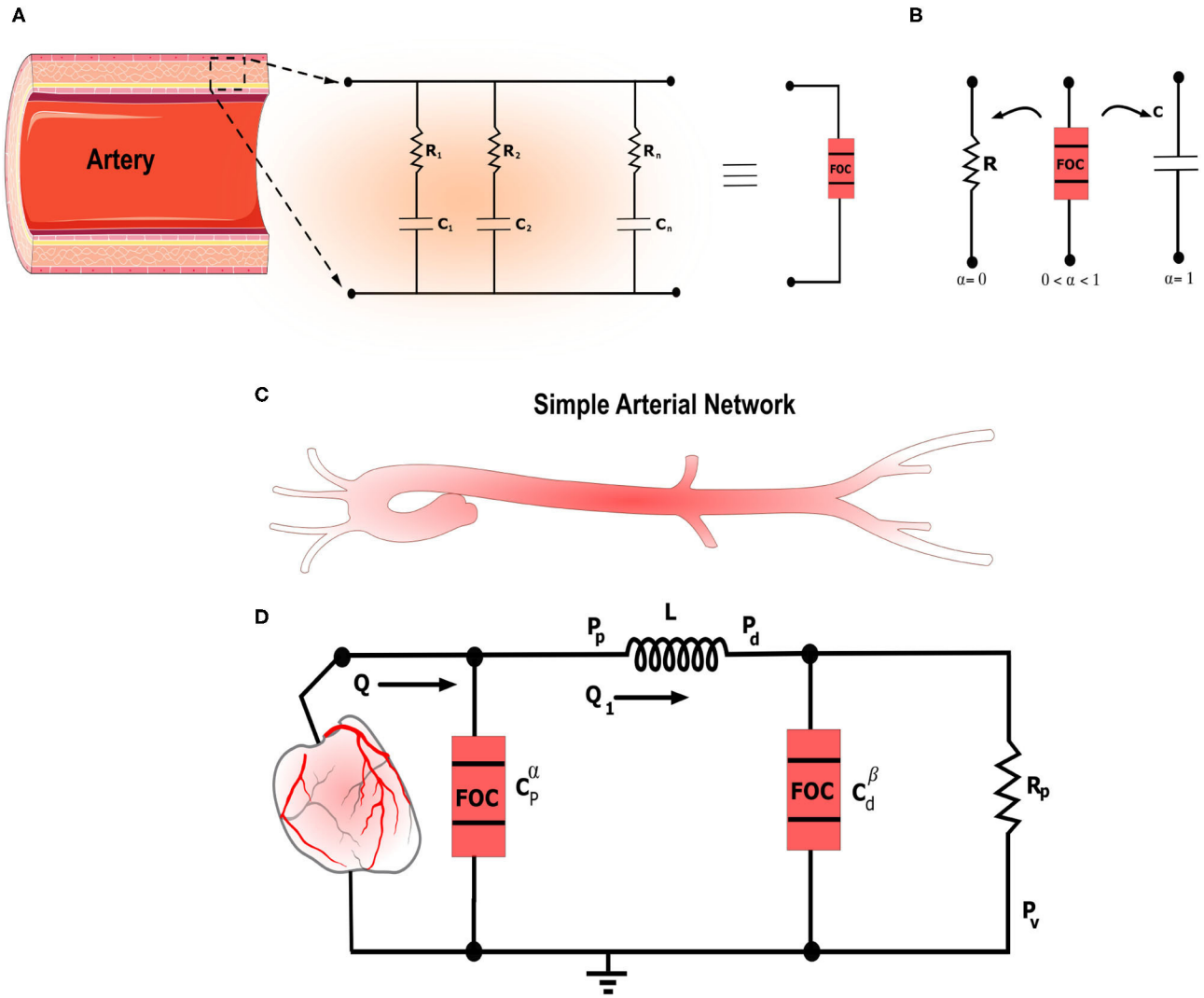

FIGURE 1 | The figure illustrates the general framework for fractional-order modeling of the arterial system in a schematic manner. **(A)** Schematic illustrating the artery along with the equivalent *RC* tree equivalent circuit of the fractional-order capacitor. **(B)** Electrical symbols of the standard resistor and capacitor and the fractional-order capacitor. $0 < \alpha < 1$ represents the fractional differentiation order. For $\alpha = 0$ and $\alpha = 1$ the fractional-order capacitor is equivalent to the standard resistor and capacitor, respectively. **(C)** Schematic that shows simplified left ventricle-aortic-arteries sub-domains. **(D)** Electrical analog of the proposed fractional-order modified Windkessel (F-MWK) model.

2005; Craiem and Armentano, 2007; Craiem et al., 2008; Zerpa et al., 2015).

The continuous fractional integro-differential operator D_t^α is defined as follows

$$D_t^\alpha = \begin{cases} \dfrac{d^\alpha}{dt^\alpha}, & \alpha > 0, \\ 1, & \alpha = 0 \\ \int_a^t (d\tau)^\alpha, & \alpha < 0 \end{cases} \tag{1}$$

where α is the fractional differential integral order.

Several definitions for fractional-order derivative exist in the literature (Podlubny, 1999), (Lorenzo and Hartley, 1998). In this work, we consider the *Grunwald-Letnikov (GL)* definition given as:

Definition 1. *(Podlubny, 1999) The Grunwald-Letnikov derivative of order α of a function f, denoted $D_t^\alpha f(t)$, is given by:*

$$D_t^\alpha f(t) = \lim_{h \to 0} \frac{1}{h^\alpha} \sum_{i=0}^{\infty} c_i^{(\alpha)} f(t - ih), \quad \alpha > 0, \tag{2}$$

where $h > 0$ is the time step, $c_i^{(\alpha)}$ $(i = 0, 1, ...)$ are the binomial coefficients recursively computed using the following formula,

$$c_0^{(\alpha)} = 1, \; c_i^{(\alpha)} = \left(1 - \frac{1+\alpha}{i}\right) c_{i-1}^{(\alpha)}. \tag{3}$$

2.2. Fractional-Order Capacitor

Fractional-order capacitor (FOC) known as the constant phase element is a fractional-order electrical element representing the fractional-order derivative through its *curent-volatge* characteristic. In fact, the relationship between the current, $i(t)$, passing through an FOC and the voltage, $v(t)$, across it with respect to time, t, can be written as follow:

$$i(t) = C_\alpha \frac{d^\alpha}{dt^\alpha} v(t), \tag{4}$$

where C_α is a proportionality constant so-called pseudo-capacitance, expressed in units of [Farad/second$^{1-\alpha}$], (Elwakil, 2010). The conventional capacitance, C, in unit of Farad is related to C_α as $C = C_\alpha \omega^{\alpha-1}$ that is frequency-dependent. The fractional-order impedance (Z_α) is expressed as follow:

$$Z_\alpha(s) = \frac{1}{C_\alpha s^\alpha} = \underbrace{\frac{1}{C_\alpha}\omega^{-\alpha}\cos(\phi)}_{Z_r} - j\underbrace{\frac{1}{C_\alpha}\omega^{\alpha}\sin(\phi)}_{Z_i}, \tag{5}$$

where s corresponds to the *Laplace* variable and ϕ denotes the phase shift expressed as: $\phi = \alpha\pi/2$ [rad] or $\phi = 90\alpha$ [degree or °]. Z_r and Z_i are the real and imaginary parts of Z_α corresponding to the resistive and capacitive portions, respectively. From (5), it is apparent that the transition between resistive and capacitive parts is ensured by α. If $0 \leq \alpha \leqslant 1$, the bounding conditions of α will corresponds to the discrete conventional elements: the resistor at $\alpha = 0$ and the ideal capacitor at $\alpha = 1$, as illustrated in **Figure 1B**. As α goes to 0, (Z_i) convergence to 0, and thus the fractional element looks like that a pure resistor, whereas as α goes to 1, (Z_r) converges to 0 and hence, the fractional element serves as a pure capacitor, (Oustaloup et al., 2000; Krishna et al., 2011; Hartley et al., 2015; Trigeassou and Maamri, 2020). **Figure 2B** represents the schematic diagram for a FOC along with the ideal resistor and capacitor. Many studies have shown that FOC is equivalent to a resistor ladder network (RC tree circuit), (Carlson and Halijak, 1964; Si et al., 2017). This structure is similar to the electrical analogy of the generalized Kelvin-Voigt viscoelastic model. **Figure 1A** presents the equivalent RC tree circuit of FOC of any order. Bearing these properties in mind, the fractional differentiation order α parameter allows extra versatility in modeling viscoelastic systems (Vastarouchas and Psychalinos, 2017).

2.3. Apparent Arterial Compliance

Arterial compliance stands for the ability of the vessel to store the blood. Functionally, it is defined as the ratio of the incremental variation in the blood volume (dV) due to an incremental variation in distending pressure (dP). Accordingly, mathematically it is expressed as: $C = dV/dP$, (Quick et al., 1998). Over the last decades, several analytical and experimental studies have focused on modeling and characterizing vascular compliance, (Chemla et al., 1998; de Simone et al., 1999; Segers et al., 1999; Stergiopulos et al., 1999; Mackenzie et al., 2002; Westerhof et al., 2009; Haluska et al., 2010; Ge, 2018; Kaya et al., 2018). With the introduction of the well-known linear Windkessel representation of the arterial system, arterial compliance was assumed to have a single constant value for the entire cardiac cycle. Hence, the transfer function relating the blood volume variation to the blood pressure input changes was also considered constant. Accordingly, the arterial compliance was modeled within the arterial lumped parameter circuit's Windkessel as an ideal capacitor whose capacitance is constant (Westerhof et al., 2009). However, this assumption was not realistic, and its drawbacks were reflected essentially in the estimation of the hemodynamic determinants (Quick et al., 2000). In fact, it does not lead to the correct evaluation of the true value of arterial compliance (Craiem and Armentano, 2003). Besides, by analyzing the transfer function blood volume/input pressure, experimental studies have shown that this relationship is frequency-dependent, and a time delay between the arterial blood volume and the input blood pressure is observed. Hence a variation in the arterial compliance along the cardiac cycle coexists (Burattini and Natalucci, 1998; Quick et al., 1998, 2000).

In order to take into account this frequency dependence, some research investigations have promoted a new configuration where they considered the viscoelastic properties of the arterial vessel and represented the arterial compliance using the so-called *Voigt-cell* configuration (Burattini and Natalucci, 1998; Aboelkassem and Virag, 2019). This type of arterial model was known as viscoelastic Windkessel. Although the viscoelastic *Voigt-cell* has resolved some contradictions of the standard elastic lumped parameter Windkessel, this configuration does also present some limitations as it does not account for the so-called stress-relaxation experiment (Burattini and Natalucci, 1998). To overcome this restriction, high-order viscoelastic configurations have been proposed by connecting many Voigt-cells as shown in **Figure 1A**. This solution might lead to an accurate estimation of arterial compliance and its feature; however, it is deemed a very complex alternative that poses extra challenges. Indeed, the number of parameters to estimate is more significant for higher-order models, while the obtained experimental data is habitually small and insufficient to identify all the parameters. It is also known that reduced-order models are more desirable for their uniformity and simplicity of investigation (Burattini and Natalucci, 1998; Bahloul and Kirati, 2019).

Bearing this in mind, recently, an alternative modeling approach of the apparent compliance was proposed in (Bahloul and Kirati, 2021) where fractional-order tools were investigated to represent the complex phenomena underlying the apparent arterial compliance. In (Bahloul and Kirati, 2021), the authors presented fractional-order models to describe the dynamic relationship between aortic blood pressure and volume, describing the apparent vascular compliance. The proposed model employs fractional-order capacitor elements to lump the complex and frequency dependence characteristics of arterial compliance. FOC combines both resistive and capacitive properties, which the fractional differentiation order, α, can control. The validations results find that the fractional-order scheme can reconstruct the overall dynamic of the complex and frequency-dependent apparent compliance dynamic and reduce the complexity.

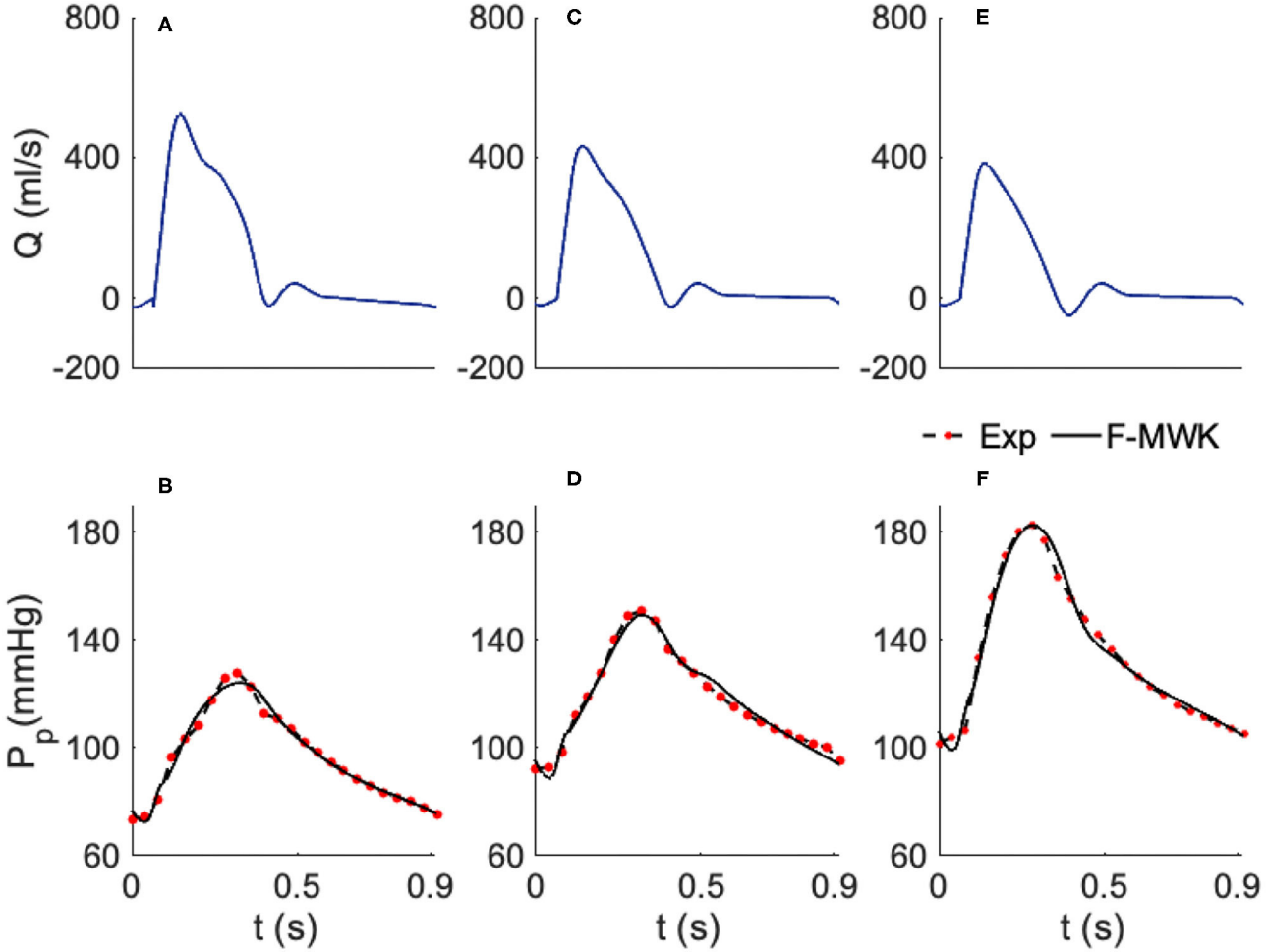

FIGURE 2 | Estimated proximal blood pressure using the proposed fractional-order modified Windkessel model along with the experimental *in-vivo* human-hypertension. **(A,C,E)** Represent the model input aortic-valve blood flow rate for each validation case of study, Pre-hypertension, Mild-hypertension, and Sever-hypertension, respectively. **(B,D,F)** Represent the pressure waveform validation results.

The vascular apparent compliance in the fractional-order domain is defined as follows:

$$Q_{stored}(t) = \frac{d^{\alpha} V}{dt^{\alpha}} = \underbrace{\frac{d^{\alpha} V(t)}{d^{\alpha} P_{in}(t)}}_{C_{app}^{\alpha}} \frac{d^{\alpha} P_{in}(t)}{dt^{\alpha}}, \tag{6}$$

where Q_{stored} is the blood stored in the arterial tree, V corresponds to the blood volume, and P_{in} is the input blood pressure.

The FOC can be an inherent lumped element that can catch vascular compliance's complex and frequency-dependent behavior. In fact, as expressed in (6), the pseudo compliance, $C_{\alpha_{app}}$, should be expressed in the unit of [ml/mmHg.sec$^{1-\alpha}$] that makes, naturally, the standard compliance (C_C), in the unit of [ml/mmHg], frequency-dependent as:

$$C_C = C_{app}^{\alpha} (j\omega)^{\alpha - 1}. \tag{7}$$

Hence, the fractional-order capacitor presents physical bases in portraying the complex and frequency dependency of the apparent vascular compliance. Besides, based on the variation of the fractional differentiation order α, the real and imaginary parts of the resultant FOC's impedance can possess various levels, so by analogy, α can control dissipative and storage mechanisms and hence the viscous and elastic component of the arterial wall. Furthermore, it is worth remarking that the equivalent circuit representation of FOC can be seen as an infinity Voigt cells branches joined in parallel. Consequently, FOC simplifies

the representation of the complex arterial network's mechanical properties by employing only two parameters (α and C_α).

2.4. Fractional-Order Modified Windkessel Model

The modified Windkessel model (MWK) is one of the simplest arterial representation that lumps the arterial network into two main compartments, proximal and distal, (Goldwyn and Watt, 1967). Taking into account that the proximal arteries close to the heart have different properties in comparison to the distal ones, MWK splits the total arterial compliance used in the original arterial Windkessel into two capacitances: C_p represents the compliance of the large arteries which are commonly elastic and C_d depicts the compliance of muscular arteries that are more stiffer. Clinical studies demonstrated that C_d is very sensitive to vasodilatory experiments, a property apparent in distal arteries. Other investigations have also shown that C_d is reduced with aging and hypertension. The latest properties make these capacitance as potential indicators of cardiovascular risk, (Francis, 2007). MWK comprises an inductor, L, between the two capacitance accounting for the inertance of the flowing blood. Also, it lumps the peripheral resistance into a resistor R_p and the venous pressure into a constant P_v. Based on the electrical analogy, the pumping heart is modeled as a pulsating current source.

In this study, we propose a general version of the MWK using fractional-order framework. We present the fractional-order modified Windkessel (F-MWK) representation as shown in **Figure 1D**. The proposed model comprises two fractional-order capacitor C_p^α and C_d^β to take into account the apparent vascular compliance of the large and small arteries, respectively. **Figure 1D** shows the schematic of F-MWK. As the proposed model contains two fractional-order storage elements and one integer-order one, three states are needed to describe the dynamic of the system. The aortic blood flow $Q(t)$ ejected from the left ventricle is considered the input to the system. P_p denotes the aortic proximal pressure and P_d represents the distal blood pressure. Q_1 represents the blood flow throughout the inertia L. Applying the Kirchhoff's voltage and current laws to the circuit shown in **Figure 1D**. We obtain the following equations:

$$\begin{cases} C_p^\alpha \cdot \dfrac{d^\alpha}{dt^\alpha} P_p(t) + Q_1(t) = Q(t) \\ \dfrac{P_p(t)}{L} - \dfrac{P_d(t)}{L} = \dfrac{dQ_1(t)}{dt} \\ C_d^\beta \cdot \dfrac{d^\beta}{dt^\beta} P_d(t) + \dfrac{P_d(t) - P_v}{R_p} = Q_1(t) \end{cases} \tag{8}$$

The resulting pseudo-state space representation is then:

$$D_t^q x(t) = Ax(t) + B(x), \tag{9}$$

where $D_t^q = [D_t^\alpha, D_t^\gamma, D_t^\beta]^{tr}$ is the fractional-order derivative operator for all the states. $(\cdot)^{tr}$ denotes the transpose of the row vector. In this study $\gamma = 1$ as we used an integer-order inductor to connect the proximal and distal compartments. $xx = [P_p, Q_1, P_d]^{tr}$ denotes the pseudo-states vector representing the aortic proximal, the blood flow throughout the inductor, and the distal pressure, respectively. The matrix A representing the lumped parameters is expressed as:

$$A = \begin{bmatrix} 0 & -\dfrac{1}{C_p^\alpha} & 0 \\ \dfrac{1}{L} & 0 & -\dfrac{1}{L} \\ 0 & \dfrac{1}{C_d^\beta} & -\dfrac{1}{R_p C_d^\beta} \end{bmatrix} \tag{10}$$

B is written as:

$$\begin{bmatrix} \dfrac{Q(t)}{C_p^\alpha} & 0 & \dfrac{P_d(t) - P_v}{R_p} \end{bmatrix}^{tr} \tag{11}$$

Remark 1. *If we were to assume that the pressure's drop across the blood inductor, L, is negligible, in this case, the proximal pressure is equal to the distal one. In addition, the F-MWK reduces to the simplest fractional-order two-element Windkessel model as proposed in (Bahloul and Laleg-Kirati, 2020) with an equivalent arterial compliance* $C_a^q = C_p^\alpha + C_d^\beta$.

3. DATA AND ANALYSIS

3.1. *In-vivo* Human Hypertension Datasets

The proposed model was applied and validated using two real clinical datasets for human hypertension (Nichols et al., 1993; Li et al., 2017). The first *in-vivo* dataset ($n = 3$) was extracted and digitized from aging, and hypertensive studies (Nichols et al., 1993; Aboelkassem and Virag, 2019)). The data consists of measured aortic blood flow rate and aortic blood pressure for three human subjects suffering from three different hypertension stages, particularly Pre-hypertension, mild-hypertension, and severe hypertension. Their cardiac cycle is $T = 0.92\ s$. The second clinical dataset was obtained from data supplement publicly available at in (Mariscal-Harana et al., 2021). The dataset was originally used in a study about forward and backward pressure waveform morphology analysis in hypertension, (Li et al., 2017). The dataset consists of 158 subjects assessed for hypertension ($n = 158$, 81 male, aged 46 ± 17 years, mean $\pm$ SD). Based on (Li et al., 2017) the patients were recruited from those who were diagnosed with hypertension at Guy's and St Thomas' Hypertension Clinic. 48% of the subject were on treatment and hence their blood pressure were settled to the normal values (normotensive). More details about the collection of this data such as the consent approval and the measurement tools can be fount in (Mariscal-Harana et al., 2021). In addition to the aortic waveforms the dataset contains extra chracteristic of the subjects such as the height, weight, measurements of systolic (SBP) and diastolic (DBP) blood pressure, cardiac output, stroke volume and heart rate. As in this study we focus on the investigation of fractional-order framework for the assessment of hypertension, we divided the patients of this dataset into 4 groups corresponding to the range of SBP and DBP of the central

blood pressure pulse: Group 1, normotension (DBP $<$ 80 AND SBP $<$ 120); Group 2, pre-hypertesion (80 $\leq$ DBP $\leq$ 85 OR 120 $\leq$ SBP $\leq$ 130); Group 3, hypertension (85 $\leq$ DBP $\leq$ 90 OR 130 $<$ SBP $\leq$ 140) and Group 4, severe-hypertension (DBP $>$ 90 OR SBP $>$ 140). The characteristics of each group are listed in **Table 1**.

3.2. Parameters Identification of the Models

For the numerical implementation of the F-MWK the definition of *Grunwald-Letnikov (GL)* given in definition 1 is used Podlubny (1999). The time validation of the proximal pressure waveforms (P_p) was performed using two clinical hypertension real datasets. The cost function we used to calculate signal dissimilarity is the L_2-norm of the difference between the two signals. It can be formally described as follows:

$$\underset{\Theta}{\text{Minimize}} \left\| P_p - \hat{P}_p(\Theta) \right\|_2, \tag{12}$$

The optimizer algorithm uses the measured aortic root flow rate as an input and compute the required model parameters, $\Theta = \{C_p^{\alpha}, L, C_d^{\beta}, R_p, P_v, \alpha, \beta\}$, which minimize the pressure root mean square error (RMSE), i.e., the difference between measured and calculated aortic root pressure as:

$$\text{RMSE} = \sqrt{\frac{1}{N}\sum_{i=1}^{n}(P_{p[i]} - \hat{P}_{p[i]})^2}. \tag{13}$$

where N denotes the number of samples per P_p pressure signal. The estimation process was based on a non-linear least square minimization routine applying the well-known MATLAB – R2020b, function fmincon. The estimate of Θ is $\hat{\Theta}$ were found *via* the solution of the inverse problem of the estimated proximal blood pressure ($\hat{P_p}$) and the real one (P_p). Initialized by Θ_0 and using a nonlinear programming solver, the inverse algorithm iteratively predicts the set of parameters $\hat{\Theta}$ which minimizes the objective function. In this process, we constrained all the parameters to be positive to guarantee physical properties (Lower_bounds = [0], Upper_bounds = [∞] and. Once a tolerance of error was reached, the convergence of the method is confirmed, the *fmincon* function exits and yields an output of the optimal set of model parameters estimates $\hat{\Theta}^*$.

In addition, to evaluate the performance of the estimation, we calculate the relative error, R.E.(%) and the correlation coefficient, ρ defined as:

$$\begin{cases} \text{R.E.}(\%) = \dfrac{||P_p - \hat{P}_p||_2}{||P_p||_2} \times 100\% \\ \rho = \dfrac{\sum_{i=1}^{n}(P_p - \bar{P_p})(\hat{P_p} - \bar{\hat{P}_p})}{\sqrt{\sum_{i=1}^{n}(P_p - \bar{P_p})^2}\sqrt{\sum_{i=1}^{n}(\hat{P_p} - \bar{\hat{P}_p})^2}}, \end{cases} \tag{14}$$

where $\bar{.}$ represents the average operator.

TABLE 1 | Characteristics of the hypertensive clinical dataset 2.

Subjects	Pulse pressure groups			
	Group 1 (n = 55)	**Group 2 (n = 41)**	**Group 3 (n = 36)**	**Group 4 (n = 26)**
Sex, male, [%]	45.45	58.53	50	50
Characteristic	DBP $<$ 80 AND SBP $<$ 120	80 $\leq$ DBP $\leq$ 85 OR 120 $\leq$ SBP $\leq$ 130	85 $\leq$ DBP $\leq$ 90 OR 130 $<$ SBP $\leq$ 140	DBP $>$ 90 OR SBP $>$ 140
Age (years)	45.34 ± 16.7	43.63 ± 17.52	47.88 ± 17.33	49.92 ± 14.28
Height (m)	1.68 ± 0.10	1.72 ± 0.09	1.69 ± 0.07	1.68 ± 0.07
Weight (Kg)	74.76 ± 15.68	79.69 ± 13.75	77.81 ± 14.50	80.18 ± 17.16
DBP (mmHg)	70.40 ± 6.24	82.65 ± 7.03	88.36 ± 7.29	95.53 ± 15.76
SBP (mmHg)	105.23 ± 10.10	124.88 ± 8.02	136.71 ± 11.52	159.03 ± 18.05
MBP (mmHg)	86.38 ± 7.29	102.02 ± 5.46	110.30 ± 6.58	123.70 ± 15.02
HR (beats/min)	57.68 ± 13.62	65.14 ± 17.06	60.98 ± 14.47	64.09 ± 12.01
PWV (m/s)	3.42 ± 01.03	3.99 ± 1.09	4.77 ± 01.57	5.46 ± 1.50

3.3. Sensitivity Analysis for the Apparent Compliance

In order to study how the variation in the apparent arterial compliance modulus and phase is associated with the variations of the different input parameters factors, a global sensitivity analysis based on *variance method* has been performed. Variance-Based Sensitivity Analysis (VBSA) is a valuable step in the model calibration process, estimating the model parameters. In fact, it provides a relevant insight on how changes in the estimates of the parameters (the inputs of the model) map into variations of the performance metric that evaluates the model fit. A detailed review with practical workflow about the sensitivity analysis literature can be found in (Pianosi et al., 2015, 2016; Wagener and Pianosi, 2019).

In this study, we evaluate the VBSA of the fractional-order arterial compliance using *First-order indices* known also as *"main effect"* and the *total-order indices* so-called *"total effect."* The *"main effect"* indices measure the direct contribution of the output variation from individual input factor or, equivalently, the expected reduction in output variance that can be obtained when fixing a specific input (Pianosi et al., 2016). The *First-order indices* is defined as:

$$\text{VBSA}_\text{F} = \frac{V_{x\sim i}[E_{x\sim i}(y|x_i)]}{V(y)} = \frac{V(y) - [E_{x\sim i}(y|x_i)]}{V(y)} \tag{15}$$

where E denotes expected value, V denotes the variance, x denotes the input, y denotes the output, and $x \sim i$ denotes "all input factors but the ith."

$$\text{VBSA}_\text{T} = \frac{E_{x\sim i}[V_{x_i}(y|x \sim i)]}{V(y)} = 1 - \frac{V_{x\sim i}[E_{x_i}(y|x \sim i)]}{V(y)} \tag{16}$$

4. RESULTS

In this section, we show the results of applying the proposed model for both subjects of the clinical dataset 1 and the groups of the clinical dataset 2 as described in **Table 1**. To fully identify the proposed fractional-order model the parameters and the fractional differentiation orders have to be estimated using the measured flow and pressure waveforms. In addition, we present the result of applying the variance-based global sensitivity analysis technique to the proposed arterial representation and the analysis of ranking the lumped parameters in order of importance based on $VBSA_F$ and $VBSA_T$.

4.1. Model Calibration

The list of the optimized F-MWK parameters and their numerical values are shown in **Table 2**. For clinical dataset 2, the parameter estimates' mean value and standard deviation (mean ± SD) are presented per group. The optimized parameters for each subject are then used to reconstruct the aortic proximal blood pressure waveform (P_p). The pressure root mean square error RMSE and the percentage relative error [*R.E.* (%)] along with the correlation coefficient (ρ) between the real aortic pressures and the reconstructed ones are also listen in **Table 2** as performances. In the following we present the detailed analysis of the proposed fractional-order model and its validation against each in-human hypertension clinical datasets.

4.1.1. Human Hypertension Dataset 1

In order to validate and check the ability of the F-MWK in reconstructing the proximal blood pressure at various levels of hypertension conditions, namely the Pre-hypertension, Mild-hypertension, and severe hypertension in this part, we use human data from the hypertensive study, (Nichols et al., 1993). The lumped model parameters are identified using the aortic blood flow (Q) as an input. The reconstructed proximal blood pressures after applying F-MWK using the identified parameters along with the experimental *in-vivo* waveform are shown in **Figures 2A,C,E** represent the model input aortic-valve blood flow rate (Q) for each hypertension condition level and **Figures 2B,D,F** represent the pressure waveform validation results. Based on this result, it is clear that the proposed fractional-order model captured the main features of the proximal aortic pressure waveform, including the maximum value (peak systolic value) and the dicrotic notch. The model conforms better in detecting these features in the cases of Mild-hypertension and Severe-hypertensive level, where the percentage relative errors were 1.9 and 2.19%, respectively. The correlation coefficients for all the studied cases are around 0.99, which confirms the model's capability to catch the explicit details of the arterial blood pressure morphology.

In addition, the model presents a better performance in terms of RMSE than the models presented in Aboelkassem and Virag (2019) namely the hybrid Windkessl-Womersley (WK-W) model. for instance, the RMSE value was around 3.02 in the case of F-MWK; however, it is equal to 4.12 in the case of (WK-W). It is worth noting that WK-W is a hybrid model that consists of the proximal and distal compartments similar to F-MWK; however, these two compartments are connected by

TABLE 2 | The optimized parameters and corresponding RMSE, *R.E.*(%) and ρ of the fractional-order modified Windkessel model for each subject of the hypertension clinical dataset 1 and different groups of the clinical hypertension dataset 2.

		Parameters estimates							Performances		
		C_p^{α}	L	C_d^{β}	R_p	P_v	α	β	*RMSE*	*R.E. (%)*	ρ
Dataset 1	Pre-hypertension	1.48	0.052	0.37	0.81	10.69	1.001	0.771	2.23	2.26	0.99
	Mild-hypertension	0.58	0.010	0.55	2.52	15	1.023	0.540	2.27	1.90	0.99
	Severe-hypertension	0.54	0.087	0.34	3.64	15	1.000	0.452	3.025	2.19	0.99
Dataset 2	Group 1	2.77 ± 1.50	0.023 ± 0.020	2.39 ± 1.28	3.10 ± 1.37	13.90 ± 4.11	1.114 ± 0.03	0.466 ± 0.10	1.48 ± 0.50	1.70 ± 0.59	0.99 ± 0.005
	Group 2	2.00 ± 1.23	0.027 ± 0.015	1.68 ± 1.01	2.52 ± 1.05	11.85 ± 2.94	1.111 ± 0.03	0.498 ± 0.18	1.66 ± 0.45	1.62 ± 0.44	0.99 ± 0.005
	Group 3	1.61 ± 1.24	0.038 ± 0.022	1.34 ± 0.85	2.95 ± 1.24	12.37 ± 3.43	1.112 ± 0.04	0.501 ± 0.12	1.90 ± 0.50	1.70 ± 0.45	0.99 ± 0.003
	Group 4	1.13 ± 0.58	0.036 ± 0.018	0.98 ± 0.47	2.09 ± 1.12	11.88 ± 3.26	1.130 ± 0.05	0.572 ± 0.19	2.34 ± 0.62	1.87 ± 0.44	0.99 ± 0.002

For each group the numerical mean value and standard deviation (mean ± SD) of the estimates and performance are presented.

a tube to represent the aorta where the blood flow is expressed by the Womersley solution of the Navier-Stokes equations. Accordingly, the fractional-order framework can reproduce an accurate performance similarly to more complex systems. By interpreting the numerical values of the proximal and distal pseudocapacitances (C_p^α, C_d^β) and the corresponding fractional differentiation-orders (α, β), we notice a clear decrease of these parameters from Pre-hypertension level to the Sever-hypertension level.

On one side, this result demonstrates the fractional-order behavior within the distal arterial network. In fact, β is less than the integer-order and takes values between 0 and 1. In addition, as the level of hypertension increases, the fractional differentiation order decreases. Furthermore, from equation (7), it is obvious that as β alters from 1 to 0, the FOC's resistive part increases. Accordingly, the results of the identified fractional-order parameters are consistent with the clinical investigations, which have revealed that the vascular remodeling in resistive arteries is strongly associated with the progression and severity of hypertension's disease.

4.1.2. Human Hypertension Dataset 2

To further validate and interpret the efficiency of the developed model, we explore the second clinical dataset that consists of 158 human subjects examined as hypertensive patients. A portion of the studied population is under treatment, and their high blood pressures were controlled and regulated to be within the normal values. The main objective of investigating this type of data is to keep the generality of the proposed model and demonstrate that this model can be employed in different physiological conditions. In fact, the dataset presents patients of different ages, gender, weight, and hemodynamic characteristics as listen in **Table 1**.

Basically, we divided this data into four classes based on the peak systolic blood pressure and diastolic values, SBP and DBP, respectively. The thresholds of SBP and DBP were set in a manner that: Group 1 consists of patients with regulated blood pressure levels that can be considered as a normotensive subset, Group 2 consists of patients with a bit high SBP and DBP, which some studies consider it as Pre-hypertension stage, Group 3 consist of patients with high-level blood pressure values which is indeed thought as hypertension subset, and Group 4 with the highest SBP and DBP is supposed to present the severe-hypertensive samples. **Figure 3** summarizes the result of the proximal aortic blood pressure reconstruction of a representative patient from each group. The proposed model can capture all the waveforms details, including the dicrotic notch and the peak systolic value. It is worth noting that the selected patients present different aortic input blood flow profiles.

As shown in **Table 2** the values of the performance indexes, namely RMSE, *R.E.*(%) and ρ, indicate that the proposed model was able to reconstruct the proximal blood pressure using the optimized lumped parameters. The RMSE values do not exceed 3 in all cases, and the smallest value is around 1.48 ± 0.50 for group 1, and the largest one is 2.34 ± 0.62 for group 4. Also the smallest *R.E.* is around $1.62\% \pm 0.44\%$ obtained for group 2 and the largest one is $1.70\% \pm 0.59\%$ for group 1. The correlation coefficient is around 0.99 for all the groups.

By checking the optimized values of the fractional-order parameter, namely the pseudocapacitance (C_p^α, C_p^β) and their corresponding fractional differentiation orders (α, β), we noticed that C_p^α and C_p^β decrease from group 1, which considered representative of the normotensive population to group 4 that corresponds to the subset with severe-hypertensive level based on the value of SBP and DBP. However, α and β slightly increase from groups 1 to 4. This result is different from the one found with the clinical subset 1. This can be explained by the fact that the presented model is not globally identifiable. It is very challenging to find unique values for the pairs (C_p^α, α) and C_d^β, β. Accordingly, it is more pertinent to evaluate the complex and frequency-dependent compliance C_C that conveys the relationship between the fractional differentiation order and the pseudocapacitance *via* the expression (9). The following section focuses on the evaluation and analysis of C_{C_h} at the cardiac frequency for both proximal and distal compliances.

4.2. Variance Based Sensitivity Analysis

Generally, to simulate the proximal blood pressure waveform, we feed F-MWK with the identified set of the values of the lumped parameters, which can be regarded as a scalar input of the proposed model. In order to test and understand the effect of varying one of the inputs at a time on the output signal dynamic and morphology and study the interactive effect between the inputs and the output, we conduct a variance-based sensitivity analysis (VBSA) as explained in the method section.

Two indices based on VBSA were evaluated in this study: the first-order index ($\mathrm{VBSA_F}$), which reflects the main effect contribution of each input factor to the variance of the output and ranks the importance of this input; the second one is the total effect index ($\mathrm{VBSA_T}$) which accounts for the total contribution to the output variation due to factor input evaluated by the first-order effect in addition to all higher-order effects due to interactions. In this study both indices were evaluated at each sample of the proximal aortic blood pressure waveform for the three hypertensive subject of the clinical dataset 1.

We consider a normal distribution variation of each input parameter $X \sim \mathcal{N}(\mu, \sigma^2)$ where X corresponds to the input, μ is the mean value of the distribution that is equal to the optimized value of the parameter shown in **Table 2**. (Dataset 1) and σ denotes the standard deviation that is taken to be 15% of the value of μ. **Figures 4A,C,E** show the evaluated $\mathrm{VBSA_F}(t)$ for the Pre-hypertension, Mild-hypertensive and Severe-hypertensive patients, respectively. **Figures 4B,D,F** displays the evaluated $\mathrm{VBSA_T}(t)$ for the Pre-hypertension, Mild-hypertensive and Severe-hypertensive patients, respectively. For all cases the indices were computed over one cardiac cycle.

For visualization purposes of each subject, all the parameters are listed in *y-axis*, whereas the *x-axis* represents the time samples. In addition, the normalized blood pressure waveform was plotted in the same plot. It is very clear from these results that F-MWK is very sensitive to the variation of the fractional differentiation order (α) over the whole cardiac cycle for all the hypertension levels. The rest of the parameters are less influential on the output dynamic, though their effect varies

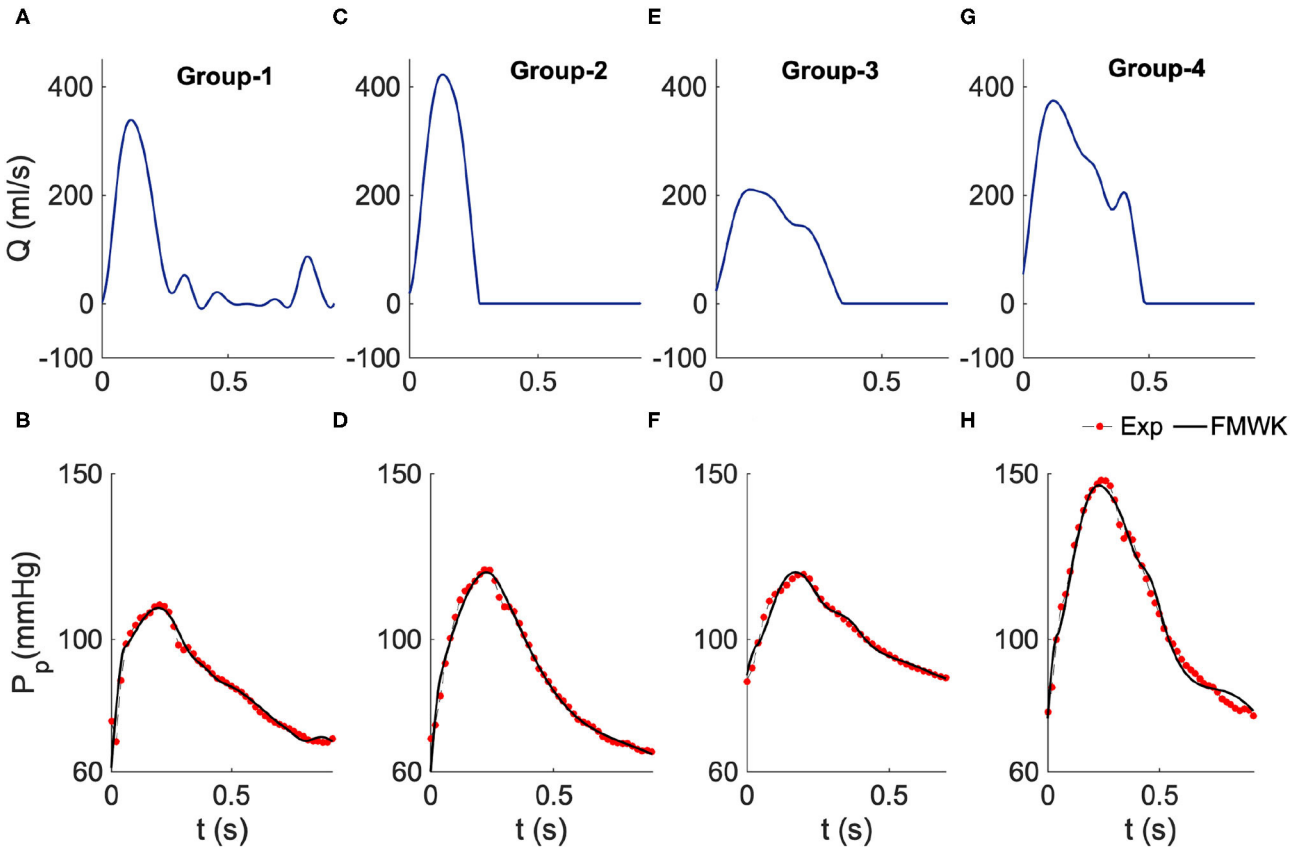

FIGURE 3 | Estimated proximal blood pressure using the proposed fractional-order modified Windkessel model along with the experimental *in-vivo* human-hypertension for samples from the different groups of the dataset 2. **(A,C,E,G)** Represent the model input aortic-valve blood flow rate for each group's sample study, Group 1, Group 2, Group 3 and Group 4, respectively. **(B,D,F,H)** Represent the pressure waveform validation results.

from one hypertension level to another. In fact, this effect is more considerable in the Mild-hypertensive case, as shown in subplot D. Generally, the difference between $VBSA_T(t)$ and $VBSA_F(t)$ measures how much the parameter is involved in the interaction with other input factors. Accordingly, the parameters are very affected by any interaction between the input factor in the case of Mild-hypertension. Based on these observations, the fractional differentiation orders might have central control in the variation of the aortic blood pressure. Accordingly, this parameter might play an important position as a bio-marker assessing the transition between viscosity and elasticity, a potential arterial stiffness index.

5. DISCUSSION

The fractional-order capacitor represented by its pseudocapacitance and the fractional differentiation order can be an inherent component in F-MWK by lumping the complex and frequency-dependent behavior of the vascular compliance as well as characterizing the hemodynamic. The sensitivity analysis and the model calibration show that the fractional-order pairs may entail valuable structural and functional physiological insight. Based on the validation results using clinical dataset 1 a clear, direct correlation between the fractional differentiation orders and the level of hypertension was found in agreement with the clinical analysis. Indeed, as the level of hypertension increases, a decrease in the numerical values of the fractional differentiation orders (α and β), as well as the pseudocapacitances (C_p^{α} and C_d^{β}), was reflected.

The concurrent decrease of the fractional-order parameters of FOC yields to the predominance of the resistive (dissipative) part on account of the capacitive (storage) part in this element. This fact is a potential representative of vascular remodeling associated with the severity of hypertension. Analyzing the fractional differentiation orders independently from the pseudo-capacitance might lead to misinterpretation. In fact, based on expression (5), these two parameters might have a compensatory inter dynamic mechanism. Accordingly, it is more appropriate to evaluate the complex fractional-order compliance that relates both parameters *via* expression (7) at the heart pulsation (ω_h), reflecting the so-called true arterial compliance. It is defined as follow:

$$C_{C_h} = C_C(\omega_h) = C_{app}^{\alpha}(j\omega_h)^{\alpha-1}. \tag{17}$$

Figure 5 shows the fractional-order compliance evaluated at the heart pulsation: **Figure 5A** represents the bar plot of the

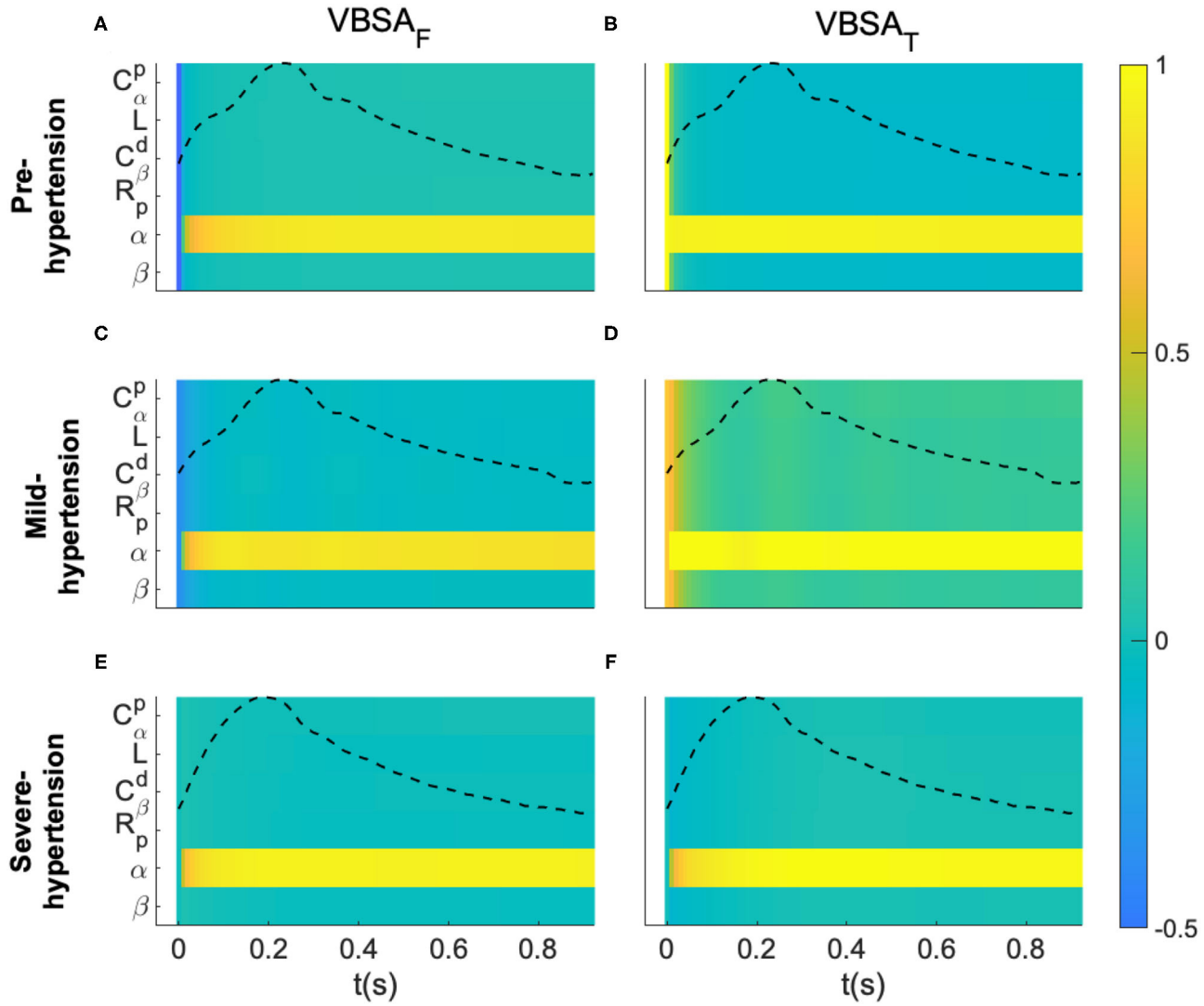

FIGURE 4 | Variance-based sensitivity analysis of the proposed fractional-order model. **(A,C,E)** Represent the first-order indices ($VBSA_F$) of the model's parameters for a Pre-hypertensive, Mild-hypertensive and Severe-hypertensive subject, respectively. **(B,D,F)** Represent the total-order indices ($VBSA_T$) of the model's parameters for a Pre-hypertensive, Mild-hypertensive and Severe-hypertensive subject, respectively. The variance based sensitivity indices were evaluated for each sample of the aortic proximal blood pressure over one cardiac cycle.

proximal ($C^p_{C_h}$) and distal ($C^d_{C_h}$) fractional-order compliance for the in-human hypertensive subjects of dataset 1; **Figure 5B** represents the error bars plot of the proximal ($C^p_{C_h}$) and distal ($C^d_{C_h}$) fractional-order compliance for the in-human hypertensive groups of dataset 2. The error in this plot corresponds to the standard error of the mean. From this figure, in all cases, $C^p_{C_h}$, which characterizes the large elastic arteries, is larger than $C^d_{C_h}$, which characterizes the small resistive vessels. In addition for both datasets, as the hypertensive increases both compliances decreases. From **Figure 5B**, the gradient from group 1 representing a normotensive population to group 2 (Pre-hypertensive) is more acute than the slopes between groups 2 and 3 and groups 3 and 4, which are approximately equal. C_{C_h} is substantially decreased from normal blood pulse pressure to the higher one.

This result is very important and demonstrates the reliability of C_{C_h} in characterizing stiffness as an important risk factor for the progression of high blood pressure. As the clinical dataset 2 provides the aortic pulse wave velocity (PWV) of each patient, in **Figure 6**. we plotted the mean values for both $C^P_{C_h}$ and $C^d_{C_h}$ for each group vs. the mean values of PWV for each group. The result shows the strong negative correlation between the PWV and C_{C_h} which is in agreement with the clinical standard that shows that PWV values substantially increase with the hypertensive level as a consequence of arterial stiffness.

The correlation with PWV (a well-established biomarker of along with the level of hypertensive reveals the potential of

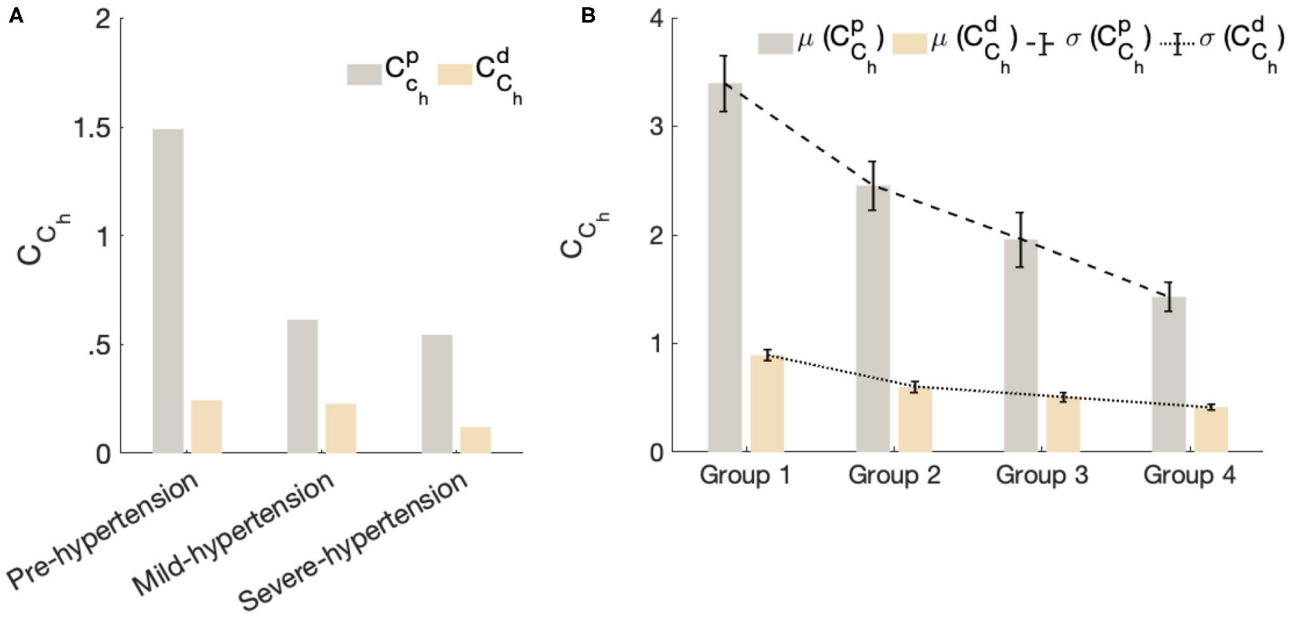

FIGURE 5 | The fractional-order compliance evaluated at the heart pulsation. **(A)** Represents bar plot of the proximal ($C^{p}_{C_h}$) and distal ($C^{d}_{C_h}$) fractional order compliance for the in-human hypertensive subjects of dataset 1. **(B)** Represents error bars plot of the proximal ($C^{p}_{C_h}$) and distal ($C^{d}_{C_h}$) fractional order compliance for the in-human hypertensive groups of dataset 2. Each bar in this plot represent the mean value of the evaluated fractional-order compliances per group and the error corresponds to the standard error of the mean per group.

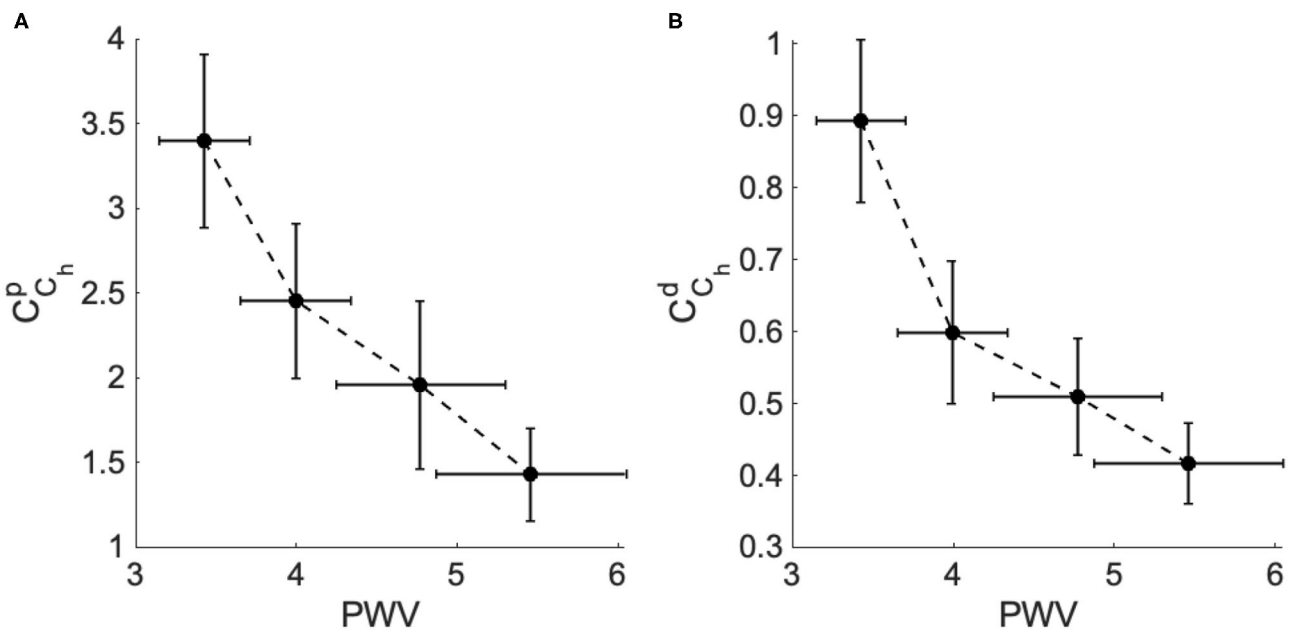

FIGURE 6 | The fractional-order compliance evaluated at the heart pulsation (C_{C_h}) vs. the arterial pulse wave velocity (PWV) for the different hypertensive groups of dataset 2. **(A)** PWV vs. the proximal fractional-order compliance ($C^{p}_{C_h}$) and **(B)** PWV vs. the distal fractional-order compliance ($C^{d}_{C_h}$).

the fractional-order parameters to improve our understanding of the structural development of vascular remodeling due to hypertension. Indeed, fractional-order parameters are considered a prospective new tool in capturing irregular vascular changes. Stress-relaxation-based viscoelastic experiments on arterial segment have reported that the fractional differentiation order parameter could be associated with vascular smooth muscles cells (VSMCs) activity, contributing to the viscoelasticity modulation in the vessels (Craiem and Armentano, 2007; Craiem et al., 2008).

In arteries, VSMCs induce the stretching of collagenous fibers, and vascular activation can modify the local viscoelastic response of the arterial wall (Armentano et al., 2006). Vascular smooth

muscle cells (VSMCs) represent an important part of blood vessels and are placed in the medium portion of the arterial vessel, known as tunica media. They are located circularly around the vascular lumen and other vascular layers. VSMCs play a crucial role in the remodeling processes of the vascular wall due to certain diseases.

In hypertension, the vascular remodeling induces different changes in the VSMCs of large and resistive small arteries: with regards to larger vessels, VSMCs experience hypertrophy remodeling, an expansion in the cellular vessel material, which results in an enlarged intima-media thickness, raised vascular stiffness, and so high blood pressure (increased pulse pressure). In the small arteries, the vascular remodeling manifests as a eutrophic phenomenon, which results in an increase in wall thickness and a reduction in lumen diameter. It can represent hypertrophic reconstruction as well.

Several clinical studies in-patient and experimental researches have revealed the marked correlation between vascular remodeling and the pathophysiology of hypertension. Low dimensional models (lumped parameters models) are quite limited in the vascular remodeling structural analysis contest, which requires an extremely complex interplay of deeply coupled multi-scale and multi-physics mechanisms. The fractional-order framework offers much promise in understanding key physiological mechanisms while reducing the order of complexity. Due to the extra fractional-order parameters, more flexibility is added to capture structural artery characteristics.

6. MODEL DEVELOPMENT AND FUTURE APPLICATIONS

Fractional order modeling (FOM) approach can be viewed as a natural generalized of the well-known blood flow arterial Windkessel model. The proposed model can be easily integrated within a closed-loop whole heart lumped parameter model representation for better understanding of the blood flow dynamics in the cardiovascular system. In this part, we list a couple of applications where the present model can be useful and is expected to perform well.

The first application is related to using the present model as a surrogate measure of arterial stiffness prediction. For example, it is commonly known that probing arterial stiffness at the arterial locations provides valuable information about the physiological state of the cardiovascular system. An increase in arterial stiffness plays a critical role in the pathogenesis of cardiovascular disorders and is identified as a major risk factor for many cardiovascular pathologies such as hypertension and coronary heart diseases. Accordingly, the present model can be used within a larger integrative computational platform for assessing arterial stiffening at different distal locations. Hence, it can be used for better understanding arterial blood flow, predicting, and diagnosing many stiffness related cardiovascular diseases.

The second application is related to the use of the pulsed wave velocity (PWV) as a standard method for assessing arterial stiffness. The PWV is functionally assessed by evaluating the time it takes for the pressure waveform to travel two known arterial sites. Despite its wider adoption in the clinical routine, the measurement process of PWV is considered a demanding task for both clinicians and patients. Since the present model have the capability of estimating the PWV. Therefore, it can be used toward developing a full scale non-invasive and easy-to-use computational tool that can overcome the challenges of the classical assessment stiffness process and hence it can be used to improve the quality of patient care.

In summary, the present model is an initial step toward developing an integrative non-invasive surrogate markers of local and global arterial stiffness. The marker is based on the fractional differentiation order that controls the transition between the resistive and capacitive parts of the fractional-order element and, by analogy, represents the viscoelastic properties of the vasculatures.

7. CONCLUSION

A novel fractional-order lumped model of the arterial system is proposed to study hypertension. The model has shown the feasibility of characterizing the proximal and distal arterial compliances using fractional-order capacitors. The *in-vivo* human validation demonstrates the ability of the proposed model in reconstructing the central blood pressure and capturing specific details of different waveforms morphology. The variation of the complex and frequency-dependent apparent arterial compliance evaluated at the heart pulsation vs. different hypertensive levels shows consistency with the clinical observations. Moreover, the correlation with the pulse wave velocity (a well-established biomarker of arterial stiffness) demonstrates the capabilities of this model, namely the fractional-order parameters. The model results are expected to improve our understanding of the structural and functional characteristics of the resulting vascular remodeling of large and small arteries in different hypertensive conditions.

DATA AVAILABILITY STATEMENT

The original contributions presented in the study are included in the article/supplementary material, further inquiries can be directed to the corresponding author/s.

AUTHOR CONTRIBUTIONS

MB: study conception and design. MB and YA: data collection. MB, YA, and T-ML-K: analysis and interpretation of results and draft manuscript preparation. All authors reviewed the results and approved the final version of the manuscript.

FUNDING

Research reported in this publication has been supported by the King Abdullah University of Science and Technology (KAUST).

ACKNOWLEDGMENTS

The authors would like to thank Dr. Ali Haneef, associate consultant cardiac surgeon and co-chairman quality management at King Faisal Cardiac Center, King Abdulaziz Medical City, National Guard Health Affairs, in the Western Region, Jeddah, KSA.

REFERENCES

Aboelkassem, Y., and Virag, Z. (2019). A hybrid windkessel-womersley model for blood flow in arteries. *J. Theor. Biol.* 462, 499–513. doi: 10.1016/j.jtbi.2018.12.005

Armentano, R. L., Barra, J. G., Santana, D. B., Pessana, F. M., Graf, S., Craiem, D., et al. (2006). Smart damping modulation of carotid wall energetics in human hypertension: effects of angiotensin-converting enzyme inhibition. *Hypertension* 47, 384–390. doi: 10.1161/01.HYP.0000205915.15940.15

Bahloul, M. A., and Kirati, T.-M. L. (2019). Fractional order models of arterial windkessel as an alternative in the analysis of the left ventricular afterload. *arXiv preprint* arXiv:1908.05239.

Bahloul, M. A., and Kirati, T.-M. L. (2021). Fractional-order model representations of apparent vascular compliance as an alternative in the analysis of arterial stiffness: an in-silico study. *Physiol. Meas.* 42, 045008. doi: 10.1088/1361-6579/abf1b1

Bahloul, M. A., and Laleg-Kirati, T.-M. (2020). Assessment of fractional-order arterial windkessel as a model of aortic input impedance. *IEEE Open J. Eng. Med. Biol.* 1, 123–132. doi: 10.1109/OJEMB.2020.2988179

Brown, I. A., Diederich, L., Good, M. E., DeLalio, L. J., Murphy, S. A., Cortese-Krott, M. M., et al. (2018). Vascular smooth muscle remodeling in conductive and resistance arteries in hypertension. *Arterioscler. Thromb. Vasc. Biol.* 38, 1969–1985. doi: 10.1161/ATVBAHA.118.311229

Burattini, R., and Natalucci, S. (1998). Complex and frequency-dependent compliance of viscoelastic windkessel resolves contradictions in elastic windkessels. *Med. Eng. Phys.* 20, 502–514.

Carlson, G., and Halijak, C. (1964). Approximation of fractional capacitors (1/s)ˆ(1/n) by a regular newton process. *IEEE Trans. Circuit Theory* 11, 210–213.

Chemla, D., Hébert, J.-L., Coirault, C., Zamani, K., Suard, I., Colin, P., et al. (1998). Total arterial compliance estimated by stroke volume-to-aortic pulse pressure ratio in humans. *Am. J. Physiol. Heart Circul. Physiol.* 274, H500–H505.

Craiem, D., and Armentano, R. (2003). The new apparent compliance concept as a simple lumped model. *Cardiovasc. Eng. Int. J.* 3, 81–83. doi: 10.1023/a:1025567616744

Craiem, D., and Armentano, R. L. (2007). A fractional derivative model to describe arterial viscoelasticity. *Biorheology* 44, 251–263.

Craiem, D., and Magin, R. L. (2010). Fractional order models of viscoelasticity as an alternative in the analysis of red blood cell (rbc) membrane mechanics. *Phys. Biol.* 7, 013001. doi: 10.1088/1478-3975/7/1/013001

Craiem, D., Rojo, F. J., Atienza, J. M., Armentano, R. L., and Guinea, G. V. (2008). Fractional-order viscoelasticity applied to describe uniaxial stress relaxation of human arteries. *Phys. Med. Biol.* 53, 4543. doi: 10.1088/0031-9155/53/17/006

de Simone, G., Roman, M. J., Koren, M. J., Mensah, G. A., Ganau, A., and Devereux, R. B. (1999). Stroke volume/pulse pressure ratio and cardiovascular risk in arterial hypertension. *Hypertension* 33, 800–805.

Doehring, T. C., Freed, A. D., Carew, E. O., and Vesely, I. (2005). Fractional order viscoelasticity of the aortic valve cusp: an alternative to quasilinear viscoelasticity. *J. Biomech. Eng.* 127, 700–708. doi: 10.1115/1.1933900

Elwakil, A. S. (2010). Fractional-order circuits and systems: an emerging interdisciplinary research area. *IEEE Circuits Syst. Mag.* 10, 40–50. doi: 10.1109/MCAS.2010.938637

Francis, S. E. (2007). *Continuous Estimation of Cardiac Output and Arterial Resistance From Arterial Blood Pressure Using a Third-Order Windkessel Model*. Ph.D. thesis, Massachusetts Institute of Technology.

Frank, O. (1899). Die grundform des arteriellen pulses. z. biol. 37, 483-526. *J. Mol. Cell Cardiol.* 22, 253–277.

Ge, Y. (2018). *A New Approach To Assess Arterial System Function With Compliance-Pressure Loop*. Ph.D. thesis, Rutgers University-School of Graduate Studies.

Goldwyn, R. M., and Watt, T. B. (1967). Arterial pressure pulse contour analysis via a mathematical model for the clinical quantification of human vascular properties. *IEEE Trans. Biomed. Eng.* BME-14, 11–17.

Gutiérrez, R. E., Rosário, J. M., and Tenreiro Machado, J. (2010). Fractional order calculus: basic concepts and engineering applications. *Math. Problems Eng.* 2010, 375858. doi: 10.1155/2010/375858

Haluska, B., Jeffriess, L., Brown, J., Carlier, S., and Marwick, T. (2010). A comparison of methods for assessing total arterial compliance. *J. Hum. Hypertension* 24, 254–262. doi: 10.1038/jhh.2009.92

Hartley, T. T., Trigeassou, J.-C., Lorenzo, C. F., and Maamri, N. (2015). Energy storage and loss in fractional-order systems. *J. Comput. Nonlin. Dyn.* 10, 8. doi: 10.1115/1.4029511

Kaya, M., Balasubramanian, V., Patel, A., Ge, Y., and Li, J. K. (2018). A novel compliance-pressure loop approach to quantify arterial compliance in systole and in diastole. *Comput. Biol. Med.* 99, 98–106. doi: 10.1016/j.compbiomed.2018.06.001

Krishna, M. S., Das, S., Biswas, K., and Goswami, B. (2011). Fabrication of a fractional order capacitor with desired specifications: a study on process identification and characterization. *IEEE Trans. Electron Devices* 58, 4067–4073. doi: 10.1109/TED.2011.2166763

Li, Y., Gu, H., Fok, H., Alastruey, J., and Chowienczyk, P. (2017). Forward and backward pressure waveform morphology in hypertension. *Hypertension* 69, 375–381. doi: 10.1161/HYPERTENSIONAHA.116.08089

Lorenzo, C., and Hartley, T. (1998). *Initialization, Conceptualization, and Application in the Generalized Fractional Calculus*. NASA TP-1998-208407.

Mackenzie, I., Wilkinson, I., and Cockcroft, J. (2002). Assessment of arterial stiffness in clinical practice. *Qjm* 95, 67–74. doi: 10.1093/qjmed/95.2.67

Magin, R. L. (2006). *Fractional Calculus in Bioengineering*, vol. 2. Redding: Begell House.

Magin, R. L. (2010). Fractional calculus models of complex dynamics in biological tissues. *Comput. Math. Appl.* 59, 1586–1593. doi: 10.1016/j.camwa.2009.08.039

Malatos, S., Raptis, A., and Xenos, M. (2016). Advances in low-dimensional mathematical modeling of the human cardiovascular system. *J. Hypertens Manag.* 2, 1–10. doi: 10.23937/2474-3690/1510017

Mariscal-Harana, J., Charlton, P. H., Vennin, S., Aramburu, J., Florkow, M. C., van Engelen, A., et al. (2021). Estimating central blood pressure from aortic flow: development and assessment of algorithms. *Am. J. Physiol. Heart Circulatory Physiol.* 320, H494–H510. doi: 10.1152/ajpheart.00241.2020

Mensah, G. A., Roth, G. A., and Fuster, V. (2019). The global burden of cardiovascular diseases and risk factors: 2020 and beyond. *J. Am. Coll. Cardiol.* 74, 2529–2532. doi: 10.1016/j.jacc.2019.10.009

Nichols, W. W., Avolio, A. P., Kelly, R. P., and O'Rourke, M. F. (1993). *Arterial Vasodilation: Mechanisms and Therapy*. London: Edward Arnold, 23–40.

Oustaloup, A., Levron, F., Mathieu, B., and Nanot, F. M. (2000). Frequency-band complex noninteger differentiator: characterization and synthesis. *IEEE Trans. Circuits Syst. I Fundam. Theory Appl.* 47, 25–39. doi: 10.1109/81.817385

Perdikaris, P., and Karniadakis, G. E. (2014). Fractional-order viscoelasticity in one-dimensional blood flow models. *Ann. Biomed. Eng.* 42, 1012–1023. doi: 10.1007/s10439-014-0970-3

Pianosi, F., Beven, K., Freer, J., Hall, J. W., Rougier, J., Stephenson, D. B., et al. (2016). Sensitivity analysis of environmental models: a systematic review with practical workflow. *Environ. Model. Softw.* 79, 214–232. doi: 10.1016/j.envsoft.2016.02.008

Pianosi, F., Sarrazin, F., and Wagener, T. (2015). A matlab toolbox for global sensitivity analysis. *Environ. Model. Softw.* 70, 80–85. doi: 10.1016/j.envsoft.2015.04.009

Podlubny, I. (1999). *Fractional Differential Equations*, vol. 198. New York, NY: Academic Press.

Quick, C. M., Berger, D. S., Hettrick, D. A., and Noordergraaf, A. (2000). True arterial system compliance estimated from apparent arterial compliance. *Ann. Biomed. Eng.* 28, 291–301. doi: 10.1114/1.268

Quick, C. M., Berger, D. S., and Noordergraaf, A. (1998). Apparent arterial compliance. *Am. J. Physiol. Heart Circul. Physiol.* 274, H1393–H1403.

Segers, P., Verdonck, P., Deryck, Y., Brimioulle, S., Naeije, R., Carlier, S., et al. (1999). Pulse pressure method and the area method for the estimation of total arterial compliance in dogs: sensitivity to wave reflection intensity. *Ann. Biomed. Eng.* 27, 480–485.

Shi, Y., Lawford, P., and Hose, R. (2011). Review of zero-d and 1-d models of blood flow in the cardiovascular system. *Biomed. Eng. Online* 10, 33. doi: 10.1186/1475-925X-10-33

Si, G., Diao, L., Zhu, J., Lei, Y., and Zhang, Y. (2017). Attempt to generalize fractional-order electric elements to complex-order ones. *Chin. Phys. B* 26, 060503. doi: 10.1088/1674-1056/26/6/060503/meta

Stergiopulos, N., Segers, P., and Westerhof, N. (1999). Use of pulse pressure method for estimating total arterial compliance in vivo. *Am. J. Physiol. Heart Circulatory Physiol.* 276, H424–H428.

Trigeassou, J.-C., and Maamri, N. (2020). *Analysis, Modeling and Stability of Fractional Order Differential Systems 2: the Infinite State Approach.* John Wiley & Sons.

Vastarouchas, C., and Psychalinos, C. (2017). "Biomedical and biological applications of fractional-order circuits," in *2017 Panhellenic Conference on Electronics and Telecommunications (PACET)* (Xanthi: IEEE), 1–4.

Wagener, T., and Pianosi, F. (2019). What has global sensitivity analysis ever done for us? a systematic review to support scientific advancement and to inform policy-making in earth system modelling. *Earth Sci. Rev.* 194, 1–18. doi: 10.1016/j.earscirev.2019.04.006

Westerhof, N., Lankhaar, J.-W., and Westerhof, B. E. (2009). The arterial windkessel. *Med. Biol. Eng. Comput.* 47, 131–141. doi: 10.1007/s11517-008-0359-2

Zerpa, J. P., Canelas, A., Sensale, B., Santana, D. B., and Armentano, R. (2015). Modeling the arterial wall mechanics using a novel high-order viscoelastic fractional element. *Appl. Math. Model.* 39, 4767–4780. doi: 10.1016/j.apm.2015.04.018

Zhou, S., Xu, L., Hao, L., Xiao, H., Yao, Y., Qi, L., et al. (2019). A review on low-dimensional physics-based models of systemic arteries: application to estimation of central aortic pressure. *Biomed. Eng. Online* 18, 41. doi: 10.1186/s12938-019-0660-3

Conflict of Interest: The authors declare that the research was conducted in the absence of any commercial or financial relationships that could be construed as a potential conflict of interest.

Publisher's Note: All claims expressed in this article are solely those of the authors and do not necessarily represent those of their affiliated organizations, or those of the publisher, the editors and the reviewers. Any product that may be evaluated in this article, or claim that may be made by its manufacturer, is not guaranteed or endorsed by the publisher.

frontiers in Physiology

ORIGINAL RESEARCH
published: 24 March 2022
doi: 10.3389/fphys.2022.834747

Role of Scar and Border Zone Geometry on the Genesis and Maintenance of Re-Entrant Ventricular Tachycardia in Patients With Previous Myocardial Infarction

Vincenzo Gionti[1], *Simone Scacchi*[2]*, *Piero Colli Franzone*[3], *Luca F. Pavarino*[3], *Roberto Dore*[1] *and Cesare Storti*[1]

[1] Divisione di Cardiologia, Istituto di Cura Città di Pavia, Pavia, Italy, [2] Dipartimento di Matematica, Università degli Studi di Milano, Milan, Italy, [3] Dipartimento di Matematica, Università degli Studi di Pavia, Pavia, Italy

OPEN ACCESS

Edited by:
Guido Caluori,
Institut de rythmologie et modélisation cardiaque (IHU-Liryc), France

Reviewed by:
James Coromilas,
Rutgers Robert Wood Johnson Medical School, United States
Sanjay Ram Kharche,
Western University, Canada

***Correspondence:**
Simone Scacchi
simone.scacchi@unimi.it

Specialty section:
This article was submitted to Integrative Physiology, a section of the journal Frontiers in Physiology

Received: 13 December 2021
Accepted: 21 February 2022
Published: 24 March 2022

Citation:
Gionti V, Scacchi S, Colli Franzone P, Pavarino LF, Dore R and Storti C (2022) Role of Scar and Border Zone Geometry on the Genesis and Maintenance of Re-Entrant Ventricular Tachycardia in Patients With Previous Myocardial Infarction. Front. Physiol. 13:834747. doi: 10.3389/fphys.2022.834747

In patients with healed myocardial infarction, the left ventricular ejection fraction is characterized by low sensitivity and specificity in the prediction of future malignant arrhythmias. Thus, there is the need for new parameters in daily practice to perform arrhythmic risk stratification. The aim of this study is to identify some features of proarrhythmic geometric configurations of scars and border zones (BZ), by means of numerical simulations based on left ventricular models derived from post myocardial infarction patients. Two patients with similar clinical characteristics were included in this study. Both patients exhibited left ventricular scars characterized by subendo- and subepicardial BZ and a transmural BZ isthmus. The scar of patient #1 was significantly larger than that of patient #2, whereas the transmural BZ isthmus and the subdendo- and subepicardial BZs of patient #2 were thicker than those of patient #1. Patient #1 was positive at electrophysiologic testing, whereas patient #2 was negative. Based on the cardiac magnetic resonance (CMR) data, we developed a geometric model of the left ventricles of the two patients, taking into account the position, extent, and topological features of scars and BZ. The numerical simulations were based on the anisotropic monodomain model of electrocardiology. In the model of patient #1, sustained ventricular tachycardia (VT) was inducible by an S2 stimulus delivered at any of the six stimulation sites considered, while in the model of patient #2 we were not able to induce sustained VT. In the model of patient #1, making the subendo- and subepicardial BZs as thick as those of patient #2 did not affect the inducibility and maintenance of VT. On the other hand, in the model of patient #2, making the subendo- and subepicardial BZs as thin as those of patient #1 yielded sustained VT. In conclusion, the results show that the numerical simulations have an effective predictive capability in discriminating patients at high arrhythmic risk. The extent of the infarct scar and the presence of transmural BZ isthmuses and thin subendo- and subepicardial BZs promote sustained VT.

Keywords: cardiac re-entry, monodomain model, infarct border zone, monomorphic ventricular tachycardia, myocardial infarction

1. INTRODUCTION

Sudden cardiac death (SCD) after myocardial infarction is a significant public healthcare burden (Fishman et al., 2010). The main goal of clinical electrophysiology in the primary prevention of major arrhythmic events is the development of accurate risk stratification algorithms. Based on the results from clinical trials, left ventricular ejection function (LVEF) and patient New York Heart Association (NYHA) functional classification are used as the principal diagnostic parameters in designing treatments to avoid future sudden cardiac death (Priori et al., 2015; Al-Khatib et al., 2018). However, other studies (Gorgels et al., 2003; Stecker et al., 2006; Sabbag et al., 2015) raise skepticism about the true role of LVEF, because this approach is characterized by low sensitivity and specificity in the prediction of malignant arrhythmias. To date, in patients with remote myocardial infarction and preserved LVEF, no non-invasive risk stratification technique has demonstrated sufficient specificity and sensitivity. Although a two-step approach including non-invasive risk factors (such as premature ventricular complexes, non-sustained ventricular tachycardia, late potentials, and prolonged QTc), and electrophysiology study (EPS) can help in the stratification of arrhythmic risk (see Gatzoulis et al., 2019), in the near future, new effective and non-invasive parameters need to be introduced for arrhythmic risk stratification. For this purpose, a full understanding of the role of each arrhythmic substrate component is necessary for outcome prediction. Besides the clinical and experimental studies, computer modeling might represent a reliable and effective tool to predict the arrhythmic risk of specific patients and the ablation target, as proposed in several recent publications (Ashikaga et al., 2013; Deng et al., 2015, 2016; Arevalo et al., 2016; Campos et al., 2021).

The scar tissue and the border zone (BZ) constitute the most common arrhythmogenic substrate in ischemic cardiomyopathy (Moran et al., 1982). In this regard, cardiac magnetic resonance (CMR) is a highly effective imaging modality for the characterization of myocardial tissue (Pattanayak and Bleumke, 2015). Histologically, a myocardial scar is not always a uniform lesion. In fact, the fibrosis areas in the scar are interrupted by viable fibers that constitute slow conduction pathways (Fenoglio et al., 1983). It is well recognized that scar heterogeneity within the myocardium at CMR is arrhythmogenic (Peters et al., 1997; Peters and Wit, 1998; de Bakker et al., 2005; Ciaccio et al., 2007). Furthermore, in most cases, stable ventricular tachycardia (VT) circuits have two scarred areas and a central isthmus or channel composed of a small mass of viable fibers (Codreanu et al., 2008).

Investigating the role of scar and BZ electrophysiological and geometric properties on the onset and maintenance of re-entry dynamics is an active research area; refer to the experimental studies (Wit et al., 1982; Dillon et al., 1988; Janse and Wit, 1989; Peters et al., 1997). Recent computational studies have investigated the pro-arrhythmic mechanisms associated with BZ tissue (Cabo and Boyden, 2003; Ciaccio et al., 2004, 2007, 2015; Cabo et al., 2006; Cabo, 2014; Connolly et al., 2015; Connolly and Bishop, 2016; Campos et al., 2018).

Our previous numerical study (Colli-Franzone et al., 2019) demonstrated, in idealized conditions, that configurations characterized by a thin subepicardial BZ and wide scar, even without transmural BZ isthmuses, facilitate the onset and perpetuation of VT re-entry. However, to our knowledge, a detailed study on patient-derived geometric configurations of scars and BZ that are more likely to promote VT is still missing in the literature.

The aim of the present investigation is to identify some features of proarrhythmic geometric configurations of scar and BZ, by means of numerical simulations based on left ventricle models derived from two post-infarction patients, similar with respect to age, gender, NYHA class, the prevalence of coronary artery disease and scar localization, but different in the outcome of EPS.

2. METHODS

We applied a four-step model: (1) selection of post-myocardial infarction patients with moderate systolic dysfunction and different vulnerability to VT at EPS; (2) identification at CMR of scar and BZ anatomic pattern of interest; (3) formulation of a mathematical model of the left ventricle, taking into account the position, extent, and topological features of the scars and BZ; and (4) modulation of the geometric features of scars and BZ.

2.1. Clinical Data

We retrospectively screened patients with prior myocardial infarction scheduled for an EPS between January 1, 2019, and July 1, 2020. The patients did not meet criteria for ICD implantation in primary prevention. The reason for referral to the EPS was arrhythmia risk stratification because of moderate left ventricular dysfunction at CMR and a history of frequent premature ventricular contractions and syncope. Of the seven patients that were screened, two patients were included because they were similar with respect to age, gender, the prevalence of coronary artery disease, scar localization, but different in EPS outcome.

For patients selection, a comprehensive patient medical history, including coronary artery disease risk factors, NYHA class, and medications at the time of EPS, was obtained. Additionally, 12-lead electrocardiography was performed and interpreted in combination with clinical and CMR data. Myocardial infarction was considered if there were previous symptoms of myocardial ischemia, pathological Q waves at 12-lead electrocardiography, loss of viable myocardium at CMR in a pattern consistent with an ischaemic etiology, and a history of a rise and/or fall of cardiac troponin (cTn) values with at least one value above the 99th percentile upper reference limit (URL), in line with a universal definition of myocardial infarction (Thygesen et al., 2018). The clinical characteristics of the two patients are reported in **Table 1**.

2.1.1. CMR Acquisition

Clinical 3-T scanners (Siemens Sonata) with phased-array receiver coils and standard protocols were used. Briefly, cine

TABLE 1 | Clinical characteristics of the two patients.

Clinical characteristics	EPS positive	EPS negative
NYHA class	II	II
Age	57 years old	59 years old
Gender	Male	Male
Hypertension	Yes	Yes
Dyslipidemia	Yes	Yes
Diabetes Mellitus	Yes	No
Tabagism	Yes	No
Obesity*	No	No
Time from MI to EPS	12 months	27 months
No. of coronaropathy	2 vessels	2 vessels

**Obesity was defined as BMI ≥ 30 Kg/m^2.*

TABLE 2 | Cardiovascular magnetic resonance (CMR) features of the two patients.

CMR characteristics	EPS positive	EPS negative
Basal-apex length	94 mm	93 mm
LV end-diastolic volume	228 ml	232 ml
LV end-diastolic diameter	57.26 mm	58.37
Wall thickness	9.2 mm	10.0 mm
LV ejection fraction	37 %	43 %
Isthmus section diameter	1.5 mm	3.1 mm
Scar location	Antero-septal	Antero-septal
Endocardial scar and BZ area	1416.11 mm^2	824.42 mm^2
Endocardial BZ thickness	1.2 mm	1.8 mm
Epicardial BZ thickness	1.3 mm	3.1 mm

images were acquired in multiple short-axis (every 10 mm throughout the entire LV) and 3 long-axis views using a steady-state free precession sequence (slice thickness, 6 mm; inter-slice gap, 4 mm; TR, 3.0 ms; TE, 1.5 ms; temporal resolution, 35–40 ms; flip angle, 60; in-plane resolution 1.71.4 mm). Delayed enhancement cardiovascular magnetic resonance (DE-CMR) was performed using a segmented inversion-recovery gradient-echo sequence (slice thickness, 6 mm; inter-slice gap, 4 mm; TR, 9.5 ms; TE, 3.8 ms; flip angle, 25; in-plane resolution 1.8x1.4 mm) 10 min after contrast administration (gadoversetamide, 0.15 mmol/kg) in the identical locations as cine-CMR. The inversion delay time was set to null signal from normal myocardium and was typically 280–360 ms.

2.1.2. CMR Analysis

All CMR analyses were performed with Digital Imaging and Communications in Medicine (DICOM) images with a custom software package. Left ventricular volumes, mass, and ejection fraction were quantitatively measured from the stack of short-axis cine images using standard techniques (Rehr et al., 1985; Walsh and Hundley, 2007). Papillary muscles were regarded as part of the ventricular cavity. For each patient, the maximum signal intensity (SI) within an infarct region in each image of the left ventricle stack was automatically determined, and the scar was defined as myocardium with SI > 50% of the maximal SI. A region of interest was then placed by a trained observer in the remote myocardium, i.e., a portion of myocardium without hyperenhancement and with normal motion, in an area free of artifacts and with uniform myocardial suppression. The signal suppression allows the objective spatial extension of the hyperenhancement area. BZ within the infarct periphery was defined as the myocardium with SI > peak remote SI but SI < 50% of maximal SI of the high SI myocardium (Amado et al., 2004; Schmidt et al., 2007). The transmural extent of hyperenhancement was measured by standard techniques (Kim et al., 2000). Each short-axis slice was segmented circumferentially into 12 wedges. For each segment, the transmural extent of total hyperenhancement was expressed as a percentage of the total segment area. For each patient, the percentage of segments with transmural extents of hyperenhancement within each quartile (0 to 25%; 26 to 50%; 51 to 75%; or > 75%) was determined. **Table 2** summarizes the CMR characteristics of the two patients, see **Figures 1**, **2**.

2.1.3. Electrophysiologic Testing

Electrophysiology study was performed using standard techniques. Briefly, programmed stimulation was performed using two drive trains (600 and 400 ms) followed by one to three ventricular extrastimuli. The extrastimuli were 2 ms in duration at two times the diastolic threshold at two right ventricular sites (apex and outflow tract), reducing the coupling interval until reaching the ventricular refractoriness or a coupling interval of 190 ms. The EPS results were classified as negative (non-inducibility with complete protocol) or positive (monomorphic VT that lasted 30 s or required cardioversion for hemodynamic compromise). Additionally, two expert operators analyzed the superficial ECG morphology of VT and interpreted it in combination with the isthmus localization at CMR. Two patients were included in the study, one with negative EPS and one with positive EPS. **Tables 1**, **2** summarize the clinical and CMR characteristics, respectively. In both patients, the maximum scar extension is localized in the mid-interventricular septum. The scar extension was greater in the patient with positive EPS, instead, the isthmus thickness was greater in the patient with negative EPS.

2.2. Computer Modeling

To model the electrical current flow through the myocardium, we assume the monodomain representation of the cardiac tissue (Colli-Franzone et al., 2014). The computational electrophysiological model considers three different types of cardiac tissue regions: healthy myocardium, necrotic scar, and the infarct BZ.

Let Ω denotes a three-dimensional portion of the myocardium. According to the monodomain model, the evolution of the transmembrane potential $v(\mathbf{x}, t)$, gating variables $\mathbf{w}(\mathbf{x}, t)$, and ionic concentrations $\mathbf{c}(\mathbf{x}, t)$ is described by the following system of non-linear partial differential equations:

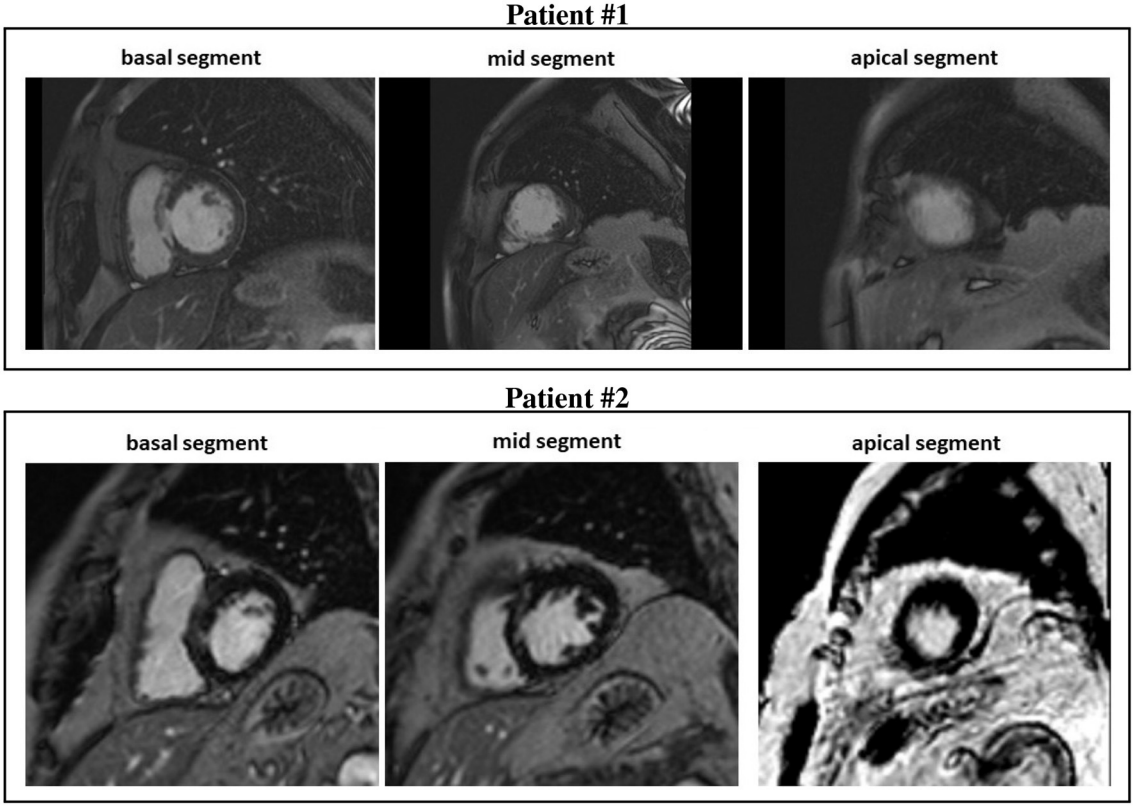

FIGURE 1 | Cardiovascular magnetic resonance (CMR) short-axis slices of the basal, mid, and apical segment of patients #1 and #2.

$$\begin{cases} c_m \partial_t v - div(D\nabla v) + i_{ion}(v, \mathbf{w}, \mathbf{c}) = i_{app} & \text{in } \Omega \\ \partial_t w - R_w(v, \mathbf{w}, \mathbf{c}) = 0, \quad \partial_t c - R_c(v, \mathbf{w}, \mathbf{c}) = 0 & \text{in } \Omega \\ \mathbf{n}^T D \nabla v = 0 & \text{on } \partial\Omega \end{cases} \tag{1}$$

with appropriate initial conditions on $v(\mathbf{x}, 0)$, $\mathbf{w}(\mathbf{x}, 0)$, and $\mathbf{c}(\mathbf{x}, 0)$. Here, c_m and i_{ion} denote the capacitance and the ionic current of the membrane per unit volume, i_{app} represents the applied current per unit volume, and D is the anisotropic conductivity tensors.

Assuming transversely isotropic properties of the intra- and extracellular media, the intra- and extracellular conductivity tensors are given by

$$D_{i,e}(\mathbf{x}) = \sigma_{\mathbf{t}}^{\mathbf{i,e}}\, \mathbf{I} + (\sigma_{\mathbf{l}}^{\mathbf{i,e}} - \sigma_{\mathbf{t}}^{\mathbf{i,e}})\mathbf{a_l}(\mathbf{x})\mathbf{a_l}(\mathbf{x})^{\mathbf{T}}, \tag{2}$$

where $\sigma_l^{i,e}$ and $\sigma_t^{i,e}$ are the conductivity coefficients of the intra- and extracellular media measured along the fiber direction $\mathbf{a}_l(\mathbf{x})$ and any cross fiber direction, respectively. According to the Monodomain model derivation presented in Colli-Franzone et al. (2005), the tensor D is given by

$$D(\mathbf{x}) = \mathbf{D_e}(\mathbf{x})(\mathbf{D_i}(\mathbf{x}) + \mathbf{D_e}(\mathbf{x}))^{-\mathbf{1}}\mathbf{D_i}(\mathbf{x}) = \sigma_{\mathbf{t}}\mathbf{I} + (\sigma_{\mathbf{l}} - \sigma_{\mathbf{t}})\, \mathbf{a_l}(\mathbf{x})\mathbf{a_l}(\mathbf{x})^{\mathbf{T}}$$

where $\sigma_{t,l} = \frac{\sigma^e_{t,l}\sigma^i_{t,l}}{\sigma^e_{t,l} + \sigma^i_{t,l}}$.

The ionic current is given by $i_{ion} = \chi I_{ion}$, where χ is the membrane surface to volume ratio and the ionic current per unit area of the membrane surface I_{ion} is given by the ten Tusscher membrane model (TP06) (ten Tusscher et al., 2004; ten Tusscher and Panfilov, 2006), available from the cellML depository (models.cellml.org/cellml). The TP06 ionic model also specifies the functions $R_w(v, \mathbf{w})$ and $R_c(v, \mathbf{w}, \mathbf{c})$ in the ordinary differential equations (ODEs) system, consisting of 17 ODEs modeling the main ionic currents dynamics.

2.3. Numerical Methods

The space discretization of the system (1) is performed by employing hexahedral isoparametric Q_1 finite elements, while the time discretization is based on splitting the ODEs of the membrane model from the reaction-diffusion PDE. Regarding the PDE, a semi-implicit scheme is adopted, where the diffusion term is treated implicitly, while the reaction term is treated explicitly. This discretization strategy yields a large-scale linear system of algebraic equations that must be solved at each time step. In order to ensure parallelization and portability of our Fortran code, we use the PETSc parallel library (Balay et al., 2020), a suite of data structures and functions for building large-scale parallel scientific applications, based on the MPI communication library. The parallel strategy employed is based on a geometric domain decomposition strategy, where each

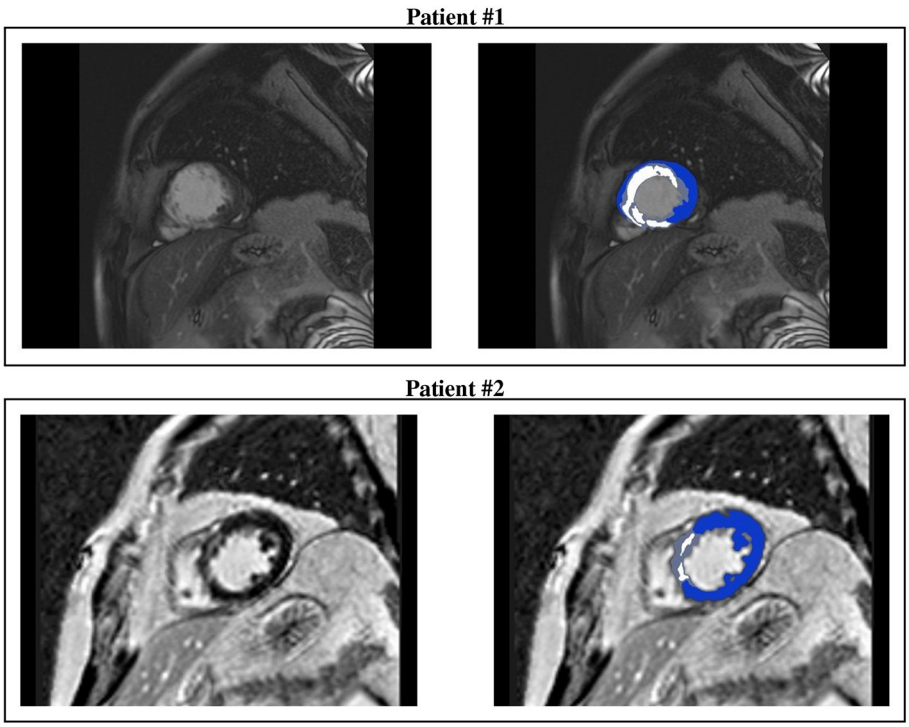

FIGURE 2 | CMR short-axis slices (left) of interest of patients #1 and #2 and the resulting ventricular segmentation (right) into non-infarcted myocardium (blue), border zone (gray), and scar (white).

subdomain is assigned to one processor and the information associated with the interior of the subdomain is uniquely owned by that processor. The processor stores all subvectors and a block of the matrices (mass, stiffness) associated with each subdomain. The linear system at each time step is solved by a parallel conjugate gradient method, preconditioned by the Block Jacobi preconditioner, with ILU(0) local solvers. For further details about the numerical procedure, refer to our previous works (Colli-Franzone et al., 2011, 2014, 2019). The simulations are run on 128 cores of the Linux Cluster Galileo of Cineca.

2.4. Simulations Setup

Computational domain. The domain H is the image of a Cartesian periodic slab using ellipsoidal coordinates, yielding a truncated ellipsoid modeling a left ventricle (LV) geometry, described by the parametric equations

$$\begin{cases} x = a(r)\cos\theta\cos\phi & \phi_{min} \le \phi \le \phi_{max}, \\ y = b(r)\cos\theta\sin\phi & \theta_{min} \le \theta \le \theta_{max}, \\ z = c(r)\sin\theta & 0 \le r \le 1, \end{cases}$$

where $a(r) = a_1 + r(a_2 - a_1)$, $b(r) = b_1 + r(b_2 - b_1)$, $c(r) = c_1 + r(c_2 - c_1)$. The parameters $a_1 = b_1$, $a_2 = b_2$, c_1, and c_2 are tuned to match the dimension of the left ventricle of the two patients (refer to **Figure 3** and **Table 3** for the geometric models and the position of scars and BZ), whereas $\phi_{min} = -\pi/2$, $\phi_{max} = 3\pi/2$, $\theta_{min} = -3\pi/8$, and $\theta_{max} = \pi/8$. We will refer to the inner surface of the truncated ellipsoid ($r = 0$) as endocardium and to the outer surface ($r = 1$) as epicardium. In all computations, a structured grid of $512 \times 256 \times 48$ hexahedral isoparametric Q_1 finite elements of size $h \approx 0.02$ cm is used in space, for a total amount of 6,447,616 mesh nodes. Fibers rotate transmurally, linearly with the depth and counterclockwise from epicardium to endocardium, for a total amount of 120°. More precisely, in a local ellipsoidal reference system $(\mathbf{e}_\phi, \mathbf{e}_\theta, \mathbf{e}_r)$, the fiber direction $\mathbf{a}_l(\mathbf{x})$ at a point $\mathbf{x}$ is given by

$$\mathbf{a}_l(\mathbf{x}) = \mathbf{e}_\phi \cos\alpha(r) + \mathbf{e}_\theta \sin\alpha(r), \text{ with } \alpha(r) = \frac{2}{3}\pi(1-r) - \frac{\pi}{4}, \quad 0 \le r \le 1.$$

The volume occupied by the left ventricular myocardial tissue of patient #1 is 141.3 cm^3, where 25.3 and 4.3 cm^3 are occupied by the scar and BZ, respectively. The volume occupied by the left ventricular myocardial tissue of patient #2 is 160.1 cm^3, where 6.9 and 5.2 cm^3 are occupied by the scar and BZ, respectively.

Parameter calibration. The values of the transversely isotropic conductivity coefficients in (2), that we use for the healthy tissue in all the numerical tests, are $\sigma_l^i = 3$, $\sigma_t^i = 0.31525$, $\sigma_l^e = 2$, and $\sigma_t^e = 1.3514$, all expressed in $m\Omega^{-1}cm^{-1}$; refer to Colli-Franzone et al. (1990, 2011) for the derivation of these conservative values. These values, coupled with the TP06 membrane model, predict conduction velocities of about 0.061 and 0.027 cm/ms for excitation layer propagating along and across the fiber direction, respectively. We remark that these conduction velocities are within the physiological range, refer to

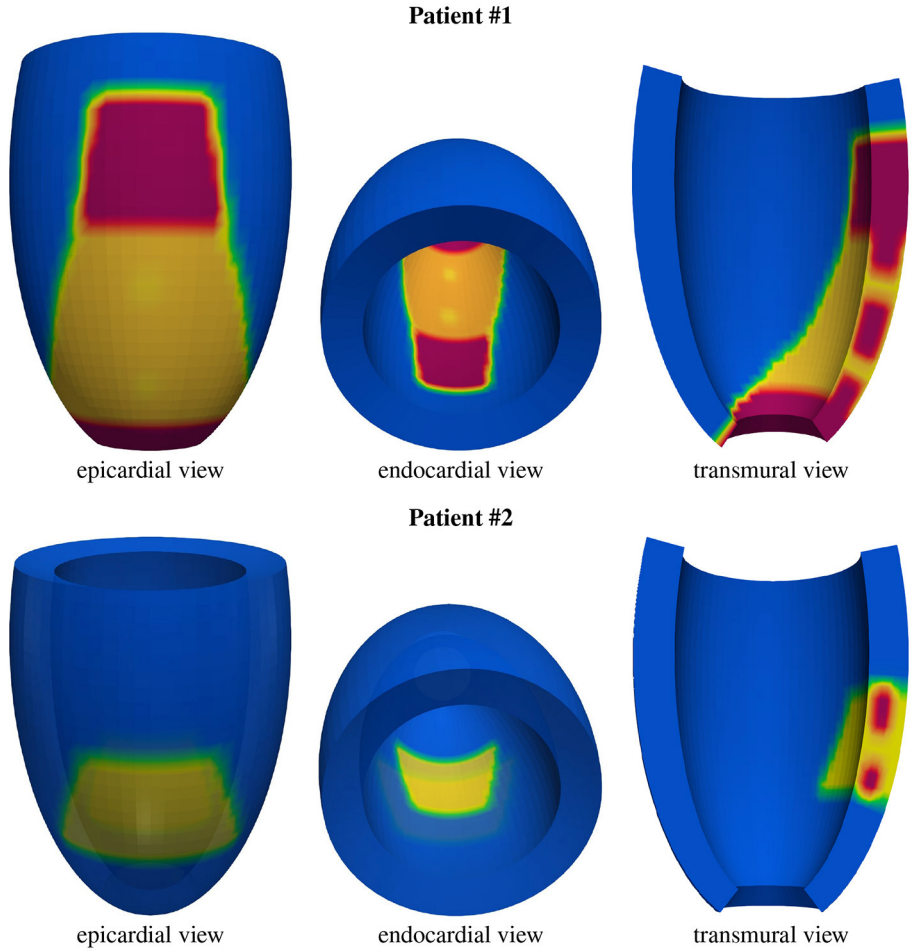

FIGURE 3 | Geometric models of the left ventricles of the two patients: healthy tissue (blue), border zone (BZ) tissue (yellow), scar tissue (red). From the transmural view, one can appreciate the transmural BZ isthmuses of the two patients.

TABLE 3 | Parameters of the truncated ellipsoidal geometries expressed in *cm*.

Patient	a_1	a_2	b_1	b_2	c_1	c_2
#1	2.5	3.5	2.5	3.5	6.5	7.1
#2	2.5	3.6	2.5	3.6	6.5	7.2

Roberts et al. (1979) and Punske et al. (2003). The membrane surface to volume ratio is $\chi = 10^3\ cm^{-1}$ and the membrane capacitance per unit volume is $c_m = \chi C_m$, where $C_m = 1\ \mu F/cm^2$ is the membrane capacitance per unit area.

Structural and functional remodeling in healed infarct generates a layer of viable myocardium cells, the so-called BZ (Pinto, 1999; Nattel et al., 2007). The BZ tissue is characterized by scar patches (de Jong et al., 2011; McDowell et al., 2011) and marked electrical and topological heterogeneity (Peters et al., 1997; Ciaccio et al., 2007).

We model the BZ by implementing a 60% reduction of fast sodium current conductance g_{Na} (Baba et al., 2005; Decker and Rudy, 2010), a 70% reduction of L-type calcium current conductance g_{CaL} (Baba et al., 2005) and a reduction of 70 and 80% of the potassium currents conductances g_{Kr} and g_{Ks}, respectively, (Jiang et al., 2000). Previous experimental studies (Yao et al., 2003) have also shown a loss of the average number of transverse gap-junctions between viable fibers in BZ tissue. We model this loss as a 75% reduction of cross fiber intracellular conductivity coefficient σ_t^i. Regarding the modeling of BZ tissue properties, we also refer to the review article (Mendonca Costa et al., 2018).

In the scar region, we assume an isotropic conductivity amounting to $0.5\ m\Omega^{-1}cm^{-1}$. To our knowledge, previous works have considered values of scar conductivity ranging between 0.05 and $0.5\ m\Omega^{-1}cm^{-1}$. We have chosen the value of 0.5 because it is the value closest to the average of the conductivities assigned in the BZ.

Stimulation protocol. Stimulations of $250\ mA/cm^3$ amplitude and $1\ ms$ duration are applied in a small subendocardial volume located in six different sites depending on the simulation points displayed in **Figure 4**: apical stimulation

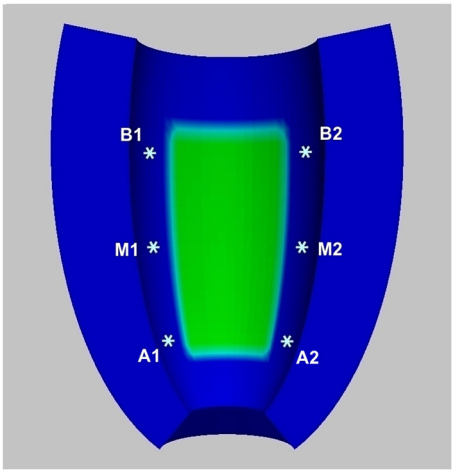

FIGURE 4 | Schematic representation of stimulation sites.

at points A1 or A2; central stimulation at points M1 or M2; basal stimulation at points B1 or B2. For each stimulation point, we first apply five pacing stimuli (S1) at a basic cycle length (BCL) of 500 *ms*. Then, a premature stimulus (S2) is delivered 350 *ms* after S1. If S2 does not generate a re-entrant arrhythmia, the S1-S2 coupling interval is shortened in steps of 10 *ms* until arrhythmia is induced or the S2 fails to trigger excitation. If an arrhythmia is not induced, an additional S3, and if necessary S4, is delivered in the same manner as S2 (initially delivered 350 *ms* after the previous stimulus, and then shortened until arrhythmia is induced or the stimulus fails). The final simulation time is 4 *s*. We consider a re-entry sustained if it maintains until 4 *s*.

Postprocessing. The transmembrane potential distributions reported in the following are generated using Paraview-5.7.0-RC1, whereas the activation time distributions and potential waveforms are generated using Matlab_R2021a. The activation time is defined in the general point **x** as the unique instant t_A when the transmembrane potential $v(\mathbf{x}, t_A) = -50\ mV$ during the depolarization phase of the action potential.

3. RESULTS

3.1. Patient #1 LV Model

M1 stimulation site. **Figures 5**, **6** report some snapshots of the transmembrane potential on the epicardium and on two longitudinal transmural sections, after the S2 stimulus, applied at t = 350 ms, being t = 0 ms the onset of the S1 stimulus. At t = 395 ms (**Figure 5A**), the excitation layer elicited by the S2 stimulus reaches the epicardial surface, generating a breakthrough (BKT) on the right side of the scar, halfway between the apex and the base. Then, excitation spreads through epicardium, entering the BZ at t = 450 ms (**Figure 5B**) and moving around the basal portion of the scar (**Figures 5C,D**). At t = 600 ms (**Figure 5H**), both endocardial and epicardial layers enter the apical isthmus, which results in complete activation at t = 700 ms (**Figure 5M**). At the same time, the endocardial excitation layer starts to enter the central isthmus, while the epicardial excitation layer is blocked at the epicardial side of the central isthmus. The excitation layer propagates very slowly through the isthmus, from the endocardium to the epicardium (**Figures 5N,O**). At t = 975 ms, excitation exits the BZ subepicardial layer over the central isthmus, generating an epicardial BKT (**Figures 5L,P**), which induces a propagating quasi-elliptical epicardial excitation layer, with the major axis aligned with the epicardial fiber direction. This excitation layer triggers the first cycle of re-entry (**Figures 6A–H**). Furthermore, when the excitation layer reaches the healthy myocardial tissue, the propagation proceeds intramurally toward the endocardial surface, moving around the basal scar region. The re-entrant activation follows the same circuit through the central isthmus (**Figures 6I–P**) for two cycles and then dies. We report in **Figure 9A** the epicardial activation time distributions of the S2 and first reentrant excitation sequence. In order to clarify the dynamics of the excitation sequence at the level of the epicardial surface and transmurally, we have added the movies **SM_paz1_M1_epi** and **SM_paz1_M1_trans** in the **Supplementary Material**.

A2 stimulation site. **Figures 7**, **8** report some snapshots of the transmembrane potential on the epicardium and on two longitudinal transmural sections, after the S2 stimulus, applied at t = 350 ms, being t = 0 ms the onset of the S1 stimulus. At t = 450 ms (**Figure 7A**), the excitation layer elicited by the S2 stimulus spreads through the epicardial surface, entering the apical portion of BZ. Then, it proceeds toward the base, moving around the basal portion of the scar (**Figures 7B–D**). At t = 650 ms (**Figure 7H**), the endocardial excitation layer enters the apical isthmus and, propagates slowly through the isthmus from endocardium to epicardium (**Figure 7O**), it reaches the apical epicardial surface at t = 850 ms (**Figure 7N**). After the apical epicardial BKT (**Figure 7J**), excitation spreads through the epicardial BZ, generating the first cycle of re-entry (**Figures 8A–H**). The re-entrant activation then maintains, following the same circuit through the apical isthmus (**Figures 8I–P**) and thus inducing even in this case a sustained VT. We report in **Figure 9B** the epicardial activation time distributions of the S2 and first reentrant excitation sequence. In order to clarify the dynamics of the excitation sequence at the level of the epicardial surface and transmurally, we have added the movies **SM_paz1_A2_epi** and **SM_paz1_A2_trans** in the **Supplementary Material**.

A deeper investigation has shown that the apical isthmus is not able to directly generate a propagating excitation layer in the overlying epicardial area, but it releases an electrotonic current which flows into the subepicardial BZ layer, triggering the first re-entrant excitation localized on the left of the BZ (**Figure 7N**). The epicardial area overlying the apical isthmus is then excited by the re-entrant excitation at about t = 950 ms (**Figure 8A**). The same excitation phenomenon occurs during the second cycle of re-entry. In the subsequent cycles, instead, the current flowing through the isthmus is able to trigger directly the excitation when it reaches the epicardium.

Summary. Stimulations from all the six pacing sites produced re-entry, which is sustained in all cases except from site M1. These outcomes are summarized in **Figure 10**, which reports

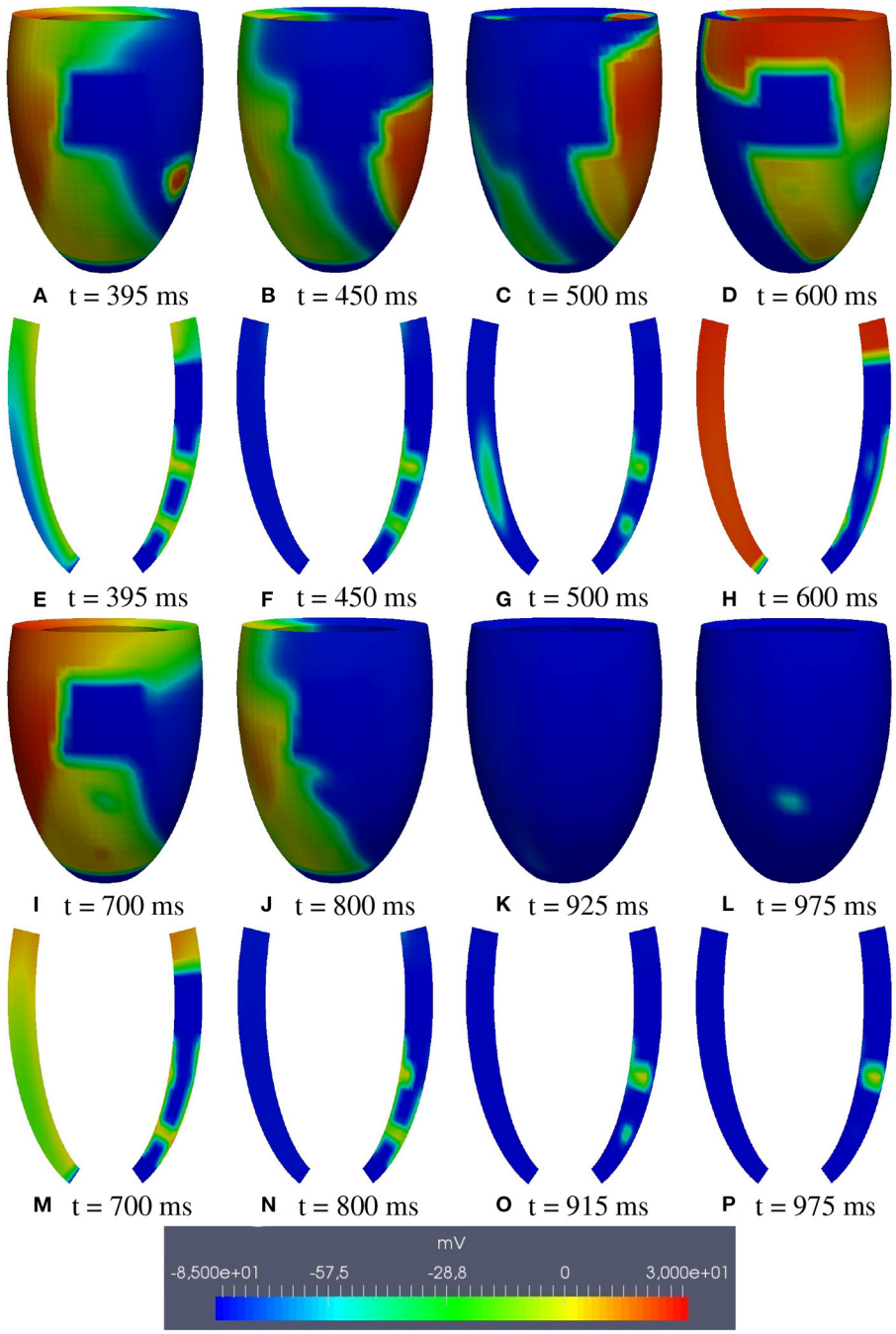

FIGURE 5 | Patient #1. M1 stimulation. **(A–P)** Transmembrane potential snapshots (t = 395–975 ms) on the epicardial surface and on a transmural section. t = 0 corresponds to the S1 stimulus. The S2 stimulus is applied at t = 350 ms.

for each simulation the transmembrane potential waveform in a sample epicardial point located in the BZ, at the exit of the transmural isthmus. We observed differences in the dynamics of re-entry among the stimulations. In stimulations B1, M1, A1, re-entry is triggered by an excitation layer that propagates through the central isthmus toward the epicardial surface. In stimulations B2, M2, A2, the pathway of re-entry follows the apical isthmus, but during the first two cycles of re-entry, the excitation propagating through the isthmus does not reach directly epicardial surface. Indeed, the electrotonic current flowing in the subepicardial BZ from the isthmus is able to trigger excitation. All subsequent cycles of re-entry are of the same type observed in stimulations B1, M1, and A1.

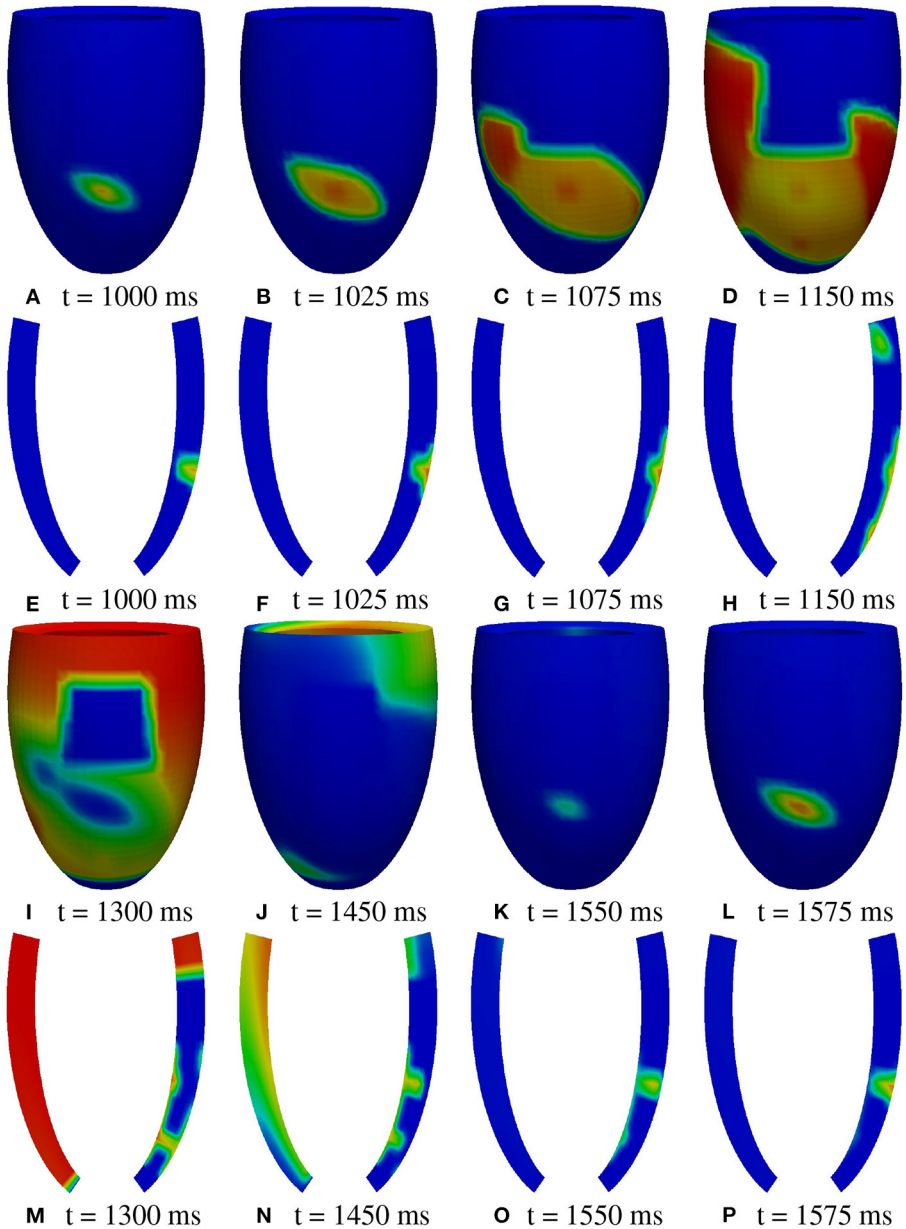

FIGURE 6 | Patient #1. M1 stimulation. **(A–P)** Transmembrane potential snapshots (t = 1,000–1,575 ms) on the epicardial surface and on a transmural section. t = 0 corresponds to the S1 stimulus. The S2 stimulus is applied at t = 350 ms. The colorbar is the same as in **Figure 5**.

3.2. Patient #2 LV Model

M2 stimulation site. We apply an S2 stimulus with an S1-S2 coupling interval of 340 ms, an S3 stimulus with an S2-S3 coupling interval of 270 ms, and an S4 stimulus with an S3-S4 coupling interval of 300 ms. **Figures 11**, **12** report some snapshots of the transmembrane potential on the epicardium and on a circumferential transmural section, after the S4 stimulus, being t = 0 ms the onset of the S3 stimulus. A conduction block occurs when the excitation layer elicited by the S4 stimulation reaches the subepicardial BZ, at about t = 450 ms, as shown in **Figure 12C**. Then, the tissue in the subepicardial BZ layers in contact with the scar does not recover completely, and an excitation layer starts to propagate from right to left after t = 600 ms (**Figures 12D–G**). When this excitation layer reaches the left lateral border separating the BZ from the healthy tissue, it triggers an intramural re-entrant excitation propagating toward both the endocardium and epicardium (**Figures 12H–J**). Excitation then propagates through the whole LV tissue (**Figures 11H–P**), but re-entry is not sustained, since it dies after the first cycle.

Summary. An analogous non-sustained re-entry phenomenon occurs in the case of the M1 stimulation site. Instead, in case of A1 stimulation site, no re-entry is observed.

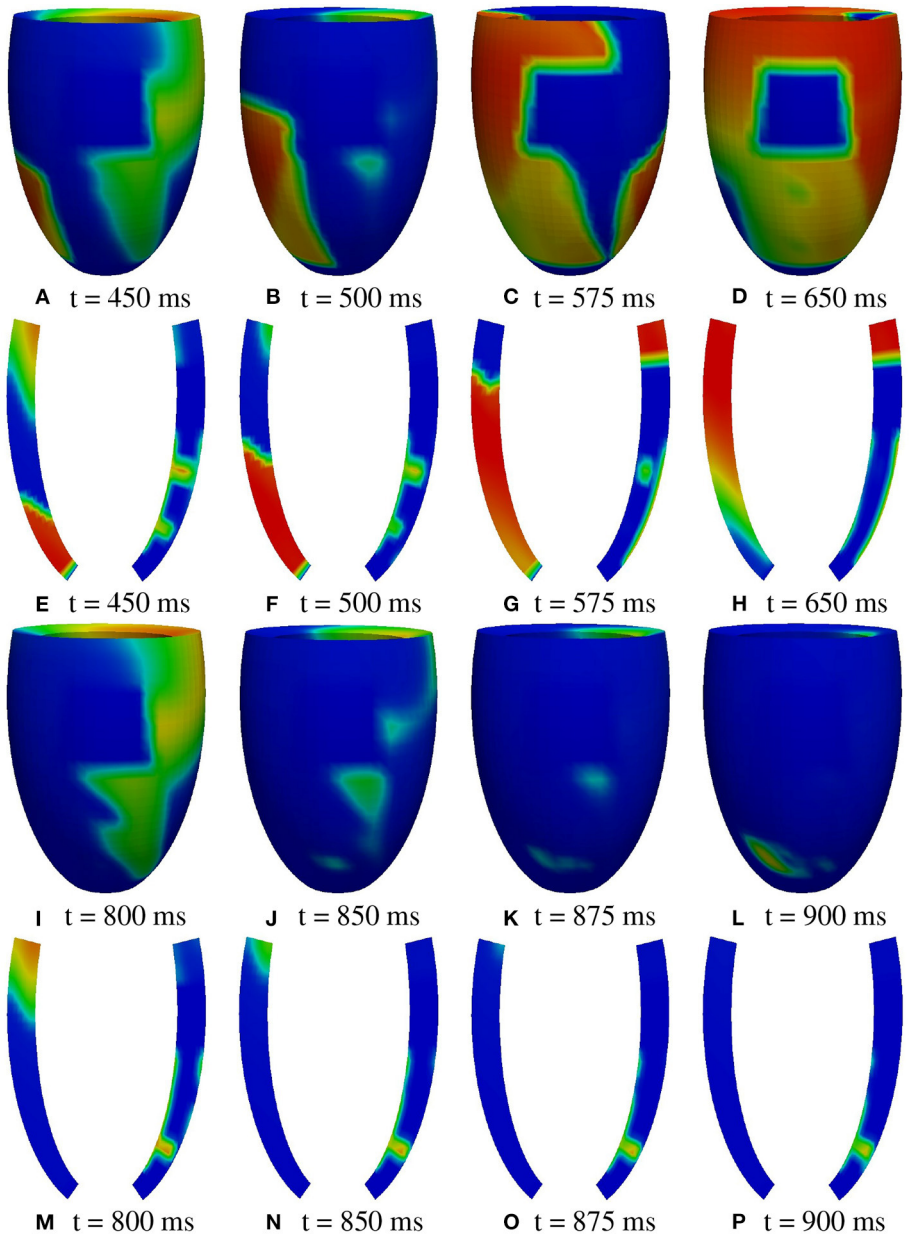

FIGURE 7 | Patient #1. A2 stimulation. **(A–P)** Transmembrane potential snapshots (t = 450–900 ms) on the epicardial surface and on a transmural section. t = 0 corresponds to the S1 stimulus. The S2 stimulus is applied at t = 350 ms. The colorbar is the same as in **Figure 5**.

From the other stimulation sites, we did not observe any sustained re-entry. Thus, irrespective of the stimulation site, sustained re-entry is never induced in the LV model of patient #2.

3.3. Modifications of Scar and BZ Configurations of Patients #1 and #2

In order to better understand the scar and BZ geometric features determining the different outcomes in the two patients, we considered the following three changes in the configuration of the BZ layer and/or the area of the isthmus section of patient#2:

- **configuration #1**: we reduce the section area of the isthmus, making it comparable with that of the central isthmus of patient #1;
- **configuration #2**: we make the subendo- and subepicardial BZ layer thickness as thin as in patient #1;
- **configuration #3**: we make the subendo- and subepicardial BZ layer thickness as thin as in patient #1 and we also reduce the

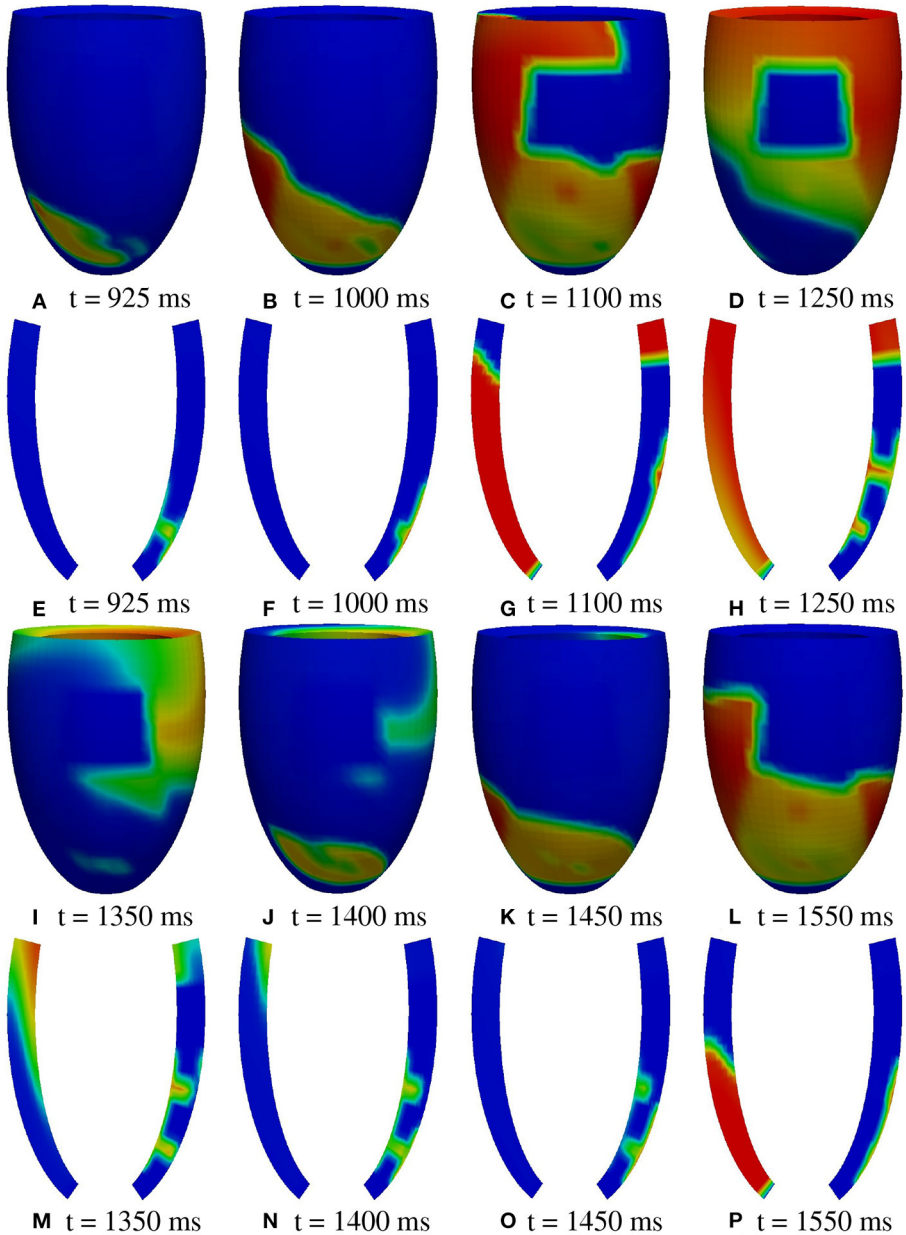

FIGURE 8 | Patient #1. A2 stimulation. **(A–P)** Transmembrane potential snapshots (t = 925–1550 ms) on the epicardial surface and on a transmural section. t = 0 corresponds to the S1 stimulus. The S2 stimulus is applied at t = 350 ms. The colorbar is the same as in **Figure 5**.

section area of the isthmus, making it comparable with that of central isthmus of patient #1.

In **configuration #1**, after a sufficiently premature S2 stimulus applied at site M1, the epicardial excitation layer blocks at the exit of the isthmus, while the endocardial excitation layer enters the isthmus, propagating toward the epicardial surface. When it reaches the exit of the isthmus, it is unable to trigger excitation into the sub-epicardial BZ. For the next 30 ms, the myocardial volume is almost completely repolarized, but inside the isthmus the transmembrane potential maintains values above the threshold, generating an electrotonic current that flows in the sub-epicardial BZ layer and at 1,024 ms it is able to trigger a re-entrant excitation. However, excitation dies after the first cycle of re-entry (see the movie **SM_paz2mod_conf1_M1_epi** in the **Supplementary Material**).

In **configuration #2**, after the S2 stimulus, the excitation layer propagating through the isthmus is able to re-excite the subepicardial BZ layer, triggering a sustained re-entry of type A (see the movie **SM_paz2mod_conf2_M1_epi** in the **Supplementary Material**).

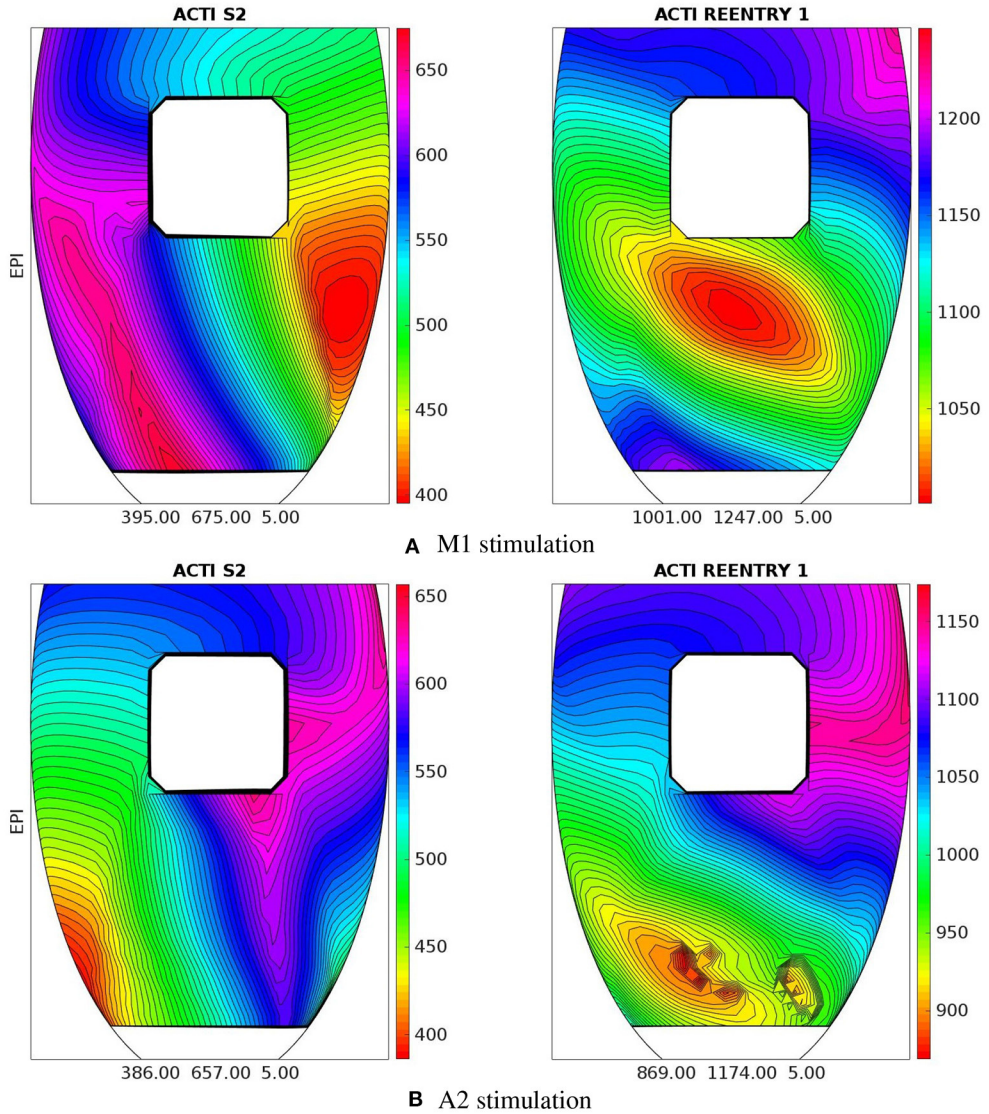

FIGURE 9 | Patient #1. Epicardial activation time distributions of S2 and first reentrant excitation sequences for M1 **(A)** and A2 **(B)** stimulations. Below each panel is reported the minimum, maximum, and isochrones step in ms of the displayed map.

In **configuration #3**, after the S2 stimulus, the excitation layer propagating through the isthmus is able to re-excite the subepicardial BZ layer, triggering a sustained re-entry of type B (see the movie **SM_paz2mod_conf3_M1_epi** in the **Supplementary Material**).

The outcomes of the previous three configurations are summarized in **Figure 13**, which reports for each simulation, the transmembrane potential waveform in a sample epicardial point located in the BZ, at the exit of the transmural isthmus.

Finally, we modified the model of patient #1 by increasing the thickness of the subendo- and subepicardial BZ, making it comparable to that of patient #2. After a sufficiently premature S2 stimulus from site M2, we were able to induce a sustained re-entry (see the movie **SM_paz1mod_M2_epi** in the **Supplementary Material**).

4. DISCUSSION

Improving arrhythmic risk stratification of patients with prior myocardial infarction and mildly reduced ejection fraction is one of the current challenges in clinical cardiology. Understanding the mechanisms (still unclear) and the scar geometric features that facilitate the onset of VT might help to identify patients at high risk.

In this work, two patients affected by infarct scar, both with LVEF $>$ 35%, have been selected for EPS. Patient #1 resulted positive, whereas patient #2 was tested negative. On the basis of the information derived from their CMR data, we have developed a finite element model of the left ventricle, taking into account the position, extent, and topological features of the scars. Then, we have run numerical simulations based on the anisotropic

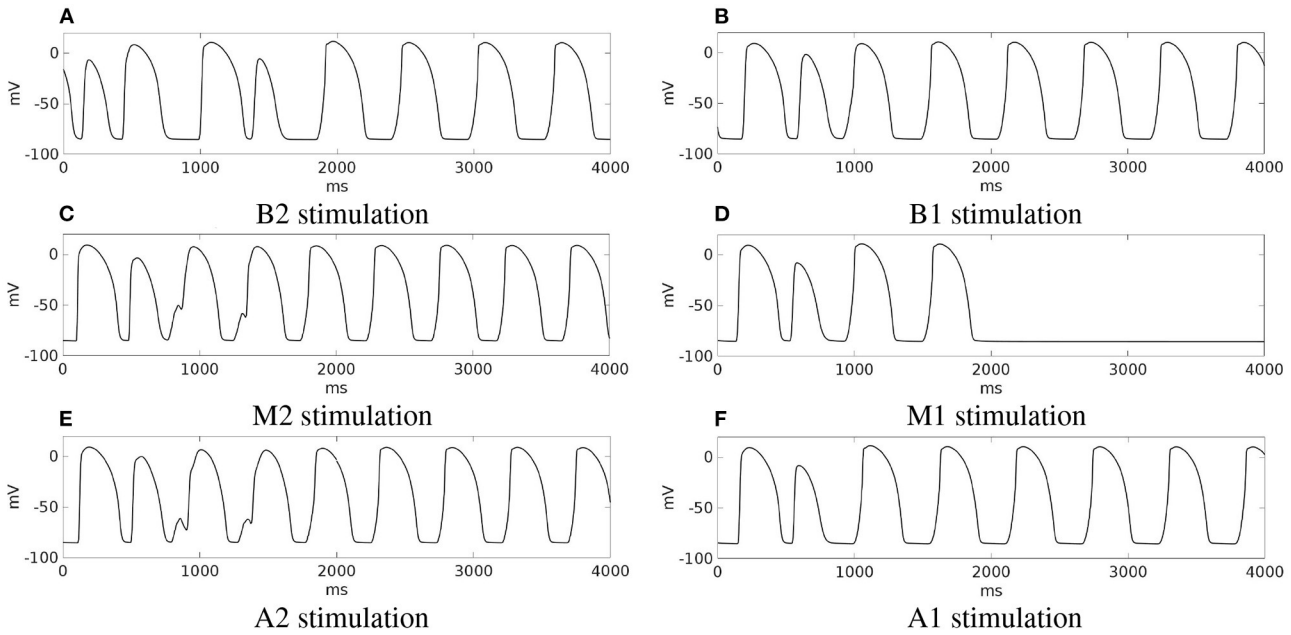

FIGURE 10 | Patient #1. **(A–F)** Transmembrane potential waveforms in the six stimulation cases, computed from an epicardial size located in the BZ, at the exit of the transmural isthmus.

Monodomain model of electrocardiology, mimicking an S1-S4 stimulation protocol, in order to

- verify whether the numerical modeling is able to reproduce the onset of VT in patient #1 and not in patient #2;
- ascertain the mechanisms that induce VT in patient #1;
- identify the geometric features of the infarct scar that facilitate the onset and maintenance of VT.

The simulation results have shown that, in patient #1, sustained VT occurs after a premature endocardial S2 stimulus. We were able to induce re-entry from all the six stimulation sites considered. Only in one case (M1 stimulation), the re-entry was not sustained. Depending on the location of the stimulus, the re-entrant circuit follows the path of the apical or central transmural isthmus. After the S2 stimulation, the excitation layer splits into two branches, one propagating through the subendocardial BZ and one through the subepicardial BZ. The mechanism that induces the onset of re-entry is the conduction block occurring when the epicardial excitation layer reaches the entrance of the apical or transmural isthmus, which is still refractory. The endocardial excitation layer instead, propagating slowly from the endocardial entrance through the isthmus, reaches the epicardial tissue, now excitable again, generating the re-entrant wave.

We identified two different exits of the re-entrant pathway:

- type A: the excitation layer propagating in the isthmus reaches the epicardial tissue, now excitable again, generating the re-entrant wave propagating over the sub-epicardium and subsequently spreading in the whole tissue (**Figures 5L**, **6A,B**, **14**–first row);
- type B: the excitation layer propagating in the isthmus reaches the sub-epicardial BZ layer, but it is not able to elicit a propagating wavefront. The electrotonic load in the isthmus generates a current flowing through the sub-epicardial BZ layer mainly along the fiber direction.The accumulation of the electrotonic current near the two lateral borders between the BZ layer and the healthy tissue elicits two propagating excitation layers spreading over the sub-epicardium and in the whole tissue (**Figures 7J–L**, **14**–second row).

Type A reentry is induced by stimulations B1, M1, A1, and the reentry circuit follows the central isthmus, whereas type B reentry is induced by stimulations B2, M2, A2, and the reentry circuit follows the apical isthmus. The different behavior can be attributed to:

- the slightly smaller section diameter of the apical isthmus with respect to the central one;
- the greater transmural thickness of the central wall with respect to the apical one;

In the LV model of patient #2, we did not observe the same mechanisms of reentry. In this case, only after the S4 stimulus, a conduction block occurs in the subepicardial BZ, generating a re-entrant wave that dies after the first cycle. Thus, we were not able to induce sustained VT in patient #2.

Consequently, the first conclusion of this study is that our computational results agree with the EPS performed on the two patients, confirming the effective predictive capability of numerical simulations in discriminating patients at high arrhythmic risk, as proposed in the pioneering papers (Ashikaga et al., 2013; Arevalo et al., 2016).

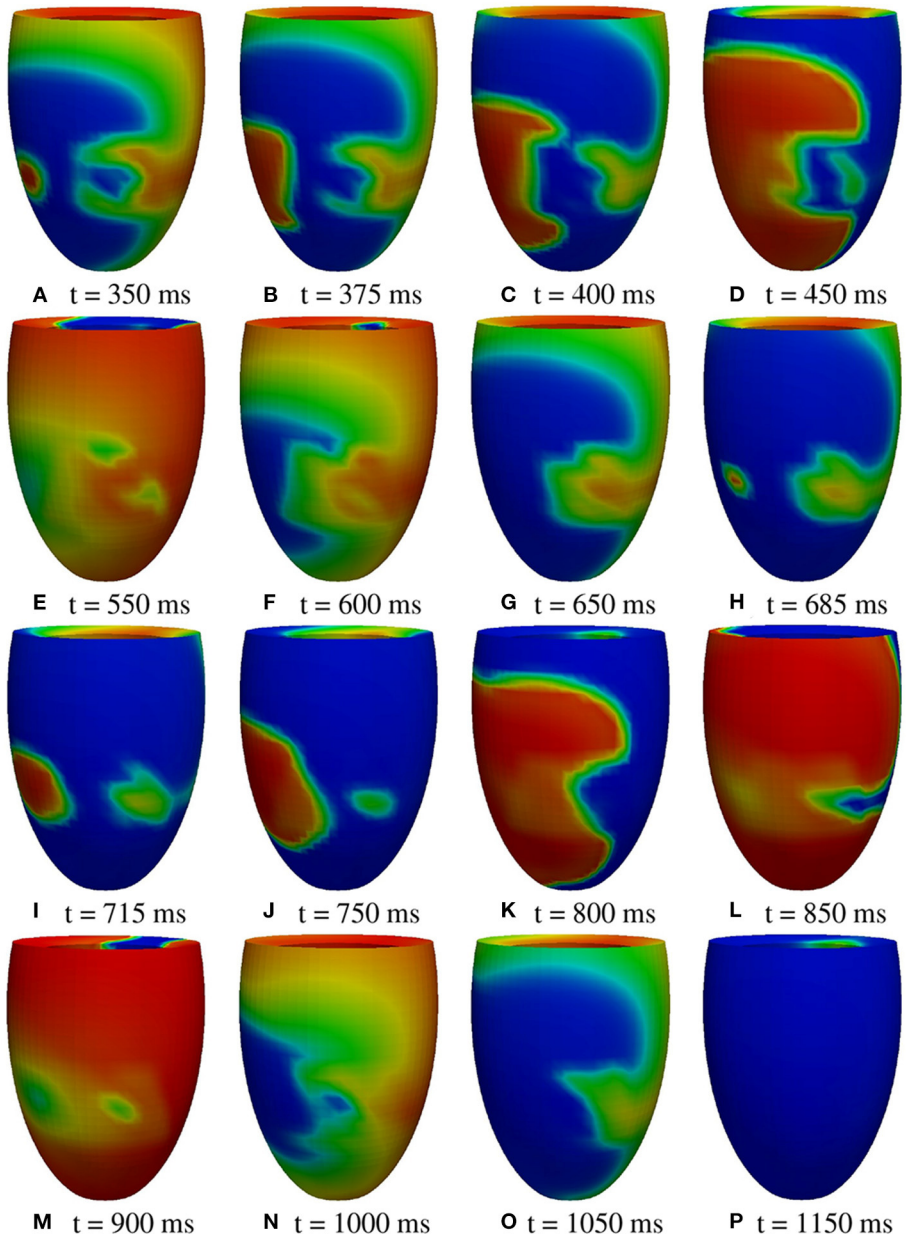

FIGURE 11 | Patient #2. M2 stimulation. **(A–P)** Transmembrane potential snapshots (t = 350–1,150 ms) on the epicardial surface. t = 0 corresponds to the S3 stimulus. The S4 stimulus is applied at t = 300 ms. The colorbar is the same as in **Figure 5**.

Analyzing the topology of the scar and BZ of the two patients, we note that in both cases, the scar is characterized by at least a transmural BZ isthmus, whereas the main differences between the two scar configurations are the following:

- the scar extent, since that of patient #1 occupies a portion of LV larger than that of patient #2;
- the isthmus thickness, since the isthmus of patient #2 is thicker than those of patient #1;
- the subendocardial and subepicardial BZs thickness, since those of patient #2 is significantly thicker than those of patient #1.

The scar extent plays an important role in determining VT, since patients with large scars are more likely to undergo VT than patients with small scars, as also observed in our previous work by Colli-Franzone et al. (2019). In order to understand whether also the thickness of the BZ plays a role in determining the onset and maintenance of sustained re-entry, we modified the configuration of the BZ layer and/or the area of the isthmus section of the two patients. The results have shown that, making the epicardial BZ of patient #2 as this as that of patient #1, even though maintaining the original small scar dimensions, sustained VT can be induced after the programmed stimulation protocol.

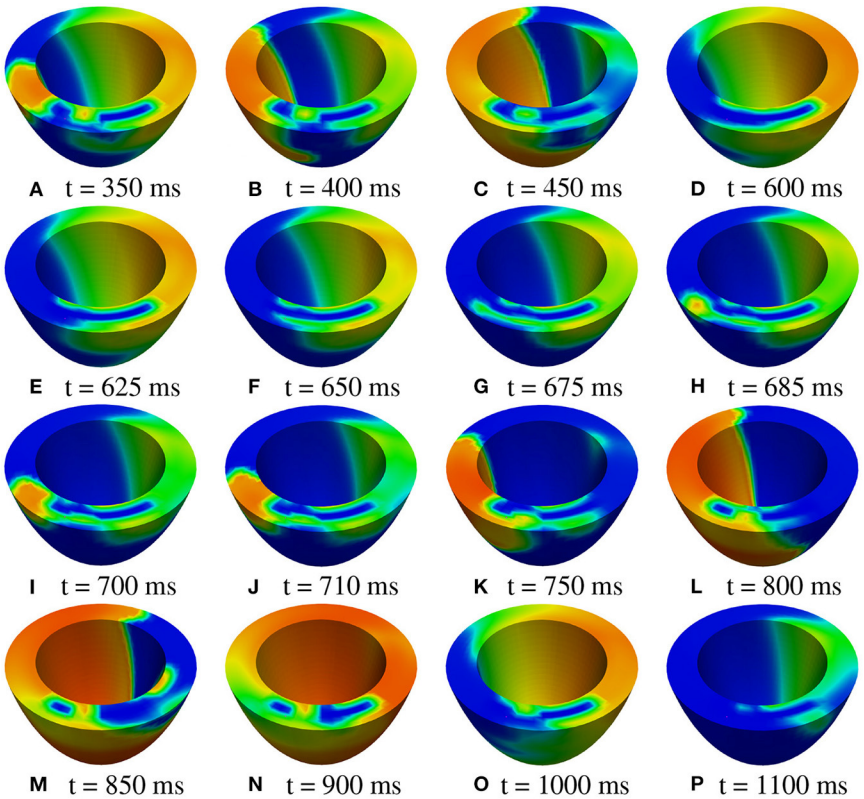

FIGURE 12 | Patient #2. M2 stimulation. **(A–P)** Transmembrane potential snapshots (t = 350–1,100 ms) on a transmural section. t = 0 corresponds to the S3 stimulus. The S4 stimulus is applied at t = 300 ms. The colorbar is the same as in **Figure 5**.

On the other hand, in patient #1, increasing the thickness of the epicardial BZ does not alter significantly the inducibility of sustained VT.

Summarizing, the second conclusion of the present work is that scar configurations with transmural BZ isthmuses and subendo- and subepicardial BZ are likely to be arrhythmogenic. The presence of a transmural BZ isthmus is crucial to determine the onset and maintenance of re-entry since the pathway followed by the simulated re-entrant circuits always passes through the isthmus. However, its thickness does not seem to affect significantly the induction of re-entry. For sufficiently large scars, such as that of patient #1 (about 1400 mm^2), sustained re-entry occurs irrespectively of the thickness of the subendo- and subepicardial BZs. On the other hand, for smaller scars, such as that of patient #2 (about 800 mm^2), thin (less than 2 *mm*) subendo- and subepicardial BZs facilitate the onset and maintenance of re-entry. This result is in agreement with previous experimental studies reported in Peters et al. (1997) and Wit et al. (1982).

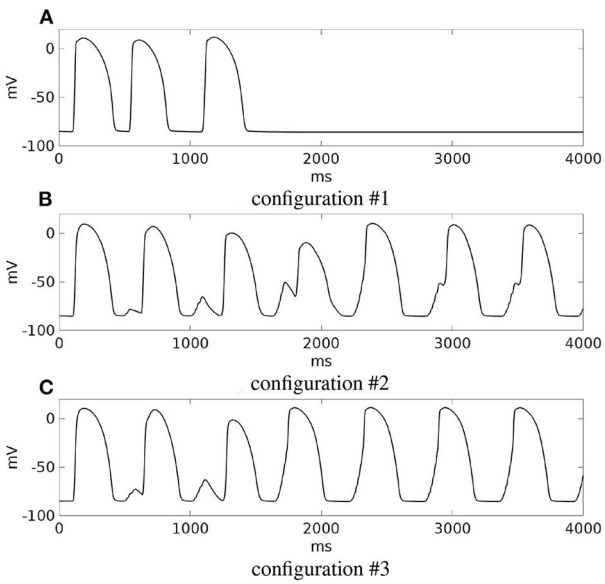

FIGURE 13 | Modifications of patient #2. **(A–C)** Transmembrane potential waveforms in the three modified configurations, computed from an epicardial size located in the BZ, at the exit of the transmural isthmus. M1 stimulation.

4.1. Clinical Implications

We identified at CMR a geometric pattern of scar and BZ, characterized by thin subendo- and subepicardial BZ

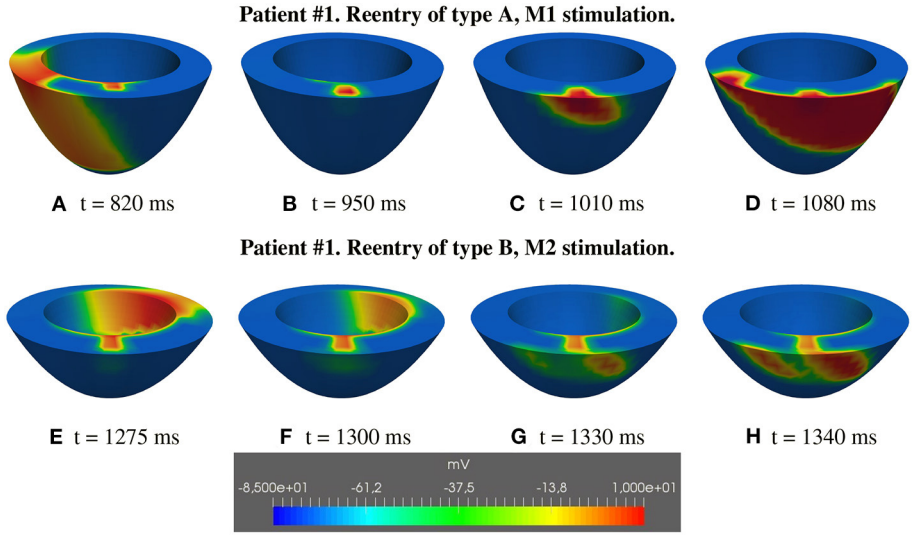

FIGURE 14 | Patient #1. Reentry of types A and B. **(A–H)** Transmembrane potential snapshots on transmural sections across the central isthmus (First row) and across the apical isthmus (Second row). t = 0 corresponds to the S1 stimulus. The S2 stimulus is applied at t = 350 ms. **First row**: Reentry of type A related to M1 stimulation. **Second row**: Reentry of type B related to M2 stimulation.

and transmural BZ isthmuses, provides a major risk for sustained VT inducibility at EPS. This information is easy to use in daily routine and could be added to known non-invasive risk factors to identify patients with ischemic cardiomyopathy and moderate systolic disfunction to submit to EPS.

4.2. Limitations

In order to reduce the computational effort, the numerical simulations were performed considering the monodomain instead of the bidomain representation of the cardiac tissue and we neglected the presence of the Purkinje network, that might play a role in influencing the patterns of reentry.

We also considered only scar formations with compact fibrosis, treated as non-conductive obstacles. A recent study (Nezlobinsky et al., 2021) has focused on the influence of various non-compact fibrotic textiles on the arrhythmogenic substrate. The BZ in our study was modeled as an electrical homogeneous tissue, with uniform thickness, instead of a highly heterogeneous region, both from the electrical and geometric point of view; (Peters et al., 1997; Ciaccio et al., 2007).

Furthermore, the electro-mechanical coupling was disregarded in our study. For the inclusion of mechanical and hemodynamical models in the numerical simulations of arrhythmias, we refer to the recent paper (Salvador et al., 2021).

DATA AVAILABILITY STATEMENT

The raw data supporting the conclusions of this article will be made available by the authors, without undue reservation.

AUTHOR CONTRIBUTIONS

VG, RD, and CS have collected and analyzed the clinical data, planned, and written the manuscript. SS, PC, and LP have developed the mathematical model and numerical solver, performed the numerical simulations, planned, and written the manuscript. All authors contributed to the article and approved the submitted version.

FUNDING

SS was supported by grants of MIUR (PRIN 2017AXL54F_003) and INdAM-GNCS. PC was supported by grants of INdAM-GNCS. LP was supported by grants of MIUR (PRIN 2017AXL54F_002) and INdAM–GNCS.

SUPPLEMENTARY MATERIAL

The Supplementary Material for this article can be found online at: https://www.frontiersin.org/articles/10.3389/fphys.2022.834747/full#supplementary-material

The **Supplementary Material** consists of the text file **supplementary.docx** and eight movies:

SM_paz1_M1_epi | Patient #1, M1 stimulation, evolution of the epicardial transmembrane potential distribution after the S1 stimulus (t = 0 ms) and the S2 stimulus (t = 350 ms). The reentry follows the central transmural isthmus and dies after two cycles.

SM_paz1_M1_trans | Patient #1, M1 stimulation, evolution of the transmural transmembrane potential distribution after the S1 stimulus (t = 0 ms) and the S2 stimulus (t = 350 ms). The reentry follows the central transmural isthmus and dies after two cycles.

SM_paz1_A2_epi | Patient #1, A2 stimulation, evolution of the epicardial transmembrane potential distribution after the S1 stimulus (t = 0 ms) and the S2

stimulus (t = 350 ms). The reentry follows the apical transmural isthmus and is sustained.

SM_paz1_A2_trans | Patient #1, A2 stimulation, evolution of the transmural transmembrane potential distribution after the S1 stimulus (t = 0 ms) and the S2 stimulus (t = 350 ms). The reentry follows the apical transmural isthmus and is sustained.

SM_paz2mod_conf1_M1_epi | Modification of patient #2, configuration #1, M1 stimulation, evolution of the epicardial transmembrane potential distribution after the S1 stimulus (t = 0 ms) and the S2 stimulus (t = 350 ms). The reentry dies after the first cycle.

SM_paz2mod_conf2_M1_epi | Modification of patient #2, configuration #2, M1 stimulation, evolution of the epicardial transmembrane potential distribution after the S1 stimulus (t = 0 ms) and the S2 stimulus (t = 520 ms). The reentry follows the transmural isthmus and is sustained.

SM_paz2mod_conf3_M1_epi | Modification of patient #2, configuration #3, M1 stimulation, evolution of the epicardial transmembrane potential distribution after the S1 stimulus (t = 0 ms) and the S2 stimulus (t = 520 ms). The reentry follows the transmural isthmus and is sustained.

SM_paz1mod_M2_epi | Modification of patient #1, M2 stimulation, evolution of the epicardial transmembrane potential distribution after the S1 stimulus (t = 0 ms) and the S2 stimulus (t = 350 ms). The reentry follows the transmural isthmus and is sustained.

REFERENCES

Al-Khatib, S. M., Stevenson, W. G., Ackerman, M. J., Bryant, W. J., Callans, D. J., Curtis, A. B., et al. (2018). 2017 AHA/ACC/HRS guideline for management of patients with ventricular arrhythmias and the prevention of sudden cardiac death. Circulation. 138, e272-e391. doi: 10.1161/CIR.0000000000000549

Amado, L. C., Gerber, B. L., and Gupta, S. N., Rettmann, D. W., Szarf, G., Schock, R., et al. (2004). Accurate and objective infarct sizing by contrast-enhanced magnetic resonance imaging in a canine myocardial infarction model. J. Am. Coll. Cardiol. 44, 2383-2389. doi: 10.1016/j.jacc.2004.09.020

Arevalo, H. J., Vadakkumpadan, F., and Guallar, E., Jebb, A., Malamas, P., Wu, K. C., et al. (2016). Arrhythmia risk stratification of patients after myocardial infarction using personalized heart models. *Nat. Commun.* 7, 11437. doi: 10.1038/ncomms11437

Ashikaga, H., Arevalo, H., Vadakkumpadan, F., Blake, R. C., Bayer, J. D., Nazarian, S., et al. (2013). Feasibility of image-based simulation to estimate ablation target in human ventricular arrhythmia. *Heart Rhythm.* 10, 1109–1116. doi: 10.1016/j.hrthm.2013.04.015

Baba, S., Dun, W., Cabo, C., and Boyden, P. A. (2005). Remodeling in cells from different regions of the reentrant circuit during ventricular tachycardia. *Circulation.* 112, 2386–2396. doi: 10.1161/CIRCULATIONAHA.105.534784

Balay, S., Abhyankar, S., Adams, M. A., Brown, J., Brune, P., Buschelman, K., et al. (2020). *PETSc Users Manual*. Available online at: https://petsc.org/release/docs/manual/

Cabo, C. (2014). Dynamics of propagation of premature impulses in structurally remodeled infarcted myocardium: a computational analysis. *Front. Physiol.* 5, 483. doi: 10.3389/fphys.2014.00483

Cabo, C., and Boyden, P. A. (2003). Electrical remodeling of the epicardial border zone in the canine infarcted heart: a computational analysis. *Am. J. Physiol. Heart Circ. Physiol.* 284, H372–H384. doi: 10.1152/ajpheart.00512.2002

Cabo, C., Yao, J., Boyden, P. A., Chen, S., Hussain, W., Duffy, H. S., et al. (2006). Heterogeneous gap junction remodeling in reentrant circuits in the epicardial border zone of the healing canine infarct. *Cardiovasc. Res.* 72, 241–249. doi: 10.1016/j.cardiores.2006.07.005

Campos, F. O., Orini, M., Arnold, R., Whitaker, J., O'Neill, M., Razavi, R. (2021). Assessing the ability of substrate mapping techniques to guide ventricular tachycardia ablation using computational modelling. *Comput. Biol. Med.* 130, 104214. doi: 10.1016/j.compbiomed.2021.104214

Campos, F. O., Shiferaw, Y., Weber dos Santos, R., Plank, G., and Bishop, M. J. (2018). Microscopic isthmuses and fibrosis within the border zone of infarcted hearts promote calcium-mediated ectopy and conduction block. *Front. Phys.* 6, 57. doi: 10.3389/fphy.2018.00057

Ciaccio, E. J., Ashikaga, H., Kaba, R. A., Cervantes, D., Hopenfeld, B., Wit, A. L., et al. (2007). Model of reentrant ventricular tachycardia based on infarct border zone geometry predicts reentrant circuit features as determined by activation mapping. *Heart Rhythm.* 4, 1034–1045. doi: 10.1016/j.hrthm.2007.04.015

Ciaccio, E. J., Chow, A. W., Davies, D. W., Wit, A. L., and Peters, N. S. (2004). Localization of the isthmus in reentrant circuits by analysis of electrograms derived from clinical noncontact mapping during sinus rhythm and ventricular tachycardia. *J. Cardiovasc. Electrophysiol.* 15, 27–36. doi: 10.1046/j.1540-8167.2004.03134.x

Ciaccio, E. J., Coromilas, J., Ashikaga, H., Cervantes, D. O., Wit, A. L., Peters, N. S., et al. (2015). Model of unidirectional block formation leading to reentrant ventricular tachycardia in the infarct border zone of postinfarction canine hearts. *Comput. Biol. Med.* 62, 254–263. doi: 10.1016/j.compbiomed.2015.04.032

Codreanu, A., Odille, F., Aliot, E., Marie, P.-Y., Magnin-Poull, I., Andronache, M., et al. (2008). Electroanatomic characterization of post-infarct scars. *J. Am. Coll. Cardiol.* 52, 839–842. doi: 10.1016/j.jacc.2008.05.038

Colli-Franzone, P., Gionti, V., Pavarino, L. F., Scacchi, S., and Storti, C. (2019). Role of infarct scar dimensions, border zone repolarization properties and anisotropy in the origin and maintenance of cardiac reentry. *Math. Biosci.* 315, 108228. doi: 10.1016/j.mbs.2019.108228

Colli-Franzone, P., Guerri, L., and Tentoni, S. (1990). Mathematical modeling of the excitation process in myocardial tissue: influence of fiber rotation on wavefront propagation and potential field. *Math. Biosci.* 101, 155-235. doi: 10.1016/0025-5564(90)90020-Y

Colli-Franzone, P., Pavarino, L. F., and Scacchi, S. (2011). Exploring anodal and cathodal make and break cardiac excitation mechanisms in a 3d anisotropic bidomain model. *Math. Biosci.* 230, 96–114. doi: 10.1016/j.mbs.2011.02.002

Colli-Franzone, P., Pavarino, L. F., and Scacchi, S. (2014). *Mathematical Cardiac Electrophysiology*. vol. 13 (New York, NY: Springer).

Colli-Franzone, P., Pavarino, L. F., and Taccardi, B. (2005). Simulating patterns of excitation, repolarization and action potential duration with cardiac bidomain and monodomain models. *Math. Biosci.* 197, 35–66. doi: 10.1016/j.mbs.2005.04.003

Connolly, A., Trew, M. L., Smaill, B. H., Plank, G., and Bishop, M. J. (2015). Local gradients in electrotonic loading modulate the local effective refractory period: Implications for arrhythmogenesis in the infarct border zone. *IEEE Trans. Biomed. Eng.* 62, 2251–2259. doi: 10.1109/TBME.2015.2421296

Connolly, A. J., and Bishop, M. J. (2016). Computational representations of myocardial infarct scars and implications for arrhythmogenesis. *Clin. Med. Insights Cardiol.* 10s1, CMC.S39708. doi: 10.4137/CMC.S39708

de Bakker, J. M. T., Stein, M., and van Rijen, H. V. M. (2005). Three-dimensional anatomic structure as substrate for ventricular tachycardia/ventricular fibrillation. *Heart Rhythm* 2, 777–779. doi: 10.1016/j.hrthm.2005.03.022

de Jong, S., van Veen, T. A. B., van Rijen, H. V. M., and de Bakker, J. M. T. (2011). Fibrosis and cardiac arrhythmias. *J. Cardiovasc. Pharmacol.* 57, 630–638. doi: 10.1097/FJC.0b013e318207a35f

Decker, K. F., and Rudy, Y. (2010). Ionic mechanisms of electrophysiological heterogeneity and conduction block in the infarct border zone. *Am. J. Physiol. Heart Circ. Physiol.* 299, H1588-H1597. doi: 10.1152/ajpheart.00362.2010

Deng, D., Arevalo, H., Pashakhanloo, F., Prakosa, A., Ashikaga, H., McVeigh, E., et al. (2015). Accuracy of prediction of infarct-related arrhythmic circuits from image-based models reconstructed from low and high resolution MRI. *Front. Physiol.* 6, 282. doi: 10.3389/fphys.2015.00282

Deng, D., Arevalo, H. J., A. Prakosa, Callans, D. J., and Trayanova, N. A. (2016). A feasibility study of arrhythmia risk prediction in patients with myocardial infarction and preserved ejection fraction. *Europace* 18, iv60–iv66. doi: 10.1093/europace/euw351

Dillon, S. M., Allessie, M. A., Ursell, P. C., and Wit, A. L. (1988). Influences of anisotropic tissue structure on reentrant circuits in the epicardial border zone of subacute canine infarcts. *Circ. Res.* 63, 182-206. doi: 10.1161/01.RES.63.1.182

Fenoglio, J. J., Pham, T. D., Harken, A. H., Horowitz, L. N., Josephson, M. E., and Wit, A. L. (1983). Recurrent sustained ventricular tachycardia: structure and ultrastructure of subendocardial regions in which tachycardia originates. *Circulation* 68, 518–533. doi: 10.1161/01.cir.68.3.518

Fishman, G. I., Chugh, S. S., DiMarco, J. P., Albert, C. M., Anderson, M. E., Bonow, R. O., et al. (2010). Sudden cardiac death prediction and prevention: report from a national heart, lung, and blood institute and heart rhythm society workshop. *Circulation.* 122, 2335–2348. doi: 10.1161/CIRCULATIONAHA.110.976092

Gatzoulis, K. A., Tsiachris, D., Arsenos, P., Antoniou, C.-K., Dilaveris, P., Sideris, S., et al. (2019). Arrhythmic risk stratification in post myocardial infarction patients with preserved ejection fraction: the PRESERVE EF study. *Europ. Heart J.* 40, 2940–2949. doi: 10.1093/eurheartj/ehz260

Gorgels, A. P., Gijsbers, C., de Vreede-Swagemakers, J., Lousberg, A., and Wellens, H. J. J. (2003). Out-of-hospital cardiac arrest-the relevance of heart failure. the maastricht circulatory arrest registry. *Eur. Heart J.* 24, 1204–1209. doi: 10.1016/s0195-668x(03)00191-x

Janse, M. J., and Wit, A. L. (1989). Electrophysiological mechanisms of ventricular arrhythmias resulting from myocardial ischemia and infarction. *Physiol. Rev.* 69, 1049–1169. doi: 10.1152/physrev.1989.69.4.1049

Jiang, M., Cabo, C., Yao, J., Boyden, P. A., and Tseng, G. (2000). Delayed rectifier k currents have reduced amplitudes and altered kinetics in myocytes from infarcted canine ventricle. *Cardiovasc. Res.* 48, 34–43. doi: 10.1016/s0008-6363(00)00159-0

Kim, R. J., Wu, E., Rafael, A., Chen, E. L., Parker, M. A., Simonetti, O., et al. (2000). The use of contrast-enhanced magnetic resonance imaging to identify reversible myocardial dysfunction. *New Engl. J. Med.* 343, 1445–1453. doi: 10.1056/NEJM200011163432003

McDowell, K. S., Arevalo, H. J., Maleckar, M. M., and Trayanova, N. A. (2011). Susceptibility to arrhythmia in the infarcted heart depends on myofibroblast density. *Biophys. J.* 101, 1307–1315. doi: 10.1016/j.bpj.2011.08.009

Mendonca Costa, C., Plank, G., Rinaldi, C. A., Niederer, S. A., and Bishop, M. J. (2018). Modeling the electrophysiological properties of the infarct border zone. *Front. Physiol.* 9, 356. doi: 10.3389/fphys.2018.00356

Moran, J. M., Kehoe, R. F., Loeb, J. M., Lichtenthal, P. R., Sanders, J. H., Michaelis, L. L. (1982). Extended endocardial resection for the treatment of ventricular tachycardia and ventricular fibrillation. *Ann. Thor. Surg.* 34, 538-552. doi: 10.1016/s0003-4975(10)63001-9

Nattel, S., Maguy, A., Le Bouter, S., and Yeh, Y.-H. (2007). Arrhythmogenic ion-channel remodeling in the heart: Heart failure, myocardial infarction, and atrial fibrillation. *Physiol. Rev.* 87, 425–456. doi: 10.1152/physrev.00014.2006

Nezlobinsky, T., Okenov, A., and Panfilov, A. V. (2021). Multiparametric analysis of geometric features of fibrotic textures leading to cardiac arrhythmias. *Sci. Rep.* 11, 21111. doi: 10.1038/s41598-021-00606-x

Pattanayak, P., and Bleumke, D. A. (2015). Tissue characterization of the myocardium. Rad. Clin. North Am. 53, 413–423. doi: 10.1016/j.rcl.2014.11.005

Peters, N. S., Coromilas, J., Severs, N. J., and Wit, A. W. (1997). Disturbed connexin43 gap junction distribution correlates with the location of reentrant circuits in the epicardial border zone of healing canine infarcts that cause ventricular tachycardia. *Circulation* 95, 988–996

Peters, N. S., and Wit, A. L. (1998). Myocardial architecture and ventricular arrhythmogenesis. *Circulation* 97, 1746–1754.

Pinto, J. (1999). Electrical remodeling in ischemia and infarction. *Cardiovasc. Res.* 42, 284-297.

Priori, S. G., Blomström-Lundqvist, C., Mazzanti, A., Blom, N., Borggrefe, M., Camm, J. (2015). 2015 ESC Guidelines for the management of patients with ventricular arrhythmias and the prevention of sudden cardiac death: The Task Force for the Management of Patients with Ventricular Arrhythmias and the Prevention of Sudden Cardiac Death of the European Society of Cardiology (ESC). Endorsed by: Association for European Paediatric and Congenital Cardiology (AEPC). *Eur. Heart J.* 36, 2793–2867. doi: 10.1093/eurheartj/ehv316

Punske, B. B., Ni, Q. R. L., Lux MacLeod, R. S., Ershler, P. R., Dustman, T. J., et al. (2003). Spatial methods of epicardial activation time determination in normal hearts. *Ann. Biomed. Eng.* 31, 781–792. doi: 10.1114/1.1581877

Rehr, R. B., Malloy, C. R., Filipchuk, N. G., and Peshock, R. M. (1985). Left ventricular volumes measured by MR imaging. *Radiology.* 156, 717–719. doi: 10.1148/radiology.156.3.4023232

Roberts, D. E., Hersh, L. T., and Scher, A. M. (1979). Influence of cardiac fiber orientation on wavefront voltage, conduction velocity, and tissue resistivity in the dog. Circ. Res. 44, 701-712. doi: 10.1161/01.res.44.5.701

Sabbag, A., Suleiman, M., Laish-Farkash, A., Samania, N., Kazatsker, M., Goldenberg, I., et al. (2015). Contemporary rates of appropriate shock therapy in patients who receive implantable device therapy in a real-world setting: From the israeli ICD registry. *Heart Rhythm* 12, 2426–2433. doi: 10.1016/j.hrthm.2015.08.020

Salvador, M., Fedele, M., and Africa P. C., Sung, E., Dede', L., Prakosa, A., et al. (2021). Electromechanical modeling of human ventricles with ischemic cardiomyopathy: numerical simulations in sinus rhythm and under arrhythmia. *Comput. Med. Biol.* 136, 104674. doi: 10.1016/j.compbiomed.2021.104674

Schmidt, A., Azevedo, C. F., Cheng, A., Gupta, S. N., Bluemke, D. A., Foo, T. K., et al. (2007). Infarct tissue heterogeneity by magnetic resonance imaging identifies enhanced cardiac arrhythmia susceptibility in patients with left ventricular dysfunction. *Circulation.* 115, 2006–2014. doi: 10.1161/CIRCULATIONAHA.106.653568

Stecker, E. C., Vickers, C., Waltz, J., Socoteanu, C., John, B. T., Mariani, R., et al. (2006). Population-based analysis of sudden cardiac death with and without left ventricular systolic dysfunction. *J. Am. Coll. Card.* 47, 1161–1166. doi: 10.1016/j.jacc.2005.11.045

ten Tusscher, K. H. W. J., Noble, D., and Noble et al., P. J. (2004). A model for human ventricular tissue. *Am. J. Physiol.-Heart Circ. Physiol.* 286, H1573–H1589. doi: 10.1152/ajpheart.00109.2006

ten Tusscher, K. H. W. J., and Panfilov, A. V. (2006). Alternans and spiral breakup in a human ventricular tissue model. *Am. J. Physiol.-Heart Circ. Physiol.* 291, H1088-H1100

Thygesen, K., Alpert, J. S., Jaffe, A. S., Chaitman, B. R., Bax, J. J., Morrow, D. A., et al. (2018). Fourth universal definition of myocardial infarction (2018). *J. Am. Coll. Cardiol.* 72, 2231–2264. doi: 10.1016/j.jacc.2018.08.1038

Walsh, T. F., and Hundley, W. G. (2007). Assessment of ventricular function with cardiovascular magnetic resonance. *Cardiol. Clin.* 25, 15–33. doi: 10.1016/j.ccl.2007.01.002

Wit, A. L., Allessie, M. A., Bonke, F. I. M., Lammers, W., Smeets, J., and Fenoglio, J. J. (1982). Electrophysiologic mapping to determine the mechanism of experimental ventricular tachycardia initiated by premature impulses. *Am. J. Cardiol.* 49, 166–185.

Yao, J.-A., Hussain, W., Patel, P., Peters, N. S., Boyden, P. A., and Wit, A. L. (2003). Remodeling of gap junctional channel function in epicardial border zone of healing canine infarcts. *Circ. Res.* 92, 437–443. doi: 10.1161/01.RES.0000059301.81035.06

Conflict of Interest: The authors declare that the research was conducted in the absence of any commercial or financial relationships that could be construed as a potential conflict of interest.

frontiers | Frontiers in Physiology

ORIGINAL RESEARCH
published: 25 April 2022
doi: 10.3389/fphys.2022.838435

Identifying Acute Cardiac Hazard in Early Drug Discovery Using a Calcium Transient High-Throughput Assay in Human-Induced Pluripotent Stem Cell-Derived Cardiomyocytes

Hua Rong Lu[1], Mohamed Kreir[1], Van Ammel Karel[1], Fetene Tekle[2], Danny Geyskens[1], Ard Teisman[1] and David J. Gallacher[1]*

[1]Global Safety Pharmacology, Predictive, Investigative and Translational Toxicology, Nonclinical Safety, Beerse, Belgium, [2]Discovery and Nonclinical Safety Statistics, Statistics and Decision Sciences, Quantitative Sciences, Janssen R&D, A Division of Janssen Pharmaceutica NV, Beerse, Belgium

OPEN ACCESS

Edited by:
Guido Caluori, Institut de Rythmologie et Modélisation Cardiaque (IHU-Liryc), France

Reviewed by:
Kenneth Ginsburg, UC Davis, United States
Aslak Tveito, Simula Research Laboratory, Norway

***Correspondence:**
Hua Rong Lu
hlu@its.jnj.com

Specialty section:
This article was submitted to Integrative Physiology, a section of the journal Frontiers in Physiology

Received: *17 December 2021*
Accepted: *21 March 2022*
Published: *25 April 2022*

Citation:
Lu HR, Kreir M, Karel VA, Tekle F, Geyskens D, Teisman A and Gallacher DJ (2022) Identifying Acute Cardiac Hazard in Early Drug Discovery Using a Calcium Transient High-Throughput Assay in Human-Induced Pluripotent Stem Cell-Derived Cardiomyocytes. Front. Physiol. 13:838435. doi: 10.3389/fphys.2022.838435

Introduction: Early identification of cardiac risk is essential for reducing late-stage attrition in drug development. We adapted the previously published cardiac hazard risk-scoring system using a calcium transient assay in human stem cell-derived CMs for the identification of cardiac risks recorded from the new hiPSC-CM line and investigated its predictivity and translational value based on the screening of a large number of reference and proprietary compounds.

Methods: Evaluation of 55 reference drugs provided the translation of various pharmacological effects into a single hazard label (no, low, high, or very high hazard) using a Ca^{2+}-sensitive fluorescent dye assay recorded by -by FDSS/μCell Functional Drug Screening System (Hamamatsu on hiPSC-CM line (FCDI iCell Cardiomyocytes^2).

Results: Application of the adapted hazard scoring system in the Ca^{2+} transient assay, using a second hiPS-CM line, provided comparable scoring results and predictivity of hazard, to the previously published scoring approach, with different pharmacological drug classes, as well as screening new chemical entities (NCE's) using a single hazard label from four different scoring levels (no, low, high, or very high hazard). The scoring system results also showed minimal variability across three different lots of hiPSC-CMs, indicating good reproducibility of the cell line. The predictivity values (sensitivity and specificity) for drug-induced acute cardiac risk for QT-interval prolongation and Torsade de pointes (TdPs) were >95% and statistical modeling confirmed the prediction of proarrhythmic risk. The

Abbreviations: Amp, amplitude; bpm, beats per minute; BR, beat rate; BS, beating stop (cessation of beating); BBQL, below beat qualitative level; CiPA, Comprehensive in vitro Proarrhythmia Assay; CTD, Calcium Transient Duration; DMSO, dimethylsulfoxide; EAD, Early Afterdepolarization; FDA, Food and Drug Administration; FDSS, Functional Drug Screening System; hERG, human ether-à-go-go-related gene; HESI, Health and Environmental Sciences Institute; hSC-CMs, human stem cell-derived cardiomyocytes; hiPSC-CMs, human induced pluripotent stem sell-derived cardiomyocytes; IKr, rapidly activating delayed rectifier potassium current; NCEs, new chemical entities.; R&D, Research & Development; RLU, Relative light unit; TdP, Torsades de Pointes; VF, Ventricular fibrillation.

outcomes of the NCEs also showed consistency with findings in other well-established *in vitro* and *in vivo* cardiac risk assays.

Conclusion: Evaluation of a large list of reference compounds and internal NCEs has confirmed the applicability of the adaptations made to the previously published novel scoring system for the hiPSC-CMs. The validation also established the predictivity for drug-induced cardiac risks with good translation to other established preclinical *in vitro* and *in vivo* assays, confirming the application of this novel scoring system in different stem cell-CM lines for early cardiac hazard identification.

Keywords: stem cells, cardiomyocytes (hiPS-CMs), cardiac hazard risk, HTS assay, translation

INTRODUCTION

Early detection and elimination of new chemical entities (NCEs) with potential cardiac safety risks in drug discovery is essential for reducing late-stage attrition. Importantly, this strategy can reduce the potential risk for participants in clinical studies, and reduce wasted investment costs in late-stage development and increase the likelihood of advancing safe and effective novel therapeutics. The primary focus of cardiac safety within the current regulatory guidelines is to avoid drug-induced potentially life-threatening arrhythmias such as torsade de Pointes (TdP) (Gintant et al., 2016; Lu et al., 2017). TdP is associated with prolongation of QT-interval, which is primarily linked to the inhibition of human ether-a-go-go current (hERG), which encodes the pore forming a-subunit of rapidly activating delayed rectifier current potassium current (I_{Kr}), in various species including human. In addition to QT prolongation, other pharmacological actions can result in drug-induced cardiac toxicities such as QT shortening (Lu et al., 2008) and QRS widening (Lu et al., 2010), which are also associated with conduction abnormalities and even companying with non-TdP-like ventricular tachycardia (VT) or ventricular fibrillation (VF). These later drug-induced cardiac toxicities, which are not related to QT prolongation (or with hERG inhibition), are also to be covered during early drug discovery in pharmaceutical research and development (R&D).

Human-induced pluripotent stem-cell-derived cardiomyocytes (hiPSC-CMs) are now applied as part of early safety de-risking of NCEs (Authier et al., 2017) (2005, Ovics et al., 2020) and were evaluated in one of the workstream elements of the Comprehensive *in vitro* Proarrhythmia Assay (CiPA) initiative (Colatsky et al., 2016; Gintant et al., 2016). Within the CIPA workstream, the Myocyte Team, coordinated by the Health and Environmental Sciences Institute (HESI) and the US Food and Drug Administration (FDA), conducted studies with 28 reference drugs known to have different potential risks in humans using various technologies including microelectrode array (MEA) and voltage-sensing optical action potential recording in hiPSC-CMs (Blinova et al., 2018). The International Conference on Harmonization (ICH) final Concept paper on S7B and E14 Q&A (2018) also supports the use of human stem cell assays in preclinical safety screening Food and Drug Administration, HHS (2005). Additionally, a Ca^{2+} dye t assay to define the drug-induced QT prolongation and proarrhythmic risks of CIPA drugs was also successfully validated in hiPSC-CMs across multiple test sites (Lu et al., 2019).

Uses of Ca^{2+}-sensitive fluorescence dyes in Stem cell-CM cultures provide imaging of intracellular Ca^{2+} transients, resembling both the rise and decay of cytosolic Ca^{2+} during a cardiac action potential (Blanchette et al., 2018) (Bootman et al., 2018). The Ca^{2+} transient model in hiPSC-CMs gives multiple indirect electrophysiological readouts, and could be considered a high-throughput screening (HTS) assay for detecting drug-induced cardiac liabilities. Earlier research works showed the translational value of the Ca^{2+} transient measurement assay on hiPSC-CMs (CTCM) assay, based on the outcomes of reference drugs with known liabilities in humans (Lu et al., 2015; Rast et al., 2015; Bedut et al., 2016; Dempsey et al., 2016; Zeng et al., 2016; Watanabe et al., 2017; Kopljar et al., 2018b). The readout of Ca^{2+} transient assay is similar to that of the voltage-dye readout on hiPSC-CMs as a HTS screening assay (Mathur et al., 2015; Lu et al., 2017), but the utility of the calcium assay (CTCM) is less expensive (Kopljar et al., 2018b; Lu et al., 2019). Furthermore, hiPSC-CMs are known to have more relevant pharmacological responses in comparison with the existing hERG-mediated ion current assay and certain nonhuman action potential studies in isolated cardiac tissue or Langendorff isolated heart assays (Takasuna et al., 2017). The application of the CTCM assay, which permits HTS evaluation of a large number of NCEs, has been facilitated by the introduction of a score algorithm, which can be used to rank NCEs based on the degree of hazard in a pharmacological response manner on the assay ((Kopljar et al., 2018b). However, as the algorithm is cell-line specific, the key challenge is to implement the scoring system for other hiPSC-CM lines. A straightforward approach is needed to introduce the scoring system for different lines of hiPSC-CMs. In the current study we used data obtained from iCell Cardiomyocytes^2 to develop the algorithm for this cell line using the same principles that were employed to an earlier cell line (Cor.4U-Cardiomyocytes) (Kopljar et al., 2018b). Ideally, the HTS CTCM data from another hiPSC-CM line should be adapted to provide a similar unified score that should be able to rank NCEs, based on hazard score in a concentration-dependent manner. Additionally, we have demonstrated the predictivity and sensitivity of the CTCM assay in this cell line for assessing drug-induced acute cardiac risks, and the statistical modeling predictor for long QT

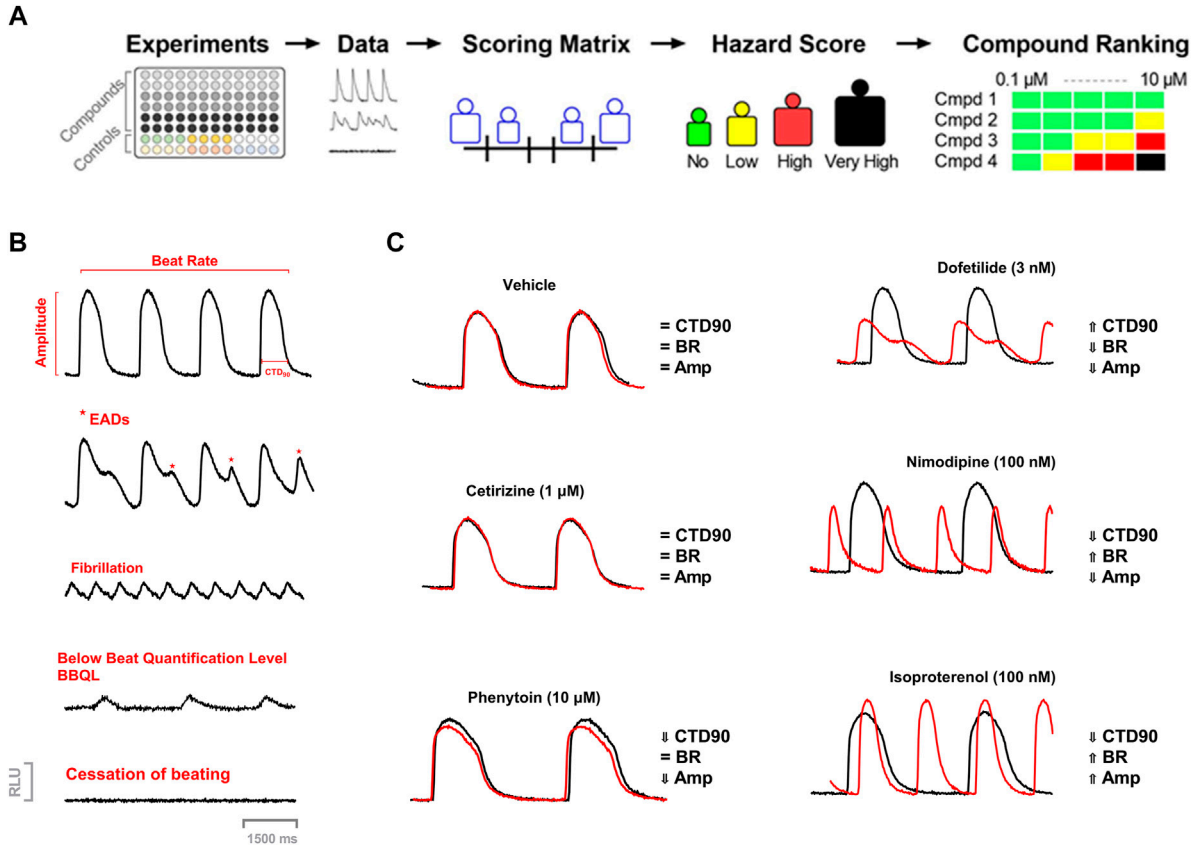

FIGURE 1 | (A) Workflow of Acute Cardiac Hazard Identification. Drugs were tested in hiPSC-CMs using calcium dye imaging. Responses in hiPSC-CMs were analyzed based on several measured parameters to define the range of hazard scores. This strategy for determining concentration-dependent hazard and ranking of compound candidates is represented schematically. **(B)** Examples of calcium transient recordings showing effects on different measured parameters, arrhythmic responses, and abnormal function: calcium transient duration at 90% of repolarization (CTD_{90}), beat rate (BR), amplitude (Amp); EAD-*like* arrhythmia, fibrillation-*like* arrhythmia, low amplitude transients (below beat quantification level; BBQL) and cessation of beating. **(C)** Example Ca^{2+} transient tracings showing tracings of vehicle, dofetilide (3 nM), nimodipine (100 nM), and isoproterenol (100 nM) at 30 min.

and TdP. We also investigated the translational value of the CTCM assay for prediction of liabilities in other established *in vitro* and *in vivo* nonclinical assays, e.g., hERG assay, isolated cardiac tissue (*in vitro*), and anesthetized guinea pigs (*in vivo*).

METHODS

The concept of cardiac hazard identification used in the current study was similar to the approach used earlier with the Cor.4u cell line (cardiomyocytes) (Kopljar et al., 2018b). In the present study, we used another cell line (iCell® Cardiomyocytes) to introduce the acute hazard score system to rank compounds based on the various parameters in the Ca^{2+} transient assay. (**Figure 1**).

Cell Culture and Reagents for the Maintenance of hiPSC-CMs

A commercially available hiPSC-CM cell line was used (iCell Cardiomyocytes^2: Catalog number R1017, Kit/lot 12,012; Fujifilm Cellular Dynamics Inc., Madison, WI, United States) for the study. Cells were pre-plated and seeded in fibronectin-coated 96-well plates at a density suited to form a monolayer and maintained in culture in a stage incubator (37°C, 5% CO_2) according to the instructions of the cell provider. The experiments with test drugs were carried out 5–7 days after plating cells on the plate to have living, beating monolayer cardiomyocytes. The beating monolayer was taken from frozen vials iCell Cardiomyocytes^2 (≈5 million cells/vial), which were plated onto three 96-well plates (≈50K/well).

To investigate whether there could be lot-to-lot variability with hiPSC-CMs, we tested 55 drugs, known cardiac risks, in one lot of iCell Cardiomyocytes^2 (Lot 12,012), 19 common reference drugs in another lot of iCell Cardiomyocytes^2 (Lot105091) as well as in iCell Cardiomyocytes (Lot 103,674) (non-square cells). The experiments with test drugs were carried out 5–7 days for iCell Cardiomyocytes^2 and 12–15 days (for iCell Cardiomyocytes) after plating cells to have living, beating monolayer cardiomyocytes (≈5 million cells/vial/96-well plates) (≈50K/well). Cells from these lot numbers were from the same donor (Apparently healthy

normal, female, Caucasian, age <18) (according to FUJIFILM Cellular Dynamics).

Calcium Transient Measurements

The method for the Ca^{2+} transient assay used in the present study has been described previously (Zeng et al., 2016; Kopljar et al., 2018a; Kopljar et al., 2018b).

On the day of the experiment, the culture medium in the 96-well plates containing the monolayers of hiPSC-CMs was replaced with Tyrode's solution (Sigma, No. T2397) supplemented with 10 mM HEPES together with KCl to yield isokalemic (4.2 mM K^+) conditions.

The Ca^{2+}-sensitive fluorescence dye Cal-520™ AM (Cat. no.21131; AAT Bioquest) was used to capture the intracellular Ca^{2+} transients in hiPSC-CMs. The protocol used was as described in Kopljar et al. (2018a). Briefly, Cal-520 was incubated for 70 min followed by a wash-out with supplemented Tyrode's solution and a 30-min recovery before starting the experiments at 37°C. On the day of the experiment, these solutions were further diluted with the supplemented Tyrode's solution. Compounds were added automatically using the Functional Drug Screen System (FDSS/μCell; Hamamatsu, Japan) head stage by adding 100 μl of the 2-fold concentrated compound solution to wells with hiPSC-CMs already containing a volume of 100 μl of the experimental solution, reaching the final intended test concentration in 0.1% DMSO.

The spontaneous beating activity of hiPSC-CMs was assessed through measurement of the Ca^{2+} fluorescence signal integrated over the whole well. Ten minutes before starting the recordings, the experimental plates were put into the FDSS system for stabilization and a baseline recording was captured for 4 min followed by compound addition. The effect of the compounds was recorded around 30 min after compound addition. The Ca^{2+} transient signals were sampled every 16 ms (frame rate of 62.5 Hz) in hiPSC-CMs maintained at 37°C during the acquisition time. Calcium transient duration at 90% of repolarization (CTD_{90}) is considered to be a surrogate for action potential duration at 90% repolarization or QT-interval of the electrocardiogram (Spencer et al., 2014). In addition, beat rate (BR = peak count/min) and amplitude (amp = difference between max. and min of every beat) were measured, and incidence of cellular arrhythmias, e.g., EAD-like activity (considered a surrogate of TdP), cessation of beating (~ stop beating), and below beating below quantification level (caused by low amplitude of the Ca^{2+} transient or by ectopic beat: BBQL) were also recorded (**Figures 1B,C**).

Compound Selection, Drug Dilution, and Addition

The compounds and their respective test concentrations were selected based on the CiPA compound list (Blinova et al., 2018 #240) and from our earlier publication (Kopljar et al., 2018b). Four DMSO stocks for each drug concentration were prepared and either used on the same day or aliquoted and frozen. Concentrated (2-fold) testing solutions (50-fold for sequential dosing) for each concentration were prepared freshly on the day of testing by diluting DMSO stocks into the experimental medium. Two-fold dilution was done when drugs were added to the experimental well to achieve targeted concentration. For sequential dosing, DMSO concentrations were adjusted sequentially up to 0.1% at the highest concentration to achieve the targeted concentration of each drug. Each compound concentration was tested in 5-6 replicates.

Dofetilide (3 nM), isoprenaline (100 nM), and nimodipine (300 nM) were used as the positive controls, while cetirizine (300 nM) was used as the negative control. A total of 55 reference compounds were used in this study with different known clinical cardiac risks.

Statistical Analysis for the Determination of the Score System

For all individual experiments, delta percent (Δ%) at 30 min with respect to the baseline value was calculated [e.g., Δ% for CTD_{90} = (CTD_{90} 30 min-CTD_{90} 0 min)/CTD_{90} 0 min) × 100]. The following two statistical approaches were used to make decisions about a compound's effect.

First, the tolerance interval (TI)-based categorization, where the Δ% values of all (pooled) DMSO wells (experiments in this study) were centered around zero (corrected with the mean) and the parametric 90–95% (p = 0.90 & 1-α = 0.95) tolerance interval (TI) was calculated (Liao et al., 2005). TIs indicate an interval where, with a certain confidence level (1- α = 0.95), a specified proportion (p = 0.90) of a sampled population falls. The lower and upper limits based on the TI values were used as cut-offs for the vehicle-corrected net effect (ΔΔ%) values of the compounds to categorize them. These ΔΔ% net effects were the values obtained after normalization for baseline (Δ% vs. baseline) per well and the aggregated compound-treated wells are vehicle corrected by subtraction with the aggregated Δ% of the corresponding DMSO wells from the same plate [e.g., ΔΔ% = median Δ% drug - median Δ% DMSO]. The categorization was made first for each concentration and then aggregated per compound and test site. If a net effect (ΔΔ%) at a given concentration of a compound was below the lower limit of the TI, then it was categorized as "decreased"; if the net effect was within the DMSO TI then it was categorized as "no effect," and if the net effect was above the upper limit of the TI then it was categorized as "increased." At the compound level, a compound was categorized as "increased" if it was in a category "increased" in at least one of the four concentrations. Similarly, a compound was categorized as decreased if it was in a category "decreased" in at least one of the four concentrations. Based on TI values, we determined the cut-off values for the hazard score system (Kopljar et al., 2018b).

Data are expressed as means ± SEM. All statistical analyses were performed using SAS® software (Copyright© 2002–2012 SAS Institute Inc.).

Sensitivity, Specificity, and Predictive Value of Potential Cardiac Risks in the Assay

Significant prolongation of CTD_{90} observed in this assay was considered a surrogate for drug-induced QT prolongation and TdP risk. Since some drugs cause QT prolongation in humans at

overdoses and/or in combination with other drugs, the predictivity values were calculated at free maximal plasma concentration in human (fC_{max}) and also at a threshold of 10 X fC_{max} or 30X fC_{max}. The list of reference drugs that have QT-prolongation and potential risk for TdP in humans was taken from the ParmaPendium® (www.pharmapendium.com) and from our recent publication (Kopljar et al., 2018b). A true positive (TP) was defined as QT prolonging drugs that significantly prolonged CTD_{90}, while true negative (TN) was defined as non-QT prolonging drugs in humans that did not prolong CTD_{90} at a tested concentration. A false negative (FN) was defined as a known QT-prolonging drug that did not prolong CTD_{90}, while a false positive (FP) was defined as a non-prolonging QT drug that significantly prolonged CTD_{90} at > 30-fold fC_{max}. Sensitivity was calculated as the % of QT-prolonging drugs correctly predicted based on CTD_{90} prolongation in this assay [TP/(TP + FN)]. Specificity was calculated as the % of non CTD_{90} prolonging drugs correctly predicted as non-QT prolonging drugs [TN/[(TN + FP)]. Positive predictive value (PPV) was calculated as: PPV = [TP/(TP + FP)], while negative predictive value (NPV) was NPV = [TN/(TN + FN)].

Statistical Modeling of Drug Proarrhythmic Potential Based on its hiPSC-CMs Effects

The modeling used in this study was primarily based on the seven predictors from the measurement parameters in MEA as given in the CiPA publication (Blinova et al., 2018), with a slight modification. Data on effects of 55 drugs with known clinical risk of TdP obtained from all experimental sites were used to construct a model that would predict TdP risk category of a drug based on its effects on hiPSC-CMs. Seven modified endpoints from hiPSC-CM experiments used as potential model predictors (Blinova et al., 2018) were: Predictor 1, drug-induced cessation of beating and early afterdepolarization (EAD) at any concentration; Predictor 2, describes the ability of a drug to induce arrhythmia-*like* events (EAD) in over 40% of wells in hiPSC-CMs; Predictor 3, CTD_{90} (ms) at the first drug concentration with statistically significant ($p \leq 0.05$) prolongation or shortening; Predictor 4, reflects the amount of drug-induced repolarization prolongation (CTD_{90}% of baseline) at the lowest concentration where statistically significant change from the baseline was observed or maximum prolongation at any of the studied concentrations; Predictors 5 and 6, account for concentrations of a drug relative to its fC_{max} when prolongation of CTD_{90} or incidence of arrhythmia-*like* event was first observed; and Predictor 7, an estimated amount of CTD_{90} prolongation that a drug would induce at its clinical fC_{max}. We added predictor 8 that includes drug-induced cessation of beating in ≥40% of wells at any concentration, which added an extra value to detect drug-induced slow conduction time or inhibiting spontaneous beating.

Logistic regression models (Model 1 and Model 2) were then used (high or intermediate risk vs. low risk–Model 1, and high vs. low and intermediate-risk vs. low risk–Model 2) on all eight risk predictors according to the CiPA publication (Blinova et al., 2018).

Lot-to-Lot Variability

To investigate lot-to-lot variability in hiPSC-CMs, we tested 19 drugs with known clinical cardiac risk in other lots of iCell Cardiomyocytes^2. Fifty-five reference drugs were tested in iCell Cardiomyocytes^2 -Lot12012, 18 reference drugs were tested in iCell Cardiomyocytes^2 (Lot105091), and 18 reference drugs were tested in iCell Cardiomyocytes (Lot103674) (nonsquare cells).

Comparison of Outcomes Between the Current CTCM Human Assay in hiPSC-CMs (iCell-Cardiomyocytes^2) and the Earlier Stem Cell-Derived Cardiomyocytes (Cor.4u® Cardiomyocytes)

To investigate the reproducibility of the cardiac hazard risk predictions from the different cell lines, we compared the present data with the results of 55 reference drugs obtained from hiPSC-CMs (iCell Cardiomyocytes^2) to the data obtained from another cell line which was published previously (Kopljar et al., 2018b).

Evaluation of the Translatability of the Scored Hazard Potential of NCEs in the Calcium Transient Assay in hiPSC-CMs to Other Nonclinical *in Vitro* and *in Vivo* Cardiac Safety Assays Including Animal Models

We also evaluated the translational predictability of the risk scores of NCEs in the CTCM assay to our complementary cardiac safety models: hERG assay, isolated rabbit wedge preparation (*ex vivo*) (Lu et al., 2016), and anesthetized guinea-pig (*in vivo*) models (Kopljar et al., 2018b) using the Software - SPEcII (Unlimit-IT, Belgium). All the experiments involving the use of animals have been conducted in accordance with "The provision of the European Convention" on the protection of vertebrate animals that are used for experimental and other scientific purposes, https://rm.coe.int/168007a67b.

RESULTS

Acute Cardiac Hazard Scoring System

We applied our previously reported strategy and methodology for the development of a cardiac hazard scoring system based on phenotypic readouts from Ca^{2+} transient imaging to a different hiPSC-CM cell line (iCell Cardiomyocytes^2) (**Figure 1A**). For a qualitative evaluation of hiPSC-CMs, each test plate (i.e., 96 unique experiments) contained 0.15 DMSO controls, together with several control drugs (cetirizine, isoprenaline, nimodipine, and dofetilide). These drugs have different pharmacological classes and were served as a pharmacological reference set for

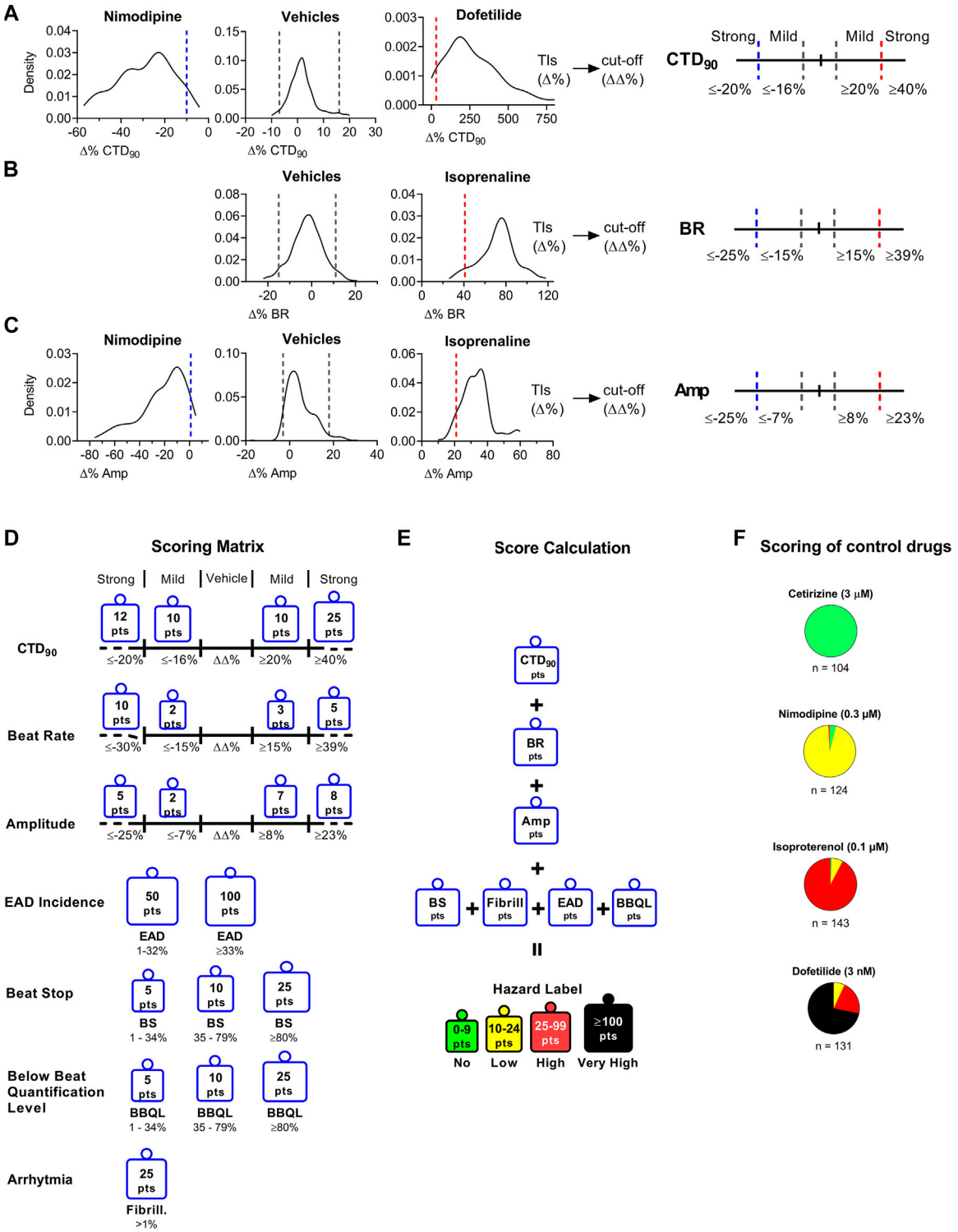

FIGURE 2 | Determination of Cutoff Values Using Statistical Tolerance Intervals (TIs) to Build a Hazard Scoring Matrix. The TIs (dashed lines within graphs) for vehicles and positive controls to determine bidirectional cutoffs for CTD_{90} to be mild or strong effects (Panel A), BR (Panel B), and Amp (Panel C). TIs from vehicle (n = 368) were applied to define the "no effect" cutoffs as well as the cut-off between "no effect" and "mild effect." Panel **(A)**: Nimodipine (300 nM; n = 173) and dofetilide (3 nM; n = 178) were used to determine "strong" CTD_{90} shortening and prolongation cut-offs, respectively. Panel **(B)**: Isoprenaline (100 nM; n = 171), and 0.1% DMSO (n = 368). TIs were used to define "strong" BR increase. Panel **(C)**: Nimodipine and isoprenaline were used to define "strong" amplitude decrease and increase, respectively. Tolerance intervals (Δ %) were corrected for vehicle offset to determine the cut-offs (ΔΔ%). **(D)**: Scoring points for hazard score identification: The scoring matrix shows a points card where for each parameter a weighted score is given depending on the size and direction of the ΔΔ% effect. **(E)**: Calculation of hazard level based on the sum of points across all parameters. **(F)**: Pie charts showing the scoring of various reference drugs over multiple studies. Cetirizine (3 μM; n = 104), isoproterenol (100 nM; n = 143), nimodipine (300 nM; n = 124), dofetilide (3 nM; n = 131). *n* indicates the number of studies; each study contained 4–8 individual experiments.

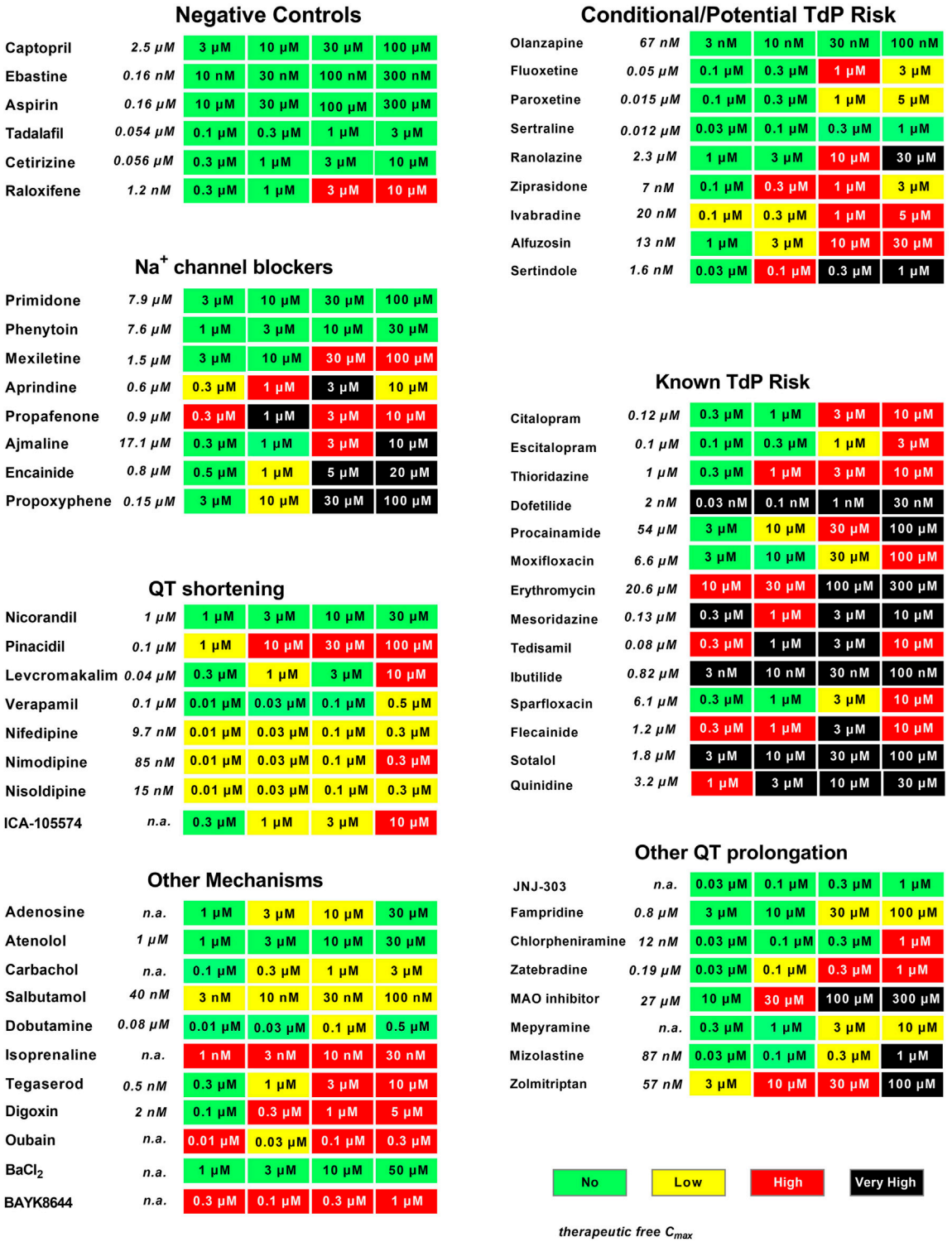

FIGURE 3 | Evaluation of reference drugs for cardiac hazard. Fifty-five reference drugs were scored for cardiac hazard using the scoring matrix. "Known TdP", "conditional TdP"/potential TdP′ groups show the marketed medicine containing these warnings in their FDA label, as well as some reference drugs that are known to block Na^+ channels, shorten QT, or have other mechanisms acting on cardiac receptors or other ion channels. Concentrations were tested according to the therapeutic fC_{max} (shown in italics), as described in our previous publication (Kopljar et al., 2018b). n. a, not available.

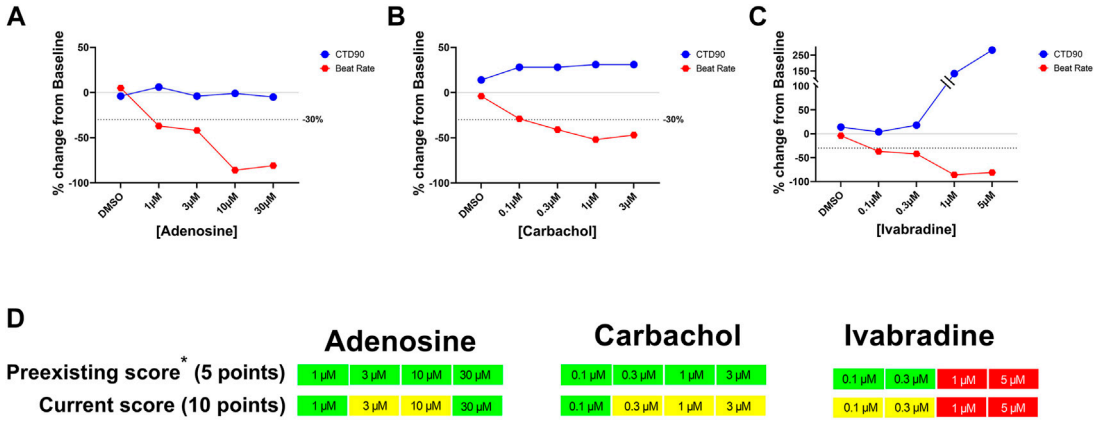

FIGURE 4 | Concentration-dependent effects of adenosine, carbachol, and ivabradine on beat rate and CTD90 in hiPSC-CMs. Panels **(A–C)**: Concentration-dependent changes in CTD_{90} and beat rate. Panel **(D)**: Identification of significant decrease in the beat rate in the current hazard scoring system by adding extra score points for decrease in beat rate (i.e., ≥30%-ΔΔ%).

the development of the hazard scoring system. Cetirizine is a real negative control known not to have any clinical cardiac liabilities. Nimodipine was used as a calcium channel antagonist and isoprenaline is a beta-adrenergic agonist. Dofetilide is a hERG blocker associated with QT prolongation and proarrhythmic TdP risk in humans. Pharmacological effects in hiPSC-CMs were investigated after a 30-min incubation period and normalized against the respective baseline recording, yielding a Δ% change in CTD_{90}, BR, and Amp.

The current hazard scoring outcome was largely similar to our previously reported scoring system for the Cor.4u cell line (Kopljar, 2018 #245, based on the TIs and its modified cut-off values of key parameters: CTD_{90}, beat rate, amplitude, and incidence of arrhythmic events (EAD and cessation of beating). The scoring matrix was determined based on the cut-offs between the different effect zones for each parameter (**Figure 2**). The "no effect" zone shows minimal changes in a parameter that is within vehicle variability, whereas "mild" and "strong" zones are determined from mild to large changes bidirectionally (e.g., CTD_{90} shortening and prolongation). The cut-off values are net changes (ΔΔ% changes vs. baseline and vehicle), which are based on the statistical tolerance intervals (TIs) (Δ% changes vs. baseline). TIs indicate an interval where, with a certain confidence level, a specified proportion of a sampled population falls. Vehicle treatments showed low variability in Δ% change for CTD_{90}, BR, and Amp with respect to baseline (**Figure 2**). Cardiac hazard scoring for the tested compound at a given concentration was given into the following risk classification hazard score (color labels): "No" (green), "Low" (yellow), "High" (red), and "Very High" (black). No hazard labeling means that a tested compound's effects were within the vehicle variability. Low hazard score indicates that the effects were outside the vehicle variability, with = low or limited risk. High hazard score gives a strong concern whereas the very high hazard score suggests potentials to cause cardiac arrhythmias-EADs.

Investigation of the Hazard Scoring System

Based on the outcomes of the positive/negative controls and the reference drug list used in another cell line (Cor.4U) (Kopljar, 2018 #245), we validated the results in this new hiPSC-CM cell line (iCell Cardiomyocytes[2]) which was essential for using the scoring system for hazard identification of NCEs. **Figure 2F** shows the hazard distribution for control drugs (at a single concentration) tested in numerous studies. Cetirizine at 1 μM (16-fold the fC_{max}) as a negative control was exclusively identified to be a no hazard agent. Nimodipine at 300 nM (15-fold fC_{max}) (n = 124) and isoproterenol (n = 143) at 100 nM (63-fold fC_{max}) are both cardio-active agents that were identified within the low and high hazard zones (95 and 92%, respectively). Dofetilide at 3 nM (2-fold f C_{max}) (n = 131) was correctly identified as yellow (8%), high (red color) (21%), or very high (black color) (71%) hazard score.

Following up, we validated the hazard scoring (as defined in **Figure 3**) using 55 reference drugs and their respective known clinical risk relative to their fC_{max}. These reference drugs are categorized based on their pharmacological mechanism or level of cardiac side effects in men (**Figure 4**). Indeed, negative control drugs have no reports of cardiac liabilities in humans and are expected to be proven to be "no hazard" for concentrations up to 10- to 30-fold fC_{max}. All negative controls were found to have "no hazard" (green). The only special case was raloxifene at clinically irrelevant concentrations (3–10 μM; ≥2500-fold the clinical fC_{max}).

We investigated the potential hazard scoring system for drugs, known to be associated with QT prolongation and a certain degree of TdP risk in humans (**Figure 3**) (These drugs were categorized into two groups according to the FDA label or described in www.torsades.org: conditional TdP/potential TdP risk, and known TdP incidence. In cases of overdose, drug–drug interactions, or in certain high-risk individuals (Woosley et al., 2018). The rank order of

incidence of EADs or degree of prolongation of CTD_{90} could be found to be co-related well to known TdP drugs > potential TdP risk or "Conditional TdP risk." Only the antidepressant olanzapine was not found to be with any hazard level, most likely because of the fact that the highest tested concentration was 100 nM, which is around fC_{max}. This concentration might be too low, since olanzapine was also only found to significantly inhibit hERG at a concentration of 6 μM, which is at 90-fold fC_{max} (Titier et al., 2005).

Although the main focus within preclinical safety pharmacology in most pharmaceutical companies is on drug-induced QT prolongation and TdP, other pharmacological mechanisms affecting different cardiac ionic currents can also result in cardiac toxicity such as, e.g., QRS widening or QT shortening. Na^+ channel blockers such as primidone and phenytoin, which are considered relatively safe in humans, had little impact on hiPSC-CMs (Green score) and another Na^+ channel blocker, mexiletine, caused some cessation of beating only at a very high concentration (100 μM = 67x fC_{max}), resulting in a Red score in the current study, similar to that in the CIPA validation study (Blinova et al., 2018). However, most Na^+ blockers also inhibit hERG current at similar concentrations, which are readily detected as CTD_{90} prolongation and incidence of EADs leading to "low" to "very high" risk (**Figure 3**).

Ca^{2+} channel antagonists resulted in strong responses in hiPSC-CMs, showing a marked decrease in amplitude companying with CTD_{90} shortening and pronounced beat rate increase. The cardiac I_{KATP} channel opener and the hERG activator (ICA-105574), which shortened CTD_{90}, were also characterized in the present study.

Additional pharmacological mechanisms including beta-adrenergic agonists (isoproterenol, dobutamine, and salbutamol), Na^+/K^+ ATPase inhibitors (digoxin and ouabain), calcium channel activator (BAYK8644), and a nonselective 5-HT_4 agonist (tegaserod), which were withdrawn from the market due to adverse cardiovascular events, were also validated in the present study and showed similar acute hazard scoring outcome as determined in Cor.4U cell line. As expected, $BaCl_2$ (an I_{K1} inhibitor) had no effect on hiPSC-CMs since it is known that most current commercial hiPSC-CMs lack functional I_{K1} channels (immature phenotype) (Goversen et al., 2018; Pourrier and Fedida 2020). Similarly, I_{Ks} inhibitor (JNJ-303) was not detected in hiPSC-CMs (Kopljar, 2018 #245).

In the previous score system with Cor.4u cell line (Kopljar et al., 2018b), significant drug-induced decrease in beat rate did not significantly impact hazard score because the maximal decrease in beat rate was only adding 5 points while the threshold for the minimal hazard score (Yellow; low risk) was 10 points. In the current updated scoring system, significant decreases induced by the muscarinic acetylcholine receptor M_2 agonist (carbachol), adenosine receptor agonist (adenosine), and funny channel current (I_f) inhibitor (ivabradine) were identified as potential "low" risk (Yellow) by adding 10 points for the decrease in beat rate by ≥ −30% (delta/delta from baseline and 0.1% DMSO control) (**Figure 4**). With this update in the scoring paradigm for changes in beat rate, we identified 29 out of ~3,000 screened reference and proprietary compounds that decreased beat rate by ≥ 30%. These 29 compounds include carbachol, adenosine, zatebradine, ivabradine, arecoline, methacholine, ibutilide, flecainide, and other internal NCEs.

Lot-to-Lot Variability

To investigate the lot-to-lot variability in responses/scores of hiPSC-CMs provided by the vendor, some of the reference drugs that prolong QT and/or have TdP risks (total of 19 compounds) were tested in different lots.

The mean baseline Ca^{2+} transient parameter values were amplitude (3,470, 2,854, and 2017 RLU), beat rate (28, 26, and 34 beats/min), and CTD_{90} (947, 1,006, and 790 ms) for lot 12,012 (iCell Cardiomyocytes^2) (n = 2,463), lot 105091 (iCell^2 Cardiomyocytes^2) (n = 521), and lot 103674 iCell Cardiomyocytes) (n = 400), respectively. There were no incidences of EADs or cessation of beating at baseline. The responses to the positive controls (isoproterenol, nimodipine, and dofetilide) and the negative controls (cetirizine or DMSO) were qualitatively similar among the three lots. For example, dofetilide (3 nM) prolonged CTD_{90} by 305% in lot 12,012 (n = 144), 330% in lot 10,591 (n = 28), and 234% in lot105091 (n = 20), and incidence of EADs was similar among the two iCell Cardiomyocytes^2 lots and the iCell Cardiomyocytes: 63, 71, and 65% incidence of EADs, respectively.

Responses to three drugs that do not prolong QT or have no TdP risk (captopril, ebastine, atenolol) were similar among the iCell Cardiomyocytes^2 and iCell Cardiomyocytes^2 lots: "no hazard"/green color, **Figure 4**). Interestingly, the cardiac risk scores for 10 drugs known to prolong QT and induced TdP were also similar in two lots of iCell Cardiomyocytes^2 and iCell Cardiomyocytes. However, EAD incidence for dl-sotalol was much higher in iCell Cardiomyocytes (10 μM) compared to the two lots of iCell-Cardiomyocytes^2 (3 and 10 μM). Five reference drugs with other mechanisms of acute cardiac risk (hERG activator, IK_{ATP} channel opener, Ca^{2+} antagonist, and Na^+ channel blockers) were also similar among the three lots with slight variations acceptable for any *in vitro* assay (**Figure 5**).

Analysis of Sensitivity, Specificity, and Predictivity Values

We analyzed the potential acute cardiac risks of 55 reference drugs with known degrees of risk in humans using the current hazard scoring system based on changes in beat rate, amplitude, CTD_{90}, and incidence of arrhythmias. We compared the cardiac risk of these 55 reference drugs based on our scoring system to the potential for clinical QT-prolongation/TdP risk, QT-shortening, QRS-prolongation, or all potential cardiac arrhythmias (i.e., non-TdP like VT/VF, bradycardia, etc.). Based on the numbers of true positives (TP),true negatives (TN), false positives (FP), and false negatives (FN), we calculated sensitivity (TP/(TP + FN)), specificity (TN/(TN + FP)), and balanced accuracy (TP + TN).

In summary, the total cardiac risks prediction was at 95%: 10 no cardiac risk drugs were all negative (green score), and for QT-prolongation/TdP risk on this CTCM assay with a balanced predictivity of 90%, sensitivity of 85%, and 95% specificity (**Figure 6**). FP was at 0 out of 43 while FN was at 2 out of 12 compounds (BaCl2 and JNJ-303: experimental drugs).

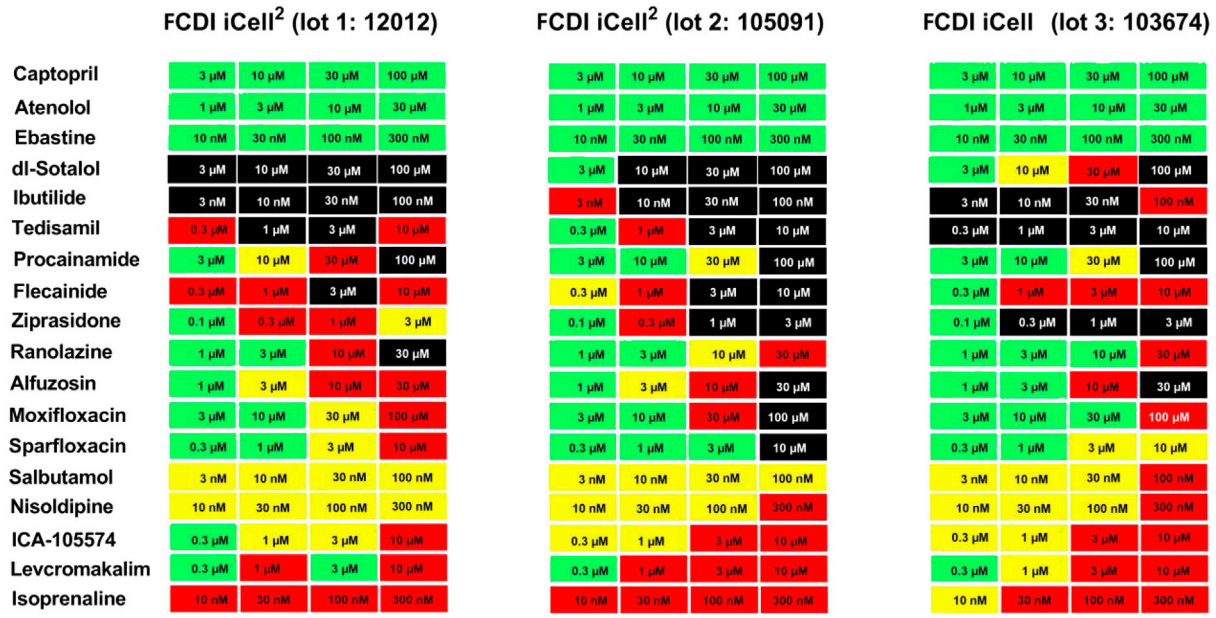

FIGURE 5 | Evaluation of Cardiac Hazard Risk of Nineteen Reference Drugs in Two iCell-Cardiomyocytes^2 Lots (12012 and 105091) and one iCell Cardiomyocyte Lot (103674). Reference drugs were scored for cardiac hazard using the described scoring matrix. "no TdP risk," "TdP risk," and "other mechanism" groups represent drug categories based on FDA labels for marketed drugs.

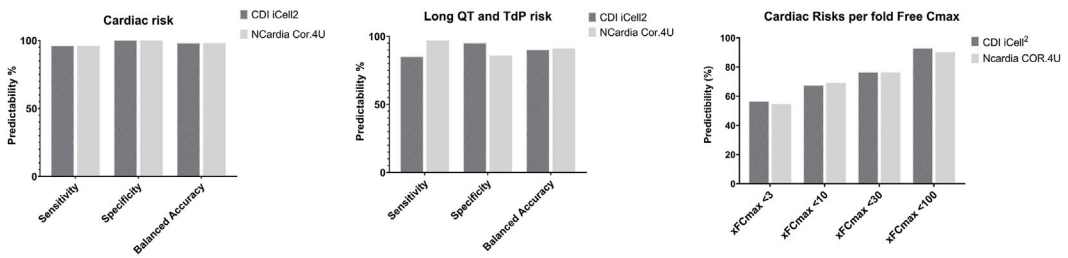

FIGURE 6 | Comparison of Sensitivity, Specificity, and Balanced Accuracy of Cardiac Risk Assessment Between iCell Cardiomyocytes^2 and Cor.4U cell line. Left Panel: Overall cardiac risk; Middle Panel: QT-prolongation and potential TdP risk; Right Panel: Cardiac risk predictability based on different multiples of fC_{max} level of the 55 reference drugs known to have potential cardiac risks in humans.

Comparison of the Acute Cardiac Hazard Cardiac Risks Between the Current Cell Line-hiPSC-CMs (iCell Cardiomyocytes^2) and Cor.4U Cell Line in the Ca^{2+} Transient Assay

Fifty-five reference drugs were tested in iCell Cardiomyocytes^2 in the current study and compared to Cor.4U in the CTCM assay (Kopljar et al., 2018b). The acute cardiac hazard scores of these 55 reference drugs were similar between the 2 cell lines. The prediction values of acute cardiac risk and QT prolongation/TdP risk in both cell lines were >90% (**Figure 5A**). When taking into account the fold over its fC_{max} (**Figure 7B**): <10 -fold fC_{max}: the predictive value with the Cor.4u cell line was slightly higher, and at <30 or <100 -fold fC_{max}, the iCell Cardiomyocytes^2 had slightly higher predictive values compared with the Cor.4u cell line. However, both cell lines were equal in defining cardiac risks in general.

Statistical Modeling of Drug Proarrhythmic Potential

In addition, we used statistical modeling of proarrhythmic potential for the 55 drugs with known clinical risk for QT-prolongation and TdP based on the results from CTCM assay and hazard scoring system. Eight endpoints from the CTCM assay were used for potential mode predictors that include seven predictors defined in the CiPA publication ((Blinova et al., 2018)), and an additional predictor: cessation of beating was included (Lu et al., 2019): Predictors 1 and 2 indicate a test drug that elicited an arrhythmia-like event (i.e., early afterdepolarization: EAD): Predictor 1 (binary): did any drug induce EAD at the tested concentration [0 = no EAD; 1 = EAD)]; Predictor 2 (binary): EAD

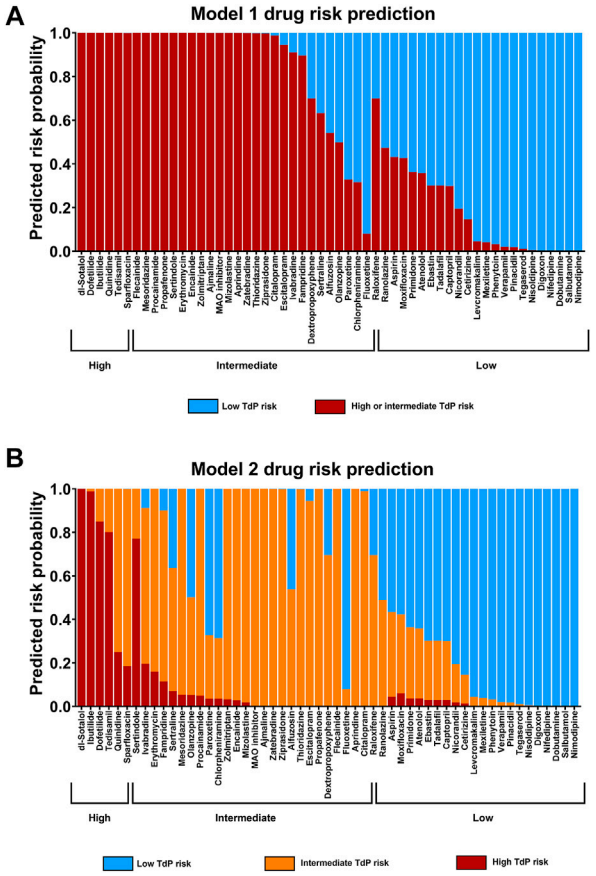

FIGURE 7 | Statistical Modeling of Cardiac Risk. **(A)** Model 1 (dichotomous model): prediction of TdP risk category as either low or intermediate and high risk combined (averaged). **(B)** Model 2; ordinal model prediction as low, intermediate, or high TdP risk category. Both models are based on the predictors published in the CiPA paper (Blinova et al., 2018), with a slight modification based on the nature of the current study.

observed at any concentrations in ≥40% wells (0 = no; 1 = yes); Predictor 3: first drug concentration with statistically significant ($p \leq 0.05$) prolongation or shortening of repolarization; Predictor 4: defined the maximal drug-induced changes in repolarization (CTD_{90}) observed at any concentration; Predictor 5: defined drug concentration (multiple of fC_{max}) at the first statistically significant ($p < 0.05$) prolongation of CTD_{90}; Predictor 6: accounted for the first drug concentration relative to its clinical fC_{max} to induce EAD; Predictor 7: had drug-induced changes in CTD_{90} (ms) at ~ its free C_{max}; Predictor 8 (binary): caused cessation of beating at any concentration in ≥40% of wells (0 = no; 1 = yes).

As described in the CiPA publication, two logistic regression models for the potential TdP risk group were used: Model 1: had high or intermediate risk *vs.* low risk and Model 2: had high risk *vs.* low risk and intermediate risk *vs.* low risk.

The results of the 55 reference drugs including a large set of CiPA compounds in the statistical model are shown in **Figure 7**. The models predicted well for high- and intermediate-risk drugs as well as for low-risk drugs with identified incidence in humans. There were very limited drugs overlapping between the intermediate- and low-risk drug (e.g., raloxifene). However, the concentrations used in the study were substantially higher compared with its f C_{max} in humans (1.2 nM). Raloxifene is a selective estrogen receptor modulator that is used for women with postmenopausal osteoporosis and is not associated with QT-prolongation in clinic. Raloxifene was reported to inhibit I_{Kr} with an IC_{50} at 1.1 μM and I_{Ks} with an IC_{50} at 4.8μM, and voltage-gated Na^+ current with an IC_{50} at2.8 μM (Liu et al., 2010). This may explain the identified activity in the current assay at much higher concentrations compared with free C_{max} (>1,000 fold its C_{max}) that could be associated with some risk for QT-prolongation.

Assessment of the Hazard Potential of NCEs

Sequentially, we investigated 839 NCEs including Janssen discovery research projects based on molecules (**Figure 8A**). Compounds were tested at a wide concentration range (0.1–10 μM). Hazard evaluation identified that the most of NCEs were classified within the "no hazard" group at concentrations less than 10 μM, with a portion showing risk at the highest concentration of 10 μM. 839 NCEs (54%) were found to be no hazard over the entire tested concentration range. Additionally, for compounds with identified hazard, the levels increased in a concentration-dependent manner. At 1 μM and higher, over 50% of the compounds did show some effects associated with a certain hazard level in hiPSC-CMs, with the "high hazard" mainly at 10 μM. The proportion in the "very high" compounds, linked to arrhythmic-like EADs, was relatively small at 10 μM with some incidence also observed at lower concentrations.

Although the hazard score classification is used as an initial indicator for potential for cardiac toxicities, further analysis in other models is necessary to help to better understand the pharmacological mechanisms involved, ultimately leading to a comprehensive integrated hazard identification. Therefore, we separated the low from high hazard groups (at 1, 3, and 10 μM) in terms of the directional effect on CTD_{90} (**Figure 8B**). CTD_{90} prolongation was mainly cause of hazard labeling among compounds for all hazard-concentration combinations (**Figure 8B**). At 1 and 3 μM, high hazard identification was mostly caused by CTD_{90} prolongation, and by the combination of CTD_{90} prolongation and beat stop (cessation of beating) at 10 μM.

Translational Value of CTCM Human Assay Compared to hERG and QT Assessment

A sum of 121 compounds were tested in both the hERG patch-clamp and CTCM assays at the similar concentration ranges (**Figure 8C**). There were 66 compounds with no risk in the CTCM assay: 53 out of 66 compounds showed hERG inhibition ≥25% while 13 of 66 compounds showed no effect in the hERG assay. There were 55 of 121 compounds that had low to very high hazard score in the CTCM assay, and only 5 of these 55

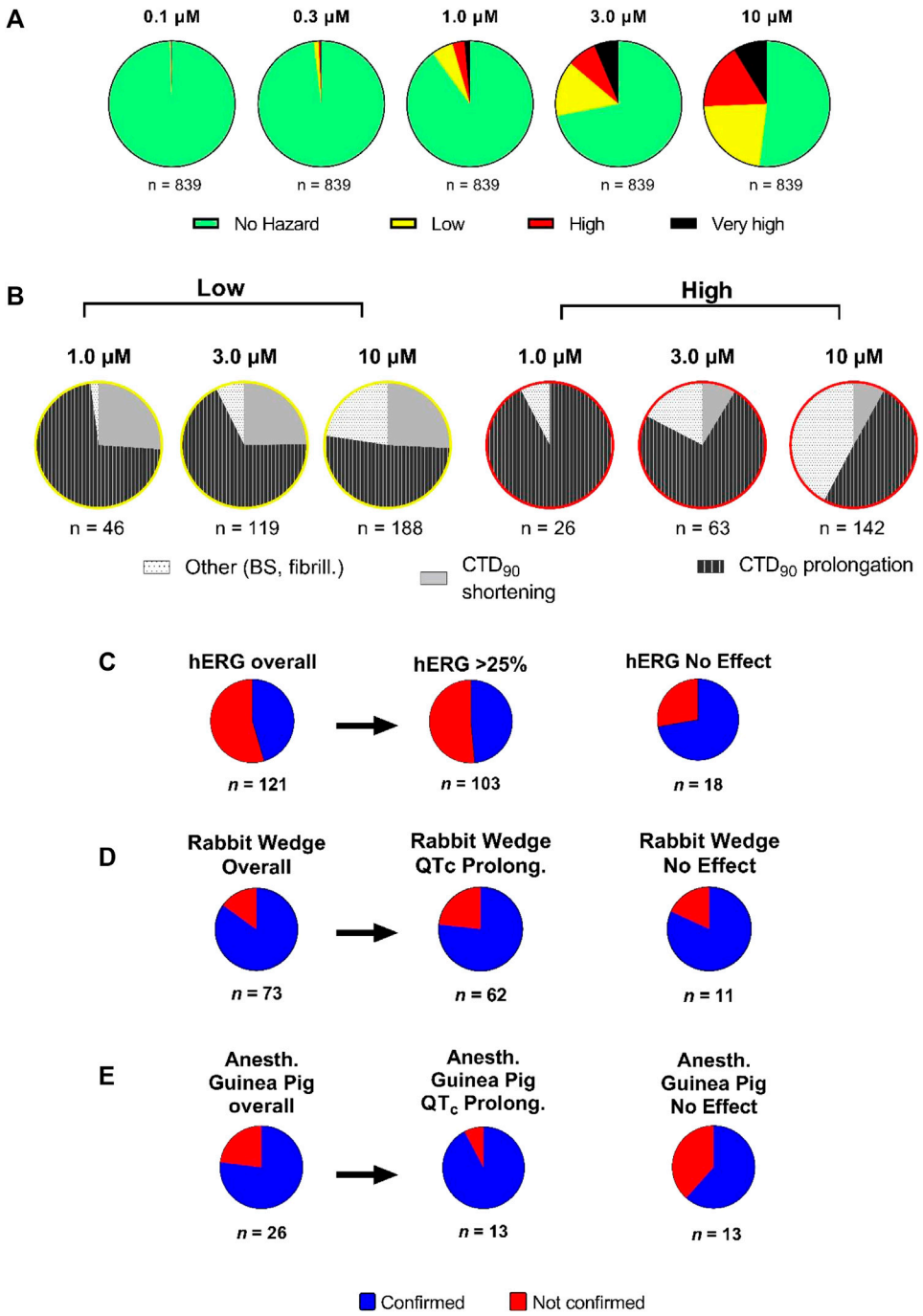

FIGURE 8 | Hazard score investigation using the scoring system on Janssen NCEs in early R&D. **(A)** Pie charts showing the concentration-dependent distribution of different hazard score levels (n = 839). **(B)** Detailed analysis of proportion of effects on CTD_{90} (increase or decrease) and incidence of beat stop (BS) or fibrillation in low and "high risk" categories by concentration (1, 3, and 10 µM) on CTCM assay. Panels **(C–E)**: The outcome of acute cardiac hazard scores in CTCM assay was compared to the inhibition among 121 compounds in the hERG assay (Panel C), to the effects on QT interval or QRS duration among 73 compounds in isolated rabbit ventricular wedge assay (Panel D), and to the effects on QTcB interval and QRS duration among 26 compounds in anesthetized guinea-pigs (Panel E). In Panel D, the left side pie: labeled Overall: including effects on both QT interval and QRS duration on a total of 73 compounds. In Panel E, the left side pie: labeled Overall: including effects on both QTcB interval and QRS duration on a total of 26 compounds. Confirmed: matching outcome between the two assays. Not Confirmed: not matching outcome between two assays.

compounds (9%) showed no effect in the hERG assay, while 50 of 55 compounds (91%) were confirmed active in the hERG assay, indicating that the drug-induced hazard scores were primarily due to inhibition of hERG current. The difference between the CTCM assay and the HERG assay could be caused by the effects on the CTCM assay not only mediated by affecting HERG current but also on other cardiac ion channels/receptors, or due to small % of false positive and negative on HERG assay.

Seventy-three compounds (acute hazard scores from the CTCM assay) were also tested in the isolated rabbit ventricular wedge preparation (**Figure 8D**). From 52 of these 73 compounds that had hazard scores in the CTCM assay, 96% (50 out of 52 compounds) had effects on either QT interval or QRS or both QRS and QT-interval in the isolated rabbit wedge assay, while only two (4%) had no effects on QRS or QT-interval in the isolated wedge preparation. Of the 21 of 73 compounds that had no hazard score in the CTCM assay 43% (9 of 21 compounds) were confirmed to have no effects in the isolated rabbit wedge preparation while 57% (12 of 21 compounds) had effects on QT interval and/or QRS: 8 compounds had QT effects; 3 had both QT and QRS effects, and 3 widened only QRS duration. However, the effects of these compounds on QT interval and QRS duration in the wedge preparation were relatively small.

Twenty-six compounds that had hazard scores in the CTCM assay were also tested in anesthetized guinea pigs (*in vivo*) (**Figure 8E**): Of the compounds that had no risk (green) in the CTCM assay, eight were also found to have no effects in anesthetized guinea-pigs in terms of changes in QRS duration and QTcB interval. One compound (terfenadine) slightly shortened CTD_{90} and caused cessation of beating in the CTCM assay, but significantly prolonged QRS duration and QTcB interval in the anesthetized guinea pig at much higher plasma levels than that of the CTCM assay. Terfenadine is known to have solubility issues *in vitro* and possibly resulting in less than nominal concentrations in the CTCM assay (Lu et al., 2012). In addition, terfenadine is rapidly metabolized in the liver to an active metabolite. Of seventeen compounds that scored yellow/red/black risk hazard scores in the CTCM assay, 71% were confirmed as positive in the anesthetized guinea pig. However, 29% of these 17 compounds (5 of 17 compounds) did not have significant effects in anesthetized guinea pigs in terms of changes in QRS duration and QTcB interval. Explanations for some of these discrepancies include: One compound slightly shortened CTD_{90} and tended to shorten QTcB interval *in vivo*; the free plasma levels of another four compounds (high plasma protein binding *in vivo*) were much lower than in the CTCM assay.

DISCUSSION

Human stem cell-derived CMs are now applied to evaluate cardiac liabilities as part of early de-risking in drug research and development (R&D). In our earlier publication ((Kopljar et al., 2018b)), we introduced a hazard scoring system to aid in the selection of new chemical entities (NCEs) devoid of acute cardiac risks. In the present study, we successfully applied the same principles of the previous hazard score system to a different hiPSC-CM line (iCell Cardiomyocytes^2), using statistical TI (s) and cut-off values for the key parameters from Ca^{2+} transient fluorescence recordings, based on DMSO controls and a validation set of 55 clinically known reference drugs that included positive and negative controls for various parameters. Statistical analysis (tolerance intervals) on a large historical data set of vehicles and control drugs helped the development of a detailed scoring system with differentiation of size and direction of effect for each parameter. We documented and confirmed the utility of various parameters [(CTD_{90}, beat rate, amplitude, cessation of beating, BBQL, fibrillation-like event and EADs)], measured in spontaneously beating hiPSC-CMs to generate a hazard identification score from data of the different pharmacological classes of drugs. To our knowledge, this is a more extensive approach relative to most other studies using hiPSC-CMs, where the focus is exclusively on APD-related parameters (e.g., field potential duration or CTD_{90}) associated with changes in the QT interval. The hazard coring system, based on the measurement of a Ca^{2+} transient in hiPSC-CMs (CTCM), can help detect and define cardiac hazards beyond drug-induced QT prolongation, such as QT shortening, beating rate changes, and slowing of conduction. This hazard score system can also identify potential hazards of drug-induced significant decreases in beating rate mediated by mechanisms such as muscarinic acetylcholine receptor M_2 stimulation (carbachol), adenosine receptor agonist (adenosine), and I_f inhibitor (ivabradine), which was lacking in our previous hazard scoring system derived from Cor.4U-cell line **Figure 8**). With the newly updated hazard score system, by adding an extra 5 points to the risk score for drug-induced decrease in beat rate (total 10 points for decreases in rate by ≥ 30%), we now are able to identify this additional hazard as a low hazard score (Yellow) in 2.9% of 3,019 NCEs tested in this cell line. We have used the hazard scoring system to simplify the analysis of complex drug-induced effects on hiPSC-CMs and provide a scoring system to identify and select safe NCEs facilitating the progress of these molecules in early R&D. Interestingly, a decrease in beat rate ≥30% has limited propensity to prolong CTD_{90} (**Figure 4**): The prolongation of CTD_{90} is still within the cut-off values of DMSO controls in these cases, which indicates that the rate dependence of CTD_{90} in this *in vitro* assay is not the same as *in vivo*, where QT interval must generally be corrected for heart rate.

The discovery and development of novel NCEs is a long and expensive process, and there is a considerable rate of attrition resulting in part to a safety concern. Therefore, an *in vitro* assay capable of detecting safety issue early in discovery and development, particularly cardiac safety, is crucial for optimized candidate selection and reduction of human risk in clinical trials and with drugs approved for use in patients This assay and the scoring system defined and described in this study can be readily applied to select the best drug candidates based on safety.

Our validation set of 55 reference drugs included the large set of CiPA compounds, used in the FDA/HESI (Blinova et al., 2018) and JiCSA (Kanda et al., 2018) studies, and showed comparable risk assessment. The models were highly predictive for high- and intermediate-risk drugs as well as for low-risk drugs, based on known risks in humans. There were a few apparent examples of

inconsistency between risk scores in the CTCM and level of risk in humans (e.g., raloxifene). Raloxifene is a selective estrogen receptor modulator that is broadly used in the treatment of postmenopausal osteoporosis and known to not prolong QT interval at therapeutic doses. In the present study, the concentrations of raloxifene used were higher than of its fC_{max} in humans (1.2 nM). Raloxifine presented with a red hazard score (high risk) but this was only observed at >2000 folds of its fC_{max}. At ~700–800 folds $fC_{max.}$ raloxifene had a green score (low risk), consistent with its clinical safety profile. Raloxifene has been reported to inhibit cardiac delayed rectifier K^+ currents at high exposures (I_{Kr}: IC_{50} = 1.1 μM and I_{Ks} = 4.8 μM), which may explain the high hazard score and potential for QT prolongation at >2000 folds its fC_{max}.

Importantly, we also documented that there was very little lot-to-lot differences in hazard scoring results for 19 common reference drugs in iCell Cardiomyocytes^2 (two lots) and iCell Cardiomyocytes (one lot).

Additionally, the specificity, sensitivity, and predictivity values for the cardiac risk assessment of 55 reference drugs were very high (>95%). The functional output of the current platform using Ca^{2+} transients enabled phenotypically relevant readouts of acute cardiac risk *in vitro*. The hazard scoring system predicted potential for long QT/TdP risk of 55 reference drugs as well as total cardiac risks (drug-induced short QT and VF-*like*) with over 95% specificity, sensitivity, and total balanced cardiac risk when compared with the known risk in humans. Importantly, the hazard scoring system predicted the cardiac risks of the 55 reference drugs mostly within the range of therapeutically relevant free plasma concentrations (fC_{max}) (**Figure 6**). The set of 55 reference drugs in the study covered a broad range of different drug classes with different pharmacological mechanisms that include both cardiovascular and noncardiovascular drugs. Using such a large set of reference drugs we were able to establish a hazard scoring system that can be applied in the selection of safe NCEs early in the drug discovery process. Although a threshold of >10-(>30- or ≤100- fold) fC_{max} was used for analyzing the scoring and assessing the predictivity of the assay, it should be noted that in many *in vitro* assays concentrations up 30-fold fC_{max} are normally considered relevant for predicting cardiac effects in humans (Redfern et al., 2003). In both the present and the CiPA stem cell validation study (Lu et al., 2019), four concentrations were used to capture fC_{max} levels with 10- and 30-fold fC_{max} margins. Additionally, cardiac and noncardiac drugs including disopyramide, terfenadine, diphenhydramine, domperidone, fluoxetine, and sertindole, etc., are known to have functional cardiac effects in *vitro* assays at much higher concentrations than their fC_{max} level (>30–100 folds fC_{max}) (Redfern et al., 2003). (Pacher et al., 2000; Eckardt et al., 2002).

To add value and gain confidence to the predictions and compound selection, screening results in this novel assay and scoring system for cardiac safety also need to be consistent with existing established early nonclinical screening assays, as well as more complex follow-up preclinical assays. Therefore, we evaluated the translational value of the current assay compared with other *in vitro* assays (such as the hERG current assay and the *ex vivo*-isolated rabbit left ventricular wedge preparation, as well as the anesthetized guinea-pig model, an established sensitive *in vivo* model to detect electrocardiographic risk (Testai et al., 2004; Lu et al., 2016)). The scoring system validation in the CTCM assay, based on reference and internal proprietary compound evaluation, was largely consistent with hERG assay results in terms of CTD_{90} prolongation, despite some false positives and negatives, as might be expected for compounds with more complex electrophysiological actions. The scoring outcome from the CTCM assay was also largely confirmed in anesthetized guinea pigs and the isolated rabbit wedge ventricular preparation (**Figures 8C–E**).

The scoring system that we developed provides a reliable way to readily identify the concentration-dependent level of cardiac risk by concentration for NCEs based on Ca^{2+} transient measurement in hiPSC-CMs using multiple functional parameters including beat rate, CTD_{90}, and amplitude. However, despite the great promise of the current scoring system for predicting acute cardiac risks, a few limitations still exist. Similar to other *in vitro* assays, the current HTS assay does not detect potential effects of active drug metabolites, which would only be detected in an *in vivo* study or by directly testing the known active metabolite in the current assay. Poor solubility may also be an issue. Moreover, similar to any *in vitro* assay using hiPSC-CMs, these cells are not fully matured, although they express key cardiac genes and have comparable function of most cardiac ion channels and receptors, and this might influence the responses to some drugs in hiPSC-CM line. That could cause difference between hiPSC-CMs and isolated cardiac tissue assays.

Our current model validation data with 55 reference drugs showed predictions of drug-induced cardiac hazard score in hiPSC-CMs (iCell-Cardiomyocytes^2) that were found to be similar to those in another cell line (Cor.4U Cardiomyocytes) (Kopljar et al., 2018b), indicating the adaptability and consistency of our scoring system approach. Screening of drug-induced effects in hiPSC-CMs can also be performed using different detection technologies, e.g., measurements of extracellular filed action potentials (Ando et al., 2017), impedance/MEA (Zhang et al., 2016; Bot et al., 2018), video motion imaging (Hayakawa et al., 2014), and voltage-sensitive dyes (Bedut et al., 2016). The principles used for the development of our scoring system could also be adapted for use in these other human cardiomyocyte systems using the same principles defined within this study.

In conclusion, the acute cardiac hazard score system applied to the Ca^{2+} transient assay using different hiPSC-CM cell lines should be useful for the identification and selection of NCEs for further investigation. The CTCM HTS assay system in our hands is user-friendly, and relatively inexpensive.

DATA AVAILABILITY STATEMENT

The original contributions presented in the study are included in the article/Supplementary Material, further inquiries can be directed to the corresponding author.

ETHICS STATEMENT

The studies involving human participants were reviewed and approved by the cell line from human Stem cells is from

commercial provider. Written informed consent to participate in this study was provided by the participants' legal guardian/next of kin.

AUTHOR CONTRIBUTIONS

All authors are employed at JNJ: HL is the first author (study design, data analysis, and wrote manuscript), MK and VK were responsible for data analysis, FT was responsible for TI and statistical modeling, DG performed experiments, AT and DG provided scientific supports. All authors agreed to be accountable for the content of the manuscript.

ACKNOWLEDGMENTS

The authors wish to thank Bruce Damiano and Rajamani Sridharan for the scientific insight and review.

REFERENCES

Ando, H., Yoshinaga, T., Yamamoto, W., Asakura, K., Uda, T., Taniguchi, T., et al. (2017). A New Paradigm for Drug-Induced Torsadogenic Risk Assessment Using Human iPS Cell-Derived Cardiomyocytes. *J. Pharmacol. Toxicol. Methods* 84, 111–127. doi:10.1016/j.vascn.2016.12.003

Authier, S., Pugsley, M. K., Koerner, J. E., Fermini, B., Redfern, W. S., Valentin, J.-P., et al. (2017). Proarrhythmia Liability Assessment and the Comprehensive *In Vitro* Proarrhythmia Assay (CiPA): An Industry Survey on Current Practice. *J. Pharmacol. Toxicol. Methods* 86, 34–43. doi:10.1016/j.vascn.2017.02.021

Bedut, S., Seminatore-Nole, C., Lamamy, V., Caignard, S., Boutin, J. A., Nosjean, O., et al. (2016). High-throughput Drug Profiling with Voltage- and Calcium-Sensitive Fluorescent Probes in Human iPSC-Derived Cardiomyocytes. *Am. J. Physiology-Heart Circulatory Physiol.* 311 (1), H44–H53. doi:10.1152/ajpheart.00793.2015

Blanchette, A. D., Grimm, F. A., Dalaijamts, C., Hsieh, N.-H., Ferguson, K., Luo, Y.-S., et al. (2018). Thorough QT/QTc in a Dish: An *In Vitro* Human Model that Accurately Predicts Clinical Concentration-QTc Relationships. *Clin. Pharmacol. Ther.* 0 (0).

Blinova, K., Dang, Q., Millard, D., Smith, G., Pierson, J., Guo, L., et al. (2018). International Multisite Study of Human-Induced Pluripotent Stem Cell-Derived Cardiomyocytes for Drug Proarrhythmic Potential Assessment. *Cel Rep.* 24 (13), 3582–3592. doi:10.1016/j.celrep.2018.08.079

Bootman, M. D., Allman, S., Rietdorf, K., and Bultynck, G. (2018). Deleterious Effects of Calcium Indicators within Cells; an Inconvenient Truth. *Cell Calcium* 73, 82–87. doi:10.1016/j.ceca.2018.04.005

Bot, C. T., Juhasz, K., Haeusermann, F., Polonchuk, L., Traebert, M., and Stoelzle-Feix, S. (2018). Cross - Site Comparison of Excitation-Contraction Coupling Using Impedance and Field Potential Recordings in hiPSC Cardiomyocytes. *J. Pharmacol. Toxicol. Methods* 93, 46–58. doi:10.1016/j.vascn.2018.06.006

Colatsky, T., Fermini, B., Gintant, G., Pierson, J. B., Sager, P., Sekino, Y., et al. (2016). The Comprehensive *In Vitro* Proarrhythmia Assay (CiPA) Initiative - Update on Progress. *J. Pharmacol. Toxicol. Methods* 81, 15–20. doi:10.1016/j.vascn.2016.06.002

Dempsey, G. T., Chaudhary, K. W., Atwater, N., Nguyen, C., Brown, B. S., McNeish, J. D., et al. (2016). Cardiotoxicity Screening with Simultaneous Optogenetic Pacing, Voltage Imaging and Calcium Imaging. *J. Pharmacol. Toxicol. Methods* 81, 240–250. doi:10.1016/j.vascn.2016.05.003

Eckardt, L., Breithardt, G., and Haverkamp, W. (2002). Electrophysiologic characterization of the antipsychotic drug sertindole in a rabbit heart model of torsade de pointes: low torsadogenic potential despite QT prolongation. *J. Pharmacol. Exp. Ther.* 300 (1), 64–71. doi:10.1124/jpet.300.1.64

Food and Drug Administration, HHS (2005). International Conference on Harmonisation; Guidance on E14 Clinical Evaluation of QT/QTc Interval Prolongation and Proarrhythmic Potential for Non-antiarrhythmic Drugs; Availability. Notice. *Fed. Regist.* 70 (202), 61134–61135.

Gintant, G., Sager, P. T., and Stockbridge, N. (2016). Evolution of Strategies to Improve Preclinical Cardiac Safety Testing. *Nat. Rev. Drug Discov.* 15 (7), 457–471. doi:10.1038/nrd.2015.34

Goversen, B., van der Heyden, M. A. G., de Boer, T. A. B. T. P., and Boer, T. D. d. (2018). The Immature Electrophysiological Phenotype of iPSC-CMs Still Hampers *In Vitro* Drug Screening: Special Focus on Ik1. *Pharmacol. Ther.* 183, 127–136. doi:10.1016/j.pharmthera.2017.10.001

Hayakawa, T., Kunihiro, T., Ando, T., Kobayashi, S., Matsui, E., Yada, H., et al. (2014). Image-based Evaluation of Contraction-Relaxation Kinetics of Human-Induced Pluripotent Stem Cell-Derived Cardiomyocytes: Correlation and Complementarity with Extracellular Electrophysiology. *J. Mol. Cell Cardiol.* 77, 178–191. doi:10.1016/j.yjmcc.2014.09.010

Kanda, Y., Yamazaki, D., Osada, T., Yoshinaga, T., and Sawada, K. (2018). Development of Torsadogenic Risk Assessment Using Human Induced Pluripotent Stem Cell-Derived Cardiomyocytes: Japan iPS Cardiac Safety Assessment (JiCSA) Update. *J. Pharmacol. Sci.* 138 (4), 233–239. doi:10.1016/j.jphs.2018.10.010

Kopljar, I., Hermans, A. N., Teisman, A., Gallacher, D. J., and Lu, H. R. (2018a). Impact of Calcium-Sensitive Dyes on the Beating Properties and Pharmacological Responses of Human iPS-Derived Cardiomyocytes Using the Calcium Transient Assay. *J. Pharmacol. Toxicol. Methods* 91, 80–86. doi:10.1016/j.vascn.2018.02.004

Kopljar, I., Lu, H. R., Van Ammel, K., Otava, M., Tekle, F., Teisman, A., et al. (2018b). Development of a Human iPSC Cardiomyocyte-Based Scoring System for Cardiac Hazard Identification in Early Drug Safety De-risking. *Stem Cel Rep.* 11 (6), 1365–1377. doi:10.1016/j.stemcr.2018.11.007

Liu, H., Yang, L., Jin, M. W., Sun, H. Y., Huang, Y., Li, G. R., et al. (2010). The Selective Estrogen Receptor Modulator Raloxifene Inhibits Cardiac Delayed Rectifier Potassium Currents and Voltage-Gated Sodium Current Without QTc Interval Prolongation. *Pharmacol Res.* 62 (5), 384–390.

Liao, C. T., Lin, T. Y., and Iyer, H. K. (2005). One- and Two-Sided Tolerance Intervals for General Balanced Mixed Models and Unbalanced One-Way Random Models. *Technometrics* 47 (3), 323–335. doi:10.1198/004017005000000102

Lu, H. R., Gallacher, D. J., and Yan, G.-X. (2016). Assessment of Drug-Induced Proarrhythmia: The Importance of Study Design in the Rabbit Left Ventricular Wedge Model. *J. Pharmacol. Toxicol. Methods* 81, 151–160. doi:10.1016/j.vascn.2016.06.006

Lu, H. R., Hermans, A. N., and Gallacher, D. J. (2012). Does terfenadine-induced ventricular tachycardia/fibrillation directly relate to its QT prolongation and Torsades de Pointes? *Br. J. Pharmacol.* 166 (4), 1490–1502. doi:10.1111/j.1476-5381.2012.01880.x

Lu, H. R., Hortigon-Vinagre, M. P., Zamora, V., Kopljar, I., De Bondt, A., Gallacher, D. J., et al. (2017). Application of Optical Action Potentials in Human Induced Pluripotent Stem Cells-Derived Cardiomyocytes to Predict Drug-Induced Cardiac Arrhythmias. *J. Pharmacol. Toxicol. Methods* 87, 53–67. doi:10.1016/j.vascn.2017.05.001

Lu, H. R., Rohrbacher, J., Vlaminckx, E., Van Ammel, K., Yan, G.-X., and Gallacher, D. J. (2010). Predicting Drug-Induced Slowing of Conduction and Pro-arrhythmia: Identifying the 'bad' Sodium Current Blockers. *Br. J. Pharmacol.* 160 (1), 60–76. doi:10.1111/j.1476-5381.2010.00646.x

Lu, H. R., Vlaminckx, E., Hermans, A. N., Rohrbacher, J., Van Ammel, K., Towart, R., et al. (2008). Predicting Drug-Induced Changes in QT Interval and Arrhythmias: QT-Shortening Drugs point to Gaps in the ICHS7B Guidelines. *Br. J. Pharmacol.* 154 (7), 1427–1438. doi:10.1038/bjp.2008.191

Lu, H. R., Whittaker, R., Price, J. H., Vega, R., Pfeiffer, E. R., Cerignoli, F., et al. (2015). High Throughput Measurement of Ca++Dynamics in Human Stem Cell-Derived Cardiomyocytes by Kinetic Image Cytometery: A Cardiac Risk Assessment Characterization Using a Large Panel of Cardioactive and Inactive Compounds. *Toxicol. Sci.* 148 (2), 503–516. doi:10.1093/toxsci/kfv201

Lu, H. R., Zeng, H., Kettenhofen, R., Guo, L., Kopljar, I., van Ammel, K., et al. (2019). Assessing Drug-Induced Long QT and Proarrhythmic Risk Using

Human Stem-Cell-Derived Cardiomyocytes in a Ca2+ Imaging Assay: Evaluation of 28 CiPA Compounds at Three Test Sites. *Toxicol. Sci.* 170 (2), 345–356. doi:10.1093/toxsci/kfz102

Mathur, A., Loskill, P., Shao, K., Huebsch, N., Hong, S., Marcus, S. G., et al. (2015). Human iPSC-Based Cardiac Microphysiological System for Drug Screening Applications. *Sci. Rep.* 5, 8883. doi:10.1038/srep08883

Ovics, P., Regev, D., Baskin, P., Davidor, M., Shemer, Y., Neeman, S., et al. (2020). Drug Development and the Use of Induced Pluripotent Stem Cell-Derived Cardiomyocytes for Disease Modeling and Drug Toxicity Screening. *Int. J. Mol. Sci.* 21 (19). doi:10.3390/ijms21197320

Pacher, P., Magyar, J., Szigligeti, P., Bányász, T., Pankucsi, C., Korom, Z., et al. (2000). Electrophysiological Effects of Fluoxetine in Mammalian Cardiac Tissues. *Naunyn-Schmiedeberg's Arch. Pharmacol.* 361 (1), 67–73. doi:10.1007/s002109900154

Pourrier, M., and Fedida, D. (2020). The Emergence of Human Induced Pluripotent Stem Cell-Derived Cardiomyocytes (hiPSC-CMs) as a Platform to Model Arrhythmogenic Diseases. *Ijms* 21 (2), 657. doi:10.3390/ijms21020657

Rast, G., Weber, J., Disch, C., Schuck, E., Ittrich, C., and Guth, B. D. (2015). An Integrated Platform for Simultaneous Multi-Well Field Potential Recording and Fura-2-Based Calcium Transient Ratiometry in Human Induced Pluripotent Stem Cell (hiPSC)-Derived Cardiomyocytes. *J. Pharmacol. Toxicol. Methods* 75, 91–100. doi:10.1016/j.vascn.2015.04.005

Redfern, W. S., Carlsson, L., Davis, A. S., Lynch, W. G., MacKenzie, I., Palethorpe, S., et al. (2003). Relationships between preclinical cardiac electrophysiology, clinical QT interval prolongation and torsade de pointes for a broad range of drugs: evidence for a provisional safety margin in drug development. *Cardiovasc. Res.* 58 (1), 32–45. doi:10.1016/s0008-6363(02)00846-5

Spencer, C. I., Baba, S., Nakamura, K., Hua, E. A., Sears, M. A. F., Fu, C.-c., et al. (2014). Calcium Transients Closely Reflect Prolonged Action Potentials in iPSC Models of Inherited Cardiac Arrhythmia. *Stem Cel Rep.* 3 (2), 269–281. doi:10.1016/j.stemcr.2014.06.003

Takasuna, K., Asakura, K., Araki, S., Ando, H., Kazusa, K., Kitaguchi, T., et al. (2017). Comprehensive *In Vitro* Cardiac Safety Assessment Using Human Stem Cell Technology: Overview of CSAHi HEART Initiative. *J. Pharmacol. Toxicol. Methods* 83, 42–54. doi:10.1016/j.vascn.2016.09.004

Testai, L., Calderone, V., Salvadori, A., Breschi, M. C., Nieri, P., and Martinotti, E. (2004). QT Prolongation in Anaesthetized guinea-pigs: an Experimental Approach for Preliminary Screening of Torsadogenicity of Drugs and Drug Candidates. *J. Appl. Toxicol.* 24 (3), 217–222. doi:10.1002/jat.975

Titier, K., Girodet, P.-O., Verdoux, H. l. n., Molimard, M., B??gaud, B., Haverkamp, W., et al. (2005). Atypical Antipsychotics. *Drug Saf.* 28 (1), 35–51. doi:10.2165/00002018-200528010-00003

Watanabe, H., Honda, Y., Deguchi, J., Yamada, T., and Bando, K. (2017). Usefulness of Cardiotoxicity Assessment Using Calcium Transient in Human Induced Pluripotent Stem Cell-Derived Cardiomyocytes. *J. Toxicol. Sci.* 42 (4), 519–527. doi:10.2131/jts.42.519

Woosley, R. L., Black, K., Heise, C. W., and Romero, K. (2018). CredibleMeds.org: What Does it Offer? *Trends Cardiovasc. Med.* 28 (2), 94–99. doi:10.1016/j.tcm.2017.07.010

Zeng, H., Roman, M. I., Lis, E., Lagrutta, A., and Sannajust, F. (2016). Use of FDSS/μCell Imaging Platform for Preclinical Cardiac Electrophysiology Safety Screening of Compounds in Human Induced Pluripotent Stem Cell-Derived Cardiomyocytes. *J. Pharmacol. Toxicol. Methods* 81, 217–222. doi:10.1016/j.vascn.2016.05.009

Zhang, X., Guo, L., Zeng, H., White, S. L., Furniss, M., Balasubramanian, B., et al. (2016). Multi-parametric Assessment of Cardiomyocyte Excitation-Contraction Coupling Using Impedance and Field Potential Recording: A Tool for Cardiac Safety Assessment. *J. Pharmacol. Toxicol. Methods* 81, 201–216. doi:10.1016/j.vascn.2016.06.004

Conflict of Interest: Authors HL, MK, VK, FT, DG, AT and DG are employed by Janssen Pharmaceutica NV.

Publisher's Note: All claims expressed in this article are solely those of the authors and do not necessarily represent those of their affiliated organizations, or those of the publisher, the editors and the reviewers. Any product that may be evaluated in this article, or claim that may be made by its manufacturer, is not guaranteed or endorsed by the publisher.

frontiers | Frontiers in Physiology

REVIEW
published: 25 April 2022
doi: 10.3389/fphys.2022.867033

Golden Standard or Obsolete Method? Review of ECG Applications in Clinical and Experimental Context

Tibor Stracina[1], *Marina Ronzhina*[2], *Richard Redina*[2,3] *and Marie Novakova*[1]*

[1]Department of Physiology, Faculty of Medicine, Masaryk University, Brno, Czech Republic, [2]Department of Biomedical Engineering, Faculty of Electrical Engineering and Communication, Brno University of Technology, Brno, Czech Republic, [3]International Clinical Research Center, St. Anne's University Hospital Brno, Brno, Czech Republic

Cardiovascular system and its functions under both physiological and pathophysiological conditions have been studied for centuries. One of the most important steps in the cardiovascular research was the possibility to record cardiac electrical activity. Since then, numerous modifications and improvements have been introduced; however, an electrocardiogram still represents a golden standard in this field. This paper overviews possibilities of ECG recordings in research and clinical practice, deals with advantages and disadvantages of various approaches, and summarizes possibilities of advanced data analysis. Special emphasis is given to state-of-the-art deep learning techniques intensely expanded in a wide range of clinical applications and offering promising prospects in experimental branches. Since, according to the World Health Organization, cardiovascular diseases are the main cause of death worldwide, studying electrical activity of the heart is still of high importance for both experimental and clinical cardiology.

Keywords: electrocardiogram, ECG recording, animal model, deep learning, ECG analysis, artificial intelligence, isolated heart, arrhythmia classification

OPEN ACCESS

Edited by:
Guido Caluori,
Institut de rythmologie et modélisation cardiaque (IHU-Liryc), France

Reviewed by:
Sharen Lee,
The Chinese University of Hong Kong, China
Erick Andres Perez Alday,
Emory University, United States

***Correspondence:**
Marie Novakova
majka@med.muni.cz

Specialty section:
This article was submitted to Integrative Physiology, a section of the journal Frontiers in Physiology

Received: *31 January 2022*
Accepted: *15 March 2022*
Published: *25 April 2022*

Citation:
Stracina T, Ronzhina M, Redina R and Novakova M (2022) Golden Standard or Obsolete Method? Review of ECG Applications in Clinical and Experimental Context. Front. Physiol. 13:867033. doi: 10.3389/fphys.2022.867033

1 INTRODUCTION

Cardiovascular disorders are the major cause of death in developed countries. Due to the change of lifestyle, their incidence increases recently also in countries where cardiovascular morbidity and consequent mortality have not been considered a problem until now. Enormous economic and social burden of such situation promotes further research of both physiological and pathophysiological cardiovascular processes.

Cardiac action starts with electrical event—membrane depolarization—which is then followed by a mechanical response, e.g., cardiac muscle contraction. After this event, called systole, the cardiac cycle continues with diastole (membrane repolarization and consequent muscle relaxation). Obtaining quite detailed information about electrical activity of the heart seems to be technically easier than obtaining comparably detailed information about mechanical events.

The first attempts to study electrical processes related to cardiac action were performed already in the 19th century (AlGhatrif and Lindsay, 2012), based on the experience with recording electrical current from skeletal muscles even a century earlier. The first successful recording of electrical activity of human heart was achieved in 1887 by the British physician and physiologist Augustus Waller (Besterman and Creese, 1979). His contribution to this area is so important that it is rather unfair that his name is not mentioned together with the so-called father of electrocardiography, Dutch physiologist and physician Willem Einthoven. Einthoven, a Nobel Prize winner in 1924, is highly recognized since he standardized the whole method: he introduced the term

"electrocardiogram" (ECG), reported a typical ECG of a healthy man with five deflections labeled P, Q, R, S, and T, and, last but not least, built a sort of the first ECG recorder based on a string galvanometer. Soon after the first clinically relevant attempts to record the human ECG curve, the method was used by other researchers who improved the recording possibilities and thus opened a new medical field—cardiology. Worth mentioning are especially Wilson and Goldberger, who introduced the central terminal thus enabled to record unipolar leads and their augmented version. All other research in heart electrophysiology proceeded from these key steps.

Concurrently to above-described milestones of ECG development and its establishment into routine clinical use, researchers were interested in electrical changes accompanying the heart activity other than whole-body models. The fundamental approach in this area is the isolated heart model. First, successful isolation and perfusion of frog heart were achieved by Elias Cyon and Carl Ludwig (Zimmer, 1998). Then, a model of isolated perfused mammalian heart was introduced by H. Newell Martin and Oscar Langendorff. The latter invented and published in 1895 a perfusion setup which is suitable for all hearts with a coronary system. Nutrition is supplied to the heart muscle by perfusion solution, administered *via* a cannula inserted into the aorta of the fully explanted heart. The hydrostatic pressure of the solution closes the aortic valve, and solution enters the coronary arteries, leaves via sinus coronarius, and drips off.

A model of isolated heart perfused according to Langendorff (also known as Langendorff's heart) is the first experimental setting which enables recording of electrical activity of the heart in the style which resembles the ECG (Olejnickova, Novakova, and Provaznik, 2015). Of course, there were some attempts to record electrical activity of the heart before introduction of this model; however, the quality of recording and consequently the scientific impact of such data were low.

2 ECG RECORDING

2.1 Clinical Perspective

From Einthoven's first ECG recording system till now, ECG recording has undergone huge transformation from a full-analog system to fully computerized ECG recorders (Rautaharju, 2016). Regardless of technological progress, the basic clinical approach—12-lead ECG recording—is still based on Einthoven, Wilson, and Goldberg's inventions. A standard 12-lead configuration contains three bipolar limb leads originally introduced by Einthoven (I, II, and III), three Goldberg's augmented unipolar limb leads (aVL, aVR, aVF), and six unipolar chest leads (V1–V6), where a Wilson central terminal serves as the reference electrode. Ten skin electrodes are placed on the left wrist or arm (LA), on the right wrist or arm (RA), on the left leg (LL), on the right leg (RL), and on the chest (V1–V6). Chest leads (V1–V6) cover small part of the chest circumference. Therefore, for specific purposes, modified chest leads, shifted to different intercostal spaces or to completely different positions, are used. For example, the leads V3R–V6R are placed on the right side of the chest mirroring leads V3–V6. Such modification is useful for diagnostics of ECG abnormalities originated in the right ventricle.

The 12-lead ECG configuration gives spatial information about the cardiac electric activity (Kalra, Lowe, and Al-Jumaily, 2019). Since ECG leads have both positive and negative poles, they may be viewed from two spatial directions. The standard 12-lead ECG system presents the "positive" ECG leads in a single well-ordered sequence in the transverse plane (chest leads V1–V6), but in two separate non-anatomical sequences in the frontal plane (I–III and aVR–aVF). Moreover, the aVR lead shows the cardiac electric activity from the right-side view, but the other eleven leads show the heart activity from the left-side view. The direction of the deflections in the aVR lead tends to be opposite to that in all other leads. In such presentation, it is usually hard to integrate consideration of lead aVR into overall ECG interpretation. To cope with such problems, an orderly presented ECG system was introduced. The so-called Cabrera system is based on two modifications of the standard 12-lead ECG: 1) changing aVR polarity (–aVR) and 2) changing re-organization of limb leads in the anatomical order (aVL, I, –aVR, II, aVF, III) (Lam, Wagner, and Pahlm, 2015). Even such modification may help to easily interpret ECG changes, and only Sweden has adopted the Cabrera system as a national standard.

Reconstruction of the cardiac vector movement from the 12-lead ECG is—despite all modifications—arduous and imagination-demanding. For such analysis, orthogonal leads are much more useful. Orthogonal leads record the electric activity from three perpendicular axes of the body (horizontal, vertical, and sagittal). Frank leads are one of the most clinically relevant orthogonal systems.

The standard 12-lead system is mostly used for ambulatory ECG recording. Also, such recording is used during the exercise stress test. Ambulatory 24 h ECG monitoring—Holter monitor—is employed in diagnostics of paroxysmal cardiac events (such as paroxysmal arrhythmias). The Holter monitor may use a 12-lead system; however, modern devices record two or three modified leads only (Kalra, Lowe, and Al-Jumaily, 2019). In case of rare symptoms, an implantable loop recorder is valuable (Giada et al., 2007). Such long-term monitor is placed under the skin on the chest and can automatically record long continuous signals (up to 3 years) (Kalra, Lowe, and Al-Jumaily, 2019). Recently, several innovative methods for ECG monitoring were introduced, including patch sensors, EPIC (electric potential integrated circuit) sensors, chest harnesses, and vest shirts (Kalra, Lowe, and Al-Jumaily, 2019; Soroudi et al., 2019). A general trend is to minimize electrodes and make devices wearable, remote-controlled, and programmable.

A typical ECG curve shows five deflections labeled P, Q, R, S, and T. The P wave reflects depolarization of the atria. Deflections Q, R, and S create a thin complex—QRS complex, which represents ventricular depolarization. The R peak is always positive (pointing upward). Deflection Q is always the negative deflection preceding R peak. Deflection S is always the negative deflection following R peak. Depending on the orientation of ECG lead, some of the deflections of the QRS complex may not be

expressed. The fifth deflection—the T wave—reflects repolarization of the ventricles. Between the end of P wave and the onset of QRS complex, a period of isoelectric line called the PQ segment is found. The PQ segment represents atrioventricular (AV) conduction or AV delay. The PQ segment together with the P wave forms a PQ interval. The PQ interval duration reflects propagation of depolarization from the atria to the ventricles. Between the end of QRS complex and the onset of T wave, there is a period of isoelectric line called the ST segment. During the ST segment, all the ventricular cardiomyocytes are fully depolarized, resting in the plateau phase of the action potential. Complete electric revolution of the ventricle is represented by a QT interval—the period from the onset of the QRS complex to the end of the T wave. The distance of two consecutive R peaks—RR interval—represents the duration of one electric cycle of the heart; therefore, it defines the heart rate. The amplitude of deflections as well as polarity of P and T waves depends on the orientation of ECG lead. This topic is out of the scope of this article, and therefore, it is not discussed here.

ECG recording plays an irreplaceable role in diagnostics of various cardiovascular diseases. Diagnostics of arrhythmias is completely based on an ECG record. Moreover, the QT interval prolongation—an independent risk factor for ventricular arrhythmias—can be detected exclusively from an ECG. Typical ECG changes, such as the ST segment elevation and T wave alteration, are related to coronary artery disease and myocardial infarction. According to the specific changes in the 12-lead ECG record, an occlusion of coronary artery can be localized. Also, left ventricular hypertrophy can be diagnosed with high sensitivity and specificity from the ECG record (Yu et al., 2021). Also, other cardiovascular diseases can manifest themselves as ECG curve alterations—for instance, myocarditis, pericarditis, myocardial fibrosis, amyloidosis, and inherited and acquired defects (such as dextrocardia, mitral stenosis, or regurgitation). ECG-based diagnostics of pulmonary embolism represents a specific issue. Although advanced techniques such as echocardiography, computed tomography, or magnetic resonance are widely used, the diagnostic role of ECG—especially in acute pulmonary embolism—is still highly valued by clinicians (Van Mieghem et al., 2004). However, it is necessary to emphasize that ECG signs of pulmonary embolism may be imitated by severe pneumonia or pneumothorax.

ECG may also help in diagnostics of numerous non-cardiovascular diseases (Van Mieghem et al., 2004). Typical ECG curve alterations are detectable in electrolyte imbalances, such as hyperkalemia and hypocalcemia. Both hyperthyroidism and hypothyroidism are presented by heart rate alterations and non-specific ST-T changes. Specific ECG changes are associated with various disorders of the central nervous system, e.g., subarachnoid hemorrhage, head trauma, and acute meningitis. Hypothermia and hyperthermia cause characteristic ECG alterations. Last but not least, there are many drugs with cardiovascular side effects. Drug-induced ECG alterations have to be considered during treatment by antiarrhythmics, beta-blockers, antibiotics, antihistamines, antipsychotics, and others.

Innovative approaches of ECG recording bring new challenges in ECG interpretation. Reduction of the employed electrodes leads to the reduction of ECG lead number. Recently, diagnostic potential of reduced-lead ECG was discussed during the PhysioNet/Computing in Cardiology Challenge (Reyna et al., 2021). The results suggest that two leads can be enough for some of the used diagnostics. However, the accuracy of the diagnostics depends also on the particular combination of leads (Reyna et al., 2021). On the contrary, a device which enables to record a high number of ECG leads has been introduced and successfully tested for detection of life-threatening events in a human phantom equipped with an ECG simulator (Wojcik et al., 2021).

2.2 Animal Perspective

The quality (sampling rate and resolution) of the ECG record is important particularly in animals of high heart rate (mice, rats).

If the electric activity is recorded directly from the surface of the heart, the term "electrogram" (EG) should be preferred. In isolated heart models, originally the electric activity was recorded by needle or hook electrodes attached directly into the cardiac muscle. However, mechanical irritation caused by electrode attachment may induce ventricular arrhythmias. To minimize it, only one pair of electrodes is usually attached, and thus, one EG lead is recorded. A less-invasive approach is possible if the isolated heart is immersed into the bath containing saline (e.g., Krebs–Henseleit or Tyrode solution). Then, an EG is recorded contact-less by electrodes placed on the inner surface of the bath (**Figure 1A**). Various numbers and positions of electrodes may be used including a two-dimensional lead system (Ronzhina et al., 2017) or three-dimensional orthogonal lead system (Janousek et al., 2010). Such approach minimizes mechanical irritation of the heart and allows to record more than one EG lead. However, moving artifacts may compromise EG analysis.

To study more complex responses of the cardiovascular system including neuro-humoral regulatory mechanisms, a whole-body animal model has to be engaged. Various animal species are used to study heart electric activity—including zebrafish, small rodents (mouse, rat, guinea pig), rabbit, dog, pig, and others. A broad range of methods are used to record the ECG in animals. Generally, the methods can be divided into two groups: 1) methods used in anesthetized animals and 2) methods enabling ECG recording in conscious animals.

In small animals, including rodents and rabbit, the ECG is frequently recorded in general anesthesia (Ha, Oh, and Kang, 2020). In anesthetized animals, needle electrodes are usually placed under the skin of thorax or limbs. Alternatively, clip or strip electrodes can be fixed to the paws. Other non-invasive approaches, such as standard skin electrodes, are less effective due to thick fur of the animals. If non-invasive attachment of the electrodes is preferred, the fur has to be shaved. Also, contact conductive ECG gel may improve the signal transduction. The position of the electrodes usually copies standard bipolar limb leads well known in human ECG. ECG recording in general anesthesia is quite common if acute events are studied, such as potential arrhythmogenicity of drugs or drug candidate substances (Marks et al., 2012; Sakaguchi et al., 2009). ECG recording using needle electrodes can also be useful to monitor cardiac activity during any surgical procedure. The

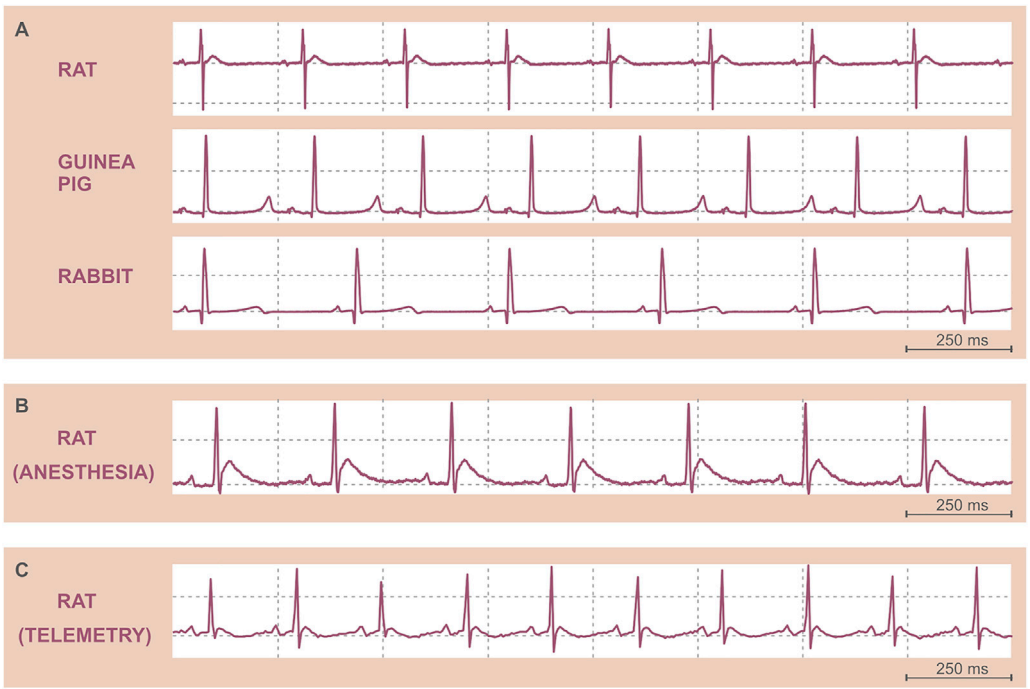

FIGURE 1 | Original ECG records. **(A)** Isolated heart electrograms of various species. **(B)** ECG in an anesthetized Sprague Dawley male rat recorded by needle electrodes. **(C)** ECG in a freely moving Wistar male rat recorded by telemetry. Note the differences in the heart rate among species **(A)** and between anesthetized **(B)** and conscious **(C)** rats.

recording of ECG in anesthetized small animals is quite easy to perform. General anesthesia minimizes the stress and ensures minimal movement of the animal (except of the breathing). However, the effect of anesthetics on the cardiac electric activity must be considered (**Figure 1B**) (Redfors, Shao, and Omerovic, 2014; Sano et al., 2016; Wren-Dail et al., 2017; Liu et al., 2019).

ECG recording in zebrafish represents a specific chapter. In the last two decades, zebrafish became a valuable model in experimental cardiology due to its fast reproduction, low maintenance cost, easy breeding, possibility of genetic manipulation, extensive developmental characterization, and optical transparency (Gut et al., 2017; Duong et al., 2021). Moreover, zebrafish cardiac electric activity is comparable to that of man (Duong et al., 2021). Therefore, several devices for ECG recording in zebrafish were introduced. Most of the approaches require anesthesia or paralysis of the fish. Recently, devices for long-term monitoring of zebrafish were developed and validated (Duong et al., 2021; Le et al., 2022).

If the unwanted effect of general anesthesia may interfere with the experimental purpose, ECG recording in conscious animals is preferred. Even in small animals, the ECG can be recorded using telemetric monitoring (Kramer et al., 2001; Ruppert et al., 2016). Telemetric systems enable to record minimally one lead of ECG in conscious, freely moving animals (**Figure 1C**). A telemetric unit—microprocessor, battery, and sensors or electrodes for recording of various biosignals—is usually implanted into the abdominal cavity or under the skin. ECG electrodes are fixed subcutaneously. After the implantation, the animal must recover. Then, the ECG can be repeatedly recorded. Such approach is highly valued in long-term studies of drug cardiotoxicity or new drug candidates' efficiency as well as in chronobiological studies. It usually allows to record the ECG simultaneously with body temperature, arterial blood pressure, or acceleration (movement) of the animal. Such polygraph may uncover subtle dysregulation of the cardiovascular system as well as disruptions of circadian cycles. However, there are some pitfalls which must be considered from the very beginning. Implantation of telemetric unit requires certain surgical skills. Also, the main advantage—recording of the ECG in freely moving animals—is a big challenge. During the movement, skeletal muscles produce a lot of electric potential changes, which cause artifacts in the ECG record. Moreover, telemetric electrodes placed under the skin may slightly change the positions due to body movement. The electrode position change results in the ECG curve change, which may affect ECG analysis. Proper fixation of the electrodes is therefore crucial. Although some approaches promise high-quality ECG recording (Tontodonati, Fasdelli, and Dorigatti, 2011), a standardized, well-reproducible, and broadly accepted procedure of telemetric electrode placement in small animals is missing. In large animals, telemetric monitoring is well established and widely used. Besides implantable telemetric systems, external sensors were introduced. ECG electrodes are placed on the inner surface of a jacket, which is securely fastened to the animal's trunk. Such fully non-invasive external telemetric system is routinely used in dogs and monkeys (Fish et al., 2017; Skinner et al., 2017). On the

TABLE 1 | Key electrophysiological characteristics in human and selected experimental animal species. AP, action potential; bpm, beats per minute; ms, milliseconds. *As in ectotherms, the heart rate and duration of ventricular AP in zebrafish vary with body temperature, and numbers indicate heart rate/ventricular AP duration at 28°C and at 19°C (in parentheses), respectively.

	Human	Dog	Rabbit	Guinea pig	Rat	Mouse	Zebrafish
Mean resting heart rate (bpm)	75	70	200	230	300	500	55 (145)*[a]
Ventricular AP (ms)	250	250	120–140	140	50	25–40	143 (311)*[a]
ST segment in ECG	Yes	Yes	Yes	Yes	No	No	Yes[a]

[a](Vornanen and Hassinen, 2016) *Unless otherwise indicated, adopted from (*Farraj, Hazari, and Cascio, 2011).

same principle, devices for small rodents were introduced. Telemetric ECG recording was used in various wild-life animal species—for instance, in humpback whale (Meijler et al., 1992). Battery lifespan, internal memory capacity, and wireless data transmission speed represent main technical limitations of all telemetric devices. Acquisition price and operating costs may also significantly limit the use of telemetric systems.

If a short-term ECG record is required, non-invasive methods are a good choice. In large well-trainable animals, it is possible to record the ECG by standard stick-on electrodes. Such procedure requires specific training, during which the animal learns to remain motionless for several minutes. In small animals, non-invasive devices usually consist of a platform equipped with electrodes, on which an animal puts its paws (Mongue-Din et al., 2007). In such approach, some restraint of the movement is indispensable. Plastic tunnel restrainers are usually used. But any restraint of movement is stressful for animal, especially for small rodents. To prevent excessive stress, proper handling of the animals must precede the recording. In well-handled rodents, restraint by hand represents a better alternative. Also, mild sedation may decrease animals' motor activity and therefore increase the quality of the ECG record. Nevertheless, restrained ECG recording technique is a valuable method for rapid screening of several animals in a short time and at low expense. Such method is particularly useful in cardiovascular phenotyping of knockout rats and mice allowing for easy detection of gross abnormalities in cardiac rhythm in a large number of animals (Mongue-Din et al., 2007).

In experimental animals, interpretation of the ECG is usually more challenging than the recording. Lack of standardization in animal ECG recording and less evidence of normal (physiological) values of ECG parameters make the interpretation difficult. The differences in cardiac electric activity among various species also must be considered—especially differences in body size, heart anatomy, and cardiac ionic channel types and their distribution and regulation. The most striking difference in ECG among the species is the RR interval duration (**Figure 1A**). In mammals, the duration of resting RR interval is directly proportional to the animal's body mass. The lower the body mass, the higher the resting heart rate. The key cardiac electrophysiological characteristics of various species are summarized in **Table 1**.

The ECG of the most frequently used laboratory animals—rat and mouse—is quite distinct from that of humans. There is no distinct ST segment in rat and mouse ECG curves due to short ventricular action potential with minimal plateau phase. The T wave begins immediately after QRS complex. Also, the resting heart rate is significantly higher than that of humans (approx. 500 bpm in mouse, 300 bpm in rat, and 75 bpm in man, respectively). Moreover, significant differences between various strains of the same species were repeatedly reported (Wehrens, Kirchhoff, and Doevendans, 2000; Azar, Sharp, and Lawson, 2011; Konopelski and Ufnal, 2016).

3 ECG ANALYSIS

After the ECG is recorded, its pre-processing and analysis may start. The ECG analysis is meant to be a process which gives valuable information about the examined subject (isolated heart model, whole-body animal model, or patient) in terms of cardiac electrophysiology. The early analyses of ECG in the beginning of the 20th century were performed only for measuring time relations in the signal. The introduction of computer technology in the middle of the 20th century opened new possibilities for the analysis of ECG. Despite all the advantages of computer technology, manual evaluation of the ECG by a cardiologist remains an indispensable part of diagnosis. The following paragraphs briefly summarize the development of ECG analysis, the basic principles of the main techniques in clinical and experimental perspectives, and, finally, the main current issues and future directions in this field. **Figure 2** illustrates the progress of ECG processing and analysis techniques in time perspective.

3.1 Pre-Computer Era

Many physiologists at the end of the 19th century were convinced that the mechanical contraction of the heart is preceded by an electrical action that could be measured. In the first attempts to record electrical potentials of the heart muscle, only heart depolarization and repolarization were recognizable (Waller, 1887). This led to the opinion that such recording would never be useful in clinical practice (Barold, 2003). As signal acquisition techniques have evolved, the quality of the signal has improved, and by the beginning of the 20th century, it was possible to distinguish in ECG five basic deflections: P, Q, R, S, and T waves (Ruiz et al., 2008). The first step in the development of ECG analysis itself was the establishment of a normal recording. At that moment, the first databases of ECG records have been introduced and used to manually measure the

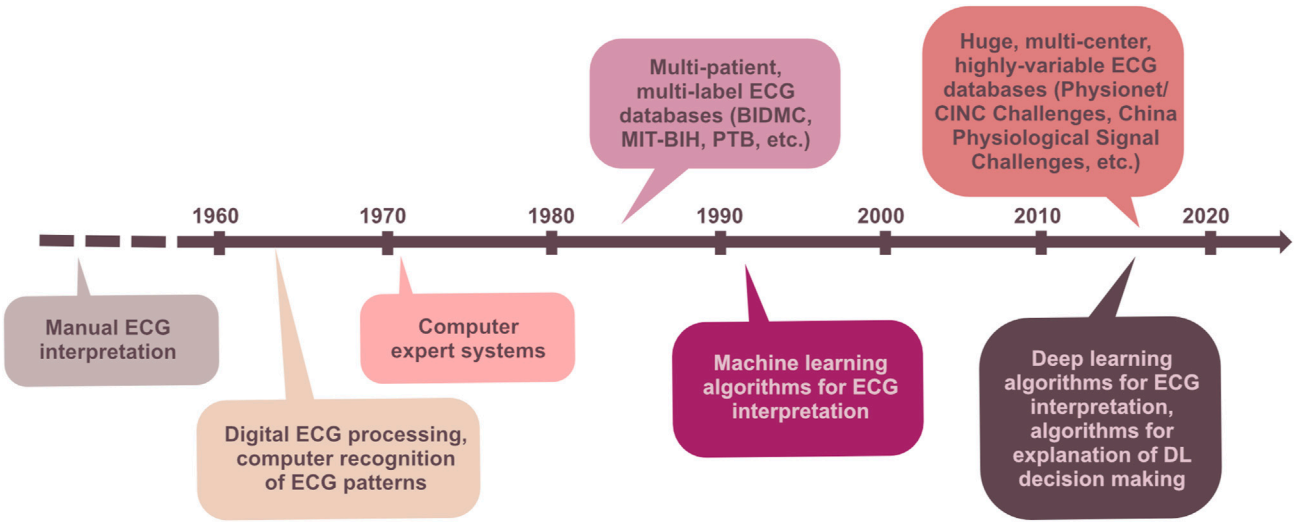

FIGURE 2 | Milestones of ECG processing and analysis in time perspective.

durations and magnitudes of the waves (Larsen and Skúlason, 1941; Simonson et al., 1949; Packard et al., 1954).

Along with the improvement of electrical activity recording, the first attempt to quantitatively describe how the heart function is transcribed into the ECG has been done. Numerous equations have been developed to identify the relationships between the heart function and ECG patterns. These equations helped to discover phenomena, which were not visible at the first glance. One of such measures, outlasting in the clinical and experimental use to present, is the QT interval corrected by Bazett's formula (Bazett, 1920). It reflects the association between the QT interval duration and the heart rate or, in other words, between electrical and mechanical systole of the heart. However, the formula has never been generally applicable; therefore, many other revisions have been developed over the years (e.g., Phang and White, 1943; Krasnoff, 1950).

From today's perspective, these pioneers have come a long way. The foundations laid by them made it possible to develop the robust and reliable computational methods in the second half of the 20th century.

3.2 Computer-Aided Analysis

3.2.1 What Are the Benefits?

Rapid development of computer technologies in the second half of the 20th century led to the extensive automation of various processes traditionally performed by human experts. In medicine, along with analysis of complex imaging data (ultrasound, CT, MRI, etc.), the diagnostics of cardiac disorders intensely uses advanced, highly intelligent computer-aided systems. Probably, the most evident benefit of the computer algorithms is in their ability to process a huge amount of data in a very short time (e.g., Brailer et al., 1997), a process desirable in both clinical and experimental applications. Another advantage is an accurate detection of specific ECG patterns, even in case of mild manifestation or several different manifestations presented in the ECG simultaneously. In such case, the low-resolution, visual diagnostics may be inaccurate or totally false, especially when provided by an inexperienced physician (e.g., Holmvang et al., 1998; Salerno et al., 2003). This limitation, however, may be partially eliminated by using the so-called collective intelligence decision-making system integrated in a special mobile application. Such system enables fast sharing of ECG data and performing the visual interpretation simultaneously by several experts (Hwang et al., 2021). The computational algorithms can analyze multi-lead data simultaneously, for the full length of the record, in a reasonable time, which is not possible by visual inspection. The decision-making process of the computer systems is reproducible, and it is not affected by human factors, such as tiredness and stress (e.g., Taddei et al., 1992). Finally, computerized ECG analysis utilizing widely available telecommunication infrastructure enables using all above benefits in areas with a lack of human experts or in telemedicine applications. In the latter, computer-aided systems play a crucial role by supporting the fast assessment of a huge amount of ECG records (Saeed and Ameen, 2021).

From medical point of view, use of the most advanced methods for ECG analysis offers a simple, widely available, cheap diagnostics tool. By accurate, sensitive, fast, and robust detection of pathological patterns in the ECG, these methods contribute to early diagnosis, selecting the correct treatment strategy, better outcomes, and improved life quality of the patients on the one side and to minimized mental and time demands of clinical staff and decreased national healthcare financial resources on the other side. Automatic prediction systems are also useful in preventive medicine.

Of course, computer algorithms make errors, especially when a low-quality signal or signal with unknown (at least by the algorithm itself) abnormality is analyzed. The computer more likely fails when similar manifestations correspond to different pathologies. In contrast to the computer algorithms, human

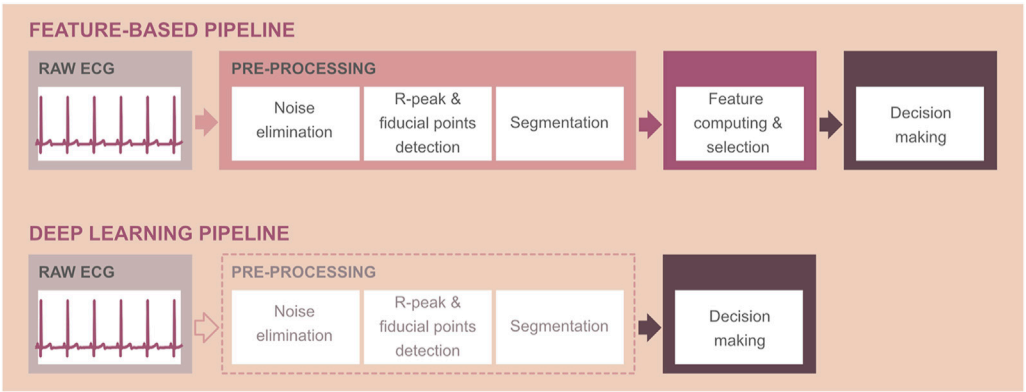

FIGURE 3 | Schematic representation of computer-aided ECG interpretation using feature-based technique (top) and deep learning approaches, which do not require the calculation of ECG features (bottom). Note: pre-processing steps are optional when using deep learning methods and depend on the application.

experts use clinical information about the patient and intuition. Therefore, all statements of the computer systems must be over-read by skilled physicians (Smulyan, 2019). Nevertheless, the decision support system based on the highly accurate algorithm may significantly improve the accuracy of physicians in ECG interpretation, as has been shown previously on myocardial ischemia detection (Tsai et al., 2003).

3.2.2 Basic Pipeline: From Digital Filters to Deep Learning Models

Traditional computer-aided ECG interpretation consists of the following steps: pre-processing, computation of so-called features, selection of the most relevant ones, and, finally, decision-making (**Figure 3**, top). ECG pre-processing usually includes suppression of noise, detection of QRS complexes and/or other fiducial points important for ECG delineation, and segmentation (e.g., Berkaya et al., 2018; Kumar and Komaragirikumar, 2018; Vidhya and Jerritta, 2022). Noise of physiological, environmental, or technical origin complicates the interpretation of the records and, thus, must be removed by appropriate methods. Most computer-aided systems use digital filters to solve this problem (see below). Noise-free ECG is suitable for accurate detection of the waves, which usually starts by detection of the most prominent deflection in ECG-QRS complex and continues by searching the peaks and onsets/offsets of the other waves in areas surrounding QRS. In some applications, the outputs of the delineation process are then used for signal segmentation into the separate beats, intervals, or waves of interest. In the next step, the most important in the whole pipeline, the quantitative descriptors—features—are calculated from the initial filtered ECG or the segments. For effective and accurate ECG interpretation, only the most relevant and informative features should be considered. Therefore, the techniques, providing careful selection of the most discriminative features or removing the irrelevant and redundant ones, are applied prior to decision-making. The final step—decision-making—is a process, which must solve specific problems. The most frequent issues related to ECG analysis are the prediction or identification of the cardiac abnormality or localization of cardiac pathological events. Nowadays, these problems are addressed by four different ways: 1) by visual or simple statistical-based expert inspection of the features using established criteria (i.e., by comparing the feature value with the physiological range); 2) by using rather simple, but transparent, human-like expert systems providing automatic analysis of the features *via* decision rules pre-determined in cooperation with clinician experts; 3) by using machine learning (ML) tools—so-called supervised learning algorithms, which are able to learn the interpretations from training data equipped with ground truth labels with no need for expert rules; and 4) by using state-of-the-art tools—so-called deep learning (DL) models.

Feature-based decision-making is usually provided by ML models, from simple linear discriminant analysis (LDA) or logistic regression to more advanced k-nearest neighbor (k-NN), decision tree, random forest, support vector machine (SVM), multiple-layer perceptron (MLP), etc. From mathematical background, most are based on using one or combination of several linear or non-linear equations, which map current input data (ECG samples or features) into the predicted output (label/diagnosis) (for further information, refer to Duda et al., 2000; Chazal et al., 2004; Osowski et al., 2004; Ince et al., 2009; Mishra and Raghav, 2010; Theodoris and Koutroumbas, 2009, etc.). In fact, they solve the classification problem by assigning each input sample (i.e., patient's ECG) to some of the pre-defined categories (e.g., normal and pathological). ML methods try to find the decision boundaries for identification of different groups of data by learning on samples with known expert interpretations. During the training process, the equation coefficients (model parameters) are adjusted by some special optimization algorithm in order to ensure mapping as accurate as possible (in other words, to ensure correct predicted output of the model). A model with optimal parameters is then able to accurately interpret new, previously unseen, data.

Both ML and DL methods are parts of artificial intelligence—a wide branch of computer science focused on developing smart systems capable of mimicking human reasoning and solving the

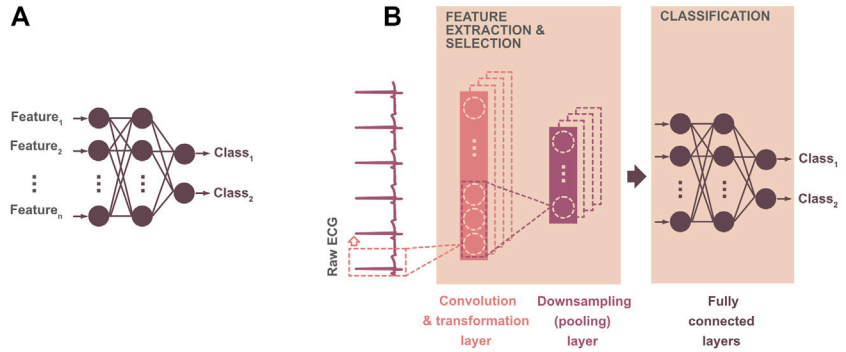

FIGURE 4 | Illustration of two binary classification models: **(A)** straightforward artificial neural network—machine learning model providing ECG classification based on the previously derived features; **(B)** 1D convolutional neural network (1D CNN)—deep learning model providing automatic extraction of the features from raw ECG by convolutional layer(s) and further assignment of the input into the class by fully connected perceptron-like layers. In a 1D CNN model, the convolutional layer consists of filters, which derive important features from the input ECG. The convolution output—feature map—is usually transformed using a linear or non-linear function (in order to simplify the training process and avoid the problem of vanishing gradient) and downsampled by calculating the average (average pooling) or by selecting maximal (max-pooling) values from the feature map. The pooling procedure leads to the reduced number of model parameters and, thus, decreased computation demand.

tasks traditionally requiring human intelligence. Deep learning is the most recent, advanced technique, extracting highly relevant complex patterns from raw ECG by itself, with no need for feature extraction (see **Figure 3**, bottom). Briefly, DL neural network models include specific layers for automatic extraction of feature maps from the input signal and layers providing the output prediction (see **Figure 4B**). Thus, DL models can be considered "all-in-one" solutions, analyzing data in a broad context and outperforming most of existing approaches in terms of time and computational requirements, as well as achieved results (e.g., Goodfellow et al., 2016; Kashou et al., 2021; Ravì et al., 2017). Reduced computational demand of the DL decision-making is caused by both the absence of pre-processing steps and fast interpretation of new data once the model is trained. Compared to the shallow MLP, the DL neural network consists of many neuron layers with different specialization (compare **Figures 4A,B**). Both shallow and deep neural networks are based on the neurons—nodes—connected to each other in such a way that the input information goes through the deep structure to the last layer, where the predicted output is generated. Each neuron is represented by a linear or non-linear equation, which maps current input data into the output. The neuron parameters—so-called weights—are actually the coefficients of the neuron equation, which are set during the optimization procedure (i.e., during model training). The mathematical operations involved in this process are rather simple: convolution between ECG samples and filter coefficients when extracting the features, linear or non-linear transformation of convolution output, linear combination between current input and neuron weights when generating predicted output, etc. (see **Figure 4B**). Nevertheless, the use of many highly coordinated neuron layers allows achieving state-of-the-art results.

Two model architectures—convolutional neural net (CNN) with feedforward information flow and recurrent neural net (RNN) with some feedback connections—are mostly used. CNNs process the input with a set of special filters to extract hidden, high-resolution patterns (Murat et al., 2020; Xue and Yu, 2021). RNNs capture the temporal relationships within the entire time-series data (Murat et al., 2020; Xue and Yu, 2021). Since both techniques have some pros and cons, many modifications have been recently introduced. For example, the long short-term memory (LSTM) network was developed to deal with the vanishing gradient problem, which leads to insufficient updation of the network weights as the training process goes through deep layers, as it is characteristic for traditional RNNs (Murat et al., 2020; Xue and Yu, 2021). More recently, both models are used together as a hybrid CNN–LSTM solution (see below) learning from the long-term, complex representations of heart activity patterns created by convolutional layers. DL models in clinical and experimental applications significantly improve the diagnostic yield of routinely used ECG. To create a well-functioning robust DL model, however, large, relevant, and highly variable ECG datasets are needed, as will be addressed below.

3.2.3 ECG Pre-Processing

3.2.3.1 Clinical Perspective

The clinical ECGs are usually corrupted with various types of noise, which may lead to errors in visual inspection and to inaccurate function of automatic delineation and interpretation algorithms. The low-frequency baseline wander, power-line interference (50/60 Hz), and high-frequency noise are those seen in raw ECG. The first one is primarily caused by respiratory movements or poor skin–electrode contact and may cause inaccurate measurement of ST segment, wave amplitudes, R-peak detection, etc. The power-line interference of high magnitude makes the analysis of low-voltage P waves impossible. The high-frequency noise, representing the myopotentials generated during skeletal muscle contraction, complicates the ECG delineation. Digital filters, implemented in a high-pass, band-pass, or low-pass mode with appropriate cut-off frequencies, are usually used to suppress above disturbances in the ECG (Satija et al., 2018; Vidhya and Jerritta, 2022). The desired characteristic of the filter is a

zero-phase shift to avoid the distortion of the signal. Special attention should be paid to elimination of the noise with frequency overlapping with the ECG spectrum. For example, inappropriate filtration of power-line interference may lead to undesired alteration (decreased amplitude or even altered morphology) of P waves and QRS complexes. Another way to eliminate noise is the ECG decomposition by so-called wavelet filters (Park et al., 1998). Besides, ML- and DL-based filtering techniques, enabling extra improvement of filtered signal characteristics, have been recently introduced (Xue and Yu, 2021).

After proper noise elimination, the R peaks and/or other fiducial points can be detected. Probably, the most famous and frequently used is the rather robust and simple Pan–Tompkins algorithm (Pan and Tompkins, 1985). Many other R-peak detectors, using searching in the initial ECG or ECG previously transformed to highlight the QRS complexes, have been developed (e.g., Liu et al., 2015; Biran and Jeremic, 2020; Walia and Kaul, 2020). However, none of them is error-free; false detections lead to false alarms and thus increase the demand on intensive care units' staff (Plesinger et al., 2016). Recently, it was shown that the false R-peak detections can be eliminated by additional validation using the advanced CNN algorithm (Silva et al., 2020).

Complete delineation of ECG can be performed by the CNN–LSTM model with a sensitivity of 97.95% (Peimankar and Puthusserypady, 2021). Another study reports use of sample-wise, so-called semantic segmentation of the raw ECG via the CNN–biLSTM network, with an overall accuracy of 95.54% (Londhe and Atulkar, 2021). Bidirectional LSTM (biLSTM) layers are the layers, where the input sequence is analyzed in the forward and backward directions resulting in better learning of important patterns. Sample-wise technique seems to have great potential in real-time applications due to its robustness and effective dealing with the continuous signal.

Another interesting study was focused on creating the mathematical models able to "extract" the waves from the ECG to make further detection of the fiducial points easier (Rueda et al., 2021). This method outperforms other recent approaches in delineating P and T waves, which are well-known as hardly recognizable and analyzable. The advantage of this algorithm against ML/DL solutions is in its robustness (in terms of required amount of training data and abnormalities present in data) and transparency (in terms of physical meaning of the process used to generate the model and delineation output itself).

Fatimah et al. (2021) compared two segmentation methods: 1) based on R-peak detection and selection of a predefined number of samples before and after the peak and 2) based on the splitting of raw signal into the frames of predefined length. Both approaches are reliable, but the second one is more suitable for real-time applications due to low computational demand.

3.2.3.2 Animal Perspective

Almost all existing methods for ECG pre-processing and analysis have been initially established for human signals. The morphology characteristics of animal ECG are like human ones. However, some differences in heart rate and ECG wave amplitudes and duration exist due to differences in ion channel expression (Bartos et al., 2015) as well as anatomical configuration and innervation of the heart. These differences should be considered when adapting the processing methods to animal applications. Little information is available regarding the processing methods, primarily due to the use of commercial, user-friendly, pre-set software. Only a few research groups develop their own algorithms for ECG pre-processing. Below, the most widespread techniques are presented.

The median filter can be successfully applied on clinical and experimental ECG data to remove low-frequency baseline wander, which complicates the signal delineation and decreases the reliability of morphology features (Steenkiste et al., 2020). For elimination of broad-band noise (such as muscle activity) in the ECG, the above-mentioned decomposition of the entire signal by discrete wavelet transform and reconstruction of "clean" ECG after removing some components containing noise is more suitable than standard linear filtration (Zhang et al., 2019). This method, however, can be sufficient in case of any type of noise, such as a high-frequency one, as shown by Steenkiste et al. (2020) in equine data application.

The narrow-band signals created by ECG wavelet decomposition are often used for accurate detection of waves and QRS complexes. First, signals with well prominent waves of interest are selected, and then the complexes are detected by threshold, which can be constant or adaptively changing according to current signal maximum amplitude or variability. This QRS detection technique was shown as more effective and accurate (sensitivity of 98% and positive predictive value of 99.1%) than the Pan–Tompkins algorithm (sensitivity of 91.5% and positive predictive value of 81.5%) in equine ECGs (Steenkiste et al., 2020). This technique can be used for complete delineation of the entire ECG (with an overall sensitivity of 99.87% and positive predictive value of 99.89%), as presented by Hejč et al. (2015) on data from isolated rabbit heart. Similar detection techniques were recently applied on the ECG recorded in larval zebrafish (Barret et al., 2021). They had to be adapted periodically since significant motion artifacts were present in data and heart rate was changed during the experimental protocol.

Kozumplík et al. (2014) introduced the QRS detector based on the estimation of signal envelope by the Teager–Kaiser energy operator and tested it on isolated rabbit heart data with a sensitivity of 99.84% and positive predictive value of 99.98%.

The first derivative of ECG and further searching for rapid deviations can be used for complete delineation of the signal as shown in detail by Huang et al. (2021) in equine ECG. Simple delineation algorithms are accurate in noise-free data. Otherwise, more robust adaptive techniques must be used, or the signal is segmented, and noisy parts are removed prior to further analysis. This can be solved by algorithms estimating ECG quality. Promising real-time algorithms offer studies by Smital et al. (2020) and Nardelli et al. (2020). These approaches can distinguish several levels of signal quality as evaluated on both human and horse ECGs.

3.2.4 Feature-Based Techniques

Features should represent well ECG patterns characteristic for investigated phenomenon (normal heart function, arrhythmias, drug-induced or stress-induced changes, structural alterations of the myocardium, etc.). The quantitative representation of heart electrical activity by a limited number of highly specific features allows to construct the efficient, robust, fast, and reliable methods for automatic identification and differentiation of various cardiac conditions, as will be shown below. Generally, three main groups of "hand-crafted" ECG features are used in computer-aided systems (e.g., Berkaya et al., 2018; Saini and Gupta, 2021; Gupta et al., 2021a):

- Time-domain features primarily representing 1) the rhythm character of the signal in terms of heart rate and duration of some important intervals (i.e., PQ, QT), 2) the morphology of ECG curve in terms of amplitude, duration, area under the curve, direction, and other shape-related characteristics of the particular waves, and 3) the statistical characteristics of ECG distribution (mean value, standard deviation, kurtosis, skewness, etc.).
- Frequency-domain or time–frequency domain features creating the new representation of ECG by using special transformation (such as Fourier transform (FT), short-term Fourier transform (STFT), and continuous or discrete wavelet transform (CWT/DWT)) and exploring the ECG spectral content and its changes in time.
- Non-linear features revealing non-linear, complex, dynamic character of ECG (hidden to the above methods) based on the chaos theory and information theory (i.e., Lyapunov exponents, Shannon entropy, correlation dimension).

Significant temporal features, intensely used in various areas, are those describing the heart rate variability (HRV). Initially, HRV analysis was introduced to investigate the vago-sympathetic balance and corresponding phenomena (Task Force of the European Society of Cardiology and the North American Society of Pacing and Electrophysiology, 1996, later Task Force Society, 1996). However, the HRV features have been also shown as useful for detection of cardiac arrhythmias, as—technically speaking—they measure the irregularity of RR intervals (or heart rate) (e.g., Task Force Society, 1996; Bernston et al., 1997; Parsi et al., 2021a). These features are calculated from the RR interval sequence (tachogram) and can be divided into three categories, i.e., time-domain (various statistical measures, such as mean or median value, standard deviation of normal interval (SDNN), root mean square of successive RR differences (RMSSD), and triangular interpolation index calculated from the histogram (TINN)), feature-domain (power and peak of very-low-, low-, and high-frequency bands, their ratios, etc.), and non-linear (parameters calculated from the Poincaré map, approximate or sample entropy, detrended fluctuation parameters, complex correlation measure, etc.) ones (Bernston et al., 1997; Tarvainen et al., 2014).

The features should reflect the studied issue. The most relevant, informative, and reliable features can be selected based on the empirical knowledge and experience of the experts, as is common in clinical routine. In computer-aided systems, special computational tools help to identify and eliminate the redundant features or those with poor ability to represent the patterns of interest. The latter often explore the inter-feature relationships (correlation analysis, principal component analysis (PCA), etc.), discriminating abilities of separate features (two-sample tests of statistical difference, as a *t*-test and others), or their combinations (linear discriminant analysis (LDA), decision tree, etc.) or searches among the feature set until the combination leading to the best performance of the model is found (forward or backward selection, sequential floating forward selection, etc.) (Guyon and Elisseeff, 2003; May et al., 2011). The reduction of feature number is desirable: it decreases computational cost and time cost of the method, enables using a simpler model, avoids the problem of model overfitting, improves model generalization, and often increases transparency and interpretability of the whole decision-making process (Duda et al., 2000; Guyon and Elisseeff, 2003, May et al., 2011; Theodoridis and Koutroumbas, 2009).

Feature-based diagnostics tools have been used for several decades and still play a crucial role in clinical and experimental research, primarily due to their transparency. Below, recent ECG applications intensely using these methods are reported.

3.2.4.1 Clinical Perspective

Fatimah et al. (2021) introduced detector of myocardial infarction using entropy, kurtosis, and energy, calculated from one-channel ECG decomposed by FT and ML classifiers, where k-NN achieved the highest accuracy (of 99.96%) outperforming other existing one-channel approaches.

Multi-lead ECG can be used to accurately detect left ventricular hypertrophy, which is a less expensive, less time-consuming, and widely available alternative to the golden standard imaging techniques. Morphological features (R and S waves or ST segment changes, QRS complex inversion, etc.) extracted from CWT-transformed ECGs perform well with ML classifiers, with the most promising accuracy (up to 97.8%) using multi-layer perceptrons (Jothiramalingam et al., 2021).

One example of using the morphology features derived from P–QRS–T segments is the recognition of different beat types, such as normal, supraventricular, and ventricular ectopic beats and fusion of ventricular and normal beats. The SVM model trained on these features performs with overall accuracy 97.8% (Zhu et al., 2019). The arrhythmia-related features can be calculated as mean, maximal, median values, etc., of ECG components derived by WT (Sangaiah et al., 2020).

A novel tool based on the multi-lead ultra-high-frequency ECG and QRS complex features has been recently introduced. It provides the quantitative description of ventricular dyssynchrony with a great potential for selecting the patients for cardiac resynchronization therapy and improving the therapy application (Jurak et al., 2020). One of the proposed features seems to be more suitable for monitoring of depolarization

patterns during the biventricular and His-bundle pacing, than common QRS duration.

A recent prospective study presents temporal, spectral, and non-linear HRV parameters as the valuable prognostic tool for evaluation of mortality risks in patients with coronary artery disease (Vuoti et al., 2021).

The most challenging recent application using HRV features is atrial fibrillation (AFIB) detection (e.g., Smisek et al., 2018; Murat et al., 2021a). Timely prediction of paroxysmal AFIB episodes using seven novel Poincaré map features achieves the accuracy over 86% for different ML models and even higher accuracy (98%) when combining with standard HRV features (Parsi et al., 2021b). McCann et al. (2021) studied ECG records from patients undergoing catheter ablation. They reported the lowest AFIB organization level in patients with failed AFIB termination during ablation using instantaneous frequency and adaptive organization index.

Novel multi-scale entropy has been shown as an accurate HRV-based tool for prediction of the malignant ventricular arrhythmia, even using a simple random forest classifier (Chen et al., 2021). Standard non-linear HRV features combined with those from 2D image representation of ECG beats can separate healthy subjects from patients with ventricular arrhythmia with an accuracy of 99.99% by using an ensemble of different ML models (Mandal et al., 2021).

A method based on only six time- and frequency-domain HRV features and a simple k-NN classifier can predict the sudden cardiac death from five-minute RR interval signals recorded by an implantable cardioverter defibrillator with an accuracy of 91.5% (Parsi et al., 2021a).

The random survival forest (RSF) ML model was used to predict spontaneous ventricular tachycardia and ventricular fibrillation events in young and adult patients with long QT syndrome (LQTS) (Lee et al., 2021). The model was trained using the combined feature set including ECG features, family history of LQTS, and occurrence of other arrhythmias. As compared to the statistical multivariate Cox regression model, the RSF model achieved more accurate results with the best precision of 0.95 and sensitivity of 0.93. In an extended multi-ethnic study, the RSF model has been also shown as a promising complex solution for predicting six different cardiovascular outcomes, including all-cause death, stroke, cardiovascular disease, coronary heart disease, atrial fibrillation, and heart failure (Ambale-Venkatesh et al., 2017). In this case, ECG features were combined with imaging features, serum biomarkers, demographic characteristics, and others in order to achieve accurate results, which outperform the output of standard cardiovascular risk scores.

3.2.4.2 Animal Perspective

The basic temporal ECG features such as heart rate and PR and QT interval duration as well as QRS complex duration are routinely used to monitor the character of impulse conduction through different parts of the heart. The assessment of the combination of these features is especially useful when evaluating the possible effects of drugs.

Detailed analysis of QT duration in rabbit protocols with drug-induced long-QT or short-QT syndrome indicated the possible effect of acute mechano-electrical function on long-QT syndrome–related arrhythmogenesis (Nimani et al., 2021). Generally, this feature is a basic marker used in a wide range of proarrhythmic research studies, including those conducted in transgenic rabbit models (Baczkó et al., 2020), larval zebrafish models (Barrett et al., 2021), and guinea pig isolated heart models (Vesely et al., 2019). So-called QT/RR coupling and—though rarely used—HRV analysis can be successfully evaluated in such studies, as previously shown in the context of haloperidol administration in isolated Sprague Dawley rat and guinea pig models (Janousek et al., 2017; Vesely et al., 2019). The prolonged QT duration was found in the methylazoxymethanol acetate rat model of schizophrenia, which has indicated the models' applicability for investigating the risk factors of ventricular arrhythmias and sudden cardiac death in patients treated with antipsychotics drugs (Stracina et al., 2016).

HRV in the isolated heart model can serve to investigate the intrinsic mechanisms of the cardiac rhythm regulation with no effect of sympathetic/parasympathetic factor (Janousek et al., 2014). Spectral HRV parameters are intensely used in toxicological studies with rodent models (Rowan et al., 2007). Time- and frequency-domain HRV features were recently used to evaluate response of cardiac autonomic modulation in mice to spontaneous and pharmacologically induced vulnerability to cardiac arrhythmias in the context of age-related changes (Piantoni et al., 2021). Due to this simple analysis, the mouse model has been shown as valuable in translational research of age-related risk of arrhythmias. In a recent study (Omoto et al., 2021), the heart rate fragmentation, representing ultra-rapid patterns of HRV, was newly shown as a reliable marker for evaluation of myocardial infarction impact on the cardiac hemodynamic parameters in a Wistar rat.

According to comprehensive overview by Mitchell and Raghav (2021), HRV analysis is commonly used to diagnose cardiac arrhythmia in a horse (in rest, during exercise, or during the treatment). Alexeenko et al. (2020) used two string measures representing the heart rate complexity to predict the paroxysmal atrial fibrillation in equine athletes.

The TINN feature has been found as associated with severity of myxomatous mitral valve disease in dogs (Rasmussen et al., 2012) and was analyzed to evaluate a risk of ventricular tachyarrhythmia and sudden cardiac death (Spier and Meurs, 2004). The Poincaré plot helped to investigate the non-linear geometrical patterns characteristic of dogs as compared to humans and to describe the specifics of impulse conduction through the sinoatrial node (Moise et al., 2020).

Morphological features were found to accurately detect ischemia in the Langendorff-perfused isolated rabbit heart with normal anatomy as well as spontaneously increased left ventricular mass (Ronzhina et al., 2017). The rhythm- and morphology-wise features were used to assess the effects of widely used voltage-sensitive dye di-4-ANEPPS on heart electrical activity in the same experimental model (Ronzhina et al., 2021). Particularly, analysis of the rhythm features revealed

the modulation effect of the dye on impulse conduction through the atria, AV node, and ventricles.

Novotna et al. (2017) investigated the usefulness of simply derived and robust features based on high-frequency components of QRS complexes (the maximal peak of QRS envelope, distance from QRS envelope maxima to R peak, and root mean square of the QRS area) to evaluate the conduction velocity in the working isolated rabbit heart under induced hemodynamic changes.

The use of ML-based methods in experimental or veterinary context is usually limited by a small amount of collected data. In case of long-term experiments, however, these techniques could be very helpful to carry out fast, robust, and reliable analysis. For example, Marsanova et al. (2017) differentiated normal sinus, ischemic, and ventricular premature beats recorded in the rabbit isolated heart during experiments with induced global ischemia by morphological and spectral ECG features and various ML models with the best accuracy of 98.6% for k-NN.

Huang et al. (2021) introduced the detector of paroxysmal atrial fibrillation in horses, which uses three consecutive intervals, QT, TQ, and RR (derived from rest, one-channel ECG), and k-NN classification algorithm.

3.2.5 All-In-One Diagnostics Solutions Based on Deep Learning

Many "all-in-one" solutions are working with a raw ECG or the pre-processed, noise-free ECG or 2D "image" representations of ECG created by converting the 1D signal into the so-called spectrogram (via STFT, CWT, etc.) or, more straightforwardly, by saving the ECG segments in some image format for further analysis. These solutions often use the hybrid model, when the first part (e.g., CNN, autoencoder) extracts the most reliable features from the input and the second part (e.g., LSTM net, fully connected layers) provides the final decision-making (classification, prediction, etc.).

Here, the overview of the most recent DL approaches is introduced. To our best knowledge, there is no all-in-one DL solution in experimental physiology applications due to limited data sources. We believe that this gap will be removed soon due to transfer of learning techniques we address in the last section and illustrate the example from the veterinary field.

3.2.5.1 Clinical Perspective – Focused Applications

Many approaches are focused on specific problems, which allows to reach promising results with a relatively simple model architecture and low time and computational requirements even in case of limited data amount. Great improvements based on DL method use were achieved in the detection of acute myocardial infarction and stable ischemic heart disease, with the detection accuracy in the range of 83–99.9% for different model configurations (CNN, ResNet, CNN–biLSTM) (Hinai et al., 2021). Myocardial infarction localization can be recognized with an accuracy of 90.20%, 99.67%, and 99.87% for biLSTM, 1D-CNN, and DenseNet, respectively (Tripathy et al., 2019; Xiong et al., 2021). The ResNet model is a CNN with residual blocks, which allows the signals to pass through several layers in the network resulting in improved training capability of the model with no information loss. DenseNet—network with so-called dense connections—"reuses" the information from each layer by sending it directly as the inputs of all subsequent layers and, thus, maximizes the flow of important inter- and intra-lead patterns between the layers. Adding dense connections increases the total number of trainable parameters in the network and thus increases the computational demand of the method. On the contrary, the overall performance of the network improves. All the above DL approaches outperform existing ML techniques based on morphological features combined with k-NN or SVM in terms of accuracy as well as time required for analysis of new patients' data (Tripathy et al., 2019; Xiong et al., 2021).

The accuracy of left ventricular hypertrophy detection reaches up to 85.8% when using CNN-extracted ECG features in combination with six-layer-perceptron–extracted demographic features, which outperform routine Sokolow-Lyon criteria and visual inspection (accuracy of 81.8 and 85.5%, respectively) (Kwon et al., 2020). Khurshid et al. (2021) trained ResNet on a 12-lead ECG to predict the LV mass and reached the output significantly correlating with the MRI-based reference values.

Left ventricular systolic dysfunction (LVSD) in critically ill patients can be accurately (71–76%) detected from ECG, which is less time-consuming and less expensive than usually used transthoracic echocardiography. Additional benefit of the DL method is its robustness and efficiency in both patients with and without atrial fibrillation, which is commonly associated with LVSD (Kashou et al., 2021). The latter increases the potential usability of this novel non-invasive, inexpensive, and fast method in acute care screening.

According to recent meta-analysis (Grün et al., 2021), CNN or CNN–LSTM models can predict heart failure from a standard raw 12-lead ECG with sensitivity 83–100% for different architectures and databases.

AFIB detection and differentiation between terminating and non-terminating AFIB episodes were recently performed via time–frequency ECG representation (by chirplet transform) and 2D CNN–biLSTM classifier with an accuracy of 99 and 75.9%, respectively (Radhakrishnan et al., 2021). The authors stated that this method outperforms those based on other representations (by STFT, CWT, and Stockwell transform) and other model architectures (CNN, attention-based, etc.). In another report (Rahul and Sharma, 2022), the AFIB detector using STFT representation and biLSTM model slightly outperformed the method using raw ECG (accuracy of 99.84 and 98.85%, respectively).

According to interesting retrospective research (Attia et al., 2019), an eight-lead ten-second ECG recorded during the sinus rhythm can be successfully used to predict the outcome in AFIB patients *via* the ResNet model with the accuracy of 79.4%. This approach offers fast, inexpensive identification of the patients with a high likelihood of AFIB by timely revealing of the structural changes in atria before the presence of any symptoms.

Detection of abnormal cardiac rhythms (in terms of the width of QRS complex, heart rate, and ECG amplitude), which can respond to electrical shock therapy with further expected

restoration of normal sinus rhythm and, consequently, normal cardiac pump function, achieved the best accuracy (91.14%) for the CNN model (Hammad et al., 2021).

3.2.5.2 Clinical Perspective—Multiple-Issue Applications

Recently, there is an effort to design approaches for differentiation of dozens of arrhythmias in ECG by only one complex model. The 1D-CNN proposed by Yildrim et al. (2018) recognizes 17 different cardiac arrhythmias from the one-channel ten-second ECG with an overall accuracy of 91.33%, in the real-time mode suitable for further implementation in mobile/cloud telemedicine applications. Haleem et al. (2021) combined the CNN–biLSTM model segmenting the raw ECGs with the 2D-CNN model, which provides final classification of the beats (previously transformed by STFT) into four categories: normal ECG, arrhythmia (97.9% accuracy), congestive heart failure (100% accuracy), and sudden cardiac death (100% accuracy). 1D ResNet can discriminate among six types of ECGs, as recently shown on a huge, unique database containing over 2 million ECGs recorded from more than 1.6 million patients (Ribeiro et al., 2020); this algorithm outperformed the accuracy of the fourth-year cardiology resident, the third-year emergency resident, and the fifth-year medical student. A similar architecture was previously used to detect abnormalities in one-channel ECG in the frame of PhysioNet Challenge 2017 with the top performance among several solutions (Clifford et al., 2017; Hannun et al., 2019).

Cinar and Tuncer (2021) combined the DL model extracting the features with SVM providing the recognition of sinus rhythm, abnormal arrhythmia, and congestive heart failure with an overall accuracy of 96.77%. The LSTM model trained on raw ECGs achieved 90.67%, and conventional feature-based ML models achieved only about 65–68% on the same dataset. By combination of complex DL and simple ML models, the authors obtained the high-performance tool on the one side and decreased computational time and improved transparency of the process on the other side.

According to Mousavi et al. (2021), the ECG can be successfully represented in the way commonly used in natural language processing, where the distinct waves and QRS complexes are considered the words and the whole ECG a sentence. This representation can be next analyzed by the DL model. The main drawback of this approach (as compared to other DL-based methods above) is the need for R-peak detection, ECG segmentation, and creating valid arrhythmia-related vocabulary required for further integer-encoded representation of ECG. This technique, however, performs better (accuracy of 74–97% depending on the database) than many other existing algorithms.

Compared to the CNN, ResNet, and CNN–biLSTM, the hybrid CNN–transformer model combined with temporal ECG features achieved higher performance in recognizing nine different beat types (Che et al., 2021). The transformer net—one of the most recent DL architectures—has been initially created as a compromise between the CNN (image pattern recognition) and the recurrent neural network (time-series sequence pattern recognition). In this model, the relevant features are driven from input data using the so-called attention mechanism. Approaches, using various transformer modifications, achieve promising results in arrhythmia classification experiments on many different ECG databases (e.g., Che et al., 2021; Hu et al., 2021; Natarajan et al., 2021; Nonaka and Seita, 2021; Meng et al., 2022).

However, adaptation of existing complex architectures, initially proposed for image (CNN, ResNet, etc.) or natural language (LSTM, biLSTM, etc.) analysis, has strong limitations as reported by the systematic study of Nonaka and Seita (2021). Novel ECG-target architectures should be developed to achieve high performance in the future.

3.3 Current Issues and Future Directions

3.3.1 Transfer Learning: Sharing the Knowledge Among Areas

Transfer learning is a research method in machine learning, where knowledge from one area is applied to solve the different, but still relevant issue. Transfer learning, when applying by proper way, may solve many different problems. One of them is a problem with heterogeneity of patients' data. It would be practically useful, if once the model is trained on some data (e.g., from healthy subjects), so that it could be directly applied on data with different diagnostics background (e.g., data from patients with rare arrhythmia). Most probably, however, this will not work well due to highly inconsistent character of patterns from two datasets. Nevertheless, successful results can be obtained when training model on one (freely available and extended) dataset and re-training it later on the other dataset consisting of samples of interest (can be small). In this case, the knowledge learned during the first training and saved in the network weights is used for analysis of the second dataset. During the re-training procedure, the weights from the first layers of the pre-trained model (extracting the relevant features from input data) remain with no changes, and only last layers (providing the classification or prediction itself) are re-trained using new data, which is computationally effective. This transferring of knowledge between the domains seems to be a way for effective usage of the models, well-established in other areas, directly in medical applications, with no extra time and source investments. It could be of special importance in problems, where there are not enough data for efficient training of the model.

DL architectures, initially proposed for image analysis, speech recognition, and other data, can be successfully used for ECG interpretation after appropriate modifications, as has been shown in clinical applications. Salem et al. (2018) recognized cardiac arrhythmias in 2D image representations of ECG using the DenseNet model, which was previously pre-trained on a huge image dataset consisting of the images of animals, objects, etc., with an overall accuracy of 97.23%. Similarly, the VGG image processing network was re-trained to detect LVH in multi-lead ECG data (Soto et al., 2021).

Bizzego et al. (2021) showed that the CNN model for heartbeat identification, initially trained on data from healthy subjects, performs poorly in data from cardiac patients. However, re-training of some layers of this network with a small amount of patients' data results in significantly improved detection

performance. Jang et al. (2021) pre-trained the convolutional autoencoder model on unlabeled one-channel ECG signals from one database and used this model later to classify 12 different rhythms in 12-lead ECG. The authors reported better performance when using the pre-trained model (overall F1-score of about 83.5%) than in case where the model weights were initiated randomly (overall F1-score of about 54.3%). Weimann and Conrad (2021) fine-tuned the weights of CNN, which was initially trained on a large publicly available ECG database, by a small set of data recorded in patients with AFIB and obtained improved performance (by 6.57%) as compared to the non-pre-trained model.

The most exciting and beneficial application of transfer learning was shown in animal data analysis, when the standard use of DL methods is strongly limited by a small amount of available data. A few published reports using DL for animal data analysis are focused mainly on image processing, e.g., detection of canine mammary tumor (Kumar et al., 2020), detection of diffuse degenerative hepatic disease in dogs (Banzato et al., 2018), and classification of the thoracic canine radiographs (Banzato et al., 2021). In animal ECG analysis, the study by Steenkuste et al. (2020) demonstrated application of DL methods by involving transfer learning technique. The CNN model pre-trained on human ECGs was used to recognize four beat types (normal, atrial premature contraction, ventricular premature contraction, and artifact) in equine ECG with an accuracy of 97.1% for the re-trained model, which outperforms the non-pre-trained model.

Aston et al. (2019) fine-tuned several pre-trained image-wise DL models (such as AlexNet, GoogLeNet, ResNet-18, SqueezeNet) *via* a newly proposed symmetric projection attractor calculated from two-lead ECG. They were used to distinguish between wild-type mice and $Scn5^{+/-}$ mutant mice suffering from impaired function of cardiac sodium channel.

From all the above, it seems that DL models can learn not only general but also more specific patterns during transfer learning. Although the DL methods have been recently applied exclusively in veterinary medicine where relatively large amounts of data are available, it seems to be reasonable—due to transfer learning technique—to expect expansion of DL models in experimental cardiology.

3.3.2 Imbalanced Data Problem: Minority Is Out of Game

The lack of data often concerns only certain groups of arrhythmias, such as those with rare incidence in the population or paroxysmal ones, where the ECG manifestation cannot be easily recorded during standard clinical examination. During the training process, the model extracts important information from input samples and uses it for final decision-making. In case of a severely imbalanced train dataset (where the categories are distributed unequally), the model will "focus" on the abnormalities from the majority group(s) and will ignore those from the minority group(s). Most of available ECG databases include much more normal sinus rhythm data than abnormal ones and, thus, are imbalanced. There are some techniques which reduce or eliminate this problem and, thus, ensure effective training of the model.

The simplest way to make the size of particular categories equal is resampling of the training dataset, where the majority class is reduced by random selection of the desired number of samples (undersampling) or the minority class is extended by random repeating of selected samples (oversampling). However, removing of samples from the training set may lead to loss of important information. Simple repeating of minority samples will not make the dataset variable and representative and may not ensure effective model training. Therefore, more sophisticated—so-called augmentation—methods are usually applied.

Augmentation techniques generate new training samples by adding some perturbation in data resulting in improved robustness of the model. First, some manipulations can be applied on initial data, such as random scaling, flipping, shifting, and noising ECG, to achieve accurate detection of multiple arrhythmias (Vicar et al., 2020; Nonaka and Seita, 2021; Do et al., 2022). The same application can profit from using the synthetic samples generated from the training ones using intuitive adaptive synthetic data sampling (ADASYN, Virgeniya and Ramaraj, 2021) or synthetic minority oversampling technique (SMOTE, Ketu and Mishra, 2021). Data samples can be generated artificially by specially trained ML or DL models (such as Gaussian mixture model (GMM), generative adversarial network (GAN), LSTM/biLSTM, CNN), as has been shown for time-series ECG (including dependent multichannel signals) and 2D spectrogram applications (e.g., Lima et al., 2019; Brophy, 2020; Hatamian et al., 2020; Hazra and Byun, 2020). Recently, a unique database of more than 120,000 artificial ECGs, generated by the GAN, has been introduced (Thambawita et al., 2021). This model was trained on more than 7,000 real patients' ECG records.

From above reports, synthetic ECGs are realistic enough to be used in practice and, consequently, contribute to the expansion of high-performance ML or DL techniques in a wide range of clinical and experimental applications. In the latter area, besides all the above, augmentation approaches, based on data generated by mathematical computational models, seem to have special potential. Models of different complexity—from molecular to organ levels—are available (e.g., Guasch et al., 2013; Henderson et al., 2009; Pagé et al., 1986) for generating the relevant, realistic, clearly interpretable electrophysiological data.

3.3.3 Understandable Means Credible: Open the Black Box

Effective interaction of a human expert (e.g., cardiologist) with the computer-aided system requires trust in the computer's decision-making. Therefore, an adoption of DL-based diagnostic systems in the routine clinical practice is limited, despite their high performance. As a result, there is a big effort in creating the tools helping to uncover the processes behind the model's prediction. Such "explaining" methods may help the experts to understand the computer-aided tools and to "safely" use their output to make the final decision. Of

course, rather transparent feature-based methods with simple ML models (such as linear discriminant function, decision tree) can be used. These are, however, less successful as DL-based systems (see above). It seems to be more suitable to use the high-performance, though non-transparent, DL algorithms and apply additional techniques to "open" the black box. Many different methods and algorithms have been proposed in the last decade to solve this issue.

Probably, the easiest solution is to visualize the outputs from those layers of deep networks, which generate the features from input data (such as convolutional layers in the CNN model, attention layers in the transformer). The generated feature maps can indicate the parts of the ECG playing the most important role in resulting diagnosis (Meng et al., 2022; Nataraja et al., 2021, etc.). The features maps can be additionally simplified by principal component analysis and used for detailed interpretation of the diagnostics model (Murat et al., 2021b).

Most comprehensive explanation can be obtained by special algorithms, such as Shapley Additive Explanations (SHAP), which assigns the importance weight to each sample by exploring the gradient, calculated when the sample enters the model (Soto et al., 2021). These weights can be then illustrated. A similar method—gradient-weighted class activation mapping (GRAD-CAM)—creates the visualization of the gradient through the entire model (Ho and Ding, 2021). Elul et al. (2021) included the spectro-temporal attention (STA) mechanism, which highlights the most important parts of ECG based on the analysis of temporal and spectral information from selected layers of the network. Other, local interpretable model-agnostic explanation technique (LIME) uses another, very simple, linear model (such as linear regression) to explain the local behavior of the black-box complex model around the sample of interest (Hughes et al., 2021).

3.3.4 Huge Amount of Data: Make It Easier With Multiple-Instance Learning

A huge amount of long-term ECG data requires a lot of time for detailed data labeling, which is crucial for accurate diagnosis and for potential use when creating the ML- or DL-based computer-aided systems. The labeling process is extremely time-consuming and expensive. Especially when each beat should be labeled separately, the risk of misinterpretations due to intensive cognitive load or poor experience of the physician is high. Therefore, multiple-instance learning (MIL) enabling model training using only global labels with no beat-wise annotations can be very useful. MIL is a type of supervised learning, which works with labeled bags of data (instead of the labeled instances) (Carbonneau et al., 2018). When properly combining with ML or DL, it can be successfully used for localization of the pathological events in ECG and generation of the detailed annotation reports, if needed, as shown in myocardial infarction detection (Sun et al., 2012), abnormal heartbeat localization (Tong et al., 2021), or premature ventricular contraction localization (Novotna et al., 2020). The accuracy of such methods is usually comparable to that of standard DL approaches, but MIL-based detectors are beneficial due to less strict requirements on the training dataset.

3.3.5 Deep Learning Expansion: Need for Control

The number of DL studies focused on cardiac arrhythmia detection and classification has intensively grown during the last five years, most probably due to the PhysioNet/Computing in Cardiology Challenge conducted in 2017, where an extended, highly variable database was introduced to the wide audience (Clifford et al., 2017). Many challenge participants applied the CNN or LSTM model to address the topic and achieved the best performance in binary (AFIB vs. non-AFIB) and multi-class (sinus rhythm, AFIB, atrial flutter, etc.) issues (Murat et al., 2021a). The growing trend in using DL is still present due to international challenges (PhysioNet/Computing in Cardiology 2020 and 2021, China Physiological Signal Challenge 2018–2021) focused on the algorithms for reliable QRS detection, supraventricular and ventricular premature contraction detection, AFIB detection or paroxysmal AFIB localization in ECG, multi-label classification of 24 different arrhythmias, or identification of the ECG leads with the highest discrimination ability. During the challenges, high-quality, freely available, and accurately labeled databases are introduced to the wide audience, which enables further development of high-performance robust algorithms (Perez Alday et al., 2021). The availability of large ECG databases, however, makes the opportunity for people with no basic knowledge in the cardiac arrhythmia domain to be involved in creating the algorithms. In this situation, one cannot expect correct and careful usage of ML or DL methods. The only way to create trustworthy diagnostic systems, which meet the true clinical needs, is close cooperation among a wide range of experts, such as clinicians, engineers, data scientists, and programmers.

Another issue, which needs to be solved soon, is a lack of the guidelines for creating and evaluating the diagnostic ML and DL algorithms. Bond et al. (2021) formulated this aspect in the context of systems for ECG interpretation as a need for best practices for "stress-testing" algorithms. They recommend to test the novel algorithms under different conditions: using both clean and noisy data, data recorded by misplaced or/and interchanged electrodes, data recorded in different hospitals by different devices and from different ethnic groups, etc. This may ensure creating the reliable, accurate, and robust algorithms useful in clinical routine support. Thus, formation of international working groups focused on the relevant guideline formulation can be expected in the near future. Best practices—after some modifications—will be further integrated in experimental applications.

4 FINAL REMARKS

The present article reviews current perspectives of ECG recording and analysis. It presents a unique combination of clinical and experimental points of view. This approach may attract a broad range of readers—not only researchers in the area of cardiology but also biomedical engineers, mathematicians, and last but not

least clinicians. Looking at the same topic from various angles and summarizing information obtained from various models may help interested readers of numerous specializations understand each other better. As a result, it might help to plan future research activities of multidisciplinary teams, consisting of both researchers and clinicians.

In the 21st century, recording of electrical activity of the heart muscle in the form of electrocardiogram may appear rather obsolete. The truth is that numerous sophisticated methods enable the researchers and clinicians to obtain information about electrical and mechanical activities of the heart and visualize these processes. On the contrary, new ways of ECG recording together with advanced methods of its analysis open new possibilities for its use.

AUTHOR CONTRIBUTIONS

MN suggested the outline of the article, was responsible for overall style, and contributed to *Introduction* and *Final Remarks*. TS wrote *ECG Recording* and contributed to design of the table and figures. MR and RR wrote *ECG Analysis* and contributed to design of figures. All authors participated in critical reading of the manuscript and review of the literature.

FUNDING

This research was funded by Masaryk University as part of project no. MUNI/A/1133/2021 with the support of the Specific University Research Grant, as provided by the Ministry of Education, Youth and Sports of the Czech Republic, and by the grant project provided by Masaryk University (No. MUNI/11/SUP/09/2022). This research was also supported by project no. LQ1605 from the National Program of Sustainability II (MEYS CR). RR is the Brno Ph.D. Talent Scholarship Holder funded by the Brno City Municipality project "Advanced Detection of Cardiac Arrhythmias Using Intracardiac ECG and Deep Learning Methods."

REFERENCES

Al Hinai, G., Jammoul, S., Vajihi, Z., and Afilalo, J. (2021). Deep Learning Analysis of Resting Electrocardiograms for the Detection of Myocardial Dysfunction, Hypertrophy, and Ischaemia: a Systematic Review. *Eur. Heart J. - Digital Health* 2, 416–423. doi:10.1093/ehjdh/ztab048

Alexeenko, V., Fraser, J. A., Bowen, M., Huang, C. L.-H., Marr, C. M., and Jeevaratnam, K. (2020). The Complexity of Clinically-normal Sinus-Rhythm ECGs Is Decreased in Equine Athletes with a Diagnosis of Paroxysmal Atrial Fibrillation. *Sci. Rep.* 10, 6822. doi:10.1038/s41598-020-63343-7

AlGhatrif, M., and Lindsay, J. (2012). A Brief Review: History to Understand Fundamentals of Electrocardiography. *J. Community Hosp. Intern. Med. Perspect.* 2, 14383. doi:10.3402/jchimp.v2i1.14383

Ambale-Venkatesh, B., Yang, X., Wu, C. O., Liu, K., Hundley, W. G., McClelland, R., et al. (2017). Cardiovascular Event Prediction by Machine Learning. *Circ. Res.* 121, 1092–1101. doi:10.1161/CIRCRESAHA.117.311312

Aston, P. J., Lyle, J. V., Bonet-Luz, E., Huang, C. L. H., Zhang, Y., Jeevaratnam, K., et al. (2019). *Deep Learning Applied to Attractor Images Derived from ECG Signals for Detection of Genetic Mutation. 2019 Computing in Cardiology*. doi:10.23919/CinC49843.2019.9005823

Attia, Z. I., Noseworthy, P. A., Lopez-Jimenez, F., Asirvatham, S. J., Deshmukh, A. J., Gersh, B. J., et al. (2019). An Artificial Intelligence-Enabled ECG Algorithm for the Identification of Patients with Atrial Fibrillation during Sinus Rhythm: a Retrospective Analysis of Outcome Prediction. *The Lancet* 394, 861–867. doi:10.1016/S0140-6736(19)31721-0

Azar, T., Sharp, J., and Lawson, D. (2011). Heart Rates of Male and Female Sprague-Dawley and Spontaneously Hypertensive Rats Housed Singly or in Groups. *J. Am. Assoc. Lab. Anim. Sci.* 50, 175–184.

Baczkó, I., Hornyik, T., Brunner, M., Koren, G., and Odening, K. E. (2020). Transgenic Rabbit Models in Proarrhythmia Research. *Front. Pharmacol.* 11, 853. doi:10.3389/fphar.2020.00853

Banzato, T., Bonsembiante, F., Aresu, L., Gelain, M. E., Burti, S., and Zotti, A. (2018). Use of Transfer Learning to Detect Diffuse Degenerative Hepatic Diseases from Ultrasound Images in Dogs: A Methodological Study. *Vet. J.* 233, 35–40. doi:10.1016/j.tvjl.2017.12.026

Banzato, T., Wodzinski, M., Burti, S., Osti, V. L., Rossoni, V., Atzori, M., et al. (2021). Automatic Classification of Canine Thoracic Radiographs Using Deep Learning. *Sci. Rep.* 11, 3964. doi:10.1038/s41598-021-83515-3

Barold, S. S. (2003). Willem Einthoven and the Birth of Clinical Electrocardiography a Hundred Years Ago. *Card. Electrophysiol. Rev.* 7, 99–104. doi:10.1023/A:1023667812925

Barrett, R., Hurst, R., Tarte, E., Müller, F., and Sik, A. (2021). *Automatic Detection of Larval Zebrafish ECG: Computational Tool for High-Throughput Cardiac Activity Analysis*. bioRxiv [Preprint] (Accessed January 12, 2022). doi:10.1101/2021.02.08.430220

Bartos, D. C., Grandi, E., and Ripplinger, C. M. (2015). Ion Channels in the Heart. *Compr. Physiol.* 5, 1423–1464. doi:10.1002/cphy.c140069

Bazett, H. C. (1920). An Analysis of the Time-Relations of Electrocardiograms. *Heart* 7, 353–370.

Berntson, G. G., Thomas Bigger, J., Jr, Eckberg, D. L., Grossman, P., Kaufmann, P. G., Malik, M., et al. (1997). Heart Rate Variability: Origins, Methods, and Interpretive Caveats. *Psychophysiology* 34, 623–648. doi:10.1111/j.1469-8986.1997.tb02140.x

Besterman, E., and Creese, R. (1979). Waller--pioneer of Electrocardiography. *Heart* 42, 61–64. doi:10.1136/hrt.42.1.61

Biran, A., and Jeremic, A. (2020). Automatic QRS Detection and Segmentation Using Short Time Fourier Transform and Feature Fusion. *IEEE Can. Conf. Electr. Comp. Eng.* doi:10.1109/CCECE47787.2020.9255676

Bizzego, A., Gabrieli, G., Neoh, M. J. Y., and Esposito, G. (2021). Improving the Efficacy of Deep-Learning Models for Heart Beat Detection on Heterogeneous Datasets. *Bioengineering* 8, 193. doi:10.3390/bioengineering8120193

Bond, R., Finlay, D., Al-Zaiti, S. S., and Macfarlane, P. (2021). Machine Learning with Electrocardiograms: A Call for Guidelines and Best Practices for 'stress Testing' Algorithms. *J. Electrocardiol.* 69, 1–6. doi:10.1016/j.jelectrocard.2021.07.003

Brailer, D. J., Kroch, E., and Pauly, M. V. (1997). The Impact of Computer-Assisted Test Interpretation on Physician Decision Making. *Med. Decis. Making* 17, 80–86. doi:10.1177/0272989X9701700109

Brophy, E. (2020). Synthesis of Dependent Multichannel ECG Using Generative Adversarial Networks. *Proc. 29th ACM Int. Conf. Inf. Knowledge Manag. (CIKM '20)*. doi:10.1145/3340531.3418509

Carbonneau, M.-A., Cheplygina, V., Granger, E., and Gagnon, G. (2018). Multiple Instance Learning: A Survey of Problem Characteristics and Applications. *Pattern Recognition* 77, 329–353. doi:10.1016/j.patcog.2017.10.009

Che, C., Zhang, P., Zhu, M., Qu, Y., and Jin, B. (2021). Constrained Transformer Network for ECG Signal Processing and Arrhythmia Classification. *BMC Med. Inform. Decis. Mak* 21, 184. doi:10.1186/s12911-021-01546-2

Chen, Z., Ono, N., Chen, W., Tamura, T., Altaf-Ul-Amin, M., Kanaya, S., et al. (2021). The Feasibility of Predicting Impending Malignant Ventricular Arrhythmias by Using Nonlinear Features of Short Heartbeat Intervals. *Comp. Methods Programs Biomed.* 205, 106102. doi:10.1016/j.cmpb.2021.106102

Çınar, A., and Tuncer, S. A. (2021). Classification of normal Sinus Rhythm, Abnormal Arrhythmia and Congestive Heart Failure ECG Signals Using LSTM and Hybrid CNN-SVM Deep Neural Networks. *Comp. Methods Biomech. Biomed. Eng.* 24 (2), 203–214. doi:10.1080/10255842.2020.1821192

Clifford, G., Liu, C., Moody, B., Lehman, L.-w., Silva, I., Li, Q., et al. (20172017). AF Classification from a Short Single Lead ECG Recording: the Physionet Computing in Cardiology Challenge 2017. *Comput. Cardiol.* doi:10.22489/CinC.2017.065-469

deChazal, P., O'Dwyer, M., and Reilly, R. B. (2004). Automatic Classification of Heartbeats Using ECG Morphology and Heartbeat Interval Features. *IEEE Trans. Biomed. Eng.* 51, 1196–1206. doi:10.1109/TBME.2004.827359

Do, E., Boynton, J., Lee, B. S., and Lustgarten, D. (2022). Data Augmentation for 12-lead ECG Beat Classification. *SN COMPUT. SCI.* 3, 70. doi:10.1007/s42979-021-00924-x

Duda, R. I., Hart, P. E., and Stork, D. G. (2000). *Pattern Classification*. 2nd edition. Wiley-Interscience. SBN 0-471-05669-3.

Duong, T., Rose, R., Blazeski, A., Fine, N., Woods, C. E., Thole, J. F., et al. (2021). Development and Optimization of an *In Vivo* Electrocardiogram Recording Method and Analysis Program for Adult Zebrafish. *Dis. Model. Mech.* 14. doi:10.1242/dmm.048827

Farraj, A. K., Hazari, M. S., and Cascio, W. E. (2011). The Utility of the Small Rodent Electrocardiogram in Toxicology. *Toxicol. Sci.* 121, 11–30. doi:10.1093/toxsci/kfr021

Fatimah, B., Singh, P., Singhal, A., Pramanick, D., S., P., and Pachori, R. B. (2021). Efficient Detection of Myocardial Infarction from Single lead ECG Signal. *Biomed. Signal Process. Control.* 68, 102678. doi:10.1016/j.bspc.2021.102678

Fish, R. E., Foster, M. L., Gruen, M. E., Sherman, B. L., and Dorman, D. C. (2017). Effect of Wearing a Telemetry Jacket on Behavioral and Physiologic Parameters of Dogs in the Open-Field Test. *J. Am. Assoc. Lab. Anim. Sci.* 56, 382–389.

Giada, F., Gulizia, M., Francese, M., Croci, F., Santangelo, L., Santomauro, M., et al. (2007). Recurrent Unexplained Palpitations (RUP) Study. *J. Am. Coll. Cardiol.* 49, 1951–1956. doi:10.1016/j.jacc.2007.02.036

Goodfellow, I., Bengio, Y., and Courville, A. (2016). *Deep Learning*. Cambridge, Massachusetts: The MIT Press. ISBN 978-0-262-03561-3.

Grün, D., Rudolph, F., Gumpfer, N., Hannig, J., Elsner, L. K., von Jeinsen, B., et al. (2021). Identifying Heart Failure in ECG Data with Artificial Intelligence-A Meta-Analysis. *Front. Digit. Health* 2, 584555. doi:10.3389/fdgth.2020.584555

Gupta, V., Mittal, M., Mittal, V., and Saxena, N. K. (2021a). A Critical Review of Feature Extraction Techniques for ECG Signal Analysis. *J. Inst. Eng. India Ser. B* 102, 1049–1060. doi:10.1007/s40031-021-00606-5

Gut, P., Reischauer, S., Stainier, D. Y. R., and Arnaout, R. (2017). Little Fish, Big Data: Zebrafish as a Model for Cardiovascular and Metabolic Disease. *Physiol. Rev.* 97, 889–938. doi:10.1152/physrev.00038.2016

Guyon, I., and Elisseeff, A. (2003). An Introduction to Variable and Feature Selection. *J. Mach Learn. Res.* 3, 1157–1182.

Ha, T. W., Oh, B., and Kang, J.-O. (2020). Electrocardiogram Recordings in Anesthetized Mice Using lead II. *JoVE* 160. doi:10.3791/61583

Haleem, M. S., Castaldo, R., Pagliara, S. M., Petretta, M., Salvatore, M., Franzese, M., et al. (2021). Time Adaptive ECG Driven Cardiovascular Disease Detector. *Biomed. Signal Process. Control.* 70, 102968. doi:10.1016/j.bspc.2021.102968

Hammad, M., Kandala, R. N. V. P. S., Abdelatey, A., Abdar, M., Zomorodi-Moghadam, M., Tan, R. S., et al. (2021). Automated Detection of Shockable ECG Signals: A Review. *Inf. Sci.* 571, 580–604. doi:10.1016/j.ins.2021.05.035

Hannun, A. Y., Rajpurkar, P., Haghpanahi, M., Tison, G. H., Bourn, C., Turakhia, M. P., et al. (2019). Cardiologist-level Arrhythmia Detection and Classification in Ambulatory Electrocardiograms Using a Deep Neural Network. *Nat. Med.* 25, 65–69. doi:10.1038/s41591-018-0268-3

Hatamian, F. N., Ravikumar, N., Vesal, S., Kemeth, F. P., Struck, M., and Maier, A. (2020). "The Effect of Data Augmentation on Classification of Atrial Fibrillation in Short Single-Lead ECG Signals Using Deep Neural Networks," in 2020 IEEE International Conference on Acoustics, Speech and Signal Processing (Barcelona, Spain: IEEE), 1264–1268.

Hazra, D., and Byun, Y.-C. (2020). SynSigGAN: Generative Adversarial Networks for Synthetic Biomedical Signal Generation. *Biology* 9, 441. doi:10.3390/biology9120441

Hejč, J., Vítek, M., Ronzhina, M., Nováková, M., and Kolářová, J. (2015). A Wavelet-Based ECG Delineation Method: Adaptation to an Experimental Electrograms with Manifested Global Ischemia. *Cardiovasc. Eng. Technol.* 6, 364–375. doi:10.1007/s13239-015-0224-z

Holmvang, L., Hasbak, P., Clemmensen, P., Wagner, G., and Grande, P. (1998). Differences between Local Investigator and Core Laboratory Interpretation of the Admission Electrocardiogram in Patients with Unstable Angina Pectoris or Non-q-wave Myocardial Infarction (A Thrombin Inhibition in Myocardial Ischemia [trim] Substudy). *Am. J. Cardiol.* 82, 54–60. doi:10.1016/S0002-9149(98)00226-4

Hu, S., Cai, W., Gao, T., Zhou, J., and Wang, M. (2021). Robust Wave-Feature Adaptive Heartbeat Classification Based on Self-Attention Mechanism Using a Transformer Model. *Physiol. Meas.* 42, 125001. doi:10.1088/1361-6579/ac3e8810.1088/1361-6579/ac3e88

Huang, Y. H., Alexeenko, V., Tse, G., Huang, C. L.-H., Marr, C. M., and Jeevaratnam, K. (2020). ECG Restitution Analysis and Machine Learning to Detect Paroxysmal Atrial Fibrillation: Insight from the Equine Athlete as a Model for Human Athletes. *Function* 2. zqaa031. doi:10.1093/function/zqaa031

Hwang, Y. M., Kim, J.-H., and Kim, Y. R. (2021). Comparison of mobile Application-Based ECG Consultation by Collective Intelligence and ECG Interpretation by Conventional System in a Tertiary-Level Hospital. *Korean Circ. J.* 51, 351–357. doi:10.4070/kcj.2020.0364

Ince, T., Kiranyaz, S., and Gabbouj, M. (2009). A Generic and Robust System for Automated Patient-specific Classification of ECG Signals. *IEEE Trans. Biomed. Eng.* 56, 1415–1426. doi:10.1109/TBME.2009.2013934

Jang, J.-H., Kim, T. Y., and Yoon, D. (2021). Effectiveness of Transfer Learning for Deep Learning-Based Electrocardiogram Analysis. *Healthc. Inform. Res.* 27, 19–28. doi:10.4258/hir.2021.27.1.19

Janousek, O., Kolárová, J., Nováková, M., and Provazník, I. (2010). Three-dimensional Electrogram in Spherical Coordinates: Application to Ischemia Analysis. *Physiol. Res.* 59, S51–S58. doi:10.33549/physiolres.932013

Janousek, O., Ronzhina, M., Kolarova, J., Provaznik, I., Stracina, T., Olejnickova, V., et al. (2014). "Fractal Dimension of *In-Vivo* and *Ex-Vivo* Rabbit HRV Series," in Proceedings of the 41th International Congress on Electrocardiology. ISBN: 9788096967278.

Janousek, O., Stracina, T., Ronzhina, M., Hejc, J., Stark, T., Ruda, J., et al. (20172017). The Effect of Haloperidol Administration on Heart Rate Variability in Isolated Heart of Schizophrenia-like and Control Rats. *Comput. Cardiol.* 44, 1–4. doi:10.22489/CinC.2017.150-161

Jothiramalingam, R., Jude, A., Patan, R., Ramachandran, M., Duraisamy, J. H., and Gandomi, A. H. (2021). Machine Learning-Based Left Ventricular Hypertrophy Detection Using Multi-lead ECG Signal. *Neural Comput. Applic* 33, 4445–4455. doi:10.1007/s00521-020-05238-2

Jurak, P., Curila, K., Leinveber, P., Prinzen, F. W., Viscor, I., Plesinger, F., et al. (2020). Novel Ultra-high-frequency Electrocardiogram Tool for the Description of the Ventricular Depolarization Pattern before and during Cardiac Resynchronization. *J. Cardiovasc. Electrophysiol.* 31, 300–307. doi:10.1111/jce.14299

Kalra, A., Lowe, A., and Al-Jumaily, A. (2019). Critical Review of Electrocardiography Measurement Systems and Technology. *Meas. Sci. Technol.* 30, 012001. doi:10.1088/1361-6501/aaf2b7

Kaplan Berkaya, S., Uysal, A. K., Sora Gunal, E., Ergin, S., Gunal, S., and Gulmezoglu, M. B. (2018). A Survey on ECG Analysis. *Biomed. Signal Process. Control.* 43, 216–235. doi:10.1016/j.bspc.2018.03.003

Kashou, A. H., Mulpuru, S. K., Deshmukh, A. J., Ko, W.-Y., Attia, Z. I., Carter, R. E., et al. (2021). An Artificial Intelligence-Enabled ECG Algorithm for Comprehensive ECG Interpretation: Can it Pass the 'Turing Test'? *Cardiovasc. Digital Health J.* 2, 164–170. doi:10.1016/j.cvdhj.2021.04.002

Kashou, A. H., Noseworthy, P. A., Lopez-Jimenez, F., Attia, Z. I., Kapa, S., Friedman, P. A., et al. (2021). The Effect of Cardiac Rhythm on Artificial Intelligence-Enabled ECG Evaluation of Left Ventricular Ejection Fraction Prediction in Cardiac Intensive Care Unit Patients. *Int. J. Cardiol.* 339, 54–55. doi:10.1016/j.ijcard.2021.07.001

Ketu, S., and Mishra, P. K. (2021). Empirical Analysis of Machine Learning Algorithms on Imbalance Electrocardiogram Based Arrhythmia Dataset for Heart Disease Detection. *Arab J. Sci. Eng.* 47, 1447–1469. doi:10.1007/s13369-021-05972-2

Khurshid, S., Friedman, S., Pirruccello, J. P., Di Achille, P., Diamant, N., Anderson, C. D., et al. (2021). Deep Learning to Predict Cardiac Magnetic Resonance-Derived Left Ventricular Mass and Hypertrophy from 12-lead ECGs. *Circ. Cardiovasc. Imaging* 14, e012281. doi:10.1161/CIRCIMAGING.120.012281

Konopelski, P., and Ufnal, M. (2016). Electrocardiography in Rats: a Comparison to Human. *Physiol. Res.* 65, 717–725. doi:10.33549/physiolres.933270

Kozumplik, J., Ronzhina, M., Janousek, O., Kolarova, J., Provaznik, I., and Novakova, M. (20142014). QRS Complex Detection in Experimental Orthogonal Electrograms of Isolated Rabbit Hearts. *Comput. Cardiol.*, 1085–1088. ISBN: 978-1-4799-4347- 0.

Kramer, K., Kinter, L., Brockway, B. P., Voss, H. P., Remie, R., and Van Zutphen, B. L. (2001). The Use of Radiotelemetry in Small Laboratory Animals: Recent Advances. *Contemp. Top. Lab. Anim. Sci.* 40, 8–16.

Krasnoff, S. O. (1950). The Duration of the Q-T Interval in Myocardial Infarction. *Am. Heart J.* 39, 523–531. doi:10.1016/0002-8703(50)90251-1

Kumar, A., KomaragiriKumar, R. M., and Kumar, M. (2018). From Pacemaker to Wearable: Techniques for ECG Detection Systems. *J. Med. Syst.* 42, 34. doi:10.1007/s10916-017-0886-1

Kumar, A., Singh, S. K., Saxena, S., Lakshmanan, K., Sangaiah, A. K., Chauhan, H., et al. (2020). Deep Feature Learning for Histopathological Image Classification of Canine Mammary Tumors and Human Breast Cancer. *Inf. Sci.* 508, 405–421. doi:10.1016/j.ins.2019.08.072

Kwon, J.-M., Jeon, K.-H., Kim, H. M., Kim, M. J., Lim, S. M., Kim, K.-H., et al. (2020). Comparing the Performance of Artificial Intelligence and Conventional Diagnosis Criteria for Detecting Left Ventricular Hypertrophy Using Electrocardiography. *EP Europace* 22, 412–419. doi:10.1093/europace/euz324

Lam, A., Wagner, G. S., and Pahlm, O. (2015). The Classical versus the Cabrera Presentation System for Resting Electrocardiography: Impact on Recognition and Understanding of Clinically Important Electrocardiographic Changes. *J. Electrocardiol.* 48, 476–482. doi:10.1016/j.jelectrocard.2015.05.011

Larsen, K., and Skúlason, T. (1941). The normal Electrocardiogram. *Am. Heart J.* 22, 625–644. doi:10.1016/S0002-8703(41)90545-8

Le, T., Zhang, J., Nguyen, A. H., Trigo Torres, R. S., Vo, K., Dutt, N., et al. (2022). A Novel Wireless ECG System for Prolonged Monitoring of Multiple Zebrafish for Heart Disease and Drug Screening Studies. *Biosens. Bioelectron.* 197, 113808. doi:10.1016/j.bios.2021.113808

Lee, S., Zhou, J., Jeevaratnam, K., Wong, W. T., Wong, I. C. K., Mak, C., et al. (2021). Paediatric/young versus Adult Patients with Long QT Syndrome. *Open Heart* 8, e001671. doi:10.1136/openhrt-2021-001671

Lima, J. L. P., Macedo, D., and Zanchettin, C. (2019). "Heartbeat Anomaly Detection Using Adversarial Oversampling," in 2019 International Joint Conference on Neural Networks (IJCNN). doi:10.1109/IJCNN.2019.8852242

Liu, J., Tan, X., Huang, C., and Ji, X. (2015). "A Dual-lead Fusion Detection Algorithm of QRS," in Third International Conference on Cyberspace Technology (Beijing, China: IET), 1–6.

Liu, X., Rabin, P. L., Yuan, Y., Kumar, A., Vasallo, P., Wong, J., et al. (2019). Effects of Anesthetic and Sedative Agents on Sympathetic Nerve Activity. *Heart Rhythm* 16, 1875–1882. doi:10.1016/j.hrthm.2019.06.017

Londhe, A. N., and Atulkar, M. (2021). Semantic Segmentation of ECG Waves Using Hybrid Channel-Mix Convolutional and Bidirectional LSTM. *Biomed. Signal Process. Control.* 63, 102162. doi:10.1016/j.bspc.2020.102162

Mandal, S., Mondal, P., and Roy, A. H. (2021). Detection of Ventricular Arrhythmia by Using Heart Rate Variability Signal and ECG Beat Image. *Biomed. Signal Process. Control.* 68, 102692. doi:10.1016/j.bspc.2021.102692

Marks, L., Borland, S., Philp, K., Ewart, L., Lainée, P., Skinner, M., et al. (2012). The Role of the Anaesthetised guinea-pig in the Preclinical Cardiac Safety Evaluation of Drug Candidate Compounds. *Toxicol. Appl. Pharmacol.* 263, 171–183. doi:10.1016/j.taap.2012.06.007

Maršánová, L., Ronzhina, M., Smíšek, R., Vítek, M., Němcová, A., Smital, L., et al. (2017). ECG Features and Methods for Automatic Classification of Ventricular Premature and Ischemic Heartbeats: A Comprehensive Experimental Study. *Sci. Rep.* 7, 11239. doi:10.1038/s41598-017-10942-6

McCann, A., Vesin, J.-M., Pruvot, E., Roten, L., Sticherling, C., and Luca, A. (2021). ECG-based Indices to Characterize Persistent Atrial Fibrillation before and during Stepwise Catheter Ablation. *Front. Physiol.* 12, 654053. doi:10.3389/fphys.2021.654053

Meijler, F. L., Wittkampf, F. H. M., Brennen, K. R., Baker, V., Wassenaar, C., and Bakken, E. E. (1992). Electrocardiogram of the Humpback Whale (Megaptera Noaeangliae) with Specific Reference to Atrioventricular Transmission and Ventricular Excitation. *J. Am. Coll. Cardiol.* 20, 475–479. doi:10.1016/0735-1097(92)90120-c

Meng, L., Tan, W., Ma, J., Wang, R., Yin, X., and Zhang, Y. (2022). Enhancing Dynamic ECG Heartbeat Classification with Lightweight Transformer Model. *Artif. Intelligence Med.* 124, 102236. doi:10.1016/j.artmed.2022.102236

Mishra, A. K., and Raghav, S. (2010). Local Fractal Dimension Based ECG Arrhythmia Classification. *Biomed. Signal Process. Control.* 5, 114–123. doi:10.1016/j.bspc.2010.01.002

Mitchell, K. J., and Schwarzwald, C. C. (2021). Heart Rate Variability Analysis in Horses for the Diagnosis of Arrhythmias. *Vet. J.* 268, 105590. doi:10.1016/j.tvjl.2020.105590

Moïse, N. S., Flanders, W. H., and Pariaut, R. (2020). Beat-to-beat Patterning of Sinus Rhythm Reveals Non-linear Rhythm in the Dog Compared to the Human. *Front. Physiol.* 10, 1548. doi:10.3389/fphys.2019.01548

Mongue-Din, H., Salmon, A., Fiszman, M. Y., and Fromes, Y. (2007). Non-invasive Restrained ECG Recording in Conscious Small Rodents: a New Tool for Cardiac Electrical Activity Investigation. *Pflugers Arch. - Eur. J. Physiol.* 454, 165–171. doi:10.1007/s00424-006-0197-8

Mousavi, S., Afghah, F., Khadem, F., and Acharya, U. R. (2021). ECG Language Processing (ELP): A New Technique to Analyze ECG Signals. *Comp. Methods Programs Biomed.* 202, 105959. doi:10.1016/j.cmpb.2021.105959

Murat, F., Sadak, F., Yildirim, O., Talo, M., Murat, E., Karabatak, M., et al. (2021a). Review of Deep Learning-Based Atrial Fibrillation Detection Studies. *Ijerph* 18, 11302. doi:10.3390/ijerph182111302

Murat, F., Yildirim, O., Talo, M., Baloglu, U. B., Demir, Y., and Acharya, U. R. (2020). Application of Deep Learning Techniques for Heartbeats Detection Using ECG Signals-Analysis and Review. *Comput. Biol. Med.* 120, 103726. doi:10.1016/j.compbiomed.2020.103726

Murat, F., Yildirim, O., Talo, M., Demir, Y., Tan, R.-S., Ciaccio, E. J., et al. (2021b). Exploring Deep Features and ECG Attributes to Detect Cardiac Rhythm Classes. *Knowledge-Based Syst.* 232, 107473. doi:10.1016/j.knosys.2021.107473

Nardelli, M., Lanata, A., Valenza, G., Felici, M., Baragli, P., and Scilingo, E. P. (2020). A Tool for the Real-Time Evaluation of ECG Signal Quality and Activity: Application to Submaximal Treadmill Test in Horses. *Biomed. Signal Process. Control.* 56, 101666. doi:10.1016/j.bspc.2019.101666

Natarajan, A., Boverman, G., Chang, Y., Antonescu, C., and Rubin, J. (2021). Convolution-free Waveform Transformers for Multi-lead ECG Classification. *Comput. Cardiol.* 2021. doi:10.23919/CinC53138.2021.9662697

Nimani, S., Hornyik, T., Alerni, N., Lewetag, R., Giammarino, L., Perez-Feliz, S., et al. (2021). Differences in Extent of Mechano-Induced QT-Changes in SQTS, WT and LQTS Rabbit Models. *Eur. Heart J.* 42, 3213. doi:10.1093/eurheartj/ehab724.3213

Nonaka, N., and Seita, J. (2021). "RandECG: Data Augmentation for Deep Neural Network Based ECG Classification," in The 35th Annual Conference of the Japanese Society for Artificial Intelligence, 1–8.

Novotna, P., Hejc, J., Ronzhina, M., Janousek, O., Stracina, T., Olejnickova, V., et al. (2017). Analysis of Hemodynamic Related Changes in High Frequency Content of QRS Complex in Working Isolated Rabbit Heart. *Comput. Cardiol.* ISBN: 978-1-5090-0684-7. doi:10.22489/cinc.2017.293-442

Novotna, P., Vicar, T., Hejc, J., Ronzhina, M., and Kolarova, J. (2020). Deep-learning Premature Contraction Localization in 12-lead ECG from Whole Signal Annotations. *Comput. Cardiol.* doi:10.22489/CinC.2020.193

Olejnickova, V., Novakova, M., and Provaznik, I. (2015). Isolated Heart Models: Cardiovascular System Studies and Technological Advances. *Med. Biol. Eng. Comput.* 53, 669–678. doi:10.1007/s11517-015-1270-2

Omoto, A. C. M., Lataro, R. M., Silva, T. M., Salgado, H. C., Fazan, R., and Silva, L. E. V. (2021). Heart Rate Fragmentation, a Novel Approach in Heart Rate Variability Analysis, Is Altered in Rats 4 and 12 Weeks after Myocardial Infarction. *Med. Biol. Eng. Comput.* 59, 2373–2382. doi:10.1007/s11517-021-02441-8

Osowski, S., Hoai, L. T., and Markiewicz, T. (2004). Support Vector Machine-Based Expert System for Reliable Heartbeat Recognition. *IEEE Trans. Biomed. Eng.* 51, 582–589. doi:10.1109/TBME.2004.824138

Packard, J. M., Graettinger, J. S., and Graybiel, A. (1954). Analysis of the Electrocardiograms Obtained from 1000 Young Healthy Aviators. *Circulation* 10, 384–400. doi:10.1161/01.CIR.10.3.384

Pan, J., and Tompkins, W. J. (1985). A Real-Time QRS Detection Algorithm. *IEEE Trans. Biomed. Eng.* BME-32, 230–236. doi:10.1109/tbme.1985.325532

Park, K. L., Lee, K. J., and Yoon, H. R. (1998). Application of a Wavelet Adaptive Filter to Minimise Distortion of the ST-Segment. *Med. Biol. Eng. Comput.* 36, 581–586. doi:10.1007/BF02524427

Parsi, A., Byrne, D., Glavin, M., and Jones, E. (2021a). Heart Rate Variability Feature Selection Method for Automated Prediction of Sudden Cardiac Death. *Biomed. Signal Process. Control.* 65, 102310. doi:10.1016/j.bspc.2020.102310

Parsi, A., Glavin, M., Jones, E., and Byrne, D. (2021b). Prediction of Paroxysmal Atrial Fibrillation Using New Heart Rate Variability Features. *Comput. Biol. Med.* 133, 104367. doi:10.1016/j.compbiomed.2021.104367

Peimankar, A., and Puthusserypady, S. (2021). DENS-ECG: A Deep Learning Approach for ECG Signal Delineation. *Expert Syst. Appl.* 165, 113911. doi:10.1016/j.eswa.2020.113911

Perez Alday, E. A., Gu, A., J Shah, A., Robichaux, C., Ian Wong, A. K., Liu, C., et al. (2021). Classification of 12-lead ECGs: the PhysioNet/Computing in Cardiology Challenge 2020. *Physiol. Meas.* 41, 124003. doi:10.1088/1361-6579/abc960

Phang, S. H., and White, P. D. (1943). The Duration of Ventricular Systole as Measured by the Q-T Interval of the Electrocardiogram, with Especial Reference to Cardiac Enlargement with and without Congestive Failure. *Am. Heart J.* 26, 108–113. doi:10.1016/S0002-8703(43)90055-9

Piantoni, C., Carnevali, L., Molla, D., Barbuti, A., DiFrancesco, D., Bucchi, A., et al. (2021). Age-related Changes in Cardiac Autonomic Modulation and Heart Rate Variability in Mice. *Front. Neurosci.* 15, 617698. doi:10.3389/fnins.2021.617698

Plesinger, F., Klimes, P., Halamek, J., and Jurak, P. (2016). Taming of the Monitors: Reducing False Alarms in Intensive Care Units. *Physiol. Meas.* 37, 1313–1325. doi:10.1088/0967-3334/37/8/1313

Radhakrishnan, T., Karhade, J., Ghosh, S. K., Muduli, P. R., Tripathy, R. K., and Acharya, U. R. (2021). AFCNNet: Automated Detection of AF Using Chirplet Transform and Deep Convolutional Bidirectional Long Short Term Memory Network with ECG Signals. *Comput. Biol. Med.* 137, 104783. doi:10.1016/j.compbiomed.2021.104783

Rahul, J., and Sharma, L. D. (2022). Artificial Intelligence-Based Approach for Atrial Fibrillation Detection Using Normalised and Short-Duration Time-Frequency ECG. *Biomed. Signal Process. Control.* 71, 103270. doi:10.1016/j.bspc.2021.103270

Rasmussen, C. E., Falk, T., Zois, N. E., Moesgaard, S. G., Häggström, J., Pedersen, H. D., et al. (2012). Heart Rate, Heart Rate Variability, and Arrhythmias in Dogs with Myxomatous Mitral Valve Disease. *J. Vet. Intern. Med.* 26, 76–84. doi:10.1111/j.1939-1676.2011.00842.x

Rautaharju, P. M. (2016). Eyewitness to History: Landmarks in the Development of Computerized Electrocardiography. *J. Electrocardiol.* 49, 1–6. doi:10.1016/j.jelectrocard.2015.11.002

Ravi, D., Wong, C., Deligianni, F., Berthelot, M., Andreu-Perez, J., Lo, B., et al. (2017). Deep Learning for Health Informatics. *IEEE J. Biomed. Health Inform.* 21, 4–21. doi:10.1109/JBHI.2016.2636665

Redfors, B., Shao, Y., and Omerovic, E. (2014). Influence of Anesthetic Agent, Depth of Anesthesia and Body Temperature on Cardiovascular Functional Parameters in the Rat. *Lab. Anim.* 48, 6–14. doi:10.1177/0023677213502015

Reyna, M. A., Sadr, N., Perez Alday, E. A., Gu, A., Shah, A. J., Robichaux, C., et al. (20212021). Will Two Do? Varying Dimensions in Electrocardiography: The PhysioNet/Computing in Cardiology Challenge 2021. *Comput. Cardiol.* 48, 1–4.

Ribeiro, A. H., Ribeiro, M. H., Paixão, G. M. M., Oliveira, D. M., Gomes, P. R., Canazart, J. A., et al. (2020). Automatic Diagnosis of the 12-lead ECG Using a Deep Neural Network. *Nat. Commun.* 11, 1760. doi:10.1038/s41467-020-15432-4

Ronzhina, M., Olejnickova, V., Stracina, T., Novakova, M., Janousek, O., Hejc, J., et al. (2017). Effect of Increased Left Ventricle Mass on Ischemia Assessment in Electrocardiographic Signals: Rabbit Isolated Heart Study. *BMC Cardiovasc. Disord.* 17, 11. doi:10.1186/s12872-017-0652-9

Ronzhina, M., Stracina, T., Lacinova, L., Ondacova, K., Pavlovicova, M., Marsanova, L., et al. (2021). Di-4-ANEPPS Modulates Electrical Activity and Progress of Myocardial Ischemia in Rabbit Isolated Heart. *Front. Physiol.* 12, 12. doi:10.3389/fphys.2021.667065

Rowan, W. H., Campen, M. J., Wichers, L. B., and Watkinson, W. P. (2007). Heart Rate Variability in Rodents: Uses and Caveats in Toxicological Studies. *Cardiovasc. Toxicol.* 7, 28–51. doi:10.1007/s12012-007-0004-6

Rueda, C., Larriba, Y., and Lamela, A. (2021). The Hidden Waves in the ECG Uncovered Revealing a Sound Automated Interpretation Method. *Sci. Rep.* 11, 3724. doi:10.1038/s41598-021-82520-w

Ruppert, S., Vormberge, T., Igl, B.-W., and Hoffmann, M. (2016). ECG Telemetry in Conscious guinea Pigs. *J. Pharmacol. Toxicol. Methods* 81, 88–98. doi:10.1016/j.vascn.2016.04.013

Saeed, J. N., and Ameen, S. Y. (2021). Smart Healthcare for ECG Telemonitoring System. *J. Soft Comput. Data Mining* 2, 75–85. doi:10.30880/jscdm.2021.02.02.007

Saini, S. K., and Gupta, R. (2021). Artificial Intelligence Methods for Analysis of Electrocardiogram Signals for Cardiac Abnormalities: State-Of-The-Art and Future Challenges. *Artif. Intell. Rev.* 55, 1519–1565. doi:10.1007/s10462-021-09999-7

Sakaguchi, Y., Takahara, A., Nakamura, Y., Akie, Y., and Sugiyama, A. (2009). Halothane-anaesthetized, Closed-Chest, guinea-pig Model for Assessment of Drug-Induced QT-Interval Prolongation. *Basic Clin. Pharmacol. Toxicol.* 104, 43–48. doi:10.1111/j.1742-7843.2008.00312.x

Salem, M., Taheri, S., and Yuan, J.-S. (20182018). ECG Arrhythmia Classification Using Transfer Learning from 2- Dimensional Deep CNN Features. *IEEE Biomed. Circuits Syst. Conf. (Biocas)*. doi:10.1109/BIOCAS.2018.8584808

Salerno, S. M., Alguire, P. C., and Waxman, H. S. (2003). Competency in Interpretation of 12-lead Electrocardiograms: a Summary and Appraisal of Published Evidence. *Ann. Intern. Med.* 138, 751–760. doi:10.7326/0003-4819-138-9-200305060-00013

Sangaiah, A. K., Arumugam, M., and Bian, G.-B. (2020). An Intelligent Learning Approach for Improving ECG Signal Classification and Arrhythmia Analysis. *Artif. intelligence Med.* 103, 101788. doi:10.1016/j.artmed.2019.101788

Sano, Y., Ito, S., Yoneda, M., Nagasawa, K., Matsuura, N., Yamada, Y., et al. (2016). Effects of Various Types of Anesthesia on Hemodynamics, Cardiac Function, and Glucose and Lipid Metabolism in Rats. *Am. J. Physiology-Heart Circulatory Physiol.* 311, H1360–H1366. doi:10.1152/ajpheart.00181.2016

Satija, U., Ramkumar, B., and Manikandan, M. S. (2018). A Review of Signal Processing Techniques for Electrocardiogram Signal Quality Assessment. *IEEE Rev. Biomed. Eng.* 11, 36–52. doi:10.1109/RBME.2018.2810957

S., C. V., and E., R. (2021). A Novel Deep Learning Based Gated Recurrent Unit with Extreme Learning Machine for Electrocardiogram (ECG) Signal Recognition. *Biomed. Signal Process. Control.* 68, 102779. doi:10.1016/j.bspc.2021.102779

Silva, P., Luz, E., Silva, G., Moreira, G., Wanner, E., Vidal, F., et al. (2020). Towards Better Heartbeat Segmentation with Deep Learning Classification. *Sci. Rep.* 10, 20701. doi:10.1038/s41598-020-77745-0

Simonson, E., Brozek, J., and Keys, A. (1949). Variability of the Electrocardiogram in normal Young Men. *Am. Heart J.* 38, 407–422. doi:10.1016/0002-8703(49)90852-2

Skinner, M., Xing, G., Lu, J., Ren, J., and Oldman, K. (2017). Detecting Drug-Induced Changes in ECG Parameters Using Jacketed Telemetry: Effect of Different Data Reduction Techniques. *J. Pharmacol. Toxicol. Methods* 85, 38–48. doi:10.1016/j.vascn.2016.12.004

Smisek, R., Hejc, J., Ronzhina, M., Nemcova, A., Marsanova, L., Kolarova, J., et al. (2018). Multi-stage SVM Approach for Cardiac Arrhythmias Detection in Short Single-lead ECG Recorded by a Wearable Device. *Physiol. Meas.* 39, 094003. doi:10.1088/1361-6579/aad9e7

Smital, L., Haider, C. R., Vitek, M., Leinveber, P., Jurak, P., Nemcova, A., et al. (2020). Real-time Quality Assessment of Long-Term ECG Signals Recorded by Wearables in Free-Living Conditions. *IEEE Trans. Biomed. Eng.* 67, 2721–2734. doi:10.1109/TBME.2020.2969719

Smulyan, H. (2019). The Computerized ECG: Friend and Foe. *Am. J. Med.* 132, 153–160. doi:10.1016/j.amjmed.2018.08.025

Soroudi, A., Hernández, N., Berglin, L., and Nierstrasz, V. (2019). Electrode Placement in Electrocardiography Smart Garments: A Review. *J. Electrocardiol.* 57, 27–30. doi:10.1016/j.jelectrocard.2019.08.015

Soto, J. T., Hughes, J. W., Sanchez, P. A., Perez, M., Ouyang, D., and Ashley, E. (2021). Multimodal Deep Learning Enhances Diagnostic Precision in Left Ventricular Hypertrophy. *medRxiv* 13, 2125886. [Preprint] (Accessed 06Januar 12, 2022). doi:10.1101/2021.06.13.21258860

Spier, A. W., and Meurs, K. M. (2004). Assessment of Heart Rate Variability in Boxers with Arrhythmogenic Right Ventricular Cardiomyopathy. *J. Am. Vet. Med. Assoc.* 224, 534–537. doi:10.2460/javma.2004.224.534

Stracina, T., Ronzhina, M., Stark, T., Ruda, J., Olsanska, E., Vesely, P., et al. (2016). Prolonged QT Interval in Neurodevelopmental Rat Model of Schizophrenia. *Comput. Cardiol. Conf.* 1049–1052. ISBN: 978-1-5090-0895-7.7. doi:10.22489/cinc.2016.302-288

Sun, L., Lu, Y., Yang, K., and Li, S. (2012). ECG Analysis Using Multiple Instance Learning for Myocardial Infarction Detection. *IEEE Trans. Biomed. Eng.* 59, 3348–3356. doi:10.1109/TBME.2012.2213597

Taddei, A., Distante, G., Emdin, M., Pisani, P., Moody, G. B., Zeelenberg, C., et al. (1992). The European ST-T Database: Standard for Evaluating Systems for the Analysis of ST-T Changes in Ambulatory Electrocardiography. *Eur. Heart J.* 13, 1164–1172. doi:10.1093/oxfordjournals.eurheartj.a060332

Tarvainen, M. P., Niskanen, J.-P., Lipponen, J. A., Ranta-aho, P. O., and Karjalainen, P. A. (2014). Kubios HRV - Heart Rate Variability Analysis Software. *Comp. Methods Programs Biomed.* 113, 210–220. doi:10.1016/j.cmpb.2013.07.024

Task Force of the European Society of Cardiology and the North American Society of Pacing and Electrophysiology (1996). Heart Rate Variability: Standards of Measurement, Physiological Interpretation and Clinical Use. Task Force of the European Society of Cardiology and the North American Society of Pacing and Electrophysiology. *Circulation* 93, 1043–1065.

Thambawita, V., Isaksen, J. L., Hicks, S. A., Ghouse, J., Ahlberg, G., Linneberg, A., et al. (2021). DeepFake Electrocardiograms Using Generative Adversarial Networks Are the Beginning of the End for Privacy Issues in Medicine. *Sci. Rep.* 11, 21896. doi:10.1038/s41598-021-01295-2

Theodoridis, S., and Koutroumbas, K. (2009). *Pattern Recognition*. 4th edition. Elsevier. ISBN 978-1-59749-272-0.

Tong, Y., Sun, Y., Zhou, P., Shen, Y., Jiang, H., Sha, X., et al. (2021). Locating Abnormal Heartbeats in ECG Segments Based on Deep Weakly Supervised Learning. *Biomed. Signal Process. Control.* 68, 102674. doi:10.1016/j.bspc.2021.102674

Tontodonati, M., Fasdelli, N., and Dorigatti, R. (2011). An Improved Method of Electrode Placement in Configuration Lead II for the Reliable ECG Recording by Telemetry in the Conscious Rat. *J. Pharmacol. Toxicol. Methods* 63, 1–6. doi:10.1016/j.vascn.2010.03.001

Tripathy, R. K., Bhattacharyya, A., and Pachori, R. B. (2019). Localization of Myocardial Infarction from Multi-lead ECG Signals Using Multiscale Analysis and Convolutional Neural Network. *IEEE Sensors J.* 19, 11437–11448. doi:10.1109/JSEN.2019.2935552

Tsai, T. L., Fridsma, D. B., and Gatti, G. (2003). Computer Decision Support as a Source of Interpretation Error: the Case of Electrocardiograms. *J. Am. Med. Inform. Assoc.* 10, 478–483. doi:10.1197/jamia.M1279

Van Mieghem, C., Sabbe, M., and Knockaert, D. (2004). The Clinical Value of the ECG in Noncardiac Conditions. *Chest* 125, 1561–1576. doi:10.1378/chest.125.4.1561

Vesely, P., Stracina, T., Hlavacova, M., Halamek, J., Kolarova, J., Olejnickova, V., et al. (2019). Haloperidol Affects Coupling between QT and RR Intervals in guinea Pig Isolated Heart. *J. Pharmacol. Sci.* 139, 23–28. doi:10.1016/j.jphs.2018.11.004

Vicar, T., Hejc, J., Novotna, P., Ronzhina, M., and Janousek, O. (2020). ECG Abnormalities Recognition Using Convolutional Network with Global Skip Connections and Custom Loss Function. *Comput. Cardiol.* doi:10.22489/CinC.2020.189

Vidhya, R. B., and Jerritta, S. (2022). Pre-processing ECG Signals for Smart home Material Application. *Mater. Today Proc.* 49, 2955–2961. doi:10.1016/j.matpr.2021.11.367

Vornanen, M., and Hassinen, M. (2016). Zebrafish Heart as a Model for Human Cardiac Electrophysiology. *Channels* 10, 101–110. doi:10.1080/19336950.2015.1121335

Vuoti, A. O., Tulppo, M. P., Ukkola, O. H., Junttila, M. J., Huikuri, H. V., Kiviniemi, A. M., et al. (2021). Prognostic Value of Heart Rate Variability in Patients with Coronary Artery Disease in the Current Treatment Era. *PloS one* 16, e0254107. doi:10.1371/journal.pone.0254107

Walia, A., and Kaul, A. (2020). QRS Detection Using Dual Window Fourier Transform. *4th Int. Conf. Electron. Commun. Aerospace Tech. (Iceca)*, 314–318. doi:10.1109/ICECA49313.2020.9297488

Waller, A. D. (1887). A Demonstration on Man of Electromotive Changes Accompanying the Heart's Beat. *J. Physiol.* 8, 229–234. doi:10.1113/jphysiol.1887.sp000257

Wehrens, X., Kirchhoff, S., and Doevendans, P. A. (2000). Mouse Electrocardiography an Interval of Thirty Years. *Cardiovasc. Res.* 45, 231–237. doi:10.1016/s0008-6363(99)00335-1

Weimann, K., and Conrad, T. O. F. (2021). Transfer Learning for ECG Classification. *Sci. Rep.* 11, 5251. doi:10.1038/s41598-021-84374-8

Wójcik, D., Rymarczyk, T., Oleszek, M., Maciura, Ł., and Bednarczuk, P. (2021). "Diagnosing Cardiovascular Diseases with Machine Learning on Body Surface Potential Mapping Data," in SenSys 2021: Proceedings of the 19th ACM Conference on Embedded Networked Sensor Systems, 379–381. doi:10.1145/3485730.3492883

Wren-Dail, M. A., Dauchy, R. T., Blask, D. E., Hill, S. M., Ooms, T. G., Dupepe, L. M., et al. (2017). Effect of Isoflurane Anesthesia on Circadian Metabolism and Physiology in Rats. *Comp. Med.* 67, 138–146.

Xiong, P., Xue, Y., Zhang, J., Liu, M., Du, H., Zhang, H., et al. (2021). Localization of Myocardial Infarction with Multi-lead ECG Based on DenseNet. *Comp. Methods Programs Biomed.* 203, 106024. doi:10.1016/j.cmpb.2021.106024

Xue, J., and Yu, L. (2021). Applications of Machine Learning in Ambulatory ECG. *Hearts* 2, 472–494. doi:10.3390/hearts2040037

Yıldırım, Ö., Pławiak, P., Tan, R.-S., and Acharya, U. R. (2018). Arrhythmia Detection Using Deep Convolutional Neural Network with Long Duration ECG Signals. *Comput. Biol. Med.* 102, 411–420. doi:10.1016/j.compbiomed.2018.09.009

Yu, Z., Song, J., Cheng, L., Li, S., Lu, Q., Zhang, Y., et al. (2021). Peguero-Lo Presti Criteria for the Diagnosis of Left Ventricular Hypertrophy: A Systematic Review and Meta-Analysis. *PLOS ONE* 16, e0246305. doi:10.1371/journal.pone.0246305

Zhang, D., Wang, S., Li, F., Wang, J., Sangaiah, A. K., Sheng, V. S., et al. (2019). An ECG Signal De-noising Approach Based on Wavelet Energy and Sub-band Smoothing Filter. *Appl. Sci.* 9, 4968. doi:10.3390/app9224968

Zhu, W., Chen, X., Wang, Y., and Wang, L. (2019). Arrhythmia Recognition and Classification Using ECG Morphology and Segment Feature Analysis. *Ieee/acm Trans. Comput. Biol. Bioinf.* 16, 131–138. doi:10.1109/TCBB.2018.2846611

Zimmer, H.-G. (1998). The Isolated Perfused Heart and its Pioneers. *Physiology* 13, 203–210. doi:10.1152/physiologyonline.1998.13.4.203

Conflict of Interest: The authors declare that the research was conducted in the absence of any commercial or financial relationships that could be construed as a potential conflict of interest.

Publisher's Note: All claims expressed in this article are solely those of the authors and do not necessarily represent those of their affiliated organizations, or those of the publisher, the editors, and the reviewers. Any product that may be evaluated in this article, or claim that may be made by its manufacturer, is not guaranteed or endorsed by the publisher.

frontiers | Frontiers in Physiology

MINI REVIEW
published: 29 April 2022
doi: 10.3389/fphys.2022.835761

Studying Cardiac Neural Network Dynamics: Challenges and Opportunities for Scientific Computing

Nil Z. Gurel[1,2], Koustubh B. Sudarshan[3], Sharon Tam[4], Diana Ly[4], J. Andrew Armour[1,2], Guy Kember[3] and Olujimi A. Ajijola[1,2,5]*

[1]UCLA Neurocardiology Research Program of Excellence, Los Angeles, CA, United States, [2]UCLA Cardiac Arrhythmia Center, UCLA Health System, Los Angeles, CA, United States, [3]Department of Engineering Mathematics and Internetworking, Dalhousie University, Halifax, NS, Canada, [4]UCLA Department of Bioengineering, Los Angeles, CA, United States, [5]Molecular, Cellular and Integrative Physiology Program, UCLA, Los Angeles, CA, United States

Neural control of the heart involves continuous modulation of cardiac mechanical and electrical activity to meet the organism's demand for blood flow. The closed-loop control scheme consists of interconnected neural networks with central and peripheral components working cooperatively with each other. These components have evolved to cooperate control of various aspects of cardiac function, which produce measurable "functional" outputs such as heart rate and blood pressure. In this review, we will outline fundamental studies probing the cardiac neural control hierarchy. We will discuss how computational methods can guide improved experimental design and be used to probe how information is processed while closed-loop control is operational. These experimental designs generate large cardio-neural datasets that require sophisticated strategies for signal processing and time series analysis, while presenting the usual large-scale computational challenges surrounding data sharing and reproducibility. These challenges provide unique opportunities for the development and validation of novel techniques to enhance understanding of mechanisms of cardiac pathologies required for clinical implementation.

Keywords: neurocardiology, sudden cardiac death (SCD), closed-loop control, cardiac nervous system, cardiac function

OPEN ACCESS

Edited by:
Guido Caluori, INSERM Institut de Rythmologie et Modélisation Cardiaque (IHU-Liryc), France

Reviewed by:
Annika Winbo, The University of Auckland, New Zealand

****Correspondence:***
Nil Z. Gurel
gurelnil@gmail.com

Specialty section:
This article was submitted to Integrative Physiology, a section of the journal Frontiers in Physiology

Received: *14 December 2021*
Accepted: *06 April 2022*
Published: *29 April 2022*

Citation:
Gurel NZ, Sudarshan KB, Tam S, Ly D, Armour J, Kember G and Ajijola OA (2022) Studying Cardiac Neural Network Dynamics: Challenges and Opportunities for Scientific Computing. Front. Physiol. 13:835761. doi: 10.3389/fphys.2022.835761

INTRODUCTION

Beat-to-beat control of cardiac function requires adaptive adjustments of cardiac electromechanical activity to meet the organism's blood flow needs. The closed-loop cardiac control network hierarchy consists of the intrinsic cardiac nervous system, the sympathetic and parasympathetic arms of the autonomic nervous system, peripheral ganglia, spinal cord, brain stem, and higher centers in the central nervous system (Ardell et al., 2016; Shivkumar et al., 2016). Contrary to the viewpoint where the peripheral nervous system functions as a conduit for centrally-derived inputs (Yuste, 2015), neural control of cardiac function involves a hierarchy of interconnected neural networks that regionally control indices such as heart rate, blood pressure, or respiration (Ardell et al., 2016; Shivkumar et al., 2016).

Substantial experimental and clinical work has focused on neural contributions to heart rate, heart rate variability, and blood pressure anomalies and associated pathologies including heart failure, myocardial infarction, coronary artery disease, and hypertension (Sessa et al., 2018; Pan et al., 2020).

At a population level, elevated resting heart rate and blood pressure, reduced heart rate variability, and depressed baroreflex sensitivity correlate with increased risks of cardiovascular disease, mortality, arrhythmia, and negative health outcomes (Jones et al., 2008; Zhang et al., 2016; Grassi et al., 2019; Fuchs and Whelton, 2020). While these biomarkers remain relevant at a population level, their usefulness to assess risk of adverse outcomes for individual patients is limited due to regionality of the control hierarchy (Huikuri and Stein, 2013; Kember et al., 2013; Ajijola, 2016; Mitrani and Myerburg, 2016; Pan et al., 2020).

The cardiac neural control network may be characterized as a closed-loop control system with the central nervous system as one component (Armour, 2004; Leenen, 2007; Hirooka, 2010; Scherbakov and Doehner, 2018). At the peripheral level of the control hierarchy, afferent and efferent activities arise from locally interconnected feedback loops of ganglia and interconnecting neurons (Ardell et al., 2016; Shivkumar et al., 2016). While the peripheral and central levels are in constant communication, the peripheral level is independently capable of maintaining basic cardiac function (Ardell et al., 1991; Smith et al., 2001a; Smith et al., 2001b). An important consequence is that autonomic control and the heart may become compromised while continuing to maintain function as indicated by measures such as heart rate and blood pressure (Armour, 2004; Kember et al., 2013).

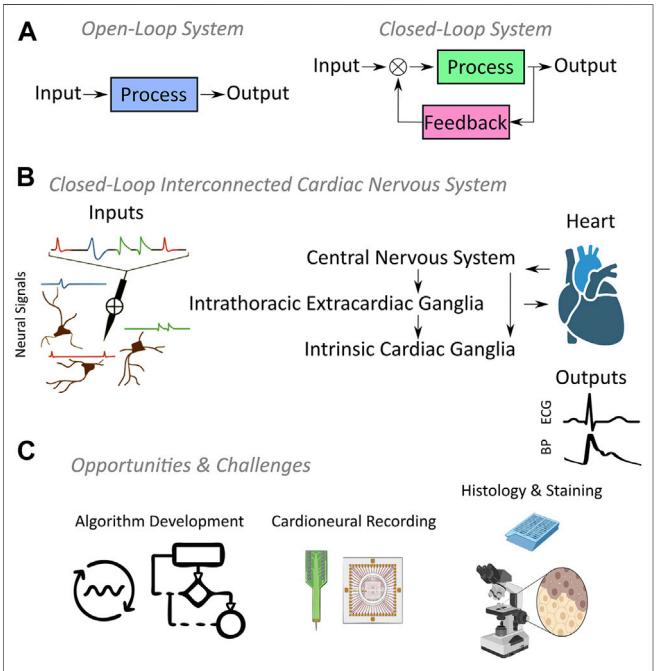

FIGURE 1 | (A) Fundamental difference between open-loop and closed-loop systems is that the system output is regulated by feedback in closed-loop systems, while open-loop systems have no feedback. **(B)** Cardiac nervous system represents a three-tier closed-loop control hierarchy where each tier exhibits neural inputs resulting in functional outputs such as the electrocardiography (ECG) or blood pressure (BP). **(C)** Open source algorithm development and novel cardioneural recording technologies supported by histologic studies will propel the field of neurocardiology forward.

Substantial progress has been made in the description of network components down to the cellular and genomic levels (Moss et al., 2021; Rajendran et al., 2019; Hanna et al., 2021), but the principles and mechanisms governing higher level function and neuro-mechanical linkages are not well defined. This is partly due to the closed-loop nature across levels of the cardiac control hierarchy: it has no simple open-loop analogue to provide a direct linkage between neural activity and functional targets (**Figure 1**). A useful strategy is to de-link levels within the control hierarchy, and this has been successfully used in experimental designs to gain insight into neural contributions to cardiac function and in clinical interventions as a last resort (Ardell et al., 1991; Smith et al., 2001a; Smith et al., 2001b). A main requirement is that experimental methods must directly measure integration within the cardiac neural control system and the linkage of this system to control targets while in closed-loop operation.

In this review, we will outline the fundamental studies focusing on closed-loop information processing within cardiac neural hierarchy. Our emphasis will be less on past achievements and more on identifying trends that are shaping the field. We will discuss how computational methods can help to guide improved experimental designs, quantify the value of small datasets, and become useful for attacking long-standing problems that span multiple scales in space and time. The size and complexity of these next generation cardio-neural datasets require sophisticated strategies for signal processing, time series analysis, and dimensionality reduction, while presenting the usual large-scale computational challenges surrounding data sharing and reproducibility. These challenges provide unique opportunities to further technological development and computational pipelines to drive improved understanding of mechanisms of cardiac pathologies.

NEURAL RECORDING LITERATURE IN CARDIAC NERVOUS SYSTEM

The cardiac nervous system offers untapped opportunities to understand mechanisms of cardiac disease and develop novel therapeutic strategies. Manipulation of the cardiac nervous system is a promising approach to mitigate the onset and progression of cardiac pathology. However, its implementation requires an understanding of the neural-mechanical linkages if safe and effective therapeutic strategies are to be developed. In **Table 1**, a representative selection of the research literature into neuro-mechanical linkages spanning the late 1960s to 2021 is provided. Earlier studies include research into anatomy and function of the stellate ganglion, right atrial ganglionated plexus, spinal cord, and nodose with single-unit recordings (Ja¨nig and Szulczyk, 1980; Armour, 1983; Armour, 1985; Armour, 1986; Gagliardi et al., 1988; Boczek-Funcke et al., 1992; Boczek-Funcke et al., 1993; Armour et al., 1998; Ardell et al., 2009; Salavatian et al., 2019a; Foreman et al., 2015; Foreman and Qin, 2009). With the advent of improved recording methods these approaches have evolved to more recent studies involving multi-unit recordings. Earlier computational methods utilized single neuron recordings and the phase relationship of a neuron's

TABLE 1 | Research literature probing into cardiac nervous system, listed as regions, recording type (single/multi unit), anesthetic agent, studied species, computational methods used, number of recording electrodes, electrode type, and software used for analysis. The reference numbers correspond to the references in the manuscript.

Ref #	Year	Region	Recording	Anesthesia	Species	Methods used	# Electrodes	Electrode type	Software
Foreman et al. (1975)	1975	spinal cord	single unit	halothane, alpha chloralose	monkey	firing rate, conduction velocity	1	platinum wire	N/A
Ja¨nig and Szulczyk, (1980)	1980	lumbar preganglionic neurons	single unit	ketamine hydrochloride, alpha chloralose	cat	firing rate, conduction velocity	1	platinum wire	N/A
Blair et al. (1981)	1981	spinal cord	single unit	ketamine, alpha chloralose	monkey	firing rate	1	stainless steel	N/A
Blair et al. (1982)	1982	spinal cord	single unit	ketamine, alpha chloralose	monkey	firing rate, conduction velocity	1	tungsten, class	N/A
Armour, (1983)	1983	stellate ganglion	single unit	sodium pentobarbital, alpha chloralose	dog	N/A	1	N/A	N/A
Ammons et al. (1983a)	1983	spinal cord	single unit	ketamine, alpha chloralose	monkey	firing rate	1	stainless steel	N/A
Ammons et al. (1983b)	1983	spinal cord	single unit	ketamine, alpha chloralose	monkey	firing rate, conduction velocity	1	stainless steel	N/A
Ammons et al. (1984a)	1984	spinal cord	single unit	ketamine, alpha chloralose	monkey	firing rate	1	stainless steel	N/A
Ammons et al. (1984b)	1984	spinal cord	single unit	ketamine, alpha chloralose	monkey	firing rate, conduction velocity	1	stainless steel	N/A
Ammons and Foreman, (1984)	1984	spinal cord	single unit	ketamine, alpha chloralose	cat	firing rate	1	carbon tipped glass	N/A
Blair et al. (1984b)	1984	spinal cord	single unit	ketamine, alpha chloralose	monkey and cat	firing rate	1	tungsten or glass	N/A
Blair et al. (1984a)	1984	spinal cord	single unit	ketamine, alpha chloralose	cat	firing rate	1	tungsten or glass	N/A
Foreman et al. (1984)	1984	spinal cord	single unit	ketamine, alpha chloralose	cat	firing rate, stimulation latency	1	stainless steel	N/A
Ammons et al. (1985b)	1985	spinal cord	single unit	ketamine, alpha chloralose	monkey	firing rate	1	stainless steel	N/A
Ammons et al. (1985a)	1985	spinal cord	single unit	ketamine, alpha chloralose	monkey	firing rate, stimulation latency	1	N/A	N/A
Armour, (1985)	1985	middle cervical ganglion	single unit	Fentanyl citrate, alpha chloralose	dog	firing rate, action potential discharge pattern, duration, SNR	1	tungsten	N/A
Armour, (1986)	1986	stellate ganglion	single unit	alpha chloralose	dog	firing rate, firing pattern, cardiac/respiration rhythmicity	1	tungsten	N/A
Brennan et al. (1987)	1987	spinal cord	single unit	ketamine, alpha chloralose	monkey	firing rate, stimulation latency	1	stainless steel	N/A
Girardot et al. (1987)	1987	spinal cord	single unit	ketamine, alpha chloralose	monkey	firing rate, stimulation latency	1	carbon-filament glass	N/A
Gagliardi et al. (1988)	1988	right atrial ganglionated plexus	single unit	Fentanyl citrate, alpha chloralose	dog	firing rate, firing pattern, cardiac/respiration rhythmicity	1	tungsten	N/A
Bolser et al. (1989)	1989	spinal cord	single unit	ketamine, alpha chloralose	cat	firing rate, stimulation latency	1	platinum-iridium	N/A
Hobbs et al. (1989)	1989	spinal cord	single unit	ketamine, alpha chloralose	monkey	firing rate, stimulation latency	1	stainless steel	N/A

(Continued on following page)

TABLE 1 | (*Continued*) Research literature probing into cardiac nervous system, listed as regions, recording type (single/multi unit), anesthetic agent, studied species, computational methods used, number of recording electrodes, electrode type, and software used for analysis. The reference numbers correspond to the references in the manuscript.

Ref #	Year	Region	Recording	Anesthesia	Species	Methods used	# Electrodes	Electrode type	Software
Chandler et al. (1991)	1991	spinal cord	single unit	ketamine, alpha chloralose	monkey	firing rate, stimulation latency	1	carbon-filament	N/A
Boczek-Funcke et al. (1992)	1992	thoracic sympathetic neurons	single unit	ketamine hydrochloride, alpha chloralose	cat	firing rate, firing pattern, cardiac/respiration rhythmicity	1	platinum wire electrodes	N/A
Boczek-Funcke et al. (1993)	1993	thoracic preganglionic neurons	single unit	ketamine hydrochloride, alpha chloralose	cat	firing rate, firing pattern, axonal conduction velocity, spontaneous activity, segmental location in spinal cord	1	platinum wire electrodes	N/A
Zhang et al. (1997)	1997	spinal cord	single unit	sodium pentobarbital	rat	firing rate, spikes per stimulus intensity	1	carbon-filament glass	N/A
Armour et al. (1998)	1998	left middle cervical and left stellate ganglion	single unit	thiopental sodium, alpha chloralose	dog	firing pattern, cross correlation (coherence), firing pattern	1	tungsten	N/A
Chandler et al. (2000)	2000	spinal cord	single unit	ketamine, alpha chloralose	monkey	firing rate, stimulation latency	1	carbon-filament glass	N/A
Qin et al. (2001)	2001	spinal cord	single unit	sodium pentobarbital	rat	firing rate, stimulation latency	1	carbon-filament glass	N/A
Chandler et al. (2002)	2002	spinal cord	single unit	ketamine, alpha chloralose	monkey	firing rate, stimulation latency	1	carbon-filament glass	N/A
Zhang et al. (2003)	2003	spinal cord	single unit	sodium pentobarbital	rat	firing rate, stimulation latency	1	carbon-filament glass	N/A
Qin et al. (2003a)	2003	spinal cord	single unit	sodium pentobarbital	rat	firing rate, stimulation latency	1	carbon-filament glass	N/A
Qin et al. (2003b)	2003	spinal cord	single unit	sodium pentobarbital	rat	firing rate, stimulation latency	1	carbon-filament glass	N/A
Qin et al. (2003c)	2003	spinal cord	single unit	sodium pentobarbital	rat	firing rate, stimulation latency	1	carbon-filament glass	N/A
Qin et al. (2004c)	2004	spinal cord	single unit	sodium pentobarbital	rat	firing rate, stimulation latency	1	carbon-filament glass	N/A
Qin et al. (2004a)	2004	spinal cord	single unit	sodium pentobarbital	rat	firing rate, stimulation latency	1	carbon-filament glass	N/A
Qin et al. (2004b)	2004	spinal cord	single unit	sodium pentobarbital	rat	firing rate, stimulation latency	1	carbon-filament glass	N/A
Qin et al. (2006)	2006	spinal cord	single unit	sodium pentobarbital	rat	firing rate, stimulation latency	1	carbon-filament glass	N/A
Qin et al. (2007)	2007	spinal cord	single unit	sodium pentobarbital	rat	firing rate, stimulation latency	1	carbon-filament glass	N/A

(Continued on following page)

TABLE 1 | (*Continued*) Research literature probing into cardiac nervous system, listed as regions, recording type (single/multi unit), anesthetic agent, studied species, computational methods used, number of recording electrodes, electrode type, and software used for analysis. The reference numbers correspond to the references in the manuscript.

Ref #	Year	Region	Recording	Anesthesia	Species	Methods used	# Electrodes	Electrode type	Software
Qin et al. (2008)	2008	spinal cord	single unit	sodium pentobarbital	rat	firing rate, stimulation latency	1	carbon-filament glass	N/A
Ardell et al. (2009)	2009	middle cervical ganglion	single unit	thiopental sodium, alpha chloralose	dog	firing pattern	1	tungsten	Spike2
Goodman-Keiser et al. (2010)	2010	spinal cord	single unit	sodium pentobarbital	rat	firing rate, stimulation latency	1	carbon-filament glass	N/A
Qin et al. (2010)	2010	spinal cord	single unit	sodium pentobarbital	rat	firing rate, stimulation latency	1	carbon-filament glass	N/A
Little et al. (2011)	2011	spinal cord	single unit	sodium pentobarbital	rat	firing rate, stimulation latency	1	carbon-filament glass	N/A
Beaumont et al. (2013)	2013	right atrial ganglionated plexus	multi unit	isoflurane	dog	template matching, principal component analysis, spike rate, conditional probability	16	platinum-iridium	Spike2
Salavatian et al. (2019a)	2019	spinal cord	single unit	isoflurone, alpha chloralose	dog	spike sorting feature of software (not specified)	1	tungsten	Spike2
Dale et al. (2020)	2020	spinal cord	multi unit	inhaled isoflurane, fentanyl, alpha chloralose	pig	firing rate, cross correlation, conditional probability	64	platinum-iridium	Spike2
Yoshie et al. (2020)	2020	stellate ganglion	multi unit	inhaled isoflurane	pig	firing rate	N/A	N/A	N/A
Omura et al. (2021)	2021	spinal cord	multi unit	inhaled isoflurane, fentanyl, alpha chloralose, bupivacaine	pig	firing rate	64	platinum-iridium	iScalDyn
Salavatian et al. (2019b)	2021	nodose	multi unit	isoflurane, alpha chloralose	pig	firing rate	16	platinum-iridium	Spike2, MATLAB
Sudarshan et al. (2021)	2021	stellate ganglion	multi unit	isoflurane, chloralose	pig	unsupervised spike detection, spike rate	16	platinum-iridium	Open source, Python

activity to common cardiac measures were considered. Functional properties of neurons were examined through the neural response to a variety of stimuli such as rhythmicity of the neural firing pattern to functional recordings such as blood pressure and respiration, mechanical touch, electrical stimulation, and pharmacological agents.

Foreman et al. (1975), Foreman et al. (1984) was the first to investigate spinal cord neurons in monkeys using single-unit platinum wire electrodes through laminectomy. These efforts were followed by Blair et al. (1981), Blair et al. (1982), Blair et al. (1984a), Blair et al. (1984b), Ammons et al. (1983a), Ammons et al. (1983b), Ammons et al. (1984a), Ammons and Foreman (1984), Ammons et al. (1984b), Ammons et al. (1985a), Ammons et al. (1985b), Brennan et al. (1987), Girardot et al. (1987), Bolser et al. (1989), Hobbs et al. (1989), and Chandler et al. (1991) in cats and monkeys using tungsten, stainless steel, platinum-iridium, and carbon-filament glass electrodes. The effects of cardiovascular stressors, noxious stressors, vagal afferent stimulation, and pharmacological agents on T1-T5 spinal, spinothalamic, and spinoreticular neurons were studied in separate investigations. These studies laid the groundwork to understand the mechanisms of cardiac pain, roles of neurotransmitters, and multi-organ architecture of spinal neurons (Foreman et al., 2015). Another set of studies focused on C1-C2 spinal neurons (Zhang et al., 1997; Chandler et al., 2000; Qin et al., 2001; Chandler et al., 2002; Qin et al., 2003a; Qin et al., 2003b; Zhang et al., 2003; Qin et al., 2004a; Qin et al., 2004b), characterization of thoracic spinal neurons receiving inputs from the heart and lower airways (Qin et al., 2003c; Qin et al., 2004c; Qin et al., 2006; Qin et al., 2007; Qin et al., 2008), and multi-organ processing of cardiac nociception (Goodman-Keiser et al., 2010; Qin et al., 2010; Little et al., 2011).

Using similar electrode technologies and methods, peripheral investigations were carried out by other groups. Ja¨nig and

Szulczyk (1980) investigated the functional properties of lumbar preganglionic sympathetic neurons in cats using single-unit platinum wire electrodes. The functional properties of the neurons were classified according to cardiac rhythmicity, reactions to different stimuli, and axon conduction velocity. Armour (1983) performed a set of experiments to study synaptic transmission in middle cervical and stellate ganglia in dogs after thoracic autonomic ganglia decentralization. Compound action potential shapes were studied based on their response to a number of pharmacological agents and electrical stimulation of an afferent cardiopulmonary nerve. In subsequent studies, extracellular neural activity of middle cervical and stellate ganglia neurons was recorded in dogs (Armour, 1985; Armour, 1986). Action potentials were identified based on predetermined signal to noise ratios, action potential duration, action potential discharge pattern, and firing rates have been quantified. Neural classifications were performed based on cardiac cycle rhythmicity, respiration, respiration rhythmicity, response to mechanical distortion of the superior vena cava, heart, thoracic aorta, thoracic wall, neck, or foreleg skin, and response to stimulation of sympathetic and/or cardiopulmonary nerves. Gagliardi et al. (1988) similarly studied right atrial ganglionated plexus neural activity in dogs by finding neurons that showed cardiac rhythmicity, respiratory rhythmicity, and responded to mechanical stimuli.

Boczek-Funcke et al. (1992) split nerve bundles into fine filaments upon perineurium incision and utilized 167 single-unit platinum wire electrodes to classify 167 single preganglionic neurons in cats, based on three reflex criteria: cardiac rhythmicity (Group 1 neurons), response to noxious stimulation of the skin (Group 2 neurons), and the coupling of neural activity to central inspiratory drive (phrenic nerve activity, Group 3 neurons). Neurons that showed lack of cardiac rhythmicity but excitability to noxious skin stimuli were labelled Group 4 neurons. A subsequent work by the same group tested whether these four, functionally distinct groups differed in the distribution of their segmental origin within the spinal cord, spontaneous activity, and axonal conduction velocity (Boczek-Funcke et al., 1993). It was reported that neurons showing different reflex patterns differed in segmental location and axonal conduction velocity. A similar stimuli-response approach was undertaken to evaluate the differential selectivity of neurons in middle cervical or stellate ganglia versus intrinsic cardiac ganglia in dogs (Armour et al., 1998). The evaluated interventions were: temporary discontinuation of respiration, alteration of respiratory rate, inferior vena cava occlusion, aortic occlusion, pharmacological agent infusion, epicardial touch, and carotid sinus stimulation. Firing patterns and cross correlation of neural firing across ganglia showed similarity and dissimilarity in reflex patterns to a wide range of stimuli. Lastly, more recent multi-probe recordings of neurons used software (Spike 2, Cambridge Electronic Design) to filter and analyze middle cervical ganglion (Ardell et al., 2009) and dorsal root ganglion (Salavatian et al., 2019a) neural recordings. The totality of evidence led to the conclusion of a thoracic nervous system acting as a distributive processor with redundant cardio-regulatory control mechanisms exerted through multiple nested feedback loops.

With the advent of linear and multi-grid microelectrode arrays, it became feasible to evaluate neural activities within and between neurons. Beaumont et al. reported activity from multiple intrinsic cardiac neurons in the right atrial ganglionated plexus in dogs using a 16-channel linear array (Beaumont et al., 2013). Following an artifact removal process based on right atrial electrogram and stimulator signals, neural activities were compared in different time windows before/after interventions by the computation of the firing rate evolution (Gagliardi et al., 1988). A Skellam distribution (Hyun-Chool Shin et al., 2010) was employed to evaluate the differences in firing rate for each intervention while differential neural to stressors were evaluated via conditional probability and a chi-squared analysis was used to compare the response characteristics of the identified intrinsic cardiac neurons. Nodose and stellate ganglia neural activity were also recorded in a separate study using 16-channel microelectrode arrays (Salavatian et al., 2019b; Yoshie et al., 2020). Spike sorting was performed via principal component analysis and k-means clustering analysis. Afterwards, individual neural activity time series were extracted to study temporal profile, calculate firing rates, and quantify firing patterns with respect to applied cardiac stressor times.

In more recent studies, neural recording technology has used 64-channel neural data distributed over eight "shanks" using penetrating high-density microarrays (Dale et al., 2020; Omura et al., 2021). These studies involved recording from the thoracic spinal cord which serves to integrate cardiac control through intraspinal reflexes. Apparent from **Table 1**, single-unit spinal cord recordings could pinpoint to a limited set of questions at a single experiment (Foreman et al., 2015), making knowledge transfer between expensive studies challenging. High-density multi-shank recordings are attractive for spinal cord research as these regions include multi-function neural populations and making it difficult to pinpoint neural activity related to cardiac control. Dale et al. (2020) used multi-shank recordings along with a number of stressors to reveal dorsal horn and sympathetic preganglionic cardiac neurons in a pig model. Principal component analysis yielded a total of 1760 identified spinal neurons, and T2 paravertebral ganglion stimulation was used to identify/activate cardiac sympathetic preganglionic neurons. Firing rate and correlation analyses were performed for neuron identification, and percentages of neurons responding to one or more stimuli were reported. Recently, a similar experimental setup and computational methods were used to study the effects of spinal anesthesia (bupivacaine) on spinal network interactions (Omura et al., 2021). Cardiac spinal neurons were identified based on their response to a wide range of interventions and bupivacaine was reported to have cardioprotective effects as it attenuates short-term coordination between local afferent-effect cardiac neurons in spinal cord.

SPIKE DETECTION AND SPIKE SORTING

Studies to date have utilized event-based analyses or snapshots of experimental data, which represent only 10% of the experimental data. Analysis of short duration event regions was possible with the use of semi-automated methods with conclusions limited to static analyses. However, development of an understanding of network interactions and space-time dynamics requires the continuous analysis of entire recordings separated into baseline and event epochs. This necessitates an order of magnitude increase in processing and has driven the construction of unsupervised spike detection and classification algorithms of large-scale datasets.

Lewicki (1998) provided the earliest exploration of the techniques and challenges encountered in spike detection and sorting from extracellular microelectrode recordings. Early spike detection was achieved via window discrimination and procedures are detailed for spike sorting based on principal component analysis and component clustering. More recent reviews (Rey et al., 2015; Lefebvre et al., 2016; Hennig et al., 2019) address common challenges and techniques that are moving closer to unsupervised algorithms needed for continuous analysis of large datasets. The algorithms are necessarily tailored to the context of specific applications and measurement equipment that present disparate features.

Our recent application is characterized by ensemble neural activity where individual neurons exhibit firing rates on the order of 1 Hz without bursting (Sudarshan et al., 2021). Neural activity detected farther from the multi-channel probe represents the superposition of attenuated activity. The superposition and attenuation eventually produce recorded signals that where individual action potentials cannot be recognized, and this is termed the "noise floor." A primary goal in analyzing multi-channel recordings is to assess network function and this is made possible by working close to the noise floor and increasing the number of recorded spikes through several orders of magnitude. We use an unsupervised approach where spikes are detected at iterated thresholds based on a competition between the number of positive and negative spikes detected at each iteration (Sudarshan et al., 2021). Regions containing spikes detected within an iteration are masked and rendered undetectable at later iterations. This approach allowed for detailed assessment of specificity over space and time of stellate ganglion population activity to specific cycles in cardiac and pulmonary dynamics during an experiment.

Following the detection of spikes, a typical spike sorting procedure involves extracting features from detected spikes and assigning them to unique clusters where each cluster would ideally represent activity from a single neuron. Rey et al. (2015) and Lefebvre et al. (2016) outlined procedures such as projection on basis functions, principal component analysis and wavelet analysis that are commonly used for feature extraction prior to clustering from detected spikes. Various clustering algorithms such as Gaussian mixtures, k-means, and density-based clustering were reviewed along with a template matching procedure for extracting activity from single neurons from the clusters. The major challenge in using these clustering methods to isolate the activity of specific neurons within a population remains the lack of an independent means to assess cluster validity. This problem is reviewed in (Foreman et al., 1975) with respect to validating spike sorting clusters with and without human-based or synthetic ground truth validations of sorted spikes. It is also explored in (Magland et al., 2020) where automated spike sorting pipelines are built for the low-dimensional spike sorting problem and compared to other approaches.

STUDY DESIGN AND DATA ANALYSIS CONSIDERATIONS

In this section, we address experimental issues that should be considered when designing and analyzing neural recording studies to probe the cardiac nervous system and a hierarchical closed-loop controller. **Table 1** lists these details for cardiac literature discussed previously.

Single-Unit vs Multi-Unit Recordings

The range of electrode technologies has also greatly diversified the type of collected neural signals. Single-unit tungsten or platinum wire single-unit electrodes have dominated the field until 2000s (Ja¨nig and Szulczyk, 1980; Armour, 1985; Boczek-Funcke et al., 1992; Armour et al., 1998). In recent years, multi-unit or multi-channel recordings have appeared in studies due to the availability of recording technologies (Beaumont et al., 2013; Dale et al., 2020; Sudarshan et al., 2021). Both single- and multi-unit electrodes have strengths and weaknesses depending on the experimental goals.

For single-unit recordings, the target neurons must be isolated and recording electrodes should be fine-tipped with low-impedance conductors for high quality recording. Single-unit recordings may record several isolated neurons with wire electrodes in separate nerve bundles (Boczek-Funcke et al., 1992). While large electrode arrays increase the amount of collected information per unit time, they may not provide sufficient isolation. The multi-unit signals involve recording of closest *neural populations*, rather than the closest single neuron. In the recent neuroscience literature, a shift in the experimental focus to interactions of neural populations and their ensemble behaviors (Yuste, 2015; Zamani Esfahlani et al., 2020) has led to the nearly exclusive use of multi-unit recordings.

Study reproducibility requires reporting details of electrode design, statistical analyses should consider the independence of data and the addition of electrode/neuron identity as covariates. Data collected from a multi-unit electrode array have more stringent methodological constraints compared to single-unit data analysis. Multi-unit recordings cannot be classified as independent if unit isolation was unassessed whereas multiple single-unit recordings may be considered independent datasets assuming isolated neurons are being recorded.

Reliance on Animal Models and Anesthesia

Open heart surgeries conducted in cardiac nervous system research studies require the use of anesthetic agents, a list of

agents have been listed in **Table 1**. In large animal models such as dogs and pigs, isoflurane inhalation followed by alpha-chloralose have been dominantly employed. Ideally, the agent should not restrict the scientific interpretation while providing stable experimental conditions showing an absence of depression of cardiovascular or autonomic activity which is a disadvantage in cardiac neural recordings.

The use of open chest preparations along with the application of anesthesia in terminal animal experiments inevitably biases both study results, interpretations, and any potential extension to humans. Yet, when experiments are tightly controlled, chronic animal model studies have been proven informative to study the nature of interactions among neural populations and their evolution from normal to pathological states. Collection of neural data from human cardiac nervous system is a more difficult and constrained task as the experiment with humans cannot be regarded as terminal. Translational failure may be explained by methodological flaws and inadequate data in animal studies. To avoid translational failure, publications should clearly indicate the study details. Systematic reviews and meta-analyses play substantial role in the selection of the most promising interpretations that could be extended to humans.

Sample Sizes and Statistical Power

There has been considerable concern surrounding reproducibility of small biomedical research datasets and contamination of literature with false positive reports due to publication pressure and lack of venues that encourage publication of negative results (Ioannidis, 2005; Button et al., 2013). This might be partly due to lack of planning in experimental design and reliance on the analysis of smaller studies compared to large clinical trials that involve dedicated personnel and a more thorough analysis. It is essential for investigators to describe number of animals, specifics of neural recording channels, neural type where relevant, along with power analyses for statistical significance and effect size for practical relevance. Effect size, a standardized measure that quantifies the size of difference or association between two groups, should be provided in addition to statistical significances to facilitate meta-analysis and reproducibility (Sullivan and Feinn, 2012).

Data and Code Sharing

Combined resources surpass the capacity of individual research laboratories or institutional efforts (Ascoli et al., 2017). To date, some effort has been made to enable data reusability such as NeuroMorpho.Org (Ascoli et al., 2007), Neurodata Without Borders (Teeters et al., 2015), and PhysioNet (Goldberger et al., 2000). An instrumental effort within the context of cardiac nervous system has been the National Institutes of Health (NIH) Common Fund's Stimulating Peripheral Activity to Relieve Conditions (SPARC) platform that encourages raw data sharing with proper labeling and a listing of computational methods/models (Osanlouy et al., 2021). In addition, computational techniques such as signal processing, machine learning, statistical analyses are central in data analysis and interpretation of results. Methods sections of research papers outline essential processing flows and mathematic/statistical information, but the complete linkage between raw data and the published results requires access to small scripts for statistical manipulations and to much larger routines used to process the raw data to a useable form. Public access to research codes, complete data pipelines used to construct all results is necessary for reproducibility, transparency of data/analysis assumptions, and the further development of software (Barnes, 2010; Ince et al., 2012).

CONCLUDING REMARKS

We are in an exciting period of study of the cardiac nervous system with the availability of high-density recording technologies and advances in open-source computational pipelines and data-analytic methods suitable for closed-loop systems. The neuroscience literature offers a wide range of novel analytical tools and interventions mostly related to open-loop brain recording studies. Such experimental designs have separated inputs and outputs (Yuste, 2015), which do not extend to cardiac studies where heart in open-loop mode would have no afferent feedback and is not experimentally realizable or meaningful. The presence of afferent signals in closed-loop mode implies that efferent cardiac inputs are returned via the afferent pathway from the heart and further affects the efferent input to the heart. In this sense, inputs and outputs are unseparated and this has necessitated the development of metrics suitable for the analysis of the dynamical state of closed-loop networked control.

The requirement to analyze continuous recordings instead of focusing on stimulus-evoked regions is driving the development of unsupervised algorithms for spike detection and classification due to a large increase in data. These analyses are leading to the discovery a highly nuanced interpretation of the neural network status in normal versus diseased states that is unavailable from event-based analyses.

Moreover, reproducibility requirements are more difficult to meet for multi-unit experimental designs where changes in probe placement, animal's autonomic status, surgical preparation, experimenter abilities, and genetic differences will lead to greater variability in experimental results. Designing elegant investigations that meet these reproducibility constraints, data, and method sharing supported by histological studies giving improved anatomical information are all required to further develop neurocardiology and improve clinical interventions.

AUTHOR CONTRIBUTIONS

NG, GK, JA, and OA conceptualized and planned the manuscript. NG, ST, and DL organized the literature. NG wrote the first draft of the manuscript. NG, KB, and GK wrote sections of the manuscript. All authors contributed to manuscript revision, read, and approved the submitted version.

FUNDING

This work was funded by the National Institutes of Health, Office of The Director DP2 OD024323-01 (OA), and U01EB025138 (GK), and National Heart Lung and Blood Institute HL159001 (OA). NG was funded by the NSF Engineering Fellows Postdoctoral Fellowship Award ID #2127509.

REFERENCES

Ajijola, O. A. (2016). Sudden Cardiac Death: We Are Not There yet. *Trends Cardiovasc. Med.* 26 (1), 34–35. doi:10.1016/j.tcm.2015.04.009

Ammons, W. S., Blair, R. W., and Foreman, R. D. (1984). Raphe Magnus Inhibition of Primate T1-T4 Spinothalamic Cells with Cardiopulmonary Visceral Input. *PAIN* 20 (3), 247–260. doi:10.1016/0304-3959(84)90014-9

Ammons, W. S., Blair, R. W., and Foreman, R. D. (1984). Greater Splanchnic Excitation of Primate T1-T5 Spinothalamic Neurons. *J. Neurophysiol.* 51 (3), 592–603. doi:10.1152/jn.1984.51.3.592

Ammons, W. S., Blair, R. W., and Foreman, R. D. (1983). Vagal Afferent Inhibition of Primate Thoracic Spinothalamic Neurons. *J. Neurophysiol.* 50 (4), 926–940. doi:10.1152/jn.1983.50.4.926

Ammons, W. S., Blair, R. W., and Foreman, R. D. (1983). Vagal Afferent Inhibition of Spinothalamic Cell Responses to Sympathetic Afferents and Bradykinin in the Monkey. *Circ. Res.* 53 (5), 603–612. doi:10.1161/01.RES.53.5.603

Ammons, W. S., and Foreman, R. D. (1984). Cardiovascular and T2-T4 Dorsal Horn Cell Responses to Gallbladder Distention in the Cat. *Brain Res.* 321 (2), 267–277. doi:10.1016/0006-8993(84)90179-3

Ammons, W. S., Girardot, M. N., and Foreman, R. D. (1985). Effects of Intracardiac Bradykinin on T2-T5 Medial Spinothalamic Cells. *Am. J. Physiology-Regulatory, Integr. Comp. Physiol.* 249 (2), R147–R152. doi:10.1152/ajpregu.1985.249.2.R147

Ammons, W. S., Girardot, M. N., and Foreman, R. D. (1985). T2-T5 Spinothalamic Neurons Projecting to Medial Thalamus with Viscerosomatic Input. *J. Neurophysiol.* 54 (1), 73–89. doi:10.1152/jn.1985.54.1.73

Ardell, J. L., Andresen, M. C., Armour, J. A., Billman, G. E., Chen, P.-S., Foreman, R. D., et al. (2016). Translational Neurocardiology: Preclinical Models and Cardioneural Integrative Aspects. *J. Physiol.* 594 (14), 3877–3909. doi:10.1113/JP271869

Ardell, J. L., Butler, C. K., Smith, F. M., Hopkins, D. A., and Armour, J. A. (1991). Activity of *In Vivo* Atrial and Ventricular Neurons in Chronically Decentralized Canine Hearts. *Am. J. Physiology-Heart Circulatory Physiol.* 260 (3), H713–H721. doi:10.1152/ajpheart.1991.260.3.H713

Ardell, J. L., Cardinal, R., Vermeulen, M., and Armour, J. A. (2009). Dorsal Spinal Cord Stimulation Obtunds the Capacity of Intrathoracic Extracardiac Neurons to Transduce Myocardial Ischemia. *Am. J. Physiology-Regulatory, Integr. Comp. Physiol.* 297 (2), R470–R477. doi:10.1152/ajpregu.90821.2008

Armour, J. A. (1985). Activity of *In Situ* Middle Cervical Ganglion Neurons in Dogs, Using Extracellular Recording Techniques. *Can. J. Physiol. Pharmacol.* 63 (6), 704–716. doi:10.1139/y85-116

Armour, J. A. (1986). Activity of *In Situ* Stellate Ganglion Neurons of Dogs Recorded Extracellularly. *Can. J. Physiol. Pharmacol.* 64 (2), 101–111. doi:10.1139/y86-016

Armour, J. A. (2004). Cardiac Neuronal Hierarchy in Health and Disease. *Am. J. Physiology-Regulatory, Integr. Comp. Physiol.* 287 (2), R262–R271. doi:10.1152/ajpregu.00183.2004

Armour, J. A., Collier, K., Kember, G., and Ardell, J. L. (1998). Differential Selectivity of Cardiac Neurons in Separate Intrathoracic Autonomic Ganglia. *Am. J. Physiology-Regulatory, Integr. Comp. Physiol.* 274 (4), R939–R949. doi:10.1152/ajpregu.1998.274.4.R939

Armour, J. A. (1983). Synaptic Transmission in the Chronically Decentralized Middle Cervical and Stellate Ganglia of the Dog. *Can. J. Physiol. Pharmacol.* 61 (10), 1149–1155. doi:10.1139/y83-171

Ascoli, G. A., Donohue, D. E., and Halavi, M. (2007). NeuroMorpho.Org: A Central Resource for Neuronal Morphologies. *J. Neurosci.* 27 (35), 9247–9251. doi:10.1523/JNEUROSCI.2055-07.2007

Ascoli, G. A., Maraver, P., Nanda, S., Polavaram, S., and Armañanzas, R. (2017). Win-win Data Sharing in Neuroscience. *Nat. Methods* 14 (2), 112–116. doi:10.1038/nmeth.4152

Barnes, N. (2010). Publish Your Computer Code: it Is Good Enough. *Nature* 467 (7317), 753. doi:10.1038/467753a

Beaumont, E., Salavatian, S., Southerland, E. M., Vinet, A., Jacquemet, V., Armour, J. A., et al. (2013). Network Interactions within the Canine Intrinsic Cardiac Nervous System: Implications for Reflex Control of Regional Cardiac Function. *J. Physiol.* 591 (18), 4515–4533. doi:10.1113/jphysiol.2013.259382

Blair, R. W., Ammons, W. S., and Foreman, R. D. (1984). Responses of Thoracic Spinothalamic and Spinoreticular Cells to Coronary Artery Occlusion. *J. Neurophysiol.* 51 (4), 636–648. doi:10.1152/jn.1984.51.4.636

Blair, R. W., Weber, R. N., and Foreman, R. D. (1981). Characteristics of Primate Spinothalamic Tract Neurons Receiving Viscerosomatic Convergent Inputs in T3-T5 Segments. *J. Neurophysiol.* 46 (4), 797–811. doi:10.1152/jn.1981.46.4.797

Blair, R. W., Weber, R. N., and Foreman, R. D. (1984). Responses of Thoracic Spinoreticular and Spinothalamic Cells to Intracardiac Bradykinin. *Am. J. Physiology-Heart Circulatory Physiol.* 246 (4), H500–H507. doi:10.1152/ajpheart.1984.246.4.H500

Blair, R. W., Weber, R. N., and Foreman, R. D. (1982). Responses of Thoracic Spinothalamic Neurons to Intracardiac Injection of Bradykinin in the Monkey. *Circ. Res.* 51 (1), 83–94. doi:10.1161/01.RES.51.1.83

Boczek-Funcke, A., Dembowsky, K., Häbler, H.-J., Jänig, W., and Michaelis, M. (1993). Spontaneous Activity, Conduction Velocity and Segmental Origin of Different Classes of Thoracic Preganglionic Neurons Projecting into the Cat Cervical Sympathetic Trunk. *J. Auton. Nervous Syst.* 43 (3), 189–200. doi:10.1016/0165-1838(93)90325-O

Boczek-Funcke, A., Dembowsky, K., Häbler, H. J., Jänig, W., McAllen, R. M., and Michaelis, M. (1992). Classification of Preganglionic Neurones Projecting into the Cat Cervical Sympathetic Trunk. *J. Physiol.* 453, 319–339. doi:10.1113/jphysiol.1992.sp019231

Bolser, D. C., Chandler, M. J., Garrison, D. W., and Foreman, R. D. (1989). Effects of Intracardiac Bradykinin and Capsaicin on Spinal and Spinoreticular Neurons. *Am. J. Physiology-Heart Circulatory Physiol.* 257 (5), H1543–H1550. doi:10.1152/ajpheart.1989.257.5.H1543

Brennan, T. J., Oh, U. T., Girardot, M.-N., Steve Ammons, W., and Foreman, R. D. (1987). Inhibition of Cardiopulmonary Input to Thoracic Spinothalamic Tract Cells by Stimulation of the Subcoeruleus-Parabrachial Region in the Primate. *J. Auton. Nervous Syst.* 18 (1), 61–72. doi:10.1016/0165-1838(87)90135-4

Button, K. S., Ioannidis, J. P. A., Mokrysz, C., Nosek, B. A., Flint, J., Robinson, E. S. J., et al. (2013). Power Failure: Why Small Sample Size Undermines the Reliability of Neuroscience. *Nat. Rev. Neurosci.* 14 (5), 365–376. doi:10.1038/nrn3475

Chandler, M. J., Hobbs, S. F., Bolser, D. C., and Foreman, R. D. (1991). Effects of Vagal Afferent Stimulation on Cervical Spinothalamic Tract Neurons in Monkeys. *PAIN* 44 (1), 81–87. doi:10.1016/0304-3959(91)90152-n

Chandler, M. J., Zhang, J., Qin, C., and Foreman, R. D. (2002). Spinal Inhibitory Effects of Cardiopulmonary Afferent Inputs in Monkeys: Neuronal Processing in High Cervical Segments. *J. Neurophysiol.* 87 (3), 1290–1302. doi:10.1152/jn.00079.2001

Chandler, M. J., Zhang, J., Qin, C., Yuan, Y., and Foreman, R. D. (2000). Intrapericardiac Injections of Algogenic Chemicals Excite Primate C1-C2 Spinothalamic Tract Neurons. *Am. J. Physiology-Regulatory, Integr. Comp. Physiol.* 279 (2), R560–R568. doi:10.1152/ajpregu.2000.279.2.R560

Dale, E. A., Kipke, J., Kubo, Y., Sunshine, M. D., Castro, P. A., Ardell, J. L., et al. (2020). Spinal Cord Neural Network Interactions: Implications for Sympathetic Control of the Porcine Heart. *Am. J. Physiology-Heart Circulatory Physiol.* 318 (4), H830–H839. doi:10.1152/ajpheart.00635.2019

Foreman, R. D., Applebaum, A. E., Beall, J. E., Trevino, D. L., and Willis, W. D. (1975). Responses of Primate Spinothalamic Tract Neurons to Electrical Stimulation of Hindlimb Peripheral Nerves. *J. Neurophysiol.* 38 (1), 132–145. doi:10.1152/jn.1975.38.1.132

Foreman, R. D., Blair, R. W., and Neal Weber, R. (1984). Viscerosomatic Convergence onto T2-T4 Spinoreticular, Spinoreticular-Spinothalamic, and Spinothalamic Tract Neurons in the Cat. *Exp. Neurol.* 85 (3), 597–619. doi:10.1016/0014-4886(84)90034-7

Foreman, R. D., Garrett, K. M., and Blair, R. W. (2015). Mechanisms of Cardiac Pain. *Compr. Physiol.* 61, 929–960. doi:10.1002/cphy.c14003210.1002/cphy.c140032

Foreman, R. D., and Qin, C. (2009). Neuromodulation of Cardiac Pain and Cerebral Vasculature: Neural Mechanisms. *Ccjm* 76 (4), S75–S79. doi:10.3949/ccjm.76.s2.15

Fuchs, F. D., and Whelton, P. K. (2020). High Blood Pressure and Cardiovascular Disease. *Hypertension* 75 (2), 285–292. doi:10.1161/HYPERTENSIONAHA.119.14240

Gagliardi, M., Randall, W. C., Bieger, D., Wurster, R. D., Hopkins, D. A., and Armour, J. A. (1988). Activity of *In Vivo* Canine Cardiac Plexus Neurons. *Am.*

J. Physiology-Heart Circulatory Physiol. 255 (4), H789–H800. doi:10.1152/ajpheart.1988.255.4.H789

Girardot, M.-N., Brennan, T. J., Martindale, M. E., and Foreman, R. D. (1987). Effects of Stimulating the Subcoeruleus-Parabrachial Region on the Non-noxious and Noxious Responses of T1-T5 Spinothalamic Tract Neurons in the Primate. *Brain Res.* 409 (1), 19–30. doi:10.1016/0006-8993(87)90737-2

Goldberger, A. L., Amaral, L. A. N., Glass, L., Hausdorff, J. M., Ivanov, P. C., Mark, R. G., et al. (2000). PhysioBank, PhysioToolkit, and PhysioNet. *Circulation* 101 (23), e215–e220. doi:10.1161/01.CIR.101.23.e215

Goodman-Keiser, M. D., Qin, C., Thompson, A. M., and Foreman, R. D. (2010). Upper Thoracic Postsynaptic Dorsal Column Neurons Conduct Cardiac Mechanoreceptive Information, but Not Cardiac Chemical Nociception in Rats. *Brain Res.* 1366, 71–84. doi:10.1016/j.brainres.2010.09.058

Grassi, G., D'Arrigo, G., Pisano, A., Bolignano, D., Mallamaci, F., Dell'Oro, R., et al. (2019). Sympathetic Neural Overdrive in Congestive Heart Failure and its Correlates: Systematic Reviews and Meta-Analysis. *J. Hypertens.* 37 (9), 1746–1756. doi:10.1097/HJH.0000000000002093

Hanna, P., Dacey, M. J., Brennan, J., Moss, A., Robbins, S., Achanta, S., et al. (2021). Innervation and Neuronal Control of the Mammalian Sinoatrial Node a Comprehensive Atlas. *Circ. Res.* 128 (9), 1279–1296. doi:10.1161/CIRCRESAHA.120.318458

Hennig, M. H., Hurwitz, C., and Sorbaro, M. (2019). "Scaling Spike Detection and Sorting for Next-Generation Electrophysiology," in In Vitro *Neuronal Networks: From Culturing Methods to Neuro-Technological Applications*. Editors M. Chiappalone, V. Pasquale, and M. Frega (Cham: Springer International Publishing), 171–184. doi:10.1007/978-3-030-11135-9_7

Hirooka, Y. (2010). Brain Perivascular Macrophages and Central Sympathetic Activation after Myocardial Infarction. *Hypertension* 55 (3), 610–611. doi:10.1161/HYPERTENSIONAHA.109.145128

Hobbs, S. F., Oh, U. T., Chandler, M. J., and Foreman, R. D. (1989). Cardiac and Abdominal Vagal Afferent Inhibition of Primate T9-S1 Spinothalamic Cells. *Am. J. Physiology-Regulatory, Integr. Comp. Physiol.* 257 (4), R889–R895. doi:10.1152/ajpregu.1989.257.4.R889

Huikuri, H. V., and Stein, P. K. (2013). Heart Rate Variability in Risk Stratification of Cardiac Patients. *Prog. Cardiovasc. Dis.* 56 (2), 153–159. doi:10.1016/j.pcad.2013.07.003

Hyun-Chool Shin, H., Aggarwal, V., Acharya, S., Schieber, M. H., and Thakor, N. V. (2010). Neural Decoding of Finger Movements Using Skellam-Based Maximum-Likelihood Decoding. *IEEE Trans. Biomed. Eng.* 57 (3), 754–760. doi:10.1109/TBME.2009.2020791

Ince, D. C., Hatton, L., and Graham-Cumming, J. (2012). The Case for Open Computer Programs. *Nature* 482 (7386), 485–488. doi:10.1038/nature10836

Ioannidis, J. P. A. (2005). Why Most Published Research Findings Are False. *Plos Med.* 2 (8), e124. doi:10.1371/journal.pmed.0020124

Ja¨nig, W., and Szulczyk, P. (1980). Functional Properties of Lumbar Preganglionic Neurones. *Brain Res.* 186 (1), 115–131. doi:10.1016/0006-8993(80)90259-0

Jones, C. M., Quinn, M. S., and Minisi, A. J. (2008). Reflex Control of Sympathetic Outflow and Depressed Baroreflex Sensitivity Following Myocardial Infarction. *Auton. Neurosci.* 141 (1), 46–53. doi:10.1016/j.autneu.2008.05.001

Kember, G., Armour, J. A., and Zamir, M. (2013). Neural Control Hierarchy of the Heart Has Not Evolved to deal with Myocardial Ischemia. *Physiol. Genomics* 45 (15), 638–644. doi:10.1152/physiolgenomics.00027.2013

Leenen, F. H. H. (2007). Brain Mechanisms Contributing to Sympathetic Hyperactivity and Heart Failure. *Circ. Res.* 101 (3), 221–223. doi:10.1161/CIRCRESAHA.107.158261

Lefebvre, B., Yger, P., and Marre, O. (2016). Recent Progress in Multi-Electrode Spike Sorting Methods. *J. Physiology-Paris* 110 (4), 327–335. Part A. doi:10.1016/j.jphysparis.2017.02.005

Lewicki, M. S. (1998). A Review of Methods for Spike Sorting: the Detection and Classification of Neural Action Potentials. *Netw. Comput. Neural Syst.* 9 (4), R53–R78. doi:10.1088/0954-898x_9_4_001

Little, J. M., Qin, C., Farber, J. P., and Foreman, R. D. (2011). Spinal Cord Processing of Cardiac Nociception: Are There Sex Differences between Male and Proestrous Female Rats? *Brain Res.* 1413, 24–31. doi:10.1016/j.brainres.2011.07.036

Magland, J., Jun, J. J., Lovero, E., Morley, A. J., Hurwitz, C. L., Buccino, A. P., et al. (2020). SpikeForest, Reproducible Web-Facing Ground-Truth Validation of Automated Neural Spike Sorters. *eLife* 9, e55167. doi:10.7554/eLife.55167

Mitrani, R. D., and Myerburg, R. J. (2016). Ten Advances Defining Sudden Cardiac Death. *Trends Cardiovasc. Med.* 26 (1), 23–33. doi:10.1016/j.tcm.2015.03.017

Moss, A., Robbins, S., Achanta, S., Kuttippurathu, L., Turick, S., Nieves, S., et al. (2021). A Single Cell Transcriptomics Map of Paracrine Networks in the Intrinsic Cardiac Nervous System. *iScience* 24 (7), 102713. doi:10.1016/j.isci.2021.102713

Omura, Y., Kipke, J. P., Salavatian, S., Afyouni, A. S., Wooten, C., Herkenham, R. F., et al. (2021). Spinal Anesthesia Reduces Myocardial Ischemia-Triggered Ventricular Arrhythmias by Suppressing Spinal Cord Neuronal Network Interactions in Pigs. *Anesthesiology* 134 (3), 405–420. doi:10.1097/ALN.0000000000003662

Osanlouy, M., Bandrowski, A., de Bono, B., Brooks, D., Cassarà, A. M., Christie, R., et al. (2021). The SPARC DRC: Building a Resource for the Autonomic Nervous System Community. *Front. Physiol.* 12, 929. doi:10.3389/fphys.2021.693735

Pan, H., Hibino, M., Kobeissi, E., and Aune, D. (2020). Blood Pressure, Hypertension and the Risk of Sudden Cardiac Death: a Systematic Review and Meta-Analysis of Cohort Studies. *Eur. J. Epidemiol.* 35 (5), 443–454. doi:10.1007/s10654-019-00593-4

Qin, C., Chandler, M. J., and Foreman, R. D. (2004). Esophagocardiac Convergence onto Thoracic Spinal Neurons: Comparison of Cervical and Thoracic Esophagus. *Brain Res.* 1008 (2), 193–197. doi:10.1016/j.brainres.2003.12.056

Qin, C., Chandler, M. J., Jou, C. J., and Foreman, R. D. (2004). Responses and Afferent Pathways of C1-C2 Spinal Neurons to Cervical and Thoracic Esophageal Stimulation in Rats. *J. Neurophysiol.* 91 (5), 2227–2235. doi:10.1152/jn.00971.2003

Qin, C., Chandler, M. J., Miller, K. E., and Foreman, R. D. (2003). Chemical Activation of Cardiac Receptors Affects Activity of Superficial and Deeper T3-T4 Spinal Neurons in Rats. *Brain Res.* 959 (1), 77–85. doi:10.1016/S0006-8993(02)03728-9

Qin, C., Chandler, M. J., Miller, K. E., and Foreman, R. D. (2001). Responses and Afferent Pathways of Superficial and Deeper C1-C2 Spinal Cells to Intrapericardial Algogenic Chemicals in Rats. *J. Neurophysiol.* 85 (4), 1522–1532. doi:10.1152/jn.2001.85.4.1522

Qin, C., Farber, J. P., and Foreman, R. D. (2008). Intraesophageal Chemicals Enhance Responsiveness of Upper Thoracic Spinal Neurons to Mechanical Stimulation of Esophagus in Rats. *Am. J. Physiology-Gastrointestinal Liver Physiol.* 294 (3), G708–G716. doi:10.1152/ajpgi.00477.2007

Qin, C., Farber, J. P., Miller, K. E., and Foreman, R. D. (2006). Responses of Thoracic Spinal Neurons to Activation and Desensitization of Cardiac TRPV1-Containing Afferents in Rats. *Am. J. Physiology-Regulatory, Integr. Comp. Physiol.* 291 (6), R1700–R1707. doi:10.1152/ajpregu.00231.2006

Qin, C., Foreman, R. D., and Farber, J. P. (2007). Characterization of Thoracic Spinal Neurons with Noxious Convergent Inputs from Heart and Lower Airways in Rats. *Brain Res.* 1141, 84–91. doi:10.1016/j.brainres.2007.01.015

Qin, C., Greenwood-Van Meerveld, B., and Foreman, R. D. (2003). Spinal Neuronal Responses to Urinary Bladder Stimulation in Rats with Corticosterone or Aldosterone onto the Amygdala. *J. Neurophysiol.* 90 (4), 2180–2189. doi:10.1152/jn.00298.2003

Qin, C., Greenwood-Van Meerveld, B., Myers, D. A., and Foreman, R. D. (2003). Corticosterone Acts Directly at the Amygdala to Alter Spinal Neuronal Activity in Response to Colorectal Distension. *J. Neurophysiol.* 89 (3), 1343–1352. doi:10.1152/jn.00834.2002

Qin, C., Kranenburg, A., and Foreman, R. D. (2004). Descending Modulation of Thoracic Viscероreceptive Transmission by C1-C2 Spinal Neurons. *Auton. Neurosci.* 114 (1), 11–16. doi:10.1016/j.autneu.2004.05.009

Qin, C., Malykhina, A. P., Thompson, A. M., Farber, J. P., and Foreman, R. D. (2010). Cross-organ Sensitization of Thoracic Spinal Neurons Receiving Noxious Cardiac Input in Rats with Gastroesophageal Reflux. *Am. J. Physiology-Gastrointestinal Liver Physiol.* 298 (6), G934–G942. doi:10.1152/ajpgi.00312.2009

Rajendran, P. S., Challis, R. C., Fowlkes, C. C., Hanna, P., Tompkins, J. D., Jordan, M. C., et al. (2019). Identification of Peripheral Neural Circuits that Regulate Heart Rate Using Optogenetic and Viral Vector Strategies. *Nat. Commun.* 10 (1), 1944. doi:10.1038/s41467-019-09770-1

Rey, H. G., Pedreira, C., and Quian Quiroga, R. (2015). Past, Present and Future of Spike Sorting Techniques. *Brain Res. Bull.* 119, 106–117. doi:10.1016/j.brainresbull.2015.04.007

Salavatian, S., Ardell, S. M., Hammer, M., Gibbons, D., Armour, J. A., and Ardell, J. L. (2019). Thoracic Spinal Cord Neuromodulation Obtunds Dorsal Root Ganglion Afferent Neuronal Transduction of the Ischemic Ventricle. *Am. J. Physiology-Heart Circulatory Physiol.* 317 (5), H1134–H1141. doi:10.1152/ajpheart.00257.2019

Salavatian, S., Yamaguchi, N., Hoang, J., Lin, N., Patel, S., Ardell, J. L., et al. (2019). Premature Ventricular Contractions Activate Vagal Afferents and Alter Autonomic Tone: Implications for Premature Ventricular Contraction-Induced Cardiomyopathy. *Am. J. Physiology-Heart Circulatory Physiol.* 317 (3), H607–H616. doi:10.1152/ajpheart.00286.2019

Scherbakov, N., and Doehner, W. (2018). Heart-brain Interactions in Heart Failure. *Card. Fail. Rev.* 4 (2), 87–91. doi:10.15420/cfr.2018.14.2

Sessa, F., Anna, V., Messina, G., Cibelli, G., Monda, V., Marsala, G., et al. (2018). Heart Rate Variability as Predictive Factor for Sudden Cardiac Death. *Aging* 10 (2), 166–177. doi:10.18632/aging.101386

Shivkumar, K., Ajijola, O. A., Anand, I., Armour, J. A., Chen, P.-S., Esler, M., et al. (2016). Clinical Neurocardiology Defining the Value of Neuroscience-Based Cardiovascular Therapeutics. *J. Physiol.* 594 (14), 3911–3954. doi:10.1113/JP271870

Smith, F. M., McGuirt, A. S., Hoover, D. B., Armour, J. A., and Ardell, J. L. (2001). Chronic Decentralization of the Heart Differentially Remodels Canine Intrinsic Cardiac Neuron Muscarinic Receptors. *Am. J. Physiology-Heart Circulatory Physiol.* 281 (5), H1919–H1930. doi:10.1152/ajpheart.2001.281.5.H1919

Smith, F. M., McGuirt, A. S., Leger, J., Armour, J. A., and Ardell, J. L. (2001). Effects of Chronic Cardiac Decentralization on Functional Properties of Canine Intracardiac Neurons *In Vitro*. *Am. J. Physiology-Regulatory, Integr. Comp. Physiol.* 281 (5), R1474–R1482. doi:10.1152/ajpregu.2001.281.5.R1474

Sudarshan, K. B., Hori, Y., Swid, M. A., Karavos, A. C., Wooten, C., Armour, J. A., et al. (2021). A Novel Metric Linking Stellate Ganglion Neuronal Population Dynamics to Cardiopulmonary Physiology. *Am. J. Physiology-Heart Circulatory Physiol.* 321, H369–H381. doi:10.1152/ajpheart.00138.2021

Sullivan, G. M., and Feinn, R. (2012). Using Effect Size-Or Why the P Value Is Not Enough. *J. Grad Med. Educ.* 4 (3), 279–282. doi:10.4300/JGME-D-12-00156.1

Teeters, J. L., Godfrey, K., Young, R., Dang, C., Friedsam, C., Wark, B., et al. (2015). Neurodata without Borders: Creating a Common Data Format for Neurophysiology. *Neuron* 88 (4), 629–634. doi:10.1016/j.neuron.2015.10.025

Yoshie, K., Rajendran, P. S., Massoud, L., Mistry, J., Swid, M. A., Wu, X., et al. (2020). Cardiac TRPV1 Afferent Signaling Promotes Arrhythmogenic Ventricular Remodeling after Myocardial Infarction. *JCI Insight* 5 (3), 02–132020. doi:10.1172/jci.insight.124477

Yuste, R. (2015). From the Neuron Doctrine to Neural Networks. *Nat. Rev. Neurosci.* 16 (8), 487–497. doi:10.1038/nrn3962

Zamani Esfahlani, F., Jo, Y., Faskowitz, J., Byrge, L., Kennedy, D. P., Sporns, O., et al. (2020). High-amplitude Cofluctuations in Cortical Activity Drive Functional Connectivity. *Proc. Natl. Acad. Sci. U.S.A.* 117 (45), 28393–28401. doi:10.1073/pnas.2005531117

Zhang, D., Shen, X., and Qi, X. (2016). Resting Heart Rate and All-Cause and Cardiovascular Mortality in the General Population: a Meta-Analysis. *Cmaj* 188 (3), E53–E63. doi:10.1503/cmaj.150535

Zhang, J., Chandler, M. J., and Foreman, R. D. (2003). Cardiopulmonary Sympathetic and Vagal Afferents Excite C1-C2 Propriospinal Cells in Rats. *Brain Res.* 969 (1), 53–58. doi:10.1016/S0006-8993(03)02277-7

Zhang, J., Chandler, M. J., Miller, K. E., and Foreman, R. D. (1997). Cardiopulmonary Sympathetic Afferent Input Does Not Require Dorsal Column Pathways to Excite C1-C3 Spinal Cells in Rats. *Brain Res.* 771 (1), 25–30. doi:10.1016/S0006-8993(97)00607-0

Conflict of Interest: University of California, Los Angeles has patents relating to cardiac neural diagnostics and therapeutics. OA is a co-founder of NeuCures, Inc.

The remaining authors declare that the research was conducted in the absence of any commercial or financial relationships that could be construed as a potential conflict of interest.

Publisher's Note: All claims expressed in this article are solely those of the authors and do not necessarily represent those of their affiliated organizations or those of the publisher, the editors, and the reviewers. Any product that may be evaluated in this article, or claim that may be made by its manufacturer, is not guaranteed or endorsed by the publisher.

frontiers | Frontiers in Physiology

ORIGINAL RESEARCH
published: 09 May 2022
doi: 10.3389/fphys.2022.838038

Dyssynchronous Left Ventricular Activation is Insufficient for the Breakdown of Wringing Rotation

Tobias Gerach[1], Stephanie Appel[1], Jacek Wilczek[2,3], Krzysztof S. Golba[2,3], Tomasz Jadczyk[4,5] and Axel Loewe[1]*

[1]Institute of Biomedical Engineering, Karlsruhe Institute of Technology (KIT), Karlsruhe, Germany, [2]Department of Electrocardiology, Upper-Silesian Heart Center, Katowice, Poland, [3]Department of Electrocardiology and Heart Failure, Medical University of Silesia, Katowice, Poland, [4]Division of Cardiology and Structural Heart Diseases, Medical University of Silesia, Katowice, Poland, [5]Interventional Cardiac Electrophysiology Group, International Clinical Research Center, St. Anne's University Hospital, Brno, Czech Republic

Cardiac resynchronization therapy is a valuable tool to restore left ventricular function in patients experiencing dyssynchronous ventricular activation. However, the non-responder rate is still as high as 40%. Recent studies suggest that left ventricular torsion or specifically the lack thereof might be a good predictor for the response of cardiac resynchronization therapy. Since left ventricular torsion is governed by the muscle fiber orientation and the heterogeneous electromechanical activation of the myocardium, understanding the relation between these components and the ability to measure them is vital. To analyze if locally altered electromechanical activation in heart failure patients affects left ventricular torsion, we conducted a simulation study on 27 personalized left ventricular models. Electroanatomical maps and late gadolinium enhanced magnetic resonance imaging data informed our in-silico model cohort. The angle of rotation was evaluated in every material point of the model and averaged values were used to classify the rotation as clockwise or counterclockwise in each segment and sector of the left ventricle. 88% of the patient models ($n = 24$) were classified as a wringing rotation and 12% ($n = 3$) as a rigid-body-type rotation. Comparison to classification based on *in vivo* rotational NOGA XP maps showed no correlation. Thus, isolated changes of the electromechanical activation sequence in the left ventricle are not sufficient to reproduce the rotation pattern changes observed *in vivo* and suggest that further patho-mechanisms are involved.

Keywords: cardiac mechanics, finite element simulation, electromechanical mapping, wringing, torsion, Lagrangian particle tracking, NOGA XP

OPEN ACCESS

Edited by:
Ovidiu Constantin Baltatu, Anhembi Morumbi University, Brazil

Reviewed by:
Lorenzo Fassina, University of Pavia, Italy
Simone Pezzuto, University of Italian Switzerland, Switzerland
Angela Lee, King's College London, United Kingdom

****Correspondence:***
Tobias Gerach
publications@ibt.kit.edu

Specialty section:
This article was submitted to Integrative Physiology, a section of the journal Frontiers in Physiology

Received: *17 December 2021*
Accepted: *14 April 2022*
Published: *09 May 2022*

Citation:
Gerach T, Appel S, Wilczek J, Golba KS, Jadczyk T and Loewe A (2022) Dyssynchronous Left Ventricular Activation is Insufficient for the Breakdown of Wringing Rotation. Front. Physiol. 13:838038. doi: 10.3389/fphys.2022.838038

1 INTRODUCTION

In the healthy human heart, left ventricular (LV) ejection and filling is supported by the twisting and untwisting of the ventricle during systole and diastole, respectively. This twisting or wringing motion is determined by several anatomical and physiological features such as age, contractility, structure of the myocardium, and muscle fiber orientation (Omar et al., 2015). Furthermore, the electrical activation pattern of the LV is heterogeneous due to the His-Purkinje system and the anisotropic conduction of the electrical potential (Sengupta et al., 2007). Consequently, the activation pattern of the LV follows an endocardial to epicardial direction. Combined with the counter-directional helical arrangement of the endo- and

epicardial muscle fibers, this results in a clockwise and counterclockwise rotation of the basal and apical segments, respectively.

In pathological cases, this wringing motion of the LV can be disrupted by dyssynchronous mechancial activation resulting in a reduced LV ejection fraction (EF) (Rüssel and Götte, 2011). Dyssynchrony may originate from different sources such as an abnormal electrical activation in patients with left bundle branch block (LBBB) or post-ischemic remodeling and geometric alterations in heart failure patients (Sillanmäki et al., 2018; Paoletti Perini et al., 2016). Multiple studies confirmed changes in LV rotational behavior in heart failure patients using MRI tagging and speckle tracking echocardiography (Popescu et al., 2009; van Dalen et al., 2008a; Sade et al., 2008; Rüssel et al., 2009a). Setser et al. (2003) specifically observed rigid-body type (RBT) rotation in patients with end-stage heart failure, meaning apical and basal segments were rotating in the same direction. Cardiac resynchronization therapy (CRT) with an implanted device is often used in patients showing ventricular dyssynchrony in an attempt to restore LV EF. However, around 30–40% of patients do not respond to this kind of intervention (Daubert et al., 2012). One reason might be a bad choice for the pacing site (Leclercq et al., 2019). Therefore, it is important to optimize CRT parameters for each patient and LV rotation has become increasingly important for this purpose (Rüssel et al., 2009b).

Jadczyk et al. (2021) investigated electromechanical coupling and scar tissue burden with respect to rotational patterns observed in patients showing heart failure with reduced ejection fraction (HFrEF) and LBBB. In their cohort of 30 patients, they found six cases showing normal wringing rotation and 24 cases showing RBT rotation. They concluded that remodeling changes the physiological gradient in electromechanical activation, which causes regional delays in mechanical activation and thus dyssynchronous contraction of the LV. In contrast, following a physiological propagation of electrical and mechanical activation, an intact electromechanical coupling (with constant electromechanical delay) will result in a wringing motion. However, due to the small number of study participants the results by Jadczyk et al. (2021) should be considered with caution. To elucidate the role of the different contributing mechanisms suggested by Jadczyk et al. (2021), we performed an in silico study under controlled conditions informed by their *in vivo* electromechanical mapping data. Specifically, we hypothesized that the altered electrical activation pattern is sufficient to change wringing rotation to RBT. Spatiotemporal electromechanical parameters including local activation time (LAT), local rotational electromechanical delay (LEMD), and total rotational electro-mechanical delay (TEMD) were combined with local scar burden derived from late-gadolinium-enhanced cardiac magnetic resonance imaging (LGE-MRI) and incorporated into the LV model. LV rotational patterns are analyzed and classified into two groups defined as normal wringing rotation and RBT. Finally, the classification based on the simulation results is compared to the clinical classification.

2 MATERIALS AND METHODS

2.1 Anatomical Finite Element Model

As a representation of the LV, we used a truncated ellipsoid with varying wall thickness. The wall thickness changes from 7 mm at the base to 3.5 mm at the apex. With a sphericity index of 1.58, the ellipsoid has a similar shape as the left ventricles of the patient cohort in Jadczyk et al. (2021). The meshes were created in Gmsh (Geuzaine and Remacle, 2009) using a fully parameterized workflow. Spatial discretization was done using the finite element method with a total of 9,237 quadratic tetrahedral elements (P2) for the LV with 53,019 degrees of freedom. Based on spatial convergence results presented in a previous study (Gerach et al., 2021, Supplement Section 2.3.2) on a similar LV geometry, this should be sufficient to reduce numerical errors to a minimum.

We applied a rule-based method based on Bayer et al. (2012)[1] to generate the local fiber and sheet architecture $\mathbf{Q} = \{\mathbf{f}_0, \mathbf{s}_0, \mathbf{n}_0\}$ of the myocardium with fiber angles of 60°at the endocardium and -60°at the epicardium (**Figure 1**) in agreement with observations from diffusion tensor MRI of human hearts (Lombaert et al., 2012). Furthermore, we computed ventricular coordinates according to Schuler et al. (2021) and used them to separate the ventricle into the 17 segments classified by the American Heart Association (AHA; Cerqueira et al., 2002). The nine segments used by the NOGA XP system (Biosense Webster, Irvine, CA, United States) were defined equally. The NOGA XP segmentation consists of four basal segments (basoseptal, basolateral, posterobasal, anterobasal), four mid-ventricular segments (midseptal, midlateral, midposterior, midanterior), and one apical segment.

2.2 Electromechanical Computational Model

The kinematics of the LV are determined by solving the governing equation for the balance of linear momentum:

$$\rho_0 \partial_t^2 \mathbf{u} - \nabla \cdot (\mathbf{F}\,\mathbf{S}(\mathbf{u}, T_a)) = \mathbf{0} \text{ in } \quad \Omega_0 \times (0, T), \tag{1}$$

$$\mathbf{F}\,\mathbf{S}(\mathbf{u}, T_a)\mathbf{N} = -k_{\text{epi}} g(\mathbf{u})\mathbf{N} \text{ on } \quad \Gamma_0^{\text{epi}} \times (0, T), \tag{2}$$

$$\mathbf{F}\,\mathbf{S}(\mathbf{u}, T_a)\mathbf{N} = -p_{\text{LV}}(t) J \mathbf{F}^{-T}\mathbf{N} \text{ on } \quad \Gamma_0^{\text{endo}} \times (0, T), \tag{3}$$

$$\partial_t \mathbf{v}(t) = \mathcal{C}\big(t, \mathbf{v}, \mathbf{z}, p_{\text{LV}}(t)\big), \tag{4}$$

$$V_{\text{LV}}^{\text{0D}}(t) = V_{\text{LV}}^{\text{3D}}(t), \tag{5}$$

where we denote $\mathbf{F} = \mathbf{I} + \nabla \mathbf{u}$ as the deformation gradient tensor with the displacement of the myocardium $\mathbf{u}$, $J = \det(\mathbf{F})$ as the Jacobian, and ρ_0 as the density in the reference configuration.

[1]This implementation of the algorithm was used: https://doi.org/10.5281/zenodo.4606575

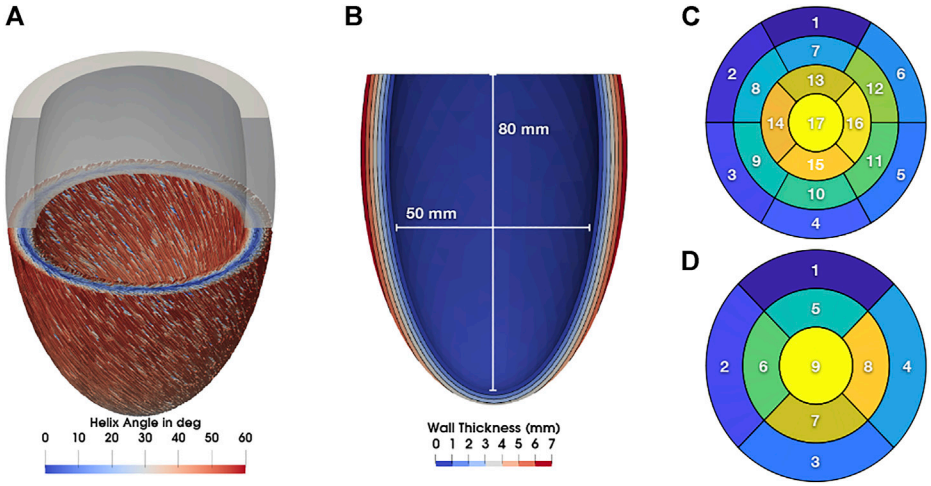

FIGURE 1 | (A) Myocyte orientation in the LV colorized with the corresponding helix angle. **(B)** Long axis cut through the LV with contours showing the wall thickness. Additionally, lengths for the calculation of the sphericity index are shown. **(C)** 17 AHA segments. **(D)** nine NOGA XP segments.

TABLE 1 | Input parameters for the electromechanical computational model.

Parameter	Value	Unit	Description
Passive biomechanics			
ϱ_0	1,082	kg/m^3	tissue density
κ	1	MPa	bulk modulus
μ	651.12	Pa	shear modulus
b_{ff}	11	-	fiber strain scaling
b_{ss}	4.4	-	radial strain scaling
b_{nn}	2.2	-	cross-fiber in-plain strain scaling
b_{fs}	7.7	-	shear strain in fiber-sheet plane scaling
b_{fn}	6.6	-	shear strain in fiber-normal plane scaling
b_{ns}	3.3	-	shear strain in sheet-normal plane scaling
Active biomechanics			
λ_0	0.7	-	minimum fiber stretch
t_{emd}	0.0	s	electromechanical delay
T_{peak}	50	kPa	peak isometric tension
t_{dur}	0.42	s	duration of active contraction
τ_{c0}	0.14	s	base time constant of contraction
ld	5.0	-	degree of length dependence
$\mathrm{ld}_{\mathrm{up}}$	0.5	s	length dependence of upstroke time
τ_r	0.05	s	time constant of relaxation
t_{cycle}	0.8	s	length of heart cycle

Furthermore, we introduce the right Cauchy-Green tensor $\mathbf{C} = \mathbf{F}^T\mathbf{F}$. The second Piola-Kirchhoff stress tensor $\mathbf{S} = \mathbf{S}(\mathbf{u}, T_a)$ incorporates both, the passive and active mechanics of the myocardium using the relationship

$$\mathbf{S}(\mathbf{u}, T_a) = 2\frac{\partial \Psi(\mathbf{C})}{\partial \mathbf{C}} + T_{\mathrm{a}}(t, \lambda_{\mathrm{f}})\frac{\mathbf{f}_0 \otimes \mathbf{f}_0}{\mathbf{f}_0 \cdot \mathbf{C}\mathbf{f}_0}. \tag{6}$$

Passive stress in cardiac tissue is modeled using a hyperelastic strain-energy function proposed by Usyk et al. (2000):

$$\begin{aligned}\Psi(\mathbf{C}) &= \frac{\kappa}{2}(\log J)^2 + \frac{\mu}{2}(\exp(Q) - 1),\\ Q &= b_{\mathrm{ff}}E_{\mathrm{ff}}^2 + b_{\mathrm{ss}}E_{\mathrm{ss}}^2 + b_{\mathrm{nn}}E_{\mathrm{nn}}^2 + b_{\mathrm{fs}}\left(E_{\mathrm{fs}}^2 + E_{\mathrm{sf}}^2\right)\\ &\quad + b_{\mathrm{fn}}\left(E_{\mathrm{fn}}^2 + E_{\mathrm{nf}}^2\right) + b_{\mathrm{ns}}\left(E_{\mathrm{ns}}^2 + E_{\mathrm{sn}}^2\right),\end{aligned} \tag{7}$$

with the directional components of the Green-Lagrange strain tensor $\mathbf{E} = \frac{1}{2}(\mathbf{C} - \mathbf{I})$, bulk modulus κ, shear modulus μ, and dimensionless orthotropic scaling factors b_{ij}, $i, j \in f, s, n$. Active stress due to the contraction of the cardiac muscle acts along the myocyte orientation $\mathbf{f}_0$ with the scalar value of the contractile force $T_{\mathrm{a}} = T_{\mathrm{a}}(t, \lambda_{\mathrm{f}})$. The simplified model by Niederer et al. (2011) is used to describe the temporal development of force generation:

$$T_{\mathrm{a}}(t, \lambda_{\mathrm{f}}) = T_{\mathrm{peak}}\phi(\lambda)\tanh^2\left(\frac{t_{\mathrm{s}}}{\tau_c}\right)\tanh^2\left(\frac{t_{\mathrm{dur}} - t_{\mathrm{s}}}{\tau_r}\right) \quad \text{for} \quad 0 < t_{\mathrm{s}} < t_{\mathrm{dur}}, \tag{8}$$

$$\begin{aligned}\phi(\lambda_{\mathrm{f}}) &= \max\{\tanh(\mathrm{ld}(\lambda_{\mathrm{f}} - \lambda_0)), 0\}, \quad \tau_c\\ &= \tau_{c0} + \mathrm{ld}_{\mathrm{up}}(1 - \phi(\lambda_{\mathrm{f}})), \quad t_{\mathrm{s}} = t - t_{\mathrm{a}} - t_{\mathrm{emd}},\end{aligned} \tag{9}$$

where λ_{f} is the fiber stretch, and t_{a} is the time of mechanical activation determined from electroanatomical mapping as detailed in **Section 2.3**. All parameters for the passive and active mechanics are given in **Table 1**.

The boundary condition in Eq. (3) is imposed on the endocardium Γ_0^{endo} to account for the pressure $p_{\mathrm{LV}}(t)$ applied by the blood inside the LV. $p_{\mathrm{LV}}(t)$ is determined by a 0D circulation model $\mathcal{C}(t, \mathbf{v}, \mathbf{z}, p_{\mathrm{LV}}(t))$ and the coupling condition in Eq. (5) ensures volume consistency, which has to be satisfied at each time step $t \in (0, T)$. Additionally, the interaction between the LV epicardium Γ_0^{epi} and the surrounding tissue (Pfaller et al., 2018; Strocchi et al., 2020) is considered by the boundary condition given in Eq. (2). The contact handling algorithm proposed by Fritz et al., (2014) is used in this study. This ensures a more realistic movement of the ventricle along the long axis of the heart with improved mitral valve displacement during systole. Since the LV is under constant stress due to the flow of blood, we have to find a suitable initial stress distribution. Therefore, we first find a stress-free state of

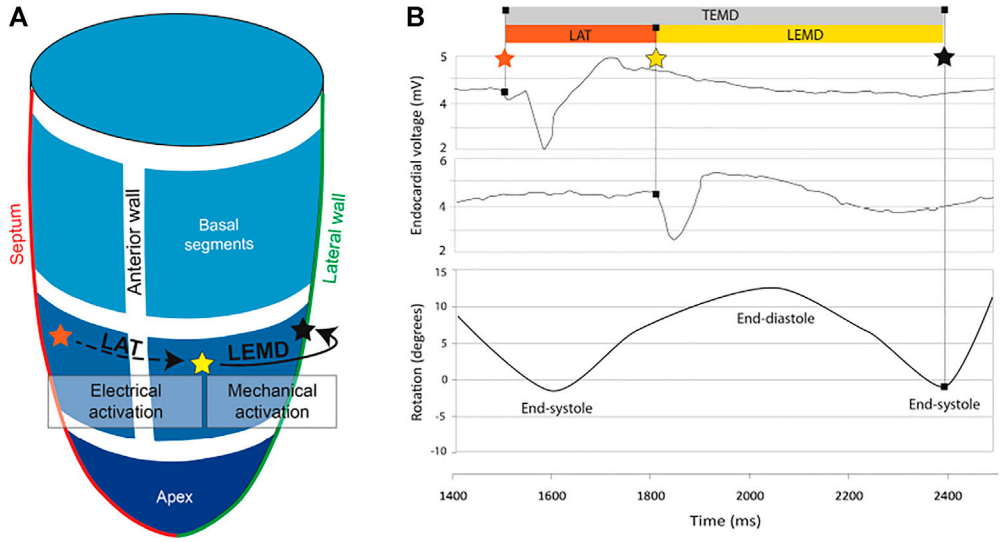

FIGURE 2 | (A) 3D model of the left ventricle showing the relation between local activation time (LAT) and local electromechanical delay. **(B)** Electromechanical parameters of the left ventricle and how they relate to endocardial voltage and rotation. The orange star indicates the first electrical activation in the LV. The yellow star indicates measured electrical activity at another location in the LV. As the tissue at this position starts to contract, the LV begins to rotate. The time when peak rotation is reached, is symbolized by a black star.

the LV by solving an inverse elasto-static problem as described in Marx et al. (2021). Then, the stress-free configuration is inflated with a pressure $p_{\mathrm{LV}} = 8$ mmHg by solving the static problem

$$\nabla \cdot (\mathbf{F}\,\mathbf{S}(\mathbf{u}, T_a = 0)) = \mathbf{0} \quad \text{in} \quad \Omega, \tag{10}$$

$$\mathbf{F}\,\mathbf{S}(\mathbf{u}, T_a = 0)\mathbf{N} = -p_{\mathrm{LV}}(t) J \mathbf{F}^{-T}\mathbf{N} \quad \text{on} \quad \Gamma^{\mathrm{endo}}, \tag{11}$$

to find the displacement $\mathbf{u}$. Finally, this displacement is used as an initial condition $\mathbf{u}_0$ for the problem described in **Eqs 1–5**.

The mathematical model described here is a reduction of the four-chamber model presented in Gerach et al. (2021) to enable the simulation of only the LV as available from the clinical data. Nevertheless, the methods for the numerical approximation of **Eqs. (1)–(5)** are equivalent to the previously published four-chamber model, which is why we omit a detailed description at this point and refer the interested reader to our previous work for further details.

2.3 Clinical Data Integration

Jadczyk et al. (2021) performed an intra-cardiac mapping study on 30 heart failure patients with reduced ejection fraction due to an ischemic etiology. The mean age of the population was 65.4 ± 6.1 years with a higher number of male participants (n = 21). Mean left ventricular ejection fraction, end-diastolic volume, and end-systolic volume were 30 ± 6%, 240.5 ± 65.8 ml and 178.4 ± 49.4 ml, respectively. All individuals presented sinus rhythm and LBBB morphology on 12-lead ECG with a mean QRS duration of 168 ± 17 ms. For the enrollment of patients, the LBBB criteria of Strauss et al. (2011) including QRS duration and morphology were used. LGE-MRI showed intensities of 11.6 ± 5.2%, 6.3 ± 4.5%, and 5.4 ± 3.2% in apical, medial, and basal segments, respectively. Patients were on optimal medical therapy in accordance to the European Society of Cardiology guidelines. There was no statistically significant difference between groups. For further information, we kindly refer the reader to the original publication (Jadczyk et al., 2021).

Jadczyk et al. (2021) acquired LV end-diastolic and end-systolic volume using transthoracic echocardiography, local scar burden using LGE-MRI, and electromechanical mapping using the NOGA XP system, which allows simultaneous measurement of local electrical activity and mechanical motion. Using the catheter, local activation time (LAT) was measured as the time that passed since the first electrical activation in the LV. The time between the LAT and the measured peak systolic rotation of the point is defined as the local electromechanical delay (LEMD). Together, both of these values give the total electromechanical delay (TEMD) as shown in **Figure 2**.

The measurements from each patient were incorporated into the LV geometry presented in **Section 2.1** by assigning the LGE-MRI data via the 17 AHA segments and LAT, LEMD, and TEMD via the nine segments of the NOGA XP system. To better differentiate between the potential influence of both, altered mechanical activation and scar burden, we first simulate all cases with only the measurements from the NOGA XP system and add local scar burden from LGE-MRI in a second run. Jadczyk et al. (2021) defined the LEMD parameter as the time interval between the local electrical activation of the segment and its peak of systolic rotation, not the onset of mechanical activation. This is an accepted approach in clinical studies of human LV mechanics (Paoletti Perini et al., 2016). Since LEMD is the only available parameter that relates to the mechanical activation including electromechanical delay, the onset of

mechanical activation is set as t_a = LAT + LEMD in each segment and assigned to the center of the endocardial surface that belongs to the corresponding segment. To avoid sharp transitions between the segments due to the low resolution of the available LEMD data, all values are interpolated over the whole endocardium using Laplacian minimization (Oostendorp et al., 1989). The resulting endocardial activation is then mapped to the volumetric myocardium using nearest neighbor interpolation and propagated transmurally with a transverse conduction velocity of $CV_{s_0} = 0.4$ m/s (Augustin et al., 2016). This adds an activation delay to all points $\mathbf{X}$ based on the distance from the endocardium $D(\mathbf{X})$:

$$t_a(\mathbf{X}) = t_a\left(\mathbf{X} \in \Gamma_0^{endo}\right) + \frac{D(\mathbf{X})}{CV_{s_0}}, \tag{12}$$

resulting in a maximal transmural delay of epicardial activation of 17.5 ms at the base where the wall thickness is 7 mm.

Local scar burden was incorporated by the percentage of enhanced area determined from LGE-MRI measurements on a segment-by-segment basis. It is assumed that the myocardium in enhanced areas was subject to remodeling processes and thus shows a decreased contractility. To reflect this in our model, the maximal contractility T_{peak} was reduced by the same amount as the percentage of the measured LGE intensity in the respective segment.

2.4 Evaluation Metrics

The main focus of this study is to determine different rotation patterns in the LV emerging from locally altered electromechanical delay. Therefore, we need to calculate the rotation angle as well as rotation direction of points located on the endocardial wall with respect to the heart's long axis. Notice that only endocardial points are evaluated since the clinical data was measured with an intracardiac mapping device. In our idealized LV model, the long axis corresponds to the z-axis of the global coordinate system in basal-apical direction. Hence, we extract all endocardial points $\mathbf{r} = \mathbf{X} \in \Gamma_0^{endo}$ in each segment, project them onto the (x, y) plane, and use the relationship

$$\cos\alpha = \frac{\mathbf{r}_{ED} \cdot \mathbf{r}_{ES}}{|\mathbf{r}_{ED}| \cdot |\mathbf{r}_{ES}|} \tag{13}$$

to calculate the angular displacement α from end-diastole (ED) to end-systole (ES). The direction of rotation was determined through

$$\det(\mathbf{r}_{ED}, \mathbf{r}_{ES}) \tag{14}$$

with values > 0 indicating counterclockwise rotation and values < 0 indicating clockwise rotation. ED and ES states are determined from the pressure-volume relationship $p_{LV}(V_{LV})$ resulting from the 0D circulation model $\mathcal{C}$. Additionally, we use Lagrangian particle tracking to visualize three dimensional trajectories of points located on the endocardium. Finally, the simulations are classified into one of two categories based on their rotational behavior: 1) wringing rotation denoted as Group A when basal segments show clockwise rotation and apical segments show counterclockwise rotation; 2) rigid-body-type (RBT) rotation denoted as Group B when the segments show either predominantly clockwise or predominantly counterclockwise rotation. The latter is realized by using a threshold of ±3° to decide whether a segment is rotating clockwise or counterclockwise, respectively. If nine or more segments show the same rotation pattern, the case is assigned to Group B.

3 RESULTS

We studied how locally altered electromechanical activation determines the diverse LV rotation patterns observed in HFrEF patients diagnosed with LBBB using in-silico models of the LV in a total of 31 cases. 30 of them were informed by patient specific measurements of LAT and LEMD using the measured data reported in Jadczyk et al. (2021) with the NOGA XP system as well as scar burden using the percentage of enhanced area from LGE-MRI. Additionally, we simulated a Control case without variations in LEMD and without scar tissue. For three of the clinical cases, simulations failed with the parameter set given in **Table 1**. Thus, simulation results are reported for 27 clinical cases. Since the rotational analysis of the simulations with and without local scar burden showed only minor differences and the classification was the same, results are reported for the cases including local scar burden unless otherwise stated.

Based on **Eqs 13**, **14**, we calculated the angle of rotation for all endocardial points and evaluated sectorial (basal, medial, apical) as well as segmental (17 AHA segments) mean values in each time step. **Figure 3** shows the dynamic rotational behavior of the LV in the basal and apical segments (left panel) as well as the sectorial mean angle of rotation during end-systole (right panel).

The results for the Control case are shown at the top. In the first 100 ms, the LV experienced a short untwist meaning that apical segments rotated clockwise with up to −3° and basal segments rotated counterclockwise with up to 1°. Right after this first phase, apical and basal segments start to rotate in the opposite direction until end-systole is reached (at about 410 ms). The mean angle of rotation was 18°, 5°, and −6° for the apical, medial, and basal sectors, respectively. At the bottom of **Figure 3**, the results for Case 18 are shown. Here, we could not observe a clear phase of untwisting. However, apical segments show opposite directions of rotation throughout the simulated heartbeat. First, anterior and septal segments showed up to −10° of clockwise rotation while lateral and inferior segments rotated counterclockwise with up to 12°. Towards end-systole however, the direction of rotation switches to the exact opposite behavior, leading to a predominantly clockwise rotation of basal and apical segments. This is reflected in the sectorial mean angle of end-systolic rotation as well. The apical sector showed significantly lower rotation compared to the Control case, whereas the medial sector switched from counterclockwise to clockwise rotation. Basal segments showed slightly lower angles of rotation compared to Control. In the Lagrangian particle tracking of the Control case (**Figure 4**), the wringing rotation

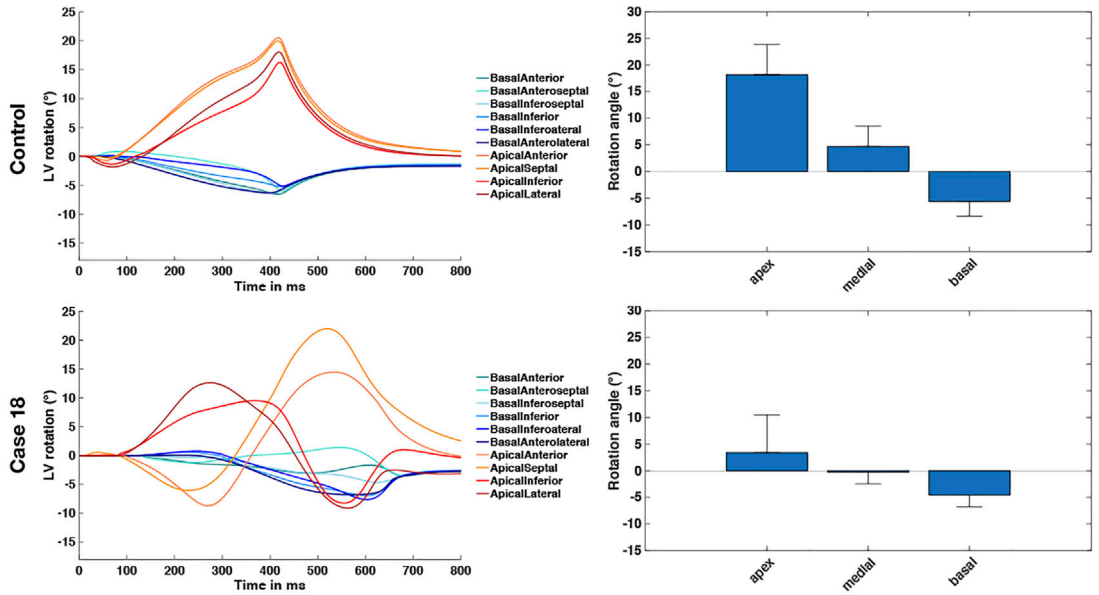

FIGURE 3 | Rotational dynamics of the basal and apical segments during one whole heart beat (left panel) and sectorial mean end-systolic rotation angle (right panel). The Control case is shown on the top and represents wringing rotation. Case 18 is shown on the bottom and was classified as RBT rotation.

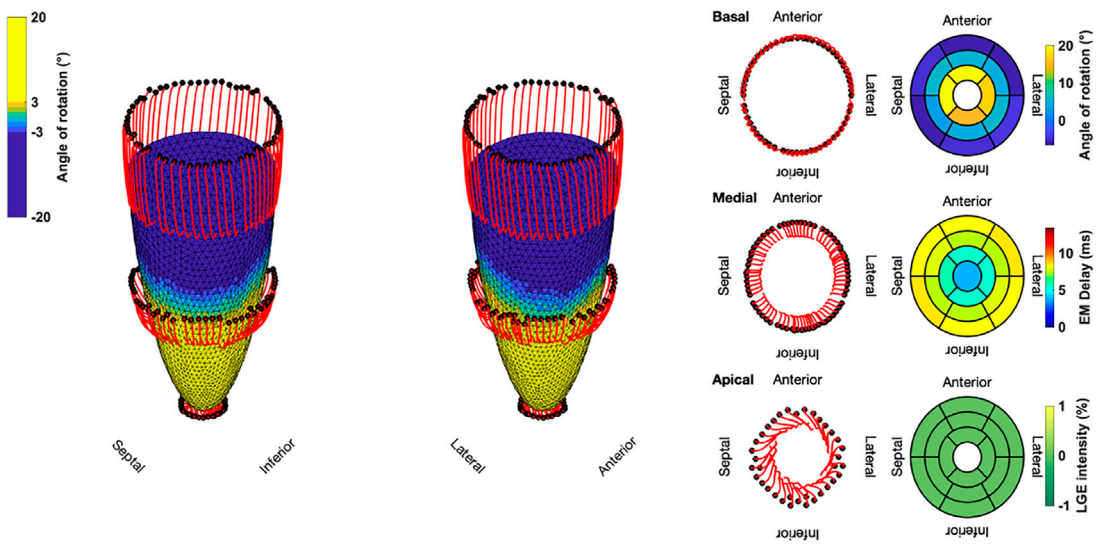

FIGURE 4 | Three-dimensional trajectories (red lines) of selected points on the endocardium in the basal, medial, and apical sectors for the Control case. The endocardial surface during end-systole is shown with rotational values depicted on the faces of the mesh. Solid black dots represent the initial positions. Bullseye plots show the segmental mean values of the angle of rotation, electromechanical (EM) delay, and LGE intensity.

could be clearly observed. Apical segments distinctly showed counterclockwise rotation up until end-systole. Additionally, we observed a translational movement towards the lateral side of the LV. In the medial and basal segments, the contraction was much more symmetrical and the myocardium in these segments rotated predominantly in a clockwise manner. However, the rotation is not as dominant as the shortening in the long axis in these segments.

Compared to the Control case, Case 18 showed a markedly different contraction pattern (**Figure 5**). Most notably, the symmetry of the homogeneous contraction pattern is lost. Inferior-lateral segments in the basal and medial sectors displayed less wall thickening, yet more shortening in the long axis compared to the Control case. Apical segments underwent a significant translation towards the anterior-lateral side of the LV with a more pronounced clockwise rotation. Due to the higher

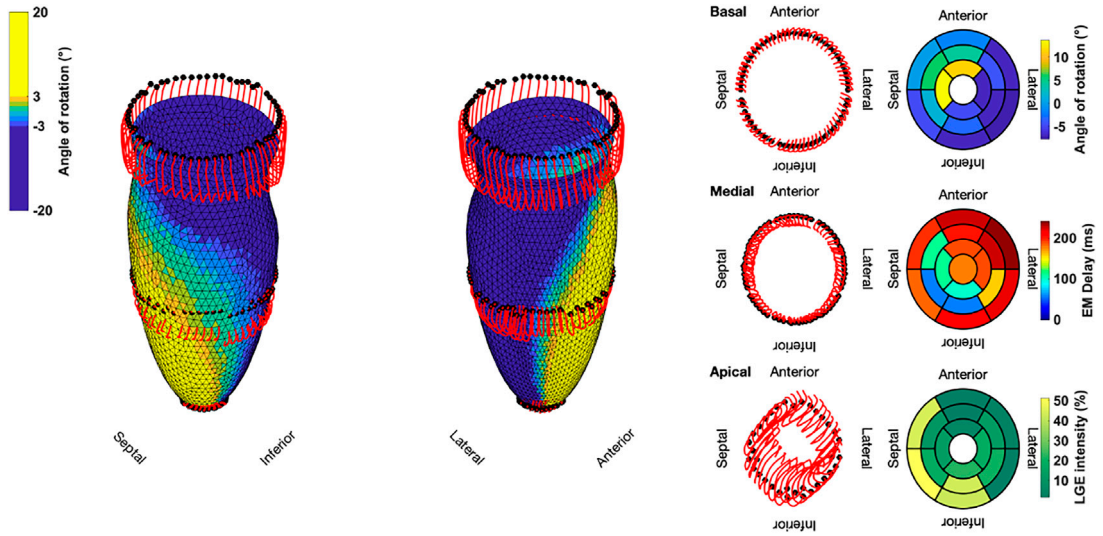

FIGURE 5 | Three-dimensional trajectories (red lines) of selected points on the endocardium in the basal, medial, and apical sectors for Case 18. The endocardial surface during end-systole is shown with rotational values depicted on the faces of the mesh. Solid black dots represent the initial positions. Bullseye plots show the segmental mean values of the angle of rotation, electromechanical (EM) delay, and LGE intensity.

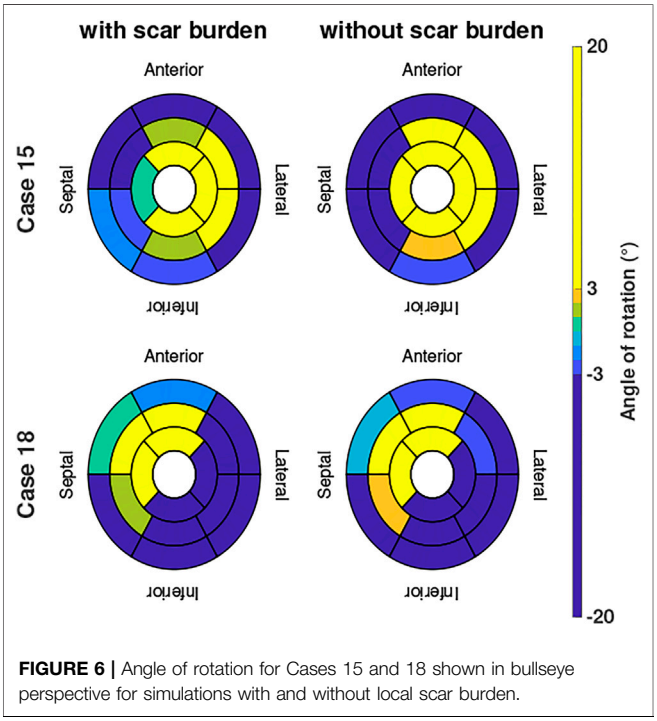

FIGURE 6 | Angle of rotation for Cases 15 and 18 shown in bullseye perspective for simulations with and without local scar burden.

LGE intensities in basal septal and basal inferior segments, the LV shows less wall thickening and less longitudinal shortening compared to the Control case.

Two examples of the difference in the evaluated angle of rotation are given in **Figure 6** in case we include or exclude local scar burden in the simulations. Case 15 (patient with the overall highest intensity values in the LGE-MRI data) showed slightly smaller rotation angles in some segments when local scar burden is incorporated into the model. With up to 5°, the change in the angle of rotation is largest in apical and medial segments. However, no change in the direction of rotation was observed. For Case 18, we observed similar changes in the magnitude of peak rotation. Angular differences occured mostly in segments with increased LGE intensity.

Lastly, the results of the binary classification for each of the 17 AHA segments in the Control case and the 27 clinically informed simulations are shown in **Figure 7**. Each segment was classified by its mean angle of rotation during end-systole. The color red depicts clockwise rotation and blue counterclockwise rotation. Cases with the majority of segments (≥9) rotating clockwise were classified as RBT rotation (Group B), which was the case for three cases (6, 10, 18). No case was classified in Group B with a predominantly counterclockwise rotation, since the basal segments rotated clockwise in the majority of cases. One repeating pattern in those three cases is that the lateral-inferior side of the LV was predominantly rotating in clockwise direction, while the anterior-septal side was dominated by counterclockwise rotation. All other cases were classified as wringing rotation (Group A). Based on the clinical recordings directly, Jadczyk et al. (2021) classified 20% of the patients in Group A (n = 6) and 80% in Group B (n = 24). Furthermore, 73% (n = 22) of patients in Group B showed clockwise RBT rotation and predominantly counterclockwise RBT rotation was observed in 7% (n = 2). Compared to the clinical classification, the in silico model results yielded matching classifications for Group A in 50% (n = 3) of the cases and in 0% of the cases for Group B.

4 DISCUSSION

We presented results of a total of 27 mechanical simulations of an idealized LV that were informed by electroanatomical maps

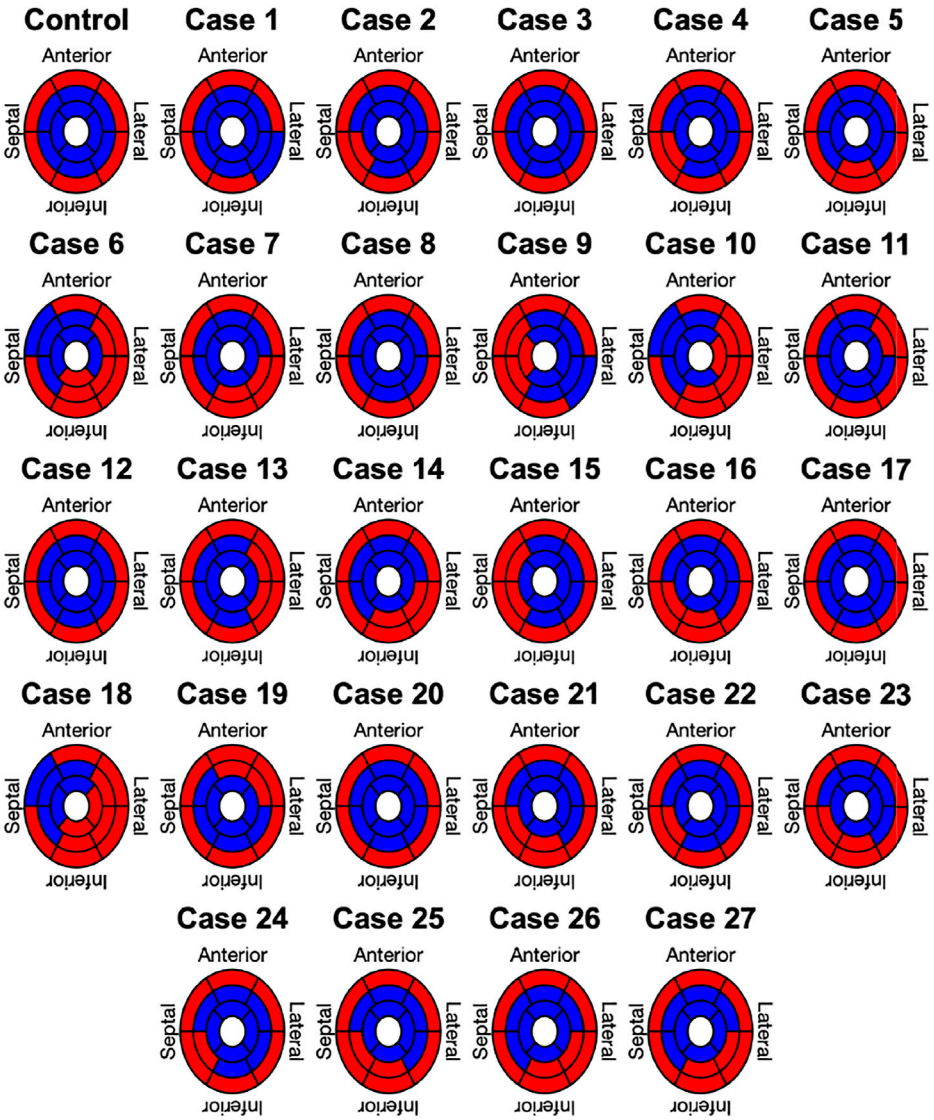

FIGURE 7 | Segment based analysis of end-systolic rotation around the long axis of the LV. A binary classification was used in each segment to determine clockwise (red) or counterclockwise (blue) rotation.

recorded with the NOGA XP system and additional LGE-MRI data. Results of one additional simulation without a patient specific input served as a control case. We evaluated the angle of rotation of each point on the endocardium and accumulated mean values on a segmental (17 AHA segments) and sectorial (basal, medial, apical) basis. Based on the segmental mean values, we determined the direction of rotation to be either clockwise (negative rotation values) or counterclockwise (positive rotation values). Finally, each simulation was classified as wringing type rotation (Group A) or RBT rotation (Group B) and compared to the clinically assessed classification.

The Control case was parameterized to yield a physiological contraction pattern that could be used as a comparison since all other cases involve data from patients suffering from HFrEF and LBBB. Hence, we presumed the electrical activation to be synchronized such that the subendocardial mechanical contraction is homogeneous throughout the LV and spreading transmurally towards the epicardium. The evaluated rotation pattern concurs with observations made in healthy individuals quantitatively and qualitatively (Stöhr et al., 2016; Lehmonen et al., 2020). First, we observed a brief untwisting (clockwise rotation of the apex and counterclockwise rotation of the base) of the LV during isovolumetric contraction. This has been observed in clinical measurements as well (Sengupta et al., 2008; Omar et al., 2015) and is linked to the initial contraction of the subendocardial layer followed by the contraction of the subepicardial layer. During ejection, the LV starts to twist normally (counterclockwise rotation of the apex and clockwise rotation of the base). Kocabay et al. (2014) reported mean rotational values of −6.9° for the base and 13° for the apex in

247 healthy volunteers using two-dimensional speckle-tracking echocardiography. With up to −6°, the Control case in this study matches these data well at the base. However, the up to 20° of rotation at the apex is larger. This can be explained by numerous factors, e.g. it is known that preload, afterload, contractility and age have an influence on the twist angle (Sengupta et al., 2008; Omar et al., 2015). Another significant factor is the choice of the apical imaging plane, since rotation values can vary widely depending on where the rotation is measured (van Dalen et al., 2008b; Stöhr et al., 2016). Based on these facts, we think that the Control case successfully represents physiological contraction in humans.

Electrical activation and consequently mechanical contraction of the LV in the pathological cases was determined by patient specific measurements of electroanatomical maps. LAT and LEMD were directly integrated into the LV model using the segments defined by the NOGA XP catheter system. LGE-MRI intensity was used as a surrogate for scar tissue in the LV. Typically, scar tissue undergoes a remodeling process that involves build-up of collagen in the myocardium (Jugdutt et al., 1996), which can result in a reorganization of the underlying fiber structure. Thus, an acknowledged way of modeling scar tissue is to impose an isotropic fiber structure with increased stiffness in the constitutive model (Niederer et al., 2011). Since we only had access to the LGE intensity as a percentage in each of the 17 AHA segments and we used the same geometrical model for all cases, it was not possible to easily implement it this way. Instead, we decided to reduce the active tension in the respective segment by the same percentage as the LGE intensity was increased with respect to the mean blood pool value (image intensity ratio, IIR). Thus, for IIR = 1.2 (20% above the mean blood pool intensity), the active tension was reduced by 20% to 0.8 × the reference value. This approach is motivated by the fact that in case of unchanged contractility, a stiffer myocardium would result in less deformation. However, this is a simplification due to the nonlinear nature of the constitutive law given in **Eq. 7**. Furthermore, we effectively smooth the effect of local scar tissue over the entire segment. Other than the altered electromechanical delay captured by the LEMD values from electroanatomical mapping and the aforementioned LGE intensity to capture the effect of scar tissue, no further patho-mechanisms were considered in the simulations. Hence, the emerging rotation patterns in the pathological cases originate from these changes only.

The classification into Group A (wringing rotation) and Group B (RBT rotation) was based on the evaluation of the mean angle of rotation in the 17 AHA segments. It clearly showed that most cases were classified into Group A. With the exception of 3 cases, all cases were classified different than in the classification based directly on the clinical rotation data, which means we cannot confirm the hypothesis postulated in Jadczyk et al. (2021) with the in silico model presented in this study. However, we identified 3 cases with predominantly clockwise rotation. Additionally to the basal segments, the medial and apical inferior-lateral side of the LV started to rotate clockwise instead of counterclockwise. Noticeably, this was accompanied by a significant translational movement of the apical region towards the anterior-lateral side of the LV. This can potentially skew the results when **Eqs 13**, **14** are used to determine the angle and direction of rotation around a fixed axis (Carreras et al., 2011), since a translation can be mistaken as a rotation. Nonetheless, the rotational dynamics shown in **Figure 3** of Case 18 show a similar pattern compared to a HFrEF case in Omar et al. (2015). There, apical rotation is reduced and undergoes both, a counterclockwise and then clockwise rotation.

Furthermore, the following limitations apply to our study:

1. LEMD was defined as the time interval between the local electrical activation of the segment and its peak systolic rotation, not the onset of mechanical activation. If we assume a similar length of active contraction in each segment, this should not pose a problem and LEMD can be interpreted as a local delay. However, different contractility can be expected especially in segments that show enhanced regions in LGE-MRI due to scar tissue and the associated tissue remodeling. This is especially important, since we observe a significantly longer time interval between electrical activation and peak systolic rotation in our simulations (489 ± 45 ms compared to the 369 ± 59 ms in the clinical measurements).
2. The presented in silico model neglects the influence of the atria and the right ventricle on rotation of the LV. Atrial data was not available for these patients at all and for the right ventricle no electroanatomical mapping data was available. Therefore, we decided to use the same LV geometrical model for all patients to isolate the effect of electromechanical activation on rotation. Especially the absence of the right ventricle might be crucial to why we can not observe clear rigid body rotation in the in silico model. The patients in the clinical cohort all presented with LBBB, meaning that the right ventricle contracted first. This might result in a lateral displacement of the septum. Consequently, an initial fraction of the active force generated by the LV contraction is spent on reversing this displacement instead of storing the entire energy in torque which ultimately results in less rotation. In our model this is not considered, which is why we might not be able to observe rigid body rotation.
3. A reason for the small differences in simulations in which scar burden was considered could be the simple way of transferring LGE intensity directly into a decrease in contractility. Although it is a straightforward approach and easy to implement, scar tissue is more complex and typically accompanied by other pathomechanisms in addition to a reduction in contractility. For example, fiber orientation in the LV of patients with dilated cardiomyopathy is typically reorganized Eggen et al. (2009). Furthermore, the stiffness of the myocardium increases and electrical conductivity decreases due to extracellular matrix remodeling Bollen et al. (2017). A detailed investigation of the effect of these additional mechanisms requires personalized LV anatomical models including information on pathological changes and was beyond the scope of this study, which focuses on the effect of dyssynchronous activation.

In conclusion, we combined a state-of-the-art model of heart mechanics and *in vivo* data of 30 patients to analyze

rotational dynamics in the LV. The main aim of this study was to investigate the specific hypothesis that dyssynchrony alone affects the kinetics of the LV in patients with HFrEF and LBBB in a way that rotational behavior is qualitatively changed. If this was the case, we would have been able to reproduce the mechanical behavior observed in the NOGA XP cardiac mapping system *in vivo*. The fact that this hypothesis was falsified shows that it is not the electromechanical activation sequence alone that determines rotational behavior suggesting that additional mechanisms are involved. Implications are that further research is required to fully understand the determinants of rotational behavior and that these further (and currently unknown) mechanisms are likely also important to be addressed therapeutically.

DATA AVAILABILITY STATEMENT

The original contributions presented in the study are included in the article/Supplementary Material, further inquiries can be directed to the corresponding author.

ETHICS STATEMENT

The studies involving human participants were reviewed and approved by Bioethical Committee, Medical University of Silesia, Katowice, Poland. The patients/participants provided their written informed consent to participate in this study.

AUTHOR CONTRIBUTIONS

TG, SA, and AL designed the study. TG and SA implemented the model, performed the simulations and analyzed the data. TG wrote the manuscript and designed figures. TJ, KG, and JW performed and analyzed NOGA electroanatomical mapping and MRI studies and provided the clinical data for this study. Moreover, TJ contributed to the analysis of *in vivo* vs. in silico electromechanical parameters. All authors revised the manuscript, have read the final version and approved the manuscript.

FUNDING

This research was funded by the Deutsche Forschungsgemeinschaft (DFG, German Research Foundation)—Project-ID 258734477—SFB 1173 and LO 2093/6-1, the Medical University of Silesia (statutory funds KNW-1-048/N/9/K) and European Union structural funds (Innovative Economy Operational Program POIG.01.01.02-00-109/09-00). We acknowledge support by the KIT-Publication Fund of Karlsruhe Institute of Technology. TJ was awarded the Anneliese and Mieczysław Koćwin Foundation Scholarship.

ACKNOWLEDGMENTS

We would like to thank Prof. Wojciech Wojakowski for his involvement in the mapping procedures and the original clinical study design.

REFERENCES

Augustin, C. M., Neic, A., Liebmann, M., Prassl, A. J., Niederer, S. A., Haase, G., et al. (2016). Anatomically Accurate High Resolution Modeling of Human Whole Heart Electromechanics: A Strongly Scalable Algebraic Multigrid Solver Method for Nonlinear Deformation. *J. Comput. Phys.* 305, 622–646. doi:10.1016/j.jcp.2015.10.045

Bayer, J. D., Blake, R. C., Plank, G., and Trayanova, N. A. (2012). A Novel Rule-Based Algorithm for Assigning Myocardial Fiber Orientation to Computational Heart Models. *Ann. Biomed. Eng.* 40, 2243–2254. doi:10.1007/s10439-012-0593-5

Bollen, I. A. E., Ehler, E., Fleischanderl, K., Bouwman, F., Kempers, L., Ricke-Hoch, M., et al. (2017). Myofilament Remodeling and Function Is More Impaired in Peripartum Cardiomyopathy Compared with Dilated Cardiomyopathy and Ischemic Heart Disease. *Am. J. Pathol.* 187, 2645–2658. doi:10.1016/j.ajpath.2017.08.022

Carreras, F., Garcia-Barnes, J., Gil, D., Pujadas, S., Li, C. H., Suarez-Arias, R., et al. (2011). Left Ventricular Torsion and Longitudinal Shortening: Two Fundamental Components of Myocardial Mechanics Assessed by Tagged Cine-MRI in normal Subjects. *Int. J. Cardiovasc. Imaging* 28, 273–284. doi:10.1007/s10554-011-9813-6

Cerqueira, M. D., Weissman, N. J., Dilsizian, V., Jacobs, A. K., Kaul, S., Laskey, W. K., et al. (2002). Standardized Myocardial Segmentation and Nomenclature for Tomographic Imaging of the Heart. A Statement for Healthcare Professionals from the Cardiac Imaging Committee of the Council on Clinical Cardiology of the American Heart Association. *J. Nucl. Cardiol.* 9, 240–245. doi:10.1067/mnc.2002.123122

Daubert, J.-C., Daubert, J.-C., Saxon, L., Adamson, P. B., Auricchio, A., Berger, R. D., et al. (2012). 2012 EHRA/HRS Expert Consensus Statement on Cardiac Resynchronization Therapy in Heart Failure: Implant and Follow-Up Recommendations and Management: A Registered branch of the European Society of Cardiology (ESC), and the Heart Rhythm Society; and in Collaboration with the Heart Failure Society of America (HFSA), the American Society of Echocardiography (ASE), the American Heart Association (AHA), the European Association of Echocardiography (EAE) of the ESC and the Heart Failure Association of the ESC (HFA). * Endorsed by the Governing Bodies of AHA, ASE, EAE, HFSA, HFA, EHRA, and HRS. *Europace* 14, 1236–1286. doi:10.1093/europace/eus222

Eggen, M. D., Swingen, C. M., and Iaizzo, P. A. (2009). "Analysis of Fiber Orientation in normal and Failing Human Hearts Using Diffusion Tensor Mri," in 2009 IEEE international symposium on biomedical imaging: from nano to macro (IEEE), 642–645. doi:10.1109/isbi.2009.5193129

Fritz, T., Wieners, C., Seemann, G., Steen, H., and Dössel, O. (2014). Simulation of the Contraction of the Ventricles in a Human Heart Model Including Atria and Pericardium. *Biomech. Model. Mechanobiol* 13, 627–641. doi:10.1007/s10237-013-0523-y

Gerach, T., Schuler, S., Fröhlich, J., Lindner, L., Kovacheva, E., Moss, R., et al. (2021). Electro-mechanical Whole-Heart Digital Twins: A Fully Coupled Multi-Physics Approach. *Mathematics* 9, 1247. doi:10.3390/math9111247

Geuzaine, C., and Remacle, J.-F. (2009). Gmsh: A 3-d Finite Element Mesh Generator with Built-In Pre- and post-processing Facilities. *Int. J. Numer. Meth. Engng.* 79, 1309–1331. doi:10.1002/nme.2579

Jadczyk, T., Kurzelowski, R., Golba, K. S., Wilczek, J., Caluori, G., Maffessanti, F., et al. (2021). Local Electromechanical Alterations Determine the Left Ventricle Rotational Dynamics in CRT-Eligible Heart Failure Patients. *Sci. Rep.* 11. doi:10.1038/s41598-021-82793-1

Jugdutt, B. I., Joljart, M. J., and Khan, M. I. (1996). Rate of Collagen Deposition during Healing and Ventricular Remodeling after Myocardial Infarction in Rat and Dog Models. *Circulation* 94, 94–101. doi:10.1161/01.cir.94.1.94

Kocabay, G., Muraru, D., Peluso, D., Cucchini, U., Mihaila, S., Padayattil-Jose, S., et al. (2014). Normal Left Ventricular Mechanics by Two-Dimensional Speckle-Tracking Echocardiography. Reference Values in Healthy Adults. *Revista Española de Cardiología (English Edition)* 67, 651–658. doi:10.1016/j.rec.2013.12.009

Leclercq, C., Burri, H., Curnis, A., Delnoy, P. P., Rinaldi, C. A., Sperzel, J., et al. (2019). Cardiac Resynchronization Therapy Non-responder to Responder Conversion Rate in the More Response to Cardiac Resynchronization Therapy with Multipoint Pacing (MORE-CRT MPP) Study: Results from Phase I. *Eur. Heart J.* 40, 2979–2987. doi:10.1093/eurheartj/ehz109

Lehmonen, L., Jalanko, M., Tarkiainen, M., Kaasalainen, T., Kuusisto, J., Lauerma, K., et al. (2020). Rotation and Torsion of the Left Ventricle with Cardiovascular Magnetic Resonance Tagging: Comparison of Two Analysis Methods. *BMC Med. Imaging* 20. doi:10.1186/s12880-020-00473-4

Lombaert, H., Peyrat, J., Croisille, P., Rapacchi, S., Fanton, L., Cheriet, F., et al. (2012). Human Atlas of the Cardiac Fiber Architecture: Study on a Healthy Population. *IEEE Trans. Med. Imaging* 31, 1436–1447. doi:10.1109/TMI.2012.2192743

Marx, L., Niestrawska, J. A., Gsell, M. A. F., Caforio, F., Plank, G., and Augustin, C. M. (2021). Efficient Identification of Myocardial Material Parameters and the Stress-free Reference Configuration for Patient-specific Human Heart Models. *Quantitative Biol.* doi:10.48550/arXiv.2101.04411

Niederer, S. A., Plank, G., Chinchapatnam, P., Ginks, M., Lamata, P., Rhode, K. S., et al. (2011). Length-dependent Tension in the Failing Heart and the Efficacy of Cardiac Resynchronization Therapy. *Cardiovasc. Res.* 89, 336–343. doi:10.1093/cvr/cvq318

Omar, A. M. S., Vallabhajosyula, S., and Sengupta, P. P. (2015). Left Ventricular Twist and Torsion. *Circ. Cardiovasc. Imaging* 8. doi:10.1161/CIRCIMAGING.115.003029

Oostendorp, T. F., van Oosterom, A., and Huiskamp, G. (1989). Interpolation on a Triangulated 3d Surface. *J. Comput. Phys.* 80, 331–343. doi:10.1016/0021-9991(89)90103-4

Paoletti Perini, A., Sacchi, S., Votta, C. D., Lilli, A., Attanà, P., Pieragnoli, P., et al. (2016). Left Ventricular Rotational Dyssynchrony before Cardiac Resynchronization Therapy. *J. Cardiovasc. Med.* 17, 469–477. doi:10.2459/jcm.0000000000000391

Pfaller, M. R., Hörmann, J. M., Weigl, M., Nagler, A., Chabiniok, R., Bertoglio, C., et al. (2018). The Importance of the Pericardium for Cardiac Biomechanics: from Physiology to Computational Modeling. *Biomech. Model. Mechanobiol* 18, 503–529. doi:10.1007/s10237-018-1098-4

Popescu, B. A., Beladan, C. C., Călin, A., Muraru, D., Deleanu, D., Roşca, M., et al. (2009). Left Ventricular Remodelling and Torsional Dynamics in Dilated Cardiomyopathy: Reversed Apical Rotation as a Marker of Disease Severity. *Eur. J. Heart Fail.* 11, 945–951. doi:10.1093/eurjhf/hfp124

Rüssel, I. K., Götte, M. J. W., Bronzwaer, J. G., Knaapen, P., Paulus, W. J., and van Rossum, A. C. (2009b). Left Ventricular Torsion. *JACC: Cardiovasc. Imaging* 2, 648–655. doi:10.1016/j.jcmg.2009.03.001

Rüssel, I. K., Götte, M. J. W., de Roest, G. J., Marcus, J. T., Tecelão, S. R., Allaart, C. P., et al. (2009a). Loss of Opposite Left Ventricular Basal and Apical Rotation Predicts Acute Response to Cardiac Resynchronization Therapy and Is Associated with Long-Term Reversed Remodeling. *J. Card. Fail.* 15, 717–725. doi:10.1016/j.cardfail.2009.04.007

Rüssel, I. K., and Götte, M. J. W. (2011). New Insights in LV Torsion for the Selection of Cardiac Resynchronisation Therapy Candidates. *Neth. Heart J.* 19, 386–391. doi:10.1007/s12471-011-0136-y

Sade, L. E., Demir, Ö., Atar, I., Müderrisoglu, H., and Özin, B. (2008). Effect of Mechanical Dyssynchrony and Cardiac Resynchronization Therapy on Left Ventricular Rotational Mechanics. *Am. J. Cardiol.* 101, 1163–1169. doi:10.1016/j.amjcard.2007.11.069

Schuler, S., Pilia, N., Potyagaylo, D., and Loewe, A. (2021). Cobiveco: Consistent Biventricular Coordinates for Precise and Intuitive Description of Position in the Heart - with MATLAB Implementation. *Med. Image Anal.* 74, 102247. doi:10.1016/j.media.2021.102247

Sengupta, P. P., Krishnamoorthy, V. K., Korinek, J., Narula, J., Vannan, M. A., Lester, S. J., et al. (2007). Left Ventricular Form and Function Revisited: Applied Translational Science to Cardiovascular Ultrasound Imaging. *J. Am. Soc. Echocardiography* 20, 539–551. doi:10.1016/j.echo.2006.10.013

Sengupta, P. P., Tajik, A. J., Chandrasekaran, K., and Khandheria, B. K. (2008). Twist Mechanics of the Left Ventricle. *JACC: Cardiovasc. Imaging* 1, 366–376. doi:10.1016/j.jcmg.2008.02.006

Setser, R. M., Kasper, J. M., Lieber, M. L., Starling, R. C., McCarthy, P. M., and White, R. D. (2003). Persistent Abnormal Left Ventricular Systolic Torsion in Dilated Cardiomyopathy after Partial Left Ventriculectomy. *J. Thorac. Cardiovasc. Surg.* 126, 48–55. doi:10.1016/S0022-5223(03)00050-3

Sillanmäki, S., Lipponen, J. A., Tarvainen, M. P., Laitinen, T., Hedman, M., Hedman, A., et al. (2018). Relationships between Electrical and Mechanical Dyssynchrony in Patients with Left Bundle branch Block and Healthy Controls. *J. Nucl. Cardiol.* 26, 1228–1239. doi:10.1007/s12350-018-1204-0

Stöhr, E. J., Shave, R. E., Baggish, A. L., and Weiner, R. B. (2016). Left Ventricular Twist Mechanics in the Context of normal Physiology and Cardiovascular Disease: a Review of Studies Using Speckle Tracking Echocardiography. *Am. J. Physiology-Heart Circulatory Physiol.* 311, H633–H644. doi:10.1152/ajpheart.00104.2016

Strauss, D. G., Selvester, R. H., and Wagner, G. S. (2011). Defining Left Bundle Branch Block in the Era of Cardiac Resynchronization Therapy. *Am. J. Cardiol.* 107, 927–934. doi:10.1016/j.amjcard.2010.11.010

Strocchi, M., Gsell, M. A. F., Augustin, C. M., Razeghi, O., Roney, C. H., Prassl, A. J., et al. (2020). Simulating Ventricular Systolic Motion in a Four-Chamber Heart Model with Spatially Varying Robin Boundary Conditions to Model the Effect of the Pericardium. *J. Biomech.* 101, 109645. doi:10.1016/j.jbiomech.2020.109645

Usyk, T. P., Mazhari, R., and McCulloch, A. D. (2000). Effect of Laminar Orthotropic Myofiber Architecture on Regional Stress and Strain in the Canine Left Ventricle. *J. Elasticity* 61, 143–164. doi:10.1023/A:1010883920374

van Dalen, B. M., Caliskan, K., Soliman, O. I. I., Nemes, A., Vletter, W. B., Ten Cate, F. J., et al. (2008a). Left Ventricular Solid Body Rotation in Non-compaction Cardiomyopathy: a Potential New Objective and Quantitative Functional Diagnostic Criterion? *Eur. J. Heart Fail.* 10, 1088–1093. doi:10.1016/j.ejheart.2008.08.006

van Dalen, B. M., Vletter, W. B., Soliman, O. I. I., ten Cate, F. J., and Geleijnse, M. L. (2008b). Importance of Transducer Position in the Assessment of Apical Rotation by Speckle Tracking Echocardiography. *J. Am. Soc. Echocardiography* 21, 895–898. doi:10.1016/j.echo.2008.02.001

Conflict of Interest: The authors declare that the research was conducted in the absence of any commercial or financial relationships that could be construed as a potential conflict of interest.

frontiers | Frontiers in Physiology

ORIGINAL RESEARCH
published: 10 May 2022
doi: 10.3389/fphys.2022.837239

Fraction of the T-Tubular Membrane as an Important Parameter in Cardiac Cellular Electrophysiology: A New Way of Estimation

Olga Švecová, Markéta Bébarová, Milena Šimurdová and Jiří Šimurda*

Department of Physiology, Faculty of Medicine, Masaryk University, Brno, Czechia

The transverse-axial tubular system (t-tubules) plays an essential role in excitation-contraction coupling in cardiomyocytes. Its remodelling is associated with various cardiac diseases. Numerous attempts were made to analyse characteristics essential for proper understanding of the t-tubules and their impact on cardiac cell function in health and disease. The currently available methodical approaches related to the fraction of the t-tubular membrane area produce diverse data. The widely used detubulation techniques cause irreversible cell impairment, thus, distinct cell samples have to be used for estimation of t-tubular parameters in untreated and detubulated cells. Our proposed alternative method is reversible and allows repetitive estimation of the fraction of t-tubular membrane (f_t) in cardiomyocytes using short-term perfusion of the measured cell with a low-conductive isotonic sucrose solution. It results in a substantial increase in the electrical resistance of t-tubular lumen, thus, electrically separating the surface and t-tubular membranes. Using the whole-cell patch-clamp measurement and the new approach in enzymatically isolated rat atrial and ventricular myocytes, a set of data was measured and evaluated. The analysis of the electrical equivalent circuit resulted in the establishment of criteria for excluding measurements in which perfusion with a low conductivity solution did not affect the entire cell surface. As expected, the final average f_t in ventricular myocytes (0.337 ± 0.017) was significantly higher than that in atrial myocytes (0.144 ± 0.015). The parameter f_t could be estimated repetitively in a particular cell (0.345 ± 0.021 and 0.347 ± 0.023 in ventricular myocytes during the first and second sucrose perfusion, respectively). The new method is fast, simple, and leaves the measured cell intact. It can be applied in the course of experiments for which it is useful to estimate both the surface and t-tubular capacitance/area in a particular cell.

OPEN ACCESS

Edited by:
Guido Caluori,
INSERM Institut de Rythmologie et Modélisation Cardiaque (IHU-Liryc), France

Reviewed by:
Michael Frisk,
University of Oslo, Norway
Ian Moench,
GlaxoSmithKline, United States
TingTing Hong,
University of Utah, United States

****Correspondence:***
Markéta Bébarová
mbebar@med.muni.cz

Specialty section:
This article was submitted to Integrative Physiology, a section of the journal Frontiers in Physiology

Received: *16 December 2021*
Accepted: *15 April 2022*
Published: *10 May 2022*

Citation:
Švecová O, Bébarová M, Šimurdová M and Šimurda J (2022) Fraction of the T-Tubular Membrane as an Important Parameter in Cardiac Cellular Electrophysiology: A New Way of Estimation. Front. Physiol. 13:837239. doi: 10.3389/fphys.2022.837239

Abbreviations: All symbols refer to the measurement in sucrose solution unless otherwise stated: C_m, Total membrane capacitance; C_t, Capacitance of t-tubular membrane; C_{Tyr}, Total membrane capacitance measured in Tyrode solution; C_s, Capacitance of surface membrane; f_t, Fraction of t-tubular membrane; $I_{K1,tail}$, Inward rectifier potassium tail current; J, Membrane current; J_1, J_2, Magnitudes of exponential components of the capacitive current; $J_{\infty,1}$, $J_{\infty,2}$, Steady-state currents at the membrane voltage U_1 and U_2; k_c, Correction factor related to C_t; R_a, Access resistance; R_{a_suc}, R_{a_Tyr}, Access resistance in sucrose and Tyrode solution; R_{el}, Microelectrode resistance; R_{ex}, Resistance of the extracellular medium; R_1, R_2, Auxiliary directly quantifiable resistances; R_{ms}, R_{mt}, Resistances of surface and t-tubular membrane; R_t, Total resistance of t-tubular lumen; τ_1, τ_2, Time constants of exponential components of the capacitive current; U, Membrane voltage; U_1, U_2, Imposed levels of membrane voltage; U_s, U_t, Membrane voltage on the surface and t-tubular membrane; U_{ms}, U_{mt}, Resting voltage of the surface and t-tubular membranes.

Keywords: sucrose, membrane capacitance, rat cardiomyocytes, new method, detubulation, t-tubules

INTRODUCTION

The transverse-axial tubular system (t-tubules) plays an essential role in excitation-contraction coupling of skeletal and cardiac myocytes by spreading depolarization from the surface membrane to the vicinity of the terminal cisternae of the sarcoplasmic reticulum, the source of Ca^{2+} that trigger cellular contraction (for a recent review, see Setterberg et al., 2021).

The contribution of the t-tubules to cardiac cell function is crucially dependent on their characteristics, both structural and functional (Orchard et al., 2009; Pásek et al., 2012; Hrabcová et al., 2013; Hong and Shaw 2017; Smith et al., 2018). The t-tubular network is extremely dynamic and its remodelling, i.e., disruption or even loss of the t-tubules, has been demonstrated in a variety of cardiac diseases including ischemia, heart failure, and hypertension (e.g., Louch et al.,2004; Heinzel et al., 2008; Dibb et al., 2009; Ibrahim et al., 2011; Crossman et al., 2011; Wagner et al., 2012; Guo et al., 2013; Bryant et al., 2015; Crossman et al., 2017; Dibb et al., 2021). These changes in the t-tubules considerably affect the electrical and mechanical function of cardiomyocytes and contribute to further progression of the cardiac pathology.

Much effort has been made to analyse the t-tubular characteristics in cardiomyocytes. The first attempt to investigate the distribution of ionic channels between the surface and t-tubular membranes was based on the diffusion delay between the extracellular solution in the t-tubules and the bulk space after a rapid change in ionic concentrations (Shepherd and McDonough 1998). Over the last 10 years, substantially improved imaging methods have contributed significantly to a better understanding of the t-tubules properties in cardiomyocytes of healthy as well as failing/ischemic hearts (e.g., Crossman et al., 2011; Wagner et al., 2012; Guo et al., 2013; Guo and Song 2014; Rog-Zielinska et al., 2021). Recently, Uchida and Lopatin (2018) described changes in diffusion accessibility of cardiac t-tubules caused by hypoosmotic shock in cardiac myocytes. Using fluorescent dextran trapping and diffusion assay and computer modelling, they concluded that the t-tubular diameter irregularity (affected by constrictions and dilatations of t-tubules) was the major contributor to the diffusional and electrical properties of t-tubules.

The widespread detubulation techniques (e.g., Kawai et al., 1999; Brette et al., 2002; Komukai et al., 2002; Brette et al., 2006) make it possible to estimate the fraction of t-tubular membrane capacitance and other t-tubular characteristics such as ionic current densities using the formamide-induced osmotic shock and consequent rapid changes of cell volume and disconnection of t-tubules from the surface membrane. A certain disadvantage of the detubulation technique is the cell impairment by the irreversible process of physical detachment of the t-tubules which disables the paired statistical testing. The hard-to-determine fraction of the t-tubules that resist detubulation can impair measurement accuracy as well (Pásek et al., 2008a). Recently, a new method of detubulation using antidepressant imipramine has emerged that allows complete detubulation to be achieved (Bourcier et al., 2019).

We propose an alternative method for the evaluation of t-tubular characteristics namely the basic parameter—the fraction of t-tubular membrane capacitance/area. The theoretical basis of another version of this method has been preliminarily published as a preprint (Šimurda et al., 2021). The method is reversible and allows repeated measurements in the same cell under control conditions (Tyrode solution) and in the presence of isotonic sucrose solution. The substantial increase in electrical resistance of the t-tubular lumen allows for the electrical separation of the surface and t-tubular membranes in isolated atrial and ventricular myocytes.

MATERIALS AND METHODS

Cell Isolation

Cardiomyocytes were isolated from atria and right ventricles of adult male Wistar rats (300 ± 20 g and 250 ± 50 g, respectively) anaesthetised by intramuscular administration of a mixture of tiletamine and zolazepam (65 mg kg^{-1}; Zoletil® 100 inj., *Virbac*, *France*), and xylazine (20 mg kg^{-1}; Xylapan® inj., *Spofa*, *Czech Republic*). The experiments were carried out with respect to recommendations of the European Community Guide for the Care and Use of Laboratory Animals; the experimental protocol was approved by the Local Committee for Animal Treatment at Masaryk University, Faculty of Medicine, and by the Ministry of Education, Youth and Sports (permission No. MSMT-29203/2012-30 and MSMT-33846/2017-3).

The dissociation procedure to obtain atrial and ventricular cardiomyocytes suitable for patch-clamp measurements was described in detail in our previous papers (e.g., Bébarová et al., 2005; Bébarová et al., 2016). In brief, the heart was retrogradely perfused *via* aorta with 0.9 mM $CaCl_2$ Tyrode solution (3–5 min) and then with nominally Ca-free Tyrode solution (~4.5 min). To isolate ventricular myocytes, the perfusion continued with the first digestion step (2.75 min), i.e., with nominally Ca-free Tyrode solution containing collagenase (type S, 0.2 mg/ml, *Yakult Pharmaceuticals*), protease (type XIV, *Sigma-Aldrich*; 0.053 mg/ml), and EGTA (*Sigma-Aldrich*; 34 μM). To isolate atrial myocytes, the first digestion step (3 min), was performed using Tyrode solution containing 0.6 μM $CaCl_2$, collagenase (Roche A, 1 mg/ml, *Roche Diagnostics GmbH*), and protease (type XIV, *Sigma-Aldrich*; 0.053 mg/ml). In the second digestion step, the protease was omitted during the isolation of both atrial (14–24 min; median: 17 min) and ventricular myocytes (10–16 min; median: 13 min). The enzyme solution was then washed out in two steps by perfusion with the low calcium Tyrode solutions (0.09 and 0.18 mM $CaCl_2$). All solutions were oxygenated with 100% O_2 at 37°C.

Subsequently, the right and left auricles or the right ventricular free wall were dissected and minced in 0.18 mM $CaCl_2$ Tyrode solution. After filtration through a nylon mesh, both atrial and ventricular isolated myocytes were exposed to gradually increasing external Ca^{2+} concentration (up to 0.9 mM within approx. 20 min).

Solutions and Chemicals

Tyrode solution with the following composition was used both during the dissociation procedure and to perfuse myocytes during the measurements (in mM): NaCl 135, KCl 5.4, $MgCl_2$ 0.9, HEPES 10, NaH_2PO_4 0.33, and glucose 10 (pH was adjusted to 7.4 with NaOH). During measurements, 0.9 mM $CaCl_2$ was added to the solution and $CoCl_2$ (2 mM) was used for inhibition of I_{Ca}. $CoCl_2$ (*Sigma-Aldrich*) was prepared as 1 M stock solution in the deionized water. Sucrose (≥99.5%, *Sigma-Aldrich*) was dissolved in the deionized water to prepare the isotonic sucrose solution (0.3 M; osmolality 300 ± 5 mOsm/kg); 5 μM $CaCl_2$ was added to maintain the membrane integrity and minimum conductivity. We have regularly checked the specific conductivity of the used distilled water (about 0.5–1.5 μS/cm). The final conductivity of the sucrose solution was ~3.5 ± 0.2 μS/cm. The solutions were applied in close vicinity of the measured cell *via* a rapid perfusion system.

A sucrose solution containing 10, 25, and 100 μM $BaCl_2$ (10 mM stock solution, $BaCl_2$ dissolved in deionized water) was used to check the Ba^{2+}-sensitive component of the membrane current during sucrose application.

To partially detubulate ventricular myocytes, the isolated cells were treated for 15 min with 75, 150, and 225 μM imipramine (according to Bourcier et al., 2019, but lower concentrations were used in our study to prevent the complete detubulation) and then they were centrifuged and the imipramine was washed using the control Tyrode solution.

The patch electrode filling solution contained (in mM): L-aspartic acid 130, KCl 25, $MgCl_2$ 1, K_2ATP 5, EGTA 1, HEPES 5, GTP 0.1, and Na_2-phosphocreatine 3 (pH 7.25 adjusted with KOH).

Electrophysiological Measurements and Evaluation

Single rod-shaped cells with well visible striations were used for recordings of the membrane current applying the whole-cell patch-clamp technique in the voltage-clamp mode. The patch pipettes were pulled from borosilicate glass capillary tubes and heat polished on a programmable horizontal puller (*Zeitz-Instrumente, Germany*). The resistance of the filled glass electrodes was below 1.5 MΩ to keep the access resistance as low as possible. For the generation of experimental protocols and data acquisition, the Axopatch 200B equipment and pCLAMP 9.2 software (*Molecular Devices*) were used. The measured ionic currents were digitally sampled at 200 kHz and stored on the hard disc. Experiments were performed at room temperature (23 ± 1°C). Experimental protocols are described in the Results.

Mathematical Simulations

All calculations according to the formulas given in the Results section and in the **Supplementary Material** were performed using the computational software MATLAB v.7.2 (*MathWorks, Inc.*).

Statistical Analysis

Evaluation of the data was performed using the computational software MATLAB R2020a (*MathWorks, Inc.*) except for the curve fitting that was performed using Clampfit 10.7 software (*Molecular Devices*). The results are presented as means ± S.E.M from *n* cells (Origin, version 2015, *OriginLab Corporation*, and GraphPad Prism, version 7.05, *GraphPad Software, Inc.*). The normality of the data distribution was tested using the Shapiro-Wilk test or Kolmogorov-Smirnov test (if $n < 8$). Paired and unpaired t-tests, and repeated measures ANOVA with the Bonferroni´s post-test were used to consider the statistical significance of the observed differences; $p < 0.05$ was considered statistically significant.

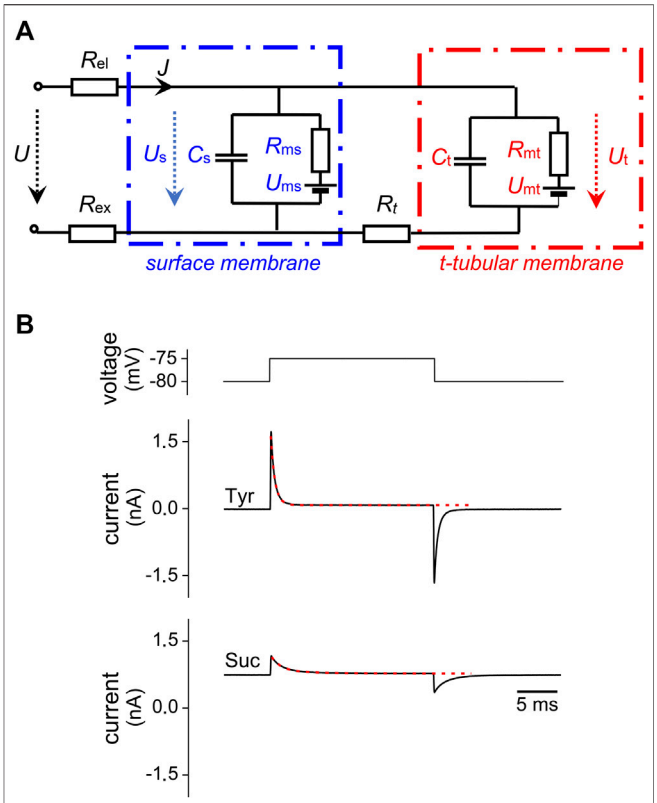

FIGURE 1 | Principle of the new method. **(A)** Scheme of the electrical equivalent circuit of cardiomyocyte; R_{el}—microelectrode resistance; R_{ex}—extracellular resistance; C_s, R_{ms}, U_{ms}, and C_t, R_{mt}, U_{mt}—membrane capacitance, membrane resistance, reversal voltage of the surface and t-tubular membranes, respectively; R_t—resistance of t-tubular lumen. The membrane resistances can be considered constant in the subthreshold range of membrane voltage. U, U_s, and U_t—the imposed voltage, surface membrane voltage, and t-tubular membrane voltage, respectively. J—the membrane current. **(B)** The imposed impulse of membrane voltage (upper panel) and representative current traces in the Tyrode (Tyr) and sucrose (Suc) solution including mono- and bi-exponential fits (red lines), respectively (middle and bottom panel).

RESULTS

A New Method for Repetitive Estimation of the Fraction of T-Tubular Membrane

The schematic diagram in **Figure 1A** represents the electrical equivalent circuit of a cardiac myocyte connected to a microelectrode. The surface membrane (capacitance C_s,

resistance R_{ms}, and reversal voltage U_{ms}) is separated from the t-tubular membrane (C_t, R_{mt}, and U_{mt}) by longitudinal resistance of the t-tubular lumen (R_t). The access resistance $R_a = R_{el} + R_{ex}$ is composed of the microelectrode resistance R_{el} and resistance of extracellular medium R_{ex}. The simple lumped equivalent circuit including the t-tubular system (similar to that applied for the same purpose by Cheng et al., 2011) was used. A model with distributed parameters of the t-tubular system of cardiomyocytes would be difficult to use for practical measurements (see the Discussion for more details).

The key idea of the proposed method is to achieve a significant increase in the electrical resistance of the t-tubular lumen R_t to electrically separate the surface and t-tubular membrane in whole-cell patch-clamp experiments. The low specific resistance of physiological solutions is associated with a low value of R_t which causes tight electrical coupling between the surface and t-tubular systems. Consequently, only the total membrane capacitance (marked C_{Tyr} in the following text) can be measured. Analysis of the electrical equivalent scheme describing cardiomyocyte in the whole-cell arrangement under conditions of a multiple increase in the resistance R_t allowed us to calculate the surface and t-tubular membrane capacitances (C_s and C_t) separately as well as to estimate the fraction of t-tubular membrane $f_t = C_t/(C_s + C_t)$. A sufficient increase in R_t was achieved by short-term perfusion of the measured cell with a low-conductive isotonic sucrose solution. The analysis was based on the resolution of two components in responses of membrane current to the imposed subthreshold voltage steps as shown in **Figure 1B** and in detail in **Supplementary Figure S1**. In the following, the symbols indicated in **Figure 1A** will refer exclusively to the values measured in the isotonic sucrose solution. C_m will indicate the total membrane capacitance estimated in the sucrose solution ($C_m = C_s + C_t$) to distinguish it from C_{Tyr}, measured in Tyrode solution.

To get an idea of the processes that take place after the application of the sucrose solution, we recorded the time course of the current at the holding voltage −80 mV (**Figure 2A**). The current was reversed and surprisingly even increased in absolute value although the access resistance R_a increased substantially in the low conductivity medium, evidently due to an increased driving force. The membrane current is likely carried preferentially by K^+ and Cl^- ions across the cell membrane. Considering the Nernst equations, the reversal voltages of all positive ions should acquire high negative values in contrast to a high positive value for Cl^-. As a result, both K^+ and Cl^- can flow out of the cell and help to maintain the electroneutrality of the media. The entry of ions from the sarcoplasm into the t-tubules can be expected to restrict the increase of R_t. The evidence of a substantial role of the inward rectifying potassium current I_{K1} is given in the Discussion.

The broader theoretical basis of the new approach was preliminarily published as a preprint (Šimurda et al., 2021) which shows that the determination of C_t is associated with a certain inaccuracy, the limit of which can be calculated from the measured data. In the present work, a new way is followed to overcome the problem of C_t estimation. It is described in the **Supplementary Material** together with an outline of the derivation of calculation formulas. In the following text, the computational relationships used to determine the basic parameters of the electrical equivalent scheme (i.e., C_s and C_t) supplemented by the calculation of f_t as an indicator of the area fraction occupied by the t-tubules will be listed.

The response of the capacitive current to subthreshold steps of membrane voltage (from the holding level U_1 = −80 mV to optional U_2) in the sucrose solution was approximated by a sum of two exponential functions and a constant (**Supplementary Figure S1**) in the Clampfit software (*Molecular Devices*). The resulting magnitudes of the exponential components (J_1 and J_2), corresponding time constants (τ_1 and τ_2), and steady-state current at the level U_2 ($J_{\infty,2}$) were supplemented by the value of the steady-state current at the holding voltage ($J_{\infty,1}$). The values of C_t, C_s, f_t, and the access resistance R_a could be calculated from the six parameters J_1, J_2, τ_1, τ_2, $J_{\infty,1}$, and $J_{\infty,2}$ using the following relationships derived in the **Supplementary Material**:

$$C_s = \frac{\tau_s}{R_a}, \text{where } \tau_s = \left(J_1 + J_2 - J_{\infty,1} + J_{\infty,2}\right)\frac{\tau_1\tau_2}{\tau_1 J_2 + \tau_2 J_1} \quad (1)$$

$$\text{and the access resistance } R_a = \frac{U_2 - U_1}{J_1 + J_2 - J_{\infty,1} + J_{\infty,2}}. \quad (2)$$

C_t is determined with an accuracy of ±4% in ventricular and ±5% in atrial cardiomyocytes (see the **Supplementary Material** for detailed explanation).

$$C_t \sim \frac{\tau_1 J_2 + \tau_2 J_1}{J_1 + J_2}\frac{k_c}{R_1}, \text{ where } R_1 = \frac{R_a}{b-1}, \text{ and } b = \frac{\tau_1^2 J_2 + \tau_2^2 J_1}{\tau_1 J_2 + \tau_2 J_1}\frac{\tau_s}{\tau_1\tau_2}. \quad (3)$$

The coefficient k_c was introduced as a correction for the mean error caused by the exchange of membrane resistances R_{mt} for R_{ms} in the approximate calculation of C_t as justified in the **Supplementary Material** (Eq. S18 and the accompanying text) and the value of k_c was set to 0.97 for ventricular and to 0.91 for atrial cardiomyocytes. The total membrane capacitance C_m and the fraction of t-tubular membrane f_t are expressed as

$$C_m = C_s + C_t, \quad f_t = \frac{C_t}{C_m}. \quad (4)$$

The experimental protocol consisted of a sequence of 300 rectangular voltage steps, 5 or 10 mV, 20 ms from the holding voltage of −80 mV applied at 25 Hz (a single step shown in **Figure 1B**, upper panel). This protocol was applied repeatedly if needed (max. 3 times). The representative current responses to a single voltage step in the Tyrode solution (Tyr) and in the isotonic sucrose solution (Suc) are illustrated in **Figure 1B**, middle and bottom panels, together with the mono-exponential fit in Tyr and bi-exponential fit in Suc (the red dashed lines). For details of evaluation of this representative cell, please see **Supplementary Figure S1**.

To obtain steady-state values of the evaluated parameters, the last 50 current responses before the sucrose wash-out were averaged and evaluated. No significant differences were observed among average values evaluated at three independent

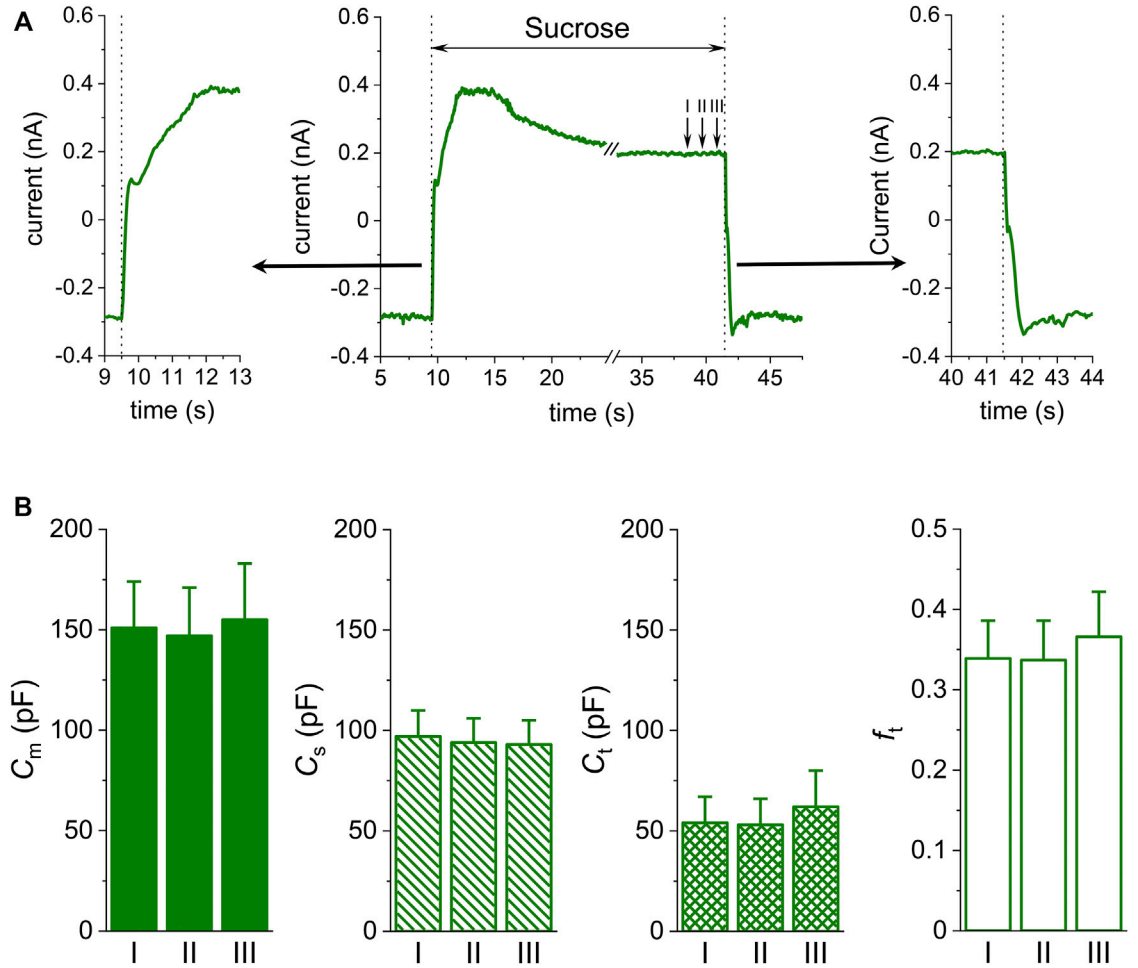

FIGURE 2 | Time course of the sucrose effect. **(A)** Changes of the membrane current at −80 mV during application and subsequent wash-out of isotonic sucrose solution in a representative cell (middle panel, the time axis is interrupted at the interval when the voltage-ramp protocol was applied; left and right panels—details of 4 s of the recording shown in the middle panel at the time of start and end of sucrose application, respectively). **(B)** Average values of basic parameters evaluated in the presence of sucrose at the steady-state in three independent intervals I, II, and III at the end of sucrose application ($n = 5$, $p > 0.05$ within the same parameter; for the approximate position of the intervals I, II, and III, please see arrows in part **(A)**.

intervals at the end of sucrose application if the protocol was repeated until the steady-state current was reached (**Figure 2B**; $n = 5$, $p > 0.05$). However, the evaluated parameters were not significantly different even if being evaluated in ~10 s from the start of the sucrose application which implies that reaching the steady-state of membrane current during sucrose application is not necessary to obtain steady-state values of the evaluated parameters (not illustrated).

Accuracy of the Parameters Estimated Using the New Method

The accuracy of the method is critically dependent on the conditions ensuring that the entire cell surface is washed with sucrose solution or Tyrode solution during rinsing. The stream washing the cell must be carefully directed which is indicated by the ratio of access resistances measured in Tyrode and sucrose solution. For cells that have not been lifted from the bottom of the chamber, there is a risk that a part of the surface is not exposed to the solution. However, the violation of the conditions of correct measurement can be revealed from the parameters obtained by the bi-exponential approximation of the capacitive current. Incomplete solution exchange strongly affects the ratio of magnitudes and time constants of both components of the analysed part of the capacitive current. The component with the shorter time constant must be sufficiently expressed. Besides the ratio of the time constants and amplitudes of both capacitive current components, an additional quantity indicating an unacceptably low resistance of t-tubular lumens was the ratio of the resistance R_1 defined in **Eq. 3** and the resistance R_2 that can be computed as

$$R_2 = \frac{R_a}{R_{ms}||(R_{mt} + R_t)} = R_a \frac{J_1 + J_2}{J_{\infty\_2} - J_{\infty\_1}}. \quad (5)$$

To decide whether a given measurement is acceptable and can be included in the overall evaluation, we applied the following criteria:

$$R_{a\_suc} - R_{a\_Tyr} > 3M\Omega, \quad (6a)$$

$$J_2/J_1 > 0.16, \quad \tau_2/\tau_1 > 0.1, \quad \text{and} \quad R_1/R_2 > 0.1. \quad (6b)$$

R_{a_suc}, and R_{a_Tyr} are access resistances in sucrose and Tyrode solution, τ_1 and J_1 refer to the component with the longer time constant, and τ_2 and J_2 to the component with the shorter time constant. In the following figures, only data from measurements fulfilling these criteria are included. For average values of R_{a_suc}, and R_{a_Tyr} in all selected cells, please see **Supplementary Figure S2**. Data selection based on the aforementioned criteria resulted in a decreased variability and, thus, in considerably increased accuracy of the resulting f_t values (**Supplementary Figure S3**).

Comparison of the Average Values in Atrial and Ventricular Cardiomyocytes

C_t, C_s, and C_m in the measured rat ventricular myocytes that passed the selection procedure described above were 47.3 ± 3.9, 92.7 ± 5.9, and 141.2 ± 8.6 pF on average, respectively (**Figure 3A**; $n = 21$). In rat atrial cardiomyocytes, C_t, C_s, and C_m were 8.4 ± 0.9, 50.4 ± 3.3, and 59.7 ± 3.6 pF on average, respectively, using the same selection criteria (**Figure 3B**; $n = 7$). It implies that f_t was significantly lower in rat atrial myocytes than that in rat ventricular myocytes (0.144 ± 0.015 vs. 0.337 ± 0.017; **Figure 3C**; $p < 0.001$) as may be expected considering the literary data and the substantially less developed t-tubular system in the atria. C_m evaluated from the data recorded during the sucrose application was significantly lower (by 23 and 18% in rat ventricular and atrial myocytes, respectively) than that evaluated in the control Tyrode solution C_{Tyr} (183.1 ± 9.9 pF in rat ventricular myocytes and 72.8 ± 4.2 pF in rat atrial myocytes; the respective C_m values—see above; $p < 0.001$ and 0.01 in rat ventricular and atrial myocytes, respectively; for a possible explanation, see the Discussion).

The value of f_t did not significantly correlate with C_{Tyr} (an indicator of the cell size) in both ventricular and atrial myocytes (**Figure 4**; for details, see the Discussion).

Repetitive Estimation of the Parameters in a Single Cell

To test the most promising advantage of the new method, we tried to apply the sucrose solution twice in the same cell (both sucrose applications were separated by a wash-out period in Tyrode solution sufficient to recover control conditions; for representative examples of rat ventricular and atrial myocytes, **Figure 5A**). The average value of f_t was not different during the first and the second sucrose application (0.345 ± 0.021 and 0.347 ± 0.023, respectively; $n = 14$, $p > 0.05$; **Figure 5B**). Hence, our new method may be used several times in the same cell, enabling testing of dynamic changes of t-tubular parameters.

DISCUSSION

A new method for estimation of the fraction of t-tubular membrane (f_t) in cardiomyocytes was developed, described,

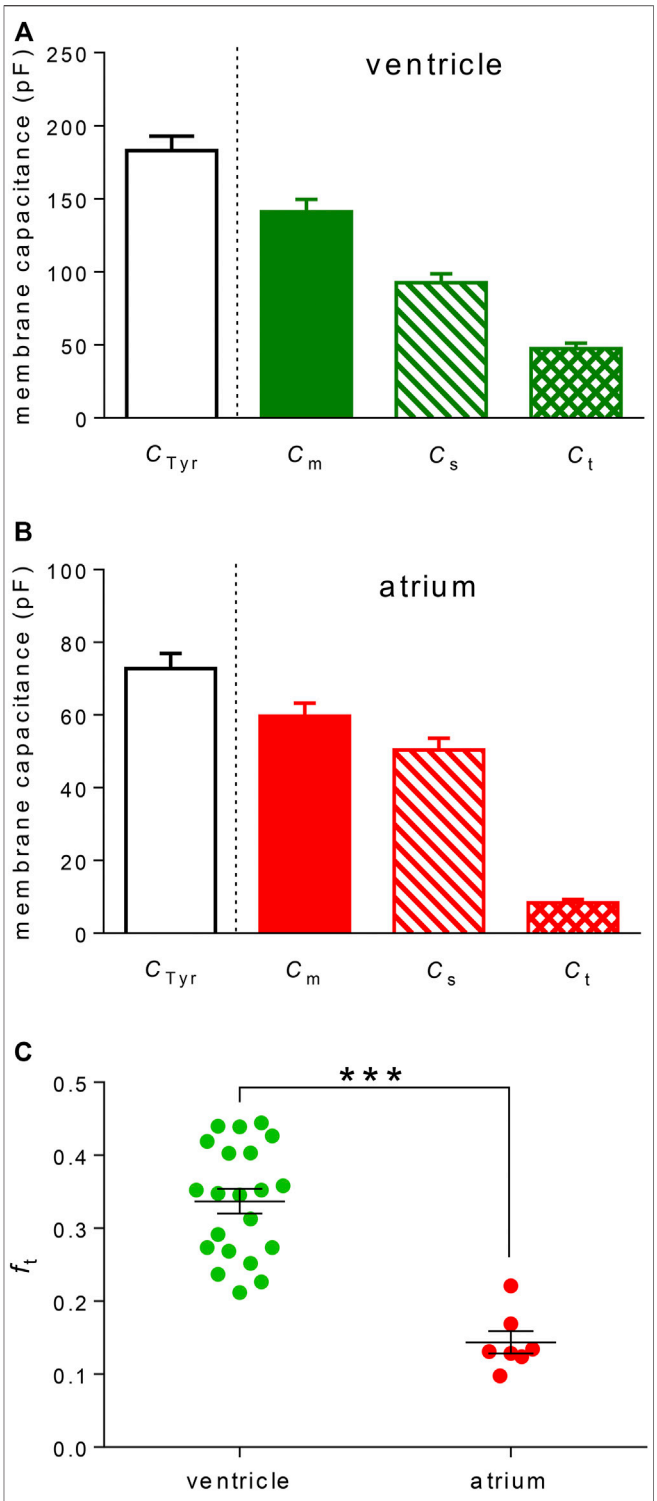

FIGURE 3 | TATS characteristics evaluated using the newly developed method. **(A,B)** Average C_{Tyr}, C_m, C_s, and C_t in ventricular **(A)** and atrial **(B)** cardiomyocytes. Values of all parameters in ventricular cells were significantly different at $p < 0.001$ ($n = 21$). In atrial cells, all parameters also significantly differed, but at various P ($p < 0.05$–0.001; $n = 7$). **(C)** The value of f_t was significantly lower in atrial vs. ventricular cardiomyocytes; ***—statistical significance at $p < 0.001$.

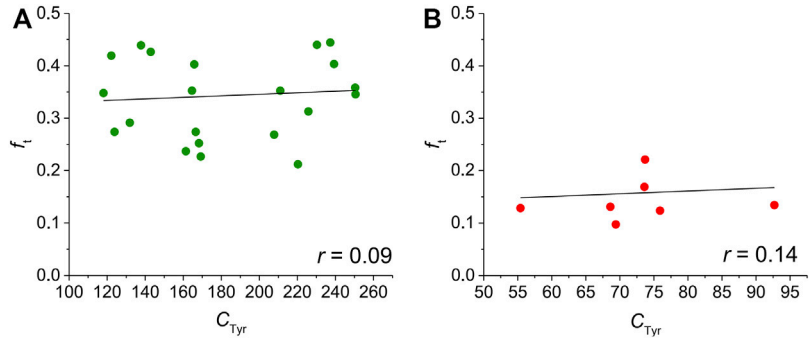

FIGURE 4 | Correlation between f_t and C_{Tyr} in ventricular **(A)** and atrial **(B)** rat cardiomyocytes. No correlation can be observed in our data ($p > 0.05$ in both ventricular and atrial myocytes).

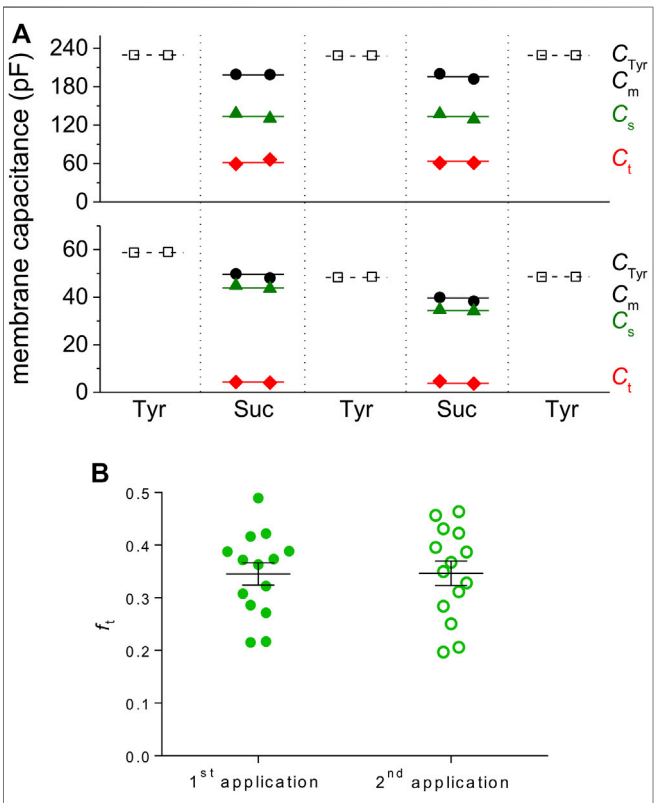

FIGURE 5 | Repeated sucrose application allows evaluation of t-tubular characteristics several times in a particular cell. **(A)** Representative examples of two sucrose applications in a row in ventricular (upper graph) and atrial (lower graph) cardiomyocytes. The perfusion time with sucrose solution did not exceed 50 s. **(B)** The evaluated f_t was not different during subsequent sucrose applications (ventricular myocytes, $n = 14$, $p > 0.05$).

and experimentally proved in this study. Short-term perfusion with isotonic sucrose solution enabled to electrically separate the surface and t-tubular membranes. The most important advantage of this new method is its reversibility which allows repetitive measurements of f_t in the same cell.

Verification of the Method and Justification of the Model

To verify our method, we investigated the effect of detubulation induced by imipramine (Bourcier et al., 2019). We first confirmed the detubulation effect of imipramine by measuring the inward rectifier potassium tail current ($I_{K1,tail}$) in Tyrode solution in both control ventricular myocytes and in ventricular myocytes pre-treated with 225 μM imipramine in which $I_{K1,tail}$ was strongly suppressed, as expected (**Supplementary Figure S4A**). As can be seen in **Figure 6**, the t-tubular membrane fraction f_t determined by our method was significantly reduced in partially detubulated ventricular cardiomyocytes in a concentration-dependent manner. At the complete detubulation, the determination of f_t fails because the method is based on the analysis of two clearly distinguishable exponential components [indicated by conditions (6b)].

A number of quantitative models have been published so far aimed at describing the electrical properties of the tubular system in skeletal muscle cells (Adrian et al., 1969; Eisenberg et al., 1972; Mathias et al., 1977; Penderson et al., 2011). These models with distributed parameters follow the results of cable theory. They are usually formulated in such a general way that they can also be applied to cardiac cells, but hardly for practical measurement of tubular membrane capacitance. Mathias et al. (1977) developed and described in detail a model (called mesh model) based on an analysis of a random network of miniature cables connecting nodes. The whole system is described by a combination of differential and difference equations. Depending on the ratio between the length constant λ and the radius a of the cell (approximately cylindrical), the solution of the system can be divided into several areas. Assuming λ >> a, a lumped approximation of the tubular system is justified in a form corresponding to our simple model, created by the luminal resistance of the tubular system in series with a parallel combination of membrane resistance and capacitance. According to the recent study of Scardigli et al. (2017), tubular length constant $\lambda = 290 \pm 90$ μm and $a \sim 13$ μm in rat ventricular myocytes resulting in $\lambda/a \sim 22$. This ratio may be however altered under conditions of sucrose solution. Both resistances determining λ will be increased, however, the actual change can only be roughly estimated. Even if, in the extreme case,

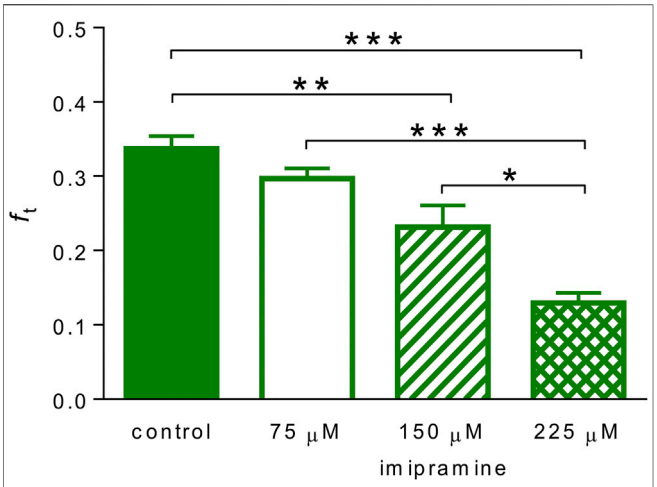

FIGURE 6 | Partial detubulation revealed by the new technique. Comparison of the fraction of the t-tubular membrane f_t in control ventricular myocytes (n = 21) and in ventricular myocytes partially detubulated using 75, 150, and 225 μM imipramine (n = 5, 8, and 8, respectively); *, **, and ***—statistical significance at p < 0.05, 0.01, and 0.001, respectively.

the luminal resistance per unit length of the tubule increased 100 times more than the resistance of the membrane, the condition λ > r would still be maintained. Lumped models of electrical properties of cardiomyocytes, including the tubular system, have already been used in other studies (Pásek et al., 2006; Pásek et al., 2008c; Cheng et al., 2011).

Origin of the Membrane Current in Sucrose

Considering the minute content of ions in the isotonic sucrose solution (supplemented only with 5 μM $CaCl_2$, the conductivity of ~3.5 μS/cm), the origin of the membrane current in sucrose is not entirely clear. The most likely candidate of the flowing current is inward rectifier potassium current I_{K1} which can be partially opposed by a negative chloride current with a high positive equilibrium voltage. We tested the effect of a specific I_{K1} inhibitor Ba^{2+} in three selected concentrations 10, 25, and 100 μM. The membrane current in sucrose was inhibited by 34, 46, and 67%, respectively (**Figure 7**). It implies that I_{K1} is the predominant component of the membrane current, especially around the holding voltage −80 mV. We tried to further support this result by measuring the effect of Ba^{2+} on $I_{K1,tail}$ induced by transient accumulation of t-tubular potassium ions (Cheng et al., 2011; Moench et al., 2013). However, this intention failed because $I_{K1,tail}$ was suppressed during application of the sucrose solution (**Supplementary Figure S4B**), very likely due to a high negative reversal voltage (see below) which prevented appearance of the inward current.

In sucrose, the resting membrane voltage considerably dropped to about −140 mV (**Figure 7B**), thus, the driving force of the ionic current was markedly enhanced. This can explain the large sucrose-induced outward current in **Figure 2A**. The shift of the resting voltage in sucrose solution corresponds well with the observations of Bouchard et al. (2004) who indicated a substantial shift of reversal voltage and decrease of slope conductance at low extracellular K^+ concentrations. **Figure 7** provides yet further evidence supporting the idea that I_{K1} is a major component of the ionic current in sucrose solution. Due to the effect of Ba^{2+}, the negative reversal voltage dropped significantly to a level around −100 mV, as can be seen clearly from the current response to the descending part of the imposed voltage ramp.

The Fraction of T-Tubular Membrane f_t Estimated by Various Techniques

Marked differences can be observed in f_t values evaluated using various techniques in ventricular myocytes, even in those from healthy hearts. Using the diffusion technique and measurements of whole-cell capacitance and cell dimensions, Shepherd and McDonough (1998) suggested f_t of 0.56 in guinea-pig ventricular myocytes, which is consistent with data acquired by imaging techniques in rat, guinea-pig, and human ventricular myocytes (over 0.5; Amsellem et al., 1995; Soeller and Cannell 1999; Ohler et al., 2009).

In contrast, studies using the often-used detubulation techniques report lower values of f_t in rat ventricular myocytes. Most data were obtained using hyperosmotic shock (e.g., f_t = 0.264 in Kawai et al., 1999, 0.29 in Brette and Orchard 2006, 0.32 in Brette et al., 2006, 0.315 in Bryant et al., 2015); later studies report values obtained from hypoosmotic shock (0.27 in Moench et al., 2013) or from the effect of imipramine (~0.4 in Bourcier et al., 2019). The value f_t = 0.337 ± 0.017 estimated by our new method (**Figure 3C**) fits well with the range of values obtained so far by detubulation approaches. Considering all these data and despite attempts to explain the differences (Pásek et al., 2008b), the true value of f_t in ventricular myocytes is still unclear, estimated somewhere between ~0.25 and 0.55.

The published data on t-tubular characteristics in atrial myocytes are even more diverse and rarer than that in ventricular cells. The t-tubules were identified by imaging techniques in atrial myocytes of various species including rat and human (e.g., Dibb et al., 2009; Wakili et al., 2010; Richards et al., 2011; Frisk et al., 2014; Glukhov et al., 2015; Yue et al., 2017). Yue et al. (2017) found out that identifiable t-tubules may be detected in more than 80% of isolated mouse atrial myocytes. However, only a minority of atrial myocytes contain well-organized t-tubules in small rodents, e.g., in the rat (~10%, Frisk et al., 2014). As expected, the value f_t estimated by our new method was significantly lower in rat atrial myocytes in comparison to that in rat ventricular myocytes (**Figure 3C**). Considering almost zero t-tubular area estimated by Caldwell et al. (2014) in the rat atria (using di-4-ANEPPS membrane staining), we were surprised by our relatively high atrial f_t value (0.144 ± 0.015). Our results agreed rather with the data published by Yue et al. (2017) who estimated the t-tubular area between 0 and 24% in mouse atrial myocytes (~10% on average in male mice using di-4-ANEPPS membrane staining). To our knowledge, the only study using formamide detubulation in atrial cells (Brette et al., 2002) suggests a value of f_t ~ 0.06. The heterogeneity of the tubular system in the atria is apparently enormous (Frisk et al., 2014).

In addition to various measurement techniques, interspecies differences and heterogeneity of t-tubular

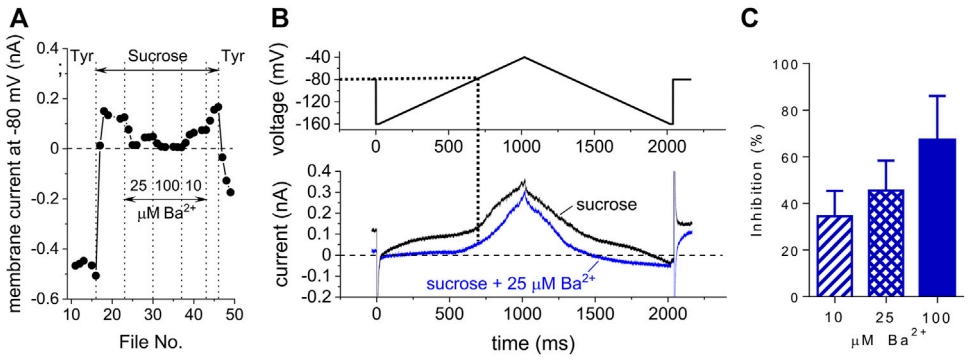

FIGURE 7 | Effect of Ba^{2+} on the membrane current in the presence of sucrose. **(A)** Time course of changes of the membrane current at –80 mV in a representative cell during consecutive application of sucrose alone and in combination with 10, 25, and 100 μM Ba^{2+}. **(B)** Changes of the membrane current during a ramp stimulation (lower panel; for the stimulation protocol, see the upper panel). **(C)** Average inhibition of the membrane current at –80 mV in sucrose at 10, 25, and 100 μM Ba^{2+} ($n = 3$).

density in both ventricular and atrial myocytes are likely the main cause of the different results (Richards et al., 2011; Caldwell et al., 2014; Frisk et al., 2014; Yue et al., 2017).

Does the Content of T-Tubules Correlate With Cell Size?

In our data, we did not observe a significant correlation between f_t and size of the cells (estimated as C_{Tyr}) in both rat ventricular and atrial myocytes (**Figure 4**). Regarding ventricular myocytes, this finding is not surprising because previous studies documented overall well-developed t-tubules in the investigated ventricular myocytes of various species including rat (e.g., Soeller and Cannell 1999; Dibb et al., 2009; Richards et al., 2011; Jayasinghe et al., 2012; Frisk et al., 2014). Therefore, no correlation between the cell size and t-tubular content may be expected and was not observed in previous studies (e.g., Richards et al., 2011; Frisk et al., 2014).

Controversial information may be found regarding t-tubular content in atrial cells of various sizes. Frisk et al. (2014) showed that the size of rat atrial myocytes without and with either disorganized or organized t-tubules did not differ (Figure 3D in Frisk et al., 2014) which agrees well with our data (**Figure 4B**). In contrast, the proportion of rat atrial myocytes with the t-tubules was higher in the wider cells in the study by Smyrnias et al. (2010); imaging identification of t-tubules). Similarly, the t-tubular content correlated with the cell width in mouse atrial myocytes (Yue et al., 2017; imaging identification of t-tubules). We missed this correlation in our data (**Figure 4B**) which may be related to the fact that we likely unintentionally selected only wider cells for our patch-clamp measurements.

More developed t-tubules could be found in wider myocytes isolated from the atria of big mammals, such as dog, horse, cow, and sheep (Wakili et al., 2010; Richards et al., 2011). As discussed by Richards et al. (2011), the difference between atrial myocytes of small rodents (rat) and big mammals may be related to the lower width of atrial myocytes of small rodents (the width of about 10 μm in rat, e.g., Dibb et al., 2009; Walden et al., 2009) and to the necessity of more developed t-tubules in wider cardiomyocytes to ensure the synchronized rise of Ca^{2+} in the whole cardiomyocyte and, thus, its synchronized contraction (reviewed by Dibb et al., 2013).

Advantages and Limitations of the New Method

As mentioned above, the most important advantage of the new method is its reversibility. It allows to directly compare parameters of the total cell membrane measured in the control Tyrode solution and the t-tubular membrane measured in the sucrose solution in the same cell. Thus, paired comparison of the differences may be done which is the preferable way of evaluation whenever it is possible. Since the estimated f_t did not differ during the first and second sucrose application in the same cells (**Figure 5**), the method may be used even for analysis of short-term changes in structure and function of the t-tubular system, induced by e.g., a transient hypoosmotic state (Moench et al., 2013) which may be relevant for the clinical practice (e.g., Kanda et al., 2004; Silveira et al., 2018). Both the paired statistical testing and analysis of short-term changes of the t-tubules are impossible when the usually used detubulation method is applied. We also plan to extend the use of the method to the estimation of other parameters characterizing the t-tubular membrane, such as the fraction of various ionic currents in the t-tubules because literary data are sparse and diverse in some cases.

A certain limitation of the method is the fact that the set of parameters obtained by the bi-exponential approximation of the capacitive current recorded in the sucrose solution does not allow an accurate calculation of all elements of the electrical equivalent circuit (**Figure 1A**). In our preliminary study (Šimurda et al., 2021), this problem was solved by an additional assumption of direct proportionality between the ratio of membrane conductivities and the ratio of membrane capacitances measured in t-tubular and surface membranes. In this work, we introduced a simpler way to estimate the t-tubular membrane capacitance $C_t \pm$ SD with the accuracy limited by the given theory. In ventricular and atrial

cardiomyocytes, the value of SD was 4% and 5%, respectively, as justified in the **Supplementary Material**.

The accurate measurements require a reliable washing of the entire cell surface with the selected solution. A violation of this condition is reflected in the set of parameters obtained by the bi-exponential approximation of the capacitive current. The condition (**Eq. 6a**) is to guarantee that the source of the perfusion solution is not too far from the measured cell. The remaining conditions (**Eq. 6b**) indicate that all parts of the cell are sufficiently washed. Unfortunately, many measured data were discarded (**Supplementary Figure S3**). Considering the fact that many measurements were discarded due to violation of conditions (**Eq. 6b**), we expect that the number of well-measured cells may be increased by lifting the measured cell slightly. It well agrees with the findings recently published by Uchida and Lopatin (2018) who emphasize the necessity of lifting the measured cell up to ensure proper t-tubular diffusion with the applied solution. It is a risky procedure, but it may help improve the diffusion of sucrose into the t-tubular system and, thus, increase the yield of our newly proposed method.

Another limitation may result from the fact that sucrose application seems to affect the estimated value of the cell membrane capacitance. C_m evaluated in the sucrose solution was significantly lower than C_{Tyr} evaluated in the Tyrode solution (**Figures 3A,B**). It is in agreement with the study by Vaughan et al. (1972) on skeletal muscle fibers. They showed that the cell membrane capacitance may be reduced if the cell is exposed to a solution with low content of ions. Anyway, the value of f_t should not be affected by this side effect of sucrose application if the surface and t-tubular membranes are affected evenly by sucrose. In addition, the actual values of C_s and C_t can be estimated by multiplying by the C_{Tyr}/C_m coefficient.

CONCLUSION

We have developed a new approach to the determination of the fraction of t-tubular membrane based on the perfusion of the measured cell with a low-conductivity isotonic solution. Its advantage over existing methods is the possibility of repeated measurements on the same cardiomyocyte and thus paired statistical testing. In the next work, we assume its extension to the measurement of t-tubular ionic current fractions. The method can be useful for studying short-term changes in the t-tubular system.

DATA AVAILABILITY STATEMENT

The raw data supporting the conclusion of this article will be made available by the authors, without undue reservation.

ETHICS STATEMENT

The animal study was reviewed and approved by the Local Committee for Animal Treatment at Masaryk University, Faculty of Medicine, and the Ministry of Education, Youth and Sports the Ministry of Education, Youth and Sports (permission No. MSMT-29203/2012-30 and MSMT-33846/2017-3).

AUTHOR CONTRIBUTIONS

OŠ—cell isolation, patch-clamp measurements, data analysis, writing of the manuscript; MB—cell isolation, patch-clamp measurements, data analysis, writing of the manuscript; MŠ—data analysis, literature search, writing of the manuscript; JŠ—development of the new method, study design, data analysis, writing of the manuscript.

FUNDING

This study was supported by the Specific University Research Grant of the Masaryk University MUNI/A/1133/2021 provided by the Ministry of Education, Youth and Sports of the Czech Republic and by the grant project NU22-02-00348 provided by the Ministry of Health of the Czech Republic.

ACKNOWLEDGMENTS

We thank B. Vyoralová for excellent technical assistance.

SUPPLEMENTARY MATERIAL

The Supplementary Material for this article can be found online at: https://www.frontiersin.org/articles/10.3389/fphys.2022.837239/full#supplementary-material

REFERENCES

Adrian, R. H., Chandler, W. K., and Hodgkin, A. L. (1969). The Kinetics of Mechanical Activation in Frog Muscle. *J. Physiol.* 204, 207–230. doi:10.1113/jphysiol.1969.sp008909

Amsellem, J., Delorme, R., Souchier, C., and Ojeda, C. (1995). Transverse-axial Tubular System in guinea Pig Ventricular Cardiomyocyte: 3D Reconstruction, Quantification and its Possible Role in K+ Accumulation-Depletion Phenomenon in Single Cells. *Biol. Cel* 85, 43–54. doi:10.1111/j.1768-322x.1995.tb00941.x

Bébarová, M., Matejovič, P., Pásek, M., Šimurdová, M., and Šimurda, J. (2005). Effect of Ajmaline on Transient Outward Current in Rat Ventricular Myocytes. *Gen. Physiol. Biophys.* 24, 27–45.

Bébarová, M., Matejovič, P., Pásek, M., Hořáková, Z., Hošek, J., Šimurdová, M., et al. (2016). Effect of Ethanol at Clinically Relevant Concentrations on Atrial Inward Rectifier Potassium Current Sensitive to Acetylcholine. *Naunyn Schmiedebergs Arch. Pharmacol.* 389, 1049–1058. doi:10.1007/s00210-016-1265-z

Bouchard, R., Clark, R. B., Juhasz, A. E., and Giles, W. R. (2004). Changes in Extracellular K+concentration Modulate Contractility of Rat and Rabbit Cardiac Myocytes via the Inward Rectifier K+currentIK1. *J. Physiol.* 556, 773–790. doi:10.1113/jphysiol.2003.058248

Bourcier, A., Barthe, M., Bedioune, I., Lechêne, P., Miled, H. B., Vandecasteele, G., et al. (2019). Imipramine as an Alternative to Formamide to Detubulate Rat Ventricular Cardiomyocytes. *Exp. Physiol.* 104, 1237–1249. doi:10.1113/EP087760

Brette, F., Komukai, K., and Orchard, C. H. (2002). Validation of Formamide as a Detubulation Agent in Isolated Rat Cardiac Cells. *Am. J. Physiology-Heart Circulatory Physiol.* 283, H1720–H1728. doi:10.1152/ajpheart.00347.2002

Brette, F., and Orchard, C. H. (2006). Density and Sub-cellular Distribution of Cardiac and Neuronal Sodium Channel Isoforms in Rat Ventricular Myocytes. *Biochem. Biophys. Res. Commun.* 348, 1163–1166. doi:10.1016/j.bbrc.2006.07.189

Brette, F., Sallé, L., and Orchard, C. H. (2006). Quantification of Calcium Entry at the T-Tubules and Surface Membrane in Rat Ventricular Myocytes. *Biophysical J.* 90, 381–389. doi:10.1529/biophysj.105.069013

Bryant, S. M., Kong, C. H. T., Watson, J., Cannell, M. B., James, A. F., and Orchard, C. H. (2015). Altered Distribution of ICa Impairs Ca Release at the T-Tubules of Ventricular Myocytes from Failing Hearts. *J. Mol. Cell Cardiol.* 86, 23–31. doi:10.1016/j.yjmcc.2015.06.012

Caldwell, J. L., Smith, C. E. R., Taylor, R. F., Kitmitto, A., Eisner, D. A., Dibb, K. M., et al. (2014). Dependence of Cardiac Transverse Tubules on the BAR Domain Protein Amphiphysin II (BIN-1). *Circ. Res.* 115, 986–996. doi:10.1161/CIRCRESAHA.116.303448

Cheng, L.-F., Wang, F., and Lopatin, A. N. (2011). Metabolic Stress in Isolated Mouse Ventricular Myocytes Leads to Remodeling of T Tubules. *Am. J. Physiology-Heart Circulatory Physiol.* 301, H1984–H1995. doi:10.1152/ajpheart.00304.2011

Crossman, D. J., Ruygrok, P. R., Soeller, C., and Cannell, M. B. (2011). Changes in the Organization of Excitation-Contraction Coupling Structures in Failing Human Heart. *PLoS ONE* 6, e17901. doi:10.1371/journal.pone.0017901

Crossman, D. J., Jayasinghe, I. D., and Soeller, C. (2017). Transverse Tubule Remodelling: a Cellular Pathology Driven by Both Sides of the Plasmalemma? *Biophys. Rev.* 9, 919–929. doi:10.1007/s12551-017-0273-7

Dibb, K. M., Clarke, J. D., Horn, M. A., Richards, M. A., Graham, H. K., Eisner, D. A., et al. (2009). Characterization of an Extensive Transverse Tubular Network in Sheep Atrial Myocytes and its Depletion in Heart Failure. *Circ. Heart Fail.* 2, 482–489. doi:10.1161/CIRCHEARTFAILURE.109.852228

Dibb, K. M., Clarke, J. D., Eisner, D. A., Richards, M. A., and Trafford, A. W. (2013). A Functional Role for Transverse (T-) Tubules in the Atria. *J. Mol. Cell Cardiol.* 58, 84–91. doi:10.1016/j.yjmcc.2012.11.001

Dibb, K. M., Louch, W. E., and Trafford, A. W. (2022). Cardiac Transverse Tubules in Physiology and Heart Failure. *Annu. Rev. Physiol.* 84, 229–255. doi:10.1146/annurev-physiol-061121-040148

Eisenberg, R. S., Vaughan, P. C., and Howell, J. N. (1972). A Theoretical Analysis of the Capacitance of Muscle Fibers Using a Distributed Model of the Tubular System. *J. Gen. Physiol.* 59, 360–373. doi:10.1085/jgp.59.3.360

Frisk, M., Koivumäki, J. T., Norseng, P. A., Maleckar, M. M., Sejersted, O. M., and Louch, W. E. (2014). Variable T-Tubule Organization and Ca2+ Homeostasis across the Atria. *Am. J. Physiology-Heart Circulatory Physiol.* 307, H609–H620. doi:10.1152/ajpheart.00295.2014

Glukhov, A. V., Balycheva, M., Sanchez-Alonso, J. L., Ilkan, Z., Alvarez-Laviada, A., Bhogal, N., et al. (2015). Direct Evidence for Microdomain-specific Localization and Remodeling of Functional L-type Calcium Channels in Rat and Human Atrial Myocytes. *Circulation* 132, 2372–2384. doi:10.1161/CIRCULATIONAHA.115.018131

Guo, A., and Song, L.-S. (2014). AutoTT: Automated Detection and Analysis of T-Tubule Architecture in Cardiomyocytes. *Biophysical J.* 106, 2729–2736. doi:10.1016/j.bpj.2014.05.013

Guo, A., Zhang, C., Wei, S., Chen, B., and Song, L.-S. (2013). Emerging Mechanisms of T-Tubule Remodelling in Heart Failure. *Cardiovasc. Res.* 98, 204–215. doi:10.1093/cvr/cvt020

Heinzel, F. R., Bito, V., Biesmans, L., Wu, M., Detre, E., von Wegner, F., et al. (2008). Remodeling of T-Tubules and Reduced Synchrony of Ca 2+ Release in Myocytes from Chronically Ischemic Myocardium. *Circ. Res.* 102, 338–346. doi:10.1161/CIRCRESAHA.107.160085

Hong, T., and Shaw, R. M. (2017). Cardiac T-Tubule Microanatomy and Function. *Physiol. Rev.* 97, 227–252. doi:10.1152/physrev.00037.2015

Hrabcová, D., Pásek, M., Šimurda, J., and Christé, G. (2013). Effect of Ion Concentration Changes in the Limited Extracellular Spaces on Sarcolemmal Ion Transport and Ca2+ Turnover in a Model of Human Ventricular Cardiomyocyte. *Int. J. Mol. Sci.* 14, 24271–24292. doi:10.3390/ijms141224271

Ibrahim, M., Gorelik, J., Yacoub, M. H., and Terracciano, C. M. (2011). The Structure and Function of Cardiac T-Tubules in Health and Disease. *Proc. R. Soc. B.* 278, 2714–2723. doi:10.1098/rspb.2011.0624

Jayasinghe, I., Crossman, D., Soeller, C., and Cannell, M. (2012). Comparison of the Organization of T-Tubules, Sarcoplasmic Reticulum and Ryanodine Receptors in Rat and Human Ventricular Myocardium. *Clin. Exp. Pharmacol. Physiol.* 39, 469–476. doi:10.1111/j.1440-1681.2011.05578.x

Kanda, M., Omori, Y., Shinoda, S., Yamauchi, T., Tamemoto, H., Kawakami, M., et al. (2004). SIADH Closely Associated with Non-functioning Pituitary Adenoma. *Endocr. J.* 51, 435–438. doi:10.1507/endocrj.51.435

Kawai, M., Hussain, M., and Orchard, C. H. (1999). Excitation-contraction Coupling in Rat Ventricular Myocytes after Formamide-Induced Detubulation. *Am. J. Physiology-Heart Circulatory Physiol.* 277, H603–H609. doi:10.1152/ajpheart.1999.277.2.H603

Komukai, K., Yamanushi, T., Orchard, C., and Brette, F. (2002). K + Current Distribution in Rat Sub-epicardial Ventricular Myocytes. *Pflugers Archiv Eur. J. Physiol.* 444, 532–538. doi:10.1007/s00424-002-0851-8

Louch, W., Bito, V., Heinzel, F. R., Macianskiene, R., Vanhaecke, J., Flameng, W., et al. (2004). Reduced Synchrony of Ca2+ Release with Loss of T-Tubules-A Comparison to Ca2+ Release in Human Failing Cardiomyocytes. *Cardiovasc. Res.* 62, 63–73. doi:10.1016/j.cardiores.2003.12.031

Mathias, R. T., Eisenberg, R. S., and Valdiosera, R. (1977). Electrical Properties of Frog Skeletal Muscle Fibers Interpreted with a Mesh Model of the Tubular System. *Biophysical J.* 17, 57–93. doi:10.1016/s0006-3495(77)85627-0

Moench, I., Meekhof, K. E., Cheng, L. F., and Lopatin, A. N. (2013). Resolution of Hyposmotic Stress in Isolated Mouse Ventricular Myocytes Causes Sealing of T-Tubules. *Exp. Physiol.* 98, 1164–1177. doi:10.1113/expphysiol.2013.072470

Ohler, A., Weisser-Thomas, J., Piacentino, V., Houser, S. R., Tomaselli, G. F., and O'Rourke, B. (2009). Two-photon Laser Scanning Microscopy of the Transverse-Axial Tubule System in Ventricular Cardiomyocytes from Failing and Non-failing Human Hearts. *Cardiol. Res. Pract.* 2009, 1–9. doi:10.4061/2009/802373

Orchard, C. H., Pásek, M., and Brette, F. (2009). The Role of Mammalian Cardiac T-Tubules in Excitation-Contraction Coupling: Experimental and Computational Approaches. *Exp. Physiol.* 94, 509–519. doi:10.1113/expphysiol.2008.043984

Pásek, M., Šimurda, J., and Christé, G. (2006). The Functional Role of Cardiac T-Tubules Explored in a Model of Rat Ventricular Myocytes. *Phil. Trans. R. Soc. A. Math. Phys. Eng. Sci.* 364, 1187–1206. doi:10.1098/rsta.2006.1764

Pásek, M., Šimurda, J., Christé, G., and Orchard, C. H. (2008a). Modelling the Cardiac Transverse-Axial Tubular System. *Prog. Biophys. Mol. Biol.* 96, 226–243. doi:10.1016/j.pbiomolbio.2007.07.021

Pásek, M., Brette, F., Nelson, A., Pearce, C., Qaiser, A., Christe, G., et al. (2008b). Quantification of T-Tubule Area and Protein Distribution in Rat Cardiac Ventricular Myocytes. *Prog. Biophys. Mol. Biol.* 96, 244–257. doi:10.1016/j.pbiomolbio.2007.07.016

Pásek, M., Šimurda, J., Orchard, C. H., and Christé, G. (2008c). A Model of the guinea-pig Ventricular Cardiac Myocyte Incorporating a Transverse-Axial Tubular System. *Prog. Biophys. Mol. Biol.* 96, 258–280. doi:10.1016/j.pbiomolbio.2007.07.022

Pásek, M., Šimurda, J., and Orchard, C. H. (2012). Role of T-Tubules in the Control of Trans-sarcolemmal Ion Flux and Intracellular Ca2+ in a Model of the Rat Cardiac Ventricular Myocyte. *Eur. Biophys. J.* 41, 491–503. doi:10.1007/s00249-012-0804-x

Penderson, T. H., Huang, C. L-H., and Fraser, J. A. (2011). An Analysis of the Relationships between Subthreshold Electrical Properties and Excitability in Skeletal Muscle. *J. Gen. Physiol.* 138, 73–93. doi:10.1085/jgp.201010510

Richards, M. A., Clarke, J. D., Saravanan, P., Voigt, N., Dobrev, D., Eisner, D. A., et al. (2011). Transverse Tubules Are a Common Feature in Large Mammalian Atrial Myocytes Including Human. *Am. J. Physiology-Heart Circulatory Physiol.* 301, H1996–H2005. doi:10.1152/ajpheart.00284.2011

Rog-Zielinska, E. A., Moss, R., Kaltenbacher, W., Greiner, J., Verkade, P., Seemann, G., et al. (2021). Nano-scale Morphology of Cardiomyocyte T-Tubule/sarcoplasmic Reticulum Junctions Revealed by Ultra-rapid High-Pressure Freezing and Electron Tomography. *J. Mol. Cell Cardiol.* 153, 86–92. doi:10.1016/j.yjmcc.2020.12.006

Scardigli, M., Crocini, C., Ferrantini, C., Gabbrielli, T., Silvestri, L., Coppini, R., et al. (2017). Quantitative Assessment of Passive Electrical Properties of the Cardiac T-Tubular System by FRAP Microscopy. *Proc. Natl. Acad. Sci. U.S.A.* 114, 5737–5742. doi:10.1073/pnas.1702188114

Setterberg, I. E., Le, C., Frisk, M., Perdreau-Dahl, H., Li, J., and Louch, W. E. (2021). The Physiology and Pathophysiology of T-Tubules in the Heart. *Front. Physiol.* 12, 718404. doi:10.3389/fphys.2021.718404

Shepherd, N., and McDonough, H. B. (1998). Ionic Diffusion in Transverse Tubules of Cardiac Ventricular Myocytes. *Am. J. Physiology-Heart Circulatory Physiol.* 275, H852–H860. doi:10.1152/ajpheart.1998.275.3.H852

Silveira, M. A. D., Seguro, A. C., da Silva, J. B., Arantes de Oliveira, M. F., Seabra, V. F., Reichert, B. V., et al. (2018). Chronic Hyponatremia Due to the Syndrome of Inappropriate Antidiuresis (SIAD) in an Adult Woman with Corpus Callosum Agenesis (CCA). *Am. J. Case Rep.* 19, 1345–1349. doi:10.12659/AJCR.911810

Šimurda, J., Šimurdová, M., Švecová, O., and Bébarová, M. (2021). *A New Approach to the Determination of Tubular Membrane Capacitance: Passive Membrane Electrical Properties under Reduced Electrical Conductivity of the Extracellular Solution*. bioRxiv preprint. doi:10.1101/2021.11.12.468264

Smith, C., Trafford, A., Caldwell, J., and Dibb, K. (2018). Physiology and Patho-Physiology of the Cardiac Transverse Tubular System. *Curr. Opin. Physiol.* 1, 153–160. doi:10.1016/j.cophys.2017.11.002

Smyrnias, I., Mair, W., Harzheim, D., Walker, S. A., Roderick, H. L., and Bootman, M. D. (2010). Comparison of the T-Tubule System in Adult Rat Ventricular and Atrial Myocytes, and its Role in Excitation-Contraction Coupling and Inotropic Stimulation. *Cell Calcium* 47, 210–223. doi:10.1016/j.ceca.2009.10.001

Soeller, C., and Cannell, M. B. (1999). Examination of the Transverse Tubular System in Living Cardiac Rat Myocytes by 2-photon Microscopy and Digital Image-Processing Techniques. *Circ. Res.* 84, 266–275. doi:10.1161/01.res.84.3.266

Uchida, K., and Lopatin, A. N. (2018). Diffusional and Electrical Properties of T-Tubules Are Governed by Their Constrictions and Dilations. *Biophys. J.* 114, 437–449. doi:10.1016/j.bpj.2017.11.3742

Vaughan, P. C., Howell, J. N., and Eisenberg, R. S. (1972). The Capacitance of Skeletal Muscle Fibers in Solutions of Low Ionic Strength. *J. Gen. Physiol.* 59, 347–359. doi:10.1085/jgp.59.3.347

Wagner, E., Lauterbach, M. A., Kohl, T., Westphal, V., Williams, G. S. B., Steinbrecher, J. H., et al. (2012). Stimulated Emission Depletion Live-Cell Super-resolution Imaging Shows Proliferative Remodeling of T-Tubule Membrane Structures after Myocardial Infarction. *Circ. Res.* 111, 402–414. doi:10.1161/CIRCRESAHA.112.274530

Wakili, R., Yeh, Y.-H., Yan Qi, X., Greiser, M., Chartier, D., Nishida, K., et al. (2010). Multiple Potential Molecular Contributors to Atrial Hypocontractility Caused by Atrial Tachycardia Remodeling in Dogs. *Circ. Arrhythmia Electrophysiol.* 3, 530–541. doi:10.1161/CIRCEP.109.933036

Walden, A. P., Dibb, K. M., and Trafford, A. W. (2009). Differences in Intracellular Calcium Homeostasis between Atrial and Ventricular Myocytes. *J. Mol. Cell Cardiol.* 46, 463–473. doi:10.1016/j.yjmcc.2008.11.003

Yue, X., Zhang, R., Kim, B., Ma, A., Philipson, K. D., and Goldhaber, J. I. (2017). Heterogeneity of Transverse-Axial Tubule System in Mouse Atria: Remodeling in Atrial-specific Na + -Ca 2+ Exchanger Knockout Mice. *J. Mol. Cell Cardiol.* 108, 50–60. doi:10.1016/j.yjmcc.2017.05.008

Conflict of Interest: The authors declare that the research was conducted in the absence of any commercial or financial relationships that could be construed as a potential conflict of interest.

Publisher's Note: All claims expressed in this article are solely those of the authors and do not necessarily represent those of their affiliated organizations, or those of the publisher, the editors and the reviewers. Any product that may be evaluated in this article, or claim that may be made by its manufacturer, is not guaranteed or endorsed by the publisher.

frontiers | Frontiers in Physiology

METHODS
published: 30 May 2022
doi: 10.3389/fphys.2022.876633

Multiple Laser Doppler Flowmetry Probes Increase the Reproducibility of Skin Blood Flow Measurements

J. Carter Luck[1], *Allen R. Kunselman*[2], *Michael D. Herr*[1], *Cheryl A. Blaha*[1], *Lawrence I. Sinoway*[1] *and Jian Cui*[1]*

[1]Penn State Health Heart and Vascular Institute, Pennsylvania State University College of Medicine, Hershey, PA, United States, [2]Department of Public Health Sciences, Pennsylvania State University College of Medicine, Hershey, PA, United States

Cutaneous microcirculatory perfusion is commonly measured using laser Doppler flowmetry (LDF) probes, which provide a continuous, non-invasive quantification of skin blood flow (SkBF). However, inhomogeneities in the skin's microvasculature density contribute to a decrease in reproducibility whenever an LDF probe is removed and replaced, as is the case during pre- and post-intervention or between-day measurements. Therefore, this study aimed to determine whether increasing the total number of individual LDF probes in a localized area improves the reproducibility of the measurement. Seven laser Doppler probes were secured in a custom-made acrylic holder designed to attach to the skin's surface easily. SkBF, local skin temperature (Tsk), and blood pressure (BP) were assessed in 11 participants (6 M, 5 F, 42 ± 15 years). SkBF and Tsk were measured from the dorsal forearm (arm trial) for 5 min. Next, the multi-laser device was moved to the lateral side of the calf (leg trial), and measurements were obtained for 5 min. Each arm and leg trial was cyclically repeated three times, and all trials were separated by intermissions lasting 10–15 min. The average SkBF and the cutaneous vascular conductance (CVC) from all possible LDF probe combinations were not statistically different across the three arm and leg trials. Two-way mixed-effects models with absolute agreement were used to compute the intraclass correlation coefficient (ICC) for CVC, and the minimum ICC increased with the addition of LDF probes. The ICC of the average CVC from seven LDF probes was 0.96 between the arm trials and 0.91 between the leg trials, which suggests that there is excellent reliability and little difference between trials following the removal and replacement of the device. Moreover, all individual ICC values from ≥3 LDF probe combinations were greater than 0.70 (i.e., good reliability). These data suggest that SkBF measurements with multiple laser Doppler probes in a custom-made holder have excellent reproducibility after replacing the probes within the same participant. Therefore, this application could provide more reproducible assessments between repeated measurements (e.g., before and after exercise or clinical procedures) where the LDF probes must be removed and replaced within the same location.

Keywords: skin blood flow, laser Doppler, thermoregulation, reproducibility, microcirculation

OPEN ACCESS

Edited by:
Chao Chen,
University of California, Davis,
United States

Reviewed by:
Manuel F Navedo,
University of California, Davis,
United States
Julie Bossuyt,
University of California, Davis,
United States

***Correspondence:**
Jian Cui
jcui@pennstatehealth.psu.edu

Specialty section:
This article was submitted to Integrative Physiology, a section of the journal Frontiers in Physiology

Received: *15 February 2022*
Accepted: *11 May 2022*
Published: *30 May 2022*

Citation:
Luck JC, Kunselman AR, Herr MD, Blaha CA, Sinoway LI and Cui J (2022) Multiple Laser Doppler Flowmetry Probes Increase the Reproducibility of Skin Blood Flow Measurements. Front. Physiol. 13:876633. doi: 10.3389/fphys.2022.876633

Abbreviations: BP, blood pressure; CVC, cutaneous vascular conductance; HR, heart rate; ICC, intraclass correlation coefficient; LDF, laser Doppler flowmetry; MAP, mean arterial blood pressure; Q1, first quartile; Q3, third quartile; SkBF, Skin blood flow; Tsk, local skin temperature.

INTRODUCTION

Laser light has been frequently used in various biomedical applications since its initial development in the 1960s (Maiman, 1960; Townes, 2007). For decades, researchers have used laser light scattering, reflection, and absorption principles and properties to quantify various physiologic parameters. The optical technique of laser-Doppler flowmetry (LDF) utilizes frequency-shifted laser light signals, which are reflected from red blood cells (erythrocytes), to quantify an index of microcirculatory perfusion in a static tissue (Holloway and Watkins, 1977; Nilsson et al., 1980a; Nilsson et al., 1980b). In human and animal experiments, these LDF probes may be applied to the skin to obtain measurements of skin blood flux (SkBF). The assessment of SkBF *via* LDF probes has provided critically useful information to further our understanding of thermoregulation and microvascular function/dysfunction. However, the LDF technique is not free from limitations, and the assessment of SkBF has been continuously criticized. Namely, it is highly susceptible to motion artifacts, and there is considerably large site-to-site and day-to-day signal heterogeneity. Thus, the inability to remove and replace the LDF probe significantly hinders the ability to obtain observations pre- and post-intervention without the use of normalization techniques (e.g., local vascular occlusion for the prepose of establishing a physiological zero or converting the raw data to a percent change from a thermoneutral baseline (33–34°C), or converting the raw data to a percentage of "maximal" SkBF at the site). Therefore, a more broadly applied method that could achieve greater reproducibility between measurements would benefit physiology researchers.

The LDF measurement is based on the Doppler principle, where laser light is applied to an otherwise static tissue at a specific wavelength (i.e., monochromatic). Due to the light-scattering and absorption properties from endogenous chromophores (e.g., erythrocytes) and other tissue components, reflected laser light becomes frequency-shifted by moving erythrocytes but remains relatively unshifted as it passes through static tissue. The broadening of the laser light, dependent on the velocity of the moving erythrocytes, is subsequently detected by photodetectors and processed by a computer. To date, LDF probes have been applied to various vascularized tissue beds (e.g., skin, muscle, liver, brain, bone, and tooth pulp) in both experiments in humans (Davis et al., 2006; Davis et al., 2008; Ghouth et al., 2018) and animals (Arvidsson et al., 1988; Lombard and Roman, 1990; Hanne et al., 2019; Allen et al., 2020). The exact sampling depth of an LDF probe is difficult to determine. It requires the identification of the individual blood vessel and erythrocyte that has interacted with the light from the LDF probe, which is both site, velocity, and time-dependent. Moreover, increased concentrations of hemoglobin molecules can shield deeper hemoglobin molecules from irradiation. Thus, the strongest signal originates from the erythrocytes closest to the light source, and the signal strength weakens with greater penetration depths. Therefore, it is generally expected that LDF penetration is shallower in tissues with relatively high hemoglobin concentrations, as is the case in skeletal muscle tissue. Whereas in cutaneous measurement, the penetration depth is expected to be slightly deeper. Using a Monte-Carlo model to simulate the diffusion of photons through biological tissue, it is roughly estimated that the sampling depth in cutaneous tissue is between 1.0 and 1.5 mm^2, yielding a sample volume of roughly ~1 mm^3 (Low et al., 2020). Thus, given the anatomical structure of the cutaneous microvasculature, it is generally believed that the LDF signal is generated by arterioles, capillaries, and post-capillary venules of the upper horizontal plexus of the dermis (Braverman et al., 1990). Due to the skin's large surface area and its superficially located capillary loops (Braverman, 2000), it serves as a readily accessible vascular bed for the investigation of microvascular function (Holowatz et al., 2008).

Similar to LDF measurement, various techniques have been employed to track changes in microvascular perfusion, namely, venous occlusion plethysmography, scanning laser-Doppler imaging, laser-Doppler speckle contrast imaging, and optical coherence tomography (Chaseling et al., 2020; Low et al., 2020). Several other methods have been used to investigate blood flow and vascular function in various regions (e.g., Doppler ultrasonography, flow-mediated dilation, pulse wave velocity, and carotid intima thickness). However, these techniques are primarily isolated to the large conduit arteries and thus, do not fully capture the downstream effects in the microvascular circulation. Other optical techniques such as near-infrared spectroscopy and pulse oximetry provide more detailed information about the interaction between oxygen and hemoglobin. However, due to the high temporal resolution, user independence, and affordability, LDF remains one of the most commonly used tools to monitor SkBF.

Although the skin is generally regarded as an excellent interrogation site for LDF probes, due to its non-invasive accessibility, SkBF measures are incredibly susceptible to motion artifacts and any slight movement or relocation of the LDF probe (Tenland et al., 1983). This is because the skin's microvascular structure and density are not evenly distributed from site to site (Braverman et al., 1990; Braverman et al., 1992; Braverman and Schechner, 1991). Indeed, several studies have repeatedly demonstrated topographical zones of high and low SkBF using sequential LDF measurements from a localized region (Braverman and Schechner, 1991; Wårdell et al., 1994). Thus, due to the small area measured by a single-point LDF probe, it has been demonstrated that the technique's reproducibility may be limited as LDF signals vary with slight movements of the probe (Tenland et al., 1983; Braverman et al., 1990; Wårdell et al., 1994; Puissant et al., 2013). Therefore, the LDF measurement is typically used to quantify temporal changes in SkBF in response to pharmacological and thermal stimuli (Low et al., 2020) in experiments where the device is secured in place for the duration of the experiment. Studies utilizing the average resting (i.e., non-normalized) SkBF values as the primary outcome measure or experimental designs where the LDF probe must be removed and replaced (e.g., between-day, pre- and post-exercise, or clinical procedure) have often been considered unreliable. To further improve reproducibility, the influence of spatial inhomogeneities must be reduced. One previous study has

TABLE 1 | Participant characteristics.

	Value
Sex, *n* (men/women)	6/5
Age, yr	42 ± 15
Height, cm	171.1 ± 7.2
Weight, kg	72.5 ± 8.1
BMI, kg/m^2	24.7 ± 1.2

Values are means ± SD. BMI, body mass index.

used signal averaging techniques of serial measurements in a localized area to improve day-to-day reproducibility (Wårdell et al., 1994). Another group has used an integrated LDF with multiple emitting fibers and two photodetectors showing that this approach improves the coefficient of variation when the device is moved to adjacent positions, 5 mm apart (Salerud and Nilsson, 1986). Based on these prior observations, the present study sought to use a custom-made integrated LDF probe holder (consisting of seven LDF probes) to test the hypothesis that the reproducibility of the LDF signal increases with the addition of individual LDF probes after the device has been removed and replaced within participants in the same location. The development of a method capable of decreasing the spatial inhomogeneities and reproducing measures of SkBF pre- and post-intervention could greatly expand the application of LDF assessments.

MATERIALS AND METHODS

Study Population

Eleven individuals (six men, five women) were invited to participate in the study. The participant characteristics are shown in **Table 1**. All participants were in good health with no history of cardiovascular, pulmonary, metabolic, or renal disease, and none were taking medications during the study. Each participant had the purposes and risks of the protocol explained to them before written informed consent was obtained. The experimental protocol was approved by the Institutional Review Board of the Penn State Milton S. Hershey Medical Center and conformed with the World Medical Association's Declaration of Helsinki.

Measurements

As described in prior reports (Cui et al., 2013; Cui et al., 2021), blood pressure (BP) was measured with an automated sphygmomanometer from the brachial artery (SureSigns VS3, Philips, Philip Medical System). Two sets of laser-Doppler flowmetry systems (MoorLab, Moor Instruments Ltd., Devon, United Kingdom) with a total of seven optical probes were used to measure SkBF. Four of the seven probes were type MP1/7-V2, which had eight glass collecting fibers in a 2 mm ring with one central glass delivery fiber (i.e., a separation distance of 1 mm). Three of the seven probes were type MP12-V2, which had one glass collecting fiber and one glass delivery fiber with 0.5 mm separation of the fibers. Signal penetration depth is multifaceted. It is dependent on the optical properties of the sample tissue and the concentration of erythrocytes in the tissue. Tissues with higher concentrations of erythrocytes will result in a slightly shallower measurement depth. In general, it can be roughly estimated that the LDF signals come from a depth of ~75% of the separation distance between the delivery and collecting fibers. Thus, the MP1/7-V2 probes are assumed to penetrate slightly further than the MP12-V2 probes. Additionally, the increased number of encircling collecting fibers in the MP1/7-V2 probes will yield a larger sample volume compared to the single-point MP12-V2 probes. All seven probes transmitted light from solid-state laser diodes at ~780 nm. Each of the probes was calibrated using a calibration kit (CAL, Moor Instruments Ltd., Devon, United Kingdom) before being used in this study.

A custom-made holder was used to mount the seven probes in a circular and equidistant configuration (**Figure 1A**). Briefly, the mount was made from a 45 mm plastic disc with a height of 11.5 mm. At 11.25 mm from the center of the circle, three small holes (1.25 mm diameter) were drilled at locations 0°, 90°, and 180°, relative to the unit circle. These three holes housed the three MP12-V2 blunt needle end delivery probes. Next, at 7.0 mm from the center of the circle, four larger tapered holes (10.25 mm down-tapered to 8.05 mm diameter) were drilled at locations 45°, 135°, 225°, and 315°, relative to the unit circle. These four tapered holes were specifically drilled to fit the contort of the MP1/7-V2 right angle probe, which has a 3 mm diameter cable. Thus a 4 mm wide by 5 mm high rectangular notch was cut to allow the cable and the right-angle probe to sit flush with the bottom of the holder. Lastly, three small 1.5 mm notches were made along the outside of the holder and used as visual landmarks while replacing the holder on the participant's skin. Furthermore, an ink marker was used to mark the skin at the location of each notch. LDF probe-to-probe separation distances were consistent (**Figure 1B**), and LDF probes were placed no closer than 8.4 mm apart. The probe holder was attached to the skin using double-sided adhesive discs (PAD, Moor Instruments Ltd., Devon, United Kingdom) and hypoallergenic tape (Transpore, 3M, St. Paul, MN, United States). To monitor the local skin temperature (Tsk), a thermocouple (TC-2000 thermocouple meters, Sable systems) attached to the skin was placed directly under the probe holder (**Figure 1**).

Experimental Protocols

The procedures were conducted with the participant in the supine position in a room with an ambient temperature of ~23°C. Three trials were performed with intermissions, during which participants were released from the testing table for 10–15 min. The seven probes were placed in the plastic holder. A thin thermocouple (Type T) was also placed under the probe holder. The probe holder was then placed on the participant's dorsal forearm, approximately at the middle position between the wrist and elbow along the line between the lateral epicondyle of the humerus and the lateral side of the styloid process of radius (**Figure 1C**). The position of the probe holder was marked using a semi-permanent marker. After

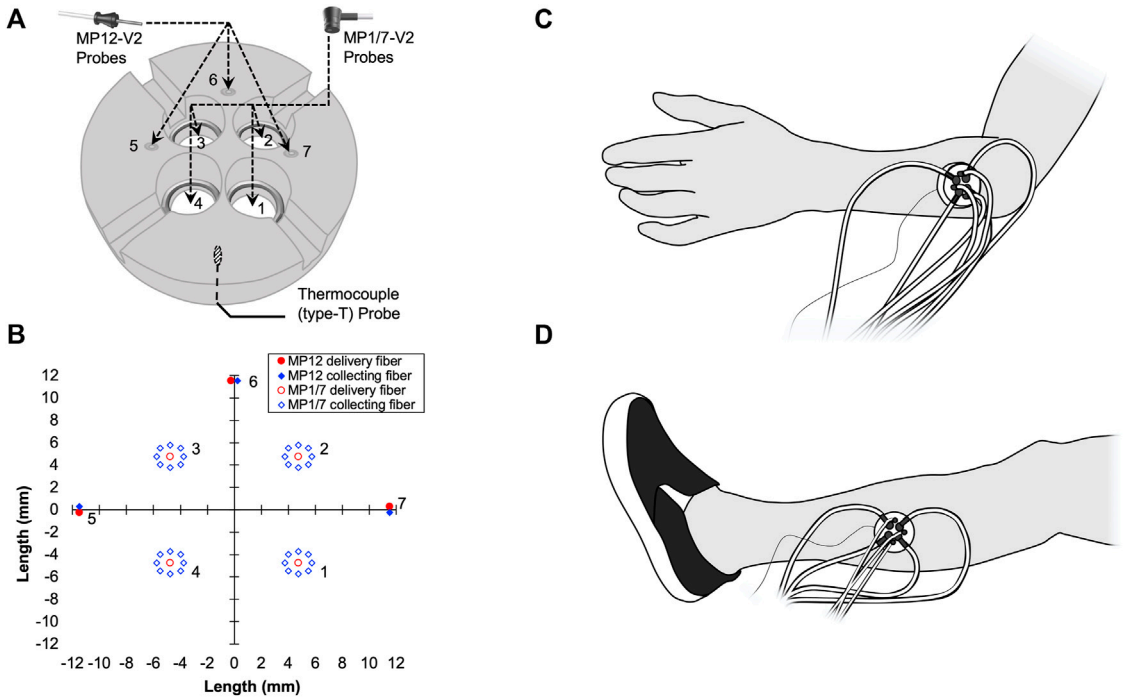

FIGURE 1 | A schematic representation of the custom-made laser Doppler flowmetry (LDF) probe holder **(A)** is shown. Four MP1/7-V2 right angle probes were placed into tapered holes (1, 2, 3, and 4). Three MP12-V2 blunt needle end delivery probes were inserted into three small holes (5, 6, and 7). A thin thermocouple (type T) used to measure skin temperature (Tsk) was placed between the bottom of the probe holder and the surface of the skin. LDF probe-to-probe separation distances in millimeters are plotted **(B)**. The location of the probe holder during the Arm Trial **(C)** and Leg Trial **(D)** are shown.

instrumentation, participants were asked to rest quietly during an acclimation period prior to the data collection while all signals of the SkBF, Tsk, and BP were monitored. The acclimation period was at least 5 min or until all signals were stable. Thereafter, SkBF and Tsk were recorded for 3 min, while BP was measured once from the contralateral arm (Arm Trial). Then, the probe holder and all of the probes were removed from the forearm. Thereafter, the probe holder and the probes were placed on the lateral aspect of the leg, which was approximately at the midpoint on the line between the tip of the head of the fibula to the tip of the lateral malleolus (**Figure 1D**). The position of the probe holder on the leg was also marked using a semi-permanent marker. Then, all signals were monitored for at least 5 min for an acclimation period. Thereafter, SkBF and Tsk were recorded for 3 min, while BP was measured once from the arm (Leg Trial). After the probe holder and all of the probes were removed from the leg, the participant was dis-instrumented and released from the testing table. Participants stayed in the laboratory for 10–15 min before lying back down on the testing table. Trials 2 and 3: The probe holder was carefully replaced on the same positions according to the markers left on the skin. The measurements on the forearm and then leg, as well as the intervals between the trials, were repeated. The order of the Arm Trial and Leg Trial was randomized amongst the participants, while the order was kept in the three trials in each individual. Because the cardiovascular variables (BP, HR, *etc.*) and thermoregulatory variables (e.g., body and skin temperatures) can change from day-to-day, these factors will directly affect SkBF. To decrease the possible influences from these factors, the three trials were performed in one laboratory visit.

Data Analysis

Data were sampled at 200 Hz *via* a data acquisition system (PowerLab, ADInstruments, Castle Hill, NSW, Australia). The mean values of the 3-min recordings of SkBF and Tsk were used as the measurement for the trial. Cutaneous vascular conductance (CVC) was calculated from the ratio of the SkBF to mean arterial pressure (MAP). The SkBF and CVC from each individual probe were calculated at first. The absolute values of BP, Tsk, SkBF, and CVC were used to examine the effects of the intervention (i.e., replacing the probes), and comparisons between the three trials were examined using repeated measures one-way ANOVA. When appropriate, Tukey *post-hoc* analyses were employed.

In this test-retest reliability study, the intraclass correlation coefficient (ICC) of the CVC was used as the primary index for the reliability of the measurement. In the present study, ICC estimates and their 95% confidence intervals were calculated using SPSS statistical software (Version 27, SPSS Inc.) based on a mean-rating (k = 3), absolute-agreement, two-way mixed-effects model (Shrout and Fleiss, 1979). The calculation of ICC for the CVC from each individual probe were performed at

TABLE 2 | Absolute hemodynamic and skin microvascular responses.

	Arm				Leg			
	Trial 1	**Trial 2**	**Trial 3**	***p*-value**	**Trial 1**	**Trial 2**	**Trial 3**	***p*-value**
Systolic arterial pressure, mmHg	119 ± 16	115 ± 17	113 ± 15*	0.002	116 ± 17	113 ± 13	110 ± 14*	0.002
Diastolic arterial pressure, mmHg	75 ± 17	74 ± 14	71 ± 15	0.051	74 ± 14	71 ± 14*	69 ± 14*	0.002
Mean arterial pressure, mmHg	90 ± 15	87 ± 14	84 ± 14*	0.002	87 ± 13	86 ± 13	83 ± 13	0.078
Heart rate, bpm	67 ± 16	65 ± 14	62 ± 14*	0.018	62 ± 17	61 ± 15	62 ± 13	0.782
Tsk, °C	29.6 ± 1.7	29.5 ± 3.1	30 ± 3.1	0.904	31.2 ± 0.7	30.9 ± 1.7	29.6 ± 3.6	0.118

Values are means ± SD. Values represent the 3-min resting period prior to replacing the laser Doppler flowmeter probes. The probes were alternated from the arm to the leg every 3 min, a total of three times (trial 1, 2, and 3). Tsk, skin temperature. P, *p-value of one-way repeated measures ANOVA; *Post-hoc, p < 0.05 vs Trial 1.*

TABLE 3 | Individual probe measures of skin blood flux and cutaneous vascular conductance.

	Arm				Leg			
	Trial 1	**Trial 2**	**Trial 3**	***p*-value**	**Trial 1**	**Trial 2**	**Trial 3**	***p*-value**
Mean SkBF, p.u.	25.5 ± 9.6	24.3 ± 9.2	23.2 ± 6.7	0.830	28.1 ± 9	28.1 ± 8.8	26.9 ± 9	0.819
Probe 1, p.u.	22.6 ± 17.1	22.5 ± 20.4	19.2 ± 10.9	0.860	23 ± 13	21.8 ± 12.6	18.8 ± 7.8	0.676
Probe 2, p.u.	16.1 ± 7.6	18 ± 9.8	18.9 ± 12.2	0.799	24.6 ± 13.3	24.1 ± 13.8	17.9 ± 7.3	0.351
Probe 3, p.u.	90.8 ± 43.8	77.9 ± 27.5	70.8 ± 19	0.342	99.9 ± 33.7	96.6 ± 26	99.6 ± 48.8	0.974
Probe 4, p.u.	15.6 ± 3.8	19.7 ± 7.9	17 ± 6.6	0.332	20.2 ± 11.8	21.7 ± 9.7	22.5 ± 12.8	0.887
Probe 5, p.u.	10.2 ± 2.4	9.3 ± 2.5	9 ± 2.2	0.432	8.9 ± 2.3	9 ± 2.2	8.9 ± 2.4	0.990
Probe 6, p.u.	13.9 ± 9.7	14.4 ± 14.3	18.2 ± 19.7	0.766	11.2 ± 6.4	13.4 ± 8.4	9.8 ± 7.6	0.525
Probe 7, p.u.	8.9 ± 5.3	8.4 ± 6.2	9.3 ± 7.1	0.947	9 ± 6.3	10.1 ± 6	10.7 ± 6.6	0.830
Mean CVC, p.u.· mmHg-1	28.7 ± 9.3	28.5 ± 10	27.9 ± 7.1	0.811	32.9 ± 10.9	33.5 ± 12.4	32.6 ± 10.2	0.930
Probe 1, p.u.· $mmHg^{-1}$	24.8 ± 4.8	25.7 ± 6.2	22.7 ± 3.2	0.904	26.5 ± 4.4	25.5 ± 4.3	23.4 ± 3.5	0.858
Probe 2, p.u.· $mmHg^{-1}$	18.3 ± 2.5	20.9 ± 2.9	22.5 ± 3.8	0.636	29 ± 4.8	29.1 ± 5.5	22.1 ± 2.8	0.466
Probe 3, p.u.· $mmHg^{-1}$	102.1 ± 12.6	92.5 ± 10.8	87.1 ± 9.2	0.622	116.5 ± 11.8	115.4 ± 11.4	118.8 ± 14.1	0.981
Probe 4, p.u.· $mmHg^{-1}$	17.9 ± 1.6	22.8 ± 2.4	20.3 ± 2.1	0.250	23.1 ± 3.8	25.3 ± 3.4	26.8 ± 4.1	0.793
Probe 5, p.u.· $mmHg^{-1}$	12 ± 1.4	11.1 ± 1.1	11.1 ± 1.1	0.839	10.7 ± 1.2	10.8 ± 1	11 ± 1.2	0.980
Probe 6, p.u.· $mmHg^{-1}$	15.4 ± 3.1	16.8 ± 4.8	20.2 ± 5.8	0.762	13.2 ± 2.5	15.9 ± 3.1	12.6 ± 3.3	0.706
Probe 7, p.u.· $mmHg^{-1}$	10.3 ± 1.8	9.8 ± 2.1	11.2 ± 2.4	0.903	11 ± 2.6	12.4 ± 2.8	13.4 ± 2.7	0.823

Mean SkBF, the average skin blood flux value from all seven LDF probes from the device; p.u., perfusion units; Mean CVC, the average cutaneous vascular conductance value from all seven LDF probes; Probe 1, 2, 3, ..., 7, are the average from all 11 participants for each individual LDF probes are shown. Values are means ± SD. P, *p-value of one-way repeated measures ANOVA.*

first. To test the effects of multiple probes, the mean values of each combination of the CVC from these probes were calculated (e.g., 35 combinations for each three probes). Then, the ICC for the mean CVC from all possible combinations (i.e., 2–7) of the probes were calculated with ICC values ≥0.70 being considered acceptable for research (Matheson G. J., 2019).

Statistical power analysis for ICC was performed using a publicly accessible add-in (Real Statistics Using Excel. www.real-statistics.com, Charles Zaiontz) for Microsoft Excel (Microsoft Corporation, Redmond, WA, United States).

The five-number summary of the distribution (i.e., minimum, Q1, median, Q3, maximum) of ICC values from the combinations of the probes were calculated and are presented with box and whiskers plots using Sigmaplot software (Version 14, Systat Software Inc.). All values are reported as means ± SD. p values of <0.05 were considered statistically significant.

RESULTS

The mean SkBF, Tsk, CVC, BPs, and HR during the three arm trials and three leg trials are shown in **Table 2**. MAP decreased along the three arm trials (Trial 1 vs Trial 3, $p < 0.05$) and did not change significantly along the leg trials. HR decreased along the three arm trials and did not change significantly along the leg trials.

Tsk remained constant across all three arm trials and three leg trials. The averaged SkBF and CVC from all probes did not change significantly along the three arm trials or three leg trials (**Table 3**). The SkBF and CVC from each individual probe during the three arm trials and three leg trials are shown in **Table 3**. The SkBF and CVC from each individual probe did not change significantly along the three arm trials or three leg trials.

The ICC values from the individual probes and the ICC values from the combinations of the probes in the arm trials and in the leg trials are presented with box and whiskers plots in **Figure 2**

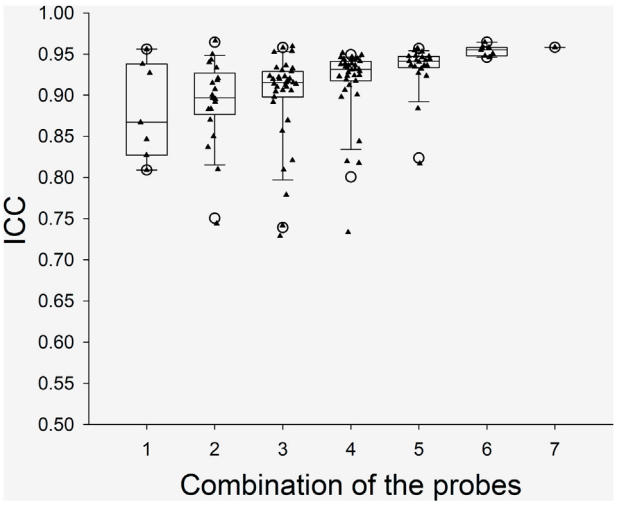

FIGURE 2 | Boxplots for the ICC between CVC values during the Arm Trials with the various probe combinations. *X* axis: the number of probes for the combinations. The calculated "Minimum" and "Maximum" values are indicated by open circles. The data below Minimum or above Maximum were outliers.

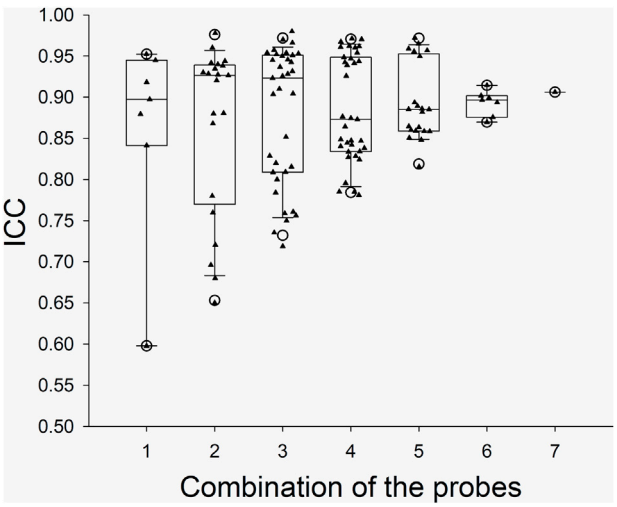

FIGURE 3 | Boxplots for the ICC between CVC values during the Leg Trials with the various probe combinations. *X* axis: the number of probes for the combinations. The calculated "Minimum" and "Maximum" values are indicated by open circles. The data below Minimum or above Maximum were outliers.

and **Figure 3**, respectively. The five-number summary of the distribution (i.e., minimum, Q1, median, Q3, maximum) of ICC values in the box and whiskers plots are shown in **Table 4**. The minimum ICC values (i.e., the lowest detected ICC), generally improved with the addition of probes in both the arm, and leg. Specifically, the lowest ICC with a single probe was only 0.598, while the lowest ICC with seven probes was 0.906, which indicates that using more probes improves the reproducibility

TABLE 4 | The five-number summary of the distribution of ICC values.

Probes (*n* =)	Combinations (*n* =)	Min	Q1	Median	Q3	Max
Arm Trial						
1	7	0.809	0.827	0.867	0.938	0.956
2	21	0.751	0.883	0.897	0.921	0.966
3	35	0.740	0.898	0.915	0.929	0.959
4	35	0.801	0.917	0.931	0.941	0.951
5	21	0.825	0.935	0.941	0.947	0.957
6	7	0.946	0.948	0.955	0.958	0.965
7	1	0.958	0.958	0.958	0.958	0.958
Leg Trial						
1	7	0.598	0.841	0.897	0.945	0.952
2	21	0.651	0.780	0.926	0.938	0.978
3	35	0.733	0.809	0.923	0.951	0.980
4	35	0.781	0.834	0.873	0.949	0.971
5	21	0.816	0.859	0.885	0.950	0.972
6	7	0.870	0.876	0.896	0.902	0.914
7	1	0.906	0.906	0.906	0.906	0.906

Data correspond to the five-number summary of the distribution (i.e. minimum, Q1, median, Q3, maximum) of ICC values which have been presented graphicly in the box and whiskers plots shown in ***Figures 2***, ***3****.*

of the CVC measurements. All data points from the arm trials using five or more probes and the leg trials with four or more probes had an ICC >0.75, which is considered indicative of good reliability between measurements (Bobak et al., 2018).

For the ICC for each of the seven single probes in the arm, the mean statistical power was 0.993 with a range of 0.989–0.997 (n = 7). For the ICC for each of the seven single probes in leg, the mean statistical power was 0.993 with a range of 0.990–0.994 (n = 7). For the averaged measurements of seven probes, the mean statistical powers were 0.991 for the arm measurements and 0.994 for the leg measurements.

DISCUSSION

The present study aimed to assess the test-retest reliability of SkBF/CVC measurements with multiple LDF probes in one holder. We found that test-retest reliability of CVC measurements increased with the addition of up to seven LDF probes in an integrated probe holder, which verified our hypothesis. These data suggest that SkBF measurements obtained with multiple LDF probes in a localized area have high reliability after removing and replacing the probes on the same participants. To our knowledge, this is the first study to provide evidence that the absolute values of SkBF/CVC after replacing the probes in the same participants can be used for analysis without the use of a normalization technique.

Integrated Laser Dopper Flux Probe Design

As illustrated in **Figures 1A,B**, the integrated LDF probe holder increases total sample volume by ~ seven-fold. The increase in sample volume is important, as previous studies have shown that

spatial inhomogeneities in microvascular density very in relatively small areas in the skin (Braverman et al., 1990; Braverman et al., 1992; Braverman, 1997, Braverman and Schechner, 1991). Thus, the contribution of spatial inhomogeneities should be reduced by simple averaging of the SkBF signals from each LDF probe. Two different types of LDF probes were used in this study to increase the total sample volume. The rationale for using a mixture of probes was related to available space within the custom probe holder, which was cut from a 45 mm diameter acrylic rod. With the addition of three smaller-diameter MP12-V2 probes, the probe-to-probe separation distance was reduced while increasing the number of probes from four to seven. The present data show that by this addition of probes within the same general area, signal reliability improves (**Figures 2**, **3**). However, it is important to note that the sampling depth between the two types of probes is slightly different. Although, determining the exact penetration depth requires the identification of the individual blood vessel and red blood cell that has interacted with the light from the LDF probe(s), which is both site, perfusion, and time-dependent. Thus, it is impossible to know the exact penetration depth. However, using Monte-Carlo modeling techniques for the diffusion of photons, it is estimated that the sampling depth in cutaneous tissue is 1.0–1.5 mm (Low et al., 2020). It is also speculated that that more superficial hemoglobin molecules could shield deeper hemoglobin molecules from irradiation. Thus, the strongest signal could likely originate from the superficial dermis vasculature (i.e., erythrocytes more superficial in relation to the device), and the signal strength weakens with greater penetration depths. In the present study, the data suggest that only four of the deeper-penetrating MP1/7-V2 probes are sufficient. As indicated by the majority of ICC values >0.75, which is considered indicative of good reliability between measurements (Bobak et al., 2018). However, the addition of the three MP12-V2 probes did indeed further improve reliability. Another potential issue is the physical displacement of the device following intermission periods between trials. The LDF probes were secured within the probe holder during measurement periods and were not moved within the probe holder itself. Additionally, an ink marker was used to outline the device and used to identify the probe location. Indeed, the present study did not appear to produce any inter-operator variability as the device was assembled, removed, and replaced by several members of the study team.

With the current integrated probe holder design, it is important to consider the possibility of probe-to-probe light contamination with the custom probe holder. We placed the probes in a configuration where probe light sources were no closer than 8.4 mm (**Figure 1B**). We selected these probe distances as they did not produce any detectible change in the absolute SkBF signal whilst the probes were individually turned on and off repeatedly. Thus, we believe that the LDF probes were placed at a sufficient separation distance to avoid probe-to-probe light contamination. Although, it must be stated that while we did not observe any change in the SkBF signals using these probe-to-probe separation distances, closer separation distances than 8.4 mm were not explicitly tested. Therefore, it remains unclear if closer separation distances produce noticeable changes in the LDF signal that can be attributed to light contamination from an adjacent probe. Studies by Braverman and collogues showed the randomly dispersed ascending arterioles, which supply the horizontal vascular network of capillaries, were at 1.5–1.7 mm intervals in the derma (Braverman et al., 1990). Thus, we believe that the ascending arterioles within the sample volumes of each of the seven individual LDF probes were most likely different.

Laser Doppler Flux and Cutaneous Vascular Conductance Responses

LDF SkBF value is a relative unit of perfusion (p.u.), commonly termed "red blood cell flux" or simply "flux," which is defined by the manufacturer using a phantom. Specifically, flux is the product of measured red blood cell concentration and velocity; thus, flux is proportional to the velocity and concentration of erythrocytes in a local tissue and is largely impacted by changes in cutaneous vasoconstriction and dilation. SkBF signals can be isolated to capillaries with a diameter of roughly 10 microns which are located in the papillary dermis 1–2 mm below the epidermal surface (Braverman, 1997). In the present study, no statistical differences were observed between the individual or mean SkBF values (**Table 2**). Thus, it is reasonable to assume that the addition of probes within the integrated probe holder contributed to the signal stability across trials at the same measurement location within each participant.

Similarly, with the SkBF values, the CVC values were not significantly different between trials in either the arm or leg (**Table 2**). The CVC was calculated as flux/mean arterial pressure. Obtaining a stable and reproducible CVC value was of particular interest in the present study due to its potential application in future studies. Indeed, in most thermoregulation studies, the main interest is on the cutaneous vascular tone (i.e., vasoconstriction and/or dilation) and less commonly focused on cutaneous blood flow itself. The BP is the main driving force for the blood flow. To decrease the effects of BP in the data, the current investigation reports CVC values, as the calculation is often used to represent the cutaneous vascular tone. In the present study, the BP decreased over time. It can be assumed that this decrease in BP is largely due to the experimental conditions in that all participants were monitored in a quiet room for over 1 h without any strong physical activity or emotional stimuli. As discussed above, the influences of this BP change should be decreased by using CVC. Temperature change (cooling or heating) can directly cause cutaneous vasoconstriction or vasodilation, which will alter CVC. In the present study, there were no changes in the skin temperature at the sites in the three trials (**Table 1**). Moreover, we could also suppose that other environmental factors such as room temperature and humidity were maintained during the study. Thus, the changes in CVC values in the present study should not be a physiological response to these factors (BP or temperature, *etc.*).

ICC of Intraindividual and Intra-site Measurements Between Three Trials

This study utilized the assessment of ICC to reflect measurement reliability between trials where the LDF probes were removed and replaced within participants and on the same skin sites (e.g., the forearm and leg). Reliability reflects the extent to which measurements can be replicated in a sample of participants. Mathematically, reliability represents a ratio of true variance over true variance plus error variance (Ebel, 1951). The evaluation of reliability is fundamental to research and clinical assessment because true values can only be estimated. The assessment of ICC during repeated tests is widely used to determine the reliability of a measurement (Carrasco et al., 2014). Although there are several models to calculate ICC, ICC reflects both degree of correlation and agreement between measurements from the same participant (i.e., class). The ICC value ranges between 0 and 1, with values closer to 1 representing stronger reliability. It has been suggested that ICC values less than 0.5 indicate poor reliability, values between 0.5 and 0.75 indicate moderate reliability, values between 0.75 and 0.9 indicate good reliability, and values greater than 0.90 indicate excellent reliability (Koo and Li, 2016).

The readings from LDF probes can be significantly altered when the site is slightly moved (Braverman et al., 1990). Therefore, the reliability of SkBF and CVC measurements with single-point LDF is low, as several prior studies have shown (Roustit et al., 2010). It has been shown previously that when a single-point probe is reapplied to the same skin sites within-participants, the reproducibility is greatly improved (Yvonne-Tee et al., 2005). Likewise, when multiple probes in proximity are averaged, the coefficient of variation is reduced (Salerud and Nilsson, 1986). Thus, we speculate that increasing the total measurement area through the addition of multiple LDF probes would help to buffer the influences from inhomogeneities in the skin microvasculature and provide a more reproducible measure of CVC between measurement trials in the same participants.

In our study, the SkBF (and thus CVC) measurements were recorded from 14 individual sites (i.e., seven in the arm and seven in the leg). The ICC of CVC was calculated from the individual sites and the possible combinations in each trial. To ensure the reliability of the measurement, we think that the minimum value from the box and whiskers plots should be predominately considered. For the data from each single probe/site, the minimum ICC values were ~0.60 and 0.81 at leg and arm, respectively, which indicate a moderate to good reliability. However, considering that the application of LDF will not be limited to the forearm, the SkBF/CVC measurement with a single probe has only moderate reliability. When multiple probes (>3) were used, the ICC values increased with the number of the probes (**Figures 2**, **3**). We speculate that the relatively reduced ICC for 1 – 2 probes could be due to the measured area being small. With the increase in the number of probes, the total measured area increased, which in turn increased the ICC. Although there was one outlier data point, the Minimum ICC of CVC with four probes was greater than 0.7, which indicates are good to excellent reliability (Cicchetti, 1994).

Limitations

In the present study, there are several limitations that must be considered when interpreting these data or implementing the proposed approach for physiology research studies. First, the intermission period, which was fixed at 10–15 min, could be initially viewed as a limitation of the study since it is unclear if the measures are reproducible with longer intermissions. However, this period was necessary to establish that any observed changes in skin blood flow, if any, were from the approach itself and not a result of "real" SkBF changes that are known to fluctuate throughout the day. The possible changes in BP, central blood volume, skin and central temperature, and environmental factors such as humidity from days to weeks will actually alter SkBF. In the current study, the SkBF/CVC remained stable between all three trials in both the arm and leg. Thus, it is unlikely that these factors significantly contributed to the measurements. Second, without the use of a normalization procedure, it remains difficult to compare between various sites and individuals using the absolute SkBF and CVC values in human studies. Indeed, a prior study has shown that the absolute resting CVC values within participants were poor between days but improved with the application of heat strain (Gemae et al., 2021). Thus, caution is advised when interpreting SkBF data where comparisons between individuals or locations are made. Third, we acknowledge that the number of the individual subjects was not large ($n = 11$) as those in prior test-retests reliability studies (Koo and Li, 2016). However, the data of the measured CVC in the three trials were quite stable, which led to high ICCs. Importantly, the ICC power calculations for both the arm and leg trials in both individual and averaged CVC conditions were sufficiently high. Thus, the total sample size in the present study was sufficient. Fourth, given the present sample size for males ($n = 6$) and females ($n = 5$) or for age range ($n = 6$ for <40 years old, $n = 5$ for >40 years old), the current study was unable to compare between biological sex or various age groups. Thus, this highlights a significant area for future investigations with more subjects. Lastly, as is the case in many physiology experiments, there may be a potential limitation of the measurement device itself as manufacturing discrepancies cause variation in the absolute values from probe to probe. It cannot be overlooked that in the present study, LDF probe 3, on average, provided higher readings across all participants than that of the other probes. This is likely due to slight differences in the manufacturing of each probe. Although each probe was calibrated using the manufacturer's calibration procedure, there may still be discrepancies between probes and connections to the light source, which is housed in a separate device. Cupping connectors that join each fiberoptic cable may also have slight variations contributing to the variable readings. However, as these readings were reproducible across all trials (i.e., there were no significant changes in the absolute values between trials), the relatively high reading from probe three did not appear to detract from the original findings of this study.

Application of Integrated Laser Doppler Flux Probes in Research

The current study shows the addition of ≥4 LDF probes in an integrated probe holder device is sufficient for physiology research in humans. Prior to the development of this approach, our laboratory and others had been significantly limited by the LDF measurement in experiments where it is not realistic to measure SkBF continuously. Until now, protocols where the lasers had to be physically removed from the participant to complete other interventions significantly confounded the comparison of the SkBF measurement. With this new approach, various experimental designs, previously confounded by the limitation of a relatively small sample volume, may be better reliably investigated. For instance, this approach can be used in the protocols using whole-body heating with water immersion, acute exercise, or exercise training over a period of days or weeks. Moreover, the data from the multiple probes could present an "averaged" condition, effectively minimizing the effects of skin inhomogeneities. In turn, the study measuring reactive changes in blood flow, we speculate that the proposed application may also accurately track "averaged" reactive changes in SkBF and CVC. Importantly, the ability to remove and replace the LDF device allows for greater application from research in the clinical setting. As patients are routinely transferred between locations for certain diagnostic tests and procedures, the proposed approach could allow for a more reliable pre- and post-assessment of SkBF and CVC. Moreover, it is speculated that this approach could be applied to monitor the skin microcirculatory function in certain disease progressions (e.g., diabetes or peripheral artery disease) within the patients, as well as track the effects of medical therapy or surgical interventions (i.e., revascularization or skin graft) over time. It is also reasonable to speculate that this approach could be applied to animal research as well. In animal models, more invasive techniques allow for the assessment of flux from various tissues, including but not limited to the skeletal muscle. However, due to the size of the animal model, a different arrangement of probes and thus a revised integrated probe holder may be necessary to facilitate a smaller sampling area. Moreover, considering that the total sizes of the organs (e.g., skin in one limb) in small animals (e.g., mice or rats) are small, the relative area measured by multiply LDF probes can be relatively much larger (e.g., over 30%). Under this condition, it is possible that measurements could be used for inter-individual and inter-site comparisons, while further studies are needed to confirm this. Thus, the approach may have even greater applicability in these experiments as well.

In conclusion, the present study showed that increasing the number of individual LDF probes in a custom-made holder increases the reliability of the LDF measurement during test retests. These results suggest that CVC measurements, obtained using multiple laser Doppler probes (number ≥4), have a sufficiently high degree of reproducibility after replacing the probes within the same participant. Thus, we suggest the values from multiple laser Doppler probes in a holder can be used in the intraindividual analysis for certain experiments where the LDF probes must be removed and replaced in the same participants (Anderson and Parrish, 1981).

DATA AVAILABILITY STATEMENT

The raw data supporting the conclusions of this article will be made available by the authors, without undue reservation.

ETHICS STATEMENT

The studies involving human participants were reviewed and approved by Institutional Review Board of the Penn State Milton S. Hershey Medical Center. The patients/participants provided their written informed consent to participate in this study.

AUTHOR CONTRIBUTIONS

JL, AK, and LS conceived and designed the research; JL, MH, CB, and JC performed the experiments; JL, AK, and JC, analyzed data; JL, JC, and LS interpreted the results of experiments; JL and JC, prepared the figures; JL and JC drafted the manuscript; JL, AK, and JC edited and revised the manuscript; JL, AK, MH, CB, LS, and JC approved the final version of the manuscript.

FUNDING

This work was supported by National Institutes of Health Grants MPI R01 HL141198 and UL1 TR002014.

ACKNOWLEDGMENTS

We would like to express appreciation to the research participants for their willingness to take part in this study. We are grateful to Samuel Pai for assisting in data analysis.

REFERENCES

Allen, L. A., Terashvili, M., Gifford, A., and Lombard, J. H. (2020). Evaluation of Cerebral Blood Flow Autoregulation in the Rat Using Laser Doppler Flowmetry. *J. Vis. Exp.* 155, 60540. doi:10.3791/60540

Anderson, R. R., and Parrish, J. A. (1981). The Optics of Human Skin. *J. Investigative Dermatology* 77, 13–19. doi:10.1111/1523-1747.ep12479191

Arvidsson, D., Svensson, H., and Haglund, U. (1988). Laser-Doppler Flowmetry for Estimating Liver Blood Flow. *Am. J. Physiology-Gastrointestinal Liver Physiology* 254, G471–G476. doi:10.1152/ajpgi.1988.254.4.G471

Bobak, C. A., Barr, P. J., and O'Malley, A. J. (2018). Estimation of an Inter-rater Intra-class Correlation Coefficient that Overcomes Common Assumption Violations in the Assessment of Health Measurement Scales. *BMC Med. Res. Methodol.* 18, 93. doi:10.1186/s12874-018-0550-6

Braverman, I. M., Keh, A., and Goldminz, D. (1990). Correlation of Laser Doppler Wave Patterns with Underlying Microvascular Anatomy. *J. Investigative Dermatology* 95, 283–286. doi:10.1111/1523-1747.ep12484917

Braverman, I. M., and Schechner, J. S. (1991). Contour Mapping of the Cutaneous Microvasculature by Computerized Laser Doppler Velocimetry. *J. Investigative Dermatology* 97, 1013–1018. doi:10.1111/1523-1747.ep12492255

Braverman, I. M. (2000). The Cutaneous Microcirculation. *J. Investigative Dermatology Symposium Proc.* 5, 3–9. doi:10.1046/j.1087-0024.2000.00010.x

Braverman, I. M. (1997). The Cutaneous Microcirculation: Ultrastructure and Microanatomical Organization. *Microcirculation* 4, 329–340. doi:10.3109/10739689709146797

Carrasco, J. L., Caceres, A., Escaramis, G., and Jover, L. (2014). Distinguishability and Agreement with Continuous Data. *Stat. Med.* 33, 117–128. doi:10.1002/sim.5896

Chaseling, G. K., Crandall, C. G., and Gagnon, D. (2020). Skin Blood Flow Measurements during Heat Stress: Technical and Analytical Considerations. *Am. J. Physiology-Regulatory, Integr. Comp. Physiology* 318, R57–R69. doi:10.1152/ajpregu.00177.2019

Cicchetti, D. V. (1994). Guidelines, Criteria, and Rules of Thumb for Evaluating Normed and Standardized Assessment Instruments in Psychology. *Psychol. Assess.* 6, 284–290. doi:10.1037/1040-3590.6.4.284

Cui, J., Boehmer, J. P., Blaha, C., Lucking, R., Kunselman, A. R., and Sinoway, L. I. (2013). Chronic Heart Failure Does Not Attenuate the Total Activity of Sympathetic Outflow to Skin during Whole-Body Heating. *Circ. Heart Fail.* 6, 271–278. doi:10.1161/CIRCHEARTFAILURE.112.000135

Cui, J., Gao, Z., Blaha, C., Luck, J. C., Brandt, K., and Sinoway, L. I. (2021). Moderate Whole Body Heating Attenuates the Exercise Pressor Reflex Responses in Older Humans. *Am. J. Physiology-Regulatory, Integr. Comp. Physiology* 320, R757–R769. doi:10.1152/ajpregu.00232.2020

Davis, S. L., Fadel, P. J., Cui, J., Thomas, G. D., and Crandall, C. G. (2006). Skin Blood Flow Influences Near-Infrared Spectroscopy-Derived Measurements of Tissue Oxygenation during Heat Stress. *J. Appl. Physiology* 100, 221–224. doi:10.1152/japplphysiol.00867.2005

Davis, S. L., Shibasaki, M., Low, D. A., Cui, J., Keller, D. M., Purdue, G. F., et al. (2008). Cutaneous Vasoconstriction during Whole-Body and Local Cooling in Grafted Skin Five to Nine Months Postsurgery. *J. Burn Care & Res.* 29, 36–41. doi:10.1097/BCR.0b013e31815f2b63

Ebel, R. L. (1951). Estimation of the Reliability of Ratings. *Psychometrika* 16, 407–424. doi:10.1007/BF02288803

Gemae, M. R., Akerman, A. P., McGarr, G. W., Meade, R. D., Notley, S. R., Schmidt, M. D., et al. (2021). Myths and Methodologies: Reliability of Forearm Cutaneous Vasodilatation Measured Using laser-Doppler Flowmetry during Whole-body Passive Heating. *Exp. Physiol.* 106, 634–652. doi:10.1113/EP089073

Ghouth, N., Duggal, M. S., BaniHani, A., and Nazzal, H. (2018). The Diagnostic Accuracy of Laser Doppler Flowmetry in Assessing Pulp Blood Flow in Permanent Teeth: A Systematic Review. *Dent. Traumatol.* 34, 311–319. doi:10.1111/edt.12424

Hanne, N. J., Easter, E. D., and Cole, J. H. (2019). Minimally Invasive Laser Doppler Flowmetry Is Suitable for Serial Bone Perfusion Measurements in Mice. *Bone Rep.* 11, 100231. doi:10.1016/j.bonr.2019.100231

Holloway, G. A., and Watkins, D. W. (1977). Laser Doppler Measurement of Cutaneous Blood Flow. *J. Investigative Dermatology* 69, 306–309. doi:10.1111/1523-1747.ep12507665

Holowatz, L. A., Thompson-Torgerson, C. S., and Kenney, W. L. (20081985). The Human Cutaneous Circulation as a Model of Generalized Microvascular Function. *J. Appl. Physiology* 105, 370–372. doi:10.1152/japplphysiol.00858.2007

Koo, T. K., and Li, M. Y. (2016). A Guideline of Selecting and Reporting Intraclass Correlation Coefficients for Reliability Research. *J. Chiropr. Med.* 15, 155–163. doi:10.1016/j.jcm.2016.02.012

Lombard, J. H., and Roman, R. J. (1990). Assessment of Muscle Blood Flow by Laser-Doppler Flowmetry during Hemorrhage in SHR. *Am. J. Physiology-Heart Circulatory Physiology* 259, H860–H865. doi:10.1152/ajpheart.1990.259.3.H860

Low, D. A., Jones, H., Cable, N. T., Alexander, L. M., and Kenney, W. L. (2020). Historical Reviews of the Assessment of Human Cardiovascular Function: Interrogation and Understanding of the Control of Skin Blood Flow. *Eur. J. Appl. Physiol.* 120, 1–16. doi:10.1007/s00421-019-04246-y

Maiman, T. H. (1960). Stimulated Optical Radiation in Ruby. *Nature* 187, 493–494. doi:10.1038/187493a0

Nilsson, G. E., Tenland, T., and Oberg, P. A. (1980b). A New Instrument for Continuous Measurement of Tissue Blood Flow by Light Beating Spectroscopy. *IEEE Trans. Biomed. Eng.* BME-27, 12–19. doi:10.1109/TBME.1980.326686

Nilsson, G. E., Tenland, T., and Oberg, P. A. (1980a). Evaluation of a Laser Doppler Flowmeter for Measurement of Tissue Blood Flow. *IEEE Trans. Biomed. Eng.* BME-27, 597–604. doi:10.1109/TBME.1980.326582

Puissant, C., Abraham, P., Durand, S., Humeau-Heurtier, A., Faure, S., Lefthériotis, G., et al. (2013). Reproducibility of Non-invasive Assessment of Skin Endothelial Function Using Laser Doppler Flowmetry and Laser Speckle Contrast Imaging. *PLoS One* 8, e61320. doi:10.1371/journal.pone.0061320

Roustit, M., Blaise, S., Millet, C., and Cracowski, J. L. (2010). Reproducibility and Methodological Issues of Skin Post-occlusive and Thermal Hyperemia Assessed by Single-point Laser Doppler Flowmetry. *Microvasc. Res.* 79, 102–108. doi:10.1016/j.mvr.2010.01.001

Tenland, T., Salerud, E. G., Nilsson, G. E., and Oberg, P. A. (1983). Spatial and Temporal Variations in Human Skin Blood Flow. *Int. J. Microcirc. Clin. Exp.* 2, 81–90.

Townes, C. H. (2007). Theodore H. Maiman (1927-2007). *Nature* 447, 654. doi:10.1038/447654a

Wardell, K., Braverman, I. M., Silverman, D. G., and Nilsson, G. E. (1994). Spatial Heterogeneity in Normal Skin Perfusion Recorded with Laser Doppler Imaging and Flowmetry. *Microvasc. Res.* 48, 26–38. doi:10.1006/mvre.1994.1036

Yvonne-Tee, G. B., Rasool, A. H. G., Halim, A. S., and Rahman, A. R. A. (2005). Reproducibility of Different Laser Doppler Fluximetry Parameters of Postocclusive Reactive Hyperemia in Human Forearm Skin. *J. Pharmacol. Toxicol. Methods* 52, 286–292. doi:10.1016/j.vascn.2004.11.003

Conflict of Interest: The authors declare that the research was conducted in the absence of any commercial or financial relationships that could be construed as a potential conflict of interest.

Publisher's Note: All claims expressed in this article are solely those of the authors and do not necessarily represent those of their affiliated organizations, or those of the publisher, the editors and the reviewers. Any product that may be evaluated in this article, or claim that may be made by its manufacturer, is not guaranteed or endorsed by the publisher.

frontiers | Frontiers in Physiology

METHODS
published: 12 July 2022
doi: 10.3389/fphys.2022.891005

An Inexpensive Open-Source Chamber for Controlled Hypoxia/Hyperoxia Exposure

Tyler C. Hillman[1], *Ryan Idnani*[2] *and Christopher G. Wilson*[1,3]*

[1]Lawrence D. Longo, MD Center for Perinatal Biology, Loma Linda, CA, United States, [2]Department of Bioengineering, College of Engineering, University of California, Berkeley, CA, United States, [3]Department of Pediatrics, School of Medicine, Loma Linda University Medical Center Loma Linda University, Loma Linda, CA, United States

Understanding hypoxia/hyperoxia exposure requires either a high-altitude research facility or a chamber in which gas concentrations are precisely and reproducibly controlled. Hypoxia-induced conditions such as hypoxic-ischemic encephalopathy (HIE), obstructive or central apneas, and ischemic stroke present unique challenges for the development of models with acute or chronic hypoxia exposure. Many murine models exist to study these conditions; however, there are a variety of different hypoxia exposure protocols used across laboratories. Experimental equipment for hypoxia exposure typically includes flow regulators, nitrogen concentrators, and premix oxygen/nitrogen tanks. Commercial hypoxia/hyperoxia chambers with environmental monitoring are incredibly expensive and require proprietary software with subscription fees or highly expensive software licenses. Limitations exist in these systems as most are single animal systems and not designed for extended or intermittent hypoxia exposure. We have developed a simple hypoxia chamber with off-the-shelf components, and controlled by open-source software for continuous data acquisition of oxygen levels and other environmental factors (temperature, humidity, pressure, light, sound, etc.). Our chamber can accommodate up to two mouse cages and one rat cage at any oxygen level needed, when using a nitrogen concentrator or premixed oxygen/nitrogen tank with a flow regulator, but is also scalable. Our system uses a *Python*-based script to save data in a text file using modules from the sensor vendor. We utilized *Python* or *R* scripts for data analysis, and we have provided examples of data analysis scripts and acquired data for extended exposure periods (≤7 days). By using FLOS (Free-Libre and open-source) software and hardware, we have developed a low-cost and customizable system that can be used for a variety of exposure protocols. This hypoxia/hyperoxia exposure chamber allows for reproducible and transparent data acquisition and increased consistency with a high degree of customization for each experimenter's needs.

Keywords: hypoxia, ischemia, neonate, stroke, inflammation, open-source

OPEN ACCESS

Edited by:
Ovidiu Constantin Baltatu, Anhembi Morumbi University, Brazil

Reviewed by:
Richard James Wilson, University of Calgary, Canada
Thorsten Schwerte, University of Innsbruck, Austria

***Correspondence:**
Christopher G. Wilson
cgwilson@llu.edu

Specialty section:
This article was submitted to Integrative Physiology, a section of the journal Frontiers in Physiology

Received: *07 March 2022*
Accepted: *08 June 2022*
Published: *12 July 2022*

Citation:
Hillman TC, Idnani R and Wilson CG (2022) An Inexpensive Open-Source Chamber for Controlled Hypoxia/Hyperoxia Exposure. Front. Physiol. 13:891005. doi: 10.3389/fphys.2022.891005

INTRODUCTION

Chronic and acute hypoxia exposure has been used in the past to study many different diseases, including hypoxic-ischemic encephalopathy (HIE) (Lacaille et al., 2019), intermittent sleep apnea (Toth and Bhargava, 2013; Arias-Cavieres et al., 2020; Lebek et al., 2020; Arias-Cavieres et al., 2021), ischemic stroke (Tsuji et al., 2013) and epilepsy (Toth and Bhargava, 2013; Lebek et al., 2020). Many studies use plethysmography (whole body and head-out) to assess short-term hypoxia and acquire other physiological data (Toth and Bhargava, 2013; Lebek et al., 2020). However, commercial plethysmography systems are comparatively expensive, typically require proprietary software for recording and monitoring pressure, volume, and flow, and may be difficult to set up without extensive technical support. Investigators focused on hyperoxia- or hypoxia-induced pathologies (neonatal HIE and stroke for example) often utilize simple hypoxia exposure systems that have rudimentary recording and environmental control (Yager, 2004). Experiments using hypoxia/hyperoxia exposure in animal models have used a variety of exposure times, oxygen concentrations, and other variables—contributing to high variability in neurological injury and making it difficult to determine the optimal hypoxia exposure settings for a given disease model. Because of this variability, there are significant challenges to reproducing experiments from different laboratories. In our laboratory, we have focused on HIE in preterm infants and have found it challenging to develop a reproducible model that will facilitate development of new HIE treatment, as have others (Rumajogee et al., 2016).

Our goal in this paper is to make our inexpensive, highly customizable open-source hypoxia chamber available to other investigators. Our chamber is useful across multiple experimental applications including: simulation of high altitudes, hypoxic ischemic stroke, sleep apnea, and other models requiring precise monitoring and control of the environment. Researchers studying HIE commonly use two types of exposures: long-chronic exposure or short-term hypoxia exposure (Vannucci and Vannucci, 2005; Lacaille et al., 2019). These exposures, however, also require animals' homeostasis to be regulated by the use of external environment regulation. For example, the Rice-Vanucci Model pups undergo 10% oxygen exposure for one to 2 hours. They must also be kept at a constant temperature to reduce experimental variability (Vannucci and Vannucci, 2005). In Lacaille et al. (2019), long-term hypoxia requires monitoring and regulation to help stabilize the animals through a 7-day chronic hypoxia exposure (Lacaille et al., 2019). However, inconsistencies in factors other than oxygen level result in outcomes with a range of severity. To help reduce this variability in outcome, regulating and recording environmental variables continuously—such as temperature and humidity—can reduce data variability (Li et al., 2009; Summa et al., 2012). For example, the temperature should be monitored during hypoxia exposure as previous work shows that mice at 22°C ambient temperature had low plasma triglycerides (TG) and low-density lipoprotein cholesterol (LDL-C) levels that increased during intermittent hypoxia while mice at an ambient temperature of 30°C had high plasma TG and LDL-C levels that did not increase during intermittent hypoxia (Jun et al., 2013). Thus, these investigators concluded that ambient temperature affects lipid metabolism during hypoxia exposure (Jun et al., 2013).

Humidity is also an important variable to quantify when performing hypoxia testing. In moist air, mice's metabolic rate was significantly lower than in dry air since evaporating the air's moisture requires heat and would increase the energy needed for respiratory and metabolic processes (Phillips et al., 1950; Xiao et al., 2020). As a result, they found that, in dry air, less oxygen was required for respiratory and metabolic processes, which delayed the effects of hypoxia compared to in more humid air (Phillips et al., 1950). Additionally, others have found that heat stress and humidity can affect lactation in rodents (Xiao et al., 2020). Alterations to animal lactation further demonstrate the critical need to monitor and regulate temperature and humidity. The relationship between chamber oxygen pressure and arterial oxygen levels (Ogawa et al., 2019) still requires further investigation; however, barometric pressure may also play a role in batch variability.

Sound monitoring within the chamber is another key variable that should be monitored to minimize the possibility of hearing loss or sound-induced stress. Exposure to auditory stress during pregnancy in mice affected reabsorption and pup survival (Jafari et al., 2017). Likewise, light levels and day/night cycles should be monitored while the mice undergo intermittent or chronic hypoxia testing as, when combined with dim light at night, mice are more likely to exhibit anxiety and depression-like behavior (Aubrecht et al., 2013). Other studies have shown that, during hypoxia exposure, dams show depressive-like behaviors that are only observed in female rats (Kanekar et al., 2015). Thus if the mice are exposed to dim light at night during the hypoxia runs, other depression-like behaviors can serve as a confounding variable.

Monitoring oxygen levels is key for assuring reproducible hypoxia exposure, since the concentration of oxygen in the chamber must be reduced (Wenger et al., 2015) and tightly controlled. Wenger and others suggest that it can require hours to achieve the desired hypoxic conditions, but hypoxia levels can be rapidly altered by a brief opening of the hypoxia chamber to disrupt the chamber's hypoxic conditions (Wenger et al., 2015). Others have found that exhaling breath with high levels of volatile organic compounds (VOC) occurs during reduced oxygen levels (Harshman et al., 2015). By ensuring that VOC concentration is similar across hypoxia runs, it is possible to ensure that hypoxic conditions do not vary between hypoxia exposures.

To reduce the cost and provide maximum customization in our chamber design, we have provided a detailed overview of our chamber and supporting software that relies upon inexpensive off-the-shelf components allowing investigators high-resolution monitoring and control over temperature, humidity, and oxygen levels without the need for proprietary software or custom fabricated equipment. We developed a system based on Free/Libre Open-Source (FLOS) principles so others can use the system for greater reproducibility experiments by labs of any

TABLE 1 | Major components and prices included in the chamber creation as of June 2022.

Cage Aspect	Item	Description	Company	Part Number	Variable, Accuracy, Percision	Quantity Used	Quantity per Unit	Cost Per Unit
Cage Structure								
	Glass Tank	Aqueon Glass Aquarium Tank - 20 Gallon	PetCo	—	Chamber	1	1	$ 49.99
	Glass Tinting	One-way window film	Amazon	—	Visual Stimulus Reduction	1	1	$ 11.99
	Acrylic Sheet	Chamber top - 1/4 x 31.5 x 14.25 in	ACME Plastics	—	Chamber Lid	1	1	$ 45.00
	Junction Box	Steel Junction Box, 254 x 254 x 101.6 mm	Newark	40T7867	Electrical Input	1	1	$ 31.60
	Cable Management	3.35 inch black cable straps	Amazon	B0881FW8TQ	Electrical Management	Variable	50	$ 9.99
Airflow								
	Bulkhead	1/2 in female PVC bulkhead fitting	Amazon	—	Airflow - In	2	2	$ 12.49
	PVC Tubing	1/2 in FPT T joint	Home Depot	—	Airflow - In	3	1	$ 1 - 3
	—	1/2 in MPT Valve	Home Depot	—	Airflow - In	2	1	$ 1 - 3
	—	1/2 in MPT Adapters (1/4, 5 and 10 in)	Home Depot	—	Airflow - In	8	1	$ 1 - 3
	—	1/2 in MPT/FPT Elbow	Home Depot	—	Airflow - In	6	1	$ 1 - 3
	Brass Tubing	1/4 in Bulkhead	Amazon	—	Airflow - Out	2	2	$ 12.89
	—	1/4 in R-angle Elbow	Amazon	—	Airflow - Out	2	2	$ 14.59
	—	1/4 in Control Valve	Amazon	—	Airflow - Out	2	2	$ 14.99
Electrical								
	Sensor PCB*	Custom PCB boards for sensor attachment	OSH Park		Sensor Mount	5	5	$ 102.50
	Raspberry Pi**	Raspberry Pi 4B, 2 GB RAM	Adafruit	4292	Microprocessor	1	1	$ 45.00
	PiCamera	Raspberry Pi Camera 2	Adafruit	3099	Image (jpg) (8 megapixel)	1	1	$ 29.95
	Power Supply	Adjustable DC Powersupply 110 V - 220 V, Output: 0 - 24 V, 20 A 480 W	Amazon	B08GFSVHLS	Power (Percision: 0.1 V)	1	1	$ 35.99
	MCP9808	High accuracy I2°C Temperature Sensor	Adafruit	1782	Temperature (Accuracy: ± 0.25°C, Percision: ± 0.0625°C)	3	1	$ 4.95
	BH1750	Light Sensor I2°C	Adafruit	4681	Light (Lux)	2	1	$ 4.50
	BME280	Temperature, Humidity & Pressure sensor I2°C	Adafruit	2652	Temperature (± 1.0°C), Humidity (± 3%), Pressure (± 1.0 hPa)	2	1	$ 14.95
	CCS811	VOC and eCO2 Sensor	Adafruit	3566	CO2 & VOC	2	1	$ 19.95
	ADS1115	4 Channel 16 bit Analog to Digital Converter	Adafruit	1085	Converter (Percision 8-860 SPS)	1	1	$ 14.95
	Voltage Regulator	3.3 V 800 mA Voltage regulator	Adafruit	2165	Voltage (Accuracy: ± 1%)	5	1	$ 1.25
	0.1 uF Capacitor	0.1 uF capacitor, max of 50 V	Adafruit	753	Voltage (Accuracy: -20%/ + 80%)	5	10	$ 1.95
	10 uF Capacitor	10 uF capacitor, max 50°V low-fequency	Adafruit	2195	Voltage (± 20%)	5	10	$ 1.95
	Power Jack	Gravitech DC Power Connector 2.1 mm x 5.5 mm	Mouser	992-CON-SOCJ-2155	Voltage	5	1	$ 1.00
	D-Sub 15 Female	D-Sub High Density DBHD15, Female	Amazon	CNR15HDM-F-10PACK	Connector	8	10	$ 12.88
	VGA Cables	UGREEN VGA, 3 meter, male to male coaxial	Amazon	B00OZL3HLO	Cable	4	1	$ 7.99
	USB Cables	Micro-USB Cable, R-angle joint	Amazon	B09C5P7YFN	Cable	1	3	$ 9.99
	USB Cables	USB-C Cable, R-angle joint	Amazon	B09CG9LZSR	Cable	1	2	$ 9.99
	DC Power Cable	DC Power Pigtail, 3ft, Male 5.5 mm x 2.1 mm plug	Amazon	B08PYWN3T7	Cable	4	2	$ 9.99
	DC Cable Extender	6 ft DC Extention Cord, male to female	Amazon	B074WJZNZD	Cable	3	4	$ 13.99

**Can be replace with breadboards and jumper cables.*

***Can also be run with Raspberry Pi 3B, 4B - 1 GB, 4B - 4 GB or 4B - 8 GB.*

Additional hardware and custom parts can be found online at: https://github.com/drcgw/hypox-chamber.git and in the ***Supplemental Material****.*

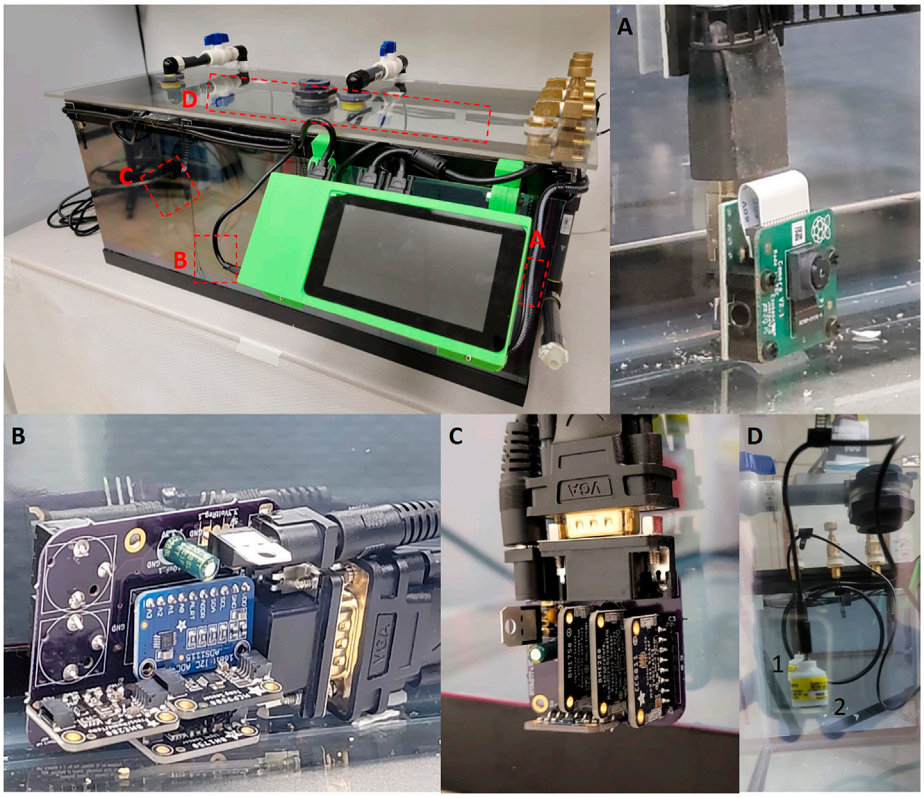

FIGURE 1 | (A) Raspberry Pi Camera version two attached to the Raspberry Pi via a HDMI cable. **(B)** Central sensor PCB board with ADS1115, MCP9808, BME280 and BH1750 sensors, the rear of the board contains two Aux jacks which allow for Teledyne sensor attachment. **(C)** External sensor breakout which contains MCP9808, BME280, BH1750 and CCS811. **(D)** Teledyne oxygen sensors hung from the roof of the chamber utilizing cable management clips. Two sensors are held by cables clips on the sealing, identified by the one and two identifiers.

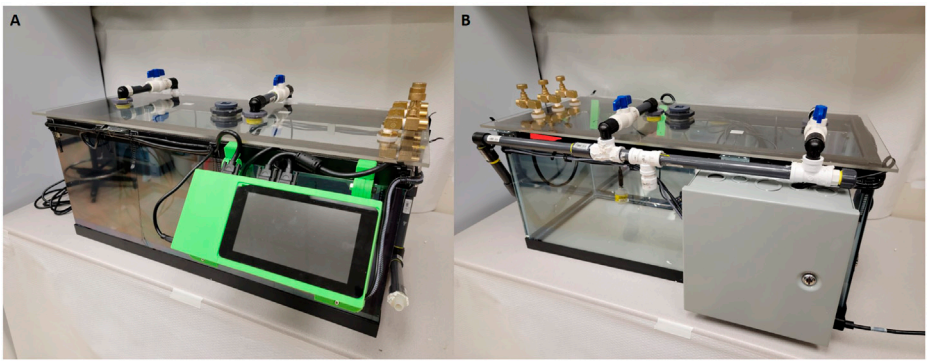

FIGURE 2 | Images of current cage design including updated sensors and revised power supply. **(A)** Front view of the chamber with a 7 inch Raspberry Pi touch screen and visible airflow systems. **(B)** Rear view of the chamber with power supply container and airflow input tubes visible.

size and funding status. By creating a system to monitor and modulate these environmental factors, we can unify these surgical models and their hypoxia exposures (Henderson et al., 2018). Our goal here is to create an inexpensive system for controlled gas exposure that will lower the bar of entry for other investigators interested in understanding physiological changes induced by hypoxia/hyperoxia.

METHODS

Chamber Components

Exposure to hypoxia during a surgical procedure elicits a stress response from the animals exposed. Therefore, to reduce and quantify variability in environmental factors, we assembled a comprehensive set of tools to monitor environmental variables

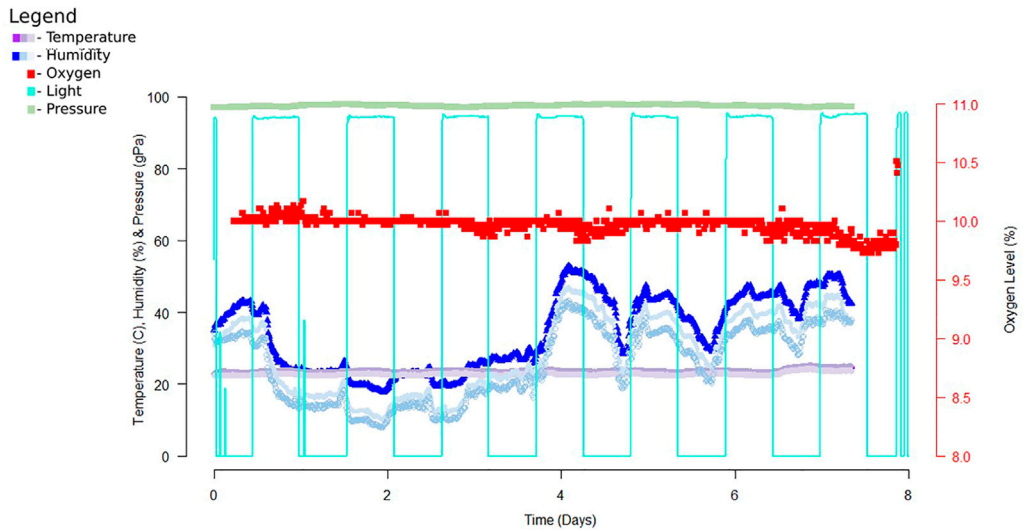

FIGURE 3 | Example data from a 7-day exposure of the chamber. Data was recorded using a Python script then analyzed with R studio. The data recorded above reports data collected from early experiments utilizing DHT22, ADS1115 and Teledyne oxygen sensor, TSL2591, and MPL3115A2. For this dataset we recorded data every 10 minutes for the entire 7 day exposure time. Since completion of this sampling we replaced these sensors with sensors of higher accuracy and precision.

and maintain them within desired ranges for a given experiment. A complete list of the parts and components of the chamber are included in the **Supplemental Material** and **Table 1**. Additionally, the Python code, PCB file, 3D files and instructions for chamber assembly can be accessed on github.com (https://github.com/drcgw/hypox-chamber.git).

Systems Recording

Temperature calibration was achieved by periodically taking temperature measurements with MCP9808, BME280, and/or BME680 sensors. Depending on the needs of the researcher we have designed the chamber to have some redundancy. The MCP9808 is a high precision (+0.0625˚C) temperature sensor with a range between -40 and 125˚C and accuracy of ±0.25 ˚C (Ada, 2021). In contrast the BME280 and BME680 are able to detect multiple variables including: temperature, humidity, pressure and total volatile organic compounds (Only BME680) but lose precision and accuracy. The accuracy and range of the BME280s sensors are: relative humidity ±3% between 0 and 100%, barometric pressure ±1 hPa between 300 and 1,100 hPa and temperature ±1.0 ˚C between -40 and 85 ˚C (Ada et al., 2015). The accuracy of the BME680s sensors are the same as the BME280 with the addition of a heated metal oxide resistor to look at total volatile organic compounds (tVOC) (Ada and Rembor, 2017). The BME280/680 sensors also have limitations regarding how many of each sensor type can be attached due to limited I2C addresses available for each sensor. The MCP9808 has eight possible addresses whereas the BME280 and BME680 only contain two I2C addresses which are duplicated for the two sensor boards (Ada and Montoya, 2017). For our chamber we utilize both MCP9808 and BME280 despite the overlapping temperature variable, we utilize the MCP9808's precision to calibrate the BME280 however, utilization of any of these three sensors will also allow for complete data collection. After these measurements were taken, the PiCamera was programmed to take a picture of a mercury thermometer located within the chamber (**Figure 1A**). After collecting the data, these images were used to determine the actual temperature in the chamber. The actual temperature in the chamber was then compared with the sensor readings to determine the precision of the sensors and calibrate the temperature sensors accordingly. Using a mercury thermometer for chamber monitoring is not practical because it violates animal health and well-being requirements and lab safety regulations.

Oxygen detection and calibration was done by pulling the voltage from a Teledyne R17A oxygen sensor using an analog-to-digital converter (ADS1115). The Teledyne R17A has a functional range of 0–100% oxygen at 25˚C with a resolution of 0.1% oxygen (Model R-17A, 2022). The voltage being recorded by the ADS1115 gets converted using the oxygen calibration data. Oxygen calibration was achieved by connecting a Teledyne R17A oxygen sensor to a hose fitting attached to a flow regulator to generate oxygen concentrations of 30, 15, 10, and 5% oxygen to develop a standard curve. Additionally, if a flow regulator is not available, the oxygen sensor can also be calibrated with premix tanks (10 & 5%) and room air (20.9%), although room oxygen is unreliable. To generate a standard curve using oxygen tanks, we attach one of the oxygen sensors to a manifold and tubing connected to tanks with different gas mixtures and expose the sensor to a given O_2 concentration for 10 min (Teledyne recommendation). The oxygen calibration script will take a series of samples every 10 s and then average the voltages to get a voltage value for the concentration being exposed. Repeat the process for at least three O_2 concentrations then create a standard curve to be used in percentage calculations. Once we established the calibration curve, the oxygen sensor's output was

measured and calculated based on the standard curve to determine the actual oxygen concentration (**Figure 1D**).

Light calibration is essential for quantifying light/dark cycle and understanding changes in physiology related to diurnal cycling. Obtaining the light by measuring lux allows us to determine if precise day/night cycles are adhered to within our animal care facility, again as a way to control the chamber environment and reduce treatment variability. To detect light the system utilizes adafruit BH1750 sensor boards (Siepert, 2021). The sensor board has a range from 0.11 lux minimum to 100,000 lux minimum with a noise reduction of 50–60 Hz. The sensor variation is ±20% with minimal infrared interference (Siepert, 2021). Additionally, the chamber walls were treated with a one-way mirror reflective coating to help minimize animals' perception of handlers during the hypoxia exposures (**Figure 2**). Any variant of one way mirror film can be used to treat the chamber walls.

Data Acquisition

Each sensor has its own function written in a master *Python* program which specifies the data recording resolution and interval that each sensor measures. These values are assigned to variables and it is easy to calculate calibration curves and obtain precise, calibrated measurements for each experimental condition measured by the on-board sensors. Our data acquisition cycle for the chamber is episodic every (10 min), using a function that saves the start and end times from the Raspberry Pi system clock and then calculates the time required to collect all the data and average over the 10 min epoch. The sampling rate can be readily adjusted within the Python program by changing the sampling interval. The data is acquired and stored throughout each 10 min acquisition period. All data is saved as comma-separated ASCII text files (.CSV) with values for raw, unprocessed data, and processed data with specific measurements. Storing data in a text file allows a great deal of flexibility since data analysis can be performed using *Python*, *R, MATLAB* or other analysis software. The caveat is, of course, that text files take up more disk space than binary files. It would be easy to add a compression function to make the files smaller but that is not currently included in our code as we use gzip or bzip2 to batch compress data files after checking them. The sensors are mounted on custom PCB boards (Central, Top, and External), which connect all the sensors back to the RaspberryPi via VGA cables (**Figures 1B, C**) which provide excellent shielding in a compact form factor.

The chamber is designed with a breakout PCB board to convert the 40 pinouts to four VGA connectors allowing for four different sensor PCB breakout boards to be attached depending on researcher needs.

Results and Analysis

Chamber monitoring allows us to record and monitor the environmental conditions within the chamber during extended hypoxia exposure, providing the ability to make real-time adjustments to the chamber's environment. During preliminary tests of the chamber, graphical time-series plots were generated to compare temperature, humidity, oxygen levels (**Figure 3**). *Python* and *R* were used to analyze and summarize chamber temperature and oxygen level data and identify changes in environmental conditions. We utilized the *Raspbian* operating system (based on *Debian GNU/Linux*), which provides remote access to the chamber software/hardware using secure shell (*ssh*). With the *Python* script collating reported values in a text file, custom analysis can be done using a variety of programs, including *Python, R, Excel*, *LibreOffice*, *GraphPad Prism,* etc. according to the user's preferences.

In our analysis, we focused on identifying time points where oxygen deviated from our tolerance of 10 ± 0.5% O_2. Deviations from our target oxygen levels were compared to other environmental variables to determine if a change in the environment was altering oxygen levels. In order to get accurate readings, oxygen concentration was determined by two-point calibration of the sensor using a vendor-supplied tank with a custom oxygen mix. The data collected provides a post-exposure view of the environmental condition of the chamber. As shown in **Figure 2**, the chamber allows for a controlled environment that can house multiple cages, for consistent exposure across several animals simultaneously, allowing us to reduce variability between exposure groups.

Control of Environment Variables

Environmental regulation is important in any experiment and being able to record multiple environmental variables can facilitate reproducibility and reliability of data. During early experiments, we found that a consistent temperature and oxygen levels led to higher survival rates in our experimental animals. This observation was supported by previous studies showing that a cold environment can lead to increased stress and affect the immune system (Meyer et al., 2007; Hankenson et al., 2018). During our hypoxia exposures, the animals have already undergone an immune challenge, so the addition of temperature stress can increase the stress on experimental animals in a given protocol. Due to this, we wished to monitor and control as chamber environment variables as possible. Environmental stress during development has been attributed to psychological stress in rodents as well, so minimizing this stress is critical in most studies (Takuma et al., 2011). The animals' environment has also been shown to affect their immune response when exposed to an inflammatory challenge (e.g. a "two hit" protocol or more complicated exposure paradigm); thus it is important to provide a controlled environment for experiments in which animals are exposed to stressors (Mueller et al., 2018).

Finally, our goal has been to provide an affordable chamber with supporting hardware and software for high-resolution data acquisition and reproducible results for experiments requiring O_2/CO_2/N_2 gas and monitoring of other environmental variables. By monitoring the environment for experimental animals, we provide a platform for more reproducible and cost-effective experiments. Alternatives that are currently used include plethysmography chambers, both head-out and whole-body, for monitoring breathing during hypoxia/hyperoxia exposure. Our open-source

system provides a more flexible foundation for rigor, transparency, and reproducibility. Commercial exposure systems can be very expensive and the investigator is often limited by their budget for multiple animal exposures. Our system lowers the cost of multiple animal exposures significantly while providing high-resolution data from the suite of sensors we have specified. We are not suggesting that our system replaces more sophisticated commercial exposure systems but, instead, provides a cost-effective alternative. Commercial plethysmography systems can provide a more extensive array of sensors and data acquisition (Ortega-Porcayo et al., 2014), and we will continue to develop and expand upon our open-source system. Finally, the ability of an open-source system allows for high customizability of the apparatus for each researcher's needs. Collaboration between labs utilizing this system can help us improve the chamber and control system while also allowing for new laboratories to develop their own custom systems (**Supplementary Table S1**).

FUTURE DIRECTIONS

The hypoxia chamber we describe has the ability to monitor and acquire data at high resolution and provide a way to standardize exposure protocols inexpensively by virtue of FLOS hardware and software. The chamber hardware and software are in constant development and we look forward to feedback for the development of additional features. An additional feature that would enhance the flexibility of our system would be to add a feedback controlled humidifier to control humidity in the chamber. A movable camera would also provide enhanced monitoring of experimental animals and a way to assess behavior and health of the animals. We also could add sound frequency and pressure measurements within the chamber. The addition of a white-noise sound suppression system to reduce the effect of environmental noise within the chamber and could mask environmental noise that might be a stressor. Including more sophisticated temperature control may be useful for some investigators and that should be possible with minimal changes to the current control circuitry and software. Finally, we intend to develop a graphical user interface (GUI) front-end to the control program to make it easier for non-technical users to use. While the chamber has several improvements that are in progress, the current system allows investigators with limited budgets to develop flexible exposure protocols and easily acquire environmental data. Even a minimal monitoring set-up will allow for a more uniform exposure system across typical hypoxia-based studies (Vannucci and Vannucci, 2005; Gunn and Bennet, 2009; Lacaille et al., 2019).

CONCLUSION

We have described a low-cost hypoxia exposure chamber that allows for high-resolution data monitoring and reporting of environmental status. Our goal in developing this chamber and associated control systems, was to provide a highly reproducible, FLOS system to facilitate low-cost physiology experiments. Use of FLOS software and hardware allows for improvements, customization, and tailoring of the chamber and software for specific experimental conditions as needed in each laboratory. We hope that, by providing this system, we can stimulate collaboration and continuous development of the chamber hardware and software. We designed the system to have a usable, minimum set of sensors acquiring temperature, humidity, light, pressure, tVOC and oxygen levels. In the future, we hope to include real-time movement monitoring to make the system more attractive to a wider range of investigators as these factors have a significant impact on experimental animals (Mueller et al., 2018). We will continue to develop this system and seek input from other investigators to maximize the system's versatility and usefulness for open, reproducible science. Our hope is that other investigators will benefit from our work and contribute to our on-going efforts to improve and expand upon the chamber hardware and software.

DATA AVAILABILITY STATEMENT

The datasets presented in this study can be found in online repositories. The names of the repository/repositories and accession number(s) can be found below: https://github.com/drcgw/hypox-chamber.

ETHICS STATEMENT

The animal study was reviewed and approved by the Loma Linda University Institutional Animal Care and Use Committee.

AUTHOR CONTRIBUTIONS

TH and CW conceived of the chamber and the ideas presented in the manuscript. RI and TH wrote the first draft of the manuscript, developed code, assembled the chamber, and collected all data presented in the manuscript. CW performed final edits.

SUPPLEMENTARY MATERIAL

The Supplementary Material for this article can be found online at: https://www.frontiersin.org/articles/10.3389/fphys.2022.891005/full#supplementary-material

REFERENCES

Ada, L. (2021). *Adafruit MCP9808 Precision I2C Temperature Sensor Guide.*

Ada, L., DiCola, T., Bearnes, B., Needell, G., Herrada, E., and Montoya, J. (2015). *Adafruit BME280 Humidity + Barometric Pressure + Temperature Sensor Breakout.*

Ada, L., and Montoya, J. (2017). I2C Addresses! the List. Available at: https://learn.adafruit.com/i2c-addresses/the-list (Accessed June 2022).

Ada, L., and Rembor, K. (2017). Adafruit BME680. Available at: https://learn.adafruit.com/adafruit-bme680-humidity-temperature-barometic-pressure-voc-gas (Accessed June 2022).

Arias-Cavieres, A., Fonteh, A., Castro-Rivera, C. I., and Garcia, A. J. (2021). Intermittent Hypoxia Causes Targeted Disruption to NMDA Receptor Dependent Synaptic Plasticity in Area CA1 of the hippocampus. *Exp. Neurol.* 344, 113808. doi:10.1016/j.expneurol.2021.113808

Arias-Cavieres, A., Khuu, M. A., Nwakudu, C. U., Barnard, J. E., Dalgin, G., and Garcia, A. J. (2020). A HIF1a-dependent Pro-oxidant State Disrupts Synaptic Plasticity and Impairs Spatial Memory in Response to Intermittent Hypoxia. *ENeuro* 7. ENEURO.0024-20.2020. doi:10.1523/ENEURO.0024-20.2020

Aubrecht, T. G., Weil, Z. M., Magalang, U. J., and Nelson, R. J. (2013). Dim Light at Night Interacts with Intermittent Hypoxia to Alter Cognitive and Affective Responses. *Am. J. Physiology-Regulatory, Integr. Comp. Physiology* 305, R78–R86. doi:10.1152/ajpregu.00100.2013

Gunn, A. J., and Bennet, L. (2009). Fetal Hypoxia Insults and Patterns of Brain Injury: Insights from Animal Models. *Clin. Perinatology* 36, 579–593. doi:10.1016/j.clp.2009.06.007

Hankenson, F. C., Marx, J. O., Gordon, C. J., and David, J. M. (2018). Effects of Rodent Thermoregulation on Animal Models in the Research Environment. *Comp. Med.* 68, 425–438. doi:10.30802/AALAS-CM-18-000049

Harshman, S. W., Geier, B. A., Fan, M., Rinehardt, S., Watts, B. S., Drummond, L. A., et al. (2015). The Identification of Hypoxia Biomarkers from Exhaled Breath under Normobaric Conditions. *J. Breath. Res.* 9, 047103. doi:10.1088/1752-7155/9/4/047103

Henderson, P., Islam, R., Bachman, P., Pineau, J., Precup, D., and Meger, D. (2018). Deep Reinforcement Learning that Matters. *Proc. AAAI Conf. Artif. Intell.* 32. doi:10.1609/aaai.v32i1.11694

Jafari, Z., Faraji, J., Mirza Agha, B., Metz, G. A. S., Kolb, B. E., and Mohajerani, M. H. (2017). The Adverse Effects of Auditory Stress on Mouse Uterus Receptivity and Behaviour. *Sci. Rep.* 7, 4720. doi:10.1038/s41598-017-04943-8

Jun, J. C., Shin, M.-K., Yao, Q., Devera, R., Fonti-Bevans, S., and Polotsky, V. Y. (2013). Thermoneutrality Modifies the Impact of Hypoxia on Lipid Metabolism. *Am. J. Physiology-Endocrinology Metabolism* 304, E424–E435. doi:10.1152/ajpendo.00515.2012

Kanekar, S., Bogdanova, O. V., Olson, P. R., Sung, Y.-H., D'Anci, K. E., and Renshaw, P. F. (2015). Hypobaric Hypoxia Induces Depression-like Behavior in Female Sprague-Dawley Rats, but Not in Males. *High Alt. Med. Biol.* 16, 52–60. doi:10.1089/ham.2014.1070

Lacaille, H., Vacher, C.-M., Bakalar, D., O'Reilly, J. J., Salzbank, J., and Penn, A. A. (2019). Impaired Interneuron Development in a Novel Model of Neonatal Brain Injury. *ENeuro* 6, 0300–0318. doi:10.1523/ENEURO.0300-18.2019

Lebek, S., Hegner, P., Schach, C., Reuthner, K., Tafelmeier, M., Maier, L. S., et al. (2020). A Novel Mouse Model of Obstructive Sleep Apnea by Bulking Agent-Induced Tongue Enlargement Results in Left Ventricular Contractile Dysfunction. *PloS One* 15, e0243844. doi:10.1371/journal.pone.0243844

Li, Q., Cheung, C., Wei, R., Hui, E. S., Feldon, J., Meyer, U., et al. (2009). Prenatal Immune Challenge Is an Environmental Risk Factor for Brain and Behavior Change Relevant to Schizophrenia: Evidence from MRI in a Mouse Model. *PLOS ONE* 4, e6354. doi:10.1371/journal.pone.0006354

Meyer, U., Yee, B. K., and Feldon, J. (2007). The Neurodevelopmental Impact of Prenatal Infections at Different Times of Pregnancy: the Earlier the Worse? *Neuroscientist* 13, 241–256. doi:10.1177/1073858406296401

Model R-17A (2022). R-17A Automotive Oxygen Sensor. Available at: https://www.teledyne-ai.com/Products/Oxygen-Sensors/Pages/R17A.aspx (Accessed June 2022).

Mueller, F. S., Polesel, M., Richetto, J., Meyer, U., and Weber-Stadlbauer, U. (2018). Mouse Models of Maternal Immune Activation: Mind Your Caging System!. *Brain, Behav. Immun.* 73, 643–660. doi:10.1016/j.bbi.2018.07.014

Ogawa, T., Fujii, N., Kurimoto, Y., and Nishiyasu, T. (2019). Effect of Hypobaria on Maximal Ventilation, Oxygen Uptake, and Exercise Performance during Running under Hypobaric Normoxic Conditions. *Physiol. Rep.* 7, e14002. doi:10.14814/phy2.14002

Ortega-Porcayo, L. A., Cabrera-Aldana, E. E., Arriada-Mendicoa, N., Gómez-Amador, J. L., Granados-García, M., and Barges-Coll, J. (2014). Operative Technique for *En Bloc* Resection of Upper Cervical Chordomas: Extended Transoral Transmandibular Approach and Multilevel Reconstruction. *Asian Spine J.* 8, 820–826. doi:10.4184/asj.2014.8.6.820

Phillips, N. E., Saxon, P. A., and Quimby, F. H. (1950). Effect of Humidity and Temperature on the Survival of Albino Mice Exposed to Low Atmospheric Pressure. *Am. J. Physiology-Legacy Content* 161, 307–311. doi:10.1152/ajplegacy.1950.161.2.307

Rumajogee, P., Bregman, T., Miller, S. P., Yager, J. Y., and Fehlings, M. G. (2016). Rodent Hypoxia–Ischemia Models for Cerebral Palsy Research: A Systematic Review. *Front. Neurol.* 7, 57. doi:10.3389/fneur.2016.00057

Siepert, B. (2021). *Adafruit BH1750 Ambient Light Sensor.*

Summa, K. C., Vitaterna, M. H., and Turek, F. W. (2012). Environmental Perturbation of the Circadian Clock Disrupts Pregnancy in the Mouse. *PLOS ONE* 7, e37668. doi:10.1371/journal.pone.0037668

Takuma, K., Ago, Y., and Matsuda, T. (2011). Preventive Effects of an Enriched Environment on Rodent Psychiatric Disorder Models. *J. Pharmacol. Sci.* 117, 71–76. doi:10.1254/jphs.11r07cp

Toth, L. A., and Bhargava, P. (2013). Animal Models of Sleep Disorders. *Comp. Med.* 63, 91–104.

Tsuji, M., Ohshima, M., Taguchi, A., Kasahara, Y., Ikeda, T., and Matsuyama, T. (2013). A Novel Reproducible Model of Neonatal Stroke in Mice: Comparison with a Hypoxia-Ischemia Model. *Exp. Neurol.* 247, 218–225. doi:10.1016/j.expneurol.2013.04.015

Vannucci, R. C., and Vannucci, S. J. (2005). Perinatal Hypoxic-Ischemic Brain Damage: Evolution of an Animal Model. *Dev. Neurosci.* 27, 81–86. doi:10.1159/000085978

Wenger, R., Kurtcuoglu, V., Scholz, C., Marti, H., and Hoogewijs, D. (2015). Frequently Asked Questions in Hypoxia Research. *Hypoxia (Auckl)* 3, 35–43. doi:10.2147/HP.S92198

Xiao, Y., Kronenfeld, J. M., and Renquist, B. J. (2020). Feed Intake-dependent and -independent Effects of Heat Stress on Lactation and Mammary Gland Development. *J. Dairy Sci.* 103, 12003–12014. doi:10.3168/jds.2020-18675

Yager, J. Y. (2004). Animal Models of Hypoxic-Ischemic Brain Damage in the Newborn. *Seminars Pediatr. Neurology* 11, 31–46. doi:10.1016/j.spen.2004.01.006

Conflict of Interest: The authors declare that the research was conducted in the absence of any commercial or financial relationships that could be construed as a potential conflict of interest.

frontiers | Frontiers in Physiology

TYPE Original Research
PUBLISHED 08 September 2022
DOI 10.3389/fphys.2022.855303

OPEN ACCESS

EDITED BY
Guido Caluori,
INSERM Institut de Rythmologie et Modélisation Cardiaque (IHU-Liryc), France

REVIEWED BY
Kenneth Scott Campbell,
University of Kentucky, United States
Wenjun Kou,
Northwestern University, United States

*CORRESPONDENCE
Takumi Washio,
washio@ut-heart.com

SPECIALTY SECTION
This article was submitted to Integrative Physiology, a section of the journal Frontiers in Physiology

RECEIVED 15 January 2022
ACCEPTED 18 July 2022
PUBLISHED 08 September 2022

CITATION
Yoneda K, Kanada R, Okada J-i, Watanabe M, Sugiura S, Hisada T and Washio T (2022), A thermodynamically consistent monte carlo cross-bridge model with a trapping mechanism reveals the role of stretch activation in heart pumping.
Front. Physiol. 13:855303.
doi: 10.3389/fphys.2022.855303

A thermodynamically consistent monte carlo cross-bridge model with a trapping mechanism reveals the role of stretch activation in heart pumping

Kazunori Yoneda[1], Ryo Kanada[2], Jun-ichi Okada[3,4], Masahiro Watanabe[1], Seiryo Sugiura[3], Toshiaki Hisada[3] and Takumi Washio[3,4]*

[1]Section Solutions Division, Healthcare Solutions Development Unit, Fujitsu Japan Limited, Shiodome City Center, Tokyo, Japan, [2]RIKEN Center for Computational Science HPC- and AI-driven Drug Development Platform Division, AI-driven Drug Discovery Collaborative Unit, Kobe, Japan, [3]UT-Heart Inc., Kashiwanoha Campus Satellite, Kashiwa, Japan, [4]Graduate School of Frontier Sciences, University of Tokyo, Kashiwanoha Campus Satellite, Kashiwa, Japan

Changes in intracellular calcium concentrations regulate heart beats. However, the decline in the left ventricular pressure during early diastole is much sharper than that of the Ca^{2+} transient, resulting in a rapid supply of blood to the left ventricle during the diastole. At the tissue level, cardiac muscles have a distinct characteristic, known as stretch activation, similar to the function of insect flight muscles. Stretch activation, which is a delayed increase in force following a rapid muscle length increase, has been thought to be related to autonomous control in these muscles. In this numerical simulation study, we introduced a molecular mechanism of stretch activation and investigated the role of this mechanism in the pumping function of the heart, using the previously developed coupling multiple-step active stiffness integration scheme for a Monte Carlo (MC) cross-bridge model and a bi-ventricular finite element model. In the MC cross-bridge model, we introduced a mechanism for trapping the myosin molecule in its post-power stroke state. We then determined the rate constants of transitions for trapping and escaping in a thermodynamically consistent manner. Based on our numerical analysis, we draw the following conclusions regarding the stretch activation mechanism: (i) the delayed force becomes larger than the original isometric force because the population of trapped myosin molecules and their average force increase after stretching; (ii) the delayed force has a duration of more than a few seconds owing to a fairly small rate constant of escape from the trapped state. For the role of stretch activation in heart pumping, we draw the following conclusions: (iii) for the regions in which the contraction force decreases earlier than the neighboring region in the end-systole phase, the trapped myosin molecules prevent further lengthening of the myocytes, which then prevents further shortening of neighboring myocytes; (iv) as a result, the contraction forces are sustained longer, resulting in a larger blood ejection, and their degeneration is synchronized.

KEYWORDS

stretch activation, Monte Carlo method, finite element method, heartbeat, excitation contraction coupling, spontaneous oscillation, cross-bridge cycle

Introduction

Stretch activation is a distinctive feature in the tension response that occurs after a small rapid stretch (lengthening of approximately 1% of the initial length) is imposed in the fiber direction to the isometrically contracting muscle. As illustrated in Figure 1A, after the rapid rise of tension during stretching (phase 1), the tension declines to a certain level (phase 2) and then rises again to a level higher than that of the original isometric force (phase 3). In the following, we refer to the force in phase 3 as the delayed force following Stelzer et al. (2006). The degree of delayed force development, or stretch activation, varies for different types of muscles. In particular, an increased delayed force is prominent in asynchronous insect flight muscles, in which stretch activation is thought to be a key factor of the spontaneous oscillations (SPOCs) that occur without intracellular Ca^{2+} regulation (Pringle 1978). Although heartbeats are regulated by the intracellular Ca^{2+} transient ($[Ca^{2+}]$), the stretch activation mechanism is thought to promote efficient switching between the systole and diastole. In our previous work on a numerical bi-ventricular model (Washio et al., 2018), we showed that stretch activation might aid in synchronizing the generation of contraction force over all of the ventricles for a non-uniform rapid rise of $[Ca^{2+}]$ during isovolumetric contraction. The stretch activation may also aid in synchronizing the degeneration of contraction force against a non-uniform slow decline of $[Ca^{2+}]$ during early diastole. In the simulation, although the total length change of cardiomyocytes in the systole and diastole was approximately 15–20% larger than the length change in the stretch activation, it was shown that the activated force can be generated locally by instantaneous small stretches at the location where the active tension is smaller than the surrounding part because of inhomogeneities of the activation level (Washio et al., 2018). In this simulation study, we assumed a trapping mechanism for strongly binding myosin molecules and modeled this mechanism using a Langevin dynamics model of the power stroke transition. However, the fairly fine time step (~0.25 ns) used in solving the Langevin equations presented an obstacle in extending this approach for clinical applications. Furthermore, we showed that a multiple-step active stiffness integration scheme that couples the Monte Carlo (MC) model with a larger time step (~5 μs) and the continuum had a much higher computational efficiency (Yoneda et al., 2021). Therefore, in this study, we introduce a stretch activation mechanism in the MC model, targeting clinical uses of beating heart simulations.

We briefly present an overview of our sarcomere model (Figure 1B) with the MC cross-bridge model used in this study (Figures 1C,D). We provide details in the Materials and Methods section. We assume that N_M (= 38) myosin molecules are arranged on the thick filament at regular intervals, except for the bare zone, whereas the thin filament is divided into N_T (= 32) segments, termed troponin/tropomyosin (T/T) units. These numbers of myosin molecules and T/T units were determined by assuming that our one-dimensional model corresponds to one of the double spirals of the actual thin filament and surrounding accessible myosin molecules (Washio et al., 2016). A myosin molecule in our cross-bridge model has one non-binding state (N_{XB}), one weakly binding state (P_{XB}), and four strong binding states (XB_{PreR}, XB_{PostR1}, XB_{PostR2}, and XB_{Trap}) (Figure 1C). Here, the trap state XB_{Trap} is added to our previous model (Yoneda et al., 2021) to reproduce the stretch activation. Ca^{2+} sensitivity is reproduced based on state transitions in the T/T units on the thin filament (Figure 1D). The coefficients k_{np} and k_{pn} in the rate constants between the non-binding state N_{XB} and the weakly binding state P_{XB} are changed according to the state of the T/T unit above the myosin molecule. Cooperativity in nearest neighbor interactions is incorporated with the factors γ^{ng} and γ^{-ng} to reproduce the force–pCa^{2+} relationship (Rice et al., 2003), where γ = 80 is used and ng = 0, 1, or 2 is the number of neighboring myosin molecules either in the weakly binding (P_{XB}) or strong binding (XB_{PreR}, XB_{PostR1}, XB_{PostR2}, and XB_{Trap}) states.

The contraction force is generated by power stroke transitions in which the lever arm swing distance increases by s_1 and s_2 in the first and second strokes, respectively (Figures 2A,B). This increase in swing distance is directly reflected by an increase in myosin rod distortion (Figure 1B). In our model, the rate constants of the power and reverse strokes are given by functions of the myosin rod distortion x such that the Boltzmann equilibrium condition is fulfilled:

$$R_i(x) \equiv \frac{r_{f,i}(x)}{r_{b,i}(x+s_i)} = \exp\left(\frac{W_{\mathrm{rod}}(x) + \Delta G_{i-1} - W_{\mathrm{rod}}(x+s_i) - \Delta G_i}{k_B T}\right), \tag{1}$$

where k_B and T denote the Boltzmann constant and temperature, respectively. ΔG_0, ΔG_1, and ΔG_2 are the free energies, respectively, at XB_{PreR}, XB_{PostR1}, and XB_{PostR2} (Figure 2B). W_{rod} is the strain energy of the myosin rod. It should be noted that the rate constants are defined as a function of distortion at the origin of the transition. With the power stroke, the free energy decrease $\Delta G_{i-1} - \Delta G_i$ is transferred to an increase in strain energy $W_{\mathrm{rod}}(x+s_i) - W_{\mathrm{rod}}(x)$. The strain energy is used for the external work *via* the half-sarcomere shortening, which corresponds to muscle shortening in the fiber direction.

Under the above formulation, the ratio R_i increases when the distortion x decreases as the sarcomere shortens. Conversely, sarcomere lengthening (as in stretch activation) causes an

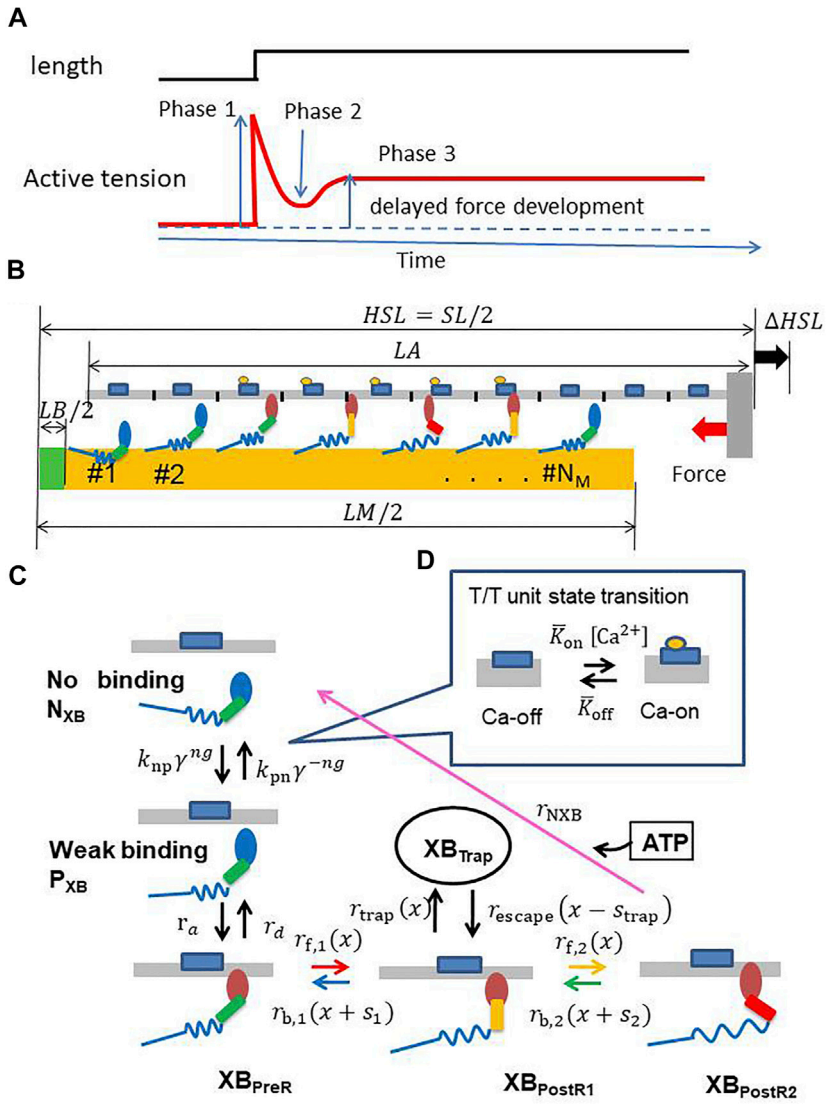

FIGURE 1
(A) A typical stretch activation response for a cardiomyocyte. Time course of the active tension (bottom) is illustrated for the response of length change (1–2%) (top) after steady-state is achieved. There is an initial increase in the active tension with the stretch (Phase 1), followed by a rapid decay in tension (Phase 2) to a minimum, and finally a delayed increase in tension (Phase 3, stretch activation). **(B)** A filament pair in the half-sarcomere model **(C)** the state transition MC model of the myosin molecule, and **(D)** the T/T unit. N_M MHs and N_T T/T units are arranged on the thick and thin filaments, respectively. The MHs in either the N_{XB} or P_{XB} states are assumed to be detached. The rate constant factors k_{np} and k_{pn} between N_{XB} and P_{XB} are affected by the state of the T/T unit above it. *ng* is an integer that takes a value of 0, 1, or 2, according to the number of neighboring MHs attached or weakly binding. $\gamma = 80$ was adopted to model the cooperativity of the MHs. The forward transitions from XB_{PreR} to XB_{PostR2} *via* XB_{PostR1} are called "power strokes," whereas the back transitions are called "reverse strokes." It should be noted that a new state, "XB_{Trap}," is introduced and interacts only with XB_{PostR1}. The transition from XB_{PostR1} to XB_{Trap} is called "trapping," whereas the opposite transition is called "escaping." The MHs connected to the extremely strained myosin rods are detached (arrows of these forced detachments are not shown).

increase in distortion x, resulting in a facilitation of reverse strokes. The chain reaction of reverse strokes and sarcomere lengthening is assumed to enable quick relaxation at the early diastole in the cardiac cycle (Washio et al., 2019; Hwang et al., 2021). However, the synchrony of this relaxation over the entire ventricular wall is needed to explain the realistic rapid decline in the left ventricular pressure. In our previous work (Washio et al., 2018), we introduced a trapping mechanism at the XB_{PostR1} state in the Langevin dynamics model to indicate the role of the stretch activation mechanism in the synchrony of relaxation. In the Langevin model, the potential that drove the power stroke was represented as a function of two parameters: the lever arm rotation distance, y, and the degree of lever arm deflection, θ. With these parameters, the total distance of the power stroke is

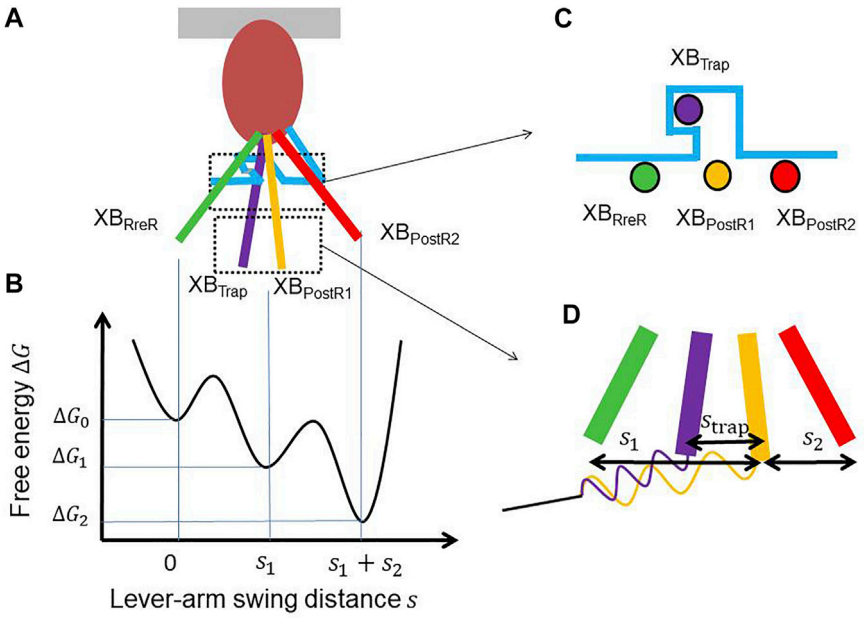

FIGURE 2
(A) Lever arm rotations at the four attached states with a hook (light blue) that traps the XB_{Trap} state. **(B)** The free energy profile that drives the power strokes. **(C)** A cross-sectional view of the lever arm positions of the four attached states. **(D)** Magnification of the lever arm rotations with the spring of the myosin rod. The distortion of the myosin rod decreases by s_{trap} during trapping, while it increases by s_{trap} while escaping.

given by $s = y - \theta$. Here, the deflection θ increases as the pulling force imposed on the lever arm increases, and a high barrier in the y-direction is assumed for the large deflection θ in the potential landscape between XB_{PreR} and XB_{PostR1}. In this way, reverse strokes from the XB_{PostR1} state to the XB_{PreR} state are prevented when the force is large. Thus, the myosin molecules in the XB_{PostR1} state with a large force are trapped. In this study, we introduce a similar trapping mechanism in our MC model based on a thermodynamically consistent formulation.

In Figure 2C, the trap mechanism is illustrated using a hook that inhibits the reverse transition to the XB_{PreR} state. The power stroke distance is slightly shortened by s_{trap} in the trapping transition from XB_{PostR1} to XB_{Trap}, while the system returns to the XB_{PostR1} state in the escaping transition from the XB_{Trap} state (Figure 2D). Thus, the ratio of the transition rates is given by:

$$T(x) \equiv \frac{r_{\text{escape}}(x)}{r_{\text{trap}}(x + s_{\text{trap}})} = \exp\left(\frac{\Delta G_{\text{trap}} + W_{rod}(x) - \Delta G_1 - W_{rod}(x + s_{\text{trap}})}{k_B T}\right), \tag{2}$$

where ΔG_{trap} is the free energy in the XB_{Trap} state. In this study, the rate constant for trapping is:

$$r_{\text{trap}}(x) = h_{\text{trap}} \tag{3}$$

and the rate constant for escaping is:

$$r_{\text{escape}}(x) = h_{\text{escape}} \exp\left(\frac{W_{rod}(x) - W_{rod}(x + s_{\text{trap}})}{k_B T}\right). \tag{4}$$

From Eq. 2, the relationship between the ratio of the coefficients h_{trap} and h_{escape} and the free energy difference is given by:

$$\frac{h_{\text{escape}}}{h_{\text{trap}}} = \exp\left(\frac{\Delta G_{\text{trap}} - \Delta G_1}{k_B T}\right). \tag{5}$$

If we assume linear elasticity for the myosin rod, the potential energy difference in Eq. 4 is represented by:

$$W_{rod}(x) - W_{rod}(x + s_{\text{trap}}) = -k_{\text{xb}} s_{\text{trap}}\left(x + \frac{1}{2} s_{\text{trap}}\right), \tag{6}$$

where k_{xb} is the spring constant of the myosin rod. Eqs 4 and 6 indicate that as the distortion x increases, the myosin molecule becomes less likely to escape from the XB_{Trap} state. Thus, the half-sarcomere lengthening (as in stretch activation) implies a rapid increase in distortion x, resulting in trapping in the XB_{Trap} state. Eqs 4 and 6 also indicate that the degree of trapping depends on the loss of the power stroke distance s_{trap}. Thus, the parameter s_{trap} has the potential to reproduce stretch activation phenomena in various muscle types (Supplementary Figures S1,S2 for the plots of the rate functions).

The structural mechanism of trapping has not yet been identified. However, the conformation change between the

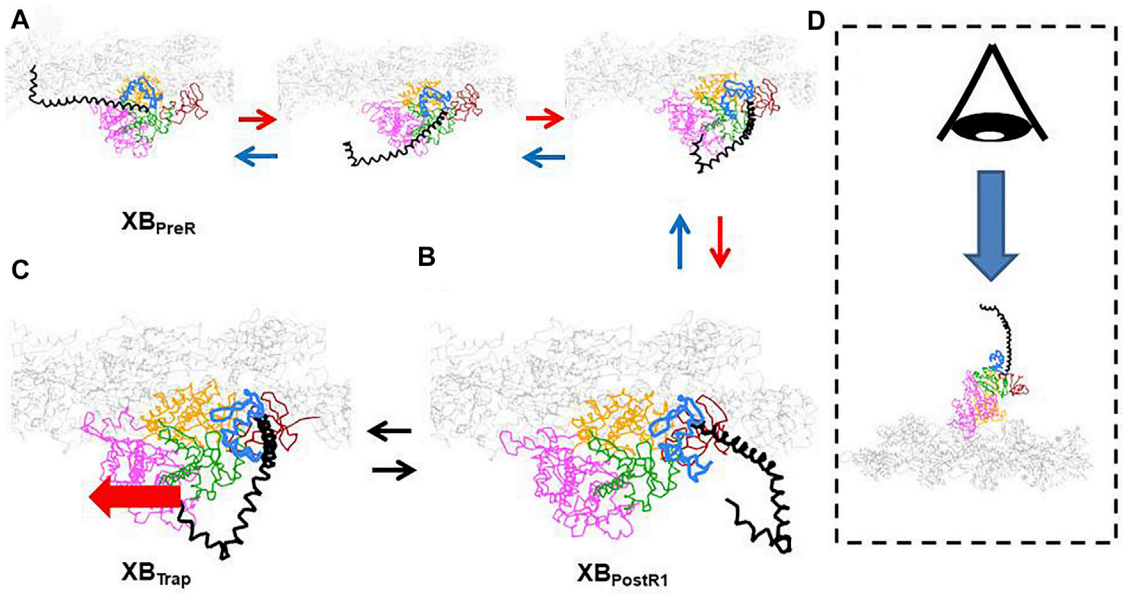

FIGURE 3
The conformation change of the myosin molecule in the first power stroke transition. **(A)** Intermediate conformations between the XB_{PreR} and XB_{PostR1} states. **(B)** Conformation in the XB_{PostR1} states **(C)** A candidate of conformation of the XB_{Trap} state with the imposed pulling force (thick red arrow). **(D)** The viewpoint for **(A–C)**. The myosin molecule is divided into the following domains: lever arm (black), converter (light blue), N-terminal (brown), central domain (green), upper 50 k (pink), and lower 50 k (orange). The thin filament is colored gray. In the XB_{Trap} state, the lever arm is trapped in the V-shaped region of the converter. The rotation of the converter might be inhibited in the case of a strong pulling force.

XB_{PreR} state and XB_{PostR1} state (Figure 3A) and the arrangement of the converter domain and the lever arm in the XB_{PostR1} state (Figure 3B) produced by our coarse-grained molecular dynamic simulation (Washio et al., 2021) indicate that the V-shaped region in the converter domain could hold the lever arm when it is strongly pulled in the opposite direction (Figure 3C). Note that these configurations of the myosin molecule are drawn from the viewpoint indicated in Figure 3D. Once the lever arm is strongly held in the V-shaped region, it might inhibit reverse rotation of the converter domain (from Figures 3A,B), resulting in trapping of the lever arm. Supplementary Video 1 shows a simulation of the power stroke transition from the XB_{PreR} state to the XB_{PostR1} state.

Determining which part of the contractile proteins is responsible for stretch activation remains controversial. Campbell and Chandra (Campbell and Chandra. 2006) reproduced stretch activation in cardiac muscle (Stelzer et al., 2006) by applying a numerical model, where they assumed that the thin filament regulatory unit (RU) was responsible. Conversely, Straight et al. (2019) proposed a myosin-based mechanism focusing on the ADP state, which corresponds to XB_{PostR1} in our MC model, although a trapping mechanism was not introduced in their model. A unique feature of our numerical model is its theoretical basement based on the Boltzmann distribution law under the strain energy for distortion of the myosin rod Eq. 2.

Materials and methods

Here, we introduce the cross-bridge MC model and its use in multiscale analyses. Cross-bridge MC models are arranged on a thick filament and interact with a thin filament. The pairs of filaments compose the half-sarcomere model (Figure 4A). Half-sarcomere models are imbedded into the myofibril model (Figure 4B) or the ventricle model (Figure 4C), where interactions of the half-sarcomere models in adjacent elements are analyzed. In the following, informative numerical results, representing basic properties of the MC cross-bridge model with the trapping mechanism are introduced to help readers understand the definitions of crucial parameters in the MC cross-bridge model.

The parameter values, which are not related to the trap model, are listed in Table 1. Some of these values came from the following references [H2021]: Hwang et al., 2021 [K2016]: Kolb et al., 2016 [L2000]: Lodish et al., 2000 [R2008]: Rice et al., 2008 [S2013]: Sato et al., 2013, and [Y2021]: Yoneda et al., 2021.

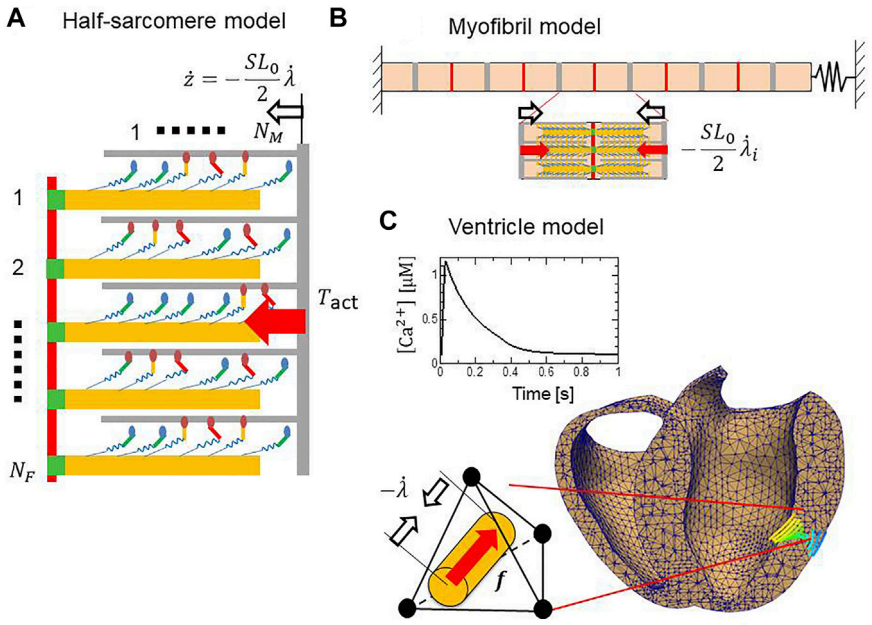

FIGURE 4
Computational models at three scales. **(A)** A half-sarcomere model consisting of N_F filament pairs. In the stretch activation test, a rapid length change was imposed after the isometric force had matured. **(B)** The myofibril model for the SPOC simulation. The half-sarcomere models were imbedded to compute the active tensions in individual half-sarcomeres, whereas their stretches provide feedback to the half-sarcomere models. **(C)** A cross-section of the finite element bi-ventricular model and the transmural change in fiber orientation. The half-sarcomere models were imbedded in tetrahedral elements to compute the contraction force in the fiber direction, whereas the stretches in the fiber direction provided feedback to the half-sarcomere models. The boxed inset shows the Ca^{2+} transient given in each element.

Parameters for the trap mechanism

Three parameters, s_{trap}, h_{trap}, and h_{escape}, characterize the trapping. We adjusted these parameters so that the experimental stretch activation results reported by Stelzer et al. (2006) were reproduced. The adjusted parameter values are s_{trap}= 1.3 nm, h_{trap}= 50 1/s, and h_{escape}= 5,000 1/s. From Eq. 5, we find that $\Delta G_{trap} - \Delta G_1$= 4.6 k_BT. According to Eq. 6, the rate constants of trapping r_{trap} and escaping r_{escape} are equal at a distortion of x= 4.8 nm in the XB_{Trap} state and $x + s_{trap}$= 6.1 nm in the XB_{PostR1} state, assuming a spring constant of k_{xb}= 2.8 pN/nm (Kaya and Higuchi, 2010) and a physiological body temperature of T= 310 K.

Control model of attachment and detachment and its effects on heart pumping

In our model, we assume that attachment, which represents the transition from the P_{XB} state to the XB_{PreR} state (Figure 1C), is allowed only in the single overlap region of the thin and thick filaments. The myosin head (MH) (# i) is situated in the single overlapping region only if the following condition is fulfilled:

$$\max\left(LA - \frac{SL}{2}, \frac{SL}{2} - LA\right) \le \frac{LB}{2} + \frac{2(i-0.5)}{n_M(LM-LB)} \le \frac{SL}{2}. \quad (7)$$

Here, the middle term is the distance from the center of the sarcomere . LM, LB, and LA represent the lengths of the thick filament, bare zone, and thin filament, respectively (Figure 1B). SL is the sarcomere length. The parameters for the sarcomere geometry were determined from cardiac sarcomeres (Rodriguez et al., 1993; Lodish et al., 2000; Rice et al., 2008; Kolb et al., 2016).

Two states (Ca-off and Ca-on) are assumed by each T/T unit (Figure 1D). The transitions between the states of the T/T unit are determined by the Ca^{2+} concentration, $[Ca^{2+}]$, and the two parameters $\bar{K}_{on}$ and $\bar{K}_{off}$. Those two parameters are defined as follows:

$$\bar{K}_{on} = \begin{cases} K'_{on} & \text{if there is an MH binding below,} \\ K_{on} & \text{otherwise.} \end{cases}$$

$$\bar{K}_{off} = \begin{cases} K'_{off} & \text{if there is an MH binding below,} \\ K_{off} & \text{otherwise.} \end{cases}$$

The transitions between the N_{XB} and P_{XB} states (Figure 1C) are affected by the status of the T/T unit above, *via* modifications of k_{np} and k_{pn}, as well as by the states of the neighboring MHs through the integer ng. The value of ng (= 0, 1, *or* 2) represents the number of neighboring MHs in the P_{XB} state or the four

TABLE 1 Parameters for the actomyosin dynamics. "Adjusted" indicates that they were adjusted to reproduce the phenomena.

Parameter	Value	Unit	References	Parameter	Value	Unit	References
ATP hydrolysis energy				**Sarcomere geometry**			
G_{ATP}	76.5	pN · nm	[Y2021]	SL_0	1.9	μ m	[R2008]
k_BT	4.28	pN · nm	$T = 310$	LM	1.65	μ m	[L2000]
Stroke size and free energy $T = 310$				LB	0.16	μ m	[K2016]
s_1	6.0	nm	[H2021]	LA	1.0	μ m	[K2016]
s_2	4.0	Nm	[H2021]	SA_0	693	nm^2	[S2013]
ΔG_{wb}	G_{ATP}	pN/nm	Adjusted	**Force regulation through T/T unit**			
ΔG_0	G_{ATP}	pN/nm	Adjusted	K'_{on}	100	1/s	[Y2021]
ΔG_1	0.7 G_{ATP}	pN/nm	Adjusted	K'_{off}	30	1/s	[Y2021]
ΔG_2	0	pN/nm	Adjusted	K_{on}	100	1/s	[Y2021]
—	—	—	—	K_{off}	150	1/s	[Y2021]
Rod distortion energy W_{rod}				K_{basic}	30	1/s	[Y2021]
k_{xb}	2.8	pN/nm	[K2010]	Q	1.6	unitless	[Y2021]
b_{xb}	0.05	Unitless	[K2010]	μ	15	unitless	[Y2021]
ξ_1	4.35	Nm	[K2010]	γ	80	unitless	[R2003]
—				**Number of elements in a sarcomere**			
Power stroke transition				N_M	38	Unitless	[Y2021]
$\bar{r}_{f,1}\bar{r}_{f,2}$	10,000	1/s	Adjusted	N_T	32	umitles	[Y2021]
$\bar{r}_{b,1}\bar{r}_{b,2}$	1,000	1/s	Adjusted	—	—	—	—
h_1	3	1/s	Adjusted	—	—	—	—
Attachment and detachment transition				—	—	—	—
c_{pre}	3,000	1/s	adjusted	—	—	—	—
r_{NXB}	225	1/s	adjusted	—	—	—	—

attached states. The corresponding T/T unit index τ for the i-th MH is given by:

$$\tau = \left\lfloor \frac{0.5LB + (i - 0.5)S_M - (SL/2 - LA)}{S_T} \right\rfloor. \quad (8)$$

Here, ⌊ ⌋ indicates the floor function, which rounds down after the decimal point. The parameter $S_M = 0.5\,(LM - LB)/N_M$ represents the spacing of the MHs, and $S_T = LA/N_T$ is the spacing of the T/T units. The corresponding T/T unit exists only if $1 \le \tau \le N_T$. Based on this correspondence, the factors k_{np} and k_{pn} of the rate constants are given by:

$$k_{\mathrm{np}} = \begin{cases} \delta_{OV} K_{\mathrm{np1}} & \text{if the T/T unit above is in the Ca} - \text{on state,} \\ \delta_{OV} K_{\mathrm{np0}} & \text{otherwise.} \end{cases} \quad (9)$$

$$k_{\mathrm{pn}} = \begin{cases} K_{\mathrm{pn1}} & \text{if the T/T unit above is in the Ca} - \text{on state,} \\ K_{\mathrm{pn0}} & \text{otherwise.} \end{cases} \quad (10)$$

Here, $\delta_{OV} = 1$ if the MH is located in the single overlapping region with the thin filament; otherwise, $\delta_{OV} = 0$. This, along with γ^{ng} or γ^{-ng} ($\gamma = 80$), represents the nearest-neighbor cooperativity of the MHs, following Rice et al. (Rice et al., 2003), which plays an important role in the force-pCa relationship, as shown in Figures 5A,B. From the cooperativity with $\gamma = 80$, the cardiac muscle in our ventricle model can relax in the diastole when [Ca^{2+}] is lower than 0.1 μM (Figure 4C), whereas the diastole deteriorates slightly with $\gamma = 40$ (Figures 5C,D). The times to reach equilibria differ substantially and are dependent on the Ca^{2+} concentration and parameter γ. Thus, cooperativity also affects the maximal rising rate of the left ventricular pressure (dP/dt_{max}), which is an important contractility index used in the medical community (Figures 5C,D).

We assume that one thin filament in the three-dimensional arrangement corresponds to two thin filaments in our half-sarcomere model. This case arises because we assumed that cooperative behavior exists along the tropomyosin molecules wrapped around the thin filament in a double-spiral fashion, and one spiral is modeled in our half-sarcomere. The constants K_{np0}, K_{np1}, K_{pn0}, and K_{pn1} are determined from Q, K_{basic}, and μ, as follows:

$$K_{\mathrm{np0}} = F_K(SL)\frac{QK_{\mathrm{basic}}}{\mu},\ K_{\mathrm{np1}} = F_K(SL)QK_{\mathrm{basic}},\ K_{\mathrm{pn0}} = K_{\mathrm{pn1}} = K_{\mathrm{basic}}\gamma^2. \quad (11)$$

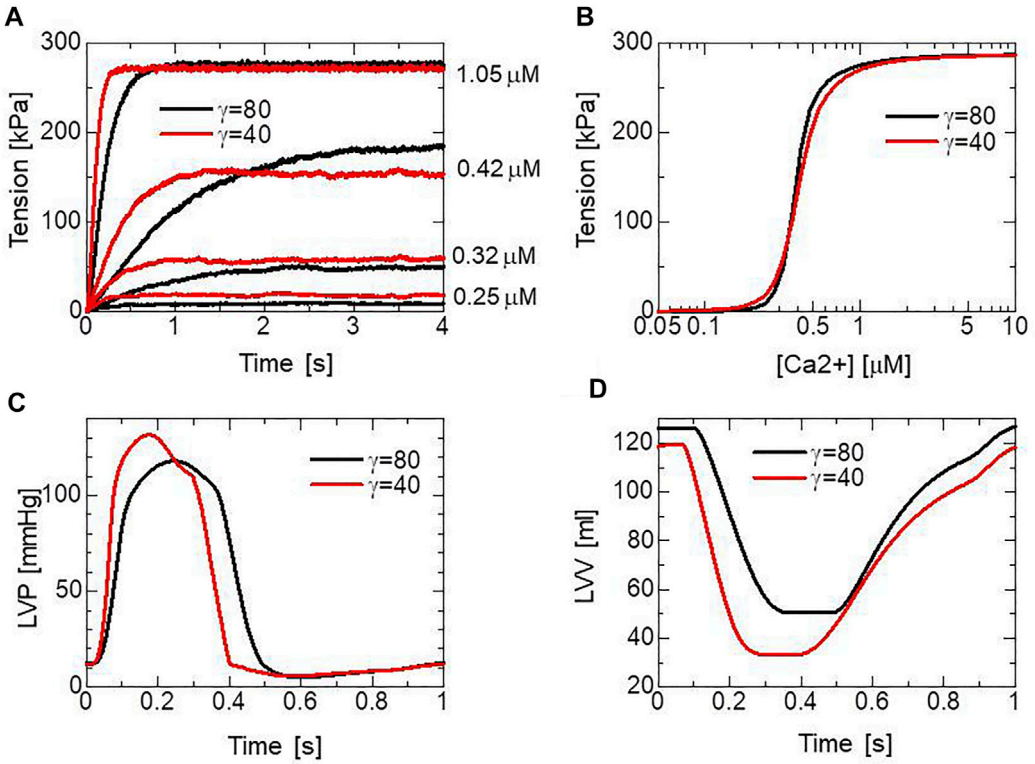

FIGURE 5
The simulated pCa-tension relationship of the MC cross-bridge model and its effects on heart pumping. **(A)** Time courses of the active tensions in the isometric contraction for [Ca^{2+}] = 0.25, 0.42, and 1.05 μM with γ= 80 (black) and γ= 40 (red). **(B)** Isometric tensions in the equilibrium states averaged over the time interval [3.5 s, 4 s] with γ= 80 (black) and γ= 40 (red). The half-sarcomere length was fixed at 1.14 μm (λ = 1.2). **(C)** Time transients of left ventricular pressures (LVP) with γ= 80 (black) and γ= 40 (red). **(D)** Time transients of the left ventricular volume (LVV) with γ= 80 (black) and γ= 40 (red).

Here, $\mu > 1$ controls the degree of cross-bridge inhibition for the T/T units in states other than Ca-on, and Q controls the ratio of binding states for the MHs. To reproduce the SL dependence in the active contraction tension, the following function $F_K(SL)$ is multiplied to define K_{np0} and K_{np1}.

$$F_K(SL) = \begin{cases} 1, & SL \geq SL_Q, \\ 1 - \alpha_Q(SL_Q - SL), & SL < SL_Q. \end{cases} \tag{12}$$

The values α_Q= 0.25 [1/ μ m] and SL_Q= 2.1 μm are used in this study.

The rate constants of attachment r_a and detachment r_d between the P_{XB} state and XB_{PreR} state are based on the assumed free energies, ΔG_{wb} and ΔG_0, of the P_{XB} state and XB_{PreR} state, respectively:

$$r_a = c_{\mathrm{pre}} \exp\left(-\frac{\Delta G_0 - \Delta G_{wb}}{k_B T} \right), \quad r_d = c_{\mathrm{pre}}. \tag{13}$$

The initial rod distortion at attachment is given stochastically based on a Boltzmann distribution determined from the rod strain energy, $W_{rod}(x)$ (Washio et al., 2016). The detachment rate constant for transitions from the XB_{PostR2} state to the N_{XB} state is r_{NXB}.

Using the rate constants, we also considered forced detachments from the XB_{PreR}, XB_{PostR1}, and XB_{PostR2} states to the N_{XB} state caused by extreme strain on the myosin rod:

$$d_{XB,i}(x) = \begin{cases} 0, & x < x_{XB,i}, \\ c_{XB,i}\left(\exp\left(a_{XB,i}\left(x - x_{XB,i}\right)\right) - 1\right), & x \geq x_{XB,i}, \\ i = 0,\ 1,\ 2. \end{cases} \tag{14}$$

Similarly, the rate constant of detachment from the XB_{Trap} state is given by:

$$d_{\mathrm{trap}}(x) = \begin{cases} 0, & x < x_{XB,t}, \\ c_{XB,t}\left(\exp\left(a_{XB,t}\left(x - x_{XB,t}\right)\right) - 1\right), & x \geq x_{XB,t}. \end{cases} \tag{15}$$

We paid close attention to the adjustments of parameters in Eqs 14 and 15 in reproducing the stretch activation. These parameters affect the degree of the increased delayed force. In this study, we used the following parameters to reproduce the characteristics of cardiac muscles: $c_{XB,0}$= 100 1/s, $c_{XB,1}$ =$c_{XB,2}$ =$c_{XB,t}$ = 20 1/s, $a_{XB,0}$= 1 1/nm,

$a_{XB,1}$ =$a_{XB,2}$ =$a_{XB,t}$ = 0.1 1/nm, $x_{XB,0}$= 3 nm, $x_{XB,1}$= 8.5 nm, $x_{XB,2}$= 13 nm, $x_{XB,t}$= 8.5 nm.

Power stroke and reverse transitions

In our model, the rate constants of the power and reverse strokes are determined from the Kramers escape theory (Kramers 1940), in which rate constants are defined by the Boltzmann factor associated with the height of the energy barrier from the origin.

$$\begin{cases} \hat{r}_{f,i}(x) = h_i \exp\left(\dfrac{\Delta G_{i-1} + W_{rod}(x) - W_{rod}(x + s_i/2)}{k_B T}\right), & (16) \\ \hat{r}_{b,i}(x + s_i) = h_i \exp\left(\dfrac{\Delta G_i + W_{rod}(x + s_i) - W_{rod}(x + s_i/2)}{k_B T}\right). & (17) \end{cases}$$

Here, $W_{rod}(x + s_i/2)$ is introduced because we assume that the barrier is given at the middle of the power stroke distances for the two states. In addition, we adopt upper limits to those transition rate constants because the power stroke transitions are thought to accompany a release of Pi and ADP from the nucleotide-binding pocket in the MH during the first and second strokes, respectively. Thus, the reverse stroke transitions must accompany a rebinding of these molecules. We assumed that the rates of chemical reactions for the release and rebinding are given by $\bar{r}_{f,i}$ and $\bar{r}_{b,i}$, respectively. With these upper limits, the temporary rate constants are modified so that the Boltzmann equilibrium in Eq. 1 is preserved:

$$r_{f,i}(x) = \begin{cases} \bar{r}_{f,i}, & x \le \bar{x}_{f,i} \\ \hat{r}_{f,i}(x), & \bar{x}_{f,i} < x \le \bar{x}_{b,i} \\ \dfrac{\hat{r}_{f,i}(x)\bar{r}_{b,i}}{\hat{r}_{b,i}(x + s_i)}, & x > \bar{x}_{b,i} \end{cases}, \quad (18)$$

$$r_{b,i}(x + s_i) = \begin{cases} \dfrac{\hat{r}_{b,i}(x + s_i)\bar{r}_{f,i}}{\hat{r}_{f,i}(x)}, & x \le \bar{x}_{f,i} \\ \hat{r}_{b,i}(x + s_i), & \bar{x}_{f,i} < x \le \bar{x}_{b,i} \\ \bar{r}_{b,i}, & x > \bar{x}_{b,i} \end{cases}. \quad (19)$$

Here, $\bar{x}_{f,i}$ and $\bar{x}_{b,i}$ are the distortions at which the temporary rates reach the upper limits ($\hat{r}_{f,i}(\bar{x}_{f,i}) = \bar{r}_{f,i}$, $\hat{r}_{b,i}(\bar{x}_{b,i} + s_i) = \bar{r}_{b,i}$).

The elastic force of a myosin rod is nonlinear with respect to the strain (Kaya and Higuchi, 2010). We assume that the myosin rod behaves as a linear spring for positive stretches, whereas nonlinear behavior is introduced for negative stretches because of the slack induced along the myosin rod. The strain energy W_{rod} is found by integrating the force F_{rod} from $x = 0$, defined by:

$$F_{rod}(x) = \begin{cases} b_{xb}k_{xb}(x + \xi_1) - F_1, & x < -\xi_1, \\ \dfrac{k_{xb}}{a_{xb}}\left(\exp(a_{xb}x) - 1\right), & -\xi_1 \le x < 0, \\ k_{xb}x, & 0 \le x. \end{cases} \quad (20)$$

Here, a_{xb} and F_1 are determined from the other parameters, so that the function F_{rod} and its first derivative are continuous at $\xi = 0$ and $-\xi_1$:

$$\begin{cases} a_{xb} = -\dfrac{(\ln b_{xb})}{\xi_1}, \\ F_1 = \dfrac{k_{xb}\left(1 - \exp(-a_{xb}\xi_1)\right)}{a_{xb}}. \end{cases} \quad (21)$$

Half-sarcomere model and its basic properties

We constructed a half-sarcomere model (Figure 5A) with n_F one-dimensional filament pairs in which the active tension generated by the bound myosin molecules is given as:

$$T_{\mathrm{act}} = \frac{2R_S}{SA_0 \cdot n_F} \sum_{\beta=1}^{n_F} \sum_{\alpha=1}^{n_M} \delta_{A,\alpha,\beta} \frac{\mathrm{d}W_{rod}\left(x_{\alpha,\beta}\right)}{\mathrm{d}x}. \quad (22)$$

Here, $\delta_{A,\alpha,\beta}$ = 1 if the MH is in an attached state; otherwise, $\delta_{A,\alpha,\beta}$ = 0. The parameter SA_0 is the cross-sectional area per thin filament in an unloaded half-sarcomere (Sato et al., 2013). The factor of 2 comes from the fact that our one-dimensional model corresponds to one of the double spirals of actin monomers along the thin filament. The parameter R_S is the sarcomere volume ratio under the unloaded condition. R_S= 0.5 is used, which indicates that 50% of the total volume is occupied by the sarcomere in the cardiac muscle.

For the feedback between sarcomere dynamics and actomyosin dynamics, the relation between the time transients of the molecular and sarcomere variables can be expressed by:

$$^{\mathrm{t}}x = {}^{t_{\mathrm{A}}}x - ({}^{\mathrm{t}}z - {}^{t_{\mathrm{A}}}z). \quad (23)$$

Here, t_A is the most recent time at which the myosin molecule was attached, ${}^{t_A}x$ is the initial distortion at the attachment, and ${}^{t}z$ is the half-sarcomere shortening length from the unloaded condition:

$$^{\mathrm{t}}z = -\frac{SL_0}{2}\left({}^{\mathrm{t}}\lambda - 1\right), \quad (24)$$

where SL_0 is the unloaded SL. Here, the stretch ${}^{\mathrm{t}}\lambda$ is the parameter given by macroscale models. The initial distortion is given from the Boltzmann distribution, assuming a fluctuation in the MH position under the potential W_{rod} (Washio et al., 2016).

The half-sarcomere shortening (${}^{t}\dot{z} > 0$) reduces the rod distortion (Eq. 23), which facilitates the power stroke (Eq. 16) and the deterioration of the reverse stroke (Eq. 17). Therefore, both the active tension and energy consumption are affected by the half-sarcomere shortening velocity. In Figure 6A, changes in the half-sarcomere length with various isotonic tensions computed using the MC cross-bridge model are depicted. In

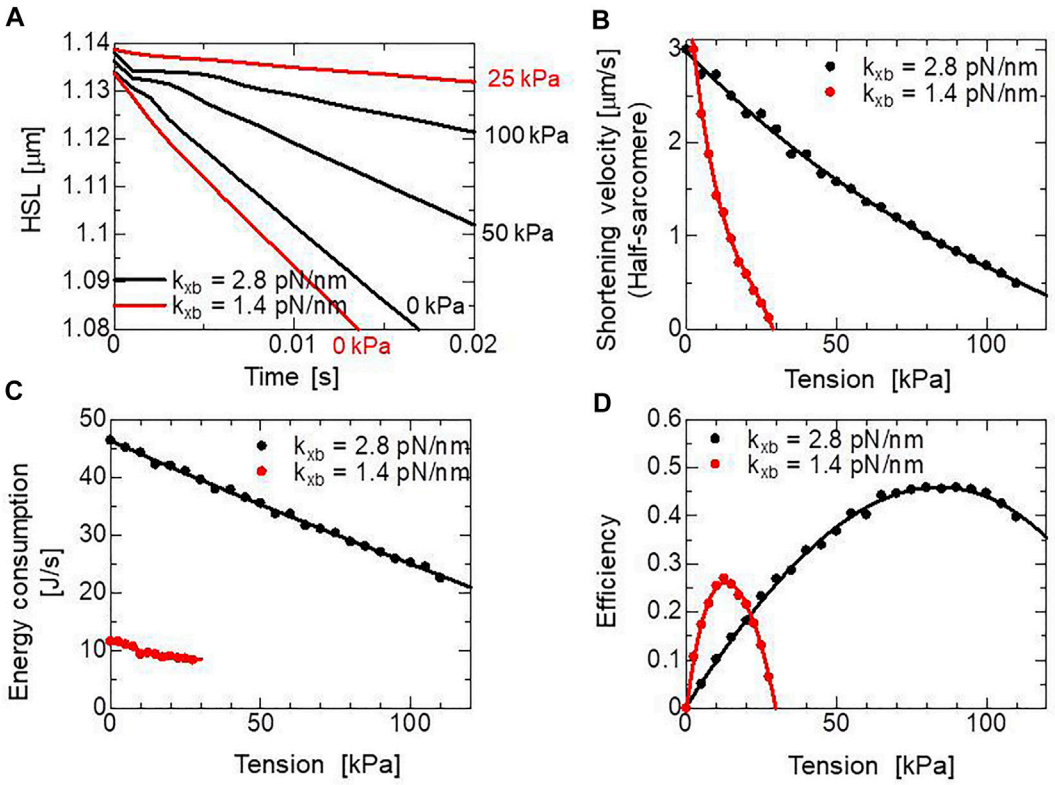

FIGURE 6
Simulated half-sarcomere length changes under isotonic conditions with the two cross-bridge model using different myosin rod stiffnesses, k_{xb} = 1.4 pN/nm and k_{xb} = 2.8 pN/nm. **(A)** Time courses of the half-sarcomere length under isotonic conditions with isotonic tensions of 0, 50, and 100 kPa for the cross-bridge model with k_{xb} = 2.8 pN/nm, and 0, 25 kPa for the cross-bridge model with k_{xb} = 1.4 pN/nm. **(B)** Half-sarcomere shortening velocities under isotonic tensions after the release starting from the half-sarcomere length at 1.14 μm (λ = 1.2). The velocities were calculated from changes of the half-sarcomere length from 1.12 to 1.09 after the release under isotonic conditions, where [Ca^{2+}] was fixed at 0.4 μM. **(C)** The energy consumption rate per the left ventricular wall volume (157 ml) of the ventricle model. **(D)** Efficiencies for shortening under isotonic conditions.

these isotonic contractions, the shortening velocities were computed over the common range of the half-sarcomere length (1.09–1.12 μm) to derive the tension-shortening velocity relationship (Figure 6B). By counting the number of detachments from the XB_{PostR2} state (Figure 1C: r_{NXB}), the energy consumption rates were evaluated assuming the detachment requires the energy G_{ATP} = 76.5 pN · nm, which is used in power stroke transitions (Figure 6C), as represented by Eq. 1. In the MC cross-bridge model, we assumed that 30% of G_{ATP} is consumed during the first power stroke (6 nm), and the remaining G_{ATP} is consumed during the second power stroke (4 nm) (See Table 1). The efficiencies were computed by dividing the work rates by the energy consumption rates (Figure 6D).

The energy loss in the cross-bridge cycle is given during the power stroke transitions and detachment from the XB_{PostR2} state. The difference between $\Delta G_i - \Delta G_{i+1}$ and $W_{rod}(x + s_i) - W_{rod}(x)$ is lost in the former, whereas the rod strain energy, $W_{rod}(x)$, at the detachment is lost in the latter. To observe the influence of the stiffness parameter k_{xb} in Eq. 20 on the dynamics in isotonic shortening, the cross-bridge performance was evaluated with the stiffness parameter k_{xb}= 1.4 pN/nm, which is half of our parameter k_{xb}= 2.8 pN/nm found by Kaya and Higuchi, 2010. In this case, the phase changes of the shortening velocity were not reproduced (Figure 6A), and the changes in the energy consumption rate for the tension is gentler than our model because the rate constants of power stoke transitions are less sensitive to the tension than the case of k_{xb}= 2.8 pN/nm. As a result, the peak efficiency is approximately half for our case (Figure 6D). The strain energy after the second power stroke ($0.5(s_1 + s_s)^2 k_{xb}$) with k_{xb}= 1.4 pN/nm is 70 pN · nm assuming isometric contraction and zero distortion at XB_{PreR}. This energy is almost equal to G_{ATP}. However, rod distortion decreases by half-sarcomere shortening until reaching XB_{PostR2} (Eq. 23) during isotonic contraction. Therefore, 75% of the energy loss is accounted for even at the optimal shortening velocity.

Coupling with macroscale models

In this study, coupling of the half-sarcomere model (Figure 4A) and the myofibril model (Figure 5B) or the ventricle model (Figure 4C) was achieved by applying the multiple-step active stiffness integration scheme in the exchange of the active tension T_{act} and stretch λ between the two scales. The macroscale model is driven by the active stress given by the active tension in the half-sarcomere model, whereas the stretch in the fiber orientation in the macroscale model provides feedback to the length change of the half-sarcomere model.

In the macroscale model, a much larger time step $\Delta T = n\Delta t$ compared with the MC time step Δt is used to save computational time. For a given stretch ${}^{T+\Delta T}\lambda$ at $T + \Delta T$, the macroscopic active tension $T_{\mathrm{act},[T,T+\Delta T]}$ over the time interval $[T, T + \Delta T]$ is determined by taking the time average of the active tension in the half-sarcomere model given for each MC step within an interval of Δt.

$$T_{\mathrm{act},[T,T+\Delta T]}\left({}^{T+\Delta T}\lambda\right) = \frac{1}{n}\sum_{k=1}^{n} T_{\mathrm{act}}\left(T + \frac{k}{n}\Delta T, \lambda^{T} + \frac{k}{n}\left({}^{T+\Delta T}\lambda - \lambda^{T}\right)\right). \quad (25)$$

The active tension T_{act} in the half-sarcomere model is given as a function of time and stretch for each MC step. The stretch for each MC step is determined by interpolating the stretches at T and $T + \Delta T$ to evaluate an appropriate stiffness of the binding myosin molecules in macroscopic Newton iterations. Note that the state transitions in the MC computations are calculated only once before the Newton iterations, assuming a stretch of $\lambda^{T+\Delta T} = \lambda^{T} + k\Delta t\lambda^{T}$ for each MC step. However, the rod distortion $\lambda^{T+\Delta T}$ is re-evaluated from Eqs 23 and 24 by replacing ${}^{T}\dot{\lambda}$ with $({}^{T+\Delta T}\lambda - {}^{T}\lambda)/\Delta T$ using the updated stretch $\lambda^{T+K\Delta T}$ in the macroscopic Newton iterations. In this study, Δt= 2.5 μs is used for the MC step, while ΔT= 0.1 ms and ΔT= 1.25 ms are used, respectively, for the myofibril and ventricle models.

For simplicity, we introduce the Newton iteration for the one half-sarcomere model under the isotonic condition, as in Figure 6A.

$$\gamma_L\dot{\lambda} + \frac{d\varphi_L}{d\lambda}(\lambda) + T_{act} - T_{iso} = 0, \quad (26)$$

where $\gamma_L = 0.01\,\mathrm{kPa}\cdot\mathrm{s}$ is the sarcomere friction, φ_L is the deformation energy for stretching in the longitudinal direction (Washio et al., 2019), and T_{iso} is the isotonic tension imposed on the cardiac muscle. Eq. 26 is discretized as:

$$\gamma_L\frac{{}^{T+\Delta T}\lambda - {}^{T}\lambda}{\Delta T} + \frac{d\varphi_L}{d\lambda}\left({}^{T+\Delta T}\lambda\right) + T_{\mathrm{act},[T,T+\Delta T]}\left({}^{T+\Delta T}\lambda\right) - T_{iso} = 0. \quad (27)$$

After executing n-times MC steps in $[T, T + \Delta T]$, where the half-sarcomere shortening length $z^{T+K\Delta T}$ at the kth step is given by assuming $\lambda^{T+K\Delta T} = {}^{T}\lambda + k\Delta t{}^{T}\dot{\lambda}$ with ${}^{T}\dot{\lambda} = ({}^{T}\lambda - {}^{T-\Delta T}\lambda)/\Delta T$, the initial solution of the Newton iteration is set as $\lambda^{T+K\Delta T} = \lambda^{T}$, and the following linearized equation of Eq. 27 at ${}^{T+\Delta T}\lambda = {}^{T+\Delta T}\lambda^{(i)}$ is iteratively solved until the magnitude of the residual $R^{(i)}$ is reduced sufficiently.

$$\left(\frac{\gamma_L}{\Delta T} + \frac{d^2\varphi_L}{d\lambda^2}\left({}^{T+\Delta T}\lambda^{(i)}\right) + K_{\mathrm{act},[T,T+\Delta T]}\left({}^{T+\Delta T}\lambda^{(i)}\right)\right)\left({}^{T+\Delta T}\lambda^{(i+1)} - {}^{T+\Delta T}\lambda^{(i)}\right) = R^{(i)}, \quad (28)$$

where the residual is given by

$$R^{(i)} = -\left(\gamma_L\frac{{}^{T+\Delta T}\lambda^{(i)} - {}^{T}\lambda}{\Delta T} + \frac{d\varphi_L}{d\lambda}\left({}^{T+\Delta T}\lambda^{(i)}\right) + T_{\mathrm{act},[T,T+\Delta T]}\left({}^{T+\Delta T}\lambda^{(i)}\right) - T_{iso}\right). \quad (29)$$

Here, $K_{\mathrm{act},[T,T+\Delta T]}\left({}^{T+\Delta T}\lambda\right)$ is the total stiffness of the binding myosin rods given as:

$$K_{\mathrm{act},[T,T+\Delta T]}\left({}^{T+\Delta T}\lambda\right) = \frac{dT_{\mathrm{act},[T,T+\Delta T]}}{d\lambda}\left({}^{T+\Delta T}\lambda\right). \quad (30)$$

See our previous work (Yoneda et al., 2021) for the actual computation of the right-hand side in Eq. 30. Under normal situations, the stiffness coefficient $K_{\mathrm{act},[T,T+\Delta T]}$ increases greatly to be much larger than $\gamma_L/\Delta T + d^2\varphi_L/d\lambda^2$ during contraction. Therefore, stiffness caused by the binding myosin rods must be correctly incorporated in the total stiffness, as in Eq. 28; otherwise, the time integration scheme generates inaccurate solutions without using a small time step ΔT in a similar order of magnitude to the MC time step Δt (Yoneda et al., 2021).

The above implicit time integration scheme can be naturally extended to more general cases where the half-sarcomere models are imbedded in different elements that interact with each other at the element interfaces. In the myofibril model (Figure 4B), two degrees of freedom, the stretches λ_i and μ_i, respectively, in the longitudinal and transverse directions, are given to each half-sarcomere element (Washio et al., 2019). For each half-sarcomere, the passive deformation energy per unit volume is given by

$$\psi(\lambda,\mu) = \varphi_L(\lambda) + \varphi_T(\mu) + \frac{1}{2}k_{LT}R_{LT}(\lambda,\mu)^2. \quad (31)$$

Here, the function φ_T is the deformation energy for the transverse stretch, and the last term is a weak penalty term associated with the inverse SL-lattice space (LS) relationship, which constrains the half-sarcomere deformation to make $|R_{LT}(\lambda,\mu)|$ small. In our model, a simple linear relation:

$$R_{LT}(\lambda,\mu) = \lambda - 1 + 2\beta_R(\mu - 1), \quad (32)$$

with $\beta_R = 2$ is applied (Washio et al., 2019). Concerning the elasticity with differences in LS between adjacent half-sarcomeres, the following deformation energy per unit volume is further applied.

$$\varphi_{TA,i}(\mu_i, \mu_{i+1}) = \begin{cases} k_{MM}(\mu_i - \mu_{i+1})^2, \ i = 1, 3, \cdots \\ k_{MZ}(\mu_i - \mu_{i+1})^2, i = 2, 4, \cdots \end{cases} \quad (33)$$

where the half-sarcomeres are separated by the M-band for the top expression, and are separated by the Z-disc for the lower expression.

Within each half-sarcomere, the following tensions act at the left and right edges:

$$T_{SR,i} = \gamma_L \dot{\lambda}_i + \frac{d\varphi_L}{d\lambda}(\lambda_i) + k_{LT} R_{LT}(\lambda_i, \mu_i) + T_{\text{act},i}, \ i = 1, \cdots, ns. \quad (34)$$

The longitudinal mechanical equilibrium condition at the element boundaries:

$$T_{\text{SR},i} - T_{\text{SR},i+1} = 0, \quad (35)$$

and the transversal mechanical equilibrium condition at each element:

$$\gamma_T \dot{\mu}_i + \frac{d\varphi_T}{d\mu}(\mu_i) + 2\beta_R k_{LT} R_{LT}(\lambda_i, \mu_i) + \frac{\partial \varphi_{TA,i-1}}{\partial \mu_i}(\mu_i, \mu_{i-1}) + \frac{\partial \varphi_{TA,i}}{\partial \mu_i}(\mu_i, \mu_{i+1}) = 0 \quad (36)$$

are simultaneously solved with the boundary condition, where one end of the myofibril is fixed and the other end is connected to a fixed linear spring (Figure 4B). The parameter γ_T is the sarcomere friction in the transverse direction, and φ_T is the deformation energy for stretching in the transverse direction (Washio et al., 2019). In our myofibril model, the rapid sarcomere lengthening in SPOCs is reproduced by the avalanche of reverse strokes at the peak contractile phase in which the population of MHs with large mechanical loads is high. From the SL-LS relationship (Eq. 32) and LS alignment with the adjacent sarcomeres (Eq. 33), the rapid lengthening of one sarcomere transversally compresses the neighboring half-sarcomere in the peak contraction phase. Then, from the SL-LS relationship, the transverse compression enlarges the longitudinal stretch, resulting in the load increments of the attached MHs. As a result, an avalanche of reverse strokes is triggered. In this way, the rapid lengthening wave travels in the myofibril model.

In the finite element ventricle model, the half-sarcomere model is imbedded in each tetrahedral element along the fiber orientation $\boldsymbol{f}$ represented by a unit vector in the reference configuration (Figure 4C). Thus, the half-sarcomere models pull each other at the element interfaces in the fiber orientation. As depicted in Figure 4C, the angle of the fibers relative to the equatorial plane varies depending on the depth of the wall, so that the direction of force developed in the wall covers a wide range. In the finite element analysis, the current position of each material point $\boldsymbol{X} \in \Omega$ in the reference (unloaded) configuration is represented by $\boldsymbol{x} = \boldsymbol{x}(\boldsymbol{X})$. Therefore, the stretch in the fiber orientation is given by

$$\lambda = \| \boldsymbol{F}\boldsymbol{f} \|, \quad (37)$$

where $\boldsymbol{F} = \partial \boldsymbol{x}/\partial \boldsymbol{X}$ is the deformation gradient tensor. The active stress $\boldsymbol{S}_{act}$ (as the second Piola-Kirchhoff stress tensor) is formulated based on considering the virtual work done by the active tension T_{act} in the fiber orientation per unit volume in the reference space as follows:

$$\delta w_{act} = -T_{act}\delta\lambda = -\frac{T_{act}}{\lambda}\frac{1}{2}\delta(\boldsymbol{f} \otimes \boldsymbol{f} : \boldsymbol{F}^T\boldsymbol{F}) = -\frac{T_{act}}{\lambda}\boldsymbol{f} \otimes \boldsymbol{f} : \boldsymbol{\delta E}, \quad (38)$$

where $\boldsymbol{\delta E} = \frac{1}{2}(\boldsymbol{\delta F}^T\boldsymbol{F} + \boldsymbol{F}^T\boldsymbol{\delta F})$ is the infinitesimal increment of the Green–Lagrange strain tensor:

$$\boldsymbol{E} = \frac{1}{2}(\boldsymbol{F}^T\boldsymbol{F} - \boldsymbol{I}). \quad (39)$$

As a result, with the active stress represented by

$$\boldsymbol{S}_{\text{act}} = \frac{T_{act}}{\lambda}\boldsymbol{f} \otimes \boldsymbol{f}, \quad (40)$$

the virtual work by the active stress per unit volume is given by

$$\delta w_{act} = -\boldsymbol{\delta E} : \boldsymbol{S}_{\text{act}}. \quad (41)$$

The equation of motion for the displacement, $\boldsymbol{u}(\boldsymbol{X}) = \boldsymbol{x}(\boldsymbol{X}) - \boldsymbol{X}$, is given as:

$$\int_\Omega \boldsymbol{\delta u} \cdot \rho \ddot{\boldsymbol{u}}\, d\Omega + \int_\Omega \boldsymbol{\delta E} : \boldsymbol{S}\, d\Omega - P_L \int_{\Gamma_L} \boldsymbol{\delta u} \cdot \boldsymbol{n}\, d\Gamma_L - P_R \int_{\Gamma_R} \boldsymbol{\delta u} \cdot \boldsymbol{n}\, d\Gamma_R = 0. \quad (42)$$

Here, $P_L = LVP$ and $P_R = RVP$ are the blood pressures in the left and right ventricular cavities, respectively. Ω is the muscle domain in the reference configuration, whereas Γ_L and Γ_R are the blood–muscle interfaces of the left and right ventricles, respectively, in the configuration at time T, and $\boldsymbol{n}$ is the normal unit vector directed from the cavity to the muscle at these surfaces. The Dirichlet boundary condition $\boldsymbol{u}(\boldsymbol{X}) \equiv 0$ is imposed on the boundary nodes around the valve rings. The second Piola–Kirchhoff stress tensor $\boldsymbol{S}$ consists of the active, passive, and viscous stresses:

$$\boldsymbol{S} \equiv \boldsymbol{S}_{\text{act}} + \boldsymbol{S}_{\text{pas}} + \boldsymbol{S}_{\text{vis}}, \quad (43)$$

where $\boldsymbol{S}_{\text{act}}$ is given by Eq. 40, and $\boldsymbol{S}_{\text{pas}} = \frac{\partial W_{pas}}{\partial \boldsymbol{E}}$ and $\boldsymbol{S}_{\text{vis}}$ are the passive and viscous stresses, respectively. The ventricle blood pressures P_L and P_R are determined through their interactions with the circulatory systems of the body and the lung. See details of the deformation potential W_{pas}, the viscous stress $\boldsymbol{S}_{\text{vis}}$, and the coupling with the circulatory system in our previous work (Yoneda et al., 2021).

Assuming a periodical solution over a heartbeat, the time integration on a cycle with the substitutions of $\dot{\boldsymbol{u}}$ and $\dot{\boldsymbol{E}}$, respectively, into $\boldsymbol{\delta u}$ and $\boldsymbol{\delta E}$ in Eq. 42 gives the relationship

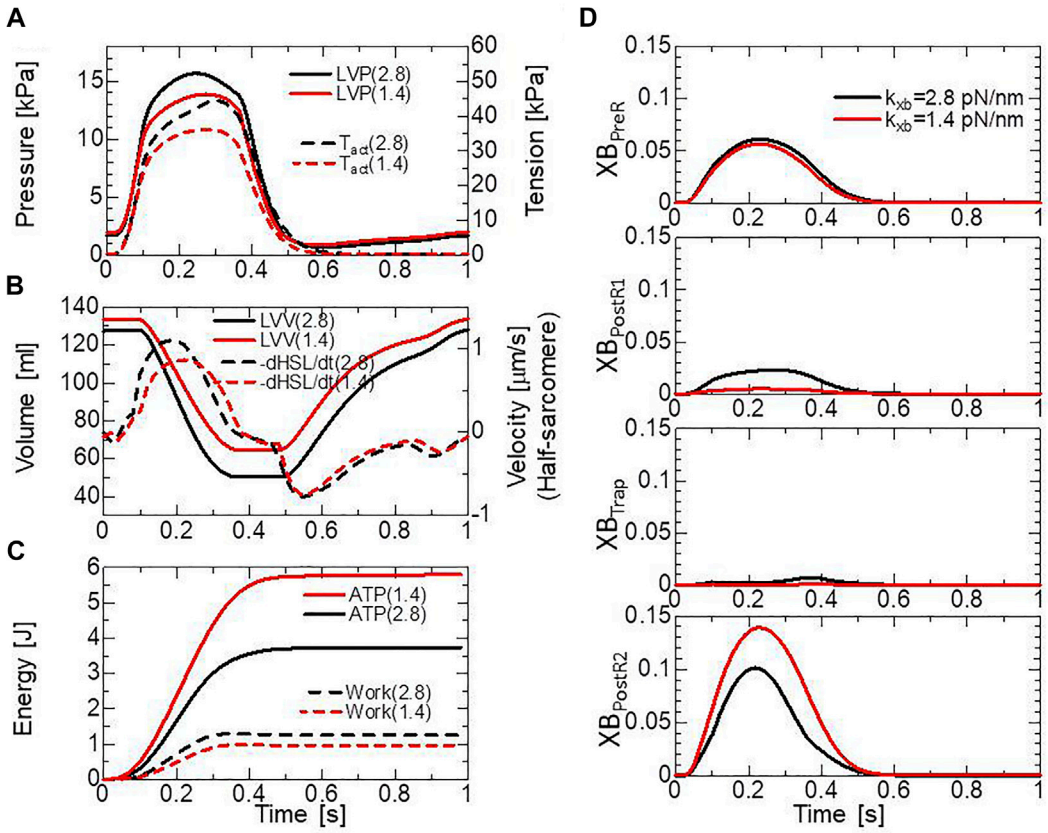

FIGURE 7
The comparison of pumping heart performance for different myosin rod distortion stiffnesses. The spring constants tested were k_{xb}= 2.8 pN/nm (black lines) and k_{xb}= 1.4 pN/nm (red lines). **(A)** Time courses of the left ventricular pressure (solid lines) and the average active tension (broken lines) over the left ventricular wall (free wall and septum). **(B)** Time courses of the left ventricular volume (solid lines) and the average half-sarcomere shortening velocity over the left ventricular wall. **(C)** Time courses of cumulative energy consumptions (solid lines) and cumulative works (broken lines) by the active tension over the left ventricular wall. **(D)** Time courses of the population ratio of attached MHs in the left ventricular wall classified according to the attached states.

between the cardiac output C_{out} and the energy production inside the cardiac muscle as follows:

$$C_{out} \equiv -\oint P_L \dot{V}_L dT - \oint P_R \dot{V}_R dT$$
$$= -\oint \int_\Omega \dot{\boldsymbol{E}} : (\boldsymbol{S}_{act} + \boldsymbol{S}_{vis})\, d\Omega dT. \quad (44)$$

Here, the inertia and the passive energy terms disappear for the sake of the periodicity assumption. If the viscous energy loss is negligible, the following work done by the active stress is almost equal to the cardiac output.

$$W_{act} \equiv -\oint \int_\Omega \dot{\lambda}\, T_{act} d\Omega dT = -\oint \int_\Omega \dot{\boldsymbol{E}} : \boldsymbol{S}_{act}\, d\Omega dT \sim C_{out} \quad (45)$$

The above relationship between the blood dynamics and muscle dynamics of the left ventricle (the left ventricular free wall and the septum) in our ventricle model is depicted in Figures 7A,B, where the two cases of the myosin rod stiffness with k_{xb}= 2.8 pN/nm (black lines) and k_{xb}= 1.4 pN/nm (red lines) are compared. The solid lines and broken lines represent, respectively, the blood dynamics and the muscle dynamics. Roughly, in the mid-systole ([0.15 s, 0.2 s]), the average active tension reaches 30–40 kPa, with a systolic blood pressure of 12–15 kPa and an average half-sarcomere shortening velocity of 1 μm/s (see also Supplementary Video 2). The relationship between the active tension and the systolic pressure agrees with the simple estimation given by the Laplace law assuming the dimension of the left ventricle in the early-systole (40 mm-diameter, 10 mm-wall thickness, the fiber helix angle twisting from −60° (epicardium) to +60° (endocardium). For example, to support blood pressure of 15 kPa, the active tension T_{act} must be roughly equal to 15 kPa × (20 mm/10 mm) × $\frac{2\pi}{3\sqrt{3}}$ ~ 36 kPa. Here, the factor $\frac{2\pi}{3\sqrt{3}}$ comes from considering the fiber helix angles. The complex distributions of the active tension and the half-sarcomere shortening velocity over the ventricular

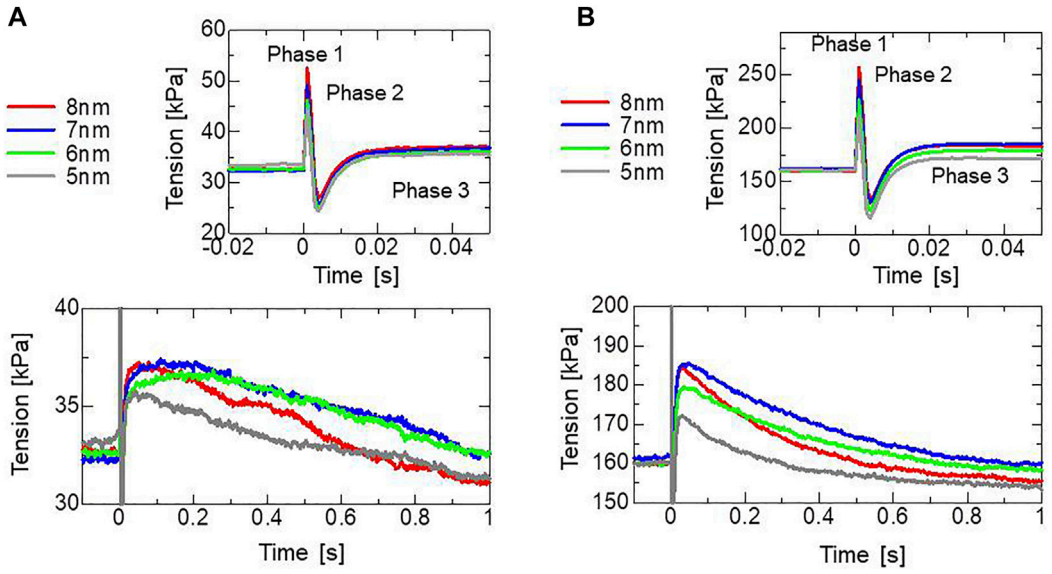

FIGURE 8
Numerical results of the stretch activation simulation. Stretches of 5, 6, 7, or 8 nm were applied over the time span of 1 ms at T = 0 s after the isometric force had matured under constant [Ca^{2+}] = 0.3 μm **(A)** and [Ca^{2+}] = 0.4 μm **(B)**. Time courses of the tensions are color-coded by the stretching as follows: 5 nm (gray), 6 nm (light green), 7 nm (blue), and 8 nm (red). Enlarged views of the top, focusing on the tension decrease on the order of seconds are depicted on the bottom.

wall (see Supplementary Video 2) make it difficult to find the correspondence to the tension-shortening velocity relationship under isotonic conditions (Figure 6B). Although the cardiac outputs and the muscle works of the two cases (the solid lines in Figures 7A,B, and the broken lines in Figure 7C) are not so different, the difference in energy consumption (the solid lines in Figure 7C) is remarkable, as indicated also in Figure 6D. The comparison of the time transients of the population ratio of the binding states (Figure 7D) indicates a shorter average dwell time in the XB_{PostR1} state and a larger population in the XB_{PostR2} state for the case of k_{xb}= 1.4 pN/nm than those for the case of k_{xb}= 2.8 pN/nm, resulting in the remarkable energy loss. Therefore, in this study, we analyzed the effects of the trapping mechanism when k_{xb}= 2.8 pN/nm.

Results

Stretch activation in the half-sarcomere model

To assess the effectiveness of the trapping mechanism, a stretch-activation test was performed for a single half-sarcomere model consisting of 32,768 filament pairs. Here, stretch lengths of 5, 6, 7, or 8 nm were applied over a 1-ms time interval after the active tension had sufficiently matured. During the simulations, the Ca^{2+} concentration ([Ca^{2+}]) was held at a constant value of 0.3 μM (Figure 8A) or 0.4 μM (Figure 8B). A greater increase in tension (the maximum in Phase 3) was observed as the stretching increased up to 7-nm stretch, corresponding to roughly +13% for a 6-nm stretch and +15% for a 7-nm stretch under [Ca^{2+}] = 0.3 μm. Here, 7 nm is 0.7% of the half-sarcomere length. These increases lasted for a few seconds after the rapid stretching. In agreement with the experimental results given by Stelzer et al. (2006), our numerical results reproduced "phase 2 (Figure 1A)" in which the force decreased to the steady-state level before stretching. The increase in tension observed by Stelzer et al. (2006) was roughly 16% for a 2% stretch and 8% for a 1% stretch. The tension increases stopped at an 8-nm stretch in the simulation result. In the numerical model, the stretch is directly linked to the shift of the thin filament relative to the thick filament (Figure 3A), while the stretch of the sarcomere may be relaxed by intermediate substances such as Z-lines or intercalated disks in the experimental conditions, as analyzed in the Discussion Section 4.3. Note that we assumed a cross-bridge model under physiological conditions identical to those of a living heart, which differ from the experimental conditions in many aspects, such as temperature.

Focusing on the result for a 7-nm stretch (Figures 9A–F), compared with the pre-stretch steady state, the lasting increase in tension apparently arose from a lasting increase in the population of the XB_{Trap} state (Figures 9C,D). The effect of the XB_{Trap} state is more emphasized when the individual contributions in the active tension of the attached states are plotted (Figures 9E,F). In the

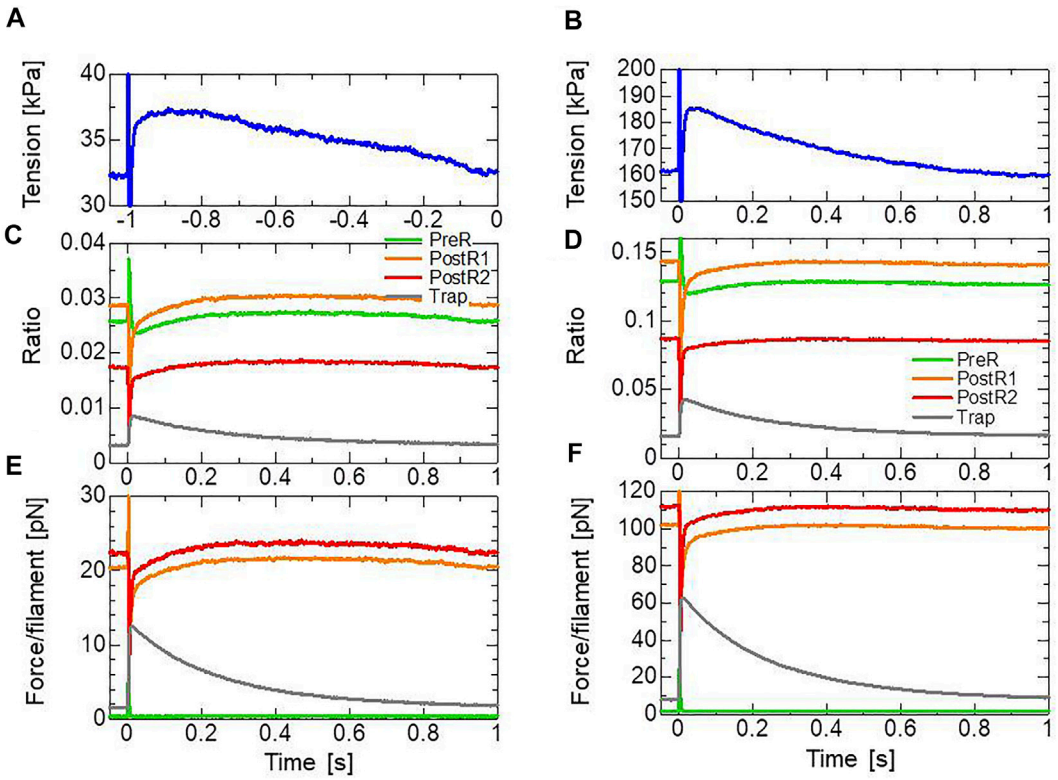

FIGURE 9
Transients of the four attached states during and after the 1-ms stretching in the stretch activation test with [Ca^{2+}] = 0.3 μm (left) and [Ca^{2+}] = 0.4 μm (right). **(A,B)** Time courses of the tension for a 7-nm stretch. **(C,D)** Time courses of the population ratio of the attached states: XB_{PreR} (green), XB_{PostR1} (orange), XB_{PostR2} (red), and XB_{Trap} (gray). **(E,F)** Time courses of the force per thin filament in each state.

half-sarcomere model, we assumed that one thin filament is surrounded by 76 (= 38 × 2) myosin molecules. In the steady state before stretching, filament forces of roughly 20 and 22 pN are generated by myosin molecules in the XB_{PostR1} (2.9%) and XB_{PostR2} (1.7%) states, respectively, when [Ca^{2+}] = 0.3 μm. Thus, the average force per molecule is 9.1 and 17.0 pN, respectively, in the XB_{PostR1} and XB_{PostR2} states. Because we assumed a force constant of k_{xb} = 2.8 pN/nm for the myosin rod distortion x, the above forces are generated by distortions of 3.3 and 6.1 nm, respectively. After the stretch, a filament force of 12 pN is produced by the myosin molecules in the XB_{Trap} state (~0.9%). Thus, the average force is roughly 17.5 pN per trapped myosin molecule. This average force is slightly larger than experimentally observed maximal forces (~15 pN) (Hwang et al., 2021). As analyzed in Section 2.4 and Section 2.5, our setting of the force constant (k_{xb} = 2.8 pN/nm) seems reasonable with respect to the efficiency in both the isotonic contraction and heart pumping. Furthermore, it may be difficult to measure the maximal force produced by a single myosin molecule under the sarcomeric condition. In particular, the force measured in the filament direction depends on the angle between the myosin rod (S2) and the thick filament, and the maximal force under a similar condition to the stretch activation environment has not been reported.

As observed by Stelzer et al. (2006), the MC cross-bridge model also reproduced the different behaviors in Phase 3 (Figure 1A) in the different activation levels. In our model, this difference is made by the differences in the time courses of the population ratio of the attached states (Figures 9C,D) that are produced by the cooperativity effects, as shown in Figure 5A.

Effects of the trap mechanism on SPOCs in a single myofibril model

The effects of the trap mechanism on SPOCs of a single myofibril model consisting of 40 half-sarcomeres were investigated (Figures 10A,B). Here, 2048 filament pairs were imbedded in each half-sarcomere model. SPOCs were produced for all Ca^{2+} concentrations ([Ca^{2+}]) in the no-trap model. In contrast, SPOCs were reproduced only for the intermediate concentration ([Ca^{2+}] = 0.4 μM) between the states of relaxation and contraction in the trap model, as observed by Fabiato and Fabiato (Fabiato and Fabiato, 1978).

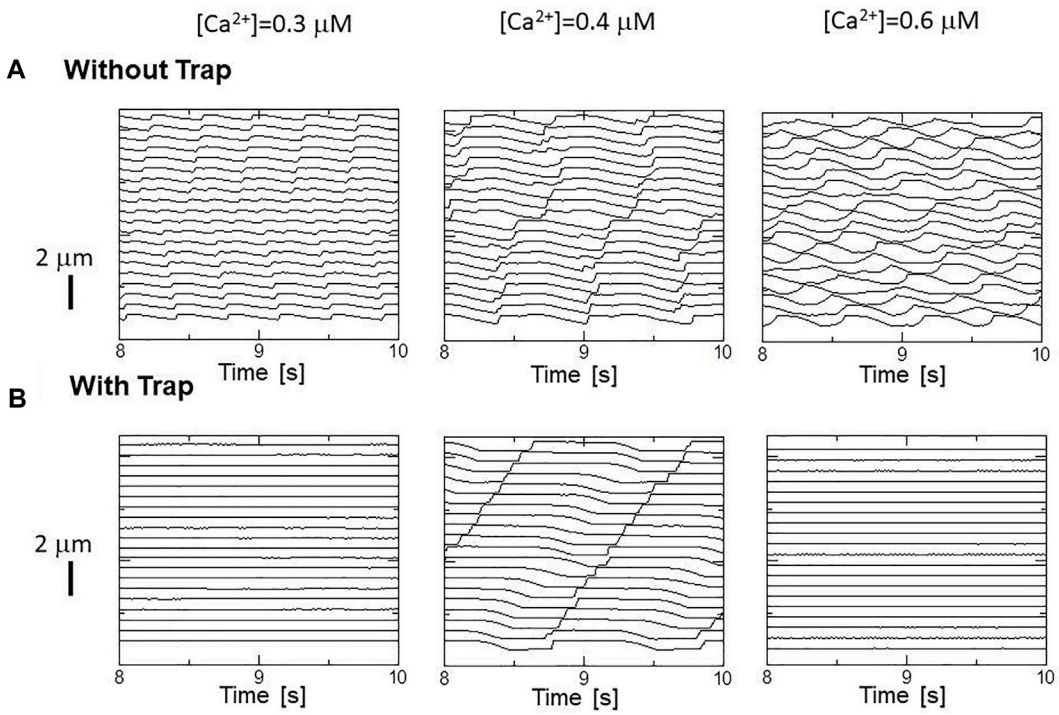

FIGURE 10
Sarcomere length changes in the myofibril model under activations with different constant calcium concentrations [Ca^{2+}] = 0.3 μM (left), 0.4 μM (center), 0.6 μM (right), for **(A)** the no-trap model and **(B)** the trap model.

Therefore, the trap mechanism may contribute to the [Ca^{2+}] dependence of the SPOCs by inhibiting the reverse stroke for certain amounts of myosin molecules in the XB_{PostR1} state. For the low Ca^{2+} concentration ([Ca^{2+}] = 0.3 μM), the lengthening was prevented by myosin molecules trapped in the XB_{Trap} state despite the oscillating XB_{PostR2} concentration in the trap model, as indicated by a small increase in the XB_{Trap} state for each reduction in the XB_{PostR2} state (Figure 11A). For the intermediate Ca^{2+} concentration ([Ca^{2+}] = 0.4 μM), the SPOCs are similar for both cases (Figure 11B). For the high Ca^{2+} concentration ([Ca^{2+}] = 0.6 μM), the sarcomeres were shortened to the minimum length, which is almost equal to the thick filament length of *LM* ~ 1.6 μM, as shown in Figure 1B. At this length, the population of the attached MHs is small because of the small single overlap region of the two filaments. Thus, lengthening was prevented in the same way as that observed for the low Ca^{2+}-concentration case in the trap model (Figure 11C).

Effects in beating ventricle simulation

Beating-ventricle simulations were performed using a finite element ventricle model with the same setup as our previous work (Yoneda et al., 2021). In each element, a sarcomere model consisting of 16 filament pairs was imbedded along the appropriate fiber orientation **f**. The distribution of the fiber orientations was found by an optimization algorithm based on the isovolumetric active tension (Washio et al., 2020) according to the impulses given by the active tension. Portions of the helical fiber structure are depicted in Figure 4C. The heart rate was set to 60 beats per minute, and the Ca^{2+} transient (Figure 4C) generated by the mid-myocardial cell model proposed by ten Tusscher panflov, (2006) was applied. Transmural delays of the Ca^{2+} transient determined by the distances from the endocardial surfaces of the left and right ventricles under a transmural conduction velocity of 52 cm/s, as measured by Taggart et al. (2000), were adopted. By comparing the trap and no-trap models in Figures 12A,B, one can see that the trap mechanism contributes to maintaining both the high pressure in the last half of the systolic phase and the rapid pressure decrease at the end of the systolic phase (Figure 12A). As a result, the blood volume ejected from the left ventricle in the trap model increased from 71 to 78 mL, while the ATP energy consumption of the left ventricular wall was almost equivalent (Figure 12C). This trend implies that the trap mechanism increases blood ejection without increasing energy consumption. It should be noted that the ATP consumption rates were computed by counting the detachments of MHs in the XB_{PostR2} state transferred to those in the N_{XB} state,

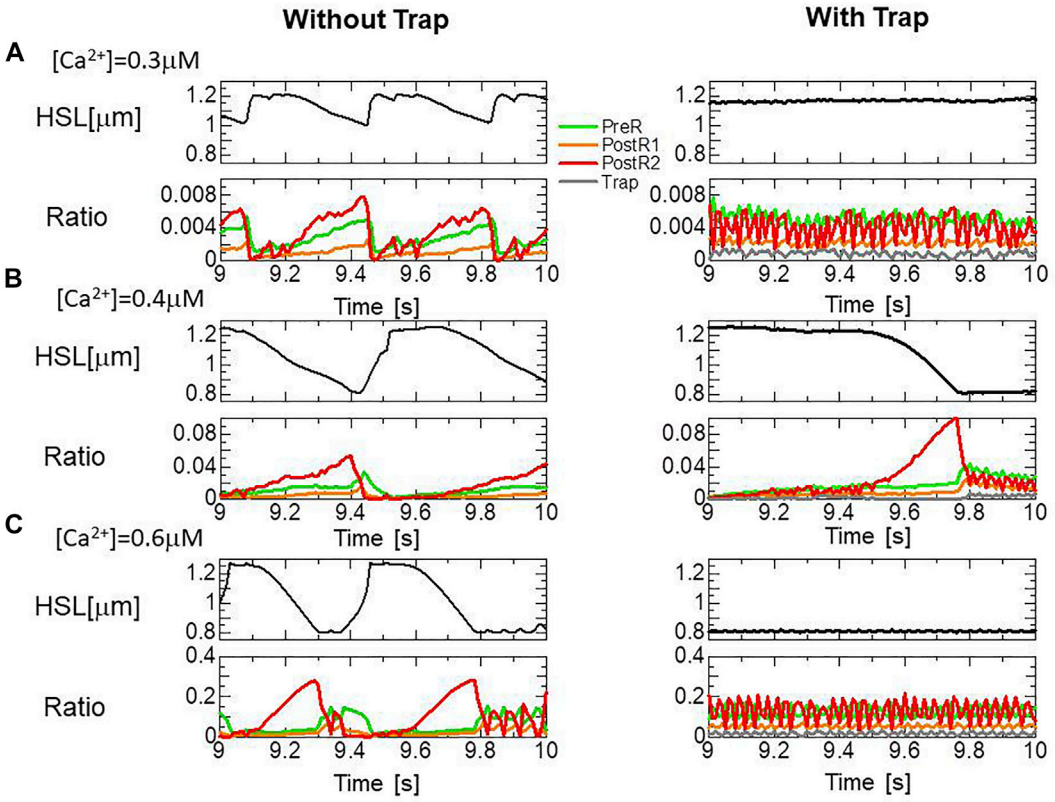

FIGURE 11
Transitions of the four attached states for the no-trap model (left) and the trap model (right) during SPOCs in a half-sarcomere model imbedded in the myofibril model. Time courses are shown for the half-sarcomere length (black) and the population ratio of binding states: XB_{PreR} (green), XB_{PostR1} (orange), XB_{PostR2} (red), and XB_{Trap} (gray), for the no-trap model (left) and the trap model (right). **(A)** $[Ca^{2+}]$ = 0.3 μM **(B)** $[Ca^{2+}]$ = 0.4 μM, and **(C)** $[Ca^{2+}]$ = 0.6 μM.

which was controlled by the rate constant r_{NXB} and the forced detachments defined by Eqs 14 and 15. As shown in Figures 12A,B slight increase in the population of MHs in the XB_{Trap} state can be seen at the end of the systolic phase (Figures 12D,E). This increase corresponds to a prolonged ejection time in the trap model, as shown in Figure 12A.

In the systolic phase, the cardiac myocytes within the shared fiber bundle support each other by pulling their neighbors *via* contractile forces, with the active tension in Eq. 22 playing the greatest role. Therefore, based on the mechanical equilibrium condition in the fiber direction, the active tensions must be almost equal. Consequently, if there is a loss of active tension at one point of the fiber bundle prior to the remaining parts in the early-systole or in the end-systolic phase, this portion would be lengthened quickly, and the sarcomeres in the remaining parts would be shortened until a mechanical equilibrium is reached. Because this transition accompanies decreases in the active tension owing to the loss of distortion in the myosin rods, stopping this process as early as possible is desirable to maintain blood pressure. The trapping mechanism can achieve this goal, as shown in Figures 13A–C, which depict the distributions of the active tension generated by the individual states XB_{PostR2} and XB_{Trap} in the end-systolic phase. The degenerated forces of the XB_{PostR2} state in the no-trap model (Figure 13A) are compensated by the force generated by the XB_{Trap} state in the trap model (Figure 13B). Furthermore, the forces of the XB_{PostR2} state in the trap model around the degenerated regions in the no-trap model (Figure 13C) are well maintained, owing to the contributions of the reinforced regions *via* the trap mechanism. As shown in the frequencies of transitions (Figure 14), the reverse power stroke contributes to diastolic relaxation to the same extent as the detachment from the XB_{PostR2} state (Figure 14A). Although the difference between the trapping and escaping frequencies averaged over the left ventricular wall (Figure 14B) is relatively small, the two peaks of the difference in Figure 14C agree with the differences in LVP between the trap model and the no-trap model in Figure 12A. Figure 14C also indicates that a certain extent of the trapped MHs is forced to detach because of the extreme distortion (Eq. 15).

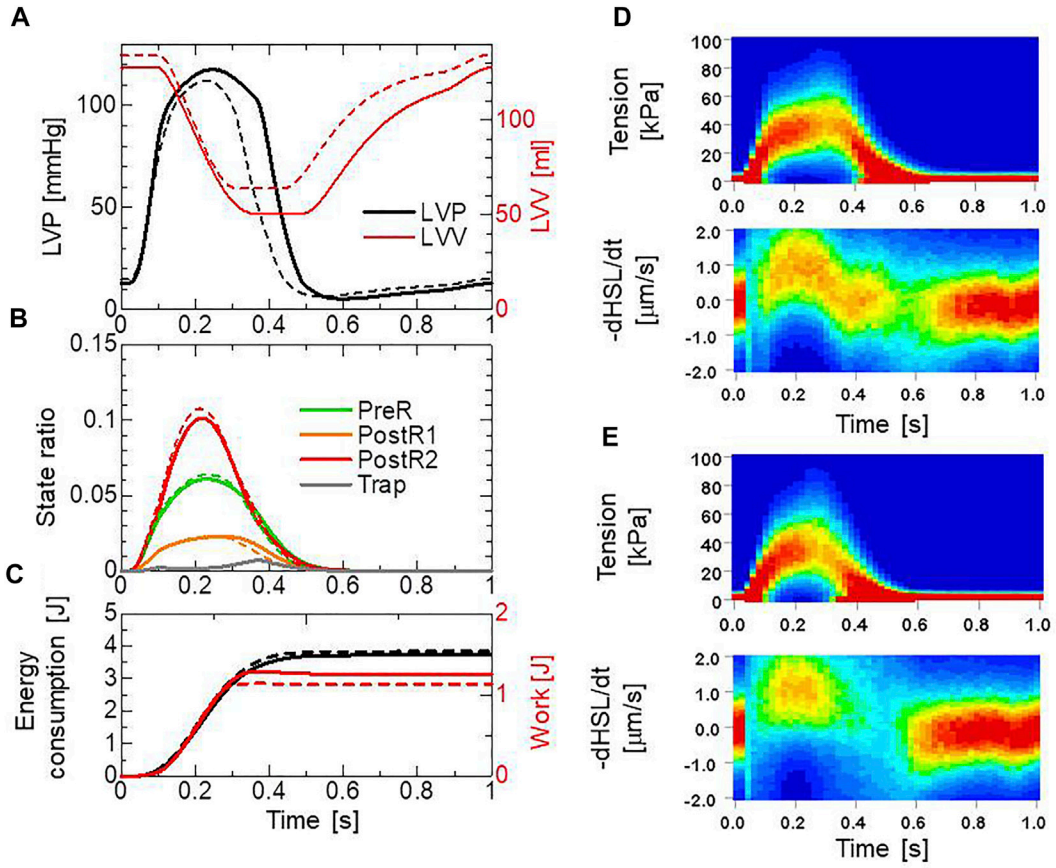

FIGURE 12
Numerical results of the beating ventricle simulation using the bi-ventricular FEM. **(A)** Time courses of the left ventricular pressure (black) and volume (red) for the no-trap MH model (broken lines) and the trap model (solid lines). **(B)** Time courses of the population ratio of attached MHs in the left ventricular wall classified according to the attached states: XB_{PreR} (green), XB_{PostR1} (orange), XB_{PostR2} (red), and XB_{Trap} (gray), for the no-trap model (broken lines) and the trap model (solid lines). **(C)** Time courses of the cumulative ATP energy consumption (black) and work (red) in the left ventricular wall for the no-trap model (broken line) and the trap model (solid line). **(D)** Contours of the tension distribution (upper) and the half-sarcomere shortening velocity (lower) for the trap MH model. **(E)** Contours of the tension distribution (upper) and the half-sarcomere shortening velocity (lower) for the no-trap MH model.

Discussion

Effects of the trapping mechanism

In the stretch activation tests, the step length dependence was reproduced (Figure 8), similar to the experimental results of Stelzer (Stelzer et al., 2006). However, the minimum values for the rapid force decay (phase 2) in the numerical results were lower than the original isometric force before stretching and higher than the isometric force in the experimental results of Stelzer. Conversely, minimum values smaller than the original isometric force were reported for wild-type myocardium by Mamidi et al. (Mamidi et al., 2018). Thus, the level of the minimum force in phase 2 compared with the original isometric force seems to depend on the experimental conditions. In our model, the decay was determined from decreases in the XB_{PostR1} and XB_{PostR2} states owing to the reverse strokes from XB_{PostR2} to XB_{PostR1} and XB_{PostR1} to XB_{PreR}. Meanwhile, the loss of force was compensated by the increase in population and the distortions of the trapped myosin molecules in the XB_{Trap} state (Figures 9B,C). Here, the rates of reverse strokes are limited by the upper bounds $\bar{r}_{b,i}$, as in Eq. 19, and the population in the XB_{Trap} state is determined by the parameter values associated with the trap mechanism (s_{trap}, h_{trap}, and h_{escape}) in Eqs 3 and 4 and the forced detachment ($x_{XB,t}$, $c_{XB,t}$, and $a_{XB,t}$) in Eq. 15. In our trap model, these parameters were carefully chosen, focusing not only on the stretch activation phenomena, but also on the SPOCs and performance in the beating ventricle model.

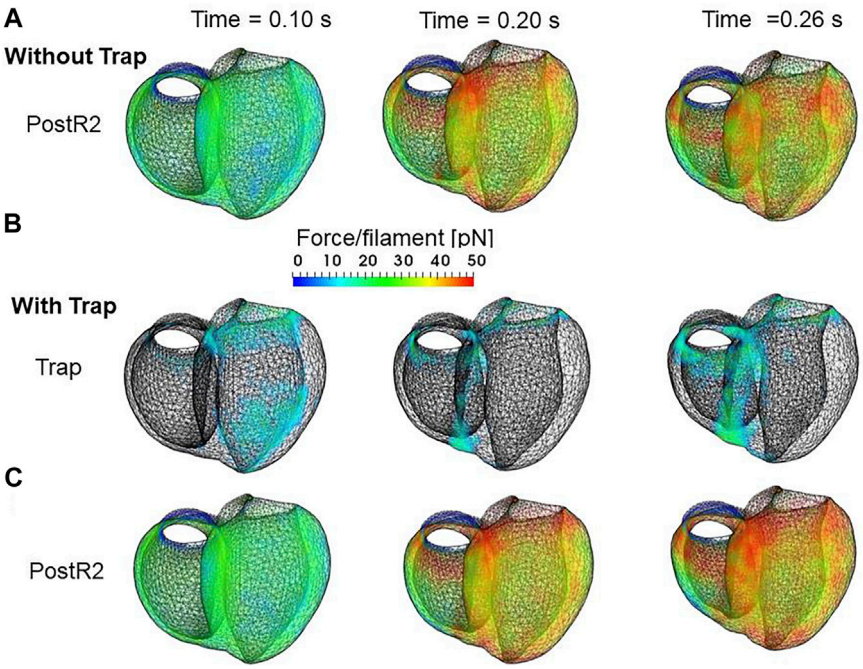

FIGURE 13
Distribution of contraction forces in the ventricles in the systolic phase at the early systole: 0.10 s (left), at the mid-systole: 0.20 s (center), and at the end-systole: 0.26 s (right) for **(A)** the XB_{PostR2} state in the no-trap model **(B)** XB_{Trap}, and **(C)** the XB_{PostR2} state in the trap model. In **(B)**, the regions in which the forces are less than 10 pN are transparent.

In our model, the trap mechanism was added to the XB_{PostR1} state, which is the state after the first power stroke. Alternatively, it might be conceivable to add a similar trap mechanism in the XB_{PostR2} state (the state after the second power stroke) if a force-dependent detachment rate constant (Greenberg et al., 2014) is adopted in the numerical model. Hwang et al. (2021) reported a much gentler increase in the reverse stroke rate constant of the first stroke compared with that of the second stroke, with a force increase of 8–14 pN. Their single-molecule experimental results support the adequacy of adding the trap mechanism to the XB_{PostR1} state.

The numerical SPOC results indicate that the trap mechanism affects the calcium activation sensitivity for the relaxation dynamics in an advantageous manner. The trap mechanism prevents sarcomere lengthening at high or low levels of calcium activation (Figure 10). The sarcomere lengthening maximizes the single overlap region between the two filaments, resulting in a facilitation of re-activation. Thus, the prevention of lengthening at low calcium levels (Figure 11A) stops weak re-activation, leading to a smooth relaxation of muscle in the diastolic phase (Figure 12A). Conversely, the prevention of lengthening at high calcium levels (Figure 11C) stops sarcomere shortening in the neighboring cardiomyocytes, causing a retention of high active tension in the fiber bundle (Figures 13B,C).

Advantages of MC simulations

The above-mentioned features for heartbeats are similar to those found in our previous work (Washio et al., 2018) with the Langevin dynamics model. However, the new MC model produced better results in the tension response for the step length changes and SPOCs owing to the simpler adjustment of related parameters. In a previous study, MC simulations were performed for a three-dimensional half-sarcomere model consisting of three myosin filaments and 13 thin filaments implemented with 360 myosin molecules and 1,170 binding sites to examine the impact of filament compliance on Ca^{2+} activation (Chase et al., 2004). However, these simulations were conducted only under steady-state conditions and were not coupled with a macroscopic finite element model (FEM). Moreover, in the beating ventricle simulation, the computation cost per beat was 1.5 h when 320 cores of a conventional parallel computer system were used for the MC model (Yoneda et al., 2021), while the cost was 105 h when 1920 cores of the same computer system were used (Washio et al., 2018). The former simulation was performed for a bi-ventricular FEM consisting of 45,000 tetrahedral elements with 16 filament pairs, while the latter was performed for a smaller FEM consisting of 7,900 elements with eight filament pairs. The improvements of the MC model, such as those demonstrated in the current study, will lead to better predictions in clinical applications (Kariya et al., 2020).

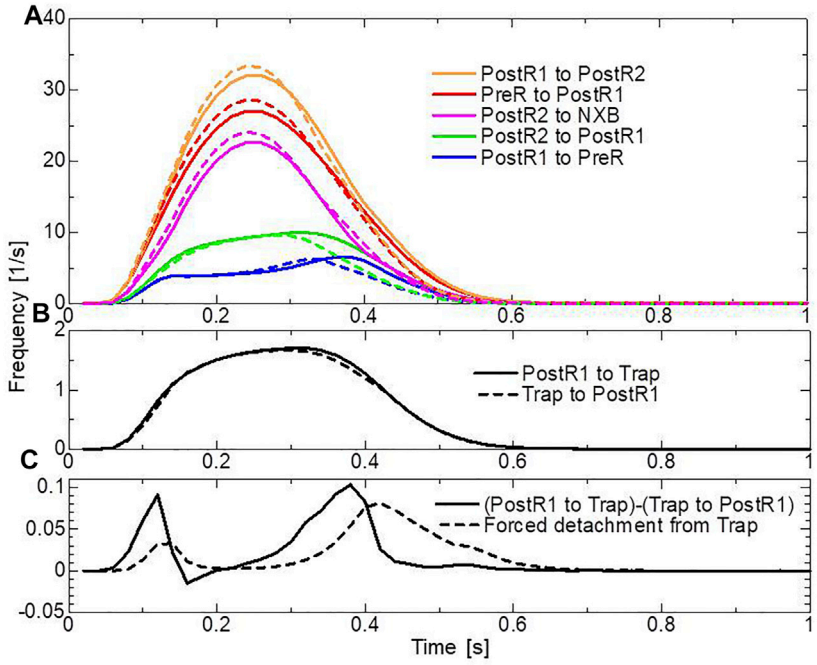

FIGURE 14
Transition frequencies of binding MHs during a heartbeat. **(A)** The frequencies per MH of the transitions from XB_{PostR1} to XB_{PostR2} (orange), XB_{Pre} to XB_{PostR1} (red), XB_{PostR2} to N_{XB} (pink), XB_{PostR2} to XB_{PostR1} (green), and XB_{PostR1} to XB_{PreR} (blue). The solid and broken lines represent the trap model and the no-trap model, respectively. **(B)** Frequencies per MH of trapping (solid line) and escaping (broken line). **(C)** The difference between the trapping frequency and the escaping frequency (solid line), and the frequency of the forced detachment from XB_{Trap}.

Limitations

Smith et al. argued that multiple working strokes are required for a cross-bridge cycle to satisfy energetic constraints and demonstrated that a cross-bridge cycling model with three strokes can reproduce various experimental findings observed for frog muscle, including absolute values of active tension, stiffness, and ATPase rate; the phase-2 tension response to a length release; and the transient tension rise during ramp stretching (Smith et al., 2008a; Smith et al., 2008b). This line of reasoning led us to adopt a model with two strokes with lengths of 6.0 and 4.0 nm to realize the 10-nm stroke suggested by the crystal structure of myosin molecules. In the three-stroke model of Smith et al., the first two strokes, which each have a length of 5.0 nm, occur around the Pi release, and a third small stroke was implemented to account for the strain-dependent ADP release rate. Although we did not explicitly define the relationship between strokes and the nucleotide released in our model, these points should be examined by comparing our results against various experimental findings in future work.

The average force of the trapped MH was larger than the maximal force ever observed experimentally. In our model, this discrepancy comes from our stiffness parameter k_{xb}= 2.8 pN/nm for nearly a 10 nm stretch, assuming linear elasticity. The force function, F_{rod}, in Eq. 20 may be improved by reducing the stiffness for substantial distortions. Further investigation and modification of the detachment rate function in Eq. 15 represent future tasks.

In our model, we didn't account for the elasticity of the components, such as the thin and thick filaments and the Z-band in the sarcomere. Namely, we assumed that all of the sarcomere components (except for the myosin rods) are rigid. Thus, the macroscopic stretch change $\Delta\lambda$ is directly reflected in the distortion increase $\Delta x = SL_0\Delta\lambda/2$. However, in the actual setting, the distortion increase might be somewhat relaxed because of the elasticities. For example, if we assume a linear elasticity of the Z-line with a spring constant of k_Z and N_{xb} attached myosin molecules per thin filament, we have:

$$\begin{cases} N_{xb}k_{xb}\Delta x = k_Z\Delta Z, \\ \Delta x + \Delta Z = \dfrac{SL_0\Delta\lambda}{2}. \end{cases} \tag{46}$$

By eliminating the Z-line distortion increment ΔZ in Eq. 46, we obtain:

$$\left(1 + \frac{N_{xb}k_{xb}}{k_Z}\right)\Delta x = \frac{SL_0\Delta\lambda}{2}. \tag{47}$$

Thus, the distortion increment Δx decreases as the number of attached myosin molecules increases. Here, the magnitude of the distortion increment Δx corresponds to the strength of trapping for myosin molecules in the XB_{Trap} state. Because N_{xb} is smaller for a lower activation, Eq. 47 may give a straightforward explanation of the experimental findings reported by Stelzer (Stelzer et al., 2006), who reported that the stretch activation is most pronounced at low levels of Ca^{2+} activation. Apart from these considerations, the effect of filament compliance on the realignment of cross-bridges reported by Chase et al. (Chase et al., 2004) is an important issue that should be included in future modeling studies.

Razumova et al. modeled and compared three possible mechanisms of cooperativity: 1) interactions between adjacent T/T RUs, 2) interactions between adjacent cycling cross-bridges, and 3) a facilitation of the transition to the on-state of a RU by the adjacent attached cross-bridge, which all control the open and closed states of the thin filament (Razumova et al., 2000). Their results clearly demonstrated distinct roles of these interactions in the maximal force and cooperativity; however, their formulations are conceptual and thus do not represent specific molecular interactions. McKillop and Geeves proposed a three-state (blocked, closed, and open) model of thin filament activation, which is compatible with X-ray diffraction data (McKillop and Geeves, 1993). Smith et al. further attempted to establish the relation between RU–RU interactions and physical entities (Smith et al., 2003) by modeling the flexible-chain-like structure of the tropomyosin molecule with a continuous-flexible-chain model. In this regard, the RU–RU model used in this study is also empirical and lacks a relation to a physical entity. Moreover, only part of the above-mentioned mechanism of cooperativity was considered.

In the finite element ventricular model, a single half-sarcomere model was imbedded in each tetrahedral element, and the half-sarcomere length changed according to the stretch of the element in the fiber direction. This is nothing but assuming that the movements of sarcomeres contained in each element are perfectly synchronized. In reality, there may be time lags in the length changes between the neighboring sarcomeres particularly in the relaxation phase. In our future work, the issue will be studied by using the homogenization method (Washio et al., 2013) whereby the bundle of myofibril models is imbedded in each element.

Data availability statement

The raw data supporting the conclusion of this article will be made available by the authors, without undue reservation.

Author contributions

TH, SS, and MW designed the project; RK, J-IO, and KY prepared the input data for the computer simulations; TW designed and conceived the trap model and ran the simulations; TW and KY analyzed the simulation data; TW, RK, J-IO, and KY developed the simulation code with input from SS, TH, MW, TW, and KY wrote the paper with input from SS, TH, and MW.

Funding

This work was supported by the MEXT under the "Program for Promoting Research on the Supercomputer Fugaku" (hp200121) and by AMED under Grant Number JP21he2102003. The computational resources of Supercomputer Fugaku were provided by the RIKEN Center for Computational Science.

Acknowledgments

We thank Rosalie Tran, and Kristi Hatch, from Edanz (https://jp.edanz.com/ac) for editing a draft of this manuscript.

Conflict of interest

TW, JO, SS, and TH are employed by UT-Heart Inc. KY and MW were employed by Fujitsu Japan, Limited.

The authors declare that the research was conducted in the absence of any commercial or financial relationships that could be construed as a potential conflict of interest.

Publisher's note

Supplementary material

The Supplementary Material for this article can be found online at: https://www.frontiersin.org/articles/10.3389/fphys.2022.855303/full#supplementary-material

References

Campbell, K. B., and Chandra, M. (2006). Functions of stretch activation in heart muscle. *J. Gen. Physiol.* 127 (2), 89–94. doi:10.1085/jgp.200509483

Chase, P. B., Macpherson, J. M., and Daniel, T. L. (2004). A spatially explicit nanomechanical model of the half-sarcomere: Myofilament compliance affects Ca^{2+}-activation. *Ann. Biomed. Eng.* 32 (11), 1559–1568. doi:10.1114/b:abme.0000049039.89173.08

Fabiato, A., and Fabiato, F. (1978). Myofilament-generated tension oscillations during partial calcium activation and activation dependence of the sarcomere length-tension relation of skinned cardiac cells. *J. Gen. Physiol.* 72 (5), 667–699. doi:10.1085/jgp.72.5.667

Greenberg, M. J., Shuman, H., and Ostap, E. M. (2014). Inherent force-dependent properties of β-cardiac myosin contribute to the force-velocity relationship of cardiac muscle. *Biophys. J.* 107 (12), L41–L44. doi:10.1016/j.bpj.2014.11.005

Hwang, Y., Washio, T., Hisada, T., Higuchi, H., and Kaya, M. (2021). A reverse stroke characterizes the force generation of cardiac myofilaments, leading to an understanding of heart function. *Proc. Natl. Acad. Sci. U. S. A.* 118 (23), e2011659118. doi:10.1073/pnas.2011659118

Kariya, T., Washio, T., Okada, J., Nakagawa, M., Watanabe, M., Kadooka, Y., et al. (2020). Personalized perioperative multi-scale, multi-physics heart simulation of double outlet right ventricle. *Ann. Biomed. Eng.* 48 (6), 1740–1750. doi:10.1007/s10439-020-02488-y

Kaya, M., and Higuchi, H. (2010). Non-linear elasticity and an 8 nm working stroke of single myosin molecules in myofilaments. *Science* 329 (5992), 686–689. doi:10.1126/science.1191484

Kolb, J., Li, F., Methawasin, M., Adler, M., Escobar, Y. N., Nedrud, J., et al. (2016). Thin filament length in the cardiac sarcomere varies with sarcomere length but is independent of titin and nebulin. *J. Mol. Cell. Cardiol.* 97, 286–294. doi:10.1016/j.yjmcc.2016.04.013

Kramers, H. A. (1940). Brownian motion in a field of force and the diffusion model of chemical reactions. *Physica* 7, 284–304. doi:10.1016/S0031-8914(40)90098-2

Lodish, H., Berk, A., Zipursky, S. L., Matsudaira, P., Baltimore, D., and Darnell, J. (2000). *Molecular cell biology*. 4th edition. New York: W. H. Freeman.

Mamidi, R., Li, J., Doh, C. Y., Verma, S., and Stelzer, J. E. (2018). Impact of the myosin modulator Mavacamten on force generation and cross-bridge behavior in a murine model of hypercontractility. *J. Am. Heart Assoc.* 7 (17), e009627. doi:10.1161/JAHA.118.009627

McKillop, D. F., and Geeves, M. A. (1993). Regulation of the interaction between actin and myosin subfragment 1: Evidence for three states of the thin filament. *Biophys. J.* 65 (2), 693–701. doi:10.1016/S0006-3495(93)81110-X

Pringle, J. W. S. (1978). The croonian lecture 1977-stretch activation of muscle: Function and mechanism. *Proc. R. Soc. Lond. B Biol. Sci.* 201, 107–130. doi:10.1098/rspb.1978.0035

Razumova, M. V., Bukatina, A. E., and Campbell, K. B. (2000). Different myofilament nearest-neighbor interactions have distinctive effects on contractile behavior. *Biophys. J.* 78 (6), 3120–3137. doi:10.1016/S0006-3495(00)76849-4

Rice, J. J., Stolovitzky, G., Tu, T., and de Tombe, P. P. (2003). Ising model of cardiac thin filament activation with nearest-neighbor cooperative interactions. *Biophys. J.* 84, 897–909. doi:10.1016/S0006-3495(03)74907-8

Rice, J. J., Wang, F., Bers, D. M., and de Tombe, P. P. (2008). Approximate model of cooperative activation and crossbridge cycling in cardiac muscle using ordinary differential equations. *Biophys. J.* 95 (5), 2368–2390. doi:10.1529/biophysj.107.119487

Rodriguez, E. K., Omens, J. H., Waldman, L. K., and McCulloch, A. D. (1993). Effect of residual stress on transmural sarcomere length distributions in rat left ventricle. *Am. J. Physiol.* 264, H1048–H1056. doi:10.1152/ajpheart.1993.264.4.H1048

Sato, K., Kuramoto, Y., Ohtaki, M., Shimamoto, Y., and Ishiwata, S. (2013). Locally and globally coupled oscillators in muscle. *Phys. Rev. Lett.* 111 (10), 108104. doi:10.1103/PhysRevLett.111.108104

Smith, D. A., Geeves, M. A., Sleep, J., and Mijailovich, S. M. (2008b). Towards a unified theory of muscle contraction. II: Predictions with the mean-field approximation. *Ann. Biomed. Eng.* 36 (8), 1353–1371. doi:10.1007/s10439-008-9514-z

Smith, D. A., Geeves, M. A., Sleep, J., and Mijailovich, S. M. (2008a). Towards a unified theory of muscle contraction. I: Foundations. *Ann. Biomed. Eng.* 36 (10), 1624–1640. doi:10.1007/s10439-008-9536-6

Smith, D. A., Maytum, R., and Geeves, M. A. (2003). Cooperative regulation of myosin-actin interactions by a continuous flexible chain I: Actin-tropomyosin systems. *Biophys. J.* 84 (5), 3155–3167. doi:10.1016/S0006-3495(03)70040-X

Stelzer, J. E., Larsson, L., Fitzsimons, D. P., and Moss, R. L. (2006). Activation dependence of stretch activation in mouse skinned myocardium: Implications for ventricular function. *J. Gen. Physiol.* 127 (2), 95–107. doi:10.1085/jgp.200509432

Taggart, P., Sutton, P. M., Opthof, T., Coronel, R., Trimlett, R., Pugsley, W., et al. (2000). Inhomogeneous transmural conduction during early ischaemia in patients with coronary artery disease. *J. Mol. Cell. Cardiol.* 32 (4), 621–630. doi:10.1006/jmcc.2000.1105

ten Tusscher, K. H., and Panfilov, A. V. (2006). Alternans and spiral breakup in a human ventricular tissue model. *Am. J. Physiol. Heart Circ. Physiol.* 291, H1088–H1100. doi:10.1152/ajpheart.00109.2006

Washio, T., Kanada, R., Cui, X., Okada, J., Sugiura, S., Takada, and S., et al. (2021). Semi-implicit time integration with Hessian eigenvalue corrections for a larger time step in molecular dynamics simulations. *J. Chem. Theory Comput.* 17 (9), 5792–5804. doi:10.1021/acs.jctc.1c00398

Washio, T., Okada, J., Takahashi, A., Yoneda, K., Kadooka, Y., Sugiura, S., et al. (2013). Multiscale heart simulation with cooperative stochastic cross-bridge dynamics and cellular structures. *Multiscale Model. Simul.* 11 (4), 965–999. doi:10.1137/120892866

Washio, T., Shintani, S. A., Higuchi, H., and Hisada, T. (2019). Effect of myofibril passive elastic properties on the mechanical communication between motor proteins on adjacent sarcomeres. *Sci. Rep.* 9, 9355. doi:10.1038/s41598-019-45772-1

Washio, T., Sugiura, S., Kanada, R., Okada, J., and Hisada, T. (2018). Coupling Langevin dynamics with continuum mechanics: Exposing the role of sarcomere stretch activation mechanisms to cardiac function. *Front. Physiol.* 9, 333. doi:10.3389/fphys.2018.00333

Washio, T., Sugiura, S., Okada, J., and Hisada, T. (2020). Using systolic local mechanical load to predict fiber orientation in ventricles. *Front. Physiol.* 11, 467. doi:10.3389/fphys.2020.00467

Washio, T., Yoneda, K., Okada, J., Kariya, T., Sugiura, S., and Hisada, T. (2016). Ventricular fiber optimization utilizing the branching structure. *Int. J. Numer. Method. Biomed. Eng.* 32 (7), e02753. doi:10.1002/cnm.2753

Yoneda, K., Okada, J., Watanabe, M., Sugiura, S., Hisada, T., and Washio, T. (2021). A multiple step active stiffness integration scheme to couple a stochastic cross-bridge model and continuum mechanics for uses in both basic research and clinical applications of heart simulation. *Front. Physiol.* 12, 712816. doi:10.3389/fphys.2021.712816

frontiers | Frontiers in Physiology

TYPE Original Research
PUBLISHED 19 October 2022
DOI 10.3389/fphys.2022.834328

OPEN ACCESS

EDITED BY
Geoffrey A. Head,
Baker Heart and Diabetes Institute, Australia

REVIEWED BY
Peter Latta,
Central European Institute of Technology (CEITEC), Czechia
Kyungjoon (Joon) Lim,
The University of Sydney, Australia
James Todd Pearson,
National Cerebral and Cardiovascular Center (Japan), Japan

*CORRESPONDENCE
Zdeněk Stárek,
zdenek.starek@fnusa.cz

SPECIALTY SECTION
This article was submitted to Integrative Physiology, a section of the journal Frontiers in Physics

RECEIVED 13 December 2021
ACCEPTED 03 October 2022
PUBLISHED 19 October 2022

CITATION
Odehnalová E, Valíková L, Caluori G, Kulík T, Římalová V, Jadczyk T, Dražanová E, Pavlova I, Pešl M, Kubeš V and Stárek Z (2022), Comparison of gross pathology inspection and 9.4 T magnetic resonance imaging in the evaluation of radiofrequency ablation lesions in the left ventricle of the swine heart.
Front. Physiol. 13:834328.
doi: 10.3389/fphys.2022.834328

Comparison of gross pathology inspection and 9.4 T magnetic resonance imaging in the evaluation of radiofrequency ablation lesions in the left ventricle of the swine heart

Eva Odehnalová[1], Lucia Valíková[1], Guido Caluori[1,2,3,4], Tomáš Kulík[1,5], Veronika Římalová[6], Tomasz Jadczyk[1,7], Eva Dražanová[8], Iveta Pavlova[8], Martin Pešl[1,2,9], Václav Kubeš[10] and Zdeněk Stárek[1,5]*

[1]Interventional Cardiac Electrophysiology Group, International Clinical Research Center, St. Anne's University Hospital Brno, Brno, Czech, [2]Nanotechnology, CEITEC Masaryk University, Brno, Czech, [3]IHU LIRYC, Electrophysiology and Heart Modeling Institute, Fondation Bordeaux Université, Pessac, France, [4]University Bordeaux, INSERM, Cardiothoracic Research Center of Bordeaux, Pessac, France, [5]1st Department of Internal Medicine—Cardioangiology, St. Anne's University Hospital Brno, Brno, Czech, [6]Biostatistics, International Clinical Research Center, St. Anne's University Hospital Brno, Brno, Czech, [7]Division of Cardiology and Structural Heart Diseases, Medical University of Silesia, Katowice, Poland, [8]Institute of Scientific Instruments of the Czech Academy of Sciences, Brno, Czech, [9]Department of Biology, Faculty of Medicine Masaryk University Brno, Brno, Czech, [10]Department of Pathology, University Hospital Brno, Brno, Czech

Aims: Gross pathology inspection (patho) is the gold standard for the morphological evaluation of focal myocardial pathology. Examination with 9.4 T magnetic resonance imaging (MRI) is a new method for very accurate display of myocardial pathology. The aim of this study was to demonstrate that lesions can be measured on high-resolution MRI images with the same accuracy as on pathological sections and compare these two methods for the evaluation of radiofrequency (RF) ablation lesion dimensions in swine heart tissue during animal experiment.

Methods: Ten pigs underwent radiofrequency ablations in the left ventricle during animal experiment. After animal euthanasia, hearts were explanted, flushed with ice-cold cardioplegic solution to relax the whole myocardium, fixed in 10% formaldehyde and scanned with a 9.4 T magnetic resonance system. Anatomical images were processed using ImageJ software. Subsequently, the hearts were sliced, slices were photographed and measured in ImageJ software. Different dimensions and volumes were compared.

Results: The results of both methods were statistically compared. Depth by MRI was 8.771 ± 2.595 mm and by patho 9.008 ± 2.823 mm; $p = 0.198$. Width was 10.802 ± 2.724 mm by MRI and 11.125 ± 2.801 mm by patho; $p = 0.049$. Estuary was 2.006 ± 0.867 mm by MRI and 2.001 ± 0.872 mm by patho; $p = 0.953$. The depth at the maximum diameter was 4.734 ± 1.532 mm on MRI and 4.783 ±

1.648 mm from the patho; p = 0.858. The volumes of the lesions calculated using a formula were 315.973 ± 257.673 mm^3 for MRI and 355.726 ± 255.860 mm^3 for patho; p = 0.104. Volume directly measured from MRI with the "point-by-point" method was 671.702 ± 362.299 mm^3.

Conclusion: Measurements obtained from gross pathology inspection and MRI are fully comparable. The advantage of MRI is that it is a non-destructive method enabling repeated measurements in all possible anatomical projections.

KEYWORDS

evaluation of radiofrequency ablation lesions, comparison of methods, gross pathology inspection, high-resolution MRI evaluation, animal experiments, catheter ablation of arrhythmias, ex vivo MRI scanning

1 Introduction

Gross pathological inspection (patho) and manual measurements are standard methods in autopsy evaluation of tissue (Song et al., 2017) including myocardial pathologies and radiofrequency ablation lesions (Nakagawa et al., 1995) (Dickfeld et al., 2007) (Krahn et al., 2018). Nevertheless, this method inadvertently destroys the sample, effectively preventing reevaluation and allowing only unidirectional slicing. Therefore, patho is limited to complex anatomical objects, the number of measured planes is limited, and the calculated volume is only approximate.

Magnetic resonance imaging (MRI) represents well established diagnostics non-invasive method that allow exact repeatable measurements of myocardial pathologies (Ishihara et al., 2007) (Braggion-Santos et al., 2013) (Suzuki et al., 2021). Standardly used 1.5 T and 3 T MRI allows visualization of myocardial pathologies including radiofrequency lesions "*in vivo*" (Dickfeld et al., 2007) (Badger et al., 2010) (Markman and Saman 2017) (Tofig et al., 2019) as well post-mortem. Moreover, high-resolution MRI systems are very promising and rapidly evolving imaging methods (Schneider et al., 2008) (Schneider et al., 2011) (Wech et al., 2016) (Ertürk et al., 2017) (Erturk et al., 2019) (Heo et al., 2019), which allow precise evaluation of the heart in unparalleled quality. Berte et al. described the successful use of 1.5T MRI for *in vivo* imaging of the hearts and 9.4 T MRI (Bruker) for explanted hearts in 2015, where they used high-resolution MRI for evaluation of the lesions after radiofrequency (RF) ablation in an ovine experiment (Berte et al., 2015).

RF ablation is a catheter-based non-pharmacological treatment of cardiac arrhythmias (Kalbfleisch and Langberg 1992). The principle of this method is destruction of the myocardium, which serves as an arrhythmogenic substrate with RF energy applied to the tip of the ablation catheter (Haines and Verow, 1990). RF energy creates limited thermal coagulation necrosis that heals as the non-conducting scar and treats arrhythmia (D. E. Haines and Watson 1989) (Haverkamp et al., 1989) (Nath et al., 1994) (O'Donnell and Nadurata. 2004) (D. Haines 2018). The radiofrequency lesion is histologically characterized by central thermal coagulation necrosis, where myocardial cells lose clear boundaries and transverse striping. Central necrosis is surrounded by a thin border zone consisting of a mix of healthy and damaged cells. Behind this border zone is a healthy myocardium (Delacretaz et al., 1999) (Gepstein et al., 1999) (Krahn et al., 2018). Catheter ablation of arrhythmias is a very fast-growing area of cardiology, and many experiments have been performed. To evaluate the effect of RF ablation, it is crucial to evaluate the extent of necrosis, synonymously called RF lesions. The standard method is gross pathology; however, MRI evaluation is becoming very promising as an alternative method.

Therefore, the aim of this study was to demonstrate that lesions can be measured on high-resolution MRI images with the same accuracy as on pathological sections and compare results from MRI and patho measurements of the lesions formed after experimental RF ablation in swine heart tissue.

2 Materials and methods

2.1 Permission

The animal experiment was approved by the ethics committee of the University of Veterinary and Pharmaceutical Sciences in Brno (approval number 12–2018) and by the Ministry of Education Youth and Sports (approval number MSMT-17402/2018–3). All procedures performed on pigs were in accordance with Directive 2010/63/EU of the European Parliament on the protection of animals used for scientific purposes.

2.2 Animal preparation

The animal experiment was carried out in cooperation with the Animal Center FNUSA-ICRC Brno. Ten female swine (weight, 50–55 kg; age, 6 months) were used. Each animal was weighed on a digital scale to determine the exact weight. Premedication before anesthesia was done by mixture of

ketamine 2 mg/kg + xylazine 2 mg/kg + tiletamine 2 mg/kg + zolazepam 2 mg/kg by intramuscular (i.m.) application. After this, pigs were intubated and an intravenous cannula was inserted into the ear vein. Animals were kept under mechanical ventilation with 1.5% isoflurane. Amiodarone (5 mg/kg, i. m.) was applied by very slow application to suppress ventricular fibrillation. Heparin (7.000 I.U., intravenous application) was administered before sheats were inserted into the femoral veins and then was repeated in a dose of 3500 I.U every hour. The animal arterial blood pressure was measured invasively in femoral artery. An oximeter was placed on the tongue of the animal to monitor oxygen saturation. A temperature control probe was inserted into the animal esophagus to minimize the risk of thermal damage to the esophagus. At the end of the experiment, animals were sacrificed by intravenous application (in dosage 4–6 ml/50 kg) of special mixture intended for euthanasia in animals named—T61 (Intervet International B.V., Boxmeer, Netherland).

2.3 RF ablations and examination of hearts

All pigs underwent a standard RF protocol under general anesthesia—left ventricles were ablated on the septum, on the lateral wall, on the inferior wall, on the anterior wall and in the left ventricular outflow tract (LVOT) position with a different power setting for 1 min or up until "steam pop" appeared. After completion of the ablation protocol, the animal was sacrificed and moved to the pathology room. Hearts were removed from the thoracic cavity and flushed with ice-cold cardioplegic solution (St. Thomas solution) to relax the whole myocardium. The heart was then fixed in 10% formaldehyde. Hearts were scanned with a 9.4 T magnetic resonance system (Bruker BioSpec 182 94/30USR), equipped with a volume coil 1H 198/154 mm. *Ex vivo* MRI imaging was performed in cooperation with the Institute of Scientific Instruments of the Czech Academy of Sciences. Anatomical images were processed using ImageJ software, which is intended for scientific use and is freely accessible on the website at www.imagej.net (Schindelin et al., 2015) (Rueden et al., 2017). All measurements done in ImageJ software were done manually without using any automatic processing tools. After the hearts were scanned, they were cut into 3–5-mm-thick slices, which were placed side by side, photographed by the camera (Nikon DX AF-S NIKKOR), and analyzed using the same ImageJ software. We opted for this method of analysis because manual measurement of the pathology samples is associated with a risk of inhaling toxic formaldehyde fumes. Each lesion was measured three times and evaluated by two independent observations.

As the last step, the heart was removed out from formaldehyde, rinsed under running water and several lesions with characteristic parameters (without "steam pop" effect) were cut out from the heart, with an approximate volume of 1 × 1 × 0.5 cm. The samples were rinsed again under running water, dehydrated *via* ascending ethanol series and subsequently immersed in xylene. Then the samples were immersed in liquid paraffin, and paraffin blocks were prepared. Tissue blocks were sliced into sections, fixed on the histological glass, and stained with hematoxylin and eosin and Masson's trichrome (to visualize the viability of the tissue). Masson's trichrome stains central necrosis purple, healthy myocardium is stained red, and the connective tissue is stained blue. Hematoxylin and eosin

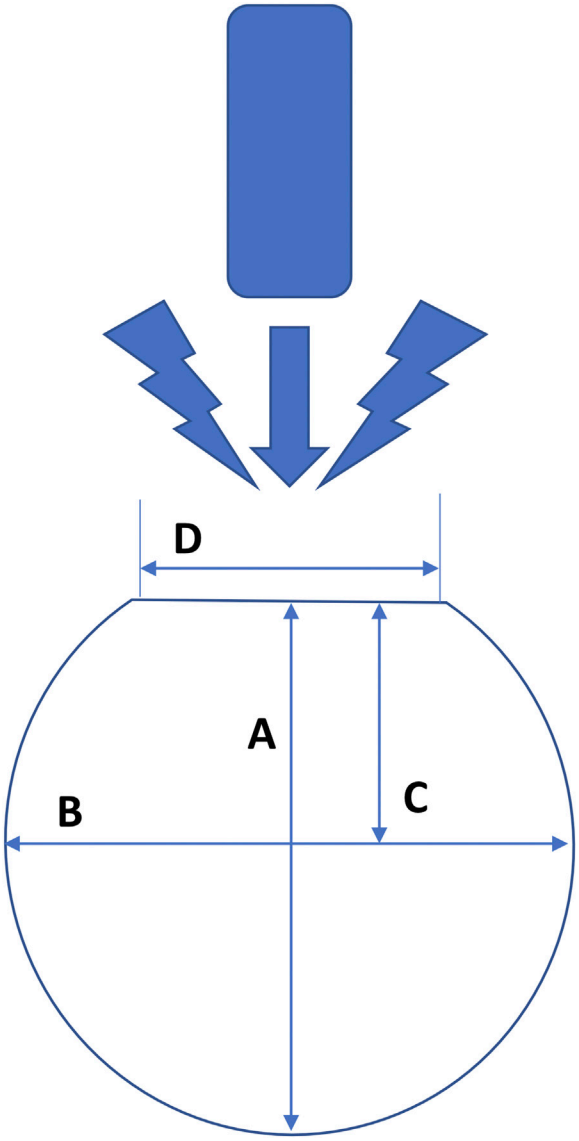

FIGURE 1
Schema of measuring the dimensions of lesions formed after radiofrequency ablation in the left ventricle of the swine hearts. **(A)** = maximum depth, **(B)** = maximum width, **(C)** = depth at the maximum diameter and **(D)** = lesion surface diameter ("estuary"). The measurement of each lesion takes place where the lesion reaches its maximum parameters.

staining was used for basic resolution. The cytoplasm is stained pink and nuclei are stained purple (Krahn et al., 2018). Slides were examined and photographed under a digital microscope (Leica DM 5000B, Leica Microsystems, Germany) at 25x, 50x and 200x magnification.

2.4 Measurement of lesions

Depth (A) of lesions was measured as the maximal distance between the point of contact of the catheter with the endocardium and the outermost apex of the lesion. *Width* (B) was measured in the place of the biggest length of the lesion. *Estuary* (D)—lesion surface diameter–was measured as a hollow in the endocardium created by catheter pressure. The *depth of the maximum diameter* (C) was measured as the distance between the *estuary* and the horizontal straight line passing through the widest point of the lesion (see Figure 1). The *volume* of the lesion was calculated from the measured parameters using the following formula (Guerra, 2013):

$$LV = \left((0.75\pi) \cdot \left(\frac{B}{2}\right)^2 \cdot (A - C) \right) - \left(0.25\pi \cdot \left(\frac{D}{2}\right)^2 \cdot (A - 2C) \right) \quad (1)$$

2.5 Measurement of lesions on MRI scans

Hearts were scanned using the 9.4 T MRI system. Every sample was removed from fixation solution, rinsed with physiological solution (0.9% NaCl, Braun) to remove all formaldehyde and submerged in a plastic jar filled with clean physiological solution and underwent MRI scanning. During immersion of the samples into a physiological solution, a syringe was used to inject a solution into the atria and ventricles, to get rid of air bubbles and blood clots, which possibly could be the cause of MRI artifacts and reduce the quality of MRI slices. All hearts were scanned once. The regions of interest (ROIs) were left heart ventricles with ablation lesions. All MRI scans were performed on a 9.4 T Bruker BioSpec 94/30USR scanner with a Bruker volume coil 1H 198/154 mm. Fast low-angle shot (FLASH) scout images were used to localize the left ventricle with ablation lesions. Proton-density (PD) weighted anatomical images were taken using FLASH sequence with TR = 1268.9 ms, TE = 4.43 ms, FA = 45.7°, FOV 100 mm x 100 mm, 8 averages, and a 256 × 256 image matrix. Eighty axial slices with a thickness of 1.0 mm were acquired; the slices covered the whole heart. The raw MRI data format was exported to the DICOM format for the further analysis. These anatomical images provided sufficient background for optimal visualization of lesions and volumetric data analysis.

Lesions were measured using ImageJ software. After image import, the ImageJ window was calibrated using the known pixel-to-mm ratio (1.024 pixel/mm). The measurement of each lesion took place in a slice, where the lesion reached its maximum parameters of d*epth* (A), *width* (B), *estuary* (D), and *depth at the maximum diameter* (C) (see Figure 1). Each lesion was bounded by a border zone that gave a low signal and was therefore displayed in black (Organ 1976) (Krahn et al., 2018). The border zone was a transition region between the necrotic, ablated and healthy, non-ablated myocardium (Ursell et al., 1985). We measured only the central completely necrotic part of the lesion. The border zone was not included in the measurement of lesion size (see Figure 2).

The *volume* of the lesions is calculated according to the abovementioned formula. In addition, we directly measured the lesion volume from MRI slices using the "point by point" method (see Figure 3) which is a variation of the Cavalieri principle. This method consists of gradually outlining the circumference of the lesion in all slices involving the measured lesion. The resulting volume is obtained by the total sum of all individually measured volumes from all slices where the lesion is displayed.

2.6 Measurement of lesions on pathology slices

As a first step, the heart was manually sliced on the macrotome (see Figure 4), a device originally developed by Templeton in 1961 (Templeton 1961) for slicing brains during histopathological examinations. The macrotome consists of the following: *a base plate* made of plexiglass with dimensions 220 × 240 × 8 mm. In the plate, there are holes with a diameter of 5 mm, which are arranged in parallel rows. The distance between the holes is 1 cm in rows along the longer side of the plate and 0.7 cm in rows along the shorter side of the plate. The next parts of the macrotome are *fixing pins*, which are 11.8 cm long and have a diameter of 0.8 cm. One end of the *pins* is tapered to a diameter of 0.5 cm and is used to insert the pin into the plate. The swine heart is placed on the plate of the macrotome and is fixed by pins all the way round. Using a long sharp knife, the heart is gradually sliced.

Every heart was removed from the fixation solution, placed in a flow box, and manually sliced using the above-mentioned macrotome to 3–5-mm-thick slices. Slices were laid side by side, and pictures were taken using a camera (see Figure 5). All hearts were photographed in this way. The whole preparation of the heart for measuring pathological sections took approximately 20 min (fix the heart on the macrotome and slice it, take a photo, and upload it to ImageJ). Photos were imported to the ImageJ program. The calibration of the software was set manually according to the settings of the caliper, which is located on each photo and shows exactly the size of 1 cm. The *depth, width, estuary, and depth at the maximum diameter* were measured in the same

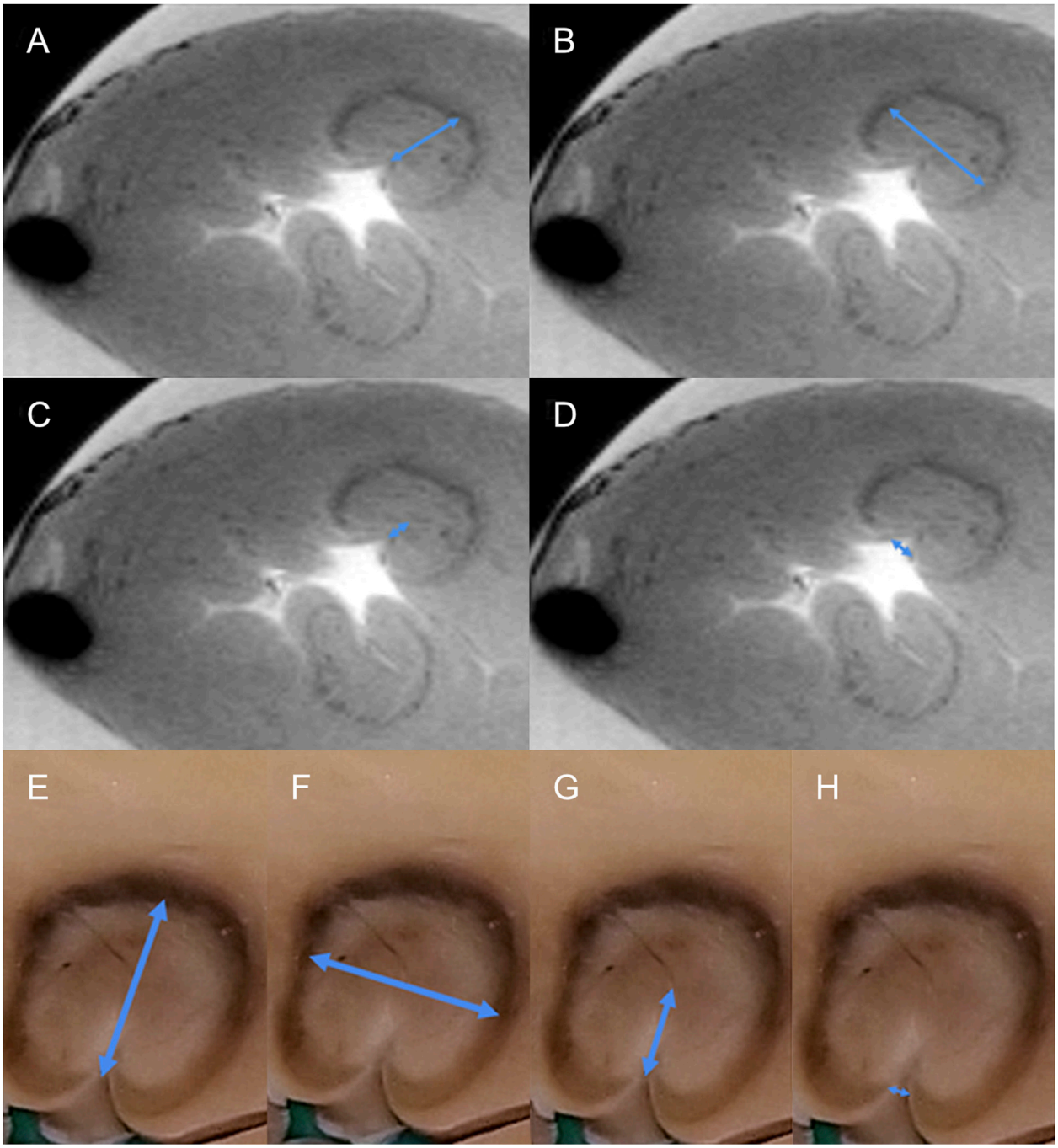

FIGURE 2
Example of measurement of the different dimensions of the radiofrequency lesion. **(A–D)**, measurement from MRI data, transverse section of the left ventricle. Two lesions are visible, the upper one is measured (blue arrows, A = depth, B = width, C = depth at the maximum diameter, and D = lesion surface diameter ("estuary). **(E–H)**, measurement from pathological samples, detail of the lesion, the same measurement as for MRI [blue arrows, E = depth, F = width, G = depth at the maximum diameter, and H = lesion surface diameter ("estuary")].

way, as in MRI scans (from photo where is the lesion in maximal dimensions, black surrounding zone not included) (see Figure 2). *The volume* of the lesions was calculated using the abovementioned formula.

2.7 Statistical analysis

All variables are described as mean ± SD, if symmetrically distributed, otherwise as median (IQR). In order to compare

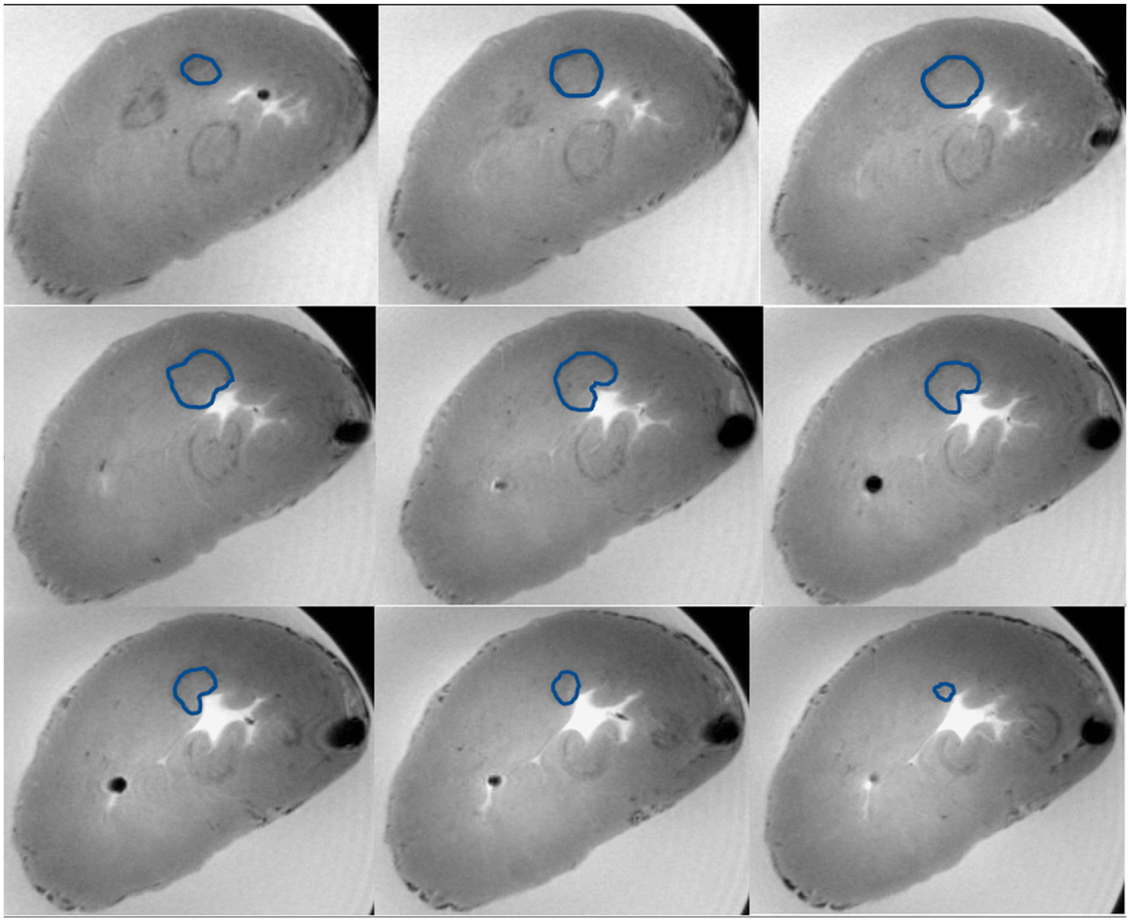

FIGURE 3
Example of volume measurement with the "point-by-point" method from MRI data. On the picture you can see nine subsequent transverse sections of the left ventricle capturing the whole radiofrequency lesion. Three lesions are visible, the upper one is measured. The measured lesion is outlined in all scans with a blue line. The resulting volume is the sum of the individual volumes from all involved MRI scans.

measurements for all within-subjects factors—method (MRI, patho), observer (two independent persons), and measurement (all lesions were measured three times by each method and observer), least squares means from multilevel (mixed-effect) models were compared separately for depth, width, estuary, depth at the maximum diameter, volume calculated by formula, and for volume directly measured from MRI with the "point-by-point" method. No interactions among factors were considered. Additionally, in the case of variable width, the measurements were split into two separate models by a factor *observer* in order to analyze the data independently on the observer. In the analysis of the time of measurement, due to skewness, the data were first log-transformed and then a least squares means from multilevel (mixed-effect) model was used to compare the methods (MRI, patho) as a single within-subjects factor. Comparison of recognized lesions was performed using the chi-square test. All tests were performed at a significance level of $\alpha = 0.05$. Statistical analysis was conducted using R version 3.6, RStudio version 1.2.1335, and package lme4 version 1.1–21.

3 Results

Histological characteristics of lesions created after RF ablation of porcine hearts are signs of coagulative necrosis characterized by karyolysis with significant cytoplasmic hypereosinophilia. Each of the lesions was loosely demarcated by a narrow border zone consisting of cardiomyocytes in different stages of cell damage. Unaffected tissue displays no tissue damage and retains the conventional morphology of cardiac tissue (see Figure 6).

A total of 99 lesions were created; the MRI method successfully evaluated 92 (92.93% from all lesions), and with

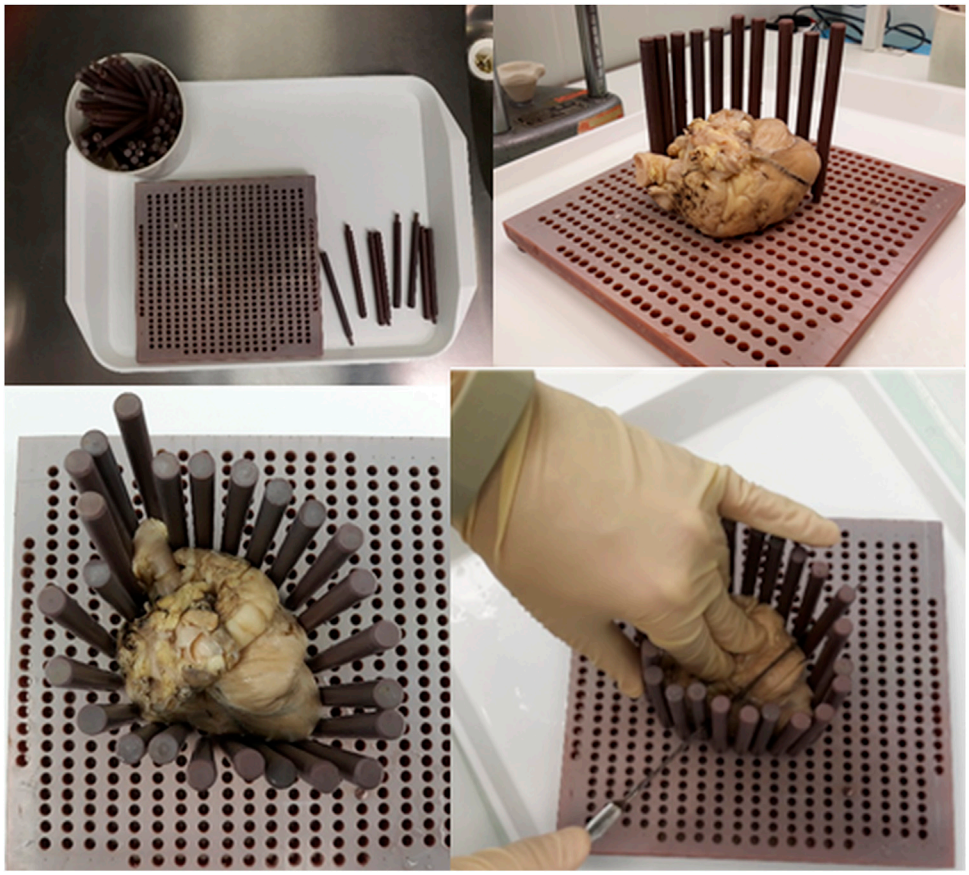

FIGURE 4
Use of the macrotome for slicing of the ventricles. In the basic plate are holes arranged in parallel rows. The swine heart is placed on the macrotome plate and fixed by pins all the way round. The heart is gradually sliced using a long sharp knife.

the patho method successfully evaluated 98 (98.99% from all lesions). No statistically significant difference was found (p = 0.755) between the two methods. *The depth* from MRI was 8.771 ± 2.595 mm, and from patho was 9.008 ± 2.823 mm; p = 0.198. *The width* of the lesion was 10.802 ± 2.724 mm on MRI, and 11.125 ± 2.801 mm with patho; p = 0.049. The limit p-value for the variable width is created by the interpersonal variability. Splitting models into two independent structures, we observed no statistically significant effect of method. The lesion values were almost identical, showing 2.006 ± 0.867 mm by MRI and 2.001 ± 0.872 mm by patho; p = 0.953. The *depth at the maximum diameter* was 4.734 ± 1.532 mm in MRI slices and 4.783 ± 1.648 mm from patho slices, p = 0.858. The *volumes* of the lesions calculated using a formula from both methods were 315.973 ± 257.673 mm^3 for MRI and 355.726 ± 255.860 mm^3 for patho; p = 0.104. *Volume* acquired from MRI by the "point-by-point" method was 671.702 ± 362.299 mm^3, which is two times larger than the volumes from the patho or MRI calculated using a formula (Table 1).

The complete time for preparing and MRI scanning was 115 ± 3 min (cleaning the heart from formaldehyde, placing it into the physiological solution, setting the MRI device, scanning the MRI sample, and controlling the quality of MRI scans after scanning). Preparing the heart for patho measurement, cutting of the slices on the macrotome for patho measurements and taking photos, took 21 ± 1 min.

The difference between the duration of measurements from MRI slices and from patho as follows: for MRI measurement, the median value was 56 s (53–59.2), whereas the median value for patho was 53 s (47–59), p = 0.001. Statistically significant differences were not found for *intrapersonal variability* (Supplementary File S1), but for *interpersonal variability* between observer 1 and observer 2, respectively, as follows: *width* was 10.418 ± 2.851 mm and 11.518 ± 2.569 mm (p < 0.0001), *depth* was 8.501 ± 2.937 mm and 9.286 ± 2.416 mm (p < 0.0001), *estuary* was 2.055 ± 0.867 mm and 1.942 ± 0.870 mm (p = 0.042), and *depth at the maximum diameter* was 4.638 ± 1.621 mm and 4.909 ± 1.558 mm (p = 0.002), respectively.

FIGURE 5
Example of a pathological picture used for measurement of radiofrequency lesions. On the picture you can see 13 subsequent transverse sections of the left ventricle. Radiofrequency lesions are visible. There is a caliper showing the exactly 1 cm, which was used to calibrate the software ImageJ.

4 Discussion

To the best of our knowledge, this is the first study focused on the comparison of two measuring methods (MRI x patho) of ablation lesions in the left ventricle. We compared two possible methods for measuring the dimensions of lesions formed in the myocardium of ventricles after RF ablation in an animal experiment. Our results showed, like the other studies (Lardo Albert et al., 2000; Dickfeld et al., 2007), that measurements obtained from pathology gross inspection (patho) and from MRI are fully comparable. For the variabiles *depth*, *estuary*, *depth at the maximum diameter*, and *volume by formula*, we found no statistically significant difference between these two methods. The limit *p*-value for the variable *width* was created by the interpersonal variability. Splitting models into two independent structures, we observed no statistically significant effect.

We found a statistically significant difference in values for directly measured *volume* from MRI ("point-by-point" method) and *volume* calculated by formula from MRI slices or patho. The reason for this is the more precise characteristics of the "point-by-point" method, where the *volume* was measured as a summary of all partial volumes obtained by manual gradual outlining of the lesion edges from all involved MRI slices. Another method of determining the lesion *volume* is to use a formula; a prerequisite for successful use of the formula is a regular oval shape of the lesion, which cannot be fully achieved in RF ablation lesions. RF lesions with higher energy settings are not precisely delineated and have a completely irregular shape (Figure 7). Therefore, using a formula to calculate volume has not been successful due to the irregular shape of the lesions. From this point of view, it seems more precise to use the "point-by-point" method.

Similar to previous studies (Dinkel et al., 2013) (Bolte et al., 2007) (Zhao et al., 2013) (Thiesse et al., 2016) (Erasmus et al., 2003) (Muenzel et al., 2012) (Lazebnik et al., 2005) we found statistically significant differences in all measured parameters for

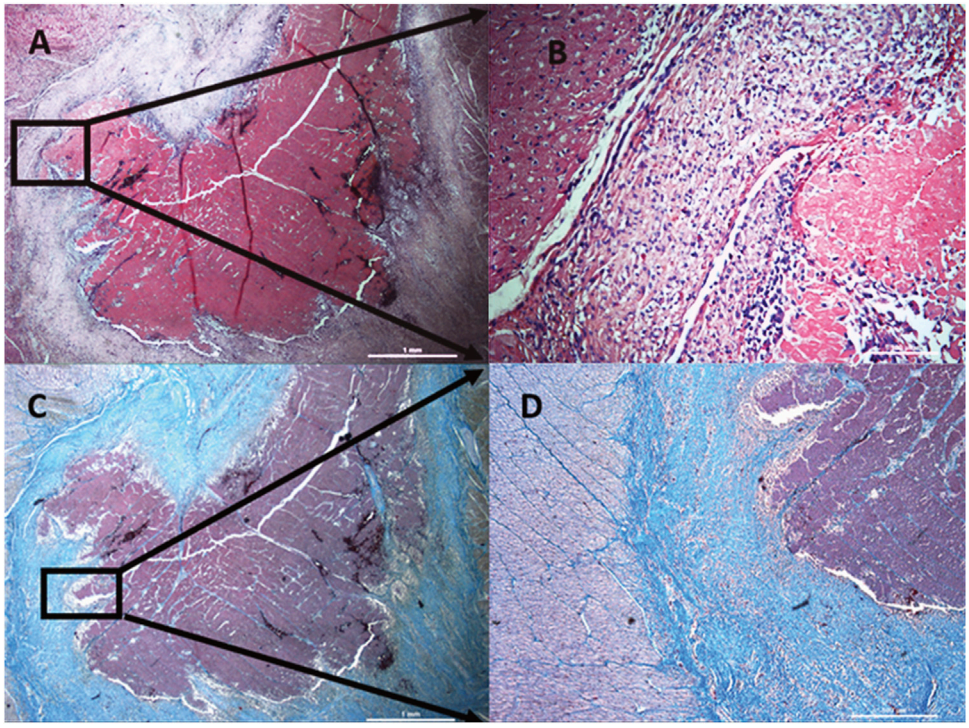

FIGURE 6
Histological characteristics of lesions created after radiofrequency ablation of porcine hearts. Lesions created by radiofrequency ablation are formed by coagulation necrosis, where cells have no borders and they are completely destroyed. Nuclei are not visible. Every lesion is surrounded by a differently wide rim consisting of cells at different stages of necrosis (damaged cell membrane and nuclei) sharply transitioning into healthy cardiomyocytes (clearly demarcated individual cells, pink cytoplasm, distinct purple nuclei). **(A)** hematoxylin-eosin staining, magnification 25x. **(B)** detail from **A**, magnification 200x, **(C)** trichrome staining, magnification 25x, **(D)** detail from **C,** magnification 50x.

TABLE 1 Comparison of evaluation of radiofrequency lesions with gross pathology inspection (patho) and MRI evaluation.

Variable	MRI	Patho	*p* value
Number of recognised lesions (N = 99)[a]	92 (92.93%)	98 (98.99%)	$p = 0.755$
Depth (mm)[b]	8.771 ± 2.595	9.008 ± 2.823	$p = 0.198$
Estuary (mm)[b]	2.006 ± 0.867	2.001 ± 0.872	$p = 0.953$
Depth at the maximum diameter (mm)[b]	4.734 ± 1.532	4.783 ± 1.648	$p = 0.858$
Volume by formula (mm3)[b]	315.973 ± 257.673	355.726 ± 255.860	$p = 0.104$
Volume by "point-by-point" method from MRI (mm3)[b]	671.702 ± 362.299	NA	NA
Width (mm)[b]	10.802 ± 2.724	11.125 ± 2.801	$p = 0.049$
Width splitted by observer			
Observer 1[c]	10.202 ± 2.826	10.620 ± 2.864	$p = 0.086$
Observer 2[c]	11.400 ± 2.484	11.629 ± 2.646	$p = 0.299$

[a] - comparison of number of recognizable lesions.
[b] - mean ± standard deviation for patho and MRI measurements. Comparison of methods was performed by comparing least squares means from mixed-effect models.
[c] - width data (with borderline statistical significance) were split by observer and two separate mixed-effect models were used to compare the MRI and patho methods.

interpersonal differences between both observers. This can be explained by the high-power values that were used and that we had several "steam pop" effects. If a "steam pop" effect occurred, there was a partial disruption of the myocardium, which spreads to the width and not to the depth of the tissue. For complex lesions such as RF lesions, is not easy to pinpoint the maximal

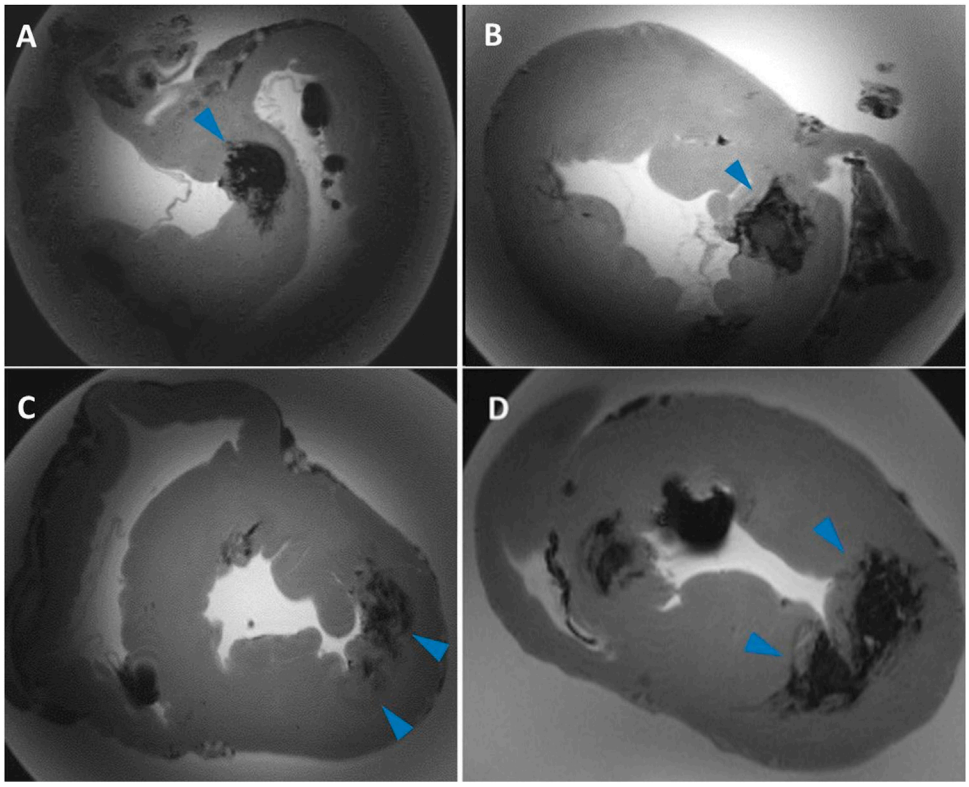

FIGURE 7
Examples of complex lesions. Transverse sections of ventricles of the swine heart on MRI scans. **(A,B)** shows the irregular shape of lesions with unclear borders. During high energy applications, a "steam pop" sometimes occurs, which causes rupture of the myocardial tissue. This rupture spreads into the myocardium and causes irregular and badly bounded lesions. **(C,D)** example of fused lesions—lesions formed so close each other that they partially merge into one.

parameters of the lesion after "steam pop" (Figure 7). Another possible explanation for the statistically significant difference in *interpersonal differences* is an individual assessment on which MRI slice the lesion reaches its maximum size. In addition, on several occasions, the individual lesions were placed close together such that they partially fused together (Figure 7). In this case, it depended on the individual evaluation of each observer as to where was the exact border of every lesion was.

No statistically significant difference was found in *intrapersonal variability*. This indicates the reproducibility of both measurement methods (see Supplementary File S1).

An important parameter for the evaluation of lesions is the time needed to perform a single measurement. We compared how long it takes to measure the basic parameters of the lesion (depth, width, estuary, and depth at the maximum diameter) from MRI slices and patho samples. The difference between the duration of measurements from MRI slices (without gradual outlining) and from patho was statistically significant (p = 0.001). The median value for MRI measurement was 56 s (53–59.2) and for patho measurement was 53 s (47–59). The difference between the duration of the measurement is significant from a statistical point of view; however, a difference of 3 s is from a practical point of view is negligible.

If outlining by the "point by point" method is included in the time measurement, the measurement of the lesion from MRI slices is significantly longer. In particular, the duration was 235.5 s (201–268.25) for overall MRI measurement and 177.5 s (144.8–208.5) for "point-by-point only." This increase in time is fully compensated by the higher accuracy of the "point-by-point" method.

In our work, we recognized 92.93% of the lesions on MRI scans compared with 75% published by (Berte et al., 2015). In our study, were created 99 lesions in total; 92 lesions (92.93%) were identified by MRI and 98 (98.99%) lesions were identified by patho. One lesion could not be traced on patho or MRI, which represents 1.01%. Three lesions were not recognized in one heart as they were covered by a single MRI artifact and could not be identified in the first scan, representing 3.03% of all lesions. Three additional lesions were identified by patho, but not recognized on MRI. These lesions were small and did not have high intensity border with an overall "ghost-like" character.

In our study, hearts underwent MRI scanning submerged in physiological solution (0.9% NaCl, Braun), which is easy to handle and obtain. On the other hand, there is a background signal on MRI scans; thus, the image background of the scan is gray and produces suboptimal contrast. The use of Fomblin Y06/6 is recommended by other authors for optimal outcomes (Bulte et al., 2003) (Lipinski et al., 2006).

In Figure 7 there is a certain inhomogeneity of the image. The shading and the brightness difference in the center and the periphery of the image is an MRI artifact occurring during the scanning of larger dimension samples. Since the hearts were not exactly the same shape and size, the artifact occurred only by some of them. This artifact did not interfere with the lesions, thus did not obstruct the image processing, and did not affect the results. Therefore we did not use any filter. For the future, we are working on the filter creating and applying it on such sample scans.

A limitation of our study is that it is an *ex vivo* model on a non-beating pig heart. Also evaluation is limited in visualization of small, not very well-demarcated lesions. As well, preparing of the heart before MRI scanning and the scanning time itself is longer than that of gross pathology inspection. Furthermore, access to a 9.4 T MRI device is required. Not negligible is also the purchase price of MRI machine and the price of the organ scanning. As the limitation of our study must be also mentioned statistically significant difference in interpersonal differences in our case. Interpersonal differences will decrease with the gradually increasing experience of the observes.

5 Conclusion

Measurements obtained from pathology gross inspection and MRI scanning did not significantly differ in absolute values; however, MRI allows a significantly more precise assessment of lesion volume. The measurement time of the lesions on MRI was significantly longer from the statistical point of view, but negligible from a practical point of view. MRI evaluation is a nondestructive method, allowing for diverse scanning angles, resulting in clear lesion definition and more precise volume assessment.

Data availability statement

The original contributions presented in the study are included in the article/Supplementary Materials, further inquiries can be directed to the corresponding author.

Ethics statement

The animal experiment was approved by the ethics committee of the University of Veterinary and Pharmaceutical Sciences in Brno (approval number 12–2018) and by the Ministry of Education Youth and Sports (approval number MSMT-17402/2018–3). All procedures performed on pigs were in accordance with Directive 2010/63/EU of the European Parliament on the protection of animals used for scientific purposes.

Author contributions

Conceptualization GC, ZS, EO, and MP; methodology GC, ZS, EO, and MP; MRI samples preparation EO, GC and IP; MRI scanning IP; formal analysis VR, TK; investigation EO, LV, ZS, GC, IP, ED and VK; writing-original draft preparation EO, ZS; writing—review and editing, GC, TK, TJ, ED, IP, and MP; supervision ZS; project administration EO, ZS; funding acquisition ZS. All authors have read and agreed to the published version of the manuscript.

Funding

This research was supported by the European Regional Development Fund-Project ENOCH (No. CZ.02.1.01/0.0/0.0/16_019/0000868) and Medical University of Silesia statutory funds (KNW-1-048/N/9/K, PCN-1-005/N/0/K. The MR measurements were supported by the grant LM2015062 "National Infrastructure for Biological and Medical Imaging (Czech-BioImaging)". This publication was supported also by Masaryk University (project "New imaging, computational and analytical methods in diagnostics and monitoring of cardiovascular disorders" MUNI/A/1462/2021) with the support of the Specific University Research Grant, as provided by the MEYS CR in 2022.

Conflict of interest

The reviewer PL declared a shared affiliation, with no collaboration, with one of the authors, GC, to the handling editor at the time of the review.

Publisher's note

Supplementary material

The Supplementary Material for this article can be found online at: https://www.frontiersin.org/articles/10.3389/fphys.2022.834328/full#supplementary-material

References

Badger, Troy J., Daccarett, Marcos, Akoum, Nazem W., YawAdjei-Poku, A., Burgon, Nathan S., Haslam, Thomas S., et al. (2010). Evaluation of left atrial lesions after initial and repeat atrial fibrillation ablation: Lessons learned from delayed-enhancement MRI in repeat ablation procedures. *Circ. Arrhythm. Electrophysiol.* 3 (3), 249–259. doi:10.1161/CIRCEP.109.868356

Berte, Benjamin, Hubert, Cochet, Magat, Julie, Naulin, Jérôme, Ghidoli, Daniele, Pillois, Xavier, et al. (2015). Irrigated needle ablation creates larger and more transmural ventricular lesions compared with standard unipolar ablation in an ovine model. *Circ. Arrhythm. Electrophysiol.* 8 (6), 1498–1506. doi:10.1161/CIRCEP.115.002963

Bolte, H., Jahnke, T., Schäfer, F. K. W., Wenke, R., Hoffmann, B., Freitag-Wolf, S., et al. (2007). Interobserver-variability of lung nodule volumetry considering different segmentation algorithms and observer training levels. *Eur. J. Radiol.* 64 (2), 285–295. doi:10.1016/j.ejrad.2007.02.031

Bulte, Jeff W. M., Einstein, Ophira, Reinhartz, Etti, Zywicke, Holly A., Douglas, Trevor, Frank, Joseph A., et al. (2003). MR microscopy of magnetically labeled neurospheres transplanted into the lewis EAE rat brain. *Magn. Reson. Med.* 50 (1), 201–205. doi:10.1002/mrm.10511

Delacretaz, E., Wtlliam, G. S., Winters, G. L., Lynch, K., Peter, L., Lynch, K., et al. (1999). Ablation of ventricular tachycardia with a saline-cooled radiofrequency catheter: Anatomic and histologic characteristics of the lesions in humans. *J. Cardiovasc. Electrophysiol.* 10 (6), 860–865. doi:10.1111/j.1540-8167.1999.tb00267.x

Dickfeld, Timm, Kato, Ritsushi, Zviman, Menekem, Nazarian, Saman, Dong, Jun, Ashikaga, Hiroshi, et al. (2007). Characterization of acute and subacute radiofrequency ablation lesions with non-enhanced magnetic resonance imaging. *Heart rhythm.* 4 (2), 208–214. doi:10.1016/j.hrthm.2006.10.019

Dinkel, J., Khalilzadeh, O., Hintze, C., Fabel, M., Puderbach, M., Eichinger, M., et al. (2013). Inter-observer reproducibility of semi-automatic tumor diameter measurement and volumetric analysis in patients with lung cancer. *Lung Cancer* 82 (1), 76–82. doi:10.1016/j.lungcan.2013.07.006

Erasmus, Jeremy, Gladish, Gregory, Broemeling, Lyle, Bradley, Sabloff, Truong, Mylene, Herbst, Roy, et al. (2003). Interobserver and intraobserver variability in measurement of non-small-cell carcinoma lung lesions: Implications for assessment of tumor response. *J. Clin. Oncol.* 21 (32), 2574–2582. doi:10.1200/JCO.2003.01.144

Erturk, M. A., Li, X., Pierre-Fancois, V., Ugurbil, K., and Gregory, J. (2019). Evolution of UHF body imaging in the human torso at 7T: Technology, applications, and future directions. *Top. Magn. Reson. Imaging* 28 (3), 101–124. doi:10.1097/RMR.0000000000000202

Ertürk, M. Arcan, Wu, Xiaoping, Eryaman, Yiğitcan, Pierre-François Van de MoorteleAuerbach, Edward J., Lagore, Russell L., et al. (2017). Toward imaging the body at 10.5 tesla. *Magn. Reson. Med.* 77 (1), 434–443. doi:10.1002/mrm.26487

Gepstein, L., Gal, H., Shpun, S., Cohen, D., and Shlomo, A. (1999). Atrial linear ablations in pigs: Chronic effects on atrial electrophysiology and pathology. *Circulation* 100 (4), 419–426. doi:10.1161/01.CIR.100.4.419

Guerra, Jose M., Jorge, E., Raga, S., Galvez-Monton, C., Alonso-Martin, C., Rodriguez-Font, E., et al. (2017). Effects of open-irrigated radiofrequency ablation catheter design on lesion formation and complications: *In vitro* comparison of 6 different devices: *In vitro* comparison of open-irrigated catheters. *J. Cardiovasc. Electrophysiol.* 24, 1157–1162. doi:10.1111/jce.12175

Haines, D. E., and Verow, A. F. (1990). Observations on electrode-tissue interface temperature and effect on electrical impedance during radiofrequency ablation of ventricular myocardium. *Circulation* 82 (3), 1034–1038. doi:10.1161/01.CIR.82.3.1034

Haines, David (2018). Biophysics of ablation: Application to technology. *J. Cardiovasc. Electrophysiol.* 15 (10), S11–S11. doi:10.1046/j.1540-8167.2004.15102.x

Haines, David E., and Watson, Denny D. (1989). Tissue heating during radiofrequency catheter ablation: A thermodynamic model and observations in isolated perfused and superfused canine right ventricular free wall. *Pacing Clin. Electrophysiol.* 12 (6), 962–976. doi:10.1111/j.1540-8159.1989.tb05034.x

Haverkamp, Wilhelm, Hindricks, Gerhard, Gulker, Hartmut, Rissel, Ulrich, Pfennings, Winnfried, Martin, Borggrefe, et al. (1989). Coagulation of ventricular myocardium using radiofrequency alternating current: Bio-physical aspects and experimental findings. *Pacing Clin. Electrophysiol.* 12 (1), 187–195. doi:10.1111/j.1540-8159.1989.tb02646.x

Heo, Dan, Lim, Soyeon, Lee, Jiye, Lee, Myung Eun, Cho, Soyoung, Jeong, Jisu, et al. (2019). Radiological assessment of effectiveness of soluble RAGE in attenuating angiotensin II-induced LVH mouse model using *in vivo* 9.4T MRI. *Sci. Rep.* 9 (23), 8475. doi:10.1038/s41598-019-44933-6

Ishihara, Yuri, Reza Nazafat, John V. Wylie, Linguraru, Marius G., Josephson, Mark E., Howe, Robert D., Manning, Warren J., et al. 2007. "MRI evaluation of RF ablation scarring for atrial fibrillation treatment." In , edited by *Kevin R. Cleary and michael I. Miga, 65090Q*. San Diego, CA. doi:10.1117/12.710323

Kalbfleisch, Steven J., and Langberg, Jonathan J. (1992). Catheter ablation with radiofrequency energy: Biophysical aspects and clinical applications. *J. Cardiovasc. Electrophysiol.* 3 (2), 173–186. doi:10.1111/j.1540-8167.1992.tb01106.x

Krahn, Philippa R. P., Singh, Sheldon M., Biswas, Labonny, Yak, Nicolas, KevanAnderson, J. T., Barry, Jennifer, et al. (2018). Cardiovascular magnetic resonance guided ablation and intra-procedural visualization of evolving radiofrequency lesions in the left ventricle. *J. Cardiovasc. Magn. Reson.* 20. doi:10.1186/s12968-018-0437-z

Lardo Albert, C., McVeigh Elliot, R., Pitayadet, J., Berger Ronald, D., Hugh, C., Lima, J., et al. (2000). Visualization and temporal/spatial characterization of cardiac radiofrequency ablation lesions using magnetic resonance imaging. *Circulation* 102 (6), 698–705. doi:10.1161/01.CIR.102.6.698

Lazebnik, R. S., Brent, D., Weinberg, M. S. B., Jonathan, S. L., and Wilson, D. L. (2005). Semiautomatic parametric model-based 3D lesion segmentation for evaluation of MR-guided radiofrequency ablation therapy. *Acad. Radiol.* 12 (12), 1491–1501. doi:10.1016/j.acra.2005.07.011

Lipinski, M. J., Vardan, J. C., Karen, C. B., Fuster, V., Fallon, J. T., Fisher, E. A., et al. (2006). MRI to detect atherosclerosis with gadolinium-containing immunomicelles targeting the macrophage scavenger receptor. *Magn. Reson. Med.* 56 (3), 601–610. doi:10.1002/mrm.20995

Markman, Timothy M., and Saman, Nazarian. (2017). Cardiac magnetic resonance for lesion assessment in the electrophysiology laboratory. *Circ. Arrhythm. Electrophysiol.* 10 (11), e005839. doi:10.1161/CIRCEP.117.005839

Muenzel, Daniela, Engels, Heinz-Peter, Bruegel, Melanie, Kehl, Victoria, Rummeny, Ernst, and Metz, Stephan (2012). Intra- and inter-observer variability in measurement of target lesions: Implication on response evaluation according to RECIST 1.1. *Radiol. Oncol.* 46 (1), 8–18. doi:10.2478/v10019-012-0009-z

Nakagawa, H., Yamanashi, W. S., Pitha, J. V., Arruda, M., Wang, X., Ohtomo, K., et al. (1995). Comparison of *in vivo* tissue temperature profile and lesion geometry for radiofrequency ablation with a saline-irrigated electrode versus temperature control in a canine thigh muscle preparation. *Circulation* 91 (8), 2264–2273. doi:10.1161/01.CIR.91.8.2264

Nath, S., DiMarco, J. P., and Haines, D. E. (1994). Basic aspects of radiofrequency catheter ablation. *J. Cardiovasc. Electrophysiol.* 5 (10), 863–876. doi:10.1111/j.1540-8167.1994.tb01125.x

Organ, L. W. (1976). Electrophysiologic principles of radiofrequency lesion making. *Appl. Neurophysiol.* 39 (2), 69–76. doi:10.1159/000102478

O'Donnell, David, and Nadurata, Voltaire (2004). Radiofrequency ablation for post infarction ventricular tachycardia. *Indian Pacing Electrophysiol. J.* 4 (2), 63–72.

Rueden, Curtis T., Johannes, Schindelin, Mark, C. H., Ellen, T. A., Eliceiri, Kevin W., Walter, A. E., et al. (2017). ImageJ2: ImageJ for the next generation of scientific image data. *BMC Bioinforma.* 18 (76), 529. doi:10.1186/s12859-017-1934-z

Santos, Braggion, Fernanda, Maria, Koenigkam-Santos, Marcel, Reis Teixeira, Sara, Volpe, G. J., and Trad, H. S. (2013). Magnetic resonance imaging evaluation of cardiac masses. *Arq. Bras. Cardiol.* 101, 263–272. doi:10.5935/abc.20130150

Schindelin, Johannes, Rueden, Curtis T., Hiner, Mark C., and Eliceiri, Kevin W. (2015). The ImageJ ecosystem: An open platform for biomedical image analysis. *Mol. Reprod. Dev.* 82 (7–8), 518–529. doi:10.1002/mrd.22489

Schneider, Jürgen E., Lanz, Titus, Barnes, Hannah, Bohl, Steffen, Lygate, Craig A., Ordidge, Roger J., et al. (2011). Accelerated cardiac magnetic resonance imaging in the mouse using an eight-channel array at 9.4 tesla: Accelerated cardiac MRI in mice at 9.4 T. *Magn. Reson. Med.* 65 (1), 60–70. doi:10.1002/mrm.22605

Schneider, Jürgen E., Lanz, Titus, Barnes, Hannah, Medway, Debra, Lygate, Craig A., Smart, Sean, et al. (2008). Ultra-fast and accurate assessment of cardiac function in rats using accelerated MRI at 9.4 tesla. *Magn. Reson. Med.* 59 (3), 636–641. doi:10.1002/mrm.21491

Song, Kyoung D., Lee, Min Woo, Rhim, Hyunchul, Kang, Tae Wook, DongCha, Ik, and Yang, Jehoon (2017). Chronological changes of radiofrequency ablation zone in rabbit liver: An *in vivo* correlation between gross pathology and histopathology. *Br. J. Radiol.* 90 (1071), 20160361. doi:10.1259/bjr.20160361

Suzuki, Atsushi, Lehmann, H. Immo, Wang, Songyun, Monahan, Kristi H., Parker, Kay D., Rettmann, Maryam E., et al. (2021). Impact of myocardial fiber orientation on lesions created by a novel heated saline-enhanced radiofrequency

needle-tip catheter: An MRI lesion validation study. *Heart rhythm.* 18 (3), 443–452. doi:10.1016/j.hrthm.2020.11.015

Templeton, McCormick (1961). A simple macrotome for soft tissues. *Stain Technol.* 36 (4), 255–256. doi:10.3109/10520296109113287

Thiesse, P., Ollivier, L., Di Stefano-Louineau, D., Négrier, S., Savary, J., Pignard, K., et al. (2016). Response rate accuracy in oncology trials: Reasons for interobserver variability. Groupe français d'Immunothérapie of the fédération nationale des centres de Lutte contre le cancer. *J. Clin. Oncol.* 15, 3507–3514. doi:10.1200/JCO.1997.15.12.3507

Tofig, Bawer J., Peter, Lukac, Nielsen, Jan M., EsbenHansen, S. S., RasmusTougaard, S., HenrikJensen, K., et al. (2019). Radiofrequency ablation lesions in low-intermediate-and normal-voltage myocardium: An *in vivo* study in a porcine heart model. *Europace* 21 (12), 1919–1927. doi:10.1093/europace/euz247

Ursell, P. C., Gardner, P. I., Albala, A., Fenoglio, J. J., Wit, A. L., and AlbAlA, A. (1985). Structural and electrophysiological changes in the epicardial border zone of canine myocardial infarcts during infarct healing. *Circ. Res.* 56 (3), 436–451. doi:10.1161/01.RES.56.3.436

Wech, Tobias, Seiberlich, Nicole, Schindele, Andreas, Grau, Vicente, Diffley, Leonie, Gyngell, Michael L., et al. (2016). Development of real-time magnetic resonance imaging of mouse hearts at 9.4 tesla – simulations and first application. *IEEE Trans. Med. Imaging* 35 (3), 912–920. doi:10.1109/TMI.2015.2501832

Zhao, Binsheng, Tan, Yongqiang, Bell, Daniel J., Marley, Sarah E., Guo, Pingzhen, Mann, Helen, et al. (2013). Exploring intra- and inter-reader variability in uni-dimensional, Bi-dimensional, and volumetric measurements of solid tumors on CT scans reconstructed at different slice intervals. *Eur. J. Radiol.* 82 (6), 959–968. doi:10.1016/j.ejrad.2013.02.018

Frontiers in Physiology

Understanding how an organism's components work together to maintain a healthy state

The second most-cited physiology journal, promoting a multidisciplinary approach to the physiology of living systems - from the subcellular and molecular domains to the intact organism and its interaction with the environment.

Discover the latest Research Topics

See more →

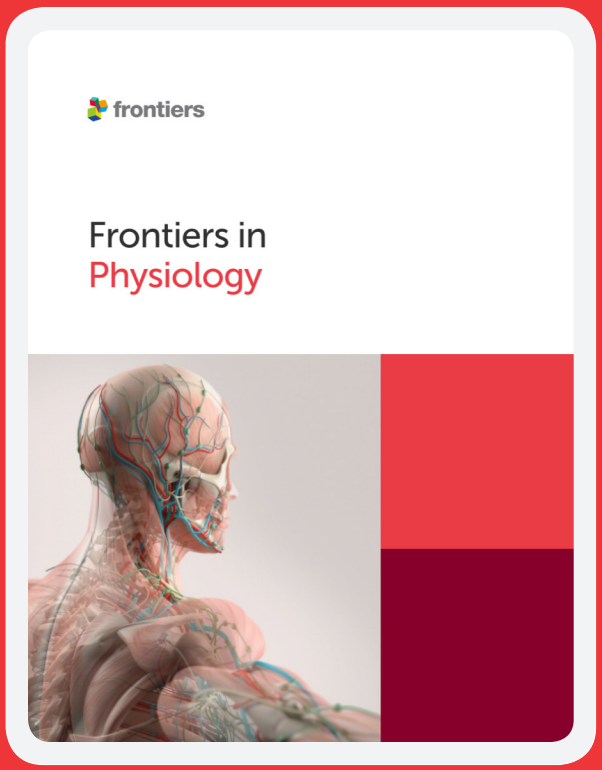

Frontiers

Avenue du Tribunal-Fédéral 34
1005 Lausanne, Switzerland
frontiersin.org

Contact us

+41 (0)21 510 17 00
frontiersin.org/about/contact